



ASTES

Advances in Science, Technology & Engineering Systems Journal

VOLUME 7-ISSUE 5 | SEPT-OCT 2022

www.astesj.com

ISSN: 2415-6698

EDITORIAL BOARD

Editor-in-Chief

Prof. Passerini Kazmerski
University of Chicago, USA

Editorial Board Members

Dr. Jiantao Shi

Nanjing Research Institute
of Electronic Technology,
China

Dr. Tariq Kamal

University of Nottingham, UK
Sakarya University, Turkey

Dr. Mohmaed Abdel Fattah

Ashabrawy
Prince Sattam bin Abdulaziz University,
Saudi Arabia

Dr. Nguyen Tung Linh

Electric Power University,
Vietnam

**Prof. Majida Ali Abed
Meshari**

Tikrit University Campus,
Iraq

Mr. Muhammad Tanveer Riaz

School of Electrical Engineering,
Chongqing University, P.R. China

**Mohamed Mohamed
Abdel-Daim**

Suez Canal University,
Egypt

Dr. Omeje Maxwell

Covenant University, Nigeria

Dr. Hung-Wei Wu

Kun Shan University, Taiwan

Dr. Heba Afify

MTI university, Cairo, Egypt

Mr. Randhir Kumar

National University of
Technology Raipur, India

Dr. Ahmet Kayabasi Karamanoglu

Mehmetbey University, Turkey

Dr. Daniele Mestriner

University of Genoa, Italy

Dr. Hongbo Du

Prairie View A&M
University, USA

Mr. Aamir Nawaz

Gomal University, Pakistan

Dr. Abhishek Shukla

R.D. Engineering College, India

Mr. Manu Mitra

University of Bridgeport, USA

Regional Editors

Dr. Maryam Asghari

Shahid Ashrafi Esfahani,
Iran

Mr. Abdullah El-Bayoumi

Cairo University, Egypt

Dr. Sabry Ali Abdallah El-Naggar

Tanta University, Egypt

Dr. Ebubekir Altuntas

Gaziosmanpasa University,
Turkey

Dr. Qichun Zhang

University of Bradford,
United Kingdom

Dr. Walid Wafik Mohamed Badawy

National Organization for Drug Control
and Research, Egypt

Dr. Gomathi Periasamy

Mekelle University, Ethiopia

Dr. Shakir Ali

Aligarh Muslim University,
India

Dr. Ayham Hassan Abazid

Jordan
University of Science and Technology,
Jordan

Editorial

In the editorial for this issue, the focus is directed towards the overarching theme of interdisciplinary collaboration and its profound impact on shaping the landscape of contemporary research. The editorial team provides a thoughtful introduction, emphasizing the synergies that emerge when researchers from diverse fields converge to address complex challenges. It underscores the importance of fostering cross-disciplinary dialogue to propel innovation and broaden the horizons of knowledge. Throughout the editorial, the symbiotic relationship between various scientific domains is explored, highlighting the interconnectedness that characterizes the modern research ecosystem. This introductory piece sets the tone for the collection of 20 papers, each offering a unique perspective and contributing to the rich tapestry of interdisciplinary exploration showcased in this special issue.

In the realm of industrial collaboration, a recent study delves into the nuanced art of musical saw bowing. The research focuses on the bowing motion, a critical element often employed by skilled players. While previous efforts have concentrated on sound feedback systems using mallet strike techniques, this study takes a unique approach. It explores the control of pressure and speed between the bow and the musical saw, aiming to achieve skilful manipulation. The investigation not only considers the sound generated by self-excited vibration but also emphasizes its inherent purity, distinct from prior studies focused on suppression. Moreover, the study showcases the adept use of an industrial collaborative humanoid robot in skilfully manipulating a musical saw with a bow [1].

Deep learning takes centre stage in another article, exploring its application in monitoring complex technical systems. The study utilizes analytical and numerical methods to model and simulate multidimensional chaotic systems. Emphasizing the Visual Thinking methodology, the research integrates visual images and calculated parameters into the Input Layer of the Recurrent Neural Network of the Deep Learning algorithm. This strategic combination enhances the quality and efficiency of monitoring complex technical systems, showcasing the potential for advanced control and interpretation [2].

A case study delves into the electrification challenges faced by remote regions, focusing on Upper Blink Water in South Africa, approximately 20km away from the national grid. The study proposes a hybrid energy system integrating solar photovoltaic (PV), a diesel generator, and battery storage. Through the use of Homer software for technical evaluations and Reticmaster software for assessing distribution line voltage drops, the results demonstrate the feasibility of supplying electricity to the isolated community. The study provides valuable insights into electricity cost optimization and diesel fuel consumption for off-grid electrification [3].

Cybersecurity in power systems takes a front seat in an article proposing an improved model to analyze the impact of cyber-attacks. The ICAPS model addresses both frequency disturbances and voltage disruption during load changes, incorporating various controllers such as LFC, AGC, AGC-PID, AVR, and AVR-PID. Through MATLAB Simulink tool experiments, the model's validity is confirmed, revealing the consequences of cyber-attacks on frequency deviations, voltage disruptions, and system oscillations. This holistic approach stands as a significant contribution to addressing the simultaneous challenges posed by cyber threats in power systems [4].

Amidst energy crises and the evolving landscape due to the COVID-19 pandemic, a study assesses the impact of integrating solar PV systems into the grid. Using the Equal Area Criterion

(EAC) method for transient stability analysis, the research focuses on power quality and stability challenges. Through MATLAB/Simulink simulations, the critical clearing time (CCT) is calculated, highlighting the positive impact of solar PV integration on the national grid's transient characteristics. The study adds a critical perspective to the ongoing discourse on sustainable energy solutions and their integration into existing power infrastructures [5].

In the realm of healthcare, a cross-sectional study investigates the effect of a flexible knee orthosis (FKO) on lateral thrust in patients with knee osteoarthritis. Leveraging a wireless 3-axis accelerometer, the study analyzes lateral thrust during walking with varying orthosis wearing pressures. The findings suggest that increased wearing pressure reduces lateral thrust, pointing to the potential effectiveness of knee orthosis in inhibiting lateral thrust in patients with knee osteoarthritis. This research contributes valuable insights into non-invasive interventions for managing knee-related conditions [6].

The semiconductor industry comes into focus with an exploration of layout arrangements for CMOS oscillators. The study evaluates various layouts, highlighting the superiority of the serpentine style in minimizing output variation on silicon. Post-layout simulations and physical fabrication validate the effectiveness of the serpentine layout style over straight and staggered alternatives. This research addresses critical challenges in CMOS oscillator realization, promising improved performance and stability on silicon [7].

Stochastic processing times in agile manufacturing take centre stage in a study conducting sensitive analysis in holding and penalty costs for the stochastic sequencing problem. Through simulation algorithms, the study compares dispatch rules, revealing the robustness of the Shortest Processing Time (SPT) rule. This research offers insights into the relationship between holding-penalty cost proportions and the most effective dispatch rules for optimizing job scheduling in agile manufacturing environments [8].

The integration of solar PV-thermal power systems is explored in-depth in another article, which proposes a model for load frequency controllers and introduces various auxiliary controllers. The study assesses controller performance using different tuning strategies and incorporates an HVDC link for stability enhancement. By focusing on stabilizing frequency and tie-power deviations, the research provides a valuable contribution to the efficient control of interlinked solar PV-thermal power systems [9].

In the mining industry, a paper presents the calibration of Discrete Element Method (DEM) parameters for modelling phosphate ore clogging. The study introduces a model contact for defining particle-cluster and particle-tipper surface interactions. Calibration methods based on repose angle determination contribute to accurate simulation, offering insights into optimal parameters for modelling phosphate clogging phenomena. This research addresses challenges in various industries by providing a reliable model for understanding and mitigating ore clogging [10].

Recognizing the challenges of video transmission in Vehicular Ad-Hoc Networks (VANETs), a study proposes a self-adaptive routing algorithm (RSAR). Leveraging the mobility characteristics of vehicles, RSAR aims to create reliable routes based on link reliability and adaptability to changing network topology. The algorithm combines heuristic Q-Learning with a decentralized network, demonstrating its effectiveness through simulations in the NS-2 environment. This research contributes to the ongoing efforts to enhance real-time video transmission in dynamic vehicular networks [11].

The design of cascade control systems for photovoltaic (PV) powered microgrids takes centre stage in another article, focusing on DC grid-connected systems. The study evaluates three cascade schemes, including digital control, model-based predictive control (MBPC), and a hybrid approach [12].

Results indicate that the combined scheme, integrating classical control with MBPC, achieves optimal stabilization of microgrid voltage with fast response and minimal overvoltage. This research offers valuable insights into the design and control strategies for enhancing the stability of PV-powered microgrids [13].

Countering the challenges of people counting in crowded spaces, a study proposes a system for automatic counting of passengers in train stations. Utilizing overhead fisheye cameras and a multi-object tracker, the system analyzes passenger trajectories to compute total train occupancy. The proposed approach demonstrates robustness against occlusions and achieves a high accuracy of counting people getting on and off trains. This research contributes to the development of intelligent systems for public transportation management [14].

Analyzing Morocco's energy mix from 2010 to 2050, a study simulates the country's electricity production trajectory. The research critically evaluates strategic decisions made at the onset of Morocco's National Energy Strategy, emphasizing the potential need for reconsideration of technology choices. This study provides a valuable contribution to the understanding of long-term renewable energy development strategies in the absence of traditional energy resources, offering insights into sustainable energy planning [15].

Efforts to reduce computational efforts in sensor and actuator networks take a sophisticated turn with a focus on model order reduction. The study decentralizes a global multi-input-multi-output system in a sensor and actuator network, resulting in multiple decentralized local single-input-single-output systems. Model order reduction techniques, including Balanced Truncation and Krylov subspace methods, are employed to minimize computational loads on decentralized nodes while preserving system properties. This research stands as a promising approach for efficient state estimation in distributed systems [16].

In the domain of EEG analysis, a novel approach introduces a machine learning algorithm for detecting artifacts in Event-Related Potential (ERP) data during an oddball paradigm. Unsupervised learning algorithms, including DBScan, are applied to identify noisy epochs, ensuring the production of a cleaner ERP dataset. By minimizing the impact of non-EEG components, this research enhances the reliability of ERP studies, contributing to improved neuroscientific insights [17].

The application of blockchain technology in the retail and insurance sectors is scrutinized through an analysis of Suning and PingAn as pioneers in implementing blockchain solutions. Using the TOE framework, the study explores success factors and highlights the impact of blockchain on digital transformation. Emphasizing industry-specific features, the research provides insights into the competitiveness of Chinese blockchain providers on the global stage, shedding light on the evolving landscape of retail and insurance with blockchain integration [18].

Text mining techniques take centre stage in a comprehensive review focusing on knowledge discovery from e-news articles. The study explores association rule extraction using two prominent algorithms, Apriori and FP-Growth. Assessing their performance in e-news article analysis, the research provides valuable insights into the use of association rules for knowledge

discovery, addressing the challenges posed by vast textual information available on the internet [19].

Navigating the complexities of battery management, a study introduces a hybrid neural network method for predicting the State-of-Health (SOH) and Remaining Useful Life (RUL) of Lithium-Ion batteries. Integrating Convolutional Neural Networks (CNN), Bidirectional Gated Recurrent Units (BGRU), and Deep Neural Networks (DNN), the proposed method aims to enhance precision in estimating battery conditions. Validation using NASA datasets demonstrates the effectiveness of the hybrid approach in achieving high estimation accuracy for improved battery performance management [20].

In summary, these 20 papers encapsulate a diverse range of cutting-edge research topics. From the nuanced art of musical saw bowing by humanoid robots to the strategic integration of blockchain technology in retail and insurance sectors, the studies contribute significantly to fields such as energy systems, manufacturing, healthcare, and information technology. These research endeavours collectively showcase the interdisciplinary nature and continuous advancements in contemporary research, offering valuable insights into the ever-evolving landscape of scientific exploration.

References:

- [1] H. Hanai, A. Mishima, A. Miura, T. Hirogaki, E. Aoyama, "Realization of Skillful Musical Saw Bowing by Industrial Collaborative Humanoid Robot," *Advances in Science, Technology and Engineering Systems Journal*, **7**(5), 1–9, 2022, doi:10.25046/aj070501.
- [2] B.I. Israfil, "Deep Learning in Monitoring the Behavior of Complex Technical Systems," *Advances in Science, Technology and Engineering Systems Journal*, **7**(5), 10–16, 2022, doi:10.25046/aj070502.
- [3] L. Mbali, O. Dzobo, "Design of an Off-Grid Hybrid Energy System for Electrification of a Remote Region: a Case Study of Upper Blink Water Community, South Africa," *Advances in Science, Technology and Engineering Systems Journal*, **7**(5), 17–26, 2022, doi:10.25046/aj070503.
- [4] M.M. Uddin, K.R. Islam, Md.M. Kabir, "An Improved Model to Analyze the Impact of Cyber-Attacks on Power Systems," *Advances in Science, Technology and Engineering Systems Journal*, **7**(5), 27–34, 2022, doi:10.25046/aj070504.
- [5] A.A. Jhumka, R.T.F.A. King, C. Ramasawmy, "Assessing the Impact of Integrating Solar PV System using the Equal Area Criterion Method," *Advances in Science, Technology and Engineering Systems Journal*, **7**(5), 35–40, 2022, doi:10.25046/aj070505.
- [6] H. Yamamoto, M. Endo, T. Baba, C. Wada, "Effect of Knee Orthosis on Lateral Thrust in Patients with Knee Osteoarthritis," *Advances in Science, Technology and Engineering Systems Journal*, **7**(5), 41–45, 2022, doi:10.25046/aj070506.
- [7] P.-Y. Lou, Y.-Y. Ho, C.-C. Wang, W.-C. Chang, "Analysis of Layout Arrangement for CMOS Oscillators to Reduce Overall Variation on Silicon," *Advances in Science, Technology and Engineering Systems Journal*, **7**(5), 46–52, 2022, doi:10.25046/aj070507.
- [8] K.H. Wai, N. Funabiki, K.T. Mon, M.Z. Htun, S.H.M. Shwe, H.H.S. Kyaw, W.-C. Kao, "A Proposal of Code Modification Problem for Self-study of Web Client Programming Using JavaScript," *Advances in Science, Technology and Engineering Systems Journal*, **7**(5), 53–61, 2022, doi:10.25046/aj070508.
- [9] E.E. Tapia, E.S.H. Gress, M. Flégl, "Sensitive Analysis in Holding and Penalty Costs for the Stochastic Sequencing Problem in Agile Manufacturing," *Advances in Science, Technology and Engineering Systems Journal*, **7**(5), 62–72, 2022, doi:10.25046/aj070509.

- [10] G. Sharma, "Frequency Oscillation Suppression of Interlinked Solar PV-Thermal Power System using HVDC Link," *Advances in Science, Technology and Engineering Systems Journal*, **7**(5), 73–78, 2022, doi:10.25046/aj070510.
- [11] B. Nasr-Eddine, S. Mohamed, A. Abdelmajid, B. Elfahim, "DEM models Calibration and Application to Simulate the Phosphate Ore Clogging," *Advances in Science, Technology and Engineering Systems Journal*, **7**(5), 79–90, 2022, doi:10.25046/aj070511.
- [12] M. Hassan, A. Badri, A. Sahel, "A Self-Adaptive Routing Algorithm for Real-Time Video Transmission in VANETs," *Advances in Science, Technology and Engineering Systems Journal*, **7**(5), 91–101, 2022, doi:10.25046/aj070512.
- [13] E.S. Gutiérrez, S.J.R. Orellana, "A DC Grid-Connected PV Microgrid Regulated via Digital and MBPC Cascade Control Strategies," *Advances in Science, Technology and Engineering Systems Journal*, **7**(5), 102–112, 2022, doi:10.25046/aj070513.
- [14] J. Calle, I. Sagastiberri, M. Aramburu, S. Cerezo, J. García, "Automatic Counting Passenger System Using Online Visual Appearance Multi-Object Tracking," *Advances in Science, Technology and Engineering Systems Journal*, **7**(5), 113–128, 2022, doi:10.25046/aj070514.
- [15] J. Slimani, A. Kadrani, I. EL Harraki, E. hadj Ezzahid, "Long-term Bottom-up Modeling of Renewable Energy Development in Morocco," *Advances in Science, Technology and Engineering Systems Journal*, **7**(5), 129–145, 2022, doi:10.25046/aj070515.
- [16] F. Friedrich, C. Ament, "Model Order Reduction and Distribution for Efficient State Estimation in Sensor and Actuator Networks," *Advances in Science, Technology and Engineering Systems Journal*, **7**(5), 146–156, 2022, doi:10.25046/aj070516.
- [17] R. Akhter, F. Beyette, "Detection Of Event-Related Potential Artifacts Of Oddball Paradigm By Unsupervised Machine Learning Algorithm," *Advances in Science, Technology and Engineering Systems Journal*, **7**(5), 157–166, 2022, doi:10.25046/aj070517.
- [18] C. Qi, Y. Lei, Y. Cai, "Blockchain Applications in Suning and PingAn," *Advances in Science, Technology and Engineering Systems Journal*, **7**(5), 167–177, 2022, doi:10.25046/aj070518.
- [19] T. Lakshika, A. Caldera, "Association Rules for Knowledge Discovery From E-News Articles: A Review of Apriori and FP-Growth Algorithms," *Advances in Science, Technology and Engineering Systems Journal*, **7**(5), 178–192, 2022, doi:10.25046/aj070519.
- [20] B. Zraibi, M. Mansouri, S.E. Loukili, S. Ben Alla, "Hybrid Neural Network Method for Predicting the SOH and RUL of Lithium-Ion Batteries," *Advances in Science, Technology and Engineering Systems Journal*, **7**(5), 193–198, 2022, doi:10.25046/aj070520.

Editor-in-chief

Prof. Passerini Kazmersk

ADVANCES IN SCIENCE, TECHNOLOGY AND ENGINEERING SYSTEMS JOURNAL

Volume 7 Issue 5

September-October 2022

CONTENTS

<i>Realization of Skillful Musical Saw Bowing by Industrial Collaborative Humanoid Robot</i>	01
Hiroaki Hanai, Akira Mishima, Atsuyuki Miura, Toshiki Hirogaki, Eiichi Aoyama	
<i>Deep Learning in Monitoring the Behavior of Complex Technical Systems</i>	10
Bahram Ismailov Israfil	
<i>Design of an Off-Grid Hybrid Energy System for Electrification of a Remote Region: a Case Study of Upper Blink Water Community, South Africa</i>	17
Lukanyo Mbali, Oliver Dzobo	
<i>An Improved Model to Analyze the Impact of Cyber-Attacks on Power Systems</i>	27
Muhammad Musleh Uddin, Kazi Rafiqul Islam, Md. Monirul Kabir	
<i>Assessing the Impact of Integrating Solar PV System using the Equal Area Criterion Method</i>	35
Abdul Ahad Jhumka, Robert Tat Fung Ah King, Chandana Ramasawmy	
<i>Effect of Knee Orthosis on Lateral Thrust in Patients with Knee Osteoarthritis</i>	41
Hiroaki Yamamoto, Masahide Endo, Tomohiro Baba, Chikamune Wada	
<i>Analysis of Layout Arrangement for CMOS Oscillators to Reduce Overall Variation on Silicon</i>	46
Pang-Yen Lou, Yung-Yuan Ho, Chua-Chin Wang, Wei-Chih Chang	
<i>Sensitive Analysis in Holding and Penalty Costs for the Stochastic Sequencing Problem in Agile Manufacturing</i>	62
Erick Esparza Tapia, Eva Selene Hernández Gress, Martin Flégl	
<i>Frequency Oscillation Suppression of Interlinked Solar PV-Thermal Power System using HVDC Link</i>	73
Gulshan Sharma	
<i>DEM models Calibration and Application to Simulate the Phosphate Ore Clogging</i>	79
Bouassale Nasr-Eddine, Sallaou Mohamed, Aittaleb Abdelmajid, Benaissa Elfahim	
<i>A Self-Adaptive Routing Algorithm for Real-Time Video Transmission in VANETs</i>	91
Marzouk Hassan, Abdelmajid Badri, Aicha Sahel	
<i>A DC Grid-Connected PV Microgrid Regulated via Digital and MBPC Cascade Control Strategies</i>	102

Elio Sánchez Gutiérrez, Sara Judith Ríos Orellana

Automatic Counting Passenger System Using Online Visual Appearance Multi-Object Tracking 113

Javier Calle, Itziar Sagastiberri, Mikel Aramburu, Santiago Cerezo, Jorge García

Long-Term Bottom-Up Modeling Of Renewable Energy Development In Morocco 129

Jabrane Slimani, Abdeslam Kadrani, Imad EL Harraki, El hadj Ezzahid

Model Order Reduction And Distribution For Efficient State Estimation In Sensor And Actuator Networks 146

Ferdinand Friedrich, Christoph Ament

Detection Of Event-Related Potential Artifacts Of Oddball Paradigm By Unsupervised Machine Learning Algorithm 157

Rafia Akhter, Fred Beyette

Blockchain Applications In Suning And PingAn 167

Cong Qi, Yue Lei, Yuejun Cai

Association Rules For Knowledge Discovery From E-News Articles: A Review Of Apriori And FP-Growth Algorithms 178

Thilini Lakshika, Amitha Caldera

Hybrid Neural Network Method for Predicting the SOH and RUL of Lithium-Ion Batteries 193

Brahim Zraibi, Mohamed Mansouri, Salah Eddine Loukili, Said Ben Alla

Realization of Skillful Musical Saw Bowing by Industrial Collaborative Humanoid Robot

Hiroaki Hanai*, Akira Mishima, Atsuyuki Miura, Toshiki Hirogaki, Eiichi Aoyama

Graduate School of Science and Engineering, Mechanical Engineering, Doshisha University, Kyotanabe, 610-0394, Japan

ARTICLE INFO

Article history:

Received: 02 May, 2022

Accepted: 19 July, 2022

Online: 09 September, 2022

Keywords:

Factory automation

Industrial collaborative

humanoid robot

Bowing

Dual arm coordination

Manufacturing system

Self-excited vibration

Wireless Measurement

FEA (Finite element analysis)

Musical saw

Sound Analysis

Tool manipulation

Tool sharing

ABSTRACT

We have been studying the application of the musical saw, an unknown and advanced tool, to a cooperative humanoid robot for industrial use. A sound feedback system using mallet strike technique and the sound generated by the technique was constructed in the previous reports. The system enables tuning to a target frequency and control to enhance the purity of the pronunciation. However, the bow manipulation often used by skilled players has not yet been examined. In addition to striking, we concentrated on bowing motion, which is used in musical saw manipulation evaluation. Furthermore, it is necessary to generate self-excited vibration by stick-slip based on manipulation. Therefore, it is necessary to control the pressure and speed between the bow and the musical saw to confirm the occurrence of self-excited vibration and the vibration itself. In this study, in addition to the generation of sound by the self-excited vibration, the pure sound nature of the vibration will be discussed. This is different from the approach to suppressing self-excited vibration that has been implemented in previous studies. Furthermore, we will show how an industrial cooperative humanoid robot can be used to manipulate a musical saw with a bow skillfully.

1. Introduction

In recent years, a lot of industrial robots employ the teaching-playback method, a human being uses a teach box or similar device to instruct the industrial robot sequentially on the work to be performed, its position, sensor output conditions, etc., and records the data at that time, which is then replayed to achieve the desired work [1-5]. This is used to build systems for industrial robots to do special work. But this method is not appropriate for multi-tasking with industrial robots because robot's movements must be determined beforehand, and teaching takes a great deal of time and labor. Therefore, it is essential to move from the teaching-playback method to a flexible system with real-time control. Real-time control here refers to the use of environmental information to provide feedback.

This study focuses on a cooperative humanoid robot with real-time control features based on movie and sound information. A humanoid robot is a robot that imitates the shape of a human being. As described below, the humanoid robot in this study has no legs,

since it specifically imitates the upper body of a human. A cooperative robot is a robot that can work without safety barriers. The utilization of humanoid robots is expanding in everyday life. Humanoid robots are marked by their ability to use human surroundings and human tools as they are, and by their meaningful human appearance [6-10]. If we put this another way, among cooperative robots, humanoid robots are expected to operate in a surrounding more similar to that of humans. When cooperative robots, including humanoid robots, work in the same environment as humans, it is inefficient for humans and robots to use different tools. Therefore, when assuming a manufacturing line in which humans and robots coexist and cooperate, the sharing of tools is a desirable form. However, this has not yet been realized. Several studies have been conducted on tasks for humanoid robots, such as working on safe interaction between industrial dual-armed robots and humans [11] and drum playing [12]. Previous research has focused on humanoid robots playing musical instruments [13] and inspecting percussion instruments [14]. There have also been studies on nail driving by humanoid robots [15] and hitting motion by a robotic arm with an elastic body.

*Corresponding Author: Hiroaki Hanai, h871hiroaki@gmail.com

But few studies have captured the sound generated as information. The information here is real-time information that allows the robot to generate its next move using, for example, PID control for deviation from the target frequency. We studied musical saw playing using a Western saw, an unknown tool among various musical instruments that is troublesome to manipulate because of its form and flexibility [16]. We studied a control system that obtains sound information in real time to find the sound frequency tuning technique and the strike positioning of the musical saw and realized a performance control by striking the saw. However, it was not possible to control sounds other than the striking of the musical saw. Manipulation by striking control is sufficient to control the position of the striking. In addition to strikes, the present study focused on bowing, which is used by skilled musical saw player. In addition to control of the sounding point, bow manipulation requires control to generate that motion. Bowing is also being studied by a violin-playing robot [17]. In these studies, the focus was on bowing movements to manipulate the violin. However, bowing manipulation using a musical saw, a tool that is challenging to manipulate, takes not only bowing motion but also sound frequency tuning control by manipulating the curvature of the musical saw and position control to manipulate the belly of the musical saw with the bow, taking more skillful tool manipulation. In this paper, we use the term "performance" to refer specifically to the way humans perform and "manipulation" to refer to the robot's advanced manipulation of the tools. The bowing motion requires a stick-slip based on the manipulation to generate a self-excited vibration. Therefore, it is necessary to control the pressure and velocity between the bow and the musical saw to determine the occurrence of self-excited oscillation and vibration. Besides the generation of sound by the self-excited vibration, the pure sound nature of the vibration needs to be discussed in this study. This way is different from the method of suppressing self-excited vibration by striking used in past works. This skillful tool manipulation will enable robots that can share the similar tools with humans and expand the scope of adaptations of cooperative robots. Therefore, as an extension of the conference at ICCAS, we attempted to discuss how to realize skillful manipulation of a musical saw by an industrial humanoid robot [18]. In our previous work, we discussed the factors important for advanced manipulation of a musical saw by a humanoid robot with a bow, based on self-excited vibration theory. Based on this theory, we modeled the bow motion of a musical saw and examined the conditions for the generation of self-excited oscillation. The three factors were defined as and bow's pressing force, sounding point and bow speed. We performed basic experiments on bow's pressing force in particular and argued that it can be controlled by a humanoid robot. However, the purity of sound was not discussed. In the present report, we especially investigate the influence of a proposed skillful manipulation on the pure sound characteristics from a musical saw. The findings of this research will contribute to the realization of a manufacturing line where humans and robots can coexist and cooperate in terms of tool sharing.

2. Experimental Device

The robot used was "Hiro" (Figure 1), a humanoid robot manufactured by Kawada Sangyo Co. A stereo camera and stereo microphone are mounted on the head, enabling multimodal control of vision and hearing as a humanoid robot. Figure 2 shows the

definition, coordinates, and direction of rotation of each joint of Hiro. He has 15 DOFs in the body and 8 DOFs in the hands (4 DOFs in one hand), for a total of 23 DOFs in control axes. The control system uses point-to-point control and trapezoidal control for speed. PTP control is a method of controlling robot motion by providing only the position and posture of the multiple work points to be taught. It focuses only on the position and posture at the taught points, and does not ask about the path or speed on the way to the taught points. Trapezoidal velocity control is a method of creating and controlling a smooth trapezoidal velocity profile by limiting the value of acceleration used to generate the trajectory. However, there is no control that commands Hiro to go halfway along the route. Table 1 summarizes the dimensions of Hiro, which is about the size of an adult woman because it is shaped to resemble a human upper body. However, the notation is in accordance with the DH law. Therefore, $L_0 = 0$ mm. Because the output power of each axis motor is limited to 80 W, Hiro is an industrial cooperative robot that can work with a person without a safety fence. Therefore, it has a one-handed payload of 2 kg. However, this payload varies slightly depending strictly on the posture of the robot arm. And we call it an industrial cooperative humanoid robot in that it can be applied to industrial applications. In addition, Table 3 shows the main specifications of the Hiro. Another major characteristic of Hiro is its twin-arm structure. This allows the robot to perform different movements with each arm, which is not possible with a single-armed robot. This allows Hiro to perform the different operations of musical saw curvature manipulation and striking in a single unit in previous studies. The repetitive positioning accuracy is 0.05 mm. Angle / linear-spherical interpolation is used for interpolation commands, but linear-spherical interpolation is used for musical saw curvature operations because linear motion is required. Angle interpolation is discussed in detail in a later section. The sampling frequency of the microphone installed in the Hiro is 44100 Hz, and its frequency response is 70 ~ 16000 Hz. It has a unidirectional directivity. Its sensitivity is -39 dB (0 dB = 1 V / 1 Pa, 1 kHz). Two cameras are mounted on the head and two on the fingertips, but since they are not used in this study, we do not describe their use in detail.

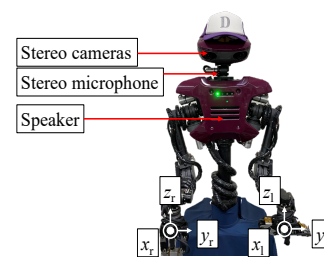


Figure 1: Humanoid robot Hiro

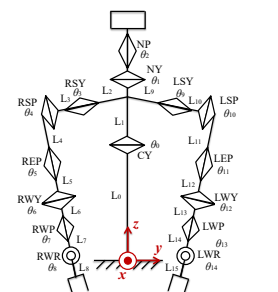


Figure 2: Composition

Table 1: Hiro dimensions (mm)

L_0	L_1	L_2, L_9	L_3, L_{10}	L_4, L_{11}	L_5, L_{12}	L_6, L_{13}	L_7, L_{14}
0	418	150	85	250	130	90	90

Table 2: Hiro specifications

Body weight	20 kg	
One-handed mass	0.3 kg	
Maximum payload (including hand)	2.0 kg	
Repeat positioning accuracy	0.05 mm or less	
Position control method	PTP control	
Interpolation	Angle / Linear-spherical interpolation	
Speed control	Trapezoidal control	
Command minimum unit	Position	0.001 mm or less
	Angle	0.001 deg.

3. Musical Saw

3.1. General musical saw playing

Define abbreviations and acronyms the first time they are used in the text, even after they have been defined in the abstract. Do not use abbreviations in the title or heads unless they are unavoidable. In this paper, a musical saw was used as an unknown tool that is highly deformable and challenging to manipulate (Fig. 3). The handle side is hereafter referred to as root and the top side as tip. Musical saws have a thickness of 1 mm. The musical saw is a so-called body-sounding instrument in which the saw itself is sounded. However, it cannot be used for cutting because it does not have a blade, or even if it does, it is not ground up. As shown in Fig. 4, the saw's operating part was held vertically between the thighs, and the tip of the saw was held in the left hand. The saw was manipulated by bowing with the right hand, as shown by the arrow direction in Fig. 4. It is well known that in the operation of the violin, the bowing motion is performed with the right hand. The musical saw performer can change the height of the sound frequency by manipulating the curvature of the S-shape [19, 20]. If the performer fixes the lower surface of the leading edge with the index finger and presses the thumb against the upper surface of the manipulated side to form an S-shape around the tip, and then controls the curvature of the entire manipulated side with the bending displacement v_1 to change sound frequency, the musical saw is manipulated. The generated sound is about 523 Hz at $v_1 = 50$ mm and 987 Hz at $v_1 = 200$ mm. For this, a force of 2.35 N and 11.95 N is required, respectively, and with Hiro's payload (2.0 kg, 19.6 N), the limit of sound generation is about 1250 Hz. In other words, the musical saw is an instrument in which the greater the amount of bending, the greater the frequency of sound.

To shape the S-shaped curved surface, a jig with rollers in contact with the upper and lower surfaces was attached to the

robot's hand to pinch the tip of the musical saw at two points in the longitudinal direction, as shown in Fig. 5. In Fig. 5, the translucent part is made of acrylic material and the white part is made of aluminum. The bending displacement v_1 of the tip shows the position of the thumb as shown in Fig. 4, while the index finger is supported by the underside of the musical saw. By controlling the curvature of the operating surface of the musical saw, the target frequency f_0 can be sounded.

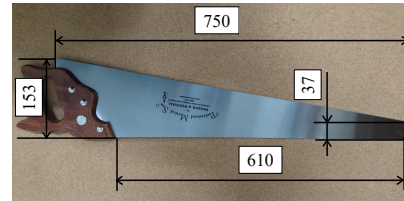


Figure 3: Musical saw

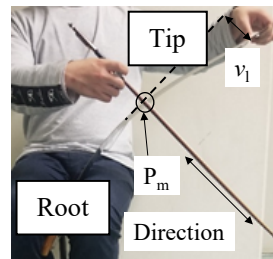


Figure 4: How to manipulate the musical saw

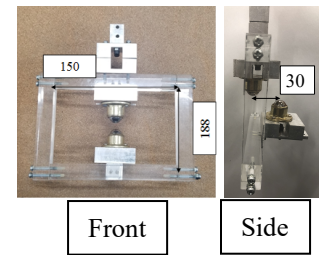


Figure 5: Jig with two rollers

3.2. Observation of vibration modes of musical saws

In a previous study [16], the mode shapes of a musical saw were investigated by sprinkling salt on a musical saw held by the device shown in Fig. 5 and rubbing it with a bow to generate self-excited vibration, as shown in Fig. 6. Based on the idea that the vibration causes fine grains to move and collect at the nodes of the vibration, the locations of the nodes are observed. The pattern thus created is called a Chladni figure. Figure 7 shows the Chladni figure for the mode with the most predominant frequency when the musical saw is struck while displacing the support.



Figure 6: Musical saw for salt spraying

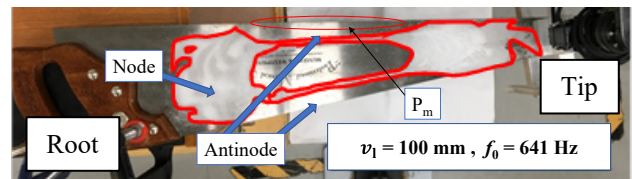


Figure 7: Observation of Chladni figures

As shown in Figure 7, lattice-like modes appeared in the musical saw. Generally, a lattice Cladoni figures appear in the oscillations of the strips. The number of nodes in the longitudinal direction (excluding the vibrating end) is m , the number of nodes

in the shortitudinal direction (excluding the vibrating end) is n , and the vibration mode is (m, n) . The vibrations of the musical saw does not reach either ends, but forming a bounded mode with no damping from the ends. Thus, (2,0) shows the mode of the musical saw used mainly for manipulation.

3.3. Natural frequency analysis of musical saws by finite element analysis (FEA) and contact area to excite sound vibration

From the Chladni figure, it is clear that the sound during bowing of the musical saw is mainly in the (2,0) mode; using FEA (Finite Element Analysis), the mode shape corresponding to the (2,0) mode was examined from the Chladni figure. The musical saw was approximated by a simple trapezoid and the analysis was performed with the saw fixed as shown in Fig. 8. The points of the contact rollers of the jig (Fig. 5) are P_1 and P_2 , which are the thumb position in Fig. 4 and the contact point by the index finger in Fig. 8, respectively, and the bending displacement v_1 is given at P_1 . Here, the material was SS400. Here, SS400 refers to general structural rolled steel. Fig. 9 shows the (2,0) mode when bending displacements $v_1 = 100, 150,$ and 200 mm were applied to both points at the tip. There are two types of sounding methods: striking and bowing, and the sounding point is different for each. In the case of striking, the bow is moved by contacting the belly position in the middle of the saw in Figure 9, and in the case of bowing, the bow is moved with contacting the edge of the saw, which is shown in P_m part among antinode areas in Figs. 4 and 7.

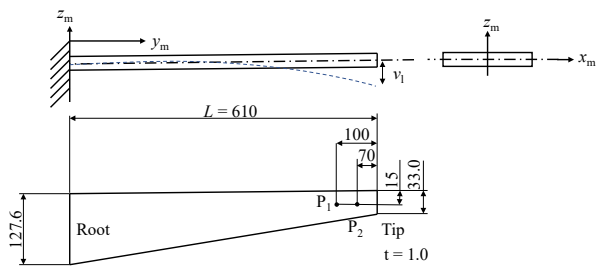


Figure 8: Trapezoidal cantilever beam model

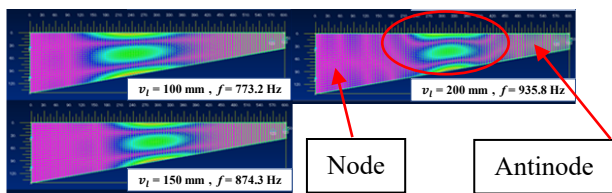


Figure 9: (2,0) mode by FEA

3.4. Flexible rubber stick for striking action of right hand

In our previous study, we developed a flexible rubber stick to realize a striking motion with a robot arm as a substitute tool of a conventional mallet, which was a flexible tool consisting of a wooden ball bolted to the end of a rubber rod (Figure 10). The striking motion in the antinode area in Fig.9 is an instantaneous excitation of the belly of the musical saw vibration. In contrast, excitation with a bow on the P_m line, as shown in Fig.7, among the antinode areas is more akin to a continuous striking motion with friction, and is expected to present difficulties, comparing a striking motion with a flexible rubber stick.

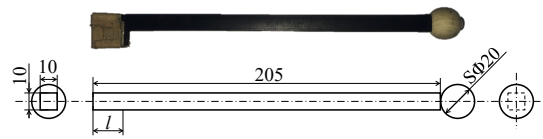


Figure 10: Flexible rubber stick to hold at right hand

4. Theory of Bow Manipulation based on Self-excited Vibration

4.1. Theoretical formula of stick-slip vibration

Headings, or heads, are organizational devices that guide the reader through your paper. There are two types: component heads and text heads.

Component heads identify the different components of your paper and are not topically subordinate to each other. Examples include Acknowledgments and References and, for these, the correct style to use is “Heading 3”. Use “figure caption” for your Figure captions, and “table head” for your table title. Run-in heads, such as “Abstract”, will require you to apply a style (in this case, italic) in addition to the style provided by the drop down menu to differentiate the head from the text.

The bowstring is rubbed against the belly of the musical saw vibration P_m (Fig. 7), and the bow is moved in the z_m direction, resulting in the bowing motion (Fig. 8). Furthermore, self-excited oscillation dominates this phenomenon caused by the frictional phenomenon that occurs at the contact field [21]. In bowing, the musical saw triggers stick-slip vibration. Since the bow moves with respect to the musical saw, stick-slip vibration is assumed to be a one-degree-of-freedom system. Fig. 11 shows a general model of self-excited vibration. In this bow movement of the musical saw, m is the equivalent mass of the musical saw and k is the equivalent stiffness of the fixed musical saw with respect to the restoring force. However, the viscosity c is not considered. Figure 11 shows a model of the sounding point when the vibration amplitude in the z_m direction of the belly shown in Fig. 8 in Fig. 9 is z_{mr} and the bow motion is v_0 . The sphere in Fig. 11 represents a musical saw and the belt represents a bow. The bow string deforms by Δx_{rm} on contact with the musical saw, generating a pressing force W . If the stiffness of the bowstring is k_b , then $W = k_b \Delta x_{rm}$.

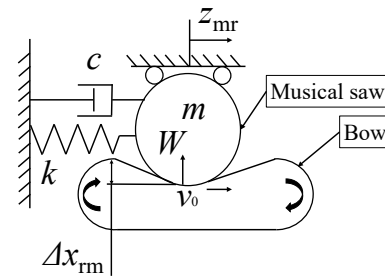


Figure 11: Model of self-excited vibration caused by friction in bowing

First, when an object moves with the belt in the right (positive direction z_{mr} -axis) direction (stick state), the frictional force acting on the object from the belt is the static frictional force in the right direction. As the object moves to the right, the restoring force increases, and when the frictional force reaches the maximum static frictional force f_s , the object begins to slide on the belt (slip state). The frictional force acting on the object is a constant dynamic frictional force f_k , and its direction is to the right.

As the object slips on the belt and comes to rest, it is accelerated to the right by the frictional force from the belt and reaches the same speed as the belt, v_0 , and then it sticks again. The frictional force acting on the object always acts in the right direction during vibration. In the sticking state, the displacement z_{mr} increases with v_0 and the formula of motion is given by:

$$m \frac{dz_{mr}^2}{dt^2} + kz_{mr} = f_k \quad (1)$$

This is because the object in the stick state is subject to dynamic friction and restoring spring forces. If f_k acts and the system is not oscillating ($\frac{dz_{mr}^2}{dt^2} = 0$), then $z_{mr} = f_k / k$. Therefore, consider the new coordinates as follows

$$y = z_{mr} - \frac{f_k}{k} \quad (2)$$

Transforming Eq. (1), we get:

$$m \frac{dy^2}{dt^2} + ky = 0 \quad (3)$$

The solution to Eq. (3) is

$$y = a \sin(\omega_n t + \varphi) \quad (4)$$

where ω_n is

$$\omega_n = \sqrt{\frac{k}{m}} \quad (5)$$

The natural angular frequencies of the vibrating system are given by this. From Eq. (2),

$$z_{mr} = a \sin(\omega_n t + \varphi) + \frac{f_k}{k} \quad (6)$$

From Eq. (6), it can be seen that in the sliding state, a constant dynamic friction force acts in the positive direction of z_{mr} , so that it oscillates with an angular frequency of ω_n around the point moved by $z_{mr} = f_k / k$. Because the restoring spring force is equal to the maximum static friction force at the point of switching to the slip state, z_s is the switching point.

$$z_s = \frac{f_s}{k} \quad (7)$$

Since the velocity at this time is v_0 , a and φ in Equation (6) can be obtained under the following conditions:

$$a = \sqrt{\left(\frac{\Delta f}{k}\right)^2 + \left(\frac{v}{\omega_n}\right)^2}, \quad \Delta f = f_s - f_k \quad (8)$$

$$\sin \varphi = \frac{\Delta f}{ak}, \quad \cos \varphi = \frac{v}{a\omega_n} \quad (9)$$

Fig. 12 shows the oscillation. The object begins to sleep from point z_s , initially moving slightly in the positive z_{mr} -axis with an initial velocity v_0 ; but, because the restoring force is larger than the kinetic frictional force f_k , it begins sliding along the negative z_{mr} -axis direction. Since the dynamic frictional force acting on the object is on the positive z_{mr} -axis, the object eventually stops and is accelerated by the frictional force acting on the positive z_{mr} -axis.

The velocity of the object reaches v_0 and begins to stick again. From Equation (8), the larger the difference between the maximum static and dynamic frictional forces, the larger the amplitude a , and the larger the equivalent stiffness k , the smaller the amplitude. When the stick time T_1 is sufficiently larger than the slip time T_2 , the frequency f is expressed as

$$f \approx \frac{1}{T_1} \quad (10)$$

After a while, T_1 and T_2 become equal and converge to the natural frequency of the system. During the transient period between the stick and slip, vibrations other than f were also occurred, generating noise at higher frequencies.

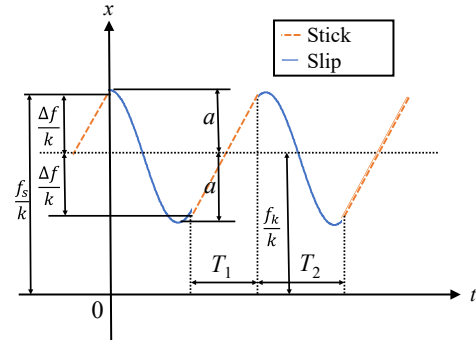


Figure 12: Stick time and slip time

It was found that the amplitude of the musical saw bow decreases as the curvature increases. Therefore, in order to determine the occurrence of self-excited oscillation and pure soundness, bow speed and bow pressure in the operation control should be considered.

4.2. Critical conditions for generating stick-slip vibrations

There are critical conditions for stick-slip vibrations. First, the governing equations must be non-dimensionalized.

$$\lambda = \frac{\Delta\mu W}{(mk)^{\frac{1}{2}} W} \quad (11)$$

$$\xi = \frac{c}{2(mk)^{\frac{1}{2}}} \quad (12)$$

However, if

$$\Delta\mu = \mu_s - \mu_k \quad (13)$$

where μ_s and μ_k are the coefficients of static and kinetic friction, respectively. W shows the pressing force in Fig. 11. With the nondimensionalization of Eq. (8) and (9), the seven independent parameters can be showed by two dimensionless quantities. The critical speed V_{cr} of self-excited vibrations owing to stick-slip is expressed by Eq. (14).

$$V_{cr} = (1 - \xi)^{2.5} (4\pi\xi mk)^{-0.5} \Delta\mu W \quad (14)$$

When the critical speed V_{cr} is exceeded, no self-excited vibration owing to stick-slip occurs. Eq. (14) was applied to the stick-slip vibration of a musical saw. The natural frequency of a musical saw is determined by the amount of bending. Other parameters are also specific to the musical saw or determined by the physical

properties of the musical saw and pine resin. Pine resin has a significant effect on friction and is also used in manipulation of a violin. Therefore, when the amount of bending was changed, the apparent equivalent stiffness k altered; however, the other parameters remained intact. Therefore, when the amount of bending is altered for the target frequency, the critical speed V_{cr} alters based on the apparent equivalent stiffness k , and the critical speed must be controlled within the range of V_{cr} based on the bending amount. As a result, it can be seen that the skillful and advanced manipulation is needed to keep the realization of musical saw bowing because there is an unstable parameter $\Delta \mu$ in Eq. (14).

5. Inspection of Bowing Manipulation

The bowing manipulation is a way of manipulating a stringed instrument, such as a violin with a bow. The three main engineering quantities in bowing are bow pressure W , bow velocity V_{cr} in Equation (14), and the sounding point in the P_m region of Fig. 9. The bow pressure is the pressing force W that the bow receives from the string, the bow velocity is the velocity at which the bow is played, and the sounding point is the point of contact with the bow. In legato playing, where the bow is manipulated smoothly, the bow must be released after making contact with the instrument in order not to cancel out the instrument's resonance. As a result, we decided to use spherical interpolation control instead of linear interpolation control for bow manipulation. The geometric model of the motion in spherical interpolation is shown in Fig. 13. f is the command distance, r is the radius of the arc, 2θ is the central angle of the arc, and Δx_r is the maximum distance between the string and the arc. In equation (13), W can vary during the motion and change V_{cr} , making spherical interpolation more suitable for manipulation than linear interpolation.

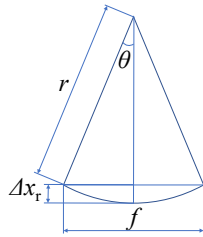


Figure 13: Spherical interpolation model

If θ is small, we obtain the following equations:

$$\Delta x_r = \frac{f^2}{8r} \tag{15}$$

$$\theta = 4 \frac{\Delta x_r}{f} \tag{16}$$

We also discuss the points needed for bowing motion. We defined the bow speed as the percentage velocity commanded by the robot. The actual velocity v_r [mm/s] and displacement Δx_r [mm] when v_c is altered are defined as the command velocity v_c [%]. The right arm of the robot was moved 300 mm in the y_r -direction

in the positive directions. The values of v_c were altered to 20 %, 30 %, and 40 %. The effect of the displacement on actual velocity is indicated in Fig. 14. The value is about 200 mm/s at $v_c = 15$ %.

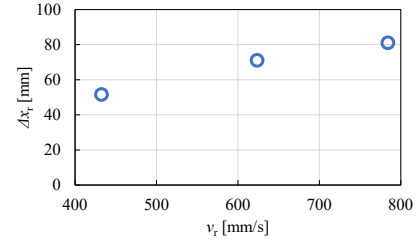


Figure 14: Effect of hand speed v_r on displacement Δx_r .

The actual velocity and displacement increase as v_c increases. The bow pressure is the pressing force W received by the bow from the musical saw, that is, the force received by the bow hairs, which is determined by the amount of displacement of the bow hairs. Furthermore, the bow speed and bow pressure can be controlled by the position of the right arm and commanded v_c . In Eq. (15) and (16), f is known and Δx_r is obtained by measurements; thus, r and θ can be estimated. r assumes a small value as the command speed increases, and θ assumes a large value as the command speed increases, and its magnitude is approximately $0.5^\circ \sim 1.5^\circ$ obtained from this experiment.

Sounding points were then inspected. We arranged the robot and the musical saw as shown in Fig. 15. And we made the robot hold the bow shown in Fig. 16. As shown in Fig. 15, the saw was installed vertically, the right hand moved the bow in the horizontal plane, and the left hand controlled the bending v_1 of the saw tip.

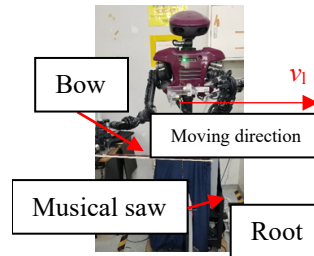


Figure 15: Holding

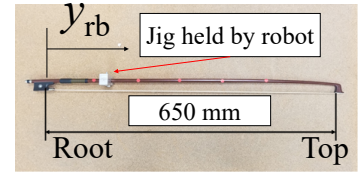


Figure 16: Bow

Figure 17 shows a model of a bowstring. In both Figures 16 and 17, the origin of the longitudinal coordinate of the bowstring is defined from the bow handle (root) to the top. Although there is literature analyzing bows, we have not found anything that identifies the stiffness of the bowstring [22]. Here, the stiffness of the bowstring, k_b , was measured. A wireless force/acceleration sensor PS-3202 manufactured by PASCO Corporation was used for the measurement. Its force resolution is 0.03 N and it can measure up to 50 N. This wireless sensor was attached to the robot's hand, and the pressing force W of the bow against the forced displacement Δx_{rm} was measured by pressing the sensing part against the bowstring from the sensor's intellect. The measurement points were $y_{tb} = 100, 300, \text{ and } 500$ mm. Figure 18 shows the results of the measurement at $y_{tb} = 100$ mm. The bowstring stiffness, k_b , was obtained by a linear least-squares approximation with an intercept of 0 N. Figure 19 summarizes the bowstring stiffness k_b at each bowstring position y_{tb} . Figure 19

shows that k_b is large at the root of the bow, but is almost constant at 1.2 N/mm from the middle to the top of the bow, which is used for playing. Therefore, the stiffness k_b of the bow string is kept constant at 1.2 N/mm during bow manipulation, and the pressing force W can be approximately controlled by controlling the forced displacement Δx_{rm} .

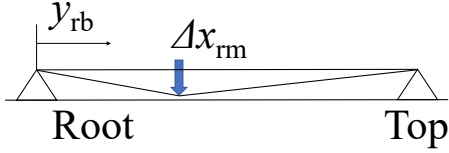


Figure 17: Bowstring model

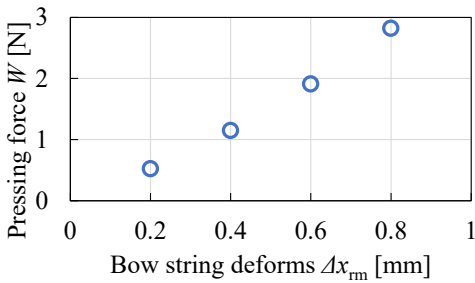


Figure 18: Stiffness of bowstring at $y_{rb} = 100$ mm

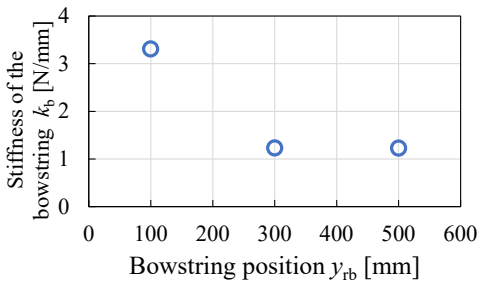


Figure 19: Stiffness of bowstring

For the bow to be held, a control was devised to reduce the resistance at the time of contact by tilting at an angle, as shown in Fig. 20, considering θ . Here, the contact area between bow and saw is the belly of the vibration. Figure 21 shows the measured amount of movement in the x_r direction and duration of sounding in the bowing stroke as the bow angle was varied from 0.5° to 2.0° in 0.5° increments. The right arm of the robot was moved 300 mm in the positive y_r -direction. Here, v_1 is 150 mm. The target frequency for this is around 700 Hz. The judgement of pure sound or noisy sound was also shown in Fig.21. The tendency can be seen that pure tones occur in the short sounding time which is less than 3s and noise tones occur in the long sounding time which is more than 3s. It tends to be difficult to keep a pure tone during long sounding time by bowing motion.

Then we give the amount of pressure ΔV on the bow when moving Δx_r in the x_r direction by Equation (17).

$$\Delta V = tl (\Delta x_r - l \tan \theta) < tl \Delta x_r \quad (17)$$

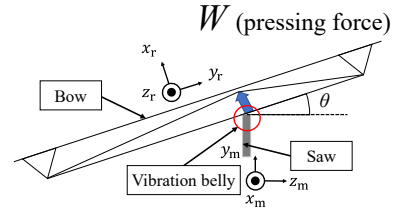


Figure 20: Control with additional angle

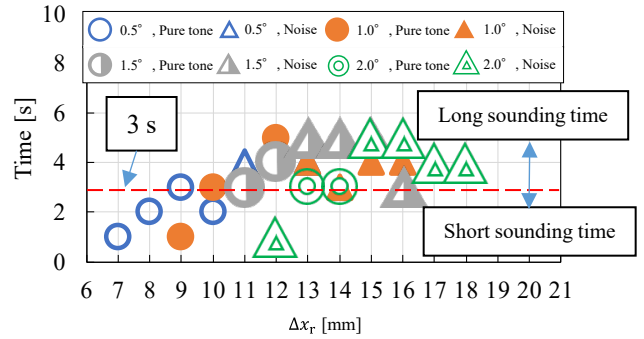


Figure 21: Effect of displacement on sound duration at $v_c = 15\%$ ($-y_r$)

As t is the thickness of the bow, and l is the width of the musical saw. Thus, while the angle reduces pressure and makes it easier to pronounce, the sound is dependent on displacement.

Next, we focused on the sound produced when the musical saw was manipulated with a bow. When a musical saw is manipulated with a bow, a noise-like sound is produced. Fig. 22 shows a comparison between the case with and without noise. Here, v_1 is 150 mm.

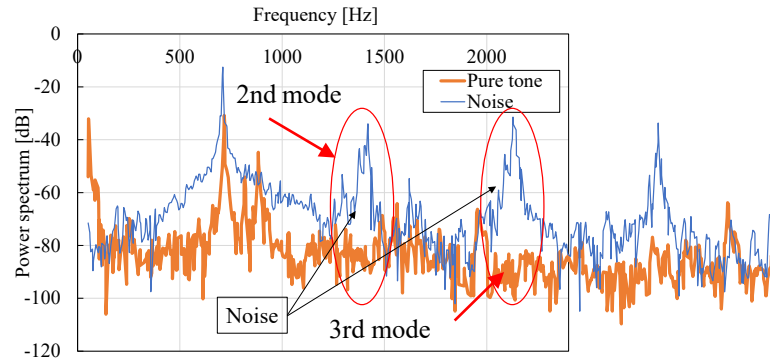


Figure 22: Comparison of pure sound and noise

The generated sound, including noise, contains second- and third-order frequencies with high sound pressure. Analysis of the vibration modes of musical saws with such higher-order frequencies yielded the results shown in Fig. 23. The analysis revealed that the higher-order vibration modes exist near the main frequency vibration modes. To improve sound quality, it is necessary to avoid excitation of this vibration mode. Here, Figure 24 shows the spectrogram of the playing sound when a skillful operator plays bowed music. Short-time Fourier transform was used for its analysis. The spectrum from 2 to 5 s, which is a short duration, in Fig. 24 shows excitation at about 700 Hz, with little excitation at other frequencies, while the spectrum from 9 to 13 s,

which is a long duration, shows significant excitation at about 700 Hz and at higher frequencies. This difference can be attributed to whether or not the higher-order vibrational modes shown in Fig. 23 were excited. It can also be seen that the higher the order frequency, the shorter the sounding time. Here, v_1 is 150 mm in both Figs. 23 and 24. As a result, it is also difficult for a skillful operator to keep a pure tone during long sounding time by bowing motion. The same skillful operation is found to be performed by industrial collaborative humanoid robot when bowing musical saw. From the above, it can be seen that the bow manipulation motion of the musical saw can be realized with the jig shown in Fig. 5, the humanoid robot equipped with the microphone shown in Fig. 15, and the bow shown in Fig. 16.

Here, we consider how well the robot performs compared to a human operator. For this purpose, we compare Figures 21 and 24. In Fig. 21, the robot is able to sustain a pure sound for about 1 to 5 s. On the other hand, Figure 24 shows that the duration of the pure sound of the human operator is about 3 s. Thus, the robot is able to produce pure sound as well as humans with its bow manipulation motion. However, the operator in Figure 24 is not a professional player.

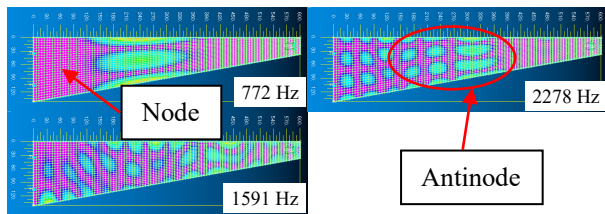


Figure 23: Observation of 2nd and 3rd order modes

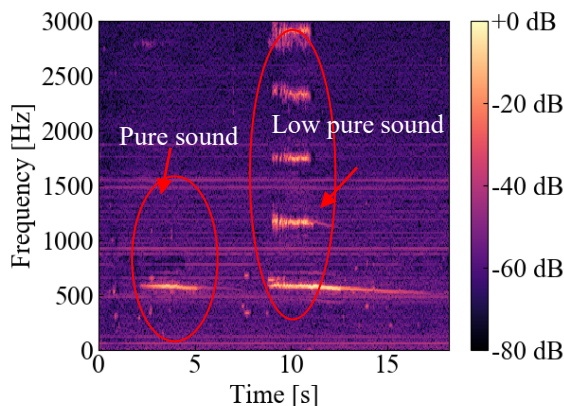


Figure 24: Spectrogram of sound by human bow performance

6. Conclusions

We studied the performance manipulation of playing a musical saw, a challenging musical instrument, by means of a robot tool and two-arm coordinated manipulation. The results are summarized as follows:

(1) We investigated the elements necessary to manipulate the bow from the theory of self-excited vibration and string friction, and derived the elements necessary to reproduce the performance control through experiments.

(2) When the amount of bending is changed with respect to the target frequency, the critical speed V_{cr} at which self-excited vibration occurs changes based on the apparent elastic modulus, and the critical speed must be controlled within the range of V_{cr} based on the amount of bending.

(3) It is also difficult for a skillful operator to keep a pure tone during long sounding time by bowing motion. Comparing bowing musical saw by skillful operator, the same skillful operation is found to be performed with an industrial collaborative humanoid robot.

This finding shows the possibility that cooperative robots, including humanoid robots, can control tools that require advanced manipulation behavior similar to that of humans. This finding may contribute to the realization of a manufacturing line where humans and robots can coexist and cooperate by sharing tools.

Conflict of Interest

The authors declare no conflict of interest.

References

- [1] M. Ratiu M. A. Prichici, "Industrial robot trajectory optimization-a review," MATEC WEB Conf., **126**, 02005, doi: <https://doi.org/10.1051/mateconf/201712602005>, 2017.
- [2] J. Arents and M. Greitans, "Smart Industrial Robot Control Trends, Challenges and Opportunities within Manufacturing," applied sciences, **12**(937), doi: 10.3390/app12020937, 2022.
- [3] L. Xiao, J. Grong and J. Chen, "Industrial Robot Control Systems: A Review," Proceedings of the 11th International Conference on Modelling, Identification and Control, 1069–1082, doi: <https://music.apple.com/jp/music-video/inori/1604319072>, 2019.
- [4] Q. Wu, Y. Liu and C. Wu, "An overview of current situations of robot industry development," ITM Web Conf., **17**, doi: 10.1051/itmconf/20181703019, 2018.
- [5] M. Botte, S. Cocuzza, N. Comand and A. Doria, "Modeling and identification of an industrial robot with a selective modal approach," applied sciences, **10**, 4619, doi: 10.3390/app10134619, 2020.
- [6] C. H. Ting, et al., "Humanoid robot: A review of the architecture, applications and future trend," Research Journal of Applied Sciences, Engineering and Technology, **7**(7), 1364–1369, doi: none, 2014.
- [7] H. Ishiguro, T. Ono, M. Imai, T. Maeda, T. Kanda and R. Nakatsu, "Robovie: an interactive humanoid robot," Industrial Robot, **28**(6), 498-504, doi: 10.1108/01439910110410051, 2001.
- [8] K. Hirai, M. Hirose, Y. Haikawa, T. Takenaka, "The development of Honda humanoid robot," Proceedings. 1998 IEEE International Conference on Robotics and Automation, no. 98CH36146, doi: 10.1109/ROBOT.1998.677288, 1998.
- [9] T. B. Sheridan, "Human–Robot Interaction: Status and Challenges," Human Factors: The Journal of the Human Factors and Ergonomics Society, 525–532, doi: 10.1177/0018720816644364, 2016.
- [10] S. A. Green, M. Billingham, X. Q. Chen, J. G. Chase, "Human-Robot Collaboration: A Literature Review and Augmented Reality Approach in Design," International Journal of Advanced Robotic Systems, **5**(1), 1-18, doi: 10.5772/5664, 2008.
- [11] A. Vick, D. Surdilovic, and J. Kruger, "Safe physical human-robot interaction with industrial dual-arm robots," 9th Workshop on Robot Motion and Control (RoMoCo), 264-269, doi: 10.1109/RoMoCo.2013.6614619, 3–5 July 2013.
- [12] S. Schaal, S. Kotosaka, and D. Sternad, "Nonlinear dynamical systems as movement primitives," in International Conference on Computational Intelligence in Robotics and Automation. Monterey, CA, October, 1999, doi: none.
- [13] J. Li, T. Hu, S. Zhang, and H. Mi., "Designing a musical robot for Chinese bamboo flute performance," in Proceedings of the Seventh International Symposium of Chinese CHI (Chinese CHI '19), ACM, New York, NY, USA, 117–120, doi: 10.1145/3332169.3332264.
- [14] Y. Kawaguchi, I. Yoshida, H. Kurumatani, T. Kikuta, and Y. Yamada, "Internal pipe inspection robot," in Proceedings of IEEE International Conference Robotics, Automation, 857–862, doi: 10.1109/ROBOT.1995.525390, 1995.

- [15] T. Tujita, S. Komizunai, Y. Nomura, T. Owa, and M. Uchiyama, "Evaluation of nailing motion for a humanoid robot," in Proceedings of the 2008 JSME Conference on Robotics and Mechatronics, Nagano, Japan, June 5–7, doi: 10.1299/jsmermd.2008_2P1-F11_1 (in Japanese).
- [16] T. Hirogaki, E. Aoyama, E. Sugiura, and Y. Kobayashi, "Investigation of impact task and application based on its hit sound feedback motion with an industrial humanoid robot," Transactions of the JSME, **83**(855), 2017, doi:10.229/transjsme.17-00132. (in Japanese).
- [17] H. Yabu, T. Aratani, and K. Shibuya, "An Algorithm for Motion Planning of Violin-playing Robot-Determining Bowing direction and Three Bowing Parameters-," The Japan Society of Mechanical Engineers, no. 14-2, 1A1-D05, 1–2, doi: 10.1299/jsmermd.2014_1A1-D05_1, 2014 (in Japanese).
- [18] H. Hanai, A. Mishima, A. Miura, T. Hirogaki and E. Aoyama, "Realization of Musical Saw Bowing by Industrial Humanoid Robot," 2021 21st International Conference on Control, Automation and Systems (ICCAS). IEEE, 2021. 1695–1700,doi: 10.23919/ICCAS52745.2021.9649856.
- [19] J. Kaneko, N. Hosoya, and K. Furuya, "Minimization of vibration and sound radiation of thin plate structures based on musical saw mechanism," in Proceedings of Dynamics and Design Conference, 111, 1–6, doi: 10.1299/jsmedmc.2010_111-1_2010 (in Japanese).
- [20] J. Lenard and J. Graebner, 1989, "Scratch My Back": A pictorial history of the musical saw and how to play it, Seada records, California.
- [21] A. D. Berman, W. A. Ducker, and J. N. Israelachvili, "Origin and Characterization of Different Stick–Slip Friction Mechanisms," LANGMUIR, **12**(19), 4559–4563, doi: 10.1021/la950896z, 1996.
- [22] S. Serafin and J. O. Smith III, "A MULTIRATE, FINITE-WIDTH, BOW-STRING INTERACTION MODEL", Proceedings of the COST G-6 Conference on Digital Audio Effects, 1 – 4, doi: none, 2000.

Deep Learning in Monitoring the Behavior of Complex Technical Systems

Bahram Ismailov Israfil*

Azerbaijan State Oil and Industry University, Department of "Instrument Engineering", Baku, AZ1010, Azerbaijan Republic

ARTICLE INFO

Article history:

Received: 15 July, 2022

Accepted: 28 August, 2022

Online: 09 September, 2022

Keywords:

Complex Vibration processes

Poincare

Lyapunov

Visual Thinking

Deep Learning

ABSTRACT

The article is devoted to the methods of monitoring and control of vibration processes occurring in the structure and units of complex and unique electromechanical equipment. The monitoring object is considered as a dynamic multidimensional information object, for the study of which analytical and numerical methods of modeling and simulation of multidimensional chaotic systems are used in the context of the scientific direction of physics of open systems. The structure of research of signals of vibration activity of equipment, description of mathematical models and algorithms based on them are presented. Demonstrative results of experiments carried out to analyze and evaluate the possibilities of controlling the behavior of a complex system using methods of influencing signals of various nature are presented. Using the methodology of Visual Thinking will improve the quality and efficiency of monitoring the vibrational activity of a complex technical object. Such a technique will make it possible to reasonably interpret the decision made to control the vibration process. The calculated parameters and the constructed visual images of the processed signals are proposed for use in the Input Layer of the Recurrent Neural Network of the Deep Learning algorithm.

1. Introduction

The analysis of vibration processes occurring in the interconnected nodes of complex power equipment is an urgent task to ensure its trouble-free, long-term and efficient operation. During operation, the equipment is exposed to electrical, mechanical, hydraulic, seismic and other forces and influences. Examples of devices with complex vibrational media are a hydraulic unit or a powerful pump design for pumping liquid. The operation of such devices is often accompanied by vibration processes with high intensity in a wide frequency range, the sources of which can be turbulent fluid flows, cavitation processes, friction in bearings of rotating assemblies, pressure pulsations on blades, etc. In the vibration signal of such devices, you can find information about the sources of vibration, beats, imbalances, resonances caused by them, or, conversely, false damping of intensity, in cases with antiphase influences from other sources of vibration. The situation becomes much more complicated when several such devices operate in parallel on the same platform, foundation. In this case, it becomes an important task to identify the cause-and-effect relationships of the true sources of vibration [1-10].

Traditionally, the process of operating complex electro-mechanical equipment is accompanied by monitoring of the vibrational environment and searching for vibration sources that can be caused by design features, transients or scenarios of technological processes. In addition, as you know, along with internal processes, equipment is exposed to external influences in the form of unpredictable changes in load, environmental impact, etc. Thus, monitoring the main parameters of the equipment allows you to identify problem areas or trends in their development at an early stage.

Monitoring the analyzed object from the standpoint of the information object will reveal previously unknown features of its dynamics, which will increase the reliability, argumentation and efficiency of the analysis. At the same time, its parameters can be presented in the form of information flows. Typically, complex dynamical systems exhibit non-linear behavior. Taking into account the nonlinear nature of the dynamic vibration processes occurring in the nodes and elements of complex technical means, their analysis and assessment should be carried out from the standpoint of the interaction of multidimensional chaotic systems [1-5, 8, 9, 11-16]. The main idea of the work is to apply the theory of chaotic systems, which connects mathematics and the studied physical processes, while the use of nonlinear recurrent analysis

*Corresponding Author: Bahram Ismailov Israfil, isbahram@gmail.com

makes it possible to simplify the study of objects presented in 2D and 3D formats.

The use of analytical-numerical methods with computer modeling and simulating of various operating modes will allow you to safely test various control strategies.

An important role is played by the visualization of the studied vibration processes, since along with the signals in the spectrum of the observed data, the use of modern methods of analysis will make it possible to reveal hidden oscillations, the effects of the manifestation of the system's memory, external influences and other information that is important for the development of a control strategy.

For the studies of the vibration activity of the control object carried out in the work, the time series obtained from the devices for collecting measuring information, the processes and functions modeled in MATLAB, as well as surrogate data were used. [2, 10, 11, 14, 15, 17, 18].

The issues of collecting measurement information and the equipment used for this are not considered in the work.

2. Research Methods Used for Analysis and Control

The research structure presented in Figure 1 [3, 19, 20, 21], covers a variety of iterative algorithms for the analysis, assessment and control of the dynamics of a complex system, the development of which takes place within the framework of an open system.

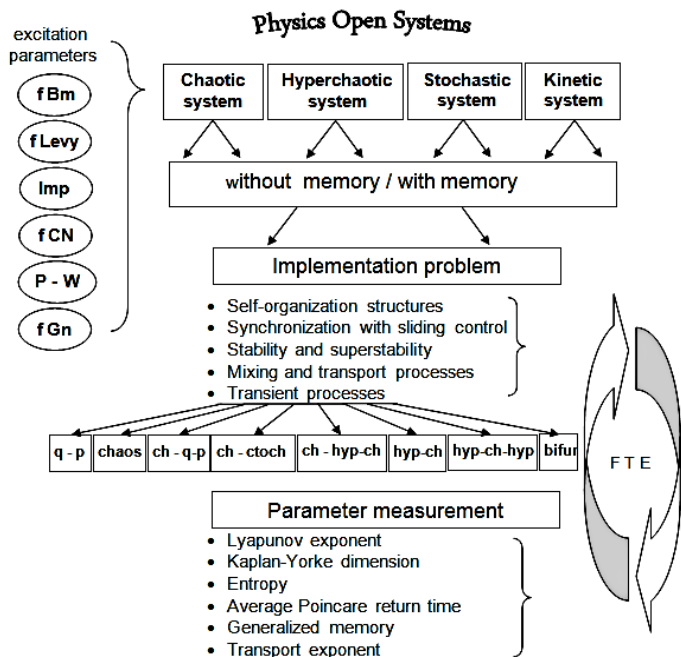


Figure 1: Structure of the study of dynamical systems

Legend:

fBm – fractional Brownian motion; fLevy – fractional Levy motion; Imp – impulsive function; fCN – fractional Colored noise; P-W – piecewise function; fGn – fractional Gaussian noise; q – p – quasi-periodic; ch – q-p – chaos – quasi-periodic; ch-stoch – chaos – stochastic; ch – hyp-ch – chaos – hyper-chaos; hyp – ch – hyp – hyper-chaos - chaos - hyper-chaos; bifur – bifurcation; F T E – fractional time evolution.

It is known that the evolution of a dynamic chaotic system is sensitive to initial conditions, the influence of system memory, as well as to minor disturbing influences.

In this work, we propose to use, for example, functions such as Brownian motion, fractional Levy motion, fractional color noise, fractional Gaussian noise, anti-synchronization, and others, as acting to correct or control the behavior of the simulated process [6, 17, 21-24]. In this case, the spectrum of changes in the nature of dynamic processes can vary from quasiperiodic to hyper chaotic processes. The choice of a particular type depends on the goals and objectives of the research.

The analysis and study of the dynamics of vibration processes was carried out according to the algorithms described below. The analysis results are visualized in the form of recurrent plots, Finite-time Lyapunov Exponent (FTLE), dependences of the Poincare return times, Lyapunov exponents, Tsallis entropy, etc. [2, 11, 12, 25-29].

The proposed mathematical model covers the most significant components affecting processes of interconnections and interactions of information flows circulating in the investigated dynamic system [10]:

$$\tau_T^\alpha \stackrel{def}{=} S_q(GM, d_f, \tau, \varepsilon, T_{st}, q - exp) \quad (1)$$

where τ_T^α - thermodynamically spectrum of the dimensions of the Poincare's return time in an open space; S_q - entropy of Tsallis; GM – generalized memory; d_f - fractal dimensions in the function of entropy of Tsallis; τ - mean return time for Poincare; ε - stability of Tsallis entropy; T_{st} - stability of thermodynamics; q -exp - exponential of Tsallis. [6, 8, 18, 19, 30-32].

The idea of modeling dynamic processes evolving within the framework of an open system is based on the thermodynamic-informational paradigm, which made it possible to connect the informative and operational components of data and knowledge.

3. Research Algorithm

Let's imagine a complex technical system as a set of interconnected pieces of equipment that demonstrate the nonlinear nature of dynamics. The structure of the research algorithm is shown in Figure 2.

Each of the components of the system is influenced as well as influenced by others. To study the behavior of such a system, it is necessary to carry out a set of measurements and calculations of informative parameters, on the basis of which it will be possible to make a decision on the continuation of monitoring or the choice of control actions for correction.

The list of measured, calculated and graphically presented data can be expanded, which will increase their overall information content. The figure 2 also shows a library of influencing functions designed to correct and control the dynamics of the observed processes. This list can also be

supplemented in the process of analyzing the response of the system in order to obtain satisfactory characteristics.

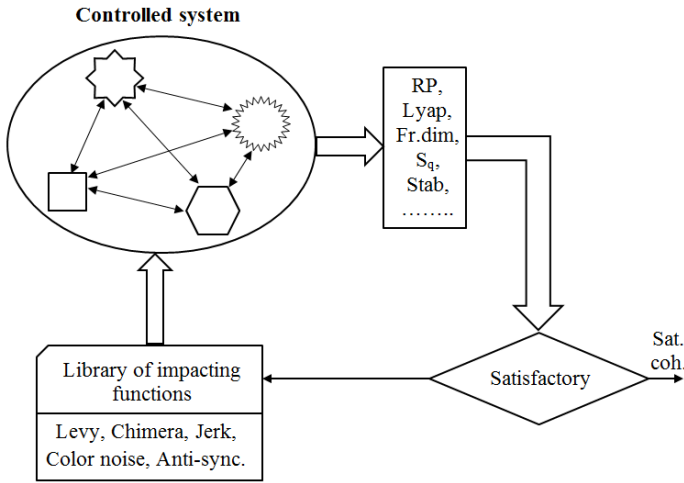


Figure 2: The structure of the research algorithm.

3.1. Interaction of System Components

Numerical modeling of the processes under study begins with the presentation of fragments of the observed time series and the selection of areas of interest. The generalized structure of the algorithm for studying the interrelationships and mutual influence of the system components, assessing the situation that has arisen and choosing the control actions [3, 11, 15, 33, 34].

Recurrent diagrams obtained as a result of non-linear recurrent analysis of observables of a connected controlled system can be used to visually assess the current situation and its dynamics:

$$PD_{i,j}^{\varepsilon,m} = \theta(\varepsilon - \|x_i - x_j\|) / \eta, \quad x \in R^m, \quad i, j = \overline{1, N}, \quad (2)$$

where N is the number of states under consideration; x_i ; ε - the size of the neighborhood of the point x at the moment i ; $\|\cdot\|$ - norm; $\theta(\cdot)$ - Heaviside function [11, 29, 35].

Considering that the time of the First Poincare recurrence times (FPRs) corresponds to a Recurrence Plot (RP) of a certain process, that is, FPRs or [8, 16]:

$$(FPRs) \sim (RPs) \quad (3)$$

Next, the most informative parameters of the system behavior are calculated, such as the Lyapunov characteristic exponents, fractional dimension, Tsallis entropy, stability indicator, etc. According to the results of the analysis of the constructed RP-s, we search for areas that meet the objectives of the research by the criterion:

$$AI(x, y, z) = \underset{\text{def}}{\underset{\text{sem}}{\text{sum}}} \underset{\text{v}}{\text{inf}} I / a^3 \quad (4)$$

where $AI(\dots)$ is the area of interest, formed on the thesis of the selection of information in such a way that it is the most

meaningful from the semantic point of view $\underset{\text{sem}}{\text{sup}}$ and the

minimum $\underset{\text{v}}{\text{inf}}$ in terms of the amount of information; a^3 -

adequately AI taking into account reflexivity, while taking into account that the measure of recurrence [8, 16]:

$$RR = \frac{I}{N^2} \sum_{i,j=1}^N R_{i,j}^{\varepsilon,m} \quad (5)$$

represents the probability of repeating trajectories when implementing a mapping

$$I(\dots) \Rightarrow C_{ref}(\eta) \quad (6)$$

The next stage is associated with the calculation of informative parameters and making a decision on the relevance of the application of impacts and, accordingly, the choice of their type. The structure shown in Figure 1 shows examples of influencing functions [3, 19, 20]. As is known, in the practice of using algorithms for controlling the behavior of chaotic systems, they are guided by the principles of actions based on the extreme sensitivity of chaotic dynamical systems to small disturbances, the effectiveness of which depends on falling into the required area. The work also used the principles of selecting areas of interest (AI) and types of impacts. In our case, the following functions were used as impacting functions: Levy flight, Chimera states, Color noise, Jerk, Anti-synchronization and others [3, 17, 22, 23].

3.2. Algorithm "Measurement – Recognition – Decision Making"

An important part of the study of the dynamics of a chaotic system are the stages: "measurement - recognition - decision making" [18, 19, 33]. Nonlinear recurrent analysis can serve as a catalyst for the implementation of the control task due to its visual images in the form of RP and their characteristic features in the form of topology, texture, color palette. The use of the Visual Thinking methodology will allow you to quickly comprehend the current situation, increase the reliability of the analysis and justify the decision on the impact on the controlled system.

The structure of the adaptive system for analyzing and controlling the behavior of fractional-order chaotic systems is shown in Figure 3.

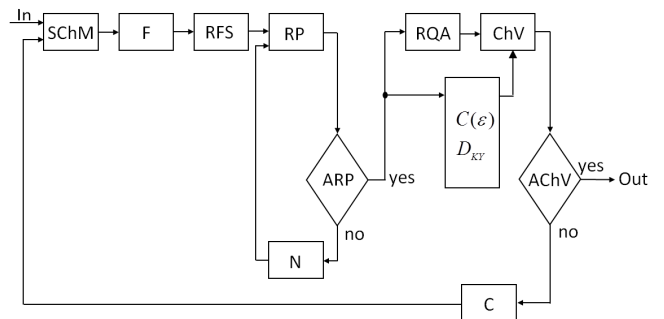


Figure 3: The structure of the adaptive system.

This structure demonstrates the application of the adaptive algorithm to the processes observed in the nodes of the power equipment of hydroelectric power plants [3, 19]. The operation of the algorithm is based on the principles of synergetic, Poincare’s return time theorem, covers the stages of analysis of measurement information, nonlinear recurrent analysis with the construction of RP, calculations of informative parameters of the system under study.

Legend:

- SChM – stochastic and chaotic mappings;
- F – filter;
- RFS – phase space reconstruction;
- RP – recurrent diagramming;
- RQA – recurrent quantitative analysis;
- ChV – characteristic vector generation;
- ARP – analysis of recurrent diagrams;
- AChV – analysis of characteristic vector;
- N – norm setting (L_1, L_2, L_∞);
- C – calculation of: correlation integral $C(\varepsilon)$, new fractional dimension of Kaplan-Yorke D_{KY} and implementation filtering chaotic information, recurrent analysis of controlled processes.

3.3. Thermodynamic Information Paradigm

It is known that in an open system the issues of energy and matter transformation are considered from the standpoint of thermodynamics. The formation of an information-theoretical approach to modeling processes in open systems contributes to the combination of dynamic and informational components, as a result of which the development of complex systems begins to be determined by its information properties as well as their relationship to the external environment [3, 10, 18, 20, 36].

The theory of dissipative structures that determine physicochemical processes was developed as an “exchange of information”, which made it possible to universalize thermodynamic categories [10, 36].

It is pertinent to note that the dynamics of nonlinear processes of dissipative systems is also described by Poincare’s theory, although they were developed for Hamiltonian systems. Also noteworthy is the relationship between metric entropy and Poincare recurrence.

3.4. Nonlinear Recurrence Analysis, Recurrence Plots

Visualization of nonlinear recurrent analysis with the representation of RP allows you to visually assess the dynamics of the system under study by its texture, topology and color scale, to study the AI allocated to test the hypothesis about the use of a control or corrective action [3, 11, 37-41]. As an example, in Figure 4 shows the operation of the algorithm for searching for the Area of Interest and extracting it on the sections of the time series of the chaotic process signal that are of interest to the researcher (color noise affects the Chen fractional system). The corresponding recurrent diagrams and distance matrices of the nonlinear recurrent analysis are constructed for the Areas of Interest highlighted on the time series chart. [37-39].

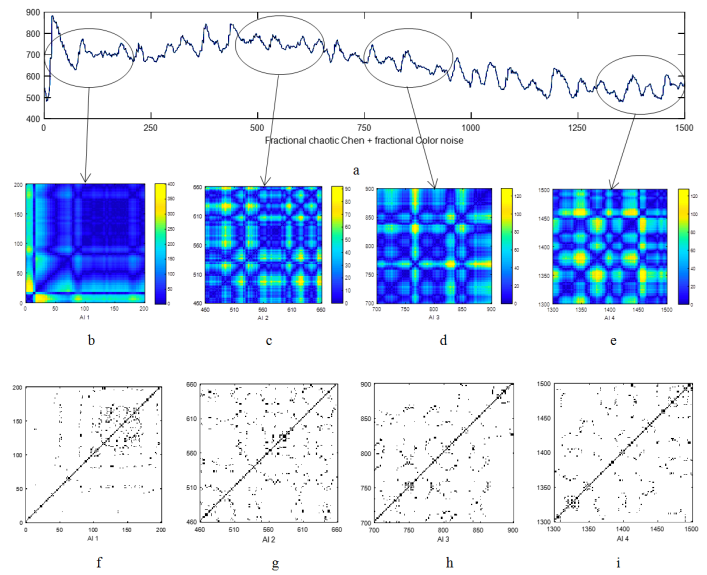


Figure 4: Interaction systems fractional Chen and Color noise: a – time series; b, c, d, e – distance matrix; f, g, h, i –recurrence plots.

3.5. Mixing Issues

Stirring is one of the key concepts in dynamical systems theory. The analysis of mixing processes of phase trajectories is an important part of studies of the behavior of chaotic systems. Lyapunov exponents, FTLE, Lagrangian coherent structures (LCS) are considered effective visual-informative indicators of the dynamics of chaotic systems, visual images of which allow one to assess the chaotic nature of the system, the presence of features on the trajectories of the system in the phase space.

An example of the spatial structure of FTLE, presented below (Figure 5), illustrates the features of phase trajectories and transitions of various states of a chaotic process during mixing and / or interaction of systems. [27, 28, 32].

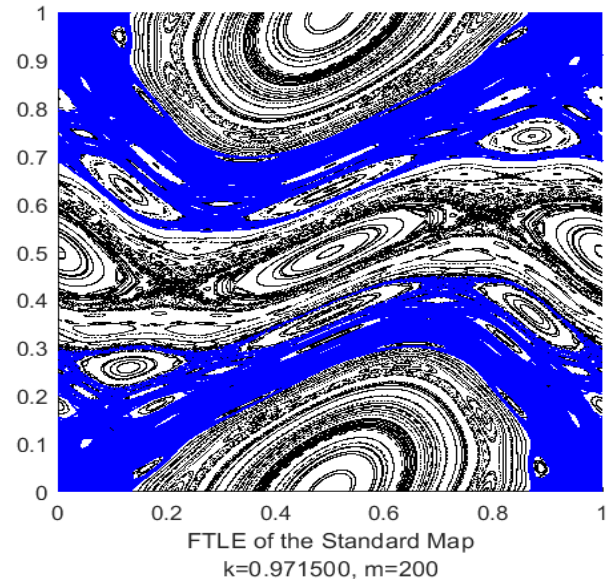


Figure 5: Visualization of characteristic parts of complex system behavior using FTLE.

4. Application of Artificial Intelligence Methodology for Research of Complex Technical Systems

The examples of visual information presented above are necessary for a comprehensive analysis and diagnostics of ongoing processes and making, on their basis, an informed decision to control or correct the behavior of a complex system.

Analysis, assessment of the situation and decision-making is the final stage of research, and is mainly based on various analytical and visual information (the value and information content of which is known to everyone), which complements knowledge based on Visual Thinking. All this predetermined further steps in the need to use artificial intelligence to solve the urgent problem of studying the behavior of complex technical systems [11, 39, 41, 42].

The above was a reasoned prerequisite for the application of the methodology Deep Learning methods based on Recurrence NN in the study of vibration processes in complex mechanical systems [11, 42-50].

The results of preliminary measurements, analyzes, simulations and transformations are used as input information for the Input Layer of Deep Learning architecture. The presented data are generalized and used as new knowledge for further analysis and evaluation using the Neural Network, which is part of the Deep Learning algorithm. As showed in Figure 6, the middle - Hidden Layer, is presented as a Recurrence NN algorithm, the work of which is to assess the dynamics of vibration processes taking into account the manifestations of system memory.

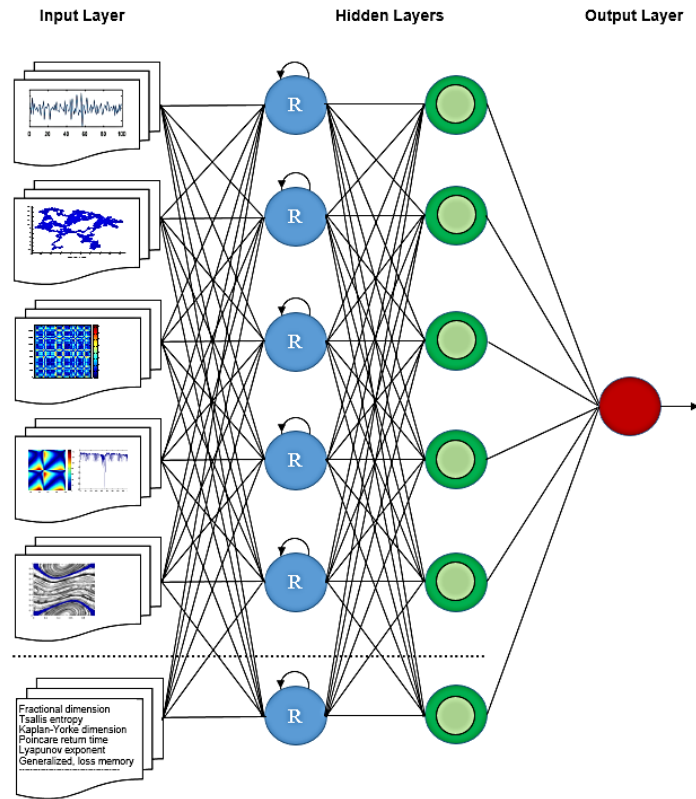


Figure 6: The structure of a recurrent neural network algorithm

Legend:

Input Layer components - time series of observed vibration processes, Levy's movements or other influences, recurrent plots of a fragment of the processes under study, stability of selected Areas of Interest, FTLE-graph of the information flow interaction area, calculated informative parameters and others; the Hidden Layer is represented by a recurrent algorithm and system memory, on which the dynamics and behavior of the system depend; the Output Layer - is the solution generated by the algorithm.

In addition, the Recurrence Neural Network algorithm in its work analyzes and uses the results of the calculated informative system parameters and the choice of control or corrective forces, taking into account the requirements of operating scenarios, etc. These algorithms may include the above-described iterative and evaluation algorithms for analyzing measurement information, visual images, time series, RP and FTLE plots, Lyapunov exponents, Tsallis entropy, fractal dimensions and other information that complements and contributes to a better understanding of the ongoing processes [27, 42, 44, 46, 48]. The solution to the problem posed to ensure the reliable operation of the monitored equipment can be represented as an output layer, in the form of recommendations to a person who decides on further actions to operate the equipment.

5. Conclusion

The article presents the main fragments of a large research work devoted to the problems of analyzing the vibration activity of complex power electromechanical equipment, presented in the form of an information model of nonlinear multidimensional chaotic processes. To generalize a large amount of parametric and visual information, modern methods of analysis and decision-making based on them were used. The structure of a deep learning algorithm based on Recurrence NN and Memory of system is substantiated and presented. Using DL to analyze and diagnose the state of a complex electromechanical system subject to vibration processes will increase the accuracy and speed of drawing conclusions about its condition and will facilitate informed decision-making based on all monitoring parameters.

Conflict of Interest

The authors declare that there is no conflict of interest regarding the publication of this paper.

Acknowledgment

The author expresses his deep gratitude to Vladimirsky E.I., for advice and assistance at the stages of writing the manuscript.

Funding

The work was not funded by third-party organizations, grants or sponsors, and was completely performed by the author as part of his research work.

References

- [1] A. Alimasi Low Frequency Vibration Visual Monitoring System Based on Multi-Modal 3DCNN-ConvLSTM. Sensors 2020, 20, 5872. 13. [doi: 10.3390/s20205872](https://doi.org/10.3390/s20205872)
- [2] B. Goswami, A Brief Introduction to Nonlinear Time Series Analysis and Recurrence Plots. Vibration. 2019, 2, 332-368. [doi: 10.3390/vibration2040021](https://doi.org/10.3390/vibration2040021)
- [3] B. Ismailov, An Analysis and Control of Dynamic Processes in Mechanical Parts of Power Equipment. International Journal of Mechanical and

- Production Engineering Research and Development (IJMPERD). **8**(5), 2018. 347-352. doi: [10.24247/ijmperdoct201839](https://doi.org/10.24247/ijmperdoct201839)
- [4] M. Ghazali, Vibration Analysis for Machine Monitoring and Diagnosis: A Systematic Review. *Hindawi, Shock and Vibration*. **2**, 2021, 25 p. doi: [10.1155/2021/9469318](https://doi.org/10.1155/2021/9469318)
- [5] G. Wojnar, R., Wieczorek A.N. and Konieczny Ł. Multidimensional Data Interpretation of Vibration Signals Registered in Different Locations for System Condition Monitoring of a Three-Stage Gear Transmission Operating under Difficult Conditions. *Sensors (Basel)*. 2021; **21**, 7808. doi: [10.3390/s21237808](https://doi.org/10.3390/s21237808)
- [6] X. Zhang, Sui T., Zhang H., Zhang Y., Liu L., Zhang Sh. An Active Vibration Control Method for Typical Piping System of Nuclear Power Plant. 2021 IEEE 10th Data Driven Control and Learning Systems Conference (DDCLS). doi: [10.1109/DDCLS52934.2021.9455612](https://doi.org/10.1109/DDCLS52934.2021.9455612)
- [7] B. Ismailov, Visualization of Measuring Experiments in a Context of Acceptance of the Decisions. 2nd world conference on soft computing. WconSC'12. Baku, 2012, 97-102.
- [8] E. Vladimírsky, Ismailov B.I. Synergetic methods of control of chaotic systems. Baku, "ELM" 2011. 240.
- [9] B.I. Ismailov The Visual Control of Vibration Dynamic System. *Eastern-European Journal of Enterprise Technologies*. **2012**(59). 25-30.
- [10] B.I. Ismailov. Thermodynamic – Informational Paradigm in the Context of the Formation of a Mathematical Model of Transient Processes in an Open System. *European Journal of Engineering Research and Science*, **2**(10), 2017. 17-20. doi: [10.24018/ejers.2017.2.10.494](https://doi.org/10.24018/ejers.2017.2.10.494)
- [11] J. Eckmann, Kamphorst S.O., Ruelle D., Recurrence Plots of Dynamical Systems. // *Europhysics Letters.*, **4**, 1987. 973-977.
- [12] H. Poincaré, Sur la probléme des trois corps et les équations de la dynamique. *Acta Mathematica*. **13**, 1–271. <https://projecteuclid.org/journals/acta-mathematica/volume-13/issue-1-2>
- [13] G. Robinson, Recurrence determine the dynamics. *Chaos* **19**, 023104. (2009). 1-6. doi: [10.1063/1.3117151](https://doi.org/10.1063/1.3117151)
- [14] Sprott J.C. *Chaos and Time Series Analysis*. Oxford University Press, 2003. 507p. <https://sprott.physics.wisc.edu/chaostsa/>
- [15] J.C. Sprott, Do We Need More Chaos Examples? *Chaos Theory and Applications (CHTA)*. **2**, Issue №: **2**. 2020. <https://dergipark.org.tr/en/pub/chaos/issue/54264>
- [16] E.I. Vladimírsky, Poincare returns time in the interaction of chaotic and stochastic systems. *Eastern-European Journal of Enterprise Technologies*. №6/4 (60). 2012. 4-8. doi: [10.15587/1729-4061.2012.5673](https://doi.org/10.15587/1729-4061.2012.5673)
- [17] D. Chen, Zhang R., Ma X., Liu S. Chaotic synchronization and anti-synchronization for a novel class of multiple chaotic systems via a sliding mode control scheme. *Nonlinear Dynamics*. **69**, 35–55, 2012. doi: [10.1007/s11071-011-0244-7](https://doi.org/10.1007/s11071-011-0244-7)
- [18] B.I. Ismailov , Simulation of Influences on the Dynamics of Transitional and Recurrent Processes of Complex Technical Systems. *International Journal of Innovative Technology and Exploring Engineering*. **9**(1), 2019. 4929- 4932. doi: [10.35940/ijitee.A8116.119119](https://doi.org/10.35940/ijitee.A8116.119119)
- [19] B.I. Ismailov, Poincare recurrence in open systems. *Journal of Multidisciplinary Engineering Science and Technology (JMEST)*. **3**(9), 2016. 5565-5569. chrome-extension://mhjfbmdgcfjbbpaeofofohoefgiehjai/index.html
- [20] E.I. Vladimírsky , Ismailov B.I. Transient and recurrence processes in open system. *International Journal of Advanced and Applied Sciences (IJAAS)*, **4**(10) 2017, 106-115. doi: [10.21833/ijaas.2017.010.015](https://doi.org/10.21833/ijaas.2017.010.015)
- [21] A. Daitche and Tél T. Memory effects in chaotic advection of inertial particles. *New Journal of Physics*. **16**, 2014. **31**, 073008 doi: [10.1088/1367-2630/16/7/073008](https://doi.org/10.1088/1367-2630/16/7/073008)
- [22] A. Dubkov, Spagnolo B., and Uchaikin V. Levy flight superdiffusion: An introduction. *International Journal of Bifurcation and Chaos*. (2008). 1-33. doi: [10.1142/S0218127408021877](https://doi.org/10.1142/S0218127408021877)
- [23] S. Murray, Metastable chimera states in community-structured oscillator networks. *Chaos* **20**, 013108, 2010. 1-5. doi: [10.1063/1.3305451](https://doi.org/10.1063/1.3305451)
- [24] T. Peng and Yan O. Torsional vibration analysis of shaft with multi inertias. *Scientific Reports*. 2022. **12**:7333. doi: [10.1038/s41598-022-11211-x](https://doi.org/10.1038/s41598-022-11211-x)
- [25] D. Marius-F., Kuznetsov N., Matlab code for Lyapunov exponents of fractional order systems. *International Journal of Bifurcation and Chaos*. **28**(05), 1850067 (2018). doi: [10.1142/S0218127418500670](https://doi.org/10.1142/S0218127418500670)
- [26] R.W. Ibrahim, and Maslina Daru. Analytic Study of Complex Fractional Tsallis' Entropy with Applications in CNNs. *Entropy*, 2018, **20**, 722; doi: [10.3390/e20100722](https://doi.org/10.3390/e20100722)
- [27] B. Sanjeeva Uncertainty in Finite-time Lyapunov Exponent computations. *Journal of Computational Dynamics*. American Institute of Mathematical Sciences **7**, №: **2**, 2020. 313–337. doi: [10.3934/jcd.2020013](https://doi.org/10.3934/jcd.2020013)
- [28] S.L. Brunton and Rowley C.W. Fast computation of finite-time Lyapunov exponent fields for unsteady flows. *Chaos* **20**, 017503 (2010). doi: [10.1063/1.3270044](https://doi.org/10.1063/1.3270044)
- [29] P. Varandas, Entropy and Poincare Recurrence from a Geometrical Viewpoint. *Nonlinearity*, **22**(10), 2009. 2365. doi: [10.1088/0951-7715/22/10/003](https://doi.org/10.1088/0951-7715/22/10/003)
- [30] B.I. Ismailov Numerical methods of control the hidden oscillations of fractional-order chaotic systems. *Journal of Multidisciplinary Engineering Science and Technology (JMEST)*. **3**(8), 2016. 5490-5494. chrome-extension://mhjfbmdgcfjbbpaeofofohoefgiehjai/index.html
- [31] E.I. Vladimírsky, Ismailov B.I. Fractional-order Chaotic Filter with Generalized Memory. *International Journal of Contemporary Applied Sciences*. **3**, No. **4**, 2016. 46-61. chrome-extension://mhjfbmdgcfjbbpaeofofohoefgiehjai/index.html
- [32] E.I. Vladimírsky Ismailov B.I. "Synchronization, control and stability of fractional order Hyperchaotic systems in the context of the generalized memory". *International Journal, of New Technology and Research (IJNTR)*, Volume-1, Issue-8, 2015. 42-48. <https://www.neliti.com/publications/263636/synchronization-control-and-stability-of-fractional-order-hyperchaotic-systems-i>
- [33] Ismailov B.I. Research of Dynamics of Coherent Behavior of a Complex Related Heterogeneous Structures. *Sciences of Europe # 27*, 2018. 60-64. <https://cyberleninka.ru/article/n/research-of-dynamics-of-coherent-behavior-of-a-complex-related-heterogeneous-structures>
- [34] E.I. Vladimírsky Ismailov B.I. Fractional Structure «MIXING – TRANSPORT» as open system. *Eastern-European Journal of Enterprise Technologies*. №4/4 (70). 2014. 4-9. doi: [10.15587/1729-4061.2014.26199](https://doi.org/10.15587/1729-4061.2014.26199)
- [35] K. Majumdar, Jayachandran S. A Geometric Analysis of Time Series Leading to Information Encoding and A New Entropy Measure. *Journal of Computational and Applied Mathematics*. 2018, **328**: 469 – 484. doi: [10.48550/arXiv.1810.05900](https://doi.org/10.48550/arXiv.1810.05900)
- [36] R. Chandrashekar, Ravikumar C. and Segar J. A Fractional entropy in Fractal phase space: properties and characterization. 2014. 22p. doi: [10.1155/2014/460364](https://doi.org/10.1155/2014/460364)
- [37] B.I. Ismailov, Nonlinear recurrent analysis in signal processing problems. *Sciences of Europe*. **1**, № **45**. 2019. 16-21. <https://cyberleninka.ru/article/n/nonlinear-recurrent-analysis-in-signal-processing-problems>
- [38] Y. Hirata, Recurrence plots for characterizing random dynamical systems. *Commun Nonlinear Sci Numer Simulat* **94** (2021) 105552. 20p. doi: [10.1016/j.cnsns.2020.105552](https://doi.org/10.1016/j.cnsns.2020.105552)
- [39] B. Hobbs and Ord A. Nonlinear dynamical analysis of GNSS data: quantification, precursors and synchronization. *Progress in Earth and Planetary Science*. 2018. 35p. doi: [10.1186/s40645-018-0193-6](https://doi.org/10.1186/s40645-018-0193-6)
- [40] A. Fragkou, Charakopoulos A., Karakasidis T. and Liakopoulos A. Non-Linear Analysis of River System Dynamics Using Recurrence Quantification Analysis. *AppliedMath*. 2022, **2**, 1–15. doi: [10.3390/appliedmath2010001](https://doi.org/10.3390/appliedmath2010001)
- [41] Y. Li and Li Z. Research on Recurrence Plot Feature Quantization Method Based on Image Texture Analysis. *Hindawi. Journal of Environmental and Public Health*. Volume 2022, Article ID 2495024, 12p. doi: [10.1155/2022/2495024](https://doi.org/10.1155/2022/2495024)
- [42] M. Evagorou, Erduran S. and Martyla T. The role of visual representations in scientific practices: from conceptual understanding and knowledge generation to 'seeing' how science works. *International Journal of STEM Education* (2015). 13p. doi: [10.1186/s40594-015-0024-x](https://doi.org/10.1186/s40594-015-0024-x)
- [43] T. Duries, Brunton S.L, Noack B.R. *Machine Learning Control - Taming Nonlinear Dynamics and Turbulence*. Springer, 2017. 211p.
- [44] S. Lee, Yu H.T., Yang H.J., Song I.S., Choi J.M., Yang J.H., Lim G.M., Kim K-S., Choi B.K. and Kwon J.W. A Study on Deep Learning Application of Vibration Data and Visualization of Defects for Predictive Maintenance of Gravity Acceleration Equipment. *Applied Sciences* 2021. **11**, Issue **4**. doi: [10.3390/app11041564](https://doi.org/10.3390/app11041564)
- [45] W.S. Lee, Flach S. Deep Learning of Chaotic Classification. *Computing Science > Machine Learning*. Science and Technology. 2020. Volume **1**, Number **4**. doi: [10.1088/2632-2153/abb6d3](https://doi.org/10.1088/2632-2153/abb6d3)
- [46] O. Avcı, Abdeljaber O., Kiranyaz S., Hussein M., Gabbouj M., Inman D.J. A review of vibration-based damage detection in civil structures: from traditional methods to Machine Learning and Deep Learning applications. *Mechanical Systems and Signal Processing*. 2021. **147**, 107077. doi: [10.1016/j.ymssp.2020.107077](https://doi.org/10.1016/j.ymssp.2020.107077)
- [47] J. Pathak, Zhixin Lu, Brian R. Hunt, Michelle Girvan, Edward Ott. Using machine learning to replicate chaotic attractors and calculate Lyapunov exponents from data. *Chaos*. **27** (12), 2017. doi: [10.1063/1.5010300](https://doi.org/10.1063/1.5010300)
- [48] T. Wang et al., Fault diagnosis of rotating machinery under time-varying speed based on order tracking and deep learning. *Journal of Vibroengineering*, **22**(2), 2020, 366-382. doi: [10.21595/jve.2019.20784](https://doi.org/10.21595/jve.2019.20784)

- [49] L. Xiong Liu J., Song B., Dang J., Yang F. and Lin H. Deep learning compound trend prediction model for hydraulic turbine time series. *International Journal of Low-Carbon Technologies* 2021, 00, 1–7. Published by Oxford University Press. [doi: 10.1093/ijlct/ctaa106](https://doi.org/10.1093/ijlct/ctaa106)
- [50] J. Xu, Hugelier S., Zhu H., Gowen A.A., Deep learning for classification of time series spectral images using combined multi-temporal and spectral features. *Analytica Chimica Acta* 1143, 2021. 9-20. [doi: 10.1016/j.aca.2020.11.018](https://doi.org/10.1016/j.aca.2020.11.018)

Design of an Off-Grid Hybrid Energy System for Electrification of a Remote Region: a Case Study of Upper Blink Water Community, South Africa

Lukanyo Mbali*, Oliver Dzobo

Department of Electrical and electronics Engineering Science, University of Johannesburg, Johannesburg, 2117, South Africa

ARTICLE INFO

Article history:

Received: 29 May, 2022

Accepted: 11 July, 2022

Online: 09 September, 2022

Keywords:

HOMER

Solar PV

Diesel generator

Upper blink water

Hybrid energy system

ABSTRACT

Electrifying or connecting remote and isolated communities to the national grid is very difficult and expensive. This challenge is due to the geographic locations of these isolated communities and terrain that needs navigation when installing transmission lines to transmit power to the communities. This article presents a case study of the design of a hybrid energy system for electrification of a remote region in South Africa. Upper blink water is about 20km away from the national grid. An effort has been made to design hybrid energy system which consists of solar photovoltaic (PV), diesel generator and battery storage. Homer software used to evaluate the technical characteristics and efficiency of the proposed hybrid energy system. Reticmaster software used to calculate the voltage drops of distribution lines to the residential houses of the communities. The results show that it is feasible to supply the isolated community with the proposed hybrid energy system. The average electricity cost is R1.1093c/kWh and the amount of diesel fuel per year is 16685L/year.

1. Introduction.

This article comes as results of previously presented and an extension of a paper originally presented in the IEEEAFRICON 2021 conference [1]. Electrical Energy is among of the most vital resources in the world and its usefulness across the globe cannot be emphasised. The use of electricity is widespread in manufacturing, telecommunication, many other field such as residential and commercially[1]. Electricity can be produce by variety of sources including nuclear, hydro, wind solar, and thermal. Electricity can be classified into two main groups namely, sources of non-renewable energy and renewable energy. The demand for energy across the world is constantly rising. The increase of energy demand is a result of population growth, economic development and the introduction of many electrical appliances. In addition, the cost of power generation, availability of resources, environmental effects, and other factors have brought many challenges to provision of electricity to many communities in the world [2]. Electrification of remote and isolated communities is a significant issue when discussing future energy access in a country[3]. South Africa has an average of 89% grid access in 2016, with renewable energy sources contributing 11%[4]. According to the 2016 statistics, coal accounted for 69 percent of South Africa's primary energy supply. Crude oil had a 14 percent share, nuclear had a 3% share and natural gas had a 3% share of the industry[4]. Many communities have been given

access to electricity through South African government programs, among other programs; through private sector investments in wind energy, small hydro and biomass[4]. Off-grid hybrid energy systems has gained a lot of popularity due to its ability to operate in remote areas where the conventional grid cannot be access. In most cases, storage units used to complement the intermittent power generation from renewable energy sources such as solar and wind. Several research studies been carried out to ascertain the feasibility of hybrid energy systems in providing electricity to remote regions [3]. Modelling and cost analysis of a hybrid energy system for a remote island in Bangladesh - St. Martin Island were done using HOMER software [5]. The proposed hybrid energy system consists of solar PV, wind turbine and diesel generator. HOMER software is used to determine the most cost effective configurations among a set of system options for electricity requirement of 53 kWh/day primary load with 10 kW peak load[5]. The results from the analysis showed that the proposed hybrid energy system gives a cost of electricity COE of USD 0.224 and a total net present cost (NPC) of USD60, 832.93. The renewable power generation contribution to the total electricity requirement for the island is 77 percent. Another case study been done for a health clinic in a rural area in southern Iraq[6]. HOMER software used to estimate the system size and its life cycle cost. The total daily load of the health clinic is 31.6 kWh. The analysis showed that the optimal system initial cost, net present cost, and electricity cost is US\$50,700, US\$60,375, and US\$0.238/kWh, respectively [6]. Based on the literature reviews,

*Corresponding Author: Lukanyo Mbali, Lukanyombali@gmail.com

the Homer software been adopted in this paper to analyse the feasibility of the proposed hybrid energy system. The analysis of the voltage drop for transmitting the power to the community residential houses conducted using Reticmaster software. Upper blink water is the community selected as a case study for design of hybrid energy system. It is located in Fort Beaufort, Eastern Cape, South Africa consisting of 43 households and is about 20km away from the national grid.

2. Case study description.

2.1. Weather and Location.

The community of Upper Blink Water is located about 20 kilometres from the national power grid. Because electricity is scarce in Upper Blink Water, an alternative energy sources required. This area considered one of the sunniest in the Eastern Cape Province. This community reached using GPS coordinates of latitude: -32034'0.01", longitude: 26032'60". Figure 1 shows the temperature range in Upper Blink Water community area. It varies between 2.6°C and 31.8°C with a median temperature of 17.5°C based on the long-term average. This data obtained from NASA (National Aeronautics and Administration) Perdition of Worldwide Energy Resource Power database[7].

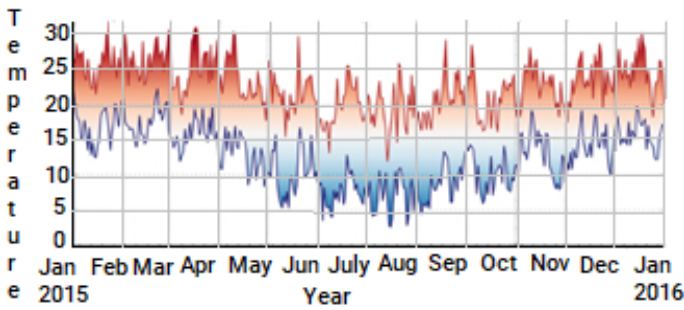


Figure 1: Ambient Temperatures throughout year.

Table 1 and Figure 2 shows the solar radiation for the considered area. The area experiences annual average radiation of 6.33 kWh/m²/d. and daily solar energy yield ranges between 2.5 kWh/m²/d and 8.8 kWh/m²/d. The highest solar radiation occurs

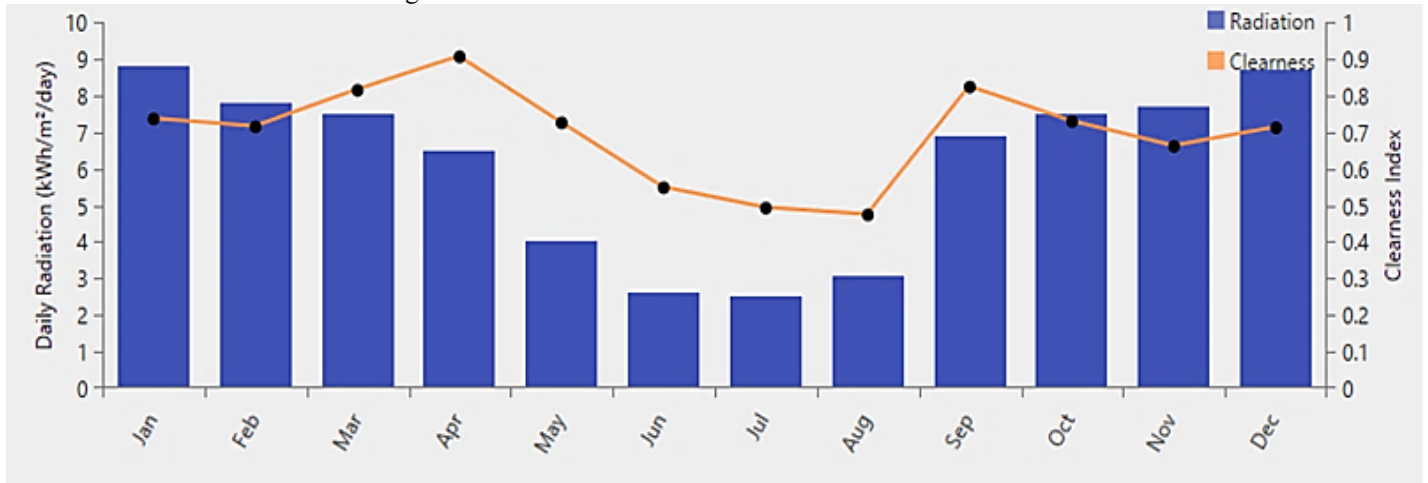


Figure 2: Monthly Average Solar Irradiance

during the summer season between Jan –Apr and Aug-Dec. The lowest solar radiation experienced during the winter season between May-July. The monthly average solar radiation data was taken from NASA (National Aeronautics and Administration) Perdition of Worldwide Energy Resource Power database[7].

Table 1: Upper Blink Water Community average solar radiation

Month	Clearness Index	Daily Radiation (kWh/m ² /day)
Jan	0.74	8.8
Feb	0.71	7.8
Mar	0.81	7.5
Apr	0.90	6.5
May	0.72	4.0
Jun	0.54	2.6
Jul	0.50	2.5
Aug	0.47	3.5
Sep	0.82	6.9
Oct	0.73	7.5
Nov	0.71	7.7
Dec	0.73	8.7

2.2. Load Model

Upper Blink Water community expected load shown in Table 2. Lights, cookers, and entertainment expected to be use by the community. The author collected data through site visits, interviews with community members, and questionnaires. Table 2 and Figure 2 summarize the results. Table 2 shows the community expected load. The details of the interviews and questionnaires not detailed in this article.

In Figure 3, all the households in the community are show with their load profiles. A peak load of 13.1kW estimated for the evening. This load expected as many people will go home after returning from work, and they will use electricity to warm the water for bath and to cook.

Table 2: Expected usage of Electricity by Upper Blink water community.

Load of the Community		Peak load (W)	Average Load(W)
Lighting	LED lights	7W	7W
Entertainment	TV/Video/Satellite	120W	120W
	Radio	20W	20W
	Laptop	50W	50W
	Smart Phone Charger	1W	1W
Cooking	Stove (4 plate)	3000W	1500W
	Stove(2 plate)	2000W	1000W

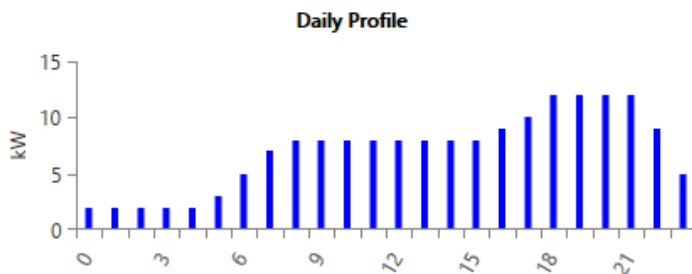


Figure 3: Load Profile for the case study.

3. Proposed Energy System Design configuration.

The HOMER software, NREL’s micro-power optimization model is employed to evaluate a range of equipment options over varying constraints to optimize the proposed hybrid energy system[8]. It gives a list of feasible system configuration options that are rank according to their cost effectiveness. Figure 4 shows a schematic block diagram for the proposed hybrid energy system.

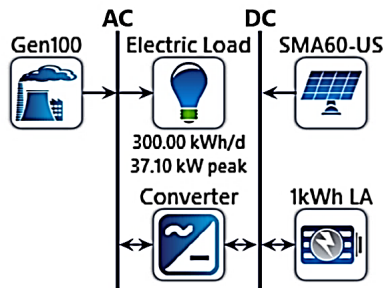


Figure 4: System Design Configuration for Upper Blink water.



3.1. System components Description

The following are the major components of the proposed hybrid energy system:

A. **Photovoltaic Cells (SMA60 – US)** PVs are the primary power converters. Solar energy converted into electricity using semiconductors. A photovoltaic cell usually produces only one or two watts of power, which is quite small. When photovoltaic cells connected together, they produce more power. These units are called modules. Each module connected to other modules to form large units known as

panels and arrays. A polycrystalline panel was considered for this research study. The efficiency of polycrystalline panels is very high. It is necessary to use a bypass diode (Schottky diode) between the battery bank and the panels to protect them from reverse current. Table 3 shows the polycrystalline solar PV cells specifications used in this paper

Table 3: Solar panel specifications[9].

Electrical Characteristics at Standard Test Conditions (STC).		
Module Type: TW P -72	325	 Solar panel
Peak Power Watts- P_m [W]	325	
Open Circuit Voltage- V_{oc} [V]	45.6	
Short Circuit Currents I_{sc} [A]	9.28	
Maximum Power Voltage - V_m [V]	37.1	
Maximum Power Current- I_m [A]		
Module efficiency [%]	16.8	
Electrical Characteristics at Normal Operating Cell Temperature (NOCT)		
Peak Power Watts- P_m [W]	225	 Solar Array
Open Circuit Voltage- V_{oc} [V]	41.4	
Short Circuit Currents I_{sc} [A]	7.26	
Maximum Power Voltage - V_m [V]	33.4	
Maximum Power Current- I_m [A]	6.74	
<p>“Note1. Standard Test Conditions (STC): irradiance 1000W/m² AM1.5: ambient temperature 25°C according to EN 60904-3; 2. Nominal Operating Cell Temperature (NOCT): Irradiance 800W/m²; Wind speed 1m/s; cell temperature 45°C; ambient temperature 20°C. Tolerance of P_m 0-+5%, Measuring uncertainty of power +-3%, Performance deviation of V_{oc} [V], I_{sc}[A], V_m [V] and I_m [A]:+-5%”</p>		

- B. **Battery Bank (315kWh LA):** The solar panels generate excess electricity that is stored in the battery. This research study utilized flooded lead acid batteries because they have a long lifespan and are inexpensive per amp hour. During the day, excess energy generated by the solar panels charges the batteries. The battery storage will discharged at night and in the early morning when the sun is not out, providing electricity to the community load. The batteries were set to a state of charge (SOC) of 30% and 90%, respectively. A combination of these settings prevents deep discharges and overcharging of the batteries respectively.
- C. **Charge Controller:** Charge controllers manage the current flowing between the batteries and the panels. The purpose of this device is to prevent battery overcharging. A charge controller usually includes special electronics that level out the charging process automatically [4]. Batteries are prevented from being overcharged by charge controllers that block reverse current. The MPPT charge controller is selected for this research study since it uses a multiple stage charge method based on the PV conditions[10].

D. *Inverter (Converter)*: By using an inverter, DC electricity can be converted to AC electricity. An inverter converts DC voltage from solar panels to AC voltage. An inverter classified according to the format of its output wave, its output power, and its type of installation. Since an inverter changes the form of electricity, sometimes referred to as a power conditioner. Modified sine waves (MSWs) or pure sine waves are both possible output waveforms of an inverter[11]. The use of MSW inverters is usually more economical and efficient than sine wave inverters, while sine wave inverters offer higher performance and can operate on virtually any load. Sunny Central Technologies' MSW inverters were selected because they have a maximum power point tracking capability (MPPT) and utility fault protection capabilities[6]. Depending on the system voltage and output voltage requirements, inverted systems with 400V AC 3-phase and 230V AC single-phase output voltages selected.

4. Proposed Energy System Sizing.

4.1. Solar PV Module sizing.

When sizing the solar panels the total daily energy (E), the average sunny hours per day, and the system voltage (Vdc) are used. A tool called the Distribution Pre electrification Tool (PET) is used to predict community electricity consumption and demand for a 15-year period[12]. This research study used 1,29kVA of After Diversity Maximum Demand (ADMD) power and 300 kWh of total load in its research. An ADMD calculated based on the government-specified income for a rural village in South Africa. Using 1.2kVA ADMD per household with a circuit breaker size of 20 Amps, a household income of R1500 per month would equal a Government pension rate of R1500 per month[12].

According to Figures 5 and 6, the site expected to have a maximum demand for electricity and electric consumption.

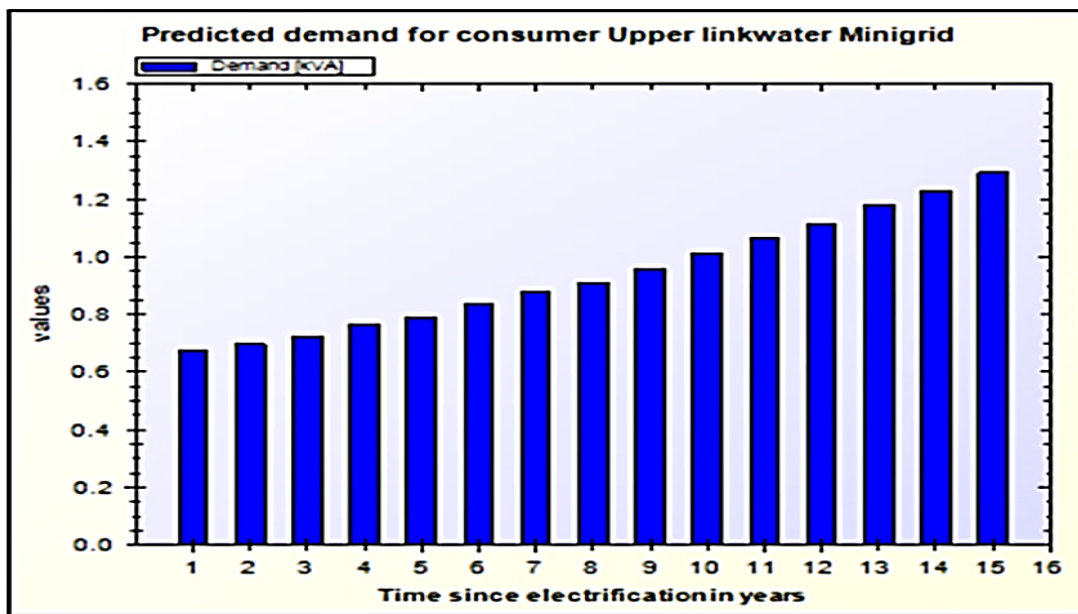


Figure 5: 15-year period-predicted electricity demand by the community[12].

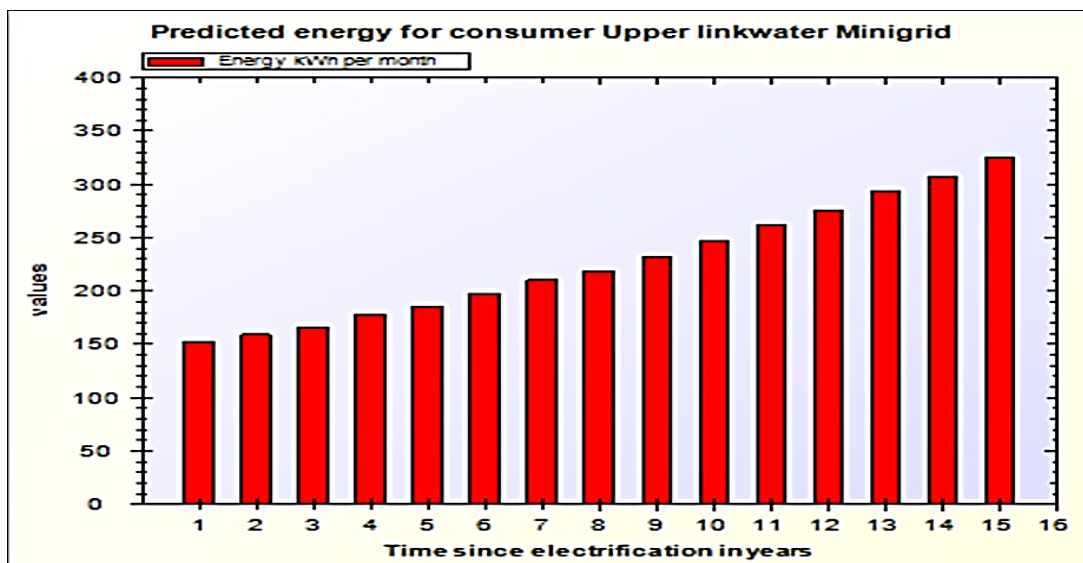


Figure 6: 15-year period-predicted electricity usage by the community[12].

Equations (1) - (5) are required to calculate the PV array (WP) and the maximum power required to operate the solar module.

$$\frac{MP(\text{Maximum Power})}{\text{Number of Households} \times (\text{ADMD})} = \text{PV array (wp)} \quad (1)$$

$$\frac{E_{tot}}{(\text{SPH} \times \text{Beff} \times \text{PV derating Factor})} \quad (2)$$

$$\frac{\text{Total Number of Modules: Nm}}{\text{PV Array size}} = \frac{\text{Modules Rating}}{\text{Modules Rating}} \quad (3)$$

$$\frac{\text{No of Modules in string: Nms}}{\text{System Voltage}} = \frac{\text{Module Normal Voltage(V)}}{\text{Module Normal Voltage(V)}} \quad (4)$$

$$\frac{\text{Number of Modules in parallel: Nps}}{\text{String in Series}} = \frac{\text{Number of Modules}}{\text{String in Series}} \quad (5)$$

where: **Etot**: Total energy Demand (Wh/d) = 300 kWh.

SPH: Solar Peak Hour (h/d) = 6.3

Beff: Battery efficiency (%) = 80%

PV der: PV derating factor (percentage) = 80%

4.2. Sizing of battery bank.

Batteries arranged into battery banks according to their voltage ratings and the needs of the system, which may be in series or parallel. The voltage of the battery usually chosen based on the energy system and the load. Batteries power photovoltaic systems connected to the grid. They are used as backup power supply during times when there is no sunshine. 12V battery voltage selected for this proposed hybrid energy system. Equations (6) - (10) are required to calculate the battery size and number of battery required for the system.

$$\frac{E_{tot}(\text{Daily Enenergy Demand})}{\text{Inverter efficiency}} = \frac{\text{Energy daily load (Edl)}}{\text{Inverter efficiency}} \quad (6)$$

$$\frac{E_{tot} \times T_{aut}}{\text{System Voltage} \times \text{DoD} \times \text{Beff}} = \text{Bttery sise(Ah)} \quad (7)$$

Equations 8 and 9 used to calculate the number of batteries required in parallel and series:

$$\frac{\text{No of Batteries (series)}}{\text{Battery Nominal Voltage(V)}} = \frac{\text{System Voltage}}{\text{Battery Nominal Voltage(V)}} \quad (8)$$

$$\frac{\text{No of batteries: (parallel)}}{\text{Rate per battery}} = \frac{\text{Total battery Size}}{\text{Rate per battery}} \quad (9)$$

$$\frac{\text{No of Batteries (Total)}}{\text{No of batteries(S)} \times \text{No of batteries (P)}} \quad (10)$$

where:

$E_{tot} \text{ (WH)} = \text{Daily energy demand}$

Beff: =Battery efficient typically: 80%

VBB =Battery nominal voltage: 2VDC

DOD= Depth of discharge: 80%

Taut: =Number of days of autonomy: two.

Selected Battery Ah Rating = 1500 Ah

Selected system voltage = 360 VDC

Since the system, voltage is 360VDC, the number of 12 volts batteries required in series is:

$$E_{tot} = \frac{Edl}{\text{Inverter eff}} = \frac{300kW}{95\%} = 315.8kW$$

$$\text{Battery Size(Ah)} = \frac{315 \text{ 800Wh} \times 2}{360 \times 80\% \times 80\%} = 1370.61Ah$$

$$\text{Number of batteries in a string} = \frac{2160}{12} = 180 \text{ batteries}$$

$$\text{Batteries (total)} = 1 \times 180 = 180.$$

4.3. Sizing of inverter (converter).

An inverter converts DC voltage from solar panels to AC voltage. An inverter classified according to the format of its output wave, its output power, and its type of installation. Since an inverter changes the form of electricity sometimes referred to as a power conditioner. Modified sine waves (MSWs) or pure sine waves are both possible output waveforms of an inverter. The use of MSW inverters is usually more economical and efficient than sine wave inverters, while sine wave inverters offer higher performance and can operate on virtually any load. Sunny Central Technologies' MSW inverters were selected because they have a maximum power point tracking capability (MPPT) and utility fault protection capabilities[6]. Depending on the system voltage and output, voltage requirements, inverted systems with 400V AC 3-phase and 230V AC single-phase output voltages are selected. The inverter selected based on the following characteristics:

- Must have a D.C input voltage of between 240 V and 480 V to minimize cable sizes.
- Must have efficiency at full load of above 95% to minimize losses.
- Must have the ability to perform maximum power point tracking to minimize the number of panels needed. Must have an in-built battery charging features.

The inverter size is determined as follows:

$$\text{Ac Loads (Total)} \times \text{Oversize Factor} = \text{Size of the inverter} = \quad (11)$$

$$\text{Inverter Size} = 55.5kW \times 1.25 \text{ (factor)} \times 1.25 = 69.34kW$$

An oversize factor of 1.25 is normally used in the sizing of an inverter for any energy system. In the case of an unexpected increase in load, the oversize factor is applied, otherwise if the actual calculated size of the inverter is used it will overheat and/or

burn due to current flow increase. The size of inverter chosen for each phase is 30 kW.

4.4. Backup Generator.

Diesel generators are also essential components of a hybrid energy system. Using different energy sources, power generators generate electricity by converting the motion of combustion engines into kinetic energy. The diesel generators (back up) selected according to their maximum power and voltage requirements. The backup generator used if the PV power generation system cannot meet the entire load.

The backup generator should have the ability to operate independently for at least a few days, providing enough energy until reaching its maximum output power. This is necessary especially during days when the sun is not shining. The backup generator selected based on the maximum power required and on the loading voltage required. The backup generator used to supply the load during the time when PV power generation supply is not able to supply the entire load. A diesel generator of 80 kW used in the case study. The backup generator is connected to the ac bus of the proposed hybrid energy system. Minimum output of the generator is set at 25 kW. The back-up generator should be able to run at least 2 days independently and supply the necessary power up to its maximum power output. Table 4 shows the specifications of the backup generator used in the case study.

Table 4: Back-up generator specifications.

Quantity	Value	Units
Electrical Production	13,677	kW
Minimum Electrical Output	25.0	kW
Maximum Electrical Output	67.2	kW
Fuel consumption	14,992	L
Specific Fuel consumption	0.365	L/kWh
Fuel Energy Input	49,120	kWh/year
Mean electrical Efficiency	31.1	%
Hours of operation	547	hrs./year
Number of starts	389	starts/year
Operational life	27.4	Yr.
Capacity Factor	1.56	%
Fixed generation cost	58.8	R/hr.
Marginal generation cost	4.87	R/kWh

4.5. Reticulation Simulation.

Reticmaster is a network analysis tool, which used to calculate voltage drops, sizing cables and calculating fault currents. The Low Voltage reticulation design chosen in this proposed design based on Eskom specifications for Low Voltage reticulation. This done in order to determine the line lengths and conductor sizes to cover the area. The distribution system consists of two main lines leaving the supply side of the proposed hybrid energy system. The total length of the distribution lines is about 2 km including minor connecting lines. All distribution lines need to fulfil Eskom standards. The electrical grounding is facilitated

at the community houses. The number of connected houses is 43 households. Table 5 shows the length of the distribution lines and the number of community houses connected.

Table 5: Length of Distribution Lines.

Northern lines	
Main line length	741 m
Line 1	114 m
Line 2	120 m
Line 3	100 m
Line 4	270 m
Line 5	82 m
Line 6	55 m
Number of Households connected	28
Southern Lines	
Main line length	595 m
Number of connections	15
Total length of Distribution lines	1 336 m
Total number of connections	43

Figure 8 shows a snapshot of part of the reticulation design using Reticmaster software.

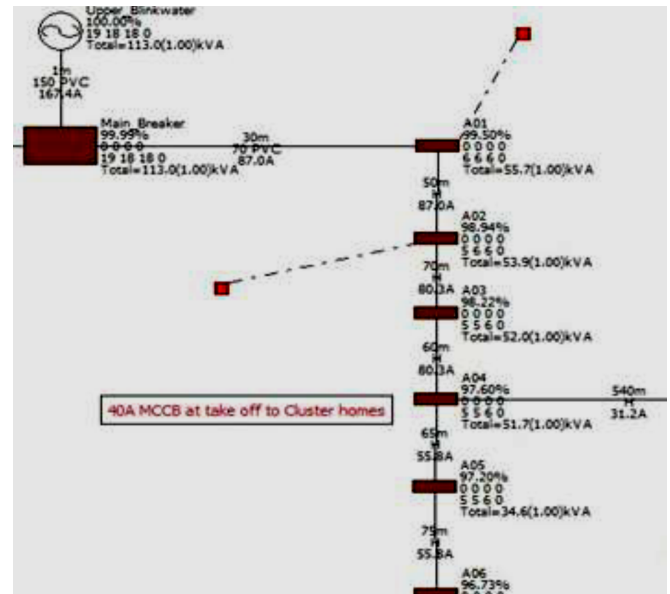


Figure 7: Low Voltage simulation using Reticmaster

Due to the layout and spread of the village, the Low Voltage lines are longer and therefore thicker conductors used so that the voltage profiles are within the statutory limits. Equations (12) and (13) used to calculate the voltage drops, sizing cables and calculating fault currents.

$$\text{Voltage Drop} = L(\text{distance}) \times Z(\text{impedance}) \times I_f(\text{Fault current}) \quad (12)$$

$$\% \text{Voltage Drop} = \frac{\text{Voltage Drop}(VD)}{\text{Phase Voltage}(V_{ph})} \times 100\% \quad (13)$$

5. Results and Discussions

The analyses and results generated or obtained from the HOMER and Reticmaster software for this proposed system. The objective is to get the lowest cost per kWh and the lowest NPC of an off-grid hybrid energy system. Table 6 and 7 optimization

results and optimal least cost off-grid hybrid energy system for Upper Blink-water.

Strategy	Charging
----------	----------

Table 6: Optimization Results for the research study.

Power Generation components (Mix)	Total Net Present Cost (NPC)	Cost of Electricity (COE)	Renewable fraction (%)
Solar PV/ Diesel Gen Battery/Inverter	R1.68M	1.23	87.2

The annual PV power production is 127 475 kWh/yr. Figure 7 shows the PV power output for the whole year. It can be clearly seen that during the winter period between May - July the PV power output is lowest. This is because of the low solar radiation experienced during this period. In summer, period between the months of September – April the solar radiation is high and thus high PV power output experienced during this period.

Table 7: Optimal least cost off-grid hybrid energy system for Upper Blink-water

Cost Summary		System Architecture		Electrical		
Total NPC	R1.68M	PV Array	60kW	Components	Production	Fraction (%)
Levelized COE	R1.23/kWh	Diesel Generator	100kW	PV Array	127,475kWh/yr	90.3
Operation Cost	R113.15	Batteries	180x 12V strings	Diesel Generator	13,677kWh/yr	9.69
		Inverter	30kW	Total	141.152kWh/yr	100
		Rectifier	30kW			
		Dispatch	Home Cycle			

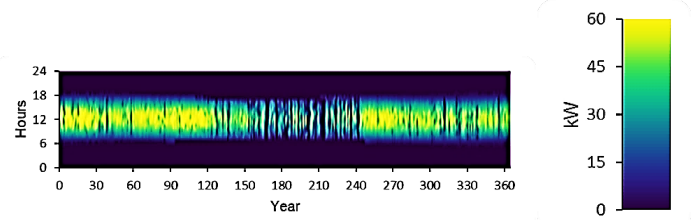


Figure 8: PV Power Output.

The total amount of electricity produced by the hybrid energy system in a given year. Figure 8 shows the electrical production proposed model. The total electrical production calculated is 141,152kWh/y.

The annual throughput of the battery bank is 56,509 kWh/y. Figure 8 shows the state of charge of the battery bank for the whole year. The graph shows that the state of charge of the battery bank is higher during summer season than in the winter period. This is because during the summer season the PV power out is very high and is able to supply the whole community load and the excess power used to charge the batteries.

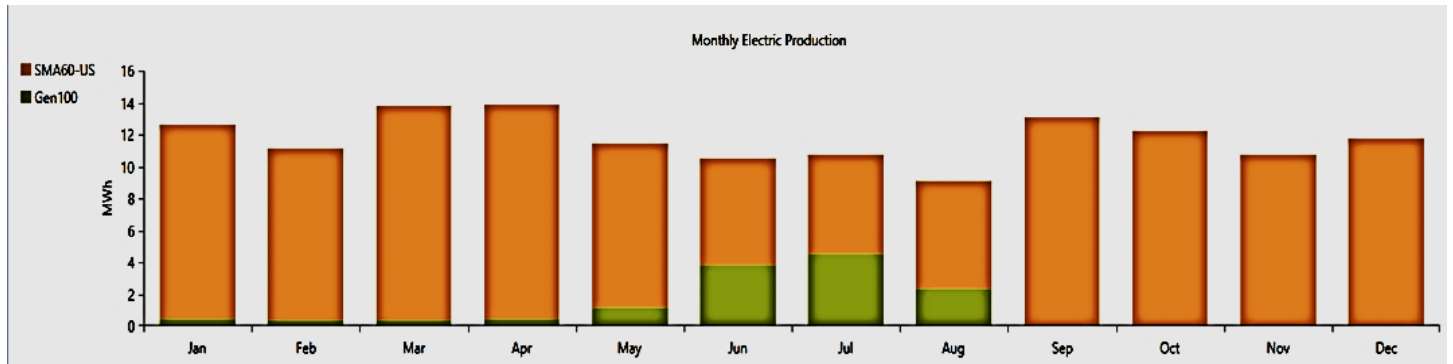


Figure 9: Electrical production for the proposed model.

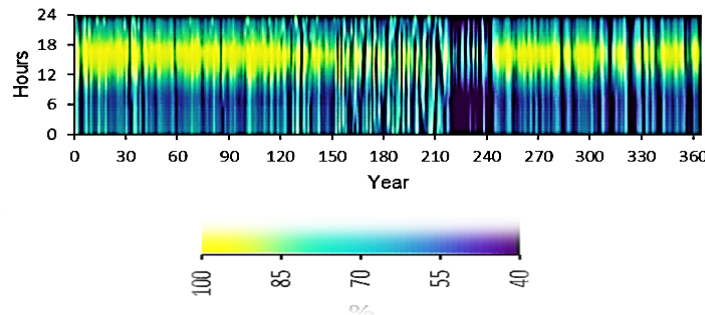


Figure 10: Battery State of charge.

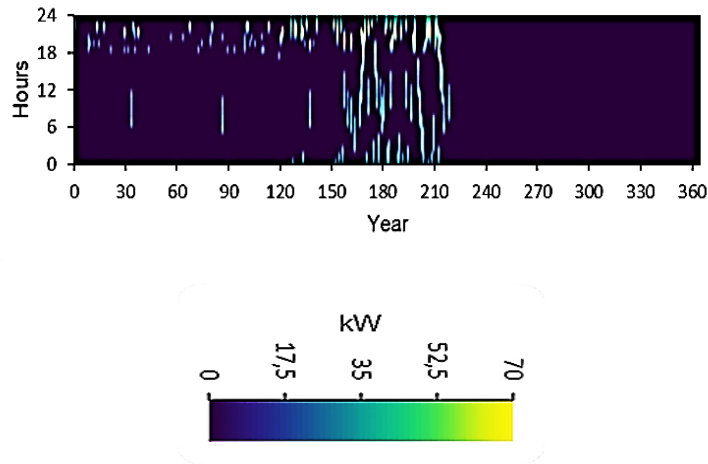


Figure 11: Generator Power Output.

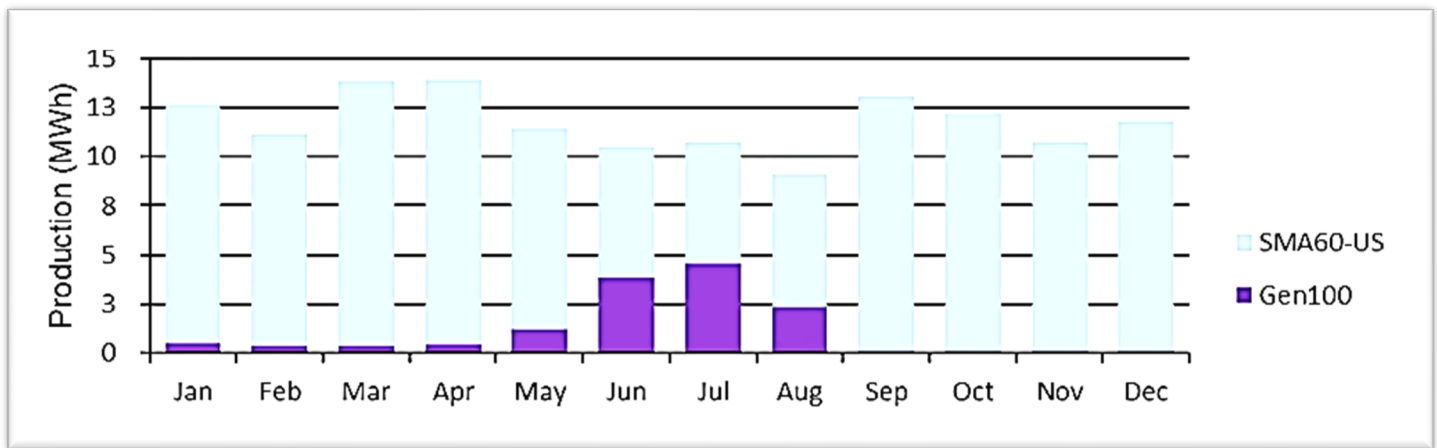


Figure 12: Energy balance of the hybrid energy system.

Figure 10 below shows the operation of the back-up generator. It is clear from the graph that the backup generator operated frequently during the winter period than in the summer period. The total number of hours of operation of the backup generator is 547 hours per year and it has 389 start-ups for the whole year. The total amount of fuel that is used by the generator is 4992 litres of diesel per year.

During the winter period between May and August shows that the PV power generation and the generator power is sometimes not adequate to supply the whole load. This indicated as energy not supplied in Figure 11. This means the operator of the hybrid energy system would have to load shed some of the community load. The shortage in electricity production by the PV generation unit is because of the low solar radiation that is experienced during the respective time. The PV power generation unit supplied 90.4% and the diesel generator only supplied 7.89 % of the total annual load for the community. The most expensive system configuration option is when only the diesel generator used to supply the total load.

Figure 12 shows the voltage drops for the different distribution lines that feeds power to the community houses. From the graph, shows that between the distances of 0 m – 156 m the maximum voltage drop is 4 %. The voltage drop increased as the length of the distribution line increases. A maximum voltage drop of 9 % occurs at a distance between 780m – 1560m.

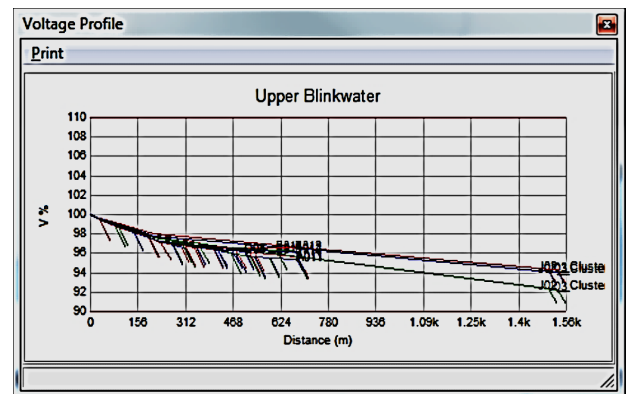


Figure 13: Voltage drops (%) vs Distance (m).

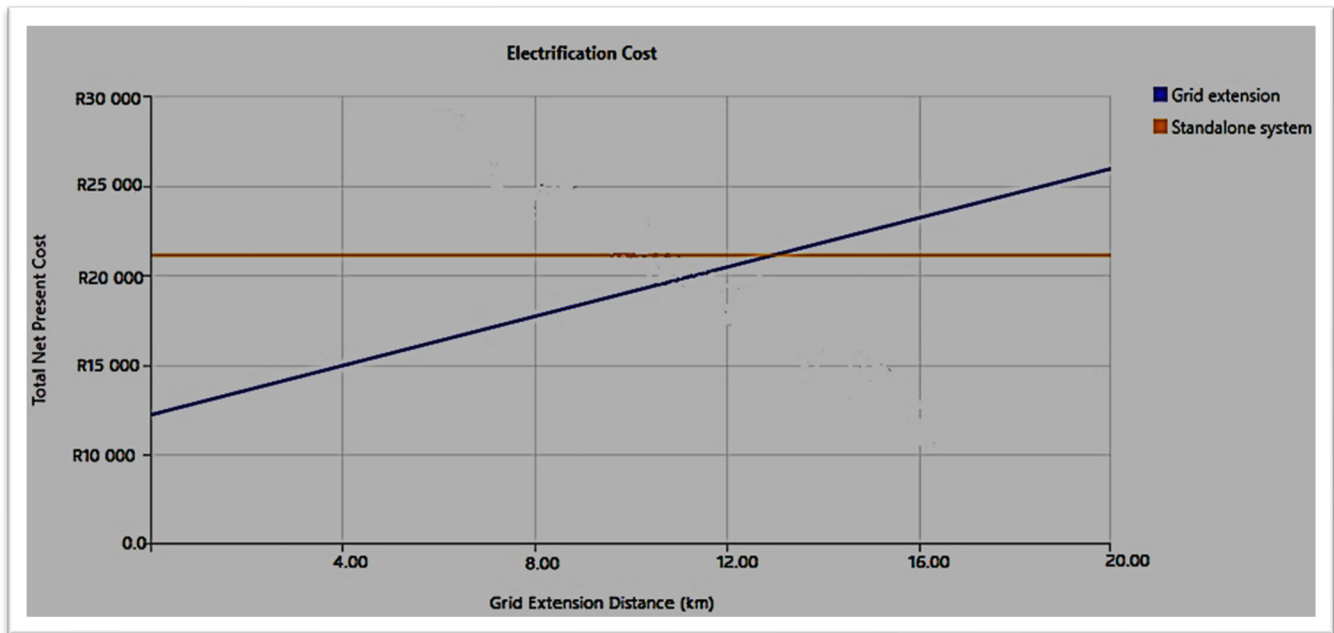


Figure 14: The breakeven distance for grid extension for proposed Upper Blink Water off grid.

When comparing grid extensions and off-grid hybrid energy systems is possible with the Grid Extension. An off-grid energy system was considered more appropriate during this research study than a grid extension. Upper Blink Water community is estimated to have an ICC (initial capital cost) of R22 000/km for the extension of the national grid. The annual O&M (operational and maintenance) cost examined is R8000/km and national grid power, power price is R0.107/kWh. Figure 14 present the results of break-even analysis showing the proposed hybrid energy system and grid extension for the electrification of Upper Blink Water. According to this figure 14, the breakeven grid extension distance is 12.2 km, which display that the designed stand-alone hybrid energy system is more cost effective than the grid extension as the nearest transformer from Upper linkwater is located 20 km away.

6. Conclusion

This article present a design of a hybrid energy system for a remote region as a case study. The main goal was to determine if solar PV could be used as an energy source for Upper Blink Water community in a reliable and cost-effective way. After many simulations conducted, it is show that solar power generation using solar panels is an effective alternative energy source where can be option for supplying isolated, remote areas where the grid extension or grid is not available. A cost-effective system configuration option for Upper Blink Water community in South Africa has been determined with the help of two software packages, HOMER and Reticmaster. The community consumes 300-kilowatt hours per day. A 60 kWp PV system, a total number 180 lead acid batteries (1500Ah, 12V), and a 30kW inverter were proposed for an off-grid hybrid energy system. Electricity costs on average was R1.1093 cents per kilowatt-hour, while the amount of diesel fuel consumed each year is 16685 litres. According to the optimal solution, stand-alone hybrid energy

systems are economically feasible for rural electrification in remote, isolated and small communities, where the national grid require extension beyond 20 km. In this case, study the breakeven distance was found to be 12 km.

Conflict of Interest

The authors declare no conflict of interest.

Acknowledgment

The authors of this paper would like to acknowledge the Eastern Cape Department of Economic Development, Environmental Affairs and Tourism (DEDEAT) who sponsored this research project, in close collaboration with the Raymond Mhlaba Local Municipality(RLM), the Lower Saxony ministry of environment (MU), DEULA-Nienburg and the Deutsches Zentrum für Luftund Raumfahrt (German Aerospace Center) DLR institute. The authors also acknowledge the University of Johannesburg.

References

- [1] L. Mbali and O. Dzobo, "Design of an off-grid hybrid pv/diesel energy system with battery storage for electrification of a remote region: A case study of upper blink water community, south africa," *IEEE AFRICON Conf.*, 2021-Sept, 2021, doi: 10.1109/AFRICON51333.2021.9570944.
- [2] A. N. R. Rt, "A nnuual repo rt 2016," 2016.
- [3] H. Tazvinga, O. Dzobo, and M. Mapako, "Towards sustainable energy system options for improving energy access in Southern Africa," *J. Energy South. Africa*, **31**(31), 59–72, 2020, doi: 10.17159/2413-3051/2020/V31I1A6504.
- [4] Department of Energy, *The South African Energy Sector Report 2019*. 2019.
- [5] N. Mahmud, "System for St. Martin Island Using HOMER," 2013.
- [6] A. Al-Karaghoul and L. L. Kazmerski, "Optimization and life-cycle cost of health clinic PV system for a rural area in southern Iraq using HOMER software," *Sol. Energy*, **84**(4), 710–714, 2010, doi: 10.1016/j.solener.2010.01.024.
- [7] NASA, "National Aeronautics and Space Administration Graphics Standards Manual Index Introduction 1 The NASA Logotype 2 Reproduction Art 3 Stationery 4 Forms 5 Publications," 1976.
- [8] Homer Energy, "Homer Pro," *Man. Homer Energy*, 1–241, 2019, [Online].

Available:

https://www.homerenergy.com/pdf/HOMER2_2.8_HelpManual.pdf.

- [9] G. A. Tumangkeng, “examining solar pv mini-grid system as a complement to grid extension for rural electrification with reference to yama community, northern ghana.,” *J. EMBA*, **1**(4), 78–85, 2013.
- [10] O. Solar and B. P. Solutions, “Backup Power Solutions MPPT 60 150 Solar Charge Controller Make the most of your energy.”
- [11] I. Guide, “Central Inverter SUNNY CENTRAL 500U.”
- [12] E. Cape, “Pre Electrification Report Project name Project number Distributor name Upper linkwater Minigrid,” 3–5, 2017.

An Improved Model to Analyze the Impact of Cyber-Attacks on Power Systems

Muhammad Musleh Uddin, Kazi Rafiqul Islam*, Md. Monirul Kabir

Department of Electrical and Electronic Engineering, Dhaka University of Engineering and Technology (DUET), Gazipur-1707, Bangladesh

ARTICLE INFO

Article history:

Received: 21 June, 2022

Accepted: 17 August, 2022

Online: 09 September, 2022

Keywords:

Load Frequency Control (LFC)

Automatic Generation Control (AGC)

Automatic voltage regulator (AVR)

Proportional-Integral-Derivative (PID) Controller

Cyber-attack and cyber-security

ABSTRACT

In this paper, an improved model has been proposed for investigating the impact of cyber-attacks on power systems regarding frequency disturbances and voltage disruption while changing the load called ICAPS. The proposed ICAPS model is formulated by five different controllers, such as LFC, AGC, AGC-PID, AVR, and AVR-PID, implemented in two sets of the system model. Specifically, a stable limit of the speed regulation of LFC, integral controller gain of AGC, and amplifier gain of AVR are determined from their characteristic equations derived from the Routh-Hurwitz array. In contrast, the Proportional-Integral-Derivative (PID) controller gains for AGC-PID and AVR-PID are determined using the tuning process. The key aspect of this paper is to obtain the impact of cyber-attacks on the power system in terms of frequency disturbances and voltage disruptions while changing the load. According to our knowledge, no one has considered these issues at a time. In order to evaluate the proposed ICAPS model and how it works, a series of experiments was conducted using the MATLAB Simulink tool. The simulation results are presented in this paper in terms of frequency deviation and voltage disruption (i.e., positive and negative biased cyber-attack) and system oscillations. Finally, the simulation results successfully identified the most severe attack in this model to prevent the power system from unstable conditions.

1. Introduction

The modern power system industry uses supreme technological innovation that enables more adaptable and efficient access to the system structure. In addition, the reliability and security of information communication technology (ICT) and digital computer techniques are crucial for the operation of power systems, which increases the risk of cyber-attacks. Due to cyber-attack, the cyber-vulnerable components of the power system and the effects of cyber-attack should be adequately analyzed [1]-[3].

The advanced control loop, sensor and communication networks are the cyber component of the power plant [4]. The sensors collect data for various parameters, which are sent to the controller to ensure stability of the power system [5]. Data is transferred using the communication network, which is one of the cyber-vulnerable components of the power system. An attacker can get it while sending data from the sensing department to the control department at the power station. The attacker can gain control over the automatic controller of a power plant after accessing confidential information. Ultimately, any change to the

controller actions may create malicious data accessing in the controller, which disrupts the stability of the system.

However, in order to investigate the impact of cyber-attack on the power system, a few works have been done in the literature (e.g., [6]-[9]). Specifically, in [6], the authors have discussed about the infrastructure of power system for identifying vulnerabilities. After that, a framework has been proposed to overcome the unstable condition of power system. Furthermore, the effect of cyber-attack on wind farms and power system networks that is also investigated in [7]. On the other hand, an anomaly detection technique has been proposed in [8] as a countermeasure against the effect of faulty data injection on AGC. The authors have investigated the impact of cyber-attack to AGC loop in the power system in [9]. It is noted that the reliability of the power system is an important factor in assessing cyber-security threats. That's why, the impact of such threats need to be estimated upon the cost of the whole power system [10]. Finally, it can be concluded that, although the existing techniques (e.g., LFC, AGC) tried to investigate the impact of cyber-attacks properly, they failed to achieve significant improvement in such cases. Therefore, the

*Corresponding Author Kazi Rafiqul Islam, Email: rafiqul@duet.ac.bd

effects of cyber-attacks should be properly analyzed to maintain the system's stability.

However, to analyze the proper deviation to be provided the system stability, the impact of cyber-attacks on power system has been presented in this paper. The proposed ICAPS is combined by five different controllers, such as, LFC, AGC, AGC-PID, AVR and AVR-PID that are implemented in two different sets of the system models, among which the first three controllers are included for one set of power system models, whereas, the rest of two controllers are for different set of system models. This work focuses on the impact of cyber-attacks on system in terms of frequency and voltage disruptions during changing the load. It should be noted that, our proposed ICAPS can perform well to investigate the impact of cyber-attacks on the power system in terms of frequency disturbances and voltage disruption during changing the load. The most serious cyber-attack on power plant is also identified successfully.

The rest of the paper has been organized into three sections, among which proposed system investigated, in Section 2. Finally, Section 3 discusses the conclusion of our paper.

2. Proposed System Modelling

In this paper, the impact of cyber-attacks on power system has been proposed to ensure the system stability. To understand the proposed model ICAPS clearly, the following five subsections need to be discussed: (i) cyber-attack impacts on LFC, (ii) cyber-attack impacts on AGC, (iii) cyber-attack impacts on AGC-PID, (iv) cyber-attack impacts on AVR, and (v) cyber-attack impacts on AVR-PID.

2.1 Cyber-Attack Impacts on LFC

A load frequency controller (LFC) is an essential power plant component. The proper operation of the LFC is important for the safe operation of the power system [11]. However, the issue is that LFC is a powerful cyber-attack tool. The load on power plant is constantly changing. It is well known that the frequency of an alternator varies as the load of power station changes. The system can become unstable as the frequency changes. Once again, it is impossible to repair the load, and the only option is to regulate the prime mover speed. In this case, LFC is a crucial part. A simple LFC is composed by a turbine, a generator, and a governor presented in Figure 1.

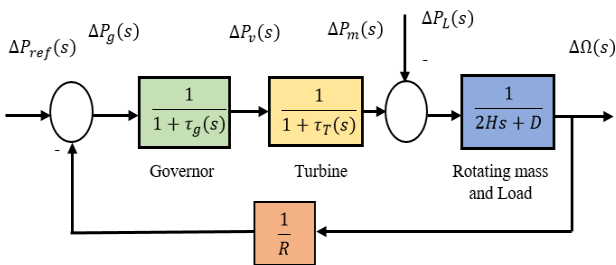


Figure 1: Isolated power system control block diagram based on LFC adapted from [12]

Whether the control system is in stable condition (i.e., not attacked by an unauthorized person), the system frequency falls than the normal value for a short time due to sudden load changes. The frequency sensor detects a decrease in the system's frequency and transmits the signal to the LFC for proper speed control. The LFC

prime mover adjusts the governor speed control based on the signal from the frequency sensor to compensate the speed and frequency of the system [12]. On the other hand, in case of an unauthorized access (i.e., cyber-attack) to the LFC loop, if any change to the speed regulation (R) occurs then that can create frequency fluctuation, which disrupts the system stability. The aim of LFC is to balance the actual (i.e., active) power in the power system by controlling the frequency of the system. In a system when the imbalance between load and generation occurs, it must be corrected within seconds to avoid frequency deviation. Depending on speed regulation (R), the governor adjusts generation with varying load demand, maintaining a stable frequency. Its value can be determined by applying Routh–Hurwitz array in its characteristics equation. The closed-loop transfer function of this system is,

$$\frac{\Delta\Omega(s)}{-\Delta P_L(s)} = \frac{(1 + \tau_g s)(1 + \tau_T s)}{(2H_s + D)(1 + \tau_g s)(1 + \tau_T s) + \frac{1}{R}} \quad (1)$$

On the other hand, the open loop transfer function of this system is,

$$KG(s)H(s) = \frac{1}{R(1 + \tau_g s)(1 + \tau_T s)(2Hs + D)} \quad (2)$$

here, R refers to speed regulation, τ_T refers to turbine time constant, τ_g refers to governor time constant, H refers to generator inertia constant, D refers to load coefficient (1% change in frequency), f refers to nominal frequency, ΔP_L refers to Change in load of the power system.

In LFC system, increasing the load demand (ΔP_L) causes a fall in generator frequency, and vice versa. The reason is that the response of the rotating mass inertia is insufficient to bring the generator frequency to the nominal value. A detailed discussion can be found in [1], whereas the block diagram of LFC system with cyber-attack point specifications shown in Figure 2.

Table 1: Parameters of Proposed LFC, AGC, and AGC-PID Power System Models, Adapted from [12]

Symbols	Parameters	Values
τ_T	Turbine time constant	0.5 s
τ_g	Governor time constant	0.25 s
H	Generator inertia constant	8s
D	Load coefficient (1% change in frequency)	1.16
R	Speed Regulation	0.04
f	Nominal frequency	50 Hz
ΔP_L	Change in load	0.25pu

The parameters used in LFC system are presented in Table I. The power station is considered an isolated power station with a turbine-rated output is 200 MW at nominal frequency of 50Hz. Considering the sudden load changes 50 MW, according to the Routh-Hurwitz array to LFC loop with considering the values of parameters mentioned in Table I and Eq. 1, the obtained value of speed regulation (R) is $R > 0.009678$. As per theoretical calculation,

it is proved that if R is equal to 0.04 then the system will be marginal stable. The frequency deviation during a cyber-attack for various R values presented in Figure 3. It is seen that the system frequency is stable for the value of $R=0.04$. It means that for stable operation of this power station, R should be equal to 0.04. It is clear that, depending on the affected value of R , cyber-attacks can be categorized into two ways: positively biased attack and negatively biased attack.

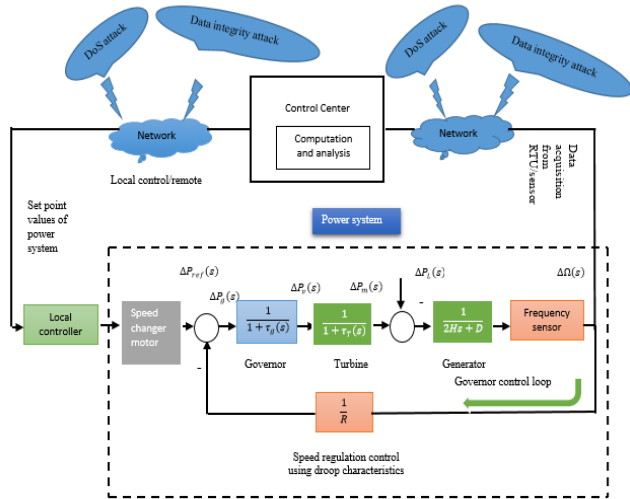


Figure 2: Attack points and general block diagram of a single-area LFC system, adapted from [1].

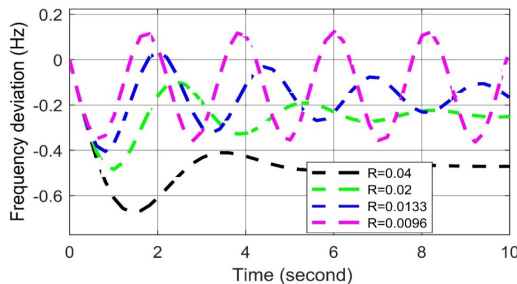


Figure 3: Frequency deviation response to different R values in LFC in case of cyber-attack.

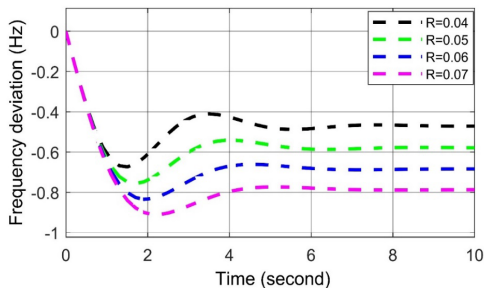


Figure 4: Frequency deviation response for positive biased cyber-attack in LFC.

2.1.1 Positively biased cyber-attack on LFC

According to the result of the cyber-attack on LFC system, the value of R increases from the set value, which is called positively biased cyber-attack. It is observed from Figure 4 that the frequency oscillation curve becomes stable quickly when the value of R increases, although the frequency decreases. According to positive bias cyber-attack, the LFC loop decreases the frequency of the

system, but it quickly returns to a stable position. However, an excessive deviation in system frequency is not permitted here since the governor's excessive deviation cannot restore the system's frequency.

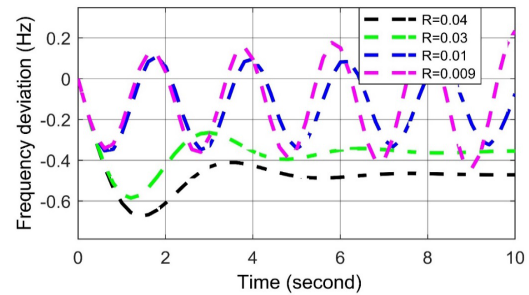


Figure 5: Frequency deviation response for negative biased cyber-attack in LFC.

2.1.2 Negatively biased cyber-attack on LFC

According to the result of the cyber-attack on LFC system, the value of R decreases from the set value, which is called negatively biased cyber-attack. It is observed from Figure 5 that, the governor can restore the system frequency when $R = 0.03$ but it takes more time than the set value $R = 0.04$. In contrast, other frequency curves never reach to a steady state in both cases (i.e., $R = 0.01$ and $R = 0.009$). As a result of the cyber-attack, speed regulation value falls down the steady state position (i.e., $R > 0.009678$), so frequency deviation is being fluctuated in nature. It increases the oscillations since the governor cannot restore the system's frequency. It can be said that the negative biased cyber-attack is very difficult to maintain a stable system condition, and such a cyber-attack can disrupt the whole system.

2.2 Cyber-Attack Impacts on AGC

It is known that changes in system loads at primary LFC result in fluctuations in the steady state frequency depending on the governor speed regulation [12]. It takes more time to restore the system frequency of the desired value (i.e., LFC primary loop). A change in LFC is required to mitigate the frequency fluctuation to zero. Adding an integral controller to the LFC system is referred to as an automatic generation control (AGC). The necessary controller gain (K_I) improves the nature of the system in such a way that the activity finally forces the frequency fluctuation to zero [2]. The K_I must be adjusted with a proper set value for a suitable transient response. Thus, it is essential to set the value of this parameter to an appropriate level for proper operation. Because of the failure to select K_I , the governor cannot restore the system's frequency. As a result of the cyber-attack, K_I is considered as a vulnerable quantity. According to unauthorized access to the AGC loop, any change to K_I may create frequency fluctuation, disrupting the system's stability. Here, the severe effect of cyber-attack on automatic generation control is analyzed. The closed-loop transfer function is shown in Eq. 3, and the block diagram of a simple AGC presented in Figure 6, consisted by some parameters mentioned in Table I. The closed loop transfer function for AGC loop as,

$$\frac{\Delta\Omega(s)}{-\Delta P_L(s)} = \frac{(1+\tau_g s)(1+\tau_T s)}{(2H_s+D)(1+\tau_g s)(1+\tau_T s)+K_I+\frac{s}{R}} \quad (3)$$

It is known that an attacker can change the values of vulnerable parameters by increasing (positive biased cyber-attack) or

decreasing (negatively biased cyber-attack) them during data manipulation [8], [13]-[14]. An attacker can operate them simultaneously or, individually. According to Equation (3) and Figure 6, the various curves for frequency deviation depending different K_I values are presented in Figure 7. The appropriate K_I value equals to 9 for the zero frequency deviation is determined here.

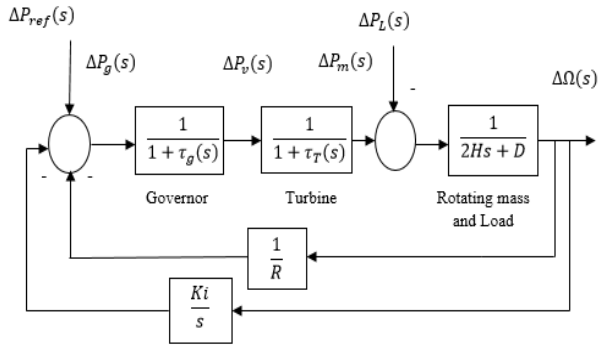


Figure 6: Isolated power system control block diagram of typical AGC

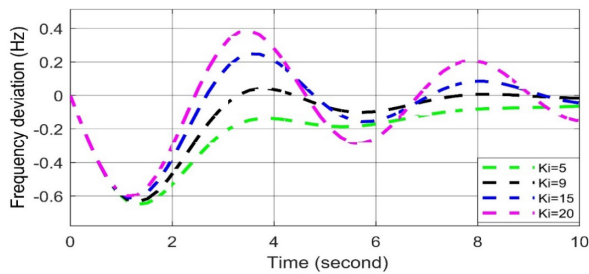


Figure 7: Frequency deviation response to different K_I values in AGC in case of cyber-attack.

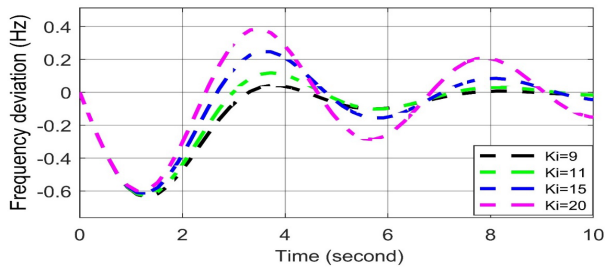


Figure 8: Frequency deviation response for positive biased cyber-attack in AGC.

2.2.1 Positively biased cyber-attack on AGC

According to the result of the cyber-attack on AGC system, the value of K_I increases from the set value, which is called positively biased cyber-attack. AGC system can lead to frequency deviation due to malicious data access. Hence, the frequency deviation of the system oscillated and became unstable. A positive biased cyber-attack's impact on the AGC is presented in Figure 8. It is observed that the frequency oscillation curve can return quickly to the stable state when the set value of $K_I = 9$. On the other hand, the frequency deviation curve oscillates slightly when $K_I = 11$. The frequency deviation curves oscillate more than the previous ones while $K_I = 15$ and 20 , respectively. The reason is that the governor cannot restore the system's frequency, which ultimately disrupts the system's stability. Thus, it can be concluded that the positive biased cyber-attack severely affects the system's frequency.

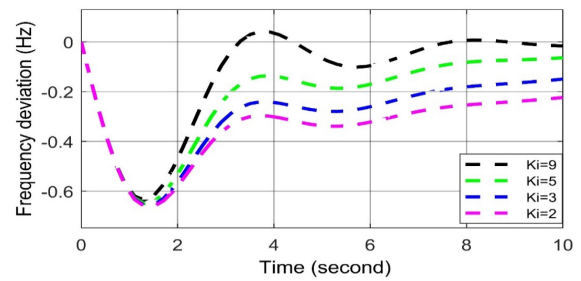


Figure 9: Frequency deviation response for negative biased cyber-attack in AGC.

2.2.2 Positively biased cyber-attack on AGC

According to the result of the cyber-attack on AGC system, the value of K_I increases from the set value, which is called positively biased cyber-attack. AGC system can lead to the frequency deviation due to malicious data access. Hence, the frequency deviation of the system is oscillated and become unstable. The impact of positive biased cyber-attack on the AGC presented in Figure 8. It is observed that the frequency oscillation curve can return quickly to the stable state when the set value of $K_I = 9$. On the other hand, the frequency deviation curve oscillates slightly when $K_I = 11$. The frequency deviation curves oscillate more than the previous ones while $K_I = 15$ and 20 , respectively. The reason is that the governor cannot restore the system's frequency, which ultimately disrupts the system's stability. Thus, it can be concluded that the positive biased cyber-attack severely affects the system's frequency.

2.2.3 Negative biased cyber-attack on AGC

According to the result of the cyber-attack on AGC system, the value of K_I decreases from the set value, which is called negatively biased cyber-attack presented in Figure 9. It is observed that because of the negative biased attack, frequency is deviated from the set value (i.e., $K_I = 9$) and an unwanted delay in restoring system frequency. As a result, the negative biased attack disables the integral controller and opposes the purpose of using the K_I . Negatively biased cyber-attack less serious than positively biased cyber-attack for frequency disturbance because it does not oscillate the nature of the frequency fluctuation.

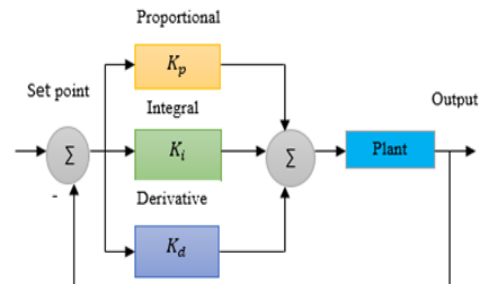


Figure 10: Block diagram of PID controller

2.3 Modelling of PID controller

In industrial applications, PID controller is the most popular approached feed-back controller. It is used to stabilize power systems, provide better frequencies, and reduce errors in the steady state. In order to evaluate the PID controller output, three different gain parameters are used in this controller, such as, the

proportional gain, integral gain, and derivative gains are used [15]-[16], exhibited in Eq. (4). The conventional PID controller structure and parameter values presented in Figure 10 and Table 2.

$$C(S) = K_p + \frac{K_i}{S} + K_d S \quad (4)$$

2.3.1 Cyber-Attack Impacts on AGC-PID

The stability of the proposed typical AGC model can be updated using a PID controller for better response. The isolated power system block diagram based on AGC-PID shown in Fig 11 and the parameters used in this model mentioned in Tables I and II. It is optimistic that cyber-attacks on AGC-PID may disrupt the stability of the frequency operation. For a suitable transient response, the PID controller gain (i.e., K_p , K_i and K_d) must be adjusted with proper tuning [2], [15]-[17]. Because of the failure of selecting the proper PID controller gain, the governor is unable to restore the frequency of the system. Thus, it is important to determine the values of these parameters optimally for proper operation. That's why, PID controller gain (i.e., K_p , K_i , and K_d) considers as the vulnerable quantity during cyber-attacks. An attacker can change the values of vulnerable parameters by increasing (i.e., positive biased cyber-attack) or, decreasing (i.e., negatively biased cyber-attack) them during data manipulation [8], [13]-[14].

Table 2: Tuning Parameters of AGC-PID controller

Symbols	Parameters	Values
K_p	Proportional gain	90.58
K_i	Integral gain	70.89
K_d	Derivative Gain	57.80

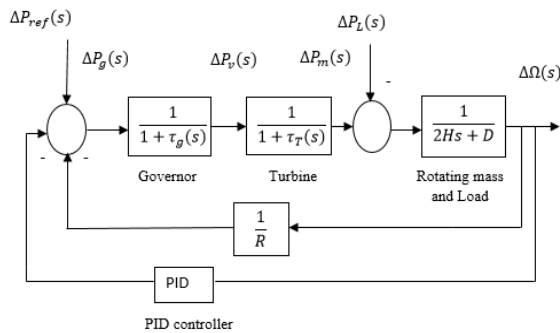


Figure 11: Block diagram of Power system control based on AGC-PID

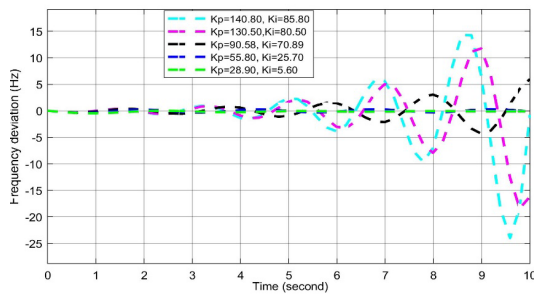


Figure 12: Frequency deviation response to different K_p and K_i values in AGC-PID in case of cyber-attack

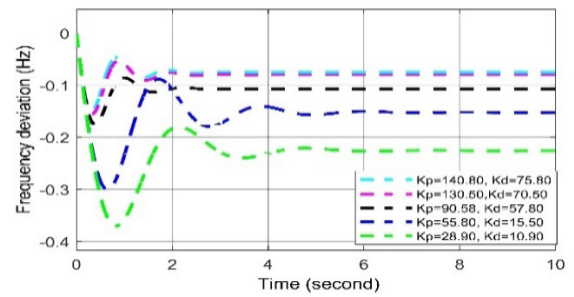


Figure 13: Frequency deviation response to different K_p and K_d values in AGC-PID in case of cyber-attack

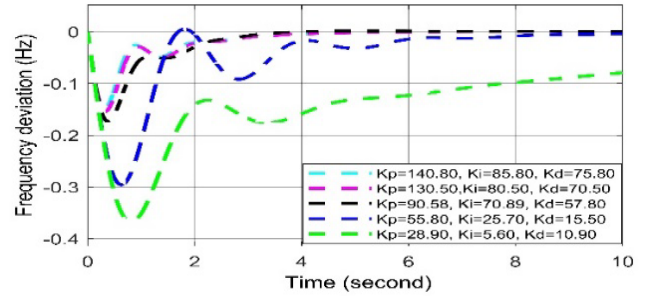


Figure 14: Frequency deviation response to different K_p , K_i and K_d (i.e., PID) values in AGC-PID in case of cyber-attack.

For positive biased cyber-attack, in Figs. (12-14), it is observed that the frequency oscillation curve can return quickly to the stable state in all cases when the set values of $K_p = 90.58$, $K_i = 70.89$, $K_d = 57.80$. When any two values among the three are being increased, the overshoot and settling time response increase. However, an excessive deviation in system frequency is not permitted here since the governor's excessive deviation cannot restore the system's frequency.

In case of negative biased cyber-attack, it is observed in Figs. (12-14) In all cases, the frequency oscillation curves are being oscillated more than the curves of set values (i.e., $K_p = 90.58$, $K_i = 70.89$, $K_d = 57.80$). Thus, it can be said that the negatively biased cyber-attack more serious than positively biased cyber-attack.

2.4. Cyber-Attack Impacts on AVR

The generator uses AVR as the primary means of controlling reactive power. The AVR control system considers the amplifier, exciter, generator, and sensor dynamics. The error signal is amplified and used to change the exciter terminal voltage by controlling the exciter field. The generated EMF changes by changing the current of the voltage generator at the exciter terminal. Thus, the reactive power is modified to keep the voltage stable [12]. It is known that cyber-attacks on the AVR is able to disrupt the stability of the voltage operation that may damage the conductor insulations and home appliances. Therefore, it is essential to consider the impact of a cyber-attack on AVR system in order to avoid such difficulty. The block diagram of AVR presented in Figure 15, where the amplifier gain (K_A) is determined using Routh-Hurwitz array. The integrated system parameters for AVR are mentioned in Table III. The closed loop transfer function for AVR loop is as,

$$\frac{V_t(s)}{V_{ref}(s)} = \frac{K_A K_E K_G K_R (1 + \tau_R S)}{(1 + \tau_A S)(1 + \tau_E S)(1 + \tau_G S)(1 + \tau_R S) + K_A K_E K_G K_R} \quad (5)$$

Figure 16 shows the terminal voltage disruptions during cyber-attack for various K_A values. It is observed that because of the cyber-attack on AVR, any changes in K_A , the voltage fluctuations are obtained that disrupt the stability of the system. It is clear that, depending on the affected value of K_A , cyber-attacks can be categorized into two ways: positively biased cyber-attack (i.e., increasing K_A) and negatively biased cyber-attack (i.e., decreasing K_A).

Table 3: Parameters of Proposed AVR System model

Parameters	Symbol and value	Time constant
Amplifier	$K_A=10$	$\tau_A=0.1s$
Exciter	$K_E=1$	$\tau_E=0.4s$
Generator	$K_G=1$	$\tau_G = 1s$
Sensor	$K_R=1$	$\tau_R = 0.05s$

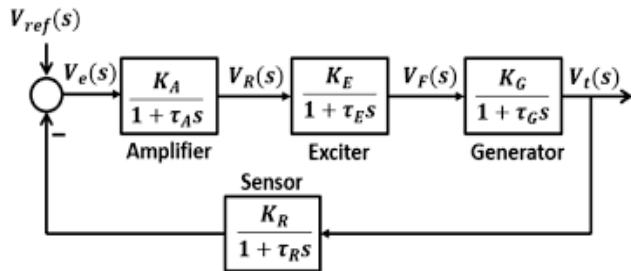


Figure 15: Power system control block diagram based on AVR, adapted from [12]

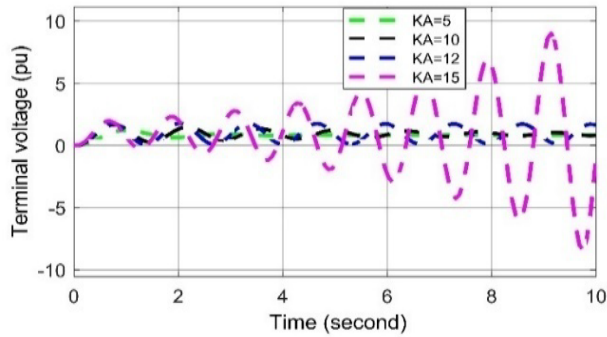


Figure 16: Voltage deviation response to different K_A values in AVR in case of cyber-attack

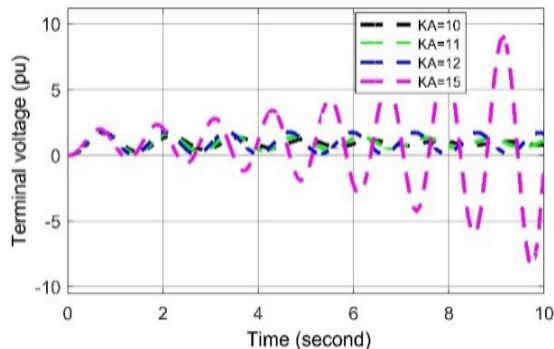


Figure 17: Voltage deviation response for positive biased cyber-attack in AVR

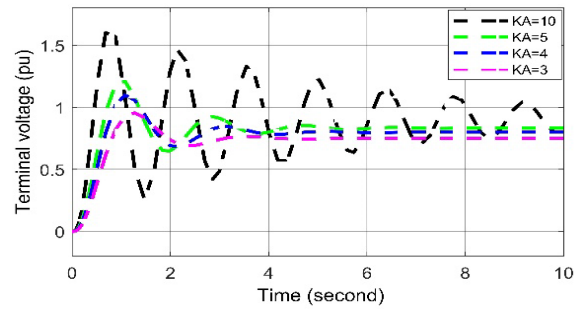


Figure 18: Voltage deviation response for negative biased cyber-attack in AVR

2.4.1 Positively biased cyber-attack on AVR

According to the result of the cyber-attack on AVR system, the value of K_A increases from the set value, which is called positively biased cyber-attack. When the cyber-attack is performed on AVR, the system's terminal voltage oscillates and becomes unstable. In the impact of positive biased cyber-attack on AVR presented in Figure 17. It is observed that the voltage fluctuation curve is oscillated in nature when the set value of $K_A = 10$. On the other hand, voltage fluctuation curves are slightly oscillated while $K_A = 11$ and 12 , respectively. Furthermore, serious voltage fluctuation is occurred in case of $K_A = 15$. The reason is that because of not selecting the proper values of K_A , the exciter is unable to restore the voltage of the system. Thus, it can be concluded that the positive biased cyber-attack on AVR severely affects voltage disturbances as oscillating in nature.

2.4.2 Negatively biased cyber-attack on AVR

According to the result of the cyber-attack on AVR system, the value of K_A decreases from the set value, which is called negatively biased cyber-attack presented in Figure 18. It is observed that because of the negative biased attack, voltage is deviated than nominal value (i.e., $K_A = 10$) and an unwanted delay in the terminal voltage. As a result, the negative biased attack disables the amplifier gain and opposes the purpose of using the K_A . Negatively biased cyber-attack less serious than positively biased cyber-attack for voltage disruptions but both are oscillate in nature.

2.5. Cyber-Attack Impacts on AVR-PID

The stability of the proposed AVR model can be updated using a PID controller for better response. The reason is that the normal AVR is suffered by two limitations: (i) availability of long-term oscillation response and (ii) larger steady-state error. PID controller has three advantages: (i) minimizing the steady-state error, (ii) decreasing the settling time, and (iii) reducing oscillation and overshoot [12]. However, during the cyber-attack on AVR-PID, for a suitable transient response, the PID controller gain (i.e., K_p , K_i and K_d) must be adjusted with proper tuning [17]-[18]. Because of the failure to select the proper PID controller gain, the exciter cannot restore the voltage of the system. Thus, it is important to determine the values of these parameters optimally for proper operation [17]. That's why PID controller gain (i.e., K_p , K_i , and K_d) considers as a vulnerable quantity during cyber-attacks. An attacker can change the values of vulnerable parameters by increasing (i.e., positive biased cyber-attack) or, decreasing (i.e., negatively biased cyber-attack) them during data manipulation [8],

[13]-[14]. Figure 19 shows the block diagram of a simple AVR-PID, where some parameters used presented in Tables II and III.

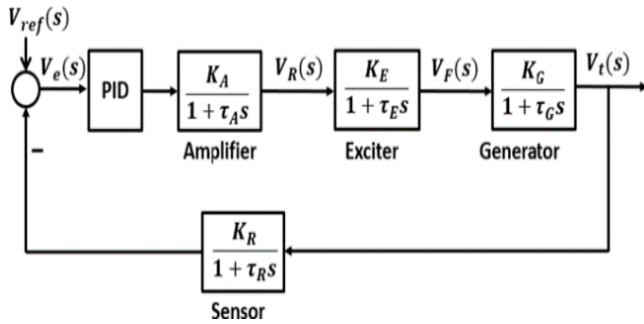


Figure 19: Power system control block diagram based on AVR-PID, adapted from [12]

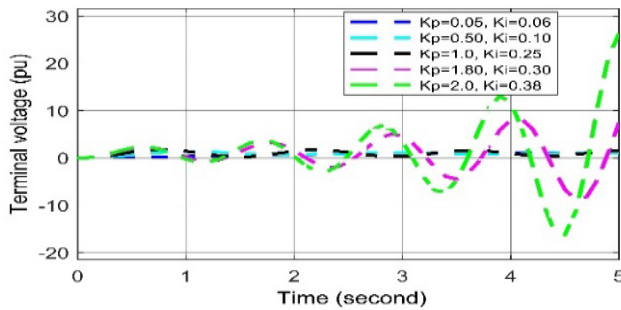


Figure 20: Voltage deviation response to different K_p and K_i values in AVR-PID in case of cyber-attack.

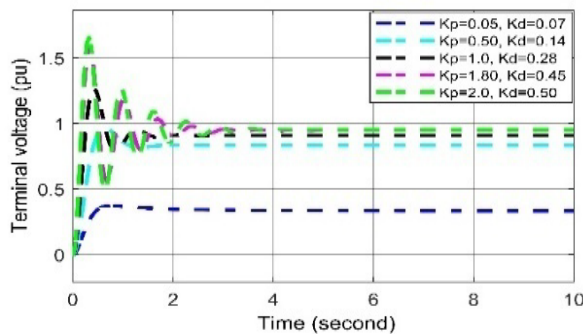


Figure 21: Voltage deviation response to different K_p and K_d values in AVR-PID in case of cyber-attack

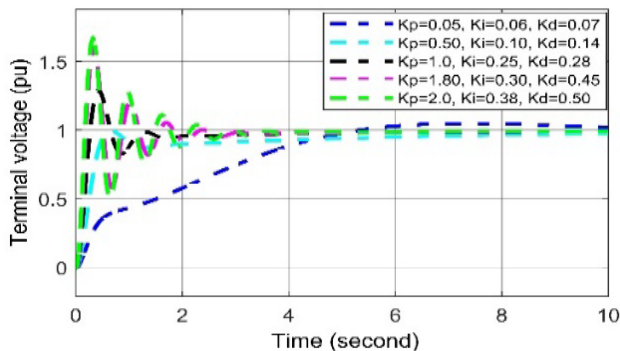


Figure 22: Voltage deviation response to different K_p , K_i and K_d values in AVR-PID in case of cyber-attack

In case of positive biased cyber-attack, in Figs. (20-22), it is observed that the voltage oscillation curve can return quickly to the stable state in all cases when the set values of $K_p = 1.0$, $K_i = 0.25$,

$K_d = 0.28$. When any two values among the three are being increased the overshoot and settling time response increasing and in order to, an unwanted delay in restoring system voltage.

For negative biased cyber-attack, it is observed in Figs. (20-22), In all cases, the voltage oscillation curves are being oscillated more than the curves of set values (i.e., $K_p = 1.0$, $K_i = 0.25$, $K_d = 0.28$), which can create voltage disturbance, which disrupts the system stability. Thus, it can be said that the negatively biased cyber-attack more serious than positively biased cyber-attack, where both forms of attacks are oscillated in nature.

3. Conclusion

The impact of cyber-attack on power systems in terms of frequency disturbances and voltage disruptions during changing loads has been investigated in this paper. In this regard, five individual controllers (i.e., LFC, AGC, AGC-PID, AVR, and AVR-PID) are introduced and incorporate two sets of system models.

In order to investigate the impact analysis properly, a series of experiments were conducted using the MATLAB-Simulink tool. The simulation results were obtained depending on the nature of the cyber-attacks shown according to the positive and negative biased cyber-attacks. It was observed that in LFC, a negative biased cyber-attack is more severe than a positive biased attack for frequency disturbance (see Figures 3-5), whereas, in AGC, a positive biased cyber-attack is more severe than a negative biased attack for frequency disturbances (see Figures 7-9). Furthermore, in AGC-PID, negative-biased cyber-attacks are more severe than positive-biased attacks for frequency disturbances (see Figures 12-14). In contrast, regarding AVR, negative-biased cyber-attack has less impact than positive-biased cyber-attack for stability in voltage disruptions, but both are oscillating in nature (see Figures. 16-18). In addition, a negative biased cyber-attack is more severe than a positive biased cyber-attack for AVR-PID, although both forms of cyber-attack oscillate in nature (see Figures 20-22).

The simulation results also confirm that, along with LFC and AGC, AVR is significant for ensuring the stability of the power system while changing the load. Finally, it can be concluded that our proposed ICAPS model is very effective in identifying the most severe attacks on the isolated power system.

In the future, we desire to achieve a reliable control system of cyber protection against unwanted access and reduce the severity of cyber-attack by considering the self-healing effectiveness process in the proposed ICAPS.

Conflict of Interest

The authors declare no conflict of interest

References

- [1] M. Mohan, N. Meskin, and H. Mehrjerdi, "A comprehensive review of the cyber-attacks and cyber-security on load frequency control of power systems," *Energies*, **13**(15), 1–33, 2020, doi: 10.3390/en13153860.
- [2] M. M. Uddin and M. M. Kabir, "Reduction of Frequency Disruption during Cyber-Attack in the Power System," 2nd International Conference on Sustainable Technologies for Industry 4.0, STI, 19–20, 2020, doi: 10.1109/STI50764.2020.9350518.
- [3] C. Chen, M. Cui, X. Wang, K. Zhang, and S. Yin, "An investigation of coordinated attack on load frequency control," *IEEE Access*, **6**, 30414–30423, 2018, doi: 10.1109/ACCESS.2018.2845300.

[4] A. Farraj, E. Hammad and D. Kundur, "On using distributed control schemes to mitigate switching attacks in smart grids," IEEE 28th Canadian Conference on Electrical and Computer Engineering (CCECE), Halifax, Canada, 1578-1582, 2015.

[5] A. K. Farraj, E. M. Hammad, A. Al Daoud, and D. Kundur, "A game-theoretic control approach to mitigate cyber switching attacks in Smart Grid systems," IEEE International Conference on Smart Grid Communications, 958-963, 2014, doi:10.1109/SmartGridComm.2014.7007772.

[6] D. Kirschen and F. Bouffard, "Keep the Lights On and the Information Flowing," IEEE Power and Energy Magazine, 7(1), 55-60, 2009, doi: 10.1109/MPE.2008.930656.

[7] J. Yan, C. C. Liu, and M. Govindarasu, "Cyber intrusion of wind farm SCADA system and its impact analysis," IEEE/PES Power Systems Conference and Exposition, PSCE, 1-6, 2011, doi: 10.1109/PSCE.2011.5772593.

[8] S. Sridhar and M. Govindarasu, "Model-based attack detection and mitigation for automatic generation control," IEEE Transactions on Smart Grid, 5(2), 580-591, 2014, doi: 10.1109/TSG.2014.2298195.

[9] M. Vrakopoulou, P. M. Esfahani, K. Margellos, J. Lygeros, and G. Andersson, "Cyber-attacks in the automatic generation control," Power Systems, 79, 303-328, 2015, doi: 10.1007/978-3-662-45928-7_11.

[10] A. Dagoumas, "Assessing the impact of cybersecurity attacks on power systems," Energies, 12(4), 2019, doi: 10.3390/en12040725.

[11] O. I. Elgerd and C. E. Fosha, "Optimum Megawatt-Frequency Control of Multiarea Electric Energy Systems," IEEE Transactions On Power Apparatus and Systems, 89, 556-563, 1970.

[12] H. Saadat, Power system analysis, McGraw-Hill, 1999.

[13] S. Biswas and A. Sarwat, "Vulnerabilities in two-area automatic generation control systems under cyberattack," Proceedings - 2016 Resilience Week, RWS, 40-45, 2016, doi: 10.1109/RWEEK.2016.7573304.

[14] S. Adepu, N. K. Kandasamy, J. Zhou, and A. Mathur, "Attacks on smart grid: power supply interruption and malicious power generation," International Journal of Information Security, 19(2), 189-211, 2020, doi: 10.1007/s10207-019-00452-z.

[15] M. M. Uddin, M. K. Saifullah, and M. M. Kabir, "PID Controller Based Automatic Generation Control for Three Area Interconnected Power System," International Conference on Information and Communication Technology for Sustainable Development, (ICICT4SD), 300-305, 2021, doi: 10.1109/ICICT4SD50815.2021.9396971.

[16] R. P. Borase, D. K. Maghade, S. Y. Sondkar, and S. N. Pawar, "A review of PID control, tuning methods and applications," International Journal of Dynamics and Control, 2020, doi: 10.1007/s40435-020-00665-4.

[17] G. Singh and J. K. Dhama, "Load Frequency and Voltage Control of Two Area Interconnected Power," International Journal of Engineering Research & Technology (IJERT), 8 (15), 1-4, 2016.

[18] M. Nagendra and M. Krishnarayalu, "PID Controller Tuning using Simulink for Multi Area Power Systems," International Journal of Engineering Research & Technology (IJERT), 1(7), 1-9, 2012.

Appendix A: List Of Abbreviations

Abbreviation	Complete Meaning
ICA	Impact of Cyber-Attacks
PS	Power System
ICAPS	Impact of Cyber-Attacks on Power System
LFC	Load frequency control
AGC	Automatic generation control
PID	Proportional, integral and derivative controller
AGC-PID	Automatic generation control-PID
AVR	Automatic voltage regulator
AVR-PID	Automatic voltage regulator-PID

Appendix B: All Simulink Models

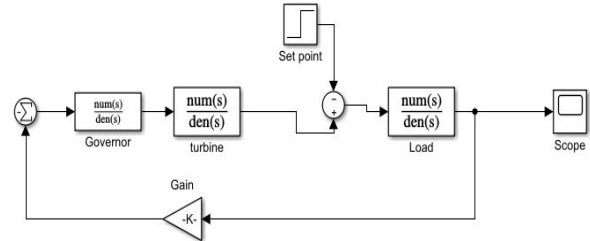


Figure 23: Simulink block diagram of LFC

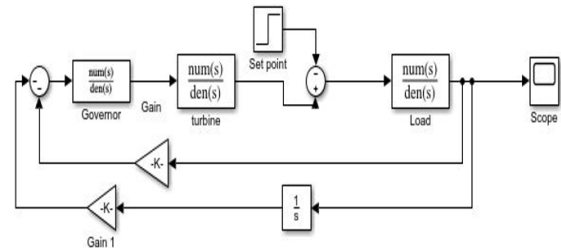


Figure 24: Simulink block diagram of AGC

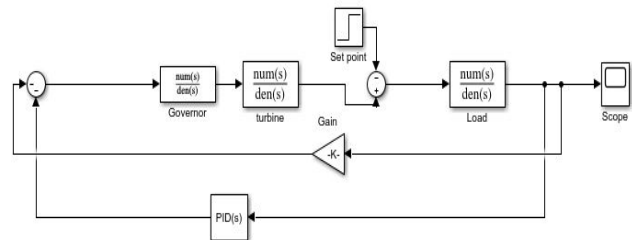


Figure 25: Simulink block diagram of AGC-PID

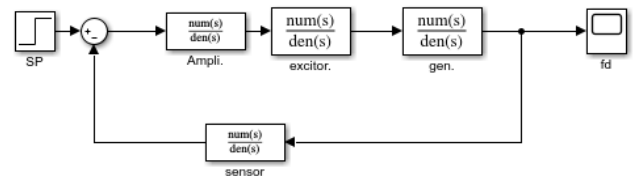


Figure 26: Simulink block diagram of AVR

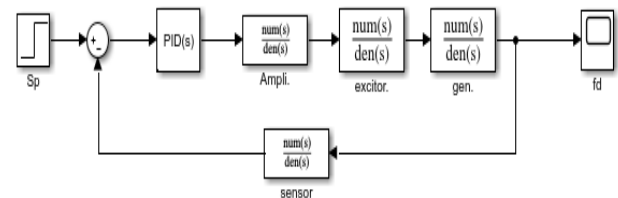


Figure 27: Simulink block diagram of AVR-PID

Assessing the Impact of Integrating Solar PV System using the Equal Area Criterion Method

Abdul Ahad Jhumka¹, Robert Tat Fung Ah King^{*1}, Chandana Ramasawmy²

¹Department of Electrical and Electronic Engineering, University of Mauritius, Reduit 80837, Mauritius

²Advanced Mechanical and Electrical Services Ltd., Rose-Hill 71364, Mauritius

ARTICLE INFO

Article history:

Received: 12 June, 2022

Accepted: 31 August, 2022

Online: 14 September, 2022

Keywords:

Equal area criterion

Transient stability

Critical clearing time

3-phase fault

Inertia

ABSTRACT

The impact of previous energy crisis gives an insight into what happens when the oil price crashes. Many countries were affected due the slow reaction in boosting the economic growth in key sectors such as oil-importing activities and the economic restructuring progress to face the challenges. But the present energy crisis resulting from the COVID-19 pandemic period and closure of many borders, has encouraged power distributors and generators to have recourse to renewable energy for grid integration. Countries such as USA, Germany, Italy, Spain and India are moving towards increasing the share of renewable energy on the grid. The increasing use of solar power systems over the past few years is being favoured for the decarbonization process. The percentage growth in integrating solar PV energy is forecasted to reach 23% in the future. This widespread application of renewable power energy sources (RES) such as wind and solar power comprise of many challenges namely power quality and stability. With this consequent increase in RES, synchronous generators are being displaced and replaced by power electronics grid interface, which reduces the overall rotating masses, hence the system inertia. Stability study in the presence of renewable energy is therefore an important aspect to be considered to meet the required power quality of the grid. This paper brings forward the use of equal area criterion (EAC) method for assessing the stability of the power system network with presence of renewable energy such as solar energy system in the generation portfolio. EAC provides an effective visual and analytical approach for transient stability analysis. The investigations have been performed within the steady and transient conditions in form of a 3-phase fault. The modelling and analysis were carried out using MATLAB/Simulink. Calculation of the critical clearing time (CCT) for stability assessment is the main contribution to knowledge. The increase in the CCT confirms that the Solar PV penetration to the grid will improve the transient characteristics of the national grid network.

1. Introduction

In 2020, the world encountered the outbreak of COVID-19 pandemic, which resulted in major energy upset across the world [1], as well the social life. A slight decrease in biofuels jobs from 2.5 million to 2.4 million was observed [2]. In reaction to this new challenge, the improvement of sustainable energy assets and renewable energy power system sources has shown its promising potential and effective strategy to meet the new energy demand. Globally, an increase of 30% in the connected capacity of solar energy was noted between 2019 and 2020. Japan, India and

Republic of Korea were the largest contributing countries in favouring the growth of solar power energy [2]. Presently, in renewable generation portfolio, wind energy occupies a major share, while the connecting capacity of solar photovoltaic (PV) system is also increasing yearly throughout the world [3]. This growing exploitation of renewable energy sources (RES) such as wind and solar energy brings many challenges to power system operators. Besides the load variation and the stochastic nature of the RES, the integration of RES brings about a subsequent reduction in the system inertia by replacing the rotating masses of the generators with power electronics devices. Hence, stability of the power grid is being disturbed with penetration of RES. Power

*Corresponding Author: Robert Tat Fung Ah King, r.ahking@uom.ac.mu

electronics technologies play a predominant role in the connection of distributed generation and renewable energy sources into the power grid and are becoming more prevalent and growing rapidly as these applications are further integrated into grid-based systems [4]. The fast evolution of power electronics devices are mainly due to development of semiconductor switches such as insulated gate bipolar transistor (IGBT) [5]. Hence the importance of studying the impact of integrating renewable energy on the stability of the power system.

Transient stability analysis (TSA) can be studied in a time-domain simulation. The nonlinear behaviour of a power system dynamics can be solved mathematically using numerical integration of the nonlinear differential equations. Time-domain simulation provides flexibility, and it can consider all components of the power system. Equal Area Criterion (EAC) method provides a direct method for transient stability. This method was first introduced in the 1930s and 1940s to assess the transient stability of the classical model of a SMIB system [6]. It is used to determine the maximum load which can be acquired by the system without exceeding the threshold limit. The principle of this method consists of the basis that when the rotor angle (δ) oscillates around the equilibrium point with constant amplitude, thus maintaining transient stability. This present research work is an extended paper from the IEEE AFRICON 2021 conference proceedings [7]. A similar model is considered for further analysis on the transient stability study using the EAC method. The transient stability margin of the system and the critical clearing time (CCT) or the critical clearing angle were also considered in the analysis. Both parameters are essential elements in the stability analysis. The critical clearing angle was obtained through modelling of the swing curve on MATLAB/Simulink while the critical clearing time was obtained through mathematical derivation.

This research paper explains the concept of the EAC with connection of renewable energy using the positive phase sequencing and interpretation of results obtained. The main objective of this research paper is to investigate on the behaviours of a power grid in terms of stability in presence of RES. The method for developing the EAC consists of reducing the multi machine system into two sets, where one set is considered as the critical cluster while the other set is comprised of the remaining machines. CCT calculation for the stability studies in the presence of renewable energy contribute to knowledge of this research work.

This research paper is categorized into the background, theory, methodology, results and conclusions.

3. Background

This section describes the background works in the transient stability field. In [7], the authors studied the stability in terms of rotor angle analysis with connection of RES. The model consisted of synchronous generators and a solar PV system connected in an IEEE 9-bus arrangement. The investigation of the study was monitored under steady state condition and under transient condition such as a 3-phase fault. The result was compared to a conventional IEEE 9-bus arrangement. The author concluded that the integration of solar PV system brought an enhancement in the

transient nature of the model under investigations due to a lower rotor angle deviation.

In [8], the authors discussed a unified approach on transient stability assessment of a multi machine power system with the initial objectives set as establishing the fundamentals of extended equal area criterion (EEAC), intrinsic limitations, basic formulations and applications to actual working conditions operating within a general threshold security limit. The proposed method consisted of using the equal area criterion as applied to a two-machine system. The EEAC thus established, gives the visual and analytical interpretation for transient stability analysis and sensitivity assessment. However, the limitation of the research is that it does not include any control, which could be applied to the system to enhance the transient stability. Other methods of applications of Artificial Intelligence (AI) to the system may enhance the transient stability particularly in presence of renewable energy.

The authors in [9] made use of a phase sequence exchange (PSE). The aim of the paper was to assess the efficiency of the PSE in a multi-machine system. The method consisted of installing two PSE devices positioned in a multi-machine system, with the first one installed at the outlet of each generator, and the second was the interconnected lines between the system. EEAC was used, and a control method was then proposed. It was observed that the use of the control methods maintained the synchronization, thus ensuring the system integrity and power quality. The efficiency of the PSE was checked against Kundur's two-area four-machine power system and the IEEE 39-bus system and compared with other emergency control methods.

In [10], the authors provided an overview of a revisited EAC with the aim of illustrating the different types of transient stability under occurrence conditions, namely type I, type II, type III and type IV. Four types of variables were discussed on the EAC, P_m , P_b , P_d , P_p where P_m is the mechanical input power while P_b , P_d , P_p are corresponding maximum power during the pre-fault, during fault and post fault. Conditions of always stable even during the fault and unstable states were investigated when $P_d < P_p$ and $P_d > P_p$. Type I was typical and widely accepted as common sense in the transient stability analysis. The study proved relevant to the development of relay protection for enhancing and maintaining the power system stability.

The authors in [11] investigated on the transient rotor angle stability during extreme conditions such as three-phase fault, the disconnection of generators, change of weather due to its stochastic nature and partial shutdown of PV generation [12]. Transient stability rating inclusive of the swing motion and damping are determined due to change of angular speed, frequency, and power output. Other factors such as critical clearing time (CCT) and loadability have been also studied in [13]. It was concluded that the transient stability rating of the grid was dependent on the extent of PV connection and type of transient events induced in the system.

In [14], the authors studied the impact of integrating photovoltaic generation penetration and together with the use of Flexible AC transmission (FACTS) devices such as STATCOM on the transient stability of a single machine infinite bus (SMIB) system based on the rotor angle stability. The system model was

created in MATLAB/Simulink software. It was concluded that with the penetration of solar PV along with the use of STATCOM was able to provide solutions to improve the behaviour of networks by damping the transient oscillations of the rotor angle for various fault conditions.

The literature survey described above shows some research gaps in the field of transient stability study in presence of renewable energy using the EAC method. Application of artificial intelligence (AI) in the transient stability has also received little attention in research. It is expected that the use of AI will enhance the use of RES by appropriate prediction of fault. However, the use of AI will not be considered within this research paper and same will be considered as further works. EAC will determine the critical clearing angle (CCA). The critical clearing time (CCT) will be determined using mathematical derivation and numerical integration. Both parameters are essential in the study of transient stability. The critical clearing angle is the maximum allowable change in the power angle δ before clearing the fault and without loss of synchronism. The critical clearing time is the maximum allowable time to remove a disturbance without interrupting the system integrity. To our knowledge, no studies of similar nature have been conducted for transient stability analysis.

4. Theory

This section explains the theory behind the single machine infinite bus (SMIB) and the equal area criterion (EAC).

4.1. Single Machine Infinite Bus (SMIB)

The diagram in Figure 1 is the equivalent representation of a SMIB in a power system through a line of reactance X_e .

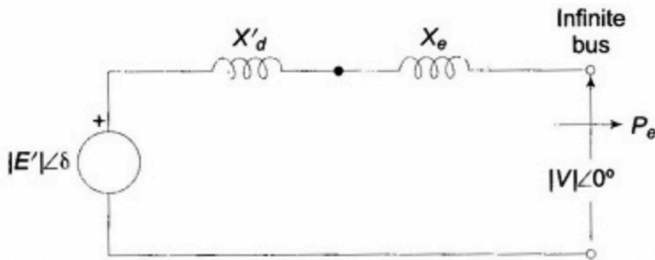


Figure 1: Arrangement of single machine

A generator operating at synchronous speed ω_m will develop an electromagnetic torque T_e and a corresponding electromagnetic power P_e . The input torque developed by the prime mover at the generator shaft is T_i , then under steady state conditions, $T_i = T_e$.

However, under disturbances, the input power, P_i is no longer equal to the output power, P_e . This gives rise to an accelerating power, ΔP which is equivalent to the accelerating torque. According to [15],

$$\Delta P = P_m - P_e = \frac{2H}{\omega_s} \frac{d^2\delta}{dt^2} \quad (1)$$

where

ΔP : Accelerating power (pu)

δ : Rotor angle (rad)

ω_s : Angular speed (rad/s).

H: Inertia (MJ/MVA)

P_m : Mechanical Power (pu)

P_e : Electrical Power (pu)

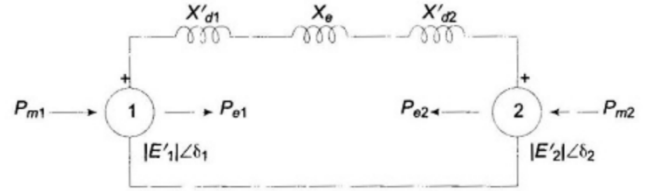


Figure 2: Two-Machine system

A two machines system operating at normal dynamic condition, i.e, steady state, the electrical power developed by the generator applications is equal to the power absorbed by the motor (network being lossless). Thus, at all time

$$P_{m1} = -P_{m2} = P_m \quad (2)$$

$$P_{e1} = -P_{e2} = P_e \quad (3)$$

The swing equations for the two machines can be written as per [13], which is detailed in (4) and (5),

$$d^2\delta_1/dt^2 = \pi f(P_m - P_e)/H_1 \quad (4)$$

$$d^2\delta_2/dt^2 = \pi f(P_e - P_m)/H_2 \quad (5)$$

Subtracting (5) from (4)

$$\frac{d^2(\delta_1 - \delta_2)}{dt^2} = \pi f \frac{(H_1 + H_2)}{H_1 H_2} (P_m - P_e) \quad (6)$$

Therefore, the accelerating power can be written as

$$P_m - P_e = \frac{H_\eta}{\pi f} \frac{d^2\delta}{dt^2} \quad (7)$$

where H_η is the equivalent system inertia.

Electrical Power interchange can be expressed as follows

$$P_e = \frac{|E'_1||E'_2|}{X'_d + X_e + X'_d} \sin \delta \quad (8)$$

A two machines system has the same form of swing and power angle equations, with that of a single machine connected to an infinite bus [16, 17].

4.2. Equal Area Criterion (EAC)

Stability assessment for a SMIB may be determined based on the rotor angle deflection. It is also possible to define the stability graphically using the power-angle diagram, which is known as the equal area criterion (EAC).

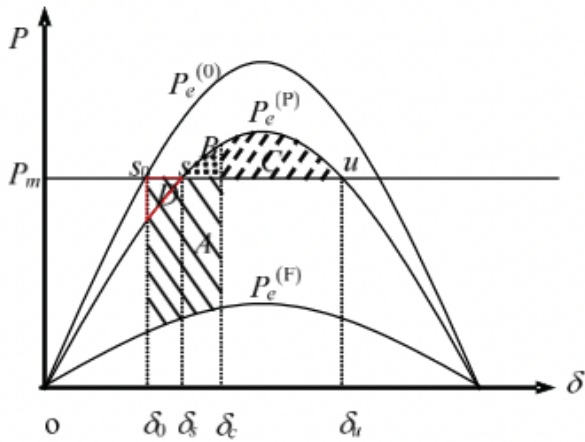


Figure 3: Power angle curve

According to [18], when

Area A < Area C: Stability is achieved within first swing operation.

Area A > Area C: System is not stable.

Area A = Area C: Machine is critically stable in the first swing.

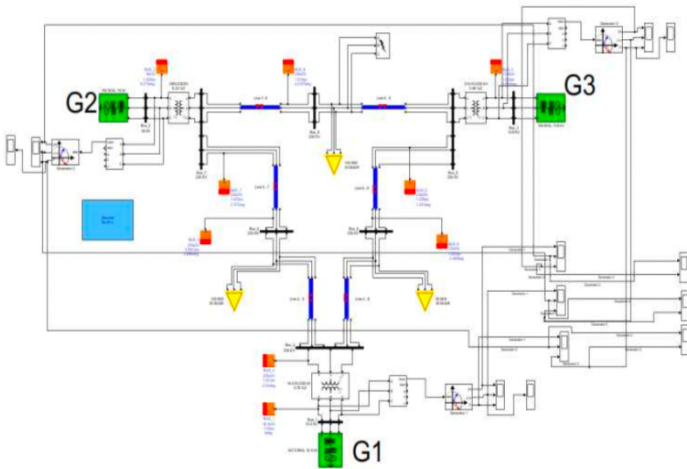


Figure 4: IEEE 9-bus arrangement

In case of a multi machine system, when

When Area A < Area C: the system is operating synchronously in the first swing.

When Area A > Area C: the system is operating asynchronously in the first swing.

When Area A = Area C: the system is operating in a critically synchronous condition within the first swing.

4.3. Methodology

The proposed system under study is comprised of an adapted IEEE 9-bus with the system frequency changed to 50 Hz. Figure 4 shows the arrangement of synchronous generators under investigation. The default values of the system's impedances were used during the study.

The power angle curve can be developed based on the impedance of the generator and the transmission line, which is shown in Figure 5.

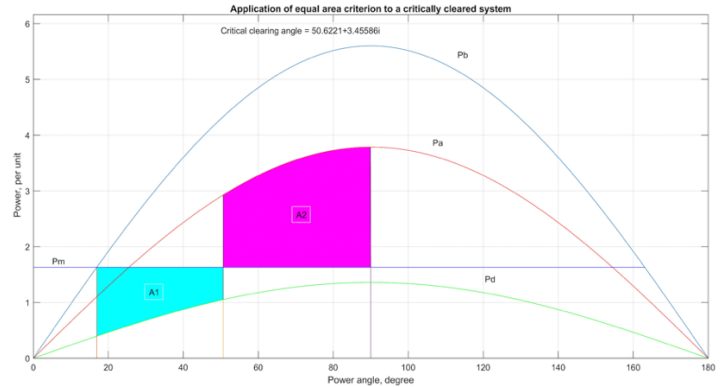


Figure 5: Power angle curve for an IEEE 9-bus arrangement

During the stability assessment of the system after the clearance of the fault, the accelerating energy (A1) and decelerating energy (A2) can be calculated using the principle laid down by [19],

$$A = \int_{\delta_2}^{\delta_1} (P_1 - P_2) d\delta \quad (9)$$

In the present condition,

$A_2 > A_1$ which implies stable state of the system.

The critical clearing time of the system is calculated with integration of (7) above, which will result in (10) according to [20]

$$t_c = \sqrt{\frac{2H_\eta (\delta_c - \delta_0)}{\pi f P}} \quad (10)$$

where t_c is the critical clearing time

H_η : Equivalent inertia (MJ/MVA)

δ_c : critical clearing angle ($^\circ$)

δ_0 : angle at steady state ($^\circ$)

f: frequency (Hz)

P: Power (MVA)

The equivalent inertia H_η can be determined using the R method which is described in [21]. The resulting critical time for the generation mix of synchronous generator is 0.4 s for an estimated inertia of 33.125 MJ/MVA.

During the integration of the solar PV system, generator G2 is displaced from the grid as per the following arrangement in Figure 6.

The first step in developing the power angle curve for this new arrangement, a single axis machine was considered, together with system impedance. The network was reduced to an equivalent circuit diagram by applying Thevenin's theorem, which is given in Figure 7.

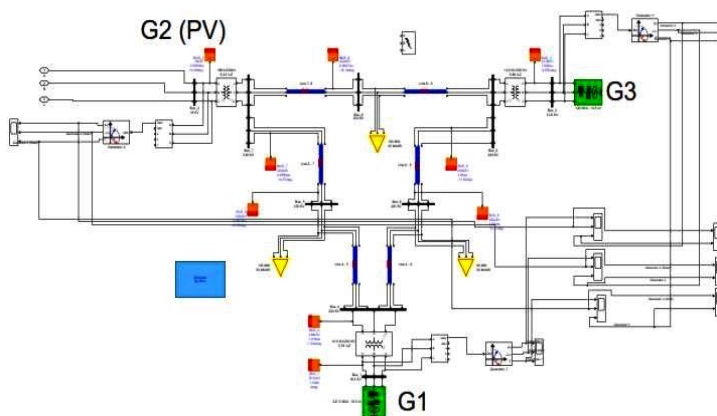


Figure 6: Solar PV system connected in an IEEE 9-bus arrangement

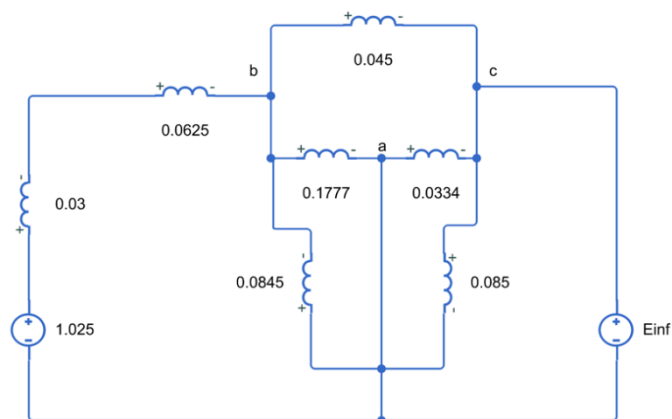


Figure 7: Equivalent circuit with solar PV integration

The result of the power angle curve is shown in Figure 8.

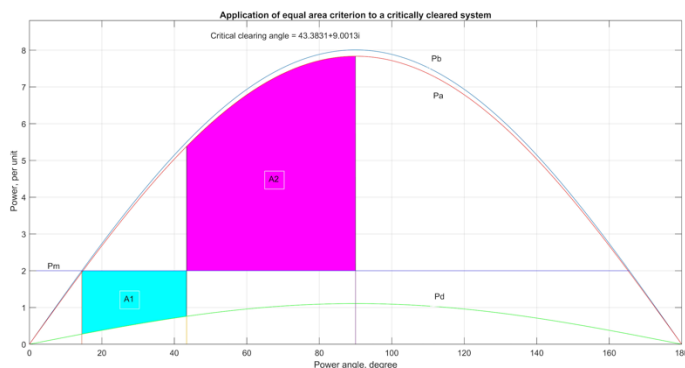


Figure 8: Equal Area Criterion with connection of renewable energy

The integration of solar PV system into the network has lowered the critical clearing angle from 50° to 43°. Using the principle as described above, it can be determined that $A_2 > A_1$, which confirmed the stable state of the system. Moreover, equation (9) in [22] was applied to determine the equivalent inertia. The estimated inertia was calculated using (11)

$$H_c = (f_{nom} CV_{dc} \Delta V_{dc}) / 2P_{res} \Delta f \quad (11)$$

According to [22], $(\Delta V_{dc}) / \Delta f$ is a constant. Allowing a maximum change of frequency of $\pm 0.5\text{Hz}$ and a dc link voltage of 500 V, the constant can be taken at 1000. An estimated value of $H_c = 6 \text{ MJ/MVA}$ can be availed from the expression above.

Upon substituting in (10) above, it is observed that the critical clearing time increased to 1.18 s.

5. Conclusion

As mentioned in the introduction, the exploitation of the solar energy is gradually increasing. It was demonstrated through this study that the system dynamics are impacted with the penetration of large-scale renewable generation. Thus, it is imperative to set the conditions for the steady state and dynamic performance of a power system for different installation scenarios of renewable power plants such as photovoltaic (PV) ones. This study can prove useful to power system operators and policy makers when it comes to the decarbonization of the power grid and its stability concept.

This research paper described the equal area criterion method as a means of transient stability analysis. Similar method can be applied in presence of renewable energy such as solar PV system. The study concluded that with solar power generating system forming part of the generation mix, an improvement of the transient stability of the grid were noted due to a decrease in the critical clearing angle from 50° to 43°.

The paper also brought about an innovative method of estimating the critical clearing time based on an estimated inertia with presence of RES. The critical clearing time was increased from 0.4s to 1.18s in the second test condition owing to the presence of solar PV system, thus confirming an enhancement in the transient stability. Further investigation needs to be worked on the application of AI to such model for fault prediction.

Conflict of Interest

The authors declare no conflict of interest.

Acknowledgment

The assistance given by Advanced Mechanical and Electrical Services Ltd. in the development of this research paper was greatly appreciated.

References

- [1] A.T. Hoang, S. Nižetić, A.I. Olcer, H.C. Ong, W.-H. Chen, C.T. Chong, S. Thomas, S.A. Bandh, X.P. Nguyen, "Impacts of COVID-19 pandemic on the global energy system and the shift progress to renewable energy: opportunities, challenges, and policy implications," *Energy Policy*, **154**, 112322, 2021, <https://doi.org/10.1016/j.enpol.2021.112322>.
- [2] IRENA, ILO, Renewable Energy and Jobs – Annual Review 2021, International Renewable Energy Agency, International Labour Organization, Abu Dhabi, Geneva, 2021.
- [3] I.S. Jha, S. Sen, K. Bhambhani, R. Kumar, "Grid integration of renewable energy sources," *International Journal of Scientific and Technical Advancements (IJSTA)*, **1**, 1-5, 2015.
- [4] M.E.T. Souza Junior, L.C.G. Freitas, "Power electronics for modern sustainable power systems: Distributed generation, microgrids and smart grids—a review," *Sustainability*, **14**, 3597, 2022, doi: 10.3390/su14063597.
- [5] J.M. Carrasco, L.G. Franquelo, J.T. Bialasiewicz, E. Galvan, R.C. Portillo Guisado, M.A.M. Prats, J.I. Leon, N. Moreno-Alfonso, "Power-electronic systems for the grid integration of renewable energy sources: a survey," *IEEE Transactions on Industrial Electronics*, **53**(4), 1002-1016, 2006, doi: 10.1109/TIE.2006.878356.
- [6] A. Bahmanyar, D. Ernst, Y. Vanaubel, Q. Gemine, C. Pache, P. Panciatici, "Extended equal area criterion revisited: a direct method for fast transient stability analysis," *Energies*, **14**, 7259, 2021, doi:10.3390/en14217259.

- [7] A.A. Jhumka, R.T.F. Ah King, C. Ramasawmy, "Rotor Angle and Inertia Analysis in Presence of Renewable Energy Source," in 2021 IEEE AFRICON Conference, 1-6, 2021, doi: 10.1109/AFRICON51333.2021.9571011.
- [8] Y. Xue, M. Pavella, "Extended equal-area criterion: an analytical ultra-fast method for transient stability assessment and preventive control of power systems," *International Journal of Electrical Power & Energy Systems*, **11**(2), 131–149, 1989, doi:10.1016/0142-0615(89)90021-5.
- [9] Y. Li, S. Huang, H. Li, J. Zhang, "Application of phase sequence exchange in emergency control of a multi-machine system," *International Journal of Electrical Power & Energy Systems*, **121**, 106136, 2020, doi:10.1016/j.ijepes.2020.106136.
- [10] Y. Sun, J. Ma, J. Kurths, M. Zhan, "Equal-area criterion in power systems revisited," *Proc. R. Soc. A*, **474**:20170733, 2018. doi:10.1098/rspa.2017.0733.
- [11] S. You, G. Kou, Y. Liu, X. Zhang, Y. Cui, M.J. Till, W. Yao, Y. Liu, "Impact of high PV penetration on the inter-area oscillations in the U.S. eastern interconnection," *IEEE Access*, **5**, 4361–4369, 2017, doi: 10.1109/ACCESS.2017.2682260.
- [12] S. Eftekharijad, V. Vittal, G. T. Heydt, B. Keel, J. Loehr, "Impact of increased penetration of photovoltaic generation on power systems," *IEEE Transactions on Power Systems*, **28**(2), 893-901, 2013, doi: 10.1109/TPWRS.2012.2216294.
- [13] B., Tamimi, C., Cañizares, K. Bhattacharya, "System stability impact of large-scale and distributed solar photovoltaic generation: the case of Ontario, Canada," *IEEE Transactions on Sustainable Energy*, **4**(3), 680–688, 2013.
- [14] S. Fettissi, D. Labeled, I. Labeled, "Influence of high PV penetration and STATCOM on rotor angle stability of SMIB transmission system," *Journal of Electrical Engineering & Technology*, 849-857, 2018.
- [15] M. Pavella, D. Ernst, D. Ruiz-Vega, *Transient stability of power systems: a unified approach to assessment and control*, Springer, 2000.
- [16] P. Kundur, N.J. Balu, M.G. Lauby, *Power system stability and control*, McGraw-Hill, 1994.
- [17] L. Fang and Y. Ji-lai, "Transient Stability Analysis with Equal Area Criterion Directly Used to a Non-Equivalent Generator Pair," in *International Conference on Power Engineering, Energy and Electrical Drives*, 386-389, 2009, doi: 10.1109/POWERENG.2009.4915162.
- [18] S. Paudyal, R. Gokaraju and M. Sachdev, "Application of Equal Area Criterion Conditions in the Time Domain for Out-of-Step Protection," in *IEEE PES General Meeting*, 1-1, 2010, doi: 10.1109/PES.2010.5589303.
- [19] H.-D. Chiang, F.F. Wu, P.P. Varaiya, "A BCU method for direct analysis of power system transient stability," *IEEE Transactions on Power Systems*, **9**(3), 1194–1208, 1994, doi:10.1109/59.336079.
- [20] F.I. Khan, T. Aziz, "Transient Stability Evaluation of a Solar PV Integrated Industrial Microgrid," in *IEEE Region 10 Symposium (TENSYP)*, 535-540, 2019, doi: 10.1109/TENSYP46218.2019.8971169.
- [21] D. Zografos, M. Ghandhari, "Estimation of Power System Inertia," in *IEEE Power and Energy Society General Meeting (PESGM)*, Boston, MA, USA, 1-5, 2016, doi: 10.1109/PESGM.2016.7741073.
- [22] R. Ghosh, N.R. Tummuru, B.S. Rajpurohit, A. Monti, "Virtual Inertia from Renewable Energy Sources: Mathematical Representation and Control Strategy," in *IEEE International Conference on Power Electronics, Smart Grid and Renewable Energy (PESGRE2020)*, 1-6, 2020, doi: 10.1109/PESGRE45664.2020.9070733.

Effect of Knee Orthosis on Lateral Thrust in Patients with Knee Osteoarthritis

Hiroaki Yamamoto^{1,2,*}, Masahide Endo³, Tomohiro Baba³, Chikamune Wada²

¹Department of Physical Therapy and Fukuoka Tenjin Medical Rehabilitation Academy, Fukuoka, 8100004, Japan

²Graduate School of Life Science and System Engineering, Kyushu Institute of Technology, Kitakyushu, 8080196, Japan

³Sakurajyuji Fukuoka Hospital, Fukuoka, 8100004, Japan

ARTICLE INFO

Article history:

Received: 01 August, 2022

Accepted: 05 September, 2022

Online: 14 September, 2022

Keywords:

Lateral Thrust

Knee Orthosis

Wearing Pressure

Knee Osteoarthritis

ABSTRACT

To examine the effects of wearing a flexible knee orthosis (FKO) on the lateral thrust in patients with knee osteoarthritis (OA) by changing the wearing pressure. This study was a cross-sectional study. Thirteen patients (mean age: 82.8 ± 7.5 years with Kellgren Lawrence Stages I and II knee OA) were included and prescribed FKO. Patient with osteoarthritis of the knee was attending outpatient rehabilitation. Using a wireless 3-axis accelerometer, we analyzed the lateral thrust in the proximal lower leg during walking (10 m) with the knee orthosis under different wearing pressures (without orthosis, using "standard force" of application, and using "tight force"). The peak values in the outward direction of the gait cycle over the three experimental conditions were selected for analysis. The mean values for patients with K-L stages I and II were calculated and compared. We found that "tight force," i.e., tightening the hook-and-loop fastener of the knee orthosis to its maximum, resulted in significantly lower lateral thrust compared to the absence of an orthosis. The effect was more pronounced in K-L Stage II patients. Our findings confirm that increasing the wearing pressure of the knee orthosis reduces lateral thrust in patients with knee OA. In Stage 1, the lateral thrust could be suppressed by the "standard force," but the lateral thrust in "Stage 2" required "tight force" to be suppressed. Knee orthosis for knee osteoarthritis were found to have the potential to inhibit lateral thrust.

1. Introduction

Knee osteoarthritis (OA) is a degenerative disease of the knee joint that affects the joint tissues, such as articular cartilage, meniscus, and ligaments [1-3]. Once the joint degeneration commences, 30% of the healthy knee joint structures will be affected within two years, while 90% of joints is affected within the next 11 years [4].

Based on the compartment affected, the disease is classified into medial, lateral, patellar, and total variety [5]. In the Japanese population, 90% of all OA patients have medial compartment OA with an internal deformity [6], which involves impairment of the periarticular ligaments and other supporting tissues, resulting in a lateral sway of the joint. Consequently, a lateral thrust is observed during walking as the outside of the knee is pushed laterally (Figure 1) [7, 8].

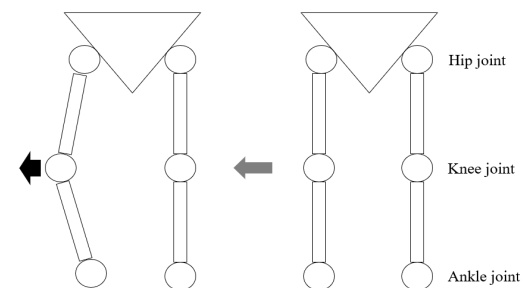


Figure 1: Schematic diagram of lateral thrust in an osteoarthritic knee during walking

The mechanical stress of repeated postures and movements in daily life is a crucial factor triggering disease onset [9]. Accordingly, a flexible knee orthosis (FKO) made of elastic materials is often used to counter these mechanical stresses. The FKO comes in a wide range of shapes, including those with bands and struts for alignment and knee stabilization. While flexible orthosis is not as supportive and does not provide as much

*Corresponding Author: Hiroaki Yamamoto, h.yamamoto.28.0321@gmail.com

corrective force as rigid knee orthosis, it is widely used by OA patients because it is inexpensive, lightweight, and easy to install [10].

It has been reported that wearing FKO reduces the knee varus moment, suggesting its role in suppressing lateral thrust [11]. Additionally, the FKO covers the entire knee, compressing and stimulating the periarticularis muscles of the knee joint. Therefore, the effect of external pressure tightness may be responsible for restricting abnormal motion and reducing the pain.

Previous studies have shown that wearing FKO suppresses the lateral thrust [11]. However, the effects of a change in wearing pressure have not been elucidated. There is evidence to support that muscle activity is improved by increasing the wearing pressure of the orthosis [12]. Therefore, the pressure exerted by the orthosis may affect muscle activity to correct deformity and lower limb alignment, thereby improving knee stability and controlling abnormal motion. The orthosis can limit abnormal motion in the initial disease to reduce pain and support stability. Accordingly, by increasing the wearing pressure of FKO, the knee joint may become relatively fixed, restricting abnormal movements and leading to pain.

Therefore, the current study investigated whether FKO with different wearing pressures can affect the lateral thrust in patients with knee OA.

2. Materials and methods

2.1 Research Participants

We included 13 patients with knee OA. The severity of knee OA was determined using the radiological Kellgren Lawrence (K-L) classification index [13], according to which, nine patients belonged to Stage I and four patients had a Stage II disease with mild varus deformity. Patients who had hip and ankle other orthopedic diseases and symptoms, or those who had resting pain or tumor in the acute phase. were excluded from the study. This is because those symptoms could affect gait. Controls and interventions were provided to all 13 patients. The study was conducted as per the Declaration of Helsinki and was approved by the Research Ethics Committee of the Sakura Juji Fukuoka Hospital, Japan (Approval ID: 2021070501). The purpose and methods of the study were explained to the research participants. Consent to participate in the study was obtained in writing.

2.2 Measurements

To measure the lateral thrust, a wireless 3-axis accelerometer (Q's TAG; Sumitomo Electric Industries, Ltd., Konohana-ku, Japan.) was used. The device allowed for measuring the knee joint external deflection angle during walking without affecting the patient's gait since the accelerometer is small and lightweight ($41 \times 41 \times 14.5 \text{ mm}^3$ and 15 g, respectively). The accelerometer was fixed to the fibular head (less affected by soft tissue-related artifacts) of the affected limb using Velcro in a standing position (Figure 2). At a sampling frequency of 200 Hz, the acquired data were wirelessly fed into a personal computer via Bluetooth. Patients were asked to walk for 10 m at a comfortable pace. Using Ogata's method [14], a sudden acceleration change in the outward direction at the beginning of the stance was defined as lateral thrust; accordingly, the peak value of outward direction of the during walking was used for analysis.



Figure 2: Placement of the accelerometer on the fibular head of the affected limb

An open-type FKO (Facilitated Supporter: (Nippon Sigma Max Co, Ltd., Shinjuku-ku, Japan) was given to all patients (Figure 3). The orthosis size was indexed by the length around the thigh—0.1 m above the center of the patella. A numerical size close to the median of the orthosis was used. The following three experimental conditions were implemented: (1) the participant did not wear the orthosis (hereafter, “control”), (2) the orthosis was fastened with appropriate force (“standard force” condition), and (3) the orthosis was fastened with a fully tightened hook-and-loop fastener (“tight force” condition). The appropriate force meant the force applied to achieve a comfortable and firm fit. All fittings were undertaken by a single physical therapist. All measurements were performed once for each research participants (Figure 4).



Figure 3: Flexible knee orthosis

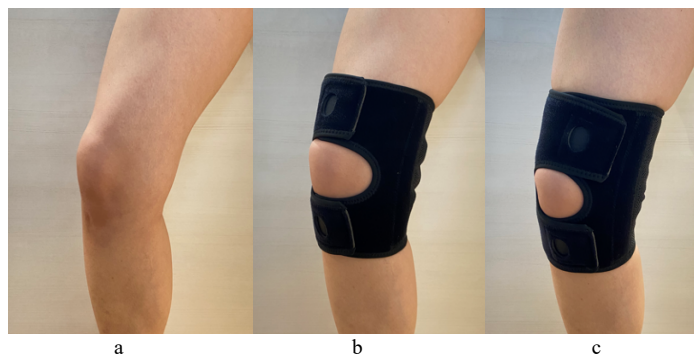


Figure 4: Different wearing pressures of the orthosis.

- a: the participant did not wear the orthosis
- b: the orthosis was fastened with appropriate force
- c: the orthosis was fastened with a fully tightened hook-and-loop fastener

The wearing pressure of the orthotics was measured using an airbag-type pressure sensor “Palm Q” (manufactured by Cape, Ltd., Osaka, Japan). According to Laplace’s law [15], the wearing pressure exerted on the lower limb is directly proportional to the tension generated from the orthotics applied to the curved surface of the lower limb. The center of the pressure sensor (10 cm²) was set to be 5 cm above the center of the patella, and the orthosis was attached on the sensor (Figure 5).



Figure 5: Palm Q sticking position.

The heel contact period was identified through vertical impact acceleration; one gait cycle was analyzed for statistical analysis (Figure 6, 7). The peak values in the outward direction of the gait cycle over the three experimental conditions were selected for analysis. Comparisons among the three experimental conditions were performed using the Friedman test and Tukey’s method. The JSTAT for Windows was used as the statistical software, and the significance level was set to 5%. The mean values for patients with K-L stages I and II were calculated and compared.



Figure 6: Measuring scenery

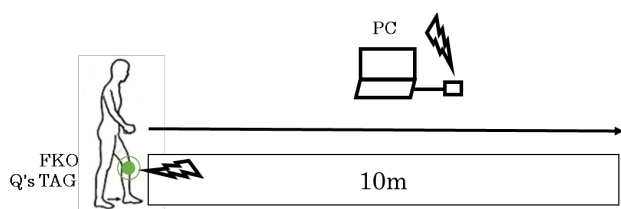


Figure 7: Schematic diagram of measuring scenery

3. Results

We included 13 patients with knee OA (6 males and 7 females) with a mean age of 82.8 ± 7.5 years (height: 156.0 ± 11.8 cm, weight: 53.2 ± 11.0 kg, and body mass index: 21.7 ± 2.3 kg/m²).

The wearing pressures were 14.3 mmHg, 41.2 mmHg for the Standard force, Tight force, respectively (Figure 8).

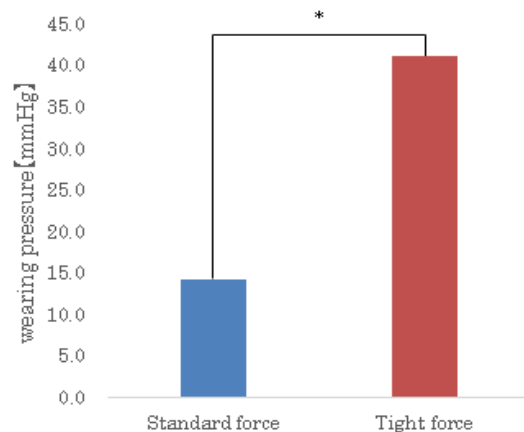


Figure 8: Comparison of wearing pressure

Conducted to quantify wearing pressure. All fittings were undertaken by a single physical therapist.

Table 1 shows the experimental results. Accordingly, our findings showed that the tight pressure condition promoted a significantly lower lateral thrust was significantly compared to the not wearing condition. Moreover, the lateral thrust was reduced by wearing a knee orthosis, and the lateral thrust tended to be further suppressed by increasing the wearing pressure (Table.1).

The mean values for lateral thrust detected in patients with Stages I and II OA are shown in Tables 2 and 3, respectively. Without the knee orthosis, lateral thrust was 15.3 m/s², but with the knee orthosis, it decreased to 11.6 m/s² in Stage I and 11.7 m/s² in Stage II. In Stage I patients, the lateral thrust tended to decrease when the patient wore the orthosis (Table 2). Regarding the wearing pressure, there was no difference between different wearing pressures.

In Stage II patients, the lateral thrust was suppressed in the “tight force” condition compared to the “control” and “standard force” conditions (Table 3). Without the knee orthosis, lateral thrust was 17.2 m/s², but with the knee orthosis, it decreased to 16.6 m/s² in Stage I and 13.5 m/s² in Stage II. Additionally, we observed that the more severe the disease, the more the lateral thrust, which was true for all conditions. In Stage 1, the lateral thrust could be suppressed by the “standard force,” but the lateral thrust in “Stage 2” required “tight force” to be suppressed.

Table. 1. Results of lateral thrust measured in patients with Stage I and II osteoarthritis.

	lateral thrust
Control	15.9±5.2
Standard force	13.1±5.5
Tight force	12.2±5.0*

all values are mean ± standard deviation; units: m/s²

* : p<0.05 (vs Control)

Table 2. Results of lateral thrust measured in patients with Stage I osteoarthritis.

	lateral thrust
Control	15.3±5.3
Standard force	11.6±4.2
Tight force	11.7±5.0

all values are mean ± standard deviation; units: m/s²

Table 3. Results of lateral thrust measured in patients with Stage II osteoarthritis

	lateral thrust
Control	17.2±5.6
Standard force	16.6±7.0
Tight force	13.5±5.6

all values are mean ± standard deviation; units: m/s²

4. Discussion

We found that the overall lateral thrust was reduced by using knee orthosis and was further reduced when the wearing pressure was increased. Furthermore, there was a significant difference between the “Tight force” condition as compared to the “Control” condition.

This reduction in lateral thrust during walking while donning FKO can be attributed to the improved fixation of the knee joint as well as the suppression of abnormal joint movement. Orthoses compensate for joint instability and abnormal movements caused by degenerated or damaged joint structures by providing external support to the joint [16]. The underlying objective is to reproduce the physiological movement of the joint as much as possible and prevent further damage to the joint structure [16]. Therefore, wearing a knee orthosis suppresses the lateral thrust to reduce the abnormal loading of the medial joint surface in the knee and the resultant pain and prevent disease progression [17].

Additionally, we observed that increasing the wearing pressure tends to suppress lateral propulsion which is probably influenced by the output of muscles around the knee joint. In a previous study, pressure stimulation changed rectus femoris muscle activity and knee angle improved jumping movements [18, 19]. Likewise, a study comparing muscle strength when wearing knee orthosis at different wearing pressures reported that with increments in the wearing pressure, the muscle output of the knee joint muscles increased and played an auxiliary role [20]. This is thought to be due to the fact that effective pressure stimulation is involved in suppressing muscle tone and promoting muscle flexibility [21]. A possible explanation is that the strongly stretched orthotic device works as an adjunct to the extensor muscle of the knee joint, i.e., the quadriceps [22]. Therefore, compared to the “standard force” condition, the “tight force” condition can better promote restrained abnormal movements, besides fixation of joint, which was also observed in our study.

There were certain limitations to the study results. The joint angle and muscle output were not measured; for this purpose, we plan to simultaneously measure knee joint movement and muscle power using a three-dimensional motion capture system and electromyography to correlate the effects of joint angle and muscle activity. Also, the patients were patients with mild knee OA (K-L Stages I and II); accordingly, differences in the severity of knee OA and internal and external deformities could not be localized. In

Stage I patients, wearing the orthosis tended to suppress the lateral thrust but the effect of wearing pressure was very small. Likewise, in Stage II patients, the wearing pressure of the “standard force” condition was insufficient to suppress the lateral thrust, and a “tight force” may be necessary. These findings support the concept that the greater the disease severity, the more lateral thrust, and that the patients of stages I and Stage II show different trends. In recent years, it has been reported that pain emerges from early Stage 0 and Stage I knee OA, for which prevention has been emphasized, and some reports have defined Stage II and later as knee OA [23, 24]. Correspondingly, a greater lateral thrust was observed in Stage II than in Stage I. Therefore, it is conceivable that there is a need for stronger wearing pressure in Stage II. Accordingly, there is a need to increase the wearing pressure for knee OA patients based on their disease severity. The highest compression pressure a patient can tolerate is a maximum of 60 mmHg [25]. Compression stimulation of 30-50 mmHg decreases muscle stiffness and promotes flexibility [21]. Furthermore, regarding cell activation, it has been reported that the application of 30-40 mmHg of compression causes cell phosphorylation and promotes capillary dilation [26]. Therefore, the wearing pressure should be set at about 40 mmHg. However, the generalizability of our results is limited because of the small number of patients included. Future studies must include patients with varying degrees of disease severity.

5. Conclusion

The current study analyzed the lateral thrust in patients with knee OA during walking using FKO with different wearing pressures. We found that increased wearing pressure reduced the lateral thrust during walking, more so in patients with K-L Stage II OA. However, this study is limited in referring to the severity of knee osteoarthritis and the differences in internal and external deformities because they were not localized. For further research, we plan to simultaneously measure knee joint movement and muscle power to elucidate the reasons for lateral thrust reduction.

Conflict of Interest

The authors declare no conflict of interest.

Abbreviations

osteoarthritis (OA), flexible knee orthosis (FKO)

References

- [1] W. Zhang, R.W. Moskowitz, G. Nuki, S. Abramson, R.D. Altman, N. Arden, S.B. Zeinstra, K.D. Brandt, P. Croft, M. Doherty, et al., “OARSI recommendations for the management of hip and knee osteoarthritis: part 2 OARSI evidence-based, expert consensus guidelines” *Osteoarthritis Cartilage*, **16**(2), 137–162, 2008, doi: 10.1016/j.joca.2007.12.013.
- [2] L. Sharma, “Local factors in osteoarthritis” *Current Opinion in Rheumatology*, **13**(5), 441–446, 2001, doi: 10.1097/00002281-200109000-00017.
- [3] R.A. Sch-ultz, D.C. Miller, C.S. Kerr, L. Micheli, “Mechanoreceptors in human cruciate ligaments. A histological study,” *Journal of Bone Joint Surgery AM*, **66**(7), 1072–1076, 1984, PMID: 6207177.
- [4] S. Ikeda, H. Tsumura, T. Torisulkeda, “Age-related quadriceps-dominant muscle atrophy and incident radiographic knee osteoarthritis,” *Journal of Orthopaedic Science*, **10**(2), 121–126, 2005, doi: 10.1007/s00776-004-0876-2.
- [5] T. Koshino, “Etiology of osteoarthritis of the knee, classification and clinical findings” *Rheumatism*, **25**, 191–203, 1985.
- [6] T. Koshino, “Knee osteoarthritis, knee clinic manual, 5th ed.” *Medical and*

Dental Publishing, Tokyo, 2001.

- [7] S. Knecht, B. Vanwanseele, E. Stüssi, "A review on the mechanical quality of articular cartilage - implications for the diagnosis of osteoarthritis," *Clinical Biomechanics*, **21**(10), 999–1012, 2006, doi: 10.1016/j.clinbiomech.2006.07.001.
- [8] A. Chang, K. Hayes, D. Dunlop, D. Hurwitz, J. Song, S. Cahue, R. Genge, L. Sharma, "Thrust during ambulation and the progression of knee osteoarthritis," *Arthritis and Rheumatism*, **50**(12), 3897–3903, 2004, doi: 10.1002/art.20657.
- [9] A. Mahmoudian, J.H. van Dieen, S.M. Bruijn, I.A. Baert, G.S. Faber, F.P. Luyten, S.M. Verschueren, "Varus thrust in women with early medial knee osteoarthritis and its relation with the external knee adduction moment," *Clinical Biomechanics*, **39**, 109–114, 2016, doi: 10.1016/j.clinbiomech.2016.10.006.
- [10] T. Okamoto, Y. Ishii, M. Deie "Efficacy and Challenges of Orthotic Therapy" joint surgery, **38**, 57–63, 2019, doi: <https://doi.org/10.18885/j00282.2019374740>.
- [11] T. Okamoto, M. Deie, R. Asaeda, M. Kawano, C. Terai, H. Watanabe, M. Ochi "Examination of orthotic therapy for knee osteoarthritis using gait analysis" *Separate Volume Orthopedics*, **1**(67), 121–124, 2015, doi: [org/10.15106/J04037.2015223650](https://doi.org/10.15106/J04037.2015223650).
- [12] H. Yamamoto, S. Okamatsu, K. Kitagawa, C. Wada, "Effect of knee orthosis pressure variation on muscle activities during sit-to-stand motion in patients with knee osteoarthritis," *International Journal of Environmental Research and Public Health*, **19**(3), 1341–1351, 2022, doi:10.3390/ijerph19031341
- [13] J.H. Kellgren, J.S. Lawrence, "Radiological assessment of osteoarthritis," *Annals of the Rheumatic Diseases*, **16**(4), 494–502, 1957, doi: 10.1136/ard.16.4.494.
- [14] K. Ogata, "Pathophysiology and treatment of knee osteoarthritis from the viewpoint of lateral sway," *Orthopaedic Disaster Surgery*, **38**(1), 11–18, 1995.
- [15] M. Hirai, "Clinical application of compression stockings," Especially about elasticity/elongation hardness and Laplace's law," *Veinology*, **23**(3), 239–245, 2012. doi.org/10.7134/phlebol.23.239
- [16] E. Genda, "Biomechanics of knee orthosis," *Bulletin of the Japanese Society of Prosthetic and Orthotic Education, Research and Development*, **24**(1), 9–15, 2008.
- [17] A. Chang, K. Hayes, D. Dunlop, D. Hurwitz, J. Song, S. Cahue, R. Genge, L. Sharma, "Thrust during ambulation and the progression of knee osteoarthritis," *Arthritis and Rheumatism*, **50**(12), 3897–3903, 2020, doi: 10.1002/art.20657.
- [18] D.K. Ramsey, K. Briem, M.J. Axe, L.S. Mackler, "A mechanical theory for the effectiveness of bracing for medial compartment osteoarthritis of the knee," *Journal of Bone and Joint Surgery. American Volume*, **89**(11), 2398–2407, 2007, doi: 10.2106/JBJS.F.01136
- [19] G. Hayata, T. Miyakawa, "Effect of a wearing overlap length change of the knee joint supporter during a stop-jump task," *Japanese Journal of Physical Fitness and Sports Medicine*, **63**(2), 279–285, 2014, doi: [org/10.7600/jspfsm.63.279](https://doi.org/10.7600/jspfsm.63.279).
- [20] G. Hayata, H. Oka, K. Miyagawa, "Effects of supporter and the taping on isokinetic torque of the knee joint," *University of the Pacific Rim Departmental Bulletin Paper*, **6**(27), 199–203, 2012, doi: [/10.24767/00000348](https://doi.org/10.24767/00000348).
- [21] N. Miura, K. Kurosawa, M. Hirose, T. Suzuki, "Inhibitory Effects of Pressure on Soleus Muscle Motor Neuron Excitability and Flow Volume in Healthy Adults," *physical therapy science*, **26**(6), 773–776, 2011, doi: [org/10.1589/rika.26.773](https://doi.org/10.1589/rika.26.773)
- [22] H. Takigami, "Lateral knee sway and clinical symptoms during walking in patients with knee osteoarthritis," *Yokohama Med*, **49**, 505–510, 1998.
- [23] N. Ozeki, T. Muneta, T. Saito, I. Sekiya "Concept of early knee osteoarthritis," *Bone Joint Nerve*, **6**(3), 473–479, 2016.
- [24] M. Ishijima, S. Hada, H. Kaneko, L. Liu, M. Kinoshita, H. Arita, J. Shiozawa, Y. Anwarjan, T. Aoki, Y. Takazawa, H. Ikeda, Y. Okada, K. Kaneko, "Expectations and challenges for the research of the early stage knee osteoarthritis in terms of the Kellgren-Lawrence classification," *Bone Joint Nerve*, **6**(3), 533–541, 2016.
- [25] International Society of Lymphology " The diagnosis and treatment of peripheral lymphedema 2009 Consensus Document of the International Society of Lymphology," *Lymphology*, **42**, 51–60, 2009.
- [26] JS Martin, Wesley CK, Cody TH, Anna, EM, Joshua JS, Christopher BM, Michael DG, Andreas K, David DP, Lee Z, Michael DR " Impact of external pneumatic compression target inflation pressure on transcriptome-wide RNA expression in skeletal muscle," *Physiol Rep*, **4**, 13209, 2016, doi: 10.14814/phy2.13029.

Analysis of Layout Arrangement for CMOS Oscillators to Reduce Overall Variation on Silicon

Pang-Yen Lou¹, Yung-Yuan Ho¹, Chua-Chin Wang^{1,*}, Wei-Chih Chang²

¹National Sun Yat-Sen University, Department of Electrical Engineering, 70 Lian-Hai Rd., Kaohsiung, Taiwan

²FocalTech Systems Co., Ltd, 6, Du Sing 1st Rd, East District, Hsinchu, Taiwan

ARTICLE INFO

Article history:

Received: 07 June, 2022

Accepted: 08 September, 2022

Online: 24 September, 2022

Keywords:

Oscillator

Serpentine style

Variation minimization

CMOS

On wafer

Adjustable frequency

ABSTRACT

This investigation demonstrates the analysis of various layout arrangements for oscillator (OSC) realized by CMOS technologies. Moreover, the analysis reveals that the serpentine style of OSC stages attains the minimum output variation on silicon. This investigation is firstly verified by post-layout simulations, comparing the variation with different kinds of layout arrangement for OSC designs, including serpentine layout style, straight layout style, and staggered layout style, etc. The proposed design is then realized using 0.18 μm process to justify the performance, where a straight line layout style and a serpentine layout style of OSC are physically fabricated on the same die. Besides, the on-silicon measurement is conducted to give the comparison for these two different styles of OSC designs. The proposed serpentine layout style attains the lowest layout variation when the variations are not homogeneous in different directions on the same silicon plane.

1 Introduction

Thanks to the advancement of CMOS semiconductor technologies, transistors as well as other passive devices are downsized constantly and rapidly. Under the continuous shrinking of nanometer manufacturing process, 180 nm, 90 nm, 40 nm, 28 nm, and even 16 nm, manufacturing variations on wafer become a serious threat to the functionality of logic devices. However, The reason is no matter what process is used, it is suffered from various environmental factors [1]-[14], e.g., voltage, temperature, power surge, process variations, etc. In addition to the environmental factors, the impact of the layout parasitic and arrangement is also an important issue for IC design [15]-[17]. Oscillator (OSC) is one of the major components of digital circuits, which is usually used as the clock generator.

2 Literature Survey

This investigation explores what kind of layout arrangement of OSCs composed of many identical delay stages will attains the best robustness to the variations caused by manufacturing on wafers. The theoretical analysis was verified not only by simulation results, but also physical measurement. In prior works, the measurement

results were much worse than the post-layout simulation results mainly due to lack of layout style analysis [18]-[20], and the worst frequency drift is about 0.2 GHz from 1 GHz-3 GHz in these works. Notably, many prior digital circuit design reports never gave details of their clock or OSC generator layout, e.g., [21]-[24]. To keep the simulation conditions consistent for different layout arrangement of OSCs, all OSCs are realized using the same 64 inverters for various 8×8 and 1×64 combinations in this investigation. Besides, to verify as many possibilities as possible, this investigation demonstrates the analysis of 7 layout arrangements of OSCs by post-layout simulations with full RC extract and Monte Carlo simulation results. Though the layout arrangements look similar for 7 layout arrangements of OSCs, the wiring length between buffers in these cases are not identical. This investigation analytically computes the overall wiring length to predict the RC impact and the variation effect in the different layout styles.

3 Layout Variation Analysis of Oscillator Designs

Figure 1 shows the architecture of a typical differential oscillator. It consists of a Driving Buffer, two 64-to-1 MUX arrays, 64 delay stages, and a Decoder to select the desired frequency. Although

*The corresponding author. He is also with Institute of Undersea Technology (IUT) of NSYSU, Taiwan. Tel: 886-7-5252000 ext. 4144; Fax: 886-7-5254199.

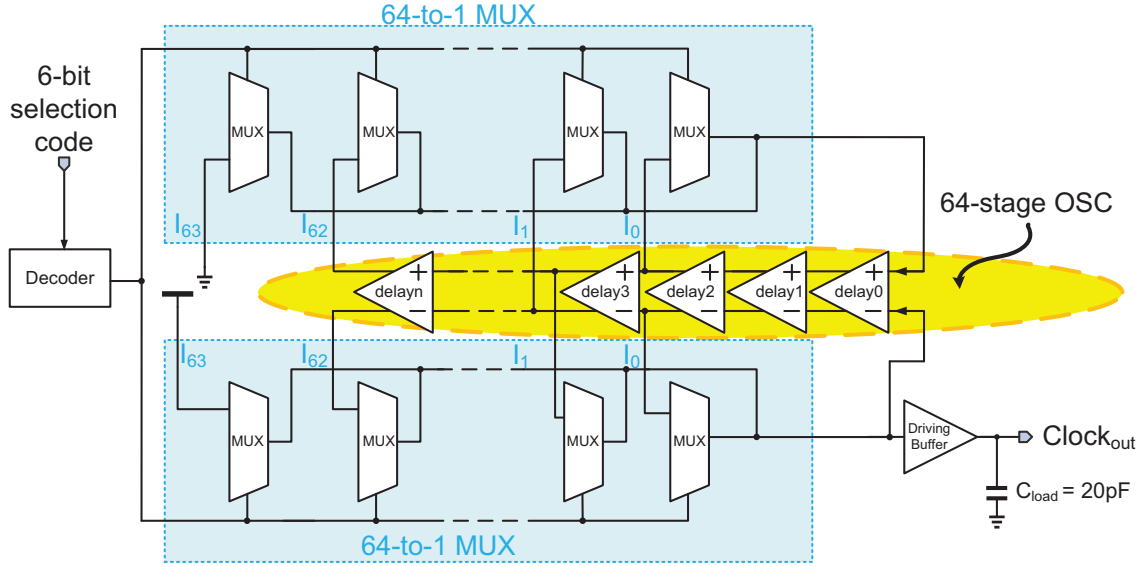


Figure 1: The architecture of the illustrative OSC with 64 delay stages

voltage variation, temperature variation, and process variation are usually considered by chip designers, there are still other variations caused by layout styles. Typical process variation on wafer are usually caused by the non-uniform and linearly degradation doping concentrations of chemical substances. Assume that the variation, $P_A(0,0)$, at the origin $A(0,0)$ has the minimum variation c . We then define the variation amount along the x axis for each buffer stage is "a", and the variation along y axis is "b" without the loss of robustness. In other words, the variation is assumed to be a linear function against the distance. And the variation amount is different in different directions on the same die (plane). For example: $B(i,j)$ delay stage has variation $P_B(i,j)$ as follows.

$$P_B(i,j) = a \cdot i + b \cdot j + c \quad (1)$$

- In the case of a straight line arrangement layout of OSC in Figure 2, the total variation $P_{total1}(i,j)$ is found as:

$$\begin{aligned} & \sum_{i=1}^{64} \sum_{j=1}^1 P_{total1}(i,j) \\ &= \sum_{i=1}^{64} \sum_{j=1}^1 (a \cdot i + b \cdot j + c) \\ &= 2080 \cdot a + 64 \cdot b + 64 \cdot c \end{aligned} \quad (2)$$

Average of variation $P_{totalaverage1}(i,j)$ is:

$$P_{totalaverage1}(i,j) = 32.5 \cdot a + b + c \quad (3)$$



Figure 2: Straight line layout style of OSC

Notably, buf# (# = 1-64) stands for inverter-based buffers.

- In Figure 3, in the case of a serpentine layout style of OSC, the total variation $P_{total2}(i,j)$ is:

$$\begin{aligned} & \sum_{i=1}^8 \sum_{j=1}^8 P_{total2}(i,j) \\ &= \sum_{i=1}^8 \sum_{j=1}^8 (a \cdot i + b \cdot j + c) \\ &= 288 \cdot a + 288 \cdot b + 64 \cdot c \end{aligned} \quad (4)$$

Average of variation $P_{totalaverage2}(i,j)$ is:

$$P_{totalaverage2}(i,j) = 4.5 \cdot a + 4.5 \cdot b + c \quad (5)$$

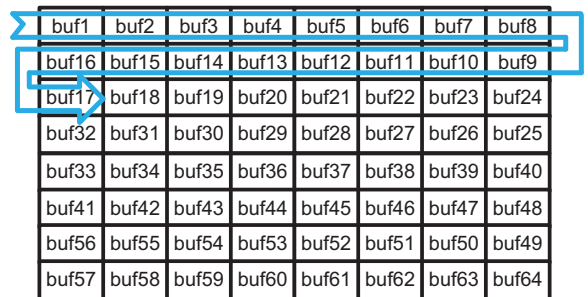


Figure 3: Serpentine layout style of OSC

Based on Eqn. (2) and (4), we make a conclusive derivation as follows.

$$P_{total1}(i, j) \geq P_{total2}(i, j)$$

$$\Rightarrow 2080 \cdot a + 64 \cdot b + 64 \cdot c \geq 288 \cdot a + 288 \cdot b + 64 \cdot c \quad (6)$$

$$\Rightarrow 8 \cdot a \geq b$$

Thus, the variation of the serpentine style is better than straight arrangement when "a" is more than or equal to one eighth of "b". This implies that if the variations in different directions are not equal, the serpentine layout style attains the better resistance to overall variations on wafer. This fact was never reported before in any prior work analytically. Notably, the similar analytic approach is applied to other layout styles as those described in the following text.

4 Results and Discussion

4.1 Simulation and Verification

In order to verify as many possibilities as possible before physical realization on silicon, this investigation demonstrates 7 layout

arrangements of OSCs as shown in Figure 4, where various arrangements and post-layout simulations with RC extract of OSCs are demonstrated. Given that the central frequency of a 64-stage OSC is 100 MHz by pre-layout simulations, it is assumed that the parasitic variation is ignored. A total of 7 different layout arrangements are shown in Figure 4, namely A, B, C, D, E, F, and G. These styles are briefly described as follows.

- A. common centroid + even-odd stage interleaved
- B. common centroid in 2 directions diagonally
- C. circle to the center
- D. serpentine
- E. line by line
- F. 2-line circle to the center
- G. straight line

The post-layout simulation of serpentine layout style shows the closest result to 100 MHz. Besides, the error between the serpentine layout style and pre-layout simulation is only 1.9%. In short, the serpentine layout style is the best arrangement proved by this post-layout simulation result.

Because of the limit of chip size and budget, we are only allowed to carry out the serpentine layout style and straight layout style on

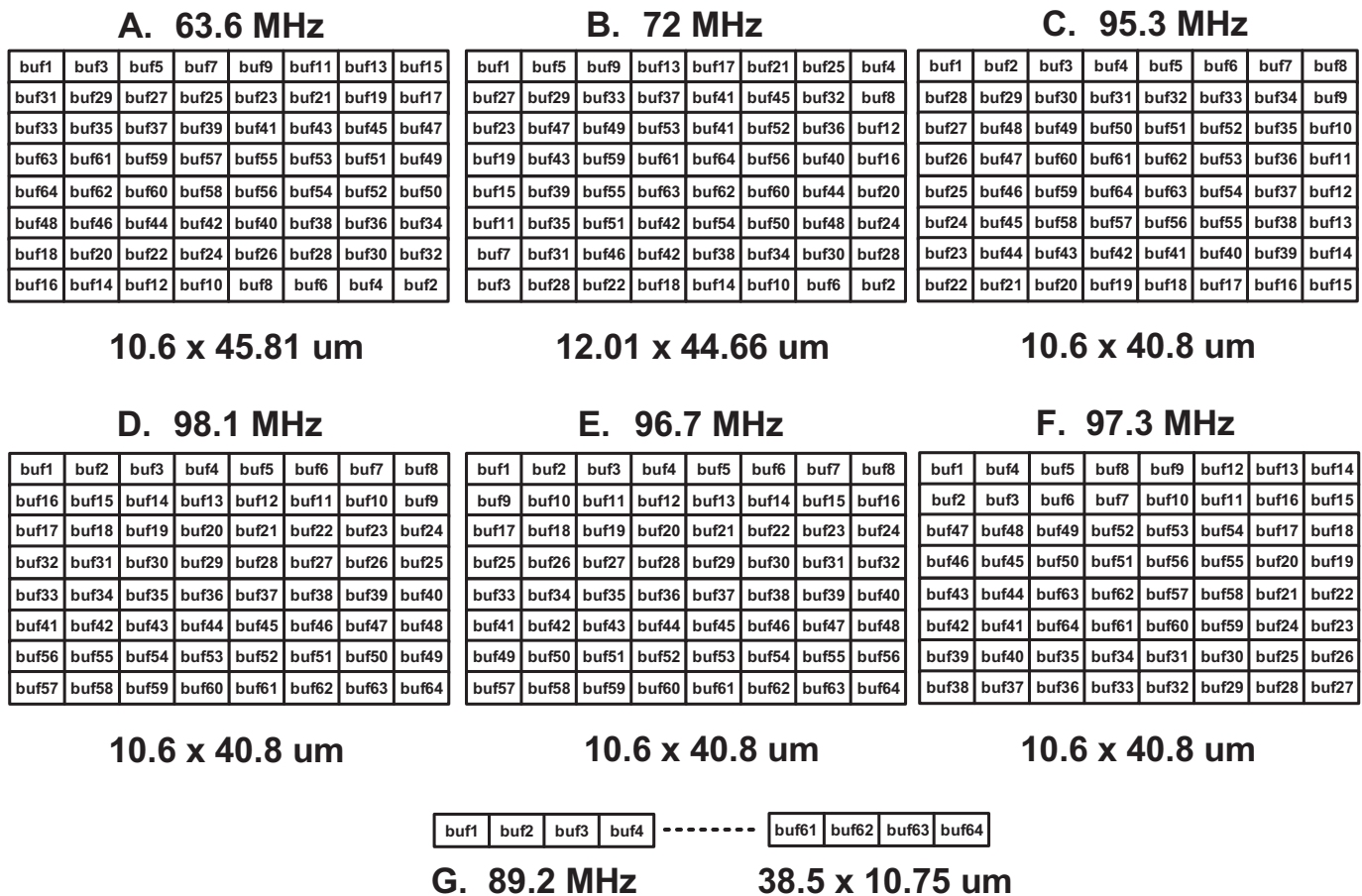


Figure 4: Various arrangements and the clock rates of OSC by post-layout simulations

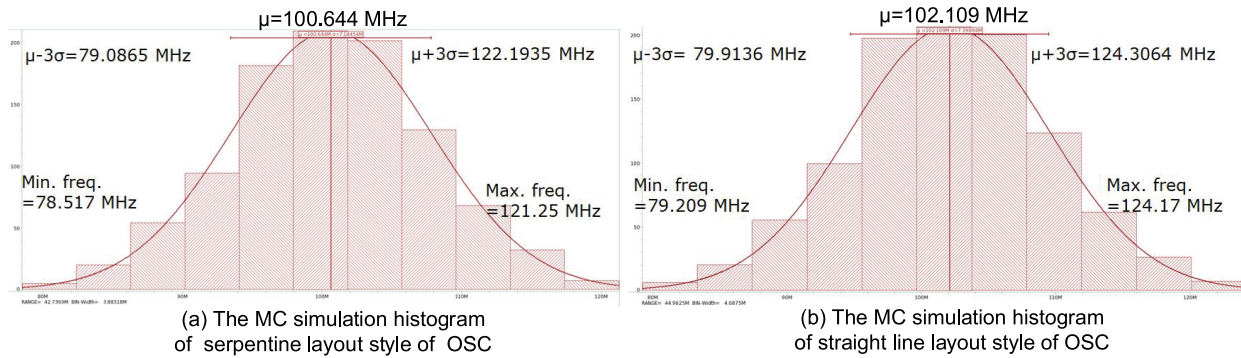


Figure 5: (a) The Monte Carlo simulation histogram of serpentine layout style of OSC; (b) The Monte Carlo simulation histogram of straight line layout style of OSC (MC times=1000)

Table 1: Comparison with prior works.

	MWCL[21]	VLSI[22]	JSSC[23]	JSSC[24]	this work	
Year	2017	2019	2019	2021	2022	
VDD (V)	1	0.8	1.2	1	3.3	
Layout arrangement	straight	straight	straight	straight	serpentine	straight
Layout variation	N/A	N/A	N/A	N/A	Yes	
Accuracy	N/A	N/A	N/A	N/A	95.5%	88.7%
Frequency range	1 MHz	3.2 GHz-4 GHz	2.1 GHz-3.1 GHz	3.6 GHz-3.6175 GHz	20 MHz-180 MHz	
Bandwidth	10 MHz	10 MHz	10 MHz	100 MHz	100 MHz	
Adjustable frequency	Yes	Yes	Yes	Yes	Yes	
Chip Area (mm ²)	0.75	1	0.25	0.00525	1.3	
Chip Area (Normalization) (10 ⁻⁴ mm ²)	1.775	2.36	0.6	0.108	0.4	
FOM	8.8	2820	11888	15700	12100, 23606 ^Δ	

$$FOM = \left(\frac{\text{Frequency range} \cdot \text{Bandwidth}}{VDD \cdot \text{Normalized Chip Area}} \right)$$

^Δ This FOM is counted only by the area of the serpentine style.

silicon. Their areas are $10.6 \times 40.8 \mu\text{m}^2$ (serpentine) and $38.5 \times 10.75 \mu\text{m}^2$ (straight line), respectively. Figure 5 shows the Monte Carlo simulation results of two different layout styles to verify the reliability, respectively. As shown in Figure 5, the central frequency of serpentine layout style is closer to 100 MHz, which is set to be the central frequency of this investigation.

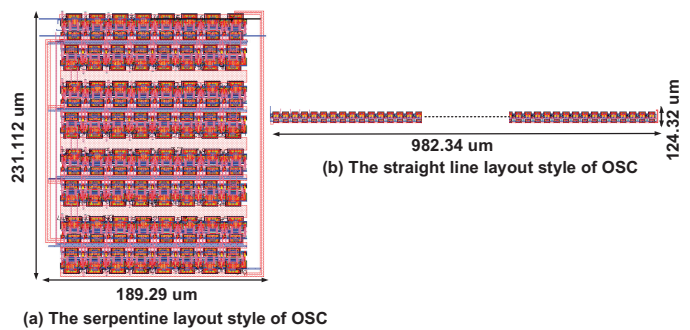


Figure 7: The enlarged layout style of OSC (a) serpentine style; (b) straight line style

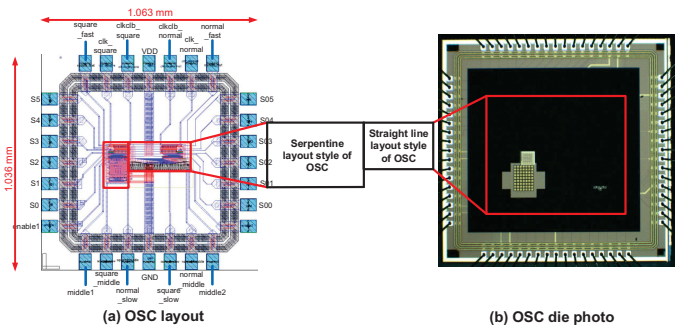


Figure 6: (a) OSC layout; (b) OSC die photo

4.2 Measurement and Performance Comparison

To verify the previous analysis, the proposed OSC designs are realized using TSMC 180 nm CMOS process. The layout and die photo of the OSCs are shown in Figure 6 (a) and (b), respectively, where the total chip area is $1.063 \times 1.063 \text{ mm}^2$, and the core area is $989 \times 344 \mu\text{m}^2$. Notably, there are 2 OSC designs (straight line,

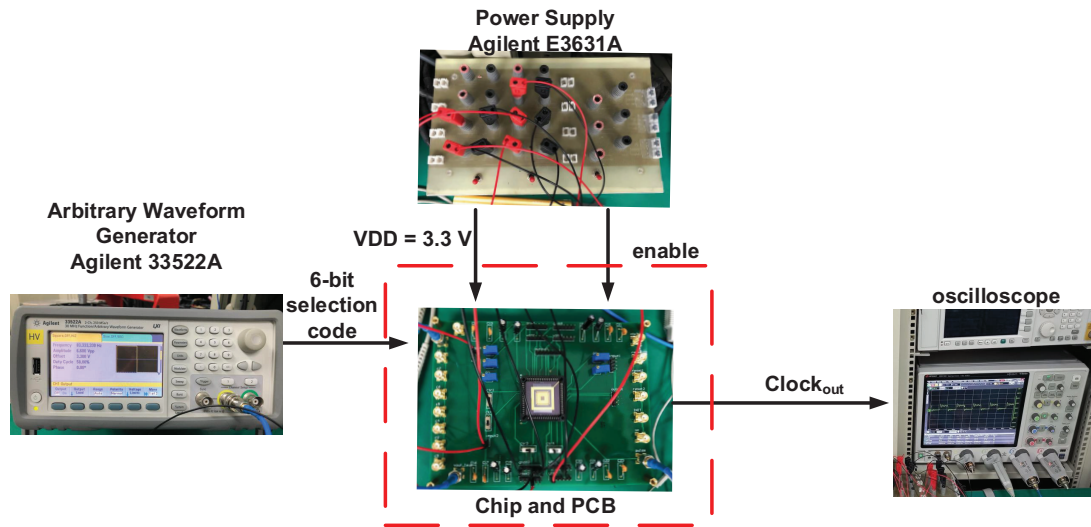


Figure 8: Measurement setup and equipment

serpentine) on the same die. The detailed layouts of the mentioned OSCs are enlarged in Figure 7. To highlight the influences from the different layout styles, the space between any two adjacent stages in Figure 7 is the same. The chip measurement setup is shown in Figure 8. The chip is soldered on the PCB to reduce noise interference. The Agilent E3631A Power Supply provides the required voltages and enable signals to the chip. Arbitrary waveform generator Agilent 33522A provide the 6-bit selection code. The oscilloscope WaveRunner610Zi is used to observe waveforms and monitor the circuit operations.

respectively. By comparing the pre-layout simulation (100 MHz) with the measurement results, the deviations of serpentine layout style and straight line layout style of OSCs are 4.5% and 11.3%, respectively.

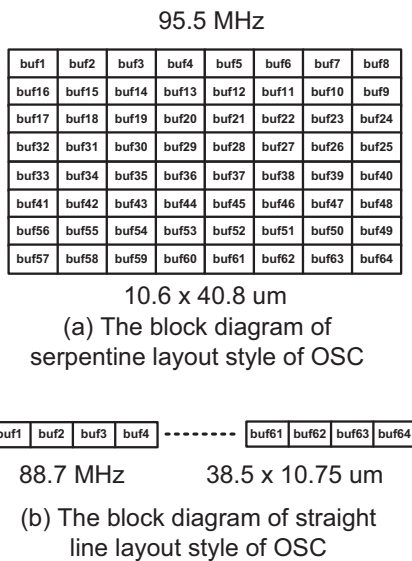


Figure 9: (a) The block diagram of serpentine layout style of OSC; (b) The block diagram of straight line layout style of OSC

Figure 9 shows the block diagrams of serpentine layout style and straight line layout style of OSCs in Figure 6 and 7. Figure 10 (a), (b) show the measurement waveforms of these 2 layout styles,

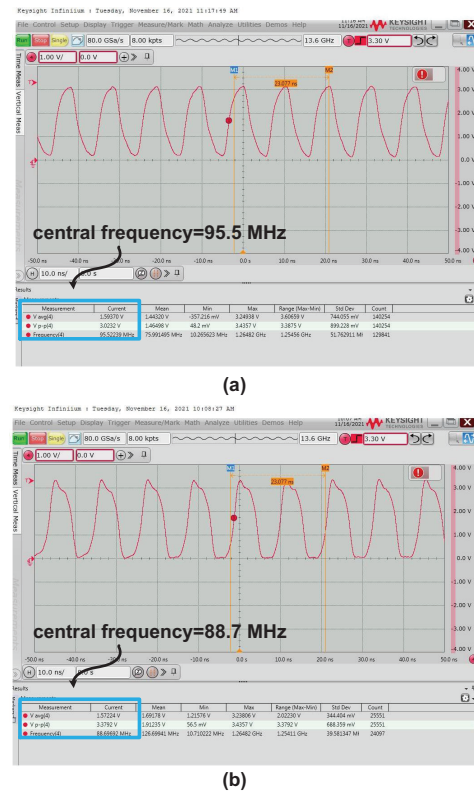


Figure 10: (a) The measurement waveform of central frequency of serpentine layout style; (b) The measurement waveform of central frequency of straight layout style

To verify the selectability of OSCs, Figure 11 shows the comparison of pre-layout simulation, post-layout simulation, and the chip measurement results by different selection codes (1-15). The

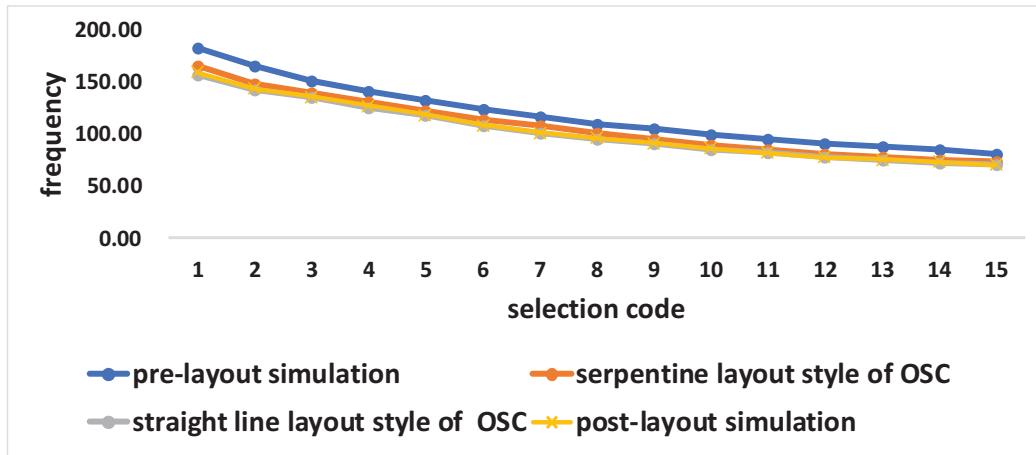


Figure 11: Comparison of pre-layout simulation, post-layout simulation, and the chip measurement results

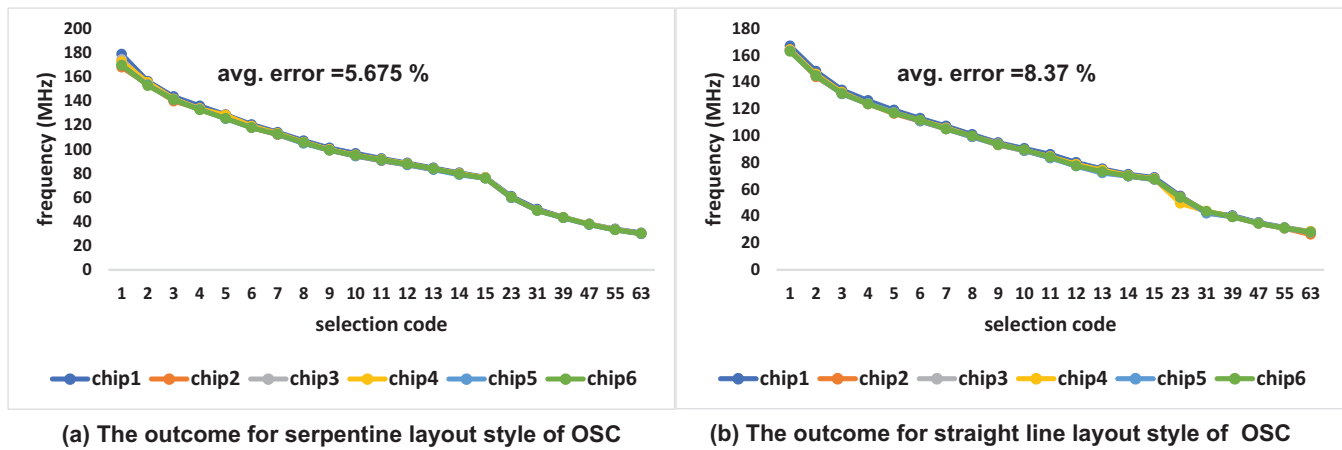


Figure 12: (a) The all chip measurement results of serpentine layout style of OSC by all different selection codes; (b) The all chip measurement results of straight line layout style of OSC by all different selection codes

measurement result of the serpentine layout style is closer to the prediction of post-layout simulations. To justify the repeatability of the chip measurement, all 6 chips are measured with 10 times and the results are shown in Figure 12. The average error of the serpentine style layout is smaller than that of the straight line counterpart. Table 1 tabulates the performance comparison of the proposed design and several recent works about layout arrangement. The proposed design achieves the second best FOM because our chip contains two layout arrangements of OSCs. In other words, the chip consumes much larger area than others. Notably, the proposed design would have the best FOM if only the area of the serpentine style is accounted for. The FOM will become 23606, simply the best of all.

5 Future Enhancement

The proposed OSC is a prototype for verifying the layout arrangement impact on CMOS oscillators. Thus, the main issue to be improved in the future is to enlarge the frequency range.

6 Conclusion

This investigation presents detailed analysis of OSC layout styles to conclude that the serpentine layout significantly reduces the variation impact. Moreover, the proposed layout method can be used to other CMOS processes. The proposed serpentine layout style can be applied in other CMOS technology nodes to make the chip performance more predictable in the early design stage.

7 Acknowledgment

This work was partially supported by FocalTech Systems Co., Ltd, Taiwan, under grant NO. N109130. The authors would like to express their deepest gratefulness to TSRI (Taiwan Semiconductor Research Institute), Taiwan, for their chip fabrication service.

References

- [1] Z. Abbas, A. Zahra, M. Olivieri, and A. Mastrandrea "Geometry scaling impact on leakage currents in FinFET standard cells based on a logic-level leakage estimation technique," *Microelectronics, Electromagnetics and Telecommunications*, **521**(4), 283-294, 2018, doi:10.1007/978-981-10-7329-8_29.
- [2] S.-K. Shin, W. Yu, Y.-H. Jun, J.-W. Kim, B.-S. Kong, and C.-G. Lee, "Slew-rate-controlled output driver having constant transition time over process, voltage, temperature, and output load variations," *IEEE Trans. on Circuits and Systems II: Express Briefs (TCAS-II)*, **54**(7), 601-605, 2007, doi:10.1109/TCSII.2007.895314.
- [3] R.-C. Kuo, H.-Y. Tseng, J.-W. Liu, and C.-C. Wang, "On-chip process and temperature compensation and self-adjusting slew rate control for output buffer," in *Asia Pacific Conf. on Postgraduate Research in Microelectronics Electronics (PrimeAsia)*, 37-40, 2011, doi:10.1109/PrimeAsia.2011.6075065.
- [4] T.-J. Lee, W. Lin, and C.-C. Wang, "Slew rate improved 2×VDD output buffer using leakage and delay compensation," in *IEEE Inter. Conf. on Electron Devices and Solid-State Circuits (EDSSC)*, 1-2, 2014, doi:10.1109/EDSSC.2014.7061267.
- [5] C.-L. Chen, H.-Y. Tseng, R.-C. Kuo, and C.-C. Wang, "On-chip MOS PVT variation monitor for slew rate self-adjusting 2×VDD output buffers," in *IEEE Inter. Conf. on IC Design Technology (ICICDT)*, 1-4, 2012, doi:10.1109/ICICDT.2012.6232876.
- [6] C.-L. Chen, H.-Y. Tseng, R.-C. Kuo, and C.-C. Wang, "A slew rate self-adjusting 2×VDD output buffer with PVT compensation," in *IEEE VLSI Design, Automation and Test (VLSI-DAT)*, 1-4, 2012, doi:10.1109/VLSI-DAT.2012.6212590.
- [7] C.-C. Wang, C.-L. Chen, R.-C. Kuo, H.-Y. Tseng, J.-W. Liu, C.-Y. Juan, "On-chip process and temperature monitor for self-adjusting slew rate control of 2×VDD output buffers," *IEEE Trans. on Circuits and Systems I: Regular Papers (TCAS-I)*, **60**(6), 1432-1440, 2013, doi:10.1109/TCSI.2012.2226515.
- [8] T.-J. Lee, K.-W. Ruan, and C.-C. Wang, "32% slew rate and 27% data rate improved 2×VDD output buffer using PVTL compensation," in *IEEE Inter. Conf. on IC Design Technology (ICICDT)*, 1-4, 2014, doi:10.1109/ICICDT.2014.6838601.
- [9] C.-C. Wang, T.-Y. Tsai, T.-J. Lee, and K.-W. Ruan, "2×VDD output buffer with 36.4% slew rate improvement using leakage current compensation," *Electronics Letters (EL)*, **53**(2), 62-64, 2017, doi:10.1049/el.2016.2351.
- [10] C.-C. Wang, T.-Y. Tsai, and W. Lin, "A 90-nm CMOS 800 MHz 2×VDD output buffer with leakage detection and output current self-adjustment," *Analog Integrated Circuits and Signal Processing (AICSP)*, **97**(2), 343-350, 2018, doi:10.1007/s10470-018-1285-3.
- [11] D. R. Dancer, "Digitally controlled ring oscillator," U.S.A. Patent US96112503, 2006.
- [12] S. Wadhwa, D. Mehrotra, and P. M. Furth, "Low voltage, wide frequency range oscillator," U.S.A. Patent US8975974B2, 2012.
- [13] C. L. Lin, "Quadrature output ring oscillator and method thereof," R.O.C. Patent TW 1547095 B, 2015.
- [14] M. More and P. Apte, "Digitally controlled oscillator with variable capacitive loading," in *International Conference on Communication and Signal Processing (ICCSP)*, 1723-1726, 2016, doi:10.1109/ICCSP.2016.7754460.
- [15] Y. Wang, L. Zhang, T. Liu, Y. Wang, R. Hu, D.-B. Fu, and G.-B. Chen, "Layout design of metal-insulator-metal capacitor array for reducing parasitic influences," in *2016 IEEE International Nanoelectronics Conference (INEC)*, 1-2, 2016, doi:10.1109/INEC.2016.7589265.
- [16] Y. S. Hristov, S. D. Kostadinov, D. G. Gaydazhiev, and I. S. Uzunov, "Influence of the layout parasitic effects on the performance of current mode amplifier designed using 32nm CMOS technology," in *2018 IEEE XXVII International Scientific Conference Electronics (ET)*, 1-4, 2018, doi: 10.1109/ET.2018.8549671.
- [17] M. Hifumi, H. Maruoka, S. Umehara, K. Yamada, J. Furuta, and K. Kobayashi, "Influence of layout structures to soft errors caused by higher-energy particles on 28/65 nm FDSOI flip-flops," in *2017 IEEE International Reliability Physics Symposium (IRPS)*, 5.1-5.4, 2017, doi:10.1109/IRPS.2017.7936406.
- [18] B. Likhterov and A. Belenky, "Traveling-wave ring oscillator — a new architecture for a transmission line based oscillator," in *2016 IEEE International Conference on the Science of Electrical Engineering (ICSEE)*, 1-5, 2016, doi:10.1109/ICSEE.2016.7806048.
- [19] B. Likhterov and A. Belenky, "Traveling-wave ring oscillator – simulations and prototype measurements for a new architecture for a transmission Line Based oscillator," in *2018 IEEE International Conference on the Science of Electrical Engineering in Israel (ICSEE)*, 1-5, 2018, doi:10.1109/ICSEE.2018.8645996.
- [20] D. Garinto, A. Syahriar and S. Budiyo, "A novel op-Amp based LC oscillator for wireless communications," in *IECON 2020 The 46th Annual Conference of the IEEE Industrial Electronics Society*, 2243-2248, 2020, doi:10.1109/ICSEE.2018.8645996.
- [21] A. Mahmoud, P. Andreani and F. Pepe, "A 2.8–3.8-GHz low-spur DTC-based DPLL with a class-D DCO in 65-nm CMOS," *IEEE Microwave and Wireless Components Letters (MWCL)*, **27**(11), 1010-1012, 2017, doi: 10.1109/LMWC.2017.2750089.
- [22] I. Taha and M. Mirhassani, "A 24-GHz DCO with high-amplitude stabilization and enhanced startup time for automotive radar," *IEEE Transactions on Very Large Scale Integration (VLSI) Systems*, **27**(10), 2260-2271, 2019, doi:10.1109/TVLSI.2019.2924018.
- [23] H. Liuet, Z. Sun, H. Huang, W. Deng, T. Siriburanon, J. Pang, Y. Wang, R. Wu, T. Somey, A. Shirane, and K. Okada, "A 265μW fractional-N digital PLL with seamless automatic switching subsampling/sampling feedback path and duty-cycled frequency-locked loop in 65nm CMOS," *IEEE Journal of Solid-State Circuits (JSSC)*, **54**(12), 3478–3492, 2019, doi:10.1109/JSSC.2019.2936967.
- [24] S. Kundu, L. Chai, K. Chandrashekar, S. Pellerano, and B. R. Carlton, "A self-calibrated 2-bit time-period comparator-Based Synthesized Fractional-N MDLL in 22-nm FinFET CMOS," *IEEE Journal of Solid-State Circuits (JSSC)*, **56**(1), 43-54, 2021, doi:10.1109/JSSC.2020.3021279.

A Proposal of Code Modification Problem for Self-study of Web Client Programming Using JavaScript

Khaing Hsu Wai¹, Nobuo Funabiki^{*1}, Khin Thet Mon¹, May Zin Htun¹, San Hay Mar Shwe¹, Htoo Htoo Sandi Kyaw², Wen-Chung Kao³

¹Department of Information and Communication Systems, Okayama University, Okayama, Japan

²Department of Computer and Information Science, Tokyo University of Agriculture and Technology, Tokyo, Japan

³Department of Electrical Engineering, National Taiwan Normal University, Taipei, Taiwan

ARTICLE INFO

Article history:

Received: 16 May, 2022

Accepted: 05 September, 2022

Online: 24 September, 2022

Keywords:

web client programming

JavaScript

HTML

CSS

code modification

coding reading

self-study

ABSTRACT

In current societies, *web application systems* take central roles in computer systems. Thus, *web client programming using JavaScript* has increased values to add dynamic features and functions in web pages by well working with *HTML* and *CSS*. In this paper, as a new type of exercise problem for its self-study, we propose a *code modification problem (CMP)*. In CMP, a source code with *HTML/CSS* elements and *JavaScript* functions for study, and the screenshots of both the original and the slightly altered web pages are provided to the students, who will need to edit the source code to generate the modified page. The goal of CMP is for students to carefully read the source code and comprehend how to use the components and functions through modifying parameters, values, or messages there. *String matching* is used to check the correctness of any answer. Through solving CMP instances, the students are expected to master the basic concepts of *web client programming*. To evaluate the proposal, we generated and assigned 25 CMP instances to 37 students in Okayama University. In addition, we offered project assignments of freely implementing source codes by referring to solved CMP instances to evaluate their learning effects. With the solution results, the validity of the proposal has been confirmed.

1 Introduction

In current societies, computer systems using software and hardware have big impacts on our daily lives. They are crucial to enhancing the capabilities of communications, calculations, and information services. By executing a lot of effective programs that have been created using various programming languages, computer systems are illustrating their powers. In computer systems, several types of programming languages have been used together, depending on the fields and applications of them. Thus, studying the commonly used plural programming languages is essential to develop effective and efficient computer systems for the students in departments of computer science (CS) or information technology (IT) in academic institutions. Especially, web application systems have taken prominent roles in computer systems with expansions of the Internet. For this reason, learning *web client programming with JavaScript* is crucial for students majoring in IT or CS.

The primary scripting language running on web browsers is *JavaScript*, which is sometimes referred as *JS*. *JavaScript* is crucial to modern *web application systems* [1]. Currently, *JavaScript* is

adopted in 97% of websites in the world, making it the most popular client-side scripting language for *web client programming*. By combining the common web technology by the *Hyper Text Markup Language (HTML)* and *Cascading Style Sheets (CSS)*, *JavaScript* can provide dynamic features on a *web page*. The structure and meaning of the page are provided in *HTML*. The layout, background colors, and fonts used in *HTML* content are described in *CSS*. Then, the *document object model (DOM)* is used for *JavaScript* interactions with them.

In order to learn a new programming language, novice students should start their study by solving simple and short exercise problems to gain the basic understanding of the grammar and key concepts for *code reading study*. If they cannot read and understand simple source codes, they are unable to properly write them by themselves for *code writing study*. This step-by-step programming learning is important for novice students. After well completing *code reading study*, novice students should move to *code writing study*. To offer step-by-step self-study environments of programming languages to novice students, the project of developing the web-based *programming learning assistant system (PLAS)* has been

*Corresponding Author: Nobuo Funabiki, 3-1-1 Tshishimanaka, Okayama University, funabiki@okayama-u.ac.jp

established. Currently, well-known programming languages of C, C++, Java, Python, and JavaScript are supported in PLAS. PLAS offers different types of exercise problems with different learning goals and difficulty levels for the step-by-step studies, as the learning materials or contents on the common system platform.

In PLAS, there exist five types of exercise problems for code reading/writing studies, namely, *grammar-concept understanding problem (GUP)*, *value trace problem (VTP)*, *element fill-in-blank problem (EFP)*, *code completion problem (CCP)*, and *code writing problem (CWP)*.

The *grammar-concept understanding problem (GUP)* [2] offers questions about the source code's keywords by defining terms like reserved words and common libraries in programming languages. The *value trace problem (VTP)* [3], [4] requests the output values of significant variables and output messages in the provided source code. The *element fill-in-blank problem (EFP)* [5], [6] asks the students to complete the missing elements in the provided source code by comprehending its syntax and semantics in order to discover the original source code. The *code completion problem (CCP)* [7], which is intended for debugging study, requests to correct and complete the provided source code when there are blank or incorrect elements in the source code. The *code writing problem (CWP)* [8] requests to complete a new source code from scratch that can pass the given test code. The correctness of the student's answer is automatically checked by *string matching* with the correct one for *GUP*, *VTP*, *EFP*, and *CCP*, and by *software testing* using test codes for *CWP*.

In PLAS, students should first solve the problems related to *code reading study*. They include *GUP* and *VTP* to understand keyword definitions and source code control flows. Next, to learn how to complete source codes by themselves, they should solve *EFP*, *CCP*, and *CWP* in this order. Then, novice students will possibly continue programming studies without dropping out, while solving the problems in PLAS step-by-step, and resulting in improved code reading and writing skills.

However, due to the fact that most web pages are written with the combination of *JavaScript*, *HTML*, and *CSS*, any type of exercise problem currently available in PLAS may not be suitable for studying *web client programming*. After studying each language separately, students must be able to relate them in the source code in *web client programming*.

In this paper, we propose a *code modification problem (CMP)* as the new exercise problem type in PLAS for effective self-study of *web client programming using JavaScript*. Since one web page is usually generated by combining the layout styles of HTML/CSS elements with JavaScript library functions, the effective way to learn them is to read and understand the sample source codes where they are included. A *CMP* instance includes a source code with the HTML/CSS elements and JavaScript functions that should be studied, as well as the two screenshots of the originally produced web page and another modified web page. Then, the original source code is requested to be modified so as to generate the second web page. This *CMP* is designed for students to carefully study the source code and understand the use of the elements/functions, while changing some parameters, values, or messages. *String matching* is used to check the correctness of any answer. It is expected that they can obtain the basic concepts of *web client programming* through

solving the given *CMP* instances.

To evaluate the proposal, we generated and assigned 25 *CMP* instances to 37 students in Okayama University. Moreover, we offered project assignments that allow students to implement source codes freely by referring to solved *CMP* instances to evaluate their learning effects. The validity of the proposal has been confirmed by their solution results.

The outlines of this paper is organized as follows: Section 2 discusses related works in literature. Section 3 proposes the *code modification problem (CMP)*. Section 4 evaluates the analysis results of *CMP*. Section 5 discusses the learning effects and learning validation after solving the *CMP* instances. Finally, Section 6 concludes this paper with future works.

2 Related Works in Literature

In this section, we discuss related works to this study in literature.

In [9], the authors proposed an educational game approach called *Reduct* to instruct novice students on fundamental JavaScript programming principles, such as functions, Booleans, equivalence, conditional expressions, and mapping functions onto sets. The designs used theories of progression design and skill learning to scaffold concepts and motivate players to create accurate mental models of the codes. The current objective of this paper is to teach up to the level of advanced and fundamental functional programming in JavaScript.

In [10], the authors described a prototype system to aid students in learning the web language JavaScript. They discussed how portable intelligent exercises activities were implemented and tested them in the web programming course. According to survey assessment data, they demonstrated that the system may assist students in learning of JavaScript, the web-based programming language.

In [11], the authors proposed the *JavaScript development environment (JDE)* for the purpose of supporting programming education. The *JDE* offers a setting in which JavaScript programming may be done anywhere, at any time. Additionally, the *JDE* may offer comprehensive snippet features that make it possible to write code using a limited number of actions. It is appropriate for usage on smartphones because it is an environment based on a browser. The *JDE* can edit HTML, CSS, and JavaScript-enabled web pages.

In [12], the authors presented contributions of an interactive e-learning course for teaching web technologies including JavaScript and HTML as a component of the Moodle platform. This course may have been taught using traditional methods of instruction, or an alternative, utilizing the *Scrum* agile software development methodology and the *EduScrum* teaching methodology.

In [13], the authors proposed an interactive serious programming game for JavaScript programming course at their university. The gamification pattern-based method was used to create this game, together with the *Technology Acceptance Model (TAM)*, and the *Technology-Enhanced Training Effectiveness Model (TETEM)*. Using pre-test and post-test knowledge evaluations, *TAM*, and *TETEM*, they presented the game's evaluation findings.

In [14], the authors made comparative descriptions of several online platforms for teaching programming and chose engaging assignments from the site used to educate students named *hacker-rank.com*. They investigated user experiences with *online coding*

platforms (OCP) and contrasted the features of various online platforms that should be utilized to teach programming to aspiring computer scientists and programmers via distance learning. In addition, they also suggested using online programming simulators to enhance computer science instruction, taking into account functionality, as well as students' preparation levels and expected results of learning.

In [15], the authors proposed a game-based learning environment to assist beginner students learning programming. It uses game creation tasks to make basic programming easier to understand and includes idea visualization approaches to let students manipulate game objects to learn important programming concepts.

In [16], in order to investigate students' perceptions of this learning environment, the authors developed a collaborative, learning environment based on the problems powered by the technology for dynamic web. The research was planned as a qualitative study. A interview format that was semi-structured was created to get the opinions of the students about the learning environment, which was supported by technologies for dynamic web and used collaboratively solving issues techniques. Their findings imply that collaborative learning techniques focused on problems and the learning environment at a community college can benefit from technologies for dynamic web pages.

3 Proposal of Code Modification Problem

In this section, the *code modification problem (CMP)* for self-study of *JavaScript* based *web client programming* in PLAS is discussed.

3.1 Definition of Code Modification Problem

In a CMP instance, a source code containing the HTML/CSS elements and the functions to be studied here, and a pair of the screenshot of the original web page generated by the code and the screenshot of the slightly altered web page are provided to students. These web pages could have different parameters, functionalities, or variables. Then, the students are requested to modify the source code to generate the altered web page. By solving the given CMP instances, it is expected that the students can master the basic concepts of *web client programming* and understand the interacted use of HTML, CSS, and JavaScript in the source code. *String matching* is used to check the correctness of any answer in the source code.

CMP is designed with the following goals:

1. Source codes of various kinds are provided along with full forms in order to assist novice students with learning *web client programming using JavaScript*.
2. By answering the questions in CMP instances correctly, students can learn how to generate web pages using various JavaScript functions.
3. As a result of using *string matching*, the student feedback is immediately provided when answers are automatically marked.
4. A novice student who has never studied *web client programming* can answer the questions without encountering serious difficulties.

3.2 Generation Procedure of CMP Instance

The following procedure can be used to generate a new CMP instance:

1. From a website or book that contains the library functions to be examined in this instance, choose a proper source code with HTML, CSS, and JavaScript to develop the web page.
2. Save the screenshot of the web page after running the source code in a web browser.
3. Identify and determine the parts of the source code that students should modify to better understand the intended functionality. Currently, this step is manually carried out. The automatic processing will be studied in future works.
4. Save the screenshot of the altered web page after running the modified source code in a web browser.
5. Due to the fact that HTML tags are not visible on web browsers, replace the HTML tags with the HTML entities according to their numbers and names.
6. Make the input text file for the newly created CMP instance that consists of the problem statement, the original source code, and the modified source code as the correct solution.
7. Using this text file, generate the CMP instance files, which are combined with the HTML, CSS, and JavaScript, for the answer interface on a web browser using the *instance generation program*. It should be noted that this program has already been implemented and used for GUP, VTP, EFP, and CCP.
8. Insert the screenshots of the original and modified web pages into the HTML file for the CMP instance.

3.3 Example of Generating CMP Instance

Next, an example web page source code will be used to discuss the details of the CMP instance generation.

3.3.1 Original Source Code

The original source code should include the fundamental JavaScript library functions for *web client programming* to be studied in this instance. The example source code in Figure 1 shows the web page that displays the *alert box* after clicking *Submit button* from accepting the user name in the input form.


```

01 <html>
02 <body>
03 <p>Submit the Form with alert box</p>
04 <form name="myForm" onsubmit="myFunction()">
05   Enter name: <input type="text" name="fname">
06   <input type="submit" value="Submit">
07 </form>
08 <script>
09 function myFunction() {
10   var x = document.forms["myForm"]["fname"].value;
11   alert("Hi, "+x+" .The form was submitted");
12 }
13 </script>
14 </body>
15 </html>
    
```

Figure 1: Original source code for CMP instance #19.

```

01 <html>
02 <body>
03 <p>Submit the Form with alert box</p>
04 <form name="myForm" onsubmit="myFunction()">
05   Password: <input type="password" name="passwd">
06   <input type="submit" value="Create Password">
07 </form>
08 <script>
09 function myFunction() {
10   var x = document.forms["myForm"]["passwd"].value;
11   alert("Your password is created.");
12 }
13 </script>
14 </body>
15 </html>
    
```

Figure 3: Modified source code for CMP instance #19.

3.3.2 Original Web Page

The screenshot of the original source code for CMP instance #19 in Figure 2 shows the web page that was created using the source code in Figure 1. This generated web page is offered as a reference for understanding the source code.

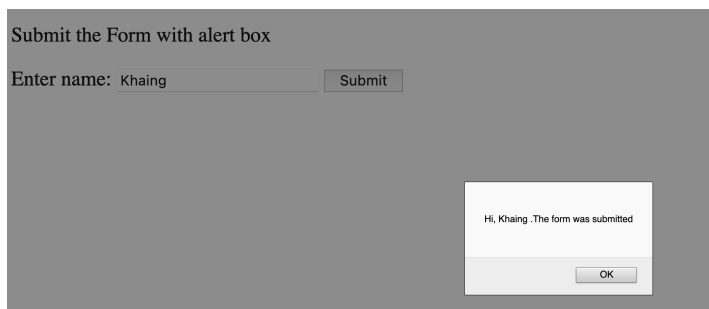


Figure 2: Web page by source code for CMP instance #19.

3.3.4 Modified Web Page

Figure 4 shows the screenshot of the altered web page by the modified source code.

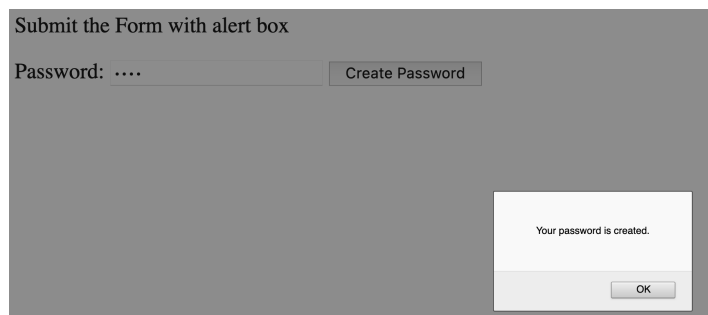


Figure 4: Modified web page for CMP instance #19.

3.3.3 Modified Source Code

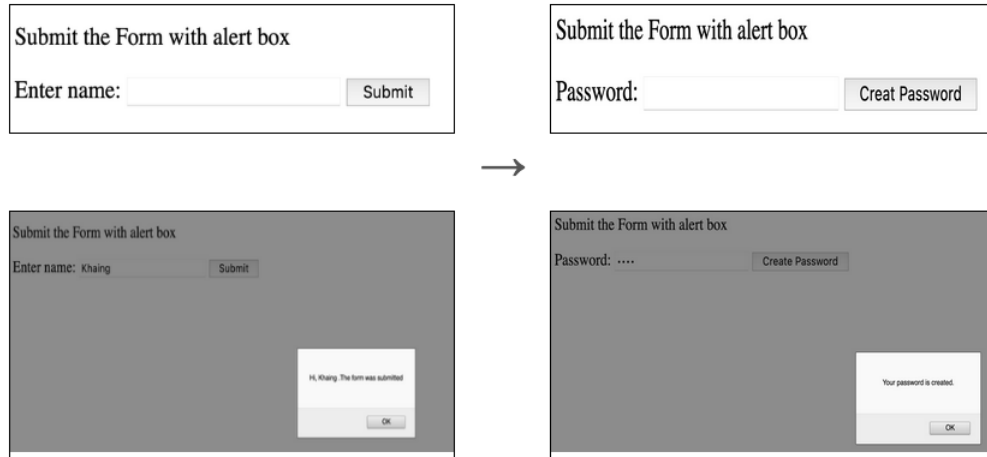
The original source code can be transformed into the modified source code by changing a few parameters and functions. It is important for students to understand the connections among the corresponding elements of HTML, CSS, and JavaScript when creating web pages. Figure 3 displays the source code for the correct answer. In this example instance, it is necessary to change the text messages in the alert box and the button, as well as the type and the name in the “input” tag.

3.4 Answer Interface

The answer interface is implemented using HTML, CSS, and JavaScript, where the JavaScript program handles the answer marking for the CMP instance. This allows both the online use and the offline use of the answer interface. In order to prevent students from cheating, the correct answers in any CMP instance are encrypted using *SHA256* [7].

Figure 5 illustrates the response interface for the CMP instance that requests the change of the form for the alert box. The source code lines in the input forms, which are indicated by red backgrounds, must be modified by students to complete this CMP instance. To better understand the source code, students can also download and run the source code, if they want to see how the web page is created and how it works.

After completing all the required changes to the input fields, the student can click the “Answer” button to confirm the validity of the answers. The relevant input form’s background color is changed to *red* if the answer on the line is incorrect. Otherwise, it turns *white*. The student can submit their answers again until every answer is verified as correct.



[Click Here To Download Source Code](#)

Modify the code to create the password. Use "password" for the type and passwrđ" for the name in 'input' tag.

Source Code

```

01:<html>
02:<body>
03:<p>Submit the Form with alert box</p>
04:<form name="myForm" onsubmit="myFunction()">
05:  Enter name: <input type="text" name="fname">
06:  <input type="submit" value="Submit">
07:</form>
08:<script>
09:function myFunction() {
10:  var x = document.forms["myForm"]["fname"].value;
11:  alert("Hi, "+x+" .The form was submitted");
12;}
13:</script>
14:</body>
15:</html>

```

the output

```

01<html>
02<body>
03<p>Submit the Form with alert box</p>
04<form name="myForm" onsubmit="myFunction()">
05  Enter name: <input type="text" name="fname">
06  <input type="submit" value="Submit">
07</form>
08<script>
09function myFunction() {
10  var x = document.forms["myForm"]["fname"].value;
11  alert("Hi, "+x+" .The form was submitted");
12}
13</script>
14</body>
15</html>

```

Answer

Answer

File Save

Figure 5: Answer interface for CMP instance #19.

4 Evaluation

This section evaluates the proposed code modification problem (CMP) for *web client programming using JavaScript*.

4.1 Evaluation of CMP Instances

In this evaluation, 25 CMP instances are generated, to examine fundamental concepts and functions in *web client programming* for performing dynamic behaviors of web pages using JavaScript, HTML, and CSS. The topic/function, the number of lines in the source code, and the number of elements that need to be modified for each CMP instance are displayed in Table 1. Other topics like using media devices will be studied in our upcoming works.

4.2 Solution Results

A total of 37 first-year master students in Okayama University, who have not taken any formal course in JavaScript programming, are assigned these 25 CMP instances. Prior to this assignment, we only offered a few websites as references to them.

4.2.1 Results of Individual Students

The results of the 37 individual students are first analyzed in our evaluations. The correct answer percentage (%) and the number of submissions in average among the 25 CMP instances are shown for each student in Figure 6.

According to the results, out of the 37 students, 22 students correctly answered the question and achieved the 100% correct rate, and 10 students scored above 90%. Only five students could not reach 90%. Among these five students, three are considered giving up answering the problems as zero answer submission attempts, and two students had not solved and submitted all the problems. Therefore, in general, the novice students can solve the generated CMP instances through self-study of *web client programming using JavaScript*.

Since each instance requires at least one submission of the answer, 25 is the least number to solve the 25 CMP instances. There are 131.4 submission times on average. These students generally submitted answers 2 – 14 times to solve one CMP instance. As a result, they carefully prepared and checked their answers before submitting them.

4.2.2 Results of Individual Instances

Next, we examine the solution results of individual 25 CMP instances. The correct answer percentage (%) and the number of submissions on average are shown for each of the 25 CMP instances among the 37 students in Figure 7.

According to the results, the instance at ID=18 gets the lowest correct rate, which is 90.8%, and the instance at ID=7 achieves the highest correct rate, which is 100%. The maximum number of submissions is 10 for the instances at ID=18 and ID=23 and the minimum ones are 3.3 for the CMP instances of the instances at ID=2, ID=17 and ID=19. Regarding the proportion of the correct answers, 30 elements/functions are needed to be changed in the instance at ID=18. In this case, we can assume that students looked

at the screenshots rather than reading the instructions. Some students had not tried to solve this problem from the answer results. In contrast, the source code of the instance at ID=7 was simple for students where they just need to change the colors and the lists.

As for the number of submission, the instances at ID=2, ID=17, and ID=23 are simple to find the necessary modifications. On the other hand, the instances at ID=18 and ID=23 require several modifications. Thus, students submitted their answers 10 times on average. In general, the CMP instances are simple to be solved. However, some instances contain long source codes, where students took time to read and understand them, and made higher submission times.

5 Project Assignment for Learning Effect Evaluation

In this section, we present *project assignments* to evaluate learning effects of the *code modification problem (CMP)* in *JavaScript-based web-client programming*.

5.1 Overview

The proposed CMP is designed for students to read a source code carefully by asking changes of some parameters, values, or messages there, and to understand how to use the HTML/CSS elements and the JavaScript library functions appearing in the code for *web client programming*. However, the CMP does not ask writing source codes by students, which will be a weak point of this approach. Thus, we will evaluate learning effects in code writing to students after solving the CMP instances.

For this purpose, we prepared two *project assignments*, requesting to design web pages and complete the source codes by referring to some given CMP instances. We made the corresponding answer interface to the project assignment that contains the *problem statement* on the requirements, the *input form* for the answer source code, the *web page output area* by running the code, and the *hint* including the sample page layout, the related CMP instances, and the short instruction video. The web page generated by running the code is shown so that students can easily test their source codes. The project assignments were assigned to the same students after solving the 25 CMP instances.

5.2 Project Assignment #1

The first project assignment is *Timer* that requires to implement the text input form, the start, stop, and clear buttons, and the time counting function by using the interval function. Figure 8 illustrates the sample web page.

5.2.1 Problem Statement

In this assignment, the problem statement is given by: “Create and develop simple “Timer” using HTML, CSS and JavaScript. You timer will count the minutes by using *setInterval* () function. You can see the hints by clicking the Hint button below. You can also try to write and run codes in the ‘Code’ area and see how your codes work in the ‘Output’ area. If your code is OK, you can save your project with your student ID.”

Table 1: Generated CMP instances.

ID	topic/function	# of lines		# of modified elements	
		HTML/CSS	JavaScript	HTML/CSS	JavaScript
1	JavaScript object	6	4	1	4
2	JavaScript class	13	10	2	2
3	JavaScript math	7	3	3	1
4	click button	10	3	2	1
5	disable button	12	20	2	3
6	circle drawing	5	14	0	5
7	unordered list	19	7	6	3
8	radio button	11	4	5	1
9	checkbox	8	12	1	1
10	information and color change	15	3	5	1
11	color form type	10	12	2	2
12	element position change	27	10	2	2
13	rotating image	14	7	1	3
14	clickable image map	23	5	3	1
15	image button with counter	22	7	3	3
16	background image position change	21	6	4	2
17	text transformation from text area	37	11	7	1
18	file input type with alert box	25	5	8	1
19	input form with alert box	9	6	2	2
20	numbers addition/subtraction from input form	33	8	3	2
21	progress bar with clicking button	23	23	4	3
22	slider control with range input type	39	9	10	1
23	bar chart drawing from input value	49	14	5	3
24	table row insertion with button	41	9	8	3
25	table column deletion with button	66	16	32	2

My Timer

Figure 8: Sample *Timer* page for assignment #1.

5.2.2 Hint

In this assignment, the hints are given by:

“For *Timer*, you will need input form to set the minutes and two buttons: start and stop for setting the timer based on the user input value. You can also see Problem #19 and #21 for the reference.

For the *layout interface*, you can create your free design for simple minute count timer. In the following example video, the timer will start as soon as the user put the input minutes value and start the timer button. The timer will be stopped and clear the interval when the user click the stop timer button.

The *setInterval()* method executes a function or evaluates an expression at specified intervals for *JavaScript library functions* (in milliseconds). Until *clearInterval()* is invoked or the window is closed, the *setInterval()* method will keep running the procedure. The ID value returned by *setInterval()* is used as the parameter for the *clearInterval()* method.”

5.2.3 Result and Discussion

Among the 37 students, only seven students completed this project assignment by making the source codes satisfying the requirements on the interface and functions. Five students among them achieved the 100% correct rate in solving the 25 CMP instances.

Feedbacks from other students who could not complete this assignment suggested that they found difficulties in combined use of HTML, CSS, and JavaScript, which usually results in long source codes. They also found difficulties in debugging source codes, because the web browser does not show any error message while running them. The use of an advanced IDE returning the error messages should be recommended to edit the source code in *web-client programming*.

Then, it was observed that the web page designs of the submitted source codes are unique from each other. Some pages show the timer with minutes and seconds, while others additionally show hours, and even years, months, and days. It is concluded that these seven students well studied *web-client programming using JavaScript*.

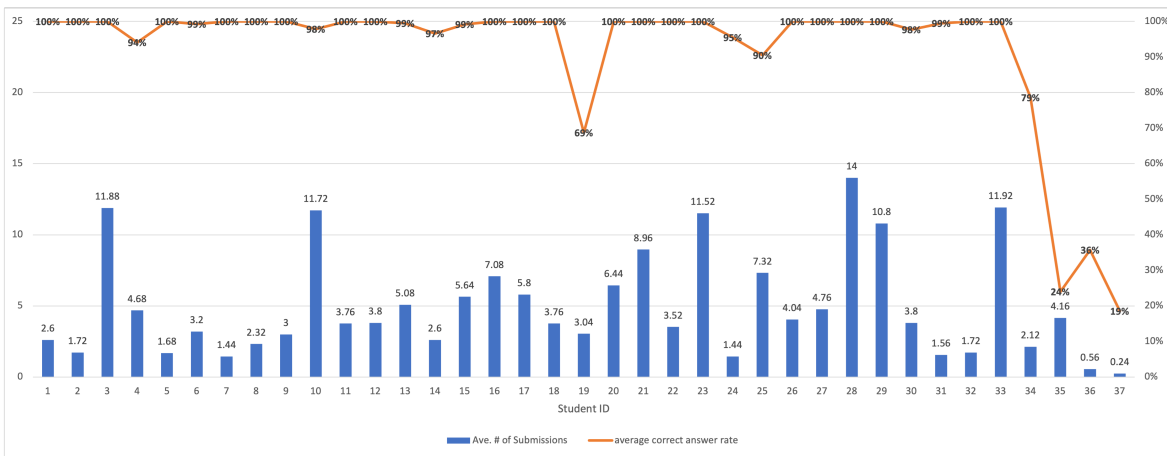


Figure 6: Results for each student.

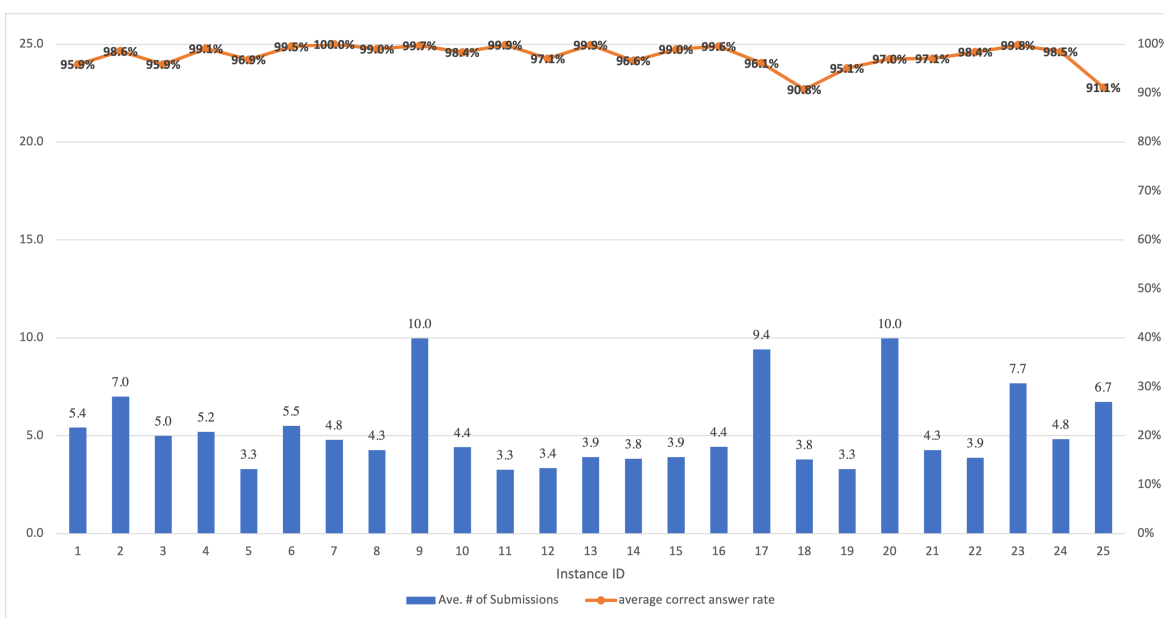


Figure 7: Solution results for individual CMP instances.

5.3 Project Assignment #2

The second project assignment is *Calculator* that requires to implement the table layout, the result area, the text input form, the calculation button, and the four arithmetic operations: addition, subtraction, multiplication, and division. Figure 9 illustrates the sample web page. Numbers (0-9), and operators (+, -, *, /, %, =) should appear in the table layout and the result area.

5.3.1 Problem Statement

In this assignment, the problem statement is given by: “Create and develop simple “Calculator” using HTML, CSS, and JavaScript. Your calculator may contain numbers (0-9), simple basic calculations (+, -, *, /, %, =) and result area to show the calculation answers. You can see the hints by clicking the Hint button below. You can also try to write and run codes in the ‘Code’ area and see how your codes work in the ‘Output’ area. If your code is OK, you can save your project with your student ID.”

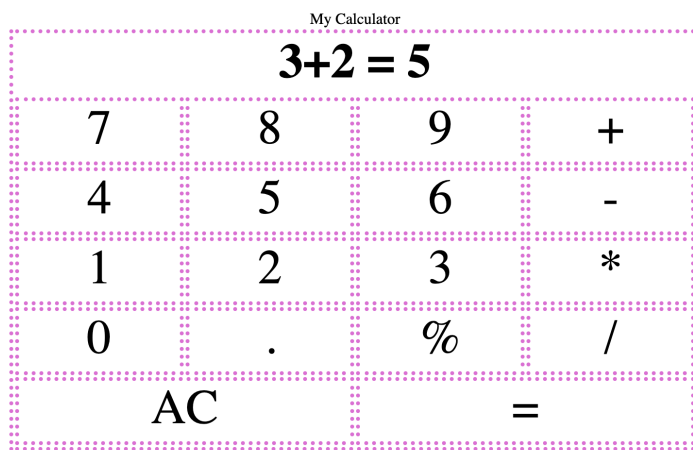


Figure 9: Sample Calculator page for assignment #2.

5.3.2 Hint

In this assignment, the hints are given by:

“For *Calculator*, you will need numbers, operators, and display area for the results.

For the *layout interface*, you can create your free design for your calculator. In the following example video, table layout and onclick function is used to get the inputs. You can also see Problem #25 for the reference.

For *JavaScript library functions*, you can use any arithmetic function for calculation in JavaScript. Here, simple *eval()* function is used in the example. But, using *eval()* in real-world applications is far more dangerous. We used it here for keeping our project simple.”

5.3.3 Result and Discussion

The same seven students completed this project assignment using the table layout design. Their implementations of the arithmetic operations are similar but not the same among them as in the first project assignment.

6 Conclusion

This paper proposed the *code modification problem (CMP)* in *programming learning assistant system (PLAS)* for self-study of *web client programming using JavaScript*. The proposed CMP is designed for students to read a source code carefully by asking changes of parameters, values, or messages there, and to understand how to use the HTML/CSS elements and JavaScript library functions appearing in the code. Students can submit the answers until achieving the correct answers and *string matching* is used to check the correctness of any answer.

For the evaluation of the proposal, 25 CMP instances, which cover the basic functions and topics of *web client programming*, were generated, and 37 first-year master students in Okayama University, who have not taken a formal JavaScript programming course, were assigned to solve them. Based on the results of their solutions, the validity of the proposal has been confirmed. Additionally, two simple project assignments were assigned to the students to evaluate learning effects in code writing abilities.

In future works, we will create CMP instances for web server programming and for other commonly used concepts and functions in web client programming, and provide them to students to evaluate the effectiveness. We will also assist students to complete the project assignments by giving hints on layout designs and code implementations.

References

- [1] S.H. Jensen, A. Moller, P. Thiemann, “Type analysis for JavaScript,” International Static Analysis Symposium, 238–255, 2009, doi:10.1007/978-3-642-03237-0-17.
- [2] S.T. Aung, N. Funabiki, Y.W. Syaifudin, H.H.S. Kyaw, S.L. Aung, N.K. Dim, W.-C. Kao, “A proposal of grammar-concept understanding problem in Java programming learning assistant system,” Journal of Advances in Information Technology, **12**(4), 342–350, 2021, doi:10.12720/jait.12.4.342-350.
- [3] K. K. Zaw, N. Funabiki, W.-C. Kao, “A proposal of value trace problem for algorithm code reading in Java programming learning assistant system,” Information Engineering Express, **1**(3), 9–18, 2015, doi:10.52731/iee.v1.i3.39.
- [4] S. H. M. Shwe, N. Funabiki, Y. W. Syaifudin, E. E. Htet, H. H. S. Kyaw, P. P. Tar, N. W. Min, T. Myint, H. A. Thant, W.-C. Kao, “Value trace problems with assisting references for Python programming self-study,” International Journal of Web Information Systems, **17**(4), 287–299, 2021, doi:10.1108/IJWIS-03-2021-0025.
- [5] N. Funabiki, Tana, K.K. Zaw, N. Ishihara, W.-C. Kao, “A graph-based blank element selection algorithm for fill-in-blank problems in Java programming learning assistant system,” IAENG International Journal of Computer Science, **44**(2), 247–260, 2017.
- [6] H.H.S. Kyaw, N. Funabiki, S.L. Aung, N.K. Dim, W.-C. Kao, “A study of element fill-in-blank problems for C programming learning assistant system,” International Journal of Information and Education Technology, **11**(6), 255–261, 2021, doi:10.18178/ijiet.2021.11.6.1520.
- [7] H.H.S. Kyaw, S.S. Wint, N. Funabiki, W.-C. Kao, “A code completion problem in Java programming learning assistant system,” IAENG International Journal of Computer Science, **47**(3), 350–359, 2020.
- [8] N. Funabiki, Y. Matsushima, T. Nakanishi, N. Amano, “A Java programming learning assistant system using test-driven development method,” IAENG International Journal of Computer Science, **40**(1), 38–46, 2013.
- [9] I. Arawjo, C.-Y. Wang, A.C. Myers, E. Andersen, F. Guimbretière, “Teaching programming with gamified semantics,” in 2017 CHI Conference on Human Factors in Computing, 4911–4923, 2017, doi:10.1145/3025453.3025711.
- [10] J. Appleton, “Introducing intelligent exercises to support web application programming students,” in 2017 International Conference on Information Communication Technologies in Education (ICICTE), 216–225, 2017.
- [11] M. Uehara, “JavaScript development environment for programming education using smartphones,” in 2019 International Symposium on Computing and Networking Workshops (CANDARW), 292–297, 2019, doi:10.1109/CANDARW.2019.00058.
- [12] P. Vostinar, “Interactive course for JavaScript in LMS Moodle,” in 2019 IEEE International Conference on Emerging eLearning Technologies and Applications (ICETA), 810–815, 2019, doi:10.1109/ICETA48886.2019.9039987.
- [13] R. Maskeliūnas, A. Kulikajevas, T. Blažauskas, R. Damaševičius, J. Swacha, “An interactive serious mobile game for supporting the learning of programming in JavaScript in the context of eco-friendly city management,” Computers, **9**(4), 1–18, 2020, doi:10.3390/computers9040102.
- [14] I. S. Zinovieva, V. O. Artemchuk, A. V. Iatsyshyn, O. O. Popov, V. O. Kovach, A. V. Iatsyshyn, Y. O. Romanenko, O. V. Radchenko, “The use of online coding platforms as additional distance tools in programming education,” Journal of Physics: Conference Series, **1840**, 2021, doi:10.1088/1742-6596/1840/1/012029.
- [15] F. W.-B. Li, C. Watson, “Game-based concept visualization for learning programming,” in 2011 International ACM Workshop on Multimedia Technologies for Distance Learning (MTDL), 37–42, 2011, doi:10.1145/2072598.2072607.
- [16] E. Ünal, H. Çakir, “Students’ views about the problem based collaborative learning environment supported by dynamic web technologies,” Malaysian Online Journal of Educational Technology, **5**(2), 1–19, 2017.

Sensitive Analysis in Holding and Penalty Costs for the Stochastic Sequencing Problem in Agile Manufacturing

Erick Esparza Tapia, Eva Selene Hernández Gress*, Martin Flégl

Tecnológico de Monterrey, School of Engineering and Sciences, Pachuca Hidalgo, 42080, México

ARTICLE INFO

Article history:

Received: 17 August, 2022

Accepted: 19 September, 2022

Online: 27 September, 2022

Keywords:

Agile manufacturing

Sensitivity

Sequencing problem

Dispatching rules

ABSTRACT

In agile manufacturing, due to the desire to meet customer's requirements, processing times are stochastic because operations could be done by robots or humans. This can cause several problems in scheduling the jobs, and it is necessary to select the dispatch rule with the least change in costs and times, to respond quickly to different processing times. In this work, some experimental tests are carried out through a simulation algorithm and the runs are made in a robot with 6 jobs where the delivery dates and the probability distribution of the processing times are known. The dispatch rules are compared, varying the ratio of Holding-Penalty cost in different proportions to analyze how the total cost is affected, which is the novelty of this work. It was found that the most robust rule is the Shortest Processing Time (SPT) no matter if $HC > PC$ or $PC \leq HC$; with less variance in cost and the least average completion time compare with the others. With the mean lowest cost and that simultaneously minimizes early, and late production average time is the Earliest Due Date (EDD), when processing times are stochastic. As the dispatch rules present different degrees of sensitivity according to the cost relationship, it is convenient to explore which is the Holding-Penalty Cost relationship, that provides greater robustness and not just selects the least expensive rule.

1. Introduction

In a manufacturing system, scheduling jobs on a single machine consists of sequencing them through a dispatch rule; that establishes the order of processing based on parameters such as the delivery date, the order of arrival or the processing time. In this sense, the objective of job scheduling is the performance optimization metric in terms of time or cost [1-3].

On the other hand, agile manufacturing refers to the production approach to re-pond quickly to uncertain aspects such as process technologies, customer demand or changing requirements; to achieve this, flexible manufacturing systems are used. In these systems, operations sequences and dispatch strategies are very important to respond in an agile manner [4]. In the present work, the process times are studied as stochastic variables, since this has significant effects in the flexible manufacturing system [5], allowing to measure how robust the solution is when processing times are used according to a certain probability distribution. Such measures can prevent wrong decisions [6]; although these times may vary due to clients requiring certain specifications and tasks

can be done by a human or a robot. Additionally, diverse customer requirements make it difficult to accurately estimate processing times.

Agile manufacturing requires managing change with flexibility while main-taining high service levels, just-in-time deliveries, and low production costs [6,7]. Given the above, for a manufacturing company that produces under an agile approach, it will be of interest to know the sensitivity of the total cost of each sequencing rule with respect to variations in the unit costs of maintaining inventory and penalties for late deliveries. The goal of analyzing such sensitivity is to control and ensure the agility of the production system in a changing environment. In this sense, knowing the sensi-tivity of the total cost for each sequencing rule would allow, for example, to determine improvement objectives in the inventory and material handling system to maintain early production at a lower cost. Also, the sensitivity analysis would lead to establish negotiation strategies with customers on penalty policies for late production and select the sequencing rule that minimizes the two above costs and, at the same time, provides greater robustness in an environment that makes these costs vary.

*Corresponding Author: Eva Selene Hernández Gress, evahgress@tec.mx

For this reason, the motivation of this article is to present a sensitivity analysis that will serve as an instrument to support decision-making in the selection of sequencing rules. Particularly, when the costs of early and late production vary due to a changing environment, it is important to select the priority rule that is the more robust. Changing the processing times is motivated by the fact that the sequencing problems not only have a combinatorial structure, but also a temporal structure [8]. More specifically, changing the processing time of activities will also change the completion time of the jobs later, changing its delivery date, the parameters used to decide the optimal sequence (such as the average number of late jobs) and, therefore, the optimal sequence. Sensitivity analysis in this area is important because we live in an environment where processing times can change [9,10], as in agile manufacturing.

The article is structured as follows. In section 2, a brief analysis of the state of the art on agile manufacturing, stochastic dispatch rules, and their sensitivity analysis is carried out. In section 3, the problem and the method used to simulate production runs with stochastic processing times are described. In section 4, the simulation results are presented, analyzing the sensitivity of the total cost per sequencing rule in two steps: first, three cases of the Holding Cost - Penalty Cost relationship (greater than, less than and equal to) are identified and how they impact the total cost. Once it is observed whether the cases are significant for the selection of sequencing rules, one of the two costs is varied while the other remains fixed to observed how the total cost changes. Finally, in section 5, the results obtained and their applicability in companies that produce under an agile approach are discussed.

2. Literature review

Since 1990, research has been done on sensitivity problems of sequencing problems, for example, in [11-13]. The precedence of operations has been studied in [14] and [15], the sensitivity of sequencing problems in parallel machines has also been experimented in [16]. In [17] the researchers examine single machine problems considering time intervals and discrete processing times, [18] and [19] also analyze similar cases. Cost sensitivity is important because costs are not always adequately estimated or vary due to changing customers' requirements. Thus, it must be resolved what would happen if these costs change [20].

There are works that present the choice for accepting or rejecting a job according to its penalty depending on its cost. For example, in [21] the researchers use a single machine with stochastic processing times. In [22] test priority rules with stochastic process times are used, but without considering cost. These authors show that the priority rules in a single machine with stochastic processing times are of current interest, because the single machine models have properties that more complex models have [4]. For example, a more complicated system that have a bottleneck is similar to a single machine model. Agile manufacturing deals with high human mix between humans and robots in collaborative manufacturing facilities, which creates uncertainty in job processing times [23-25]. Therefore, it is necessary to respond quickly to unforeseen customer demands. In this kind of manufacturing systems there is also a need of active and proactive schedules [26], in which the decision maker thinks (or rethinks) in how the activities need to be prioritized to be ready

for any possible scenario [27]. This high variation of production requirements makes it challenging to find the optimal solution at the lowest cost [28], or to find the most robust solution. For this, in [23] is proposed a sequencing and dispatch method for facilities where humans and robots are mixed, while handling uncertainty in process times to minimize the variability of the solution. In [28] the authors optimize the production line that works with parallel machines that work at different speeds, whereas in [29] propose an adaptive sequencing and dispatch method for human-robot collaborative manufacturing systems where policy is dynamically adjusted using petri nets.

In [30] they suggest a mathematical model for the sequencing problem in a mixed model with high variety. To achieve this, the authors developed a heuristic solution to minimize the variability of the workload. In [27] performed a robust programming in the automatic supply chain presenting a hybrid store flow with job shop type processes, where multiple objectives are handled in the presence of capacity changes. In [31], they performed an optimization through simulation that allows dealing with the programming of vehicles and machines in a flexible system with stochastic elements included. Furthermore, a genetic algorithm is used to reduce the number of replicas. In [32] the authors worked with an assembly line where multiple products were manufactured with different demand, delivery dates and the variation in the material, to minimize the makespan and the cost of penalty for late delivery. Table 1 presents a comparison of these works and the proposal.

Table 1: Comparison of the relevant aspects of articles that address the Sequencing Problem in Agile. Own elaboration

Work	Uncertainty and robustness	Multiple machines	Use simulation	Optimized objective	Costs sensitivity
[23]	yes	yes	yes	Variability in the solution	no
[28]	no	yes	yes	Multiobjective (production and energy)	no
[29]	yes	no	no	Idle time	no
[30]	no	yes	no	Workload	no
[27]	yes	yes	no	Makespan	no
[31]	yes	yes	yes	Multiobjective (makespan, tardiness)	no
[32]	yes	yes	no	Multiobjective (variation in material,	no

				makespan, penalty cost)	
Proposal	yes	no	yes	Total cost, total early and late production time	yes

These works present different methodologies for agile manufacturing. What is different about the proposal in this article is the cost sensitivity analysis, since the total cost as a performance metric allows to control and ensure an agile manufacturing system in a changing environment in a viable way. Additionally, to check the robustness of the solution in the dispatch rules, stochastic processing times with a normal distribution are used through the inverse transform method¹ that is explained in [33]. The normal distribution for the processing times is used because the convolution property that it has, and the sum of the processing times is needed as it will be explained later, and, last but not least, each of these times has a normal distribution. Given two normal probability density functions $G_1 = (\mu_1, \sigma_1^2)$ and $G_2 = (\mu_2, \sigma_2^2)$, it is proved in the literature [34] that the convolution of these two functions is a normal probability distribution function with mean $\mu_1 + \mu_2$ and variance $\sigma_1^2 + \sigma_2^2$. This article presents jobs that need to go through a manufacturing robot with different processing times, but sometimes need to be processed by humans to meet customer's requirements. The method to perform the sensitivity analysis is presented in section 3.

The research questions are the following:

RQ1. If lead times are stochastic, what is the priority rule for assigning jobs that should be chosen to minimize costs?

RQ2. If processing times are stochastic, what is the most robust priority rule, that is, with less variability in terms of costs?

3. Method

3.1. Problem description

Let be a problem of one robot ($m = 1$), with n jobs to be processed. Additionally,

X_j = stochastic processing time of the job j in an arbitrary distribution.

d_j = the due date of the job j , represents the shipping or completion date, and the completion of a job after a due date is allowed with a certain penalty.

c_j = time in which the job j is completed

C_{max} = the completion of the last job or makespan

To make the decisions, the priority rules listed below are used.

SPT = Shortest processing time, jobs are sorted according to processing times in ascending order.

LPT = Longest processing time, jobs are sorted according to processing times in descending order.

EDD = Earliest due date, the jobs enter the sequence according to the earliest due date and finish on the latest.

FCFS = First Coming First Served, the first that arrives is the first that is processed,

Due to the fact the job times are stochastic, these rules are compared using two considerations described in [4]: 1) stochastic dominance based on the expected value and 2) dominance based on the variance.

1) Dominance based on the expected value

1.1) The random variable X_1 is larger in expected value than X_2 if $E(X_1) \geq E(X_2)$.

1.2) The stochastically longest (most likely) random variable X_1 is compared with X_2 if $P(X_1 > t) \geq P(X_2 > t)$ for all t .

2) Dominance based on a variance

The random variable X_1 is larger in variance than X_2 if $\text{Var}(X_1) \geq \text{Var}(X_2)$.

Dominance based on expected value and variance order form another dominance call increasing convex ordering. To avoid confusion, in this case a stochastic comparison is made using Makespans subject to different scenarios (different processing times).

$$C_{max}^1 = \max(x_1^1, x_2^1, \dots, x_n^1)$$

$$C_{max}^2 = \max(x_1^2, x_2^2, \dots, x_n^2)$$

$$\text{If } C_{max}^1 \geq C_{max}^2 \text{ then } (E(C_{max}^1) \geq E(C_{max}^2)) \tag{1}$$

and their expected values are compared through the following performance measures (E = expected value)

$$E_{s \rightarrow \infty} \left(\frac{\sum_{j=1}^n c_j - d_j}{n} \right) = \text{Average days late} \tag{2}$$

$$E_{s \rightarrow \infty} \left(\frac{\sum_{j=1}^n d_j - c_j}{n} \right) = \text{Average days early} \tag{3}$$

$$E_{s \rightarrow \infty} \left(\frac{\sum_{j=1}^n c_j}{n} \right) = \text{Average completion time} \tag{4}$$

$$E_{s \rightarrow \infty} \left(\frac{\sum_{j=1}^n c_j}{\sum_{j=1}^n X_j} \right) = \text{Average jobs in system} \tag{5}$$

¹ In this case, the inverse transform method is used to generate the simulation runs and generate different processing times. This method is used because if the cumulative function of the probability distribution is known, its application is simple to use. The method is as follows:

Assume we want to generate a random variable X with a cumulative distribution function (CDF) F_X . The inverse transform sampling algorithm is defined as [33]:

www.astesj.com

1. Generate a random number $U \sim Unif(0,1)$
2. Let $X = F_X^{-1}(U)$

Then, X will follow the distribution governed by the (CDF) F_X . which was the desired result.

In addition, the total cost is calculated considering the Holding Cost (HC), which is the cost of keeping a unit in inventory, and the Penalty Cost (PC), the cost of not delivering a unit on time. Then, the expected value of the costs is given by

$$E_{s \rightarrow \infty}(\text{Lateness} * PC + \text{Earliness} * HC) = \text{Average Total Cost} \tag{6}$$

$$\left(\frac{\sum_{j=1}^n c_j - d_j}{n} \right) = \text{Lateness}$$

$$= \left(\frac{\sum_{j=1}^n d_j - c_j}{n} \right) = \text{Earliness}$$

3.2. Method case study

To exemplify the analysis method, the following case is proposed. Let suppose a robot that receives six jobs simultaneously and whose processing time corresponds to a normal distribution, with a mean, a standard deviation, and a known delivery date for each job. It is intended to minimize the total time of early and late production, and consequently, the total cost associated with holding inventory and penalties from customers. Likewise, it is considered that the robot has no setup interruptions during the processing of the six jobs and that the holding and penalty cost per unit are both the same for all the jobs.

The method to perform the sensitivity analysis of the total cost is based on the construction of a simulator of production runs with stochastic processing times, which receives the following inputs:

- A set of six jobs that arrive simultaneously.
- A mean and a standard deviation for the processing time of each job, assuming that the times follow a normal distribution.
- A due date for each job.
- An early production inventory holding cost and a late production penalty cost, per piece per day and pervasive for all jobs.
- As an example, the following parameters of the problem to perform the simulation are considered.

Table 2: Parameters used in the simulation of production runs. Own elaboration.

Job	Average (days)	Standard deviation (days)	Probability distribution	Due date (days)
A	4	1	Normal	34
B	10	1	Normal	25
C	2	0.5	Normal	18
D	14	1	Normal	30
E	12	1	Normal	14
F	6	1	Normal	22

Given the above parameters, the stochastic processing times are simulated through an inverse normal distribution function, whose calculation involves a random probability variable. Subsequently, the sequencing of jobs is performed in the robot based on the dispatch rules First Come First Served (FCFS), Shortest Processing Time (SPT), Longest Processing Time (LPT)

and Earliest Due Date (EDD). Finally, the total cost of the system per rule is obtained, whose calculation is the sum of the cost of keeping the early jobs in inventory and the penalty cost of the late jobs. This algorithm is presented in Figure 1, since it is not proving a theorem, perhaps with other examples the solution could change, but the algorithm of analysis is the same.

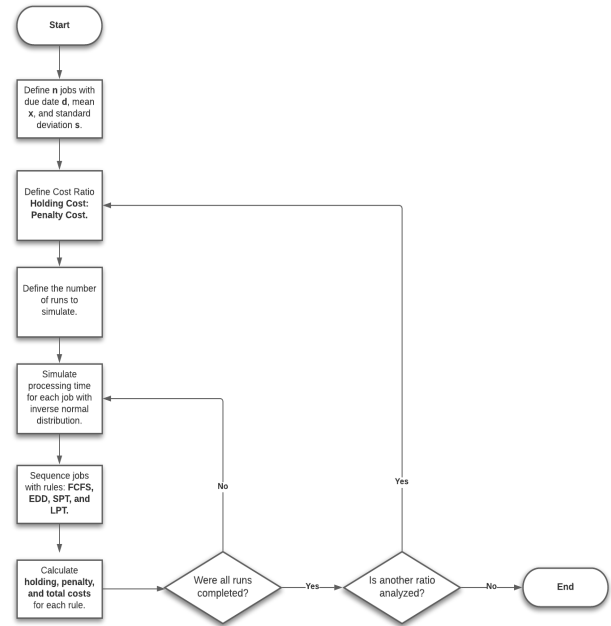


Figure 1: Algorithm to simulate production runs with stochastic processing times. Own elaboration

As the next step in the analysis, the behavior of the total cost of each rule with respect to the three cases of the Holding Cost - Penalty Cost relationship will be identified in such a way that the runs will be carried out as: 1) Holding Cost will be defined at \$4 and the Penalty Cost at \$2 for the case greater than; 2) \$2 and \$4 for the case less than; and 3) \$3 and \$3 for the case equal to. Once it has been verified if the cases of the Holding Cost - Penalty Cost relationship affect the total cost of the rules, then the degree of the sensitivity will be analyzed in each of the cases that were significant. To do this, the holding cost will be varied in a range of values between \$ 1 and \$ 500, while the penalty cost is fixed at \$ 1. Subsequently, the penalty cost will be varied in the same range, while the holding cost remains fixed at \$1. This sensitivity analysis of the total cost of the system will be carried out for each of the rules. Thus, the objective of this method is to observe how the total cost of the system changes when the following factors change: the sequencing rule used, the cases of the Holding Cost - Penalty Cost relationship, and the ratio between these costs (for example, \$5 of Holding Cost and \$1 of Penalty Cost is a 5:1 ratio). It is important to mention that a previous work deals with a scheduling model taking in account earliness/tardiness penalties [35], along with fuzzy processing times, but without considering the Holding Cost Penalty Cost ratio.

4. Results

4.1. Analysis of the holding cost – penalty cost relationship use

To begin with, it is important to analyze the three cases that could occur in the unit cost relationship per day for early and late

production presented before: Identifying the behavior of the total cost of the system for each of these three cases will allow to define if the change in the Holding Cost - Penalty Cost relationship is significant for the selection of sequencing rules in terms of the total cost.

In the first place, the behavior of the total cost is analyzed for the three cases of relationship Holding Cost – Penalty Cost; for which, the following runs were carried out in the simulator.

- 100 runs for the case Holding Cost = Penalty Cost in a 1:1 ratio
- 100 runs for the case Holding Cost > Penalty Cost in a 2:1 ratio
- 100 runs for the case Holding Cost < Penalty Cost in a 1:2 ratio

Table 3: Results of the relevant parameters of each dispatch rule for each case of the Holding Cost – Penalty Cost relationship. Own elaboration.

Case	Parameters	FCFS	EDD	SPT	LPT
Holding Cost = Penalty Cost	Total Cost	(294.11, 298.4)	(119.4, 124.9)	(283.3, 287.7)	(291.4, 303.1)
	Average days early	(7.26, 7.58)	(1.31, 1.51)	(9.55, 9.86)	(2.44, 2.63)
	Average days late	(8.84, 9.21)	(5.17, 5.57)	(6.02, 6.31)	(13.66, 16.3)
	Average completion time (min)	(25.11, 25.75)	(27.51, 28.0)	(20.20, 20.56)	(34.95, 38.5)
	Average jobs in system	(3.18, 3.22)	(3.48, 3.52)	(2.53, 2.57)	(4.42, 4.46)
Holding Cost < Penalty Cost	Total Cost	(302.7, 308.43)	(143.99, 151.7)	(262.8, 267.9)	(358, 373.8)
	Average days early	(7.155, 7.44)	(1.26, 1.46)	(9.39, 9.66)	(2.40, 2.61)
	Average days late	(8.91, 9.24)	(6.15, 6.43)	(6.15, 6.43)	(13.67, 14.3)
	Average completion time (min)	(25.32, 25.9)	(27.68, 28.22)	(20.3, 20.8)	(34.9, 35.6)
	Average jobs in system	(3.18969, 3.22358)	(3.48454, 3.51598)	(2.56231, 2.59381)	(4.40619, 4.43769)
Holding Cost > Penalty Cost	Total Cost	(281.5, 285.3)	(98.3, 101.8)	(301.8, 306.3)	(224.96, 234.21)
	Average days early	(7.01, 7.31)	(1.31, 1.51)	(9.41, 9.63)	(2.3596, 2.5765)
	Average days late	(9.054, 9.363)	(5.33, 5.704)	(6.16, 6.43)	(13.9, 14.5)
	Average completion time (min)	(25.59, 26.07)	(27.67, 28.21)	(20.39, 20.8)	(35.25, 35.87)
	Average jobs in system	(3.20, 3.23)	(3.4, 3.49)	(2.55, 2.58)	(4.41, 4.44)

It is necessary to mention that 40 runs are enough to have accurate results, but 100 are made to ensure their reliability. The simulator obtains the average value of all the runs for the following parameters in each rule: total cost, average days early, average days late, average completion time and average jobs in the system. Although the parameter of interest is the total cost, it is relevant to identify the behavior of the other parameters for each rule in each case of the relationship. Confidence intervals were made at 95% reliability, in every sample it was tested if the data were adjusted to a normal distribution, since the population variance was not known, the student's t-distribution was used [36]. The results of the analysis are shown in Table 3.

The interpretation of the results of this analysis is as follows:

- As can be seen, the magnitude of the total cost presents variations from one case to another in each rule, which will be studied in detail in the next section when carrying out the sensitivity analysis of the total cost in each case. For now, it is relevant to note that the performance of the sequencing rules does change depending on the case in which the cost relationship is found.
- In this sense, in the Holding Cost = Penalty Cost case and the Holding Cost < Penalty Cost case the same effect is observed when the order of the sequencing rules is analyzed in terms of total cost and even in the terms of the other parameters. For both cases the order of the sequencing rules from lowest to highest cost is: EDD, SPT, FCFS and LPT. However, the performance of the rules changes for the Holding Cost > Penalty Cost case, since the order of these rules from lowest to highest cost is EDD, LPT, FCFS and SPT.
- Given the above, it can be established that the three cases of the relationship Holding cost - Penalty cost identified can be grouped into only two significant cases for the selection of sequencing rules according to their performance: Holding cost > Penalty cost and Holding cost ≤ Penalty cost.
- Optimal rule: In any case of the Holding Cost - Penalty Cost relationship, the rule that generates the lowest total cost is EDD; this is because this rule minimizes the average earliness time and the average tardiness time in all cases.
- Most expensive rule: This rule depends on the two significant cases identified:
 - 1) When the Holding cost ≤ Penalty cost, the rule with the worst performance in terms of the total cost is LPT. This is because LPT is associated with the highest average completion times; therefore, this results in the highest delay times of the four sequencing rules.
 - 2) When Holding Cost > Penalty Cost the worst-performing rule is SPT. This is because SPT is associated with the lowest average completion times; therefore, this results in the highest early times of the four sequencing rules.

4.2. Sensitivity analysis of the total cost

As shown in the previous analysis, there are only two significant cases of the relationship Holding cost - Penalty cost for the selection of sequencing rules. Due to this, the sensitivity analysis of the total cost will be applied with respect to these two

cases for each of the four rules studied. The objective is to vary one of the two costs while the other remains fixed to change the ratio and visualize the effect of this change on the total cost when their relationship is found in one case or another.

In the first place, the case Holding Cost > Penalty Cost is analyzed, performing the following runs on the simulator:

- 100 runs for the Holding Cost > Penalty Cost in a 5:1 ratio
- 100 runs for the Holding Cost > Penalty Cost in a 10:1 ratio
- 100 runs for the Holding Cost > Penalty Cost in 50:1 ratio
- 100 runs for the Holding Cost > Penalty Cost in a 100:1 ratio
- 100 runs for the Holding Cost > Penalty Cost case in a 500:1 ratio

As shown, there are runs for cases where Holding Cost is 5 times greater than Penalty Cost, 10 times greater, 50 times greater, etc. It is worth mentioning that in a practical approach a very large ratio may be unrealistic, but it was analyzed for experimental purposes. Table 4 shows the average total costs of each sequencing rule with respect to each of the simulated ratios; in the same way, in Figure 2 these results were graphed by rule.

Table 4: Average total cost per sequencing rule for each ratio of the Holding Cost > Penalty Cost case. Own elaboration.

Holding Cost: Penalty Cost Ratio	Quotient	Average Total Cost			
		FCFS	EDD	SPT	LPT
05:01	5	274.47	73.21	323.3	157.63
10:01	10	493.38	111.73	612.87	221.32
50:01:00	50	2,240.00	423.12	2,884.80	837.49
100:01:00	100	4,393.56	835.98	5,719.99	1,594.16
500:01:00	500	22,155.67	4,042.66	28,723.70	7,850.70
Slope		44.2324	8.0252	57.3925	15.5683

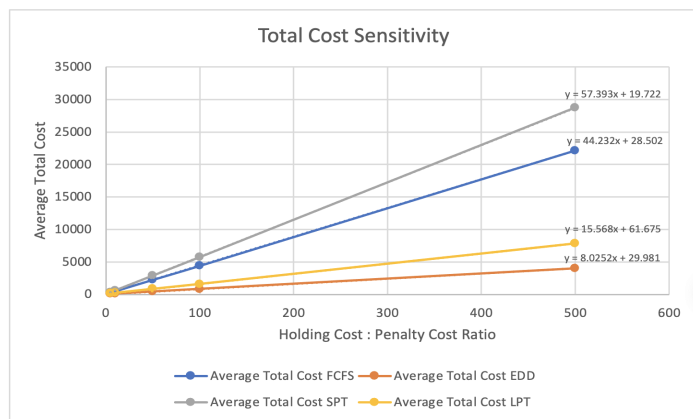


Figure 2: Sensitivity of the average total cost with respect to the costs ratio for the Holding Cost > Penalty Cost case. Own elaboration

To obtain the equations in Figure 2 a simple linear regression was performed for each rule, in which the total cost was used as the response variable and the Holding Cost: Penalty Cost ratio as the explanatory variable, whose regression model is the following:

$$Y = \beta_0 + \beta_1x + e$$

The parameters β_0 and β_1 were estimated with the least-squares method in order to define a line that fits the data by minimizing the sum of squares of the regression errors [34]. In particular, the estimation of the parameter β_1 represents the slope of the line or in this case, the degree of sensitivity of the total cost with respect to the change in the Holding Cost: Penalty Cost ratio.

The above evidence shows that with a higher holding cost, the total cost grows linearly at different speeds according to the applied sequencing rule. According to the slopes obtained in the regression of the data, it is noted that the least sensitive rule is EDD increasing \$ 8.03 for each unit that increases the Holding Cost: Penalty Cost ratio, while the most sensitive rule is SPT increasing \$ 57.39 per each unit that increases that ratio. That is, when Holding Cost > Penalty Cost the SPT rule is 7.15 times more sensitive than EDD; the other sensitivity relationships between rules are found in Table 5. Likewise, a grouping between the rules is observed, with EDD and LPT being notoriously less sensitive than FCFS and SPT for this case.

Table 5: Sensitivity relationships between the sequencing rules for the Holding cost > Penalty cost. Own elaboration.

Case: Holding Cost > Penalty cost				
Rule sensitivity:	Regarding the rule:			
	EDD	LPT	FCFS	SPT
SPT	7.15	3.69	1.3	-
FCFS	5.51	2.84	-	-
LPT	1.94	-	-	-
EDD	-	-	-	-

Second, the case Holding Cost ≤ Penalty Cost is analyzed, performing the following runs on the built simulator:

- 100 runs for the Penalty Cost case ≤ Holding Cost in a 1:1 ratio
- 100 runs for the Penalty Cost case ≤ Holding Cost in 5:1 ratio
- 100 runs for the Penalty Cost case ≤ Holding Cost in a 10:1 ratio
- 100 runs for the Penalty Cost case ≤ Holding Cost in 50:1 ratio
- 100 runs for the Penalty Cost case ≤ Holding Cost in a 100:1 ratio
- 100 runs for the Penalty Cost case ≤ Holding Cost in 500:1 ratio

It is worth mentioning that for the analysis of this case, the Holding Cost - Penalty Cost relationship was inverted to obtain an integer ratio comparable to the previous case. In this context, Table 6 shows the average total costs of each sequencing rule for each of the simulated ratios and in Figure 3 the data plotted by rule is presented.

Table 6: Average total cost per sequencing rule for each ratio of the Holding Cost ≤ Penalty Cost case. Own elaboration.

Penalty Cost: Holding Cost Ratio	Quotient	Average Total Cost			
		FCFS	EDD	SPT	LPT
01:01	1	98.71	40.84	95.29	99.65
05:01	5	314.92	170.44	244	432.55
10:01	10	593.02	339.96	434.08	855.11
50:01:00	50	2,771.24	1,643.66	1,921.44	4,231.30
100:01:00	100	5,584.92	3,381.25	3,872.48	8,635.48
500:01:00	500	27,703.64	16,749.71	19,236.98	42,487.58
Slope		55.3371	33.4991	38.3847	84.957

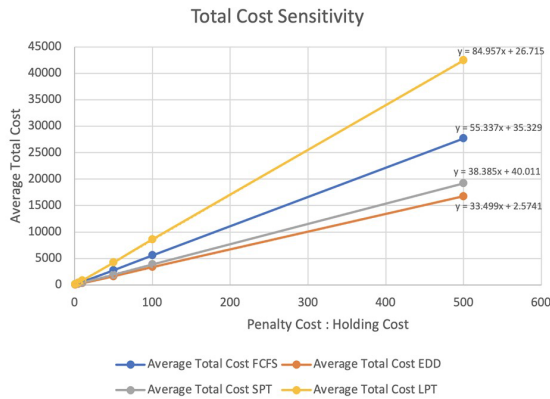


Figure 3: Sensitivity of the average total cost with respect to the cost ratio for the Holding Cost ≤ Penalty Cost case. Own elaboration

As in the previous analysis, the parameters β_0 and β_1 of the regression equations in Fig. (3) were estimated through the least-squares method, where β_1 is the parameter that represents the degree of sensitivity of the total cost with respect to the change in Holding Cost: Penalty Cost ratio for each rule.

For this case, it can be interpreted that the higher the Penalty Cost is, the total cost grows linearly with different slopes depending on the dispatch rule implemented, similar to the previous case. Again, the least sensitive rule is EDD with an increase of \$33.50 for each unit that increases the Penalty Cost: Holding Cost ratio, while the most sensitive rule is LPT with an increase of \$ 84.96 for each unit that increases the ratio. Being then 2.54 times more sensitive LPT than EDD when Holding Cost ≤ Penalty Cost. Like the previous analysis, the other sensitivity relationships between rules for this case are found in Table 7. Furthermore, the EDD and SPT rules have a similar sensitivity in both cases: Holding Cost > Penalty Cost case and Holding Cost ≤ Penalty Cost case.

Table 7: Sensitivity relationships between the sequencing rules for the Holding cost ≤ Penalty cost. Own elaboration.

Case: Holding Cost ≤ Penalty Cost				
Rule sensitivity:	Regarding the rule:			
	EDD	SPT	FCFS	LPT
LPT	2.54	2.21	1.54	

FCFS	1.65	1.44		
SPT	1.15			
EDD				

Once the analysis has been carried out for both cases, it is possible to reach the following conclusions:

- As demonstrated, a sequencing rule can present different degrees of sensitivity depending on in which of the two significant cases of the Holding Cost - Penalty Cost relationship this rule is found. For example, EDD is the optimal rule in terms of total cost for all the proportions. However, it presents a lower sensitivity and the lowest total costs when it is in the Holding Cost > Penalty Cost case than when it is in the Holding Cost ≤ Penalty Cost case, as shown in Figure 4.
- In the Holding Cost ≤ Penalty Cost case, EDD is the rule that has the lowest total cost (RQ1) however SPT is the rule that is less sensitive to cost variation as can be seen in Fig 4 (RQ2).
- Furthermore, it can be observed in Figure 4 that all the rules are less sensitive in the Holding Cost > Penalty Cost case, except the SPT rule which is less sensitive in the Holding Cost ≤ Penalty Cost case (RQ2).
- That is, when the total cost is the parameter to optimize in a changing environment, it is not only possible to choose the most economical sequencing rule, but it is also convenient to look for a Holding Cost - Penalty Cost relationship that provides less sensitivity to changes of those costs. This will not only ensure lower-cost production but will also allow the production system to respond more robustly to changes in the economic environment in this case the less sensitive is SPT rule.

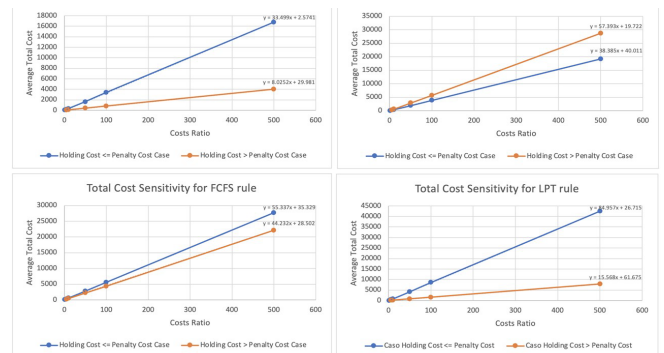


Figure 4: Comparison of the sensitivity of the total cost for each case of the Holding Cost - Penalty Cost relationship by sequencing rule, own elaboration

- Further, in Appendix A, the parameters of the simulation run where different Holding Cost - Penalty cost relationships are handled, the EDD is the rule that generates the lowest costs (RQ1), however if they are compared with the standard deviation, the SPT it is the most robust or the one with the least variation in costs (RQ2).

5. Discussion

Based on the obtained results, this section studies the applicability of the sensitivity analysis of the total cost of the

sequencing rules within organizations that manufacture under an agile approach. This study starts from the fact that sequencing rules are applied in a changing environment that constantly causes a variation in the penalty costs of late production and the holding costs of early production. Due to the above, it is relevant to point out how these costs could vary and how the sensitivity analysis could help make better decisions.

Consider the following numerical example to demonstrate the variation of penalty costs in a changing environment:

- During the negotiations of a manufacturing organization with a customer, it was determined as a policy that after the first 5 days of delay, a penalty of 2% of the volume value of the parts will be paid for each additional day of a delay; considering 5 business days in a week. It is not allowed to exceed 45% of the value of the pieces and in case of exceeding it, the contract will be canceled.
- Consider that the value of each piece is \$100 and that the manufacturing company must make quarterly deliveries of batches that vary in size from period to period, due to changing customer requirements.
- Suppose that this quarter the company delivers a batch of 1,000 pieces 10 days late, so the penalty would be 5% of the total value of \$ 100,000; that is, \$5,000 would be paid. As result, the unit penalty cost is \$5 for each piece of this batch delayed 10 days; therefore, the penalty cost for each piece per day is \$0.5.
- The following quarter, the company delivers a batch of 2000 pieces 25 days late, which implies a penalty of 20% of the total value of \$200,000; that is \$40,000. Thus, the unit penalty cost of \$20 for each piece is delayed 25 days; therefore, the penalty cost for each piece per day is \$0.8.
- Now consider that the next period, the company delivers a batch of 3,000 pieces 25 days late as well; that is, again 20% of the total value of the lot amounting to \$ 300,000. This means that a penalty of \$60,000 will be paid, the penalty unit cost also being \$20 for each piece delayed 25 days; hence, the penalty cost for each piece per day returns to \$0.8.
- Then it is observed that the penalty cost per product does not depend on the volume of late parts, as shown in the second and third quarters of the example. The lot size can vary, but if the number of days late is kept constant, arithmetically the penalty unit cost will always be the same.
- Given the above, it can be established that the unit penalty cost depends directly on the number of days of delay, for a policy like the one used in this example. However, it should be noted that variations in batch sizes could affect this cost indirectly, as larger, and fluctuating batches may require more time to complete and deliver.

On the other hand, there are multiple works that propose various mathematical models to calculate the Cost of Maintaining the inventory [37,38]. However, more works agree that the traditional method is to establish this cost as a percentage of the value of the product and keep it constant for each item and for each unit of time. In fact, in the literature, it is mentioned that this percentage ranges between 12% and 34% of the value of the product, or a reference to similar organizations, or an industry average is used [39,40]. Although previous works point out that www.astesj.com

the traditional method has deficiencies to adequately estimate the Cost of Maintaining the inventory in practice, this approach is commonly found [41]. Due to the above and for the sake of simplicity, the traditional method is used to exemplify the Holding cost variance in a changing environment, although the exercise could be adapted to a mathematical model with greater precision.

To understand the variation of Holding Cost in a constantly changing environment, consider the following example:

- Continuing with the situation raised above, the manufacturing company offers the basic model of its product at \$ 100 per piece. However, customer requirements tend to vary from one period to another and they request parts with additional finishes and machining, larger dimensions, different materials, etc. This changes the manufacturing cost and, therefore, the value of the product.
- Consider that the company has taken a traditional approach to define its Holding cost based on an industry average, representing 25% of the value of its product.
- In this sense, its base model has an annual inventory cost of \$ 25 for each part. Considering that the company works 260 days a year, there is a holding cost per piece per day of \$ 0.1 for the base model.
- Suppose that in the first quarter of the year, the customer ordered a batch of parts with additional machining and larger dimensions, increasing the value of the product by \$200 per part. Since 25% of the product value is held fixed, these parts have an annual inventory cost of \$ 50 for each part and an inventory cost per part per day of \$ 0.2 for this special specification model.
- In this way, the Holding cost increases proportionally to the value of the product, which is reasonable considering that a more valuable product may incur higher risk costs (such as obsolescence or damage), space costs, service costs (such as insurance or taxes) and even capital costs [13].

Variations in holding and penalty costs may be subject to other factors in addition to those described above. Nonetheless, in this study these conditions will be used to explain how the decision-maker could use sensitivity analysis to control and ensure the agility of the manufacturing system at a low cost. As an example, a tool was built in Excel that allows calculating the maximum number of days that a batch can be delayed to keep the Penalty Cost below the holding cost and thus remain in the case it presents lower sensitivity of the total cost with respect to the variations of these two costs. This calculator is based on the penalty policy that was described in this section and through the Solver tool, the maximum value of days of delay is found that meets the restriction $\text{Holding Cost} > \text{Penalty Cost}$.

In Figure 5 the tool built is shown, assuming that for a certain quarter there is a Holding Cost of \$ 0.80 per piece per day and the values defined in the penalty policy described above are used. As can be seen, the calculator determines that the delivery of that batch cannot be more than 24 days late, so that the Penalty Cost does not equal or exceed \$0.80.

As explained in previous sections, EDD is the optimal sequencing rule to use when the total cost is the parameter to

minimize. However, in a changing environment characterized mainly by the variation of customer requirements, in Agile Manufacturing, it is necessary to look for a Holding Cost - Penalty Cost relationship that provides greater robustness to the variations of these two costs. Through the sensitivity analysis of the total cost of the sequencing rules, it was shown that the SPT rule is more robust in terms of cost (RQ2) although EDD has the less cost (RQ1); therefore, it is convenient that the Penalty Cost can be kept varying below the Holding Cost. Otherwise, it is necessary to shorten delivery times through different Lean techniques, production planning and control, work-study, set-up time reduction techniques, theory of restrictions, etc. [42].

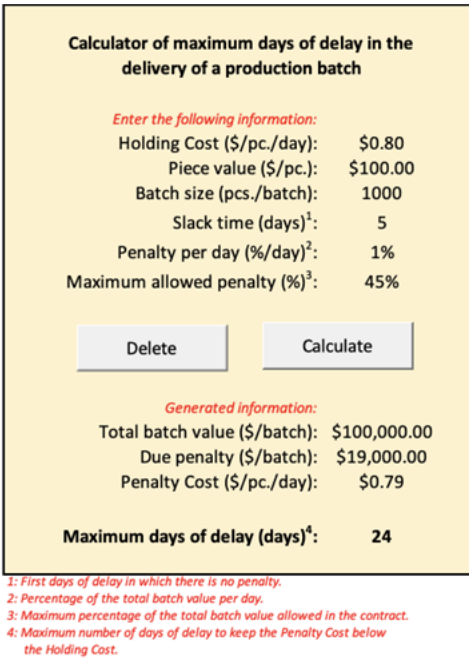


Figure 5: Calculator that determines the maximum number of days of delay to keep the Penalty Cost below the Holding Cost. Own elaboration

6. Conclusions

This article presents a sensitivity analysis that serves as an instrument to take decisions in the selection of sequencing rules when inventory maintenance and penalty costs vary in a changing environment, with the objective of reducing the total cost and to be prepared if costs vary like in Agile Manufacturing. Speaking about agile manufacturing, recent works propose the sequencing and dispatch method for facilities where humans and robots are mixed, while handling uncertainty in process times. However, these works do not present a cost sensitivity analysis; the total cost as performance metrics allows to control and ensure an agile manufacturing system in a changing environment.

The problem of the study are jobs that are to be handled by robots whose processing times follow a normal distribution with known mean and standard deviation, and that sometimes need to be handled by humans to meet customer requirements. Delivery dates are also known. The objective is to minimize the total time of early and late production, and consequently, the total cost associated with keeping the inventory and penalties from customers. Jobs are sequenced in the robot based on FCFS, SPT, LPT y EDD dispatch rules. Finally, the total

cost of the system per rule is obtained, whose calculation is the sum of the cost of keeping the early jobs in inventory and the penalty cost of the late jobs.

In order to carry out the sensitivity analysis by a rule, first the effect on the total cost of the three identified cases of the Holding Cost - Penalty Cost relationship was analyzed. After verifying that this relationship was significant for the performance of the rules, in each case the Holding Cost was varied, while the Penalty Cost was fixed and vice versa. In this sensitivity analysis, it was observed how the total cost of the system changes when the following factors vary: the sequencing rule used, the case of the Holding Cost - Penalty Cost relationship, and the ratio between both costs.

It was observed that when Holding Cost = Penalty Cost and Holding Cost < Penalty Cost, the same effect occurred in the order of the sequencing rules in terms of the total cost. In this sense, for both cases, the order of the sequencing rules from lowest to highest cost is EDD, SPT, FCFS and LPT. On the other hand, for the case Holding Cost > Penalty Cost, the order of the rules EDD is the best in terms of cost (RQ1); but the SPT rule is the most robust rule with respect to cost ratio (RQ2), no matter if $HC > PC$ or $PC \leq HC$.

Subsequently, the degree of the sensitivity of each rule regarding the movement of costs is analyzed. It can be concluded that a dispatch rule may have different degrees of sensitivity depending on which of the two significant cases of the Holding - Penalty costs relationship that rule is. For example, EDD is the optimal rule in terms of the total cost for all cases; however, it has lower sensitivity and lower total costs when it is in the case of Holding Cost > Penalty Cost than when it is in the case of Holding Cost \leq Penalty Cost. Therefore, when the total cost is the parameter to be optimized in a changing environment, it is not only possible to choose the most economical sequencing rule, but also to look for a Holding Cost - Penalty Cost relationship that gives less sensitivity to changes in costs in this case the SPT rule.

Likewise, the applicability of the presented analysis was verified. As a result, a situation was exemplified in which the Holding Cost and the Penalty Cost vary due to changes in customer requirements, either in terms of specifications or volumes requested. Finally, an Excel calculator was built based on the proposed penalty policy. With this tool, the decision-maker can estimate the maximum number of days that the delivery of a batch can be delayed to keep the Penalty Cost below the Holding Cost and, thus, maintain the cost ratio in the case with less sensitivity to total cost; through the sensitivity analysis of the total cost of the sequencing rules, it was shown that the EDD rule is the least in cost, but the SPT is the most robust. Therefore, it is convenient that the Penalty Cost is kept varying below the Holding Cost. As a result, it is shown that the present sensitivity analysis can provide tools for decision making with the objective of reducing costs in a volatile environment like Agile Manufacturing. Future work includes running the simulation with stochastic processing times for 2 or more robots and performing cost sensitivity analysis.

References

[1] A. Ghasemi, A. Ashoori, C. Heavey, "Evolutionary Learning Based Simulation Optimization for Stochastic Job Shop Scheduling Problems,"

- Applied Soft Computing, **106**, 107309, 2021, doi:10.1016/j.asoc.2021.107309.
- [2] P. Sharma, A. Jain, "Performance analysis of dispatching rules in a stochastic dynamic job shop manufacturing system with sequence-dependent setup times: Simulation approach," *CIRP Journal of Manufacturing Science and Technology*, **10**, 110–119, 2015, doi:10.1016/j.cirpj.2015.03.003.
- [3] M.A. Şahman, "A discrete spotted hyena optimizer for solving distributed job shop scheduling problems," *Applied Soft Computing*, **106**, 107349, 2021, doi:10.1016/j.asoc.2021.107349.
- [4] Pinedo Michael L., *Scheduling*, 5th ed., Springer Science, New York, 2016.
- [5] Z. Shi, S. Gao, J. Du, H. Ma, L. Shi, "Automatic Design of Dispatching Rules for Real-time optimization of Complex Production Systems," *Proceedings of the 2019 IEEE/SICE International Symposium on System Integration, SII 2019*, 55–60, 2019, doi:10.1109/SII.2019.8700391.
- [6] B. Maskell, "The age of agile manufacturing," *Supply Chain Management*, **6**(1), 5–11, 2001, doi:10.1108/13598540110380868/FULL/XML.
- [7] F. Maciá Pérez, J.V. Berna-Martinez, D. Marcos-Jorquera, I. Lorenzo Fonseca, A. Ferrándiz Colmeiro, "Cloud agile manufacturing," *IOSR Journal of Engineering*, **2**, 1045–1048, 2012.
- [8] N.G. Hall, M.E. Posner, "Sensitivity Analysis for Scheduling Problems," *Journal of Scheduling* 2004 **7**(1), 49–83, 2004, doi:10.1023/B:JOSH.0000013055.31639.F6.
- [9] D.R. Anderson, D. Sweeney, T.A. Williams, *Contemporary Management Sciences with Spreadsheets*, South Western College Publishing, Cincinnati OH, 1999.
- [10] T. Danaci, D. Toksari, "A branch-and-bound algorithm for two-competing-agent single-machine scheduling problem with jobs under simultaneous effects of learning and deterioration to minimize total weighted completion time with no-tardy jobs," *International Journal of Industrial Engineering: Theory, Applications, and Practice*, **28**(6), 577–593, 2022, doi:10.23055/ijietap.2021.28.6.7723.
- [11] A.W.J. Kolen, A.H.G. Rinnooy Kan, C.P.M. van Hoesel, A.P.M. Wagelmans, "Sensitivity analysis of list scheduling heuristics," *Discrete Applied Mathematics*, **55**(2), 145–162, 1994, doi:10.1016/0166-218X(94)90005-1.
- [12] Y.N. Sotskov, "Stability of an optimal schedule," *European Journal of Operational Research*, **55**(1), 91–102, 1991, doi:10.1016/0377-2217(91)90194-Z.
- [13] S.A. Kravchenko, Y.N. Sotskov, F. Werner, "Optimal schedules with infinitely large stability radius *," [Http://Dx.Doi.Org/10.1080/02231939508844080](http://Dx.Doi.Org/10.1080/02231939508844080), **33**(3), 271–280, 2007, doi:10.1080/02231939508844080.
- [14] R.L. Graham, E.L. Lawler, J.K. Lenstra, A.H.G.R. Kan, "Optimization and Approximation in Deterministic Sequencing and Scheduling: a Survey," *Annals of Discrete Mathematics*, **5**(C), 287–326, 1979, doi:10.1016/S0167-5060(08)70356-X.
- [15] C.A. Tovey, "A Simplified Anomaly and Reduction for Precedence Constrained Multiprocessor Scheduling," [Http://Dx.Doi.Org/10.1137/0403051](http://Dx.Doi.Org/10.1137/0403051), **3**(4), 582–584, 2006, doi:10.1137/0403051.
- [16] A. Wagelmans, *Sensitivity analysis in Combinatorial Optimization*, Erasmus University, Rotterdam, Netherlands, 1990.
- [17] P. Kouvelis, G. Yu, *A Robust Discrete Optimization Framework*, Springer, Boston, MA: 26–73, 1997, doi:10.1007/978-1-4757-2620-6_2.
- [18] R.L. Daniels, P. Kouvelis, "Robust Scheduling to Hedge Against Processing Time Uncertainty in Single-Stage Production," [Http://Dx.Doi.Org/10.1287/Mnsc.41.2.363](http://Dx.Doi.Org/10.1287/Mnsc.41.2.363), **41**(2), 363–376, 1995, doi:10.1287/MNSC.41.2.363.
- [19] P. Kouvelis, R.L. Daniels, G. Vairaktarakis, "Robust scheduling of a two-machine flow shop with uncertain processing times," *IIE Transactions* 2000 **32**:5, 421–432, 2000, doi:10.1023/A:1007640726040.
- [20] F.S. Hillier, G.J. Lieberman, *Introduction to Operations Research*, 9th ed., McGraw Hill, New York, 2010.
- [21] X. Liu, W. Li, "Approximation Algorithm for the Single Machine Scheduling Problem with Release Dates and Submodular Rejection Penalty," *Mathematics* 2020, **8**(1), 133, 2020, doi:10.3390/MATH8010133.
- [22] M. Kühn, M. Völker, T. Schmidt, "An Algorithm for Efficient Generation of Customized Priority Rules for Production Control in Project Manufacturing with Stochastic Job Processing Times," *Algorithms* 2020, Vol. 13, Page 337, **13**(12), 337, 2020, doi:10.3390/A13120337.
- [23] C. Te Yang, "An inventory model with both stock-dependent demand rate and stock-dependent holding cost rate," *International Journal of Production Economics*, **155**, 214–221, 2014, doi:10.1016/j.ijpe.2014.01.016.
- [24] H. Ding, M. Schipper, B. Matthias, "Optimized task distribution for industrial assembly in mixed human-robot environments - Case study on IO module assembly," *IEEE International Conference on Automation Science and Engineering*, **2014-January**, 19–24, 2014, doi:10.1109/COASE.2014.6899298.
- [25] M. Messner, F. Pauker, G. Mauthner, T. Frühwirth, J. Mangler, "Closed Loop Cycle Time Feedback to Optimize High-Mix / Low-Volume Production Planning," *Procedia CIRP*, **81**, 689–694, 2019, doi:10.1016/j.procir.2019.03.177.
- [26] O. Cardin, D. Trentesaux, A. Thomas, P. Castagna, T. Berger, H. Bril El-Haouzi, "Coupling predictive scheduling and reactive control in manufacturing hybrid control architectures: state of the art and future challenges," *Journal of Intelligent Manufacturing* 2015 **28**:7, **28**(7), 1503–1517, 2015, doi:10.1007/S10845-015-1139-0.
- [27] D. Ivanov, A. Dolgui, B. Sokolov, "Robust dynamic schedule coordination control in the supply chain," *Computers & Industrial Engineering*, **94**, 18–31, 2016, doi:10.1016/j.cie.2016.01.009.
- [28] A. Cataldo, A. Perizzato, R. Scattolini, "Production scheduling of parallel machines with model predictive control," *Control Engineering Practice*, **42**, 28–40, 2015, doi:10.1016/j.conengprac.2015.05.007.
- [29] A. Casalino, A.M. Zanchettin, L. Piroddi, P. Rocco, "Optimal Scheduling of Human-Robot Collaborative Assembly Operations With Time Petri Nets," *IEEE Transactions on Automation Science and Engineering*, 70–84, 2019, doi:10.1109/TASE.2019.2932150.
- [30] J. Dörmer, H.O. Günther, R. Gujjula, "Master production scheduling and sequencing at mixed-model assembly lines in the automotive industry," *Flexible Services and Manufacturing Journal* 2013 **27**:1, **27**(1), 1–29, 2013, doi:10.1007/S10696-013-9173-8.
- [31] J.T. Lin, C.C. Chiu, Y.H. Chang, "Simulation-based optimization approach for simultaneous scheduling of vehicles and machines with processing time uncertainty in FMS," *Flexible Services and Manufacturing Journal* 2017 **31**:1, **31**(1), 104–141, 2017, doi:10.1007/S10696-017-9302-X.
- [32] U. Saif, Z. Guan, L. Zhang, F. Zhang, B. Wang, J. Mirza, "Multi-objective artificial bee colony algorithm for order oriented simultaneous sequencing and balancing of multi-mixed model assembly line," *Journal of Intelligent Manufacturing* 2017 **30**:3, **30**(3), 1195–1220, 2017, doi:10.1007/S10845-017-1316-4.
- [33] M.D. Rossetti, *Simulation Modeling and Arena*, 2nd ed., Wiley & Sons, Hoboken, New Jersey, 2015.
- [34] S. Vinga, J.S. Almeida, "Rényi continuous entropy of DNA sequences," *Journal of Theoretical Biology*, **231**(3), 377–388, 2004, doi:10.1016/j.jtbi.2004.06.030.
- [35] M.H. Seyyedi, A.M.F. Saghieh, Z.N. Azimi, "A FUZZY MATHEMATICAL MODEL FOR MULTI-OBJECTIVE FLEXIBLE JOB-SHOP SCHEDULING PROBLEM WITH NEW JOB INSERTION AND EARLINESS/TARDINESS PENALTY," *International Journal of Industrial Engineering: Theory, Applications, and Practice*, **28**(3), 2021, doi:10.23055/ijietap.2021.28.3.7445.
- [36] D.C. Montgomery, G.C. Runger, *Applied Statistics and Probability for Engineers*, John Wiley & Sons, Inc., New York, 2003.
- [37] C. Te Yang, "An inventory model with both stock-dependent demand rate and stock-dependent holding cost rate," *International Journal of Production Economics*, **155**, 214–221, 2014, doi:10.1016/j.ijpe.2014.01.016.
- [38] V. Pando, J. García-Laguna, L.A. San-José, J. Sicilia, "Maximizing profits in an inventory model with both demand rate and holding cost per unit time dependent on the stock level," *Computers & Industrial Engineering*, **62**(2), 599–608, 2012, doi:10.1016/j.cie.2011.11.009.
- [39] P. Berling, "Holding cost determination: An activity-based cost approach," *International Journal of Production Economics*, **112**(2), 829–840, 2008, doi:10.1016/j.ijpe.2005.10.010.
- [40] D.M. Lambert, J.R. Stock, L.M. Ellram, *Fundamentals of Logistics Management*, McGraw-Hill Higher Education, 1998.
- [41] R. Chase, R. Jacobs, N. Aquilano, *Administración de Operaciones*, 12th ed., McGraw-Hill Education, México, 2009.
- [42] A.H. Alad, V.A. Deshpande, "A Review of Various Tools and Techniques for Lead Time Reduction," *International Journal of Engineering Development and Research*, **2**, 1159–1164, 2014.

Appendix A: Table A1. Simulation runs parameters for the sequencing rules, relations Holding cost- Penalty cost. Own elaboration. The least cost or time are marked in yellow.

HC=PC	TOTAL COST				AVERAGE DAYS EARLY				AVERAGE DAYS LATE			
	FCFS	EDD	SPT	LPT	FCFS	EDD	SPT	LPT	FCFS	EDD	SPT	LPT
MAX	324.4881235	159.0649771	304.1401985	361.5915067	9.912862035	2.640428787	11.30611191	3.078288766	11.64958743	8.293383618	8.370011627	17.7434017
MIN	269.4675854	93.83961847	258.7406446	204.7959859	5.929719946	0.329820153	7.797001287	5.549866767	7.351259754	3.317095678	4.461616566	10.73084639
AVERAGE	295.9967842	123.8274527	283.858605	299.6363908	7.337228696	1.345874035	9.448980918	2.579146079	9.107037095	5.533428893	6.320941582	14.06732008
STD	10.61578264	13.45057393	9.40800032	28.42537755	0.790493168	0.550270608	0.704534444	0.421483501	0.892360632	1.020459122	0.773334962	1.508090353
DEVIATION												
HC=PC	FCFS	EDD	SPT	LPT	FCFS	EDD	SPT	LPT	FCFS	EDD	SPT	LPT
MAX	321.6185449	121.4161522	329.7350998	267.873387	9.215549884	2.735021624	11.10431407	3.195712621	11.23147009	7.581213156	8.257477955	17.3450959
MIN	255.6703199	74.60981282	274.4851095	148.4552078	5.782360796	0.354050164	7.959006166	4.03796765	7.547518384	3.355770855	4.179971215	9.627967166
AVERAGE	285.5580209	98.48834681	306.0853378	233.6423299	7.308896674	1.334116661	9.585475621	2.595375742	9.178708394	5.539128913	6.336160241	14.27944268
STD	13.42551567	9.093664242	12.65321384	21.18601861	0.821322253	0.522455631	0.756768639	0.359164673	0.858823468	0.948782963	0.780414382	1.508620402
DEVIATION												
HC=PC, 1:2	FCFS	EDD	SPT	LPT	FCFS	EDD	SPT	LPT	FCFS	EDD	SPT	LPT
MAX	346.4918455	191.3116839	295.6890169	437.8827827	9.860566425	2.64315815	11.48715793	3.614426578	11.13822482	7.477871505	7.795189753	17.11489466
MIN	279.9573365	107.4291879	234.1946599	266.1847722	5.73020676	0.257090708	7.920432015	4.028940557	7.312814433	3.212898738	4.61296948	10.53840262
AVERAGE	305.5619438	147.877337	265.3672044	365.9036277	7.300247549	1.362278386	9.528820181	2.512579533	9.081623882	5.480416516	6.292556759	13.98969472
STD	14.44116885	19.60831141	12.91847467	39.80919538	0.728912431	0.498289029	0.681353507	0.536132671	0.818519923	0.973099995	0.702941228	1.608135218
DEVIATION												
HC=PC, 1:5	FCFS	EDD	SPT	LPT	FCFS	EDD	SPT	LPT	FCFS	EDD	SPT	LPT
MAX	771.2391279	534.0932703	615.7264943	1082.057959	10.12094097	2.378698691	11.17871365	3.10322638	11.60266095	8.813328601	8.60104996	17.53572437
MIN	527.7697303	179.9565962	364.6675416	635.9896343	6.225267756	0.230852835	8.071665664	4.051310384	6.932092255	2.523536866	4.111256227	9.994507034
AVERAGE	635.065533	347.8043775	493.1168762	873.4279955	7.320651607	1.337947633	9.53168712	2.523160935	9.120295229	5.529150099	6.312277179	14.05250107
STD	48.51650324	61.79903466	42.28943217	94.57595663	0.753230454	0.504640931	0.691182842	0.519925797	0.920097777	1.105834774	0.805122863	1.586317445
DEVIATION												
	AVERAGE COMPLETION TIME				AVERAGE # OF JOBS IN THE SYSTEM							
HC=PC	FCFS	EDD	SPT	LPT	FCFS	EDD	SPT	LPT				
MAX	29.39254348	31.70440494	24.40634367	39.23171969	3.388672672	3.6922126	2.772364825	4.613928352				
MIN	21.43453355	24.7810502	17.40844952	31.76413541	2.875157031	3.267978801	2.386071648	4.227635175				
AVERAGE	25.60314173	28.02088819	20.705294	35.32150733	3.19795433	3.501324266	2.585361927	4.414638073				
STD	1.579414546	1.459410985	1.384070457	1.552461303	0.094879817	0.085319822	0.077229507	0.084910239				
DEVIATION												
HC=PC	FCFS	EDD	SPT	LPT	FCFS	EDD	SPT	LPT				
MAX	29.27805098	30.69744624	24.01644808	38.68958606	3.514627799	3.723434761	2.751288772	4.594023707				
MIN	22.16530183	24.75859184	17.12107083	32.08965043	2.971601957	3.292437219	2.405976293	4.248711228				
AVERAGE	25.70314505	28.03845559	20.58401795	35.51740027	3.206229139	3.499382508	2.566464174	4.433535826				
STD	1.582475432	1.371870566	1.440746399	1.497465592	0.099730279	0.090110885	0.084910239	0.084910239				
DEVIATION												
HC=PC, 1:2	FCFS	EDD	SPT	LPT	FCFS	EDD	SPT	LPT				
MAX	28.67818878	30.51744867	23.29668814	38.73831039	3.467306334	3.700168464	2.751738523	4.656152823				
MIN	21.28558134	24.40307392	17.17548402	31.72285427	2.95824624	3.294826101	2.343847177	4.248261477				
AVERAGE	25.61470967	27.95147146	20.59706991	35.31044852	3.206632604	3.500258504	2.578060907	4.421939093				
STD	1.443181146	1.370470114	1.264264175	1.639137979	0.085388479	0.079226785	0.079387808	0.079387808				
DEVIATION												
HC=PC, 1:5	FCFS	EDD	SPT	LPT	FCFS	EDD	SPT	LPT				
MAX	29.17937168	32.20553242	24.1290919	38.87618297	3.388797917	3.708073203	2.730439123	4.585361866				
MIN	20.64448461	23.97817151	16.97914676	30.80123935	2.930944572	3.36616493	2.414638134	4.269560877				
AVERAGE	25.63297696	28.0245358	20.61392339	35.36267347	3.204937427	3.505027166	2.578060907	4.423623345				
STD	1.578312146	1.529210243	1.406674794	1.639137979	0.085388479	0.074121777	0.071673752	0.071673752				
DEVIATION												

Frequency Oscillation Suppression of Interlinked Solar PV-Thermal Power System using HVDC Link

Gulshan Sharma*

Department of Electrical Engineering Technology, University of Johannesburg, Johannesburg, 2006, South Africa

ARTICLE INFO

Article history:

Received: 26 August, 2022

Accepted: 31 August, 2022

Online: 10 October, 2022

Keywords:

AC Tie-line

Dynamic Responses

HVDC link

PV-Thermal Interlinked LFC

PID Design Tuning Methods

ABSTRACT

This paper looks for the merging of solar PV power plant with thermal power generation and interlinked through tie-lines approaching into an interlinked PV-Thermal model for the design and analysis of load frequency controllers. Moreover, the different models of controllers are also proposed and tested to regulate the frequency of PV-Thermal interlinked system for a certain disturbance in one of the regions of an interlinked system. The choice of auxiliary controllers is assessed utilizing assorted tuning strategies and the comparative examination of all models are shown via graphical response and via calculating numerical values to bring back the frequency and tie-line power deviations back to the standard level and to analyze the viable control activity. In addition, an HVDC link is also used between linked PV-Thermal areas to stabilize the frequency and tie-power quickly as well as to stabilize the system operation for alteration in changing loading conditions of the interlinked system.

1. Introduction

Load frequency control (LFC) is a critical process in the power system, and it determines the quality energy supply to the cutting-edge society. We fulfil this requirement by matching the power system generation with the power demand and hence frequency manages to its original value i.e., 50 Hz. However, the power demand continuously changes over the complete day and hence it shifts the frequency value from 50 Hz to either up or low from the original value and therefore the power customers are affected. Subsequently, load frequency controllers are required on the generators in position to keep the power system generation up or mo as per the power demand. This gives the electrical energy to the clients with least change from the standard and acceptable level (i.e., 50Hz).

The frequency stability reflects approximately the beginning time and moment of control activity. As there's an unbalance between the power generation and power demand, the first control action (Primary control) is initiated and tries to increase or decrease the power generation as per the requirement. The primary control loop is with the synchronous generators and known as first level of control. In any case, the action of primary control loop is limited, slow and hence unable to take the frequency of the system back to its original value and consequently the auxiliary control

activities (i.e., secondary control) plays a vital part in achieving quick reclamation to power system frequency to perceived level.

Apart from this, the regions are interconnected with the means of tie-lines which generally interchange power between the regions, and these are AC tie-lines. But they suffer with large number of technical problems and one of the major issues are transferring of disturbances between the regions and that is why these drawbacks can overcome via moving the HVDC tie-line with AC tie-lines between the regions. Advance, it is continuously fitting that each region ought to meet its claim power request whereas overseeing the power give-and-take over the tie-lines to the plan value [1-2].

In any case due to continuous change in power demand as per the client's requirement ultimately results in frequency as well as tie-line power alteration from the beginning level and hence a secondary control plan is persistently required in the system. The deviation in frequency with power deviations over tie-lines combined in a linear form is recognize as area control error (ACE). South Africa is moving ahead in orchestrate to meet its current and future power demand through cheap as well as clean sources such as sun fuelled control well known as PV based control. In any case, it is enormously troublesome to ACE deviations in the power system as the power generated through PV is exceedingly convulsive in nature.

Still, the PV based power generation is conclusion of the country considering its boundless openness, brought compelling

*Corresponding Author: Gulshan Sharma, gulshanmail2005@gmail.com

and defilement free keeping the environment of the country clean and sickness free as well as in arrange to cater the current as well as rising power demands of South Africa. An introductory exertion in frequency management reflects about is to investigate the controller plan based on classical approach [3-4].

In any case, this approach appears to be totally unsuccessful in view of set working conditions of the power system. The controller plan approach for frequency regulation have progressed over the past few years. Assorted calculations such as optimal control by seeing each state [5]; output vector feedback design seeing crucial states [6], changing structure [7] and robust controller designs [8-9] are well attempted over the last number of years to reach the LFC benchmarks. Be that as it may, most of the frequency steadiness remedies are given for well establish plants i.e. thermal power or for combination of hydro-thermal and exceptionally scarce approaches [10-13] were available for solar PV generation and integration to the existing systems. The solar PV can generate power in one of the regions and can be interlinked to thermal power via tie-lines in order to have stable operation. Further an HVDC link may prove to be more efficient in meeting the standards of solar PV-Thermal as well as to deliver quality energy to people of South Africa.

It is well-known that the managers and labour working in assorted control businesses are very comfortable with the different structures of auxiliary controller which are “PI (proportional-integral), PD (proportional-derivative), proportional-integral-derivative (PID)” to oversee industry operations in day-to-day life in different spaces as the operation of these controllers and setting the pickup values are much easier for them and these can be achieved by considering the graphical system response [14] and hardly required any numerical calculations. Although, the pickup values and the controller design play a challenging role in achieving the required control target and sometimes it is also advisable to design and check the diverse controller designs for a certain application [15]. Within the scope, this paper is set to;

- Present mathematical model of PV and thermal power interlinked through tie-line i.e., PV-Thermal. To discuss the transfer function model of HVDC link.
- Create the conventional validation of solar PV in region one with thermal power in region two and these two power generated regions are connected via help of HVDC link parallel to AC tie-lines.
- Further, to propose and to calculate the pick-up value of various auxiliary controllers for LFC using various tuning methods and to see the merits of one over other design for step disturbance.
- The outcomes are shown via graphs for various states to find the best design for the proposed LFC.
- At last, the performance of auxiliary controllers are also matched by calculating the error (integral time multiplied by absolute error) for all LFCs with and without HVDC link to show the positive benefits of using HVDC running parallel to tie-lines.

2. Details of PV-Thermal LFC Model

The PV cell is made up of current source and it is directly related to solar radiation with one diode parallel to it. It also has a

small resistance in series and its schematic representation is shown in Figure 1 [10-13]. Further the output of this cell depends on solar radiation and surface temperature. Generally, the MPPT technique is used to achieve the maximum output from PV and hence it enhances the output as well as efficiency of PV.

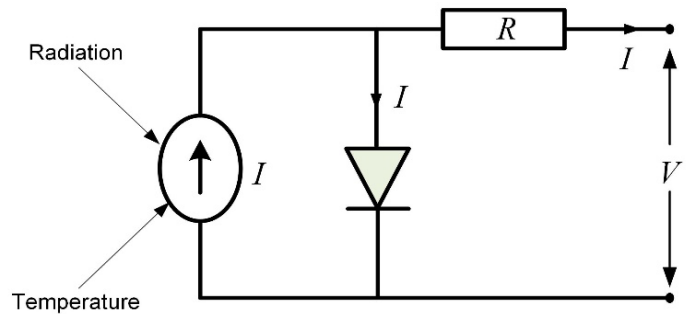


Figure 1: Representation of PV cell

The model of PV is a combination of PV panel, an inverter to convert DC power to AC power, MPPT system and filter. The complete representation in form of transfer function (TF) is as follows [10-13]:

$$G_{PV} = \frac{-18s+900}{s^2+100s+50} \tag{1}$$

The present work is the interconnection of PV with thermal power finally coming into an PV-Thermal model for frequency regulation of the power system. The TF of PV is given in equation (1) and can be used for load frequency control studies. The thermal power system includes governor to regulate the flow of steam and its output is connected to turbine with finally the shaft of turbine coupled to the power system generator. The PV-Thermal areas are interlinked via AC tie-line. The governor for thermal area in TF is as follows [13]:

$$\frac{K_g}{T_g s + 1}$$

With re-heater in TF as.

$$\frac{K_r T_r s + 1}{T_r s + 1}$$

The steam turbine TF representation is as;

$$\frac{K_t}{T_t s + 1}$$

Finally, the TF of power system generator is depicted as.

$$\frac{K_p}{T_p s + 1}$$

The interlinked PV-Thermal model for LFC is shown in Figure 2 and these areas are interlinked via AC tie-line.

However, these tie-line struggle to damp out the system oscillations quickly as well as disturbances are transferred from one area to another and hence affect the customers. These problems can be solved by running HVDC link parallel to AC.

The HVDC interface comprises of a rectifier and an inverter. The terminating points are balanced to control the rectifier and the

inverter. The first-order exchange work of dc-link is communicated as:

$$K_{DC}/(1+sT_{DC}) \quad (2)$$

Where, K_{DC} is the gain of the link as well as T_{DC} represent the responding time of HVDC link.

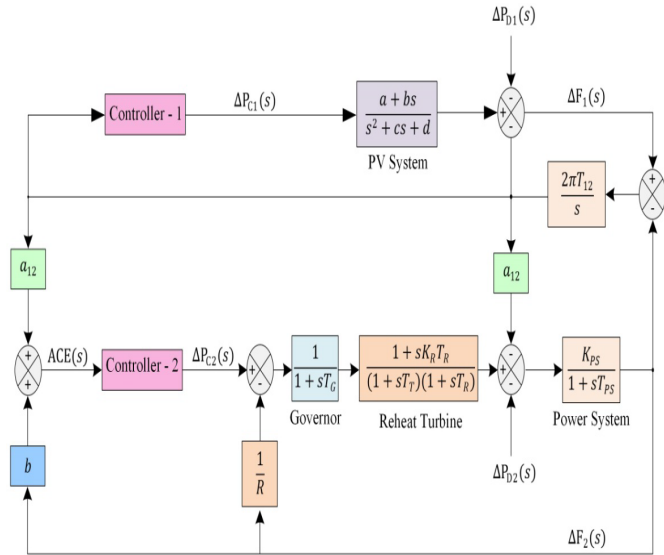


Figure 2: PV-Thermal LFC model

3. Design of Auxiliary Controllers for PV-Thermal System

One of the most common auxiliary controllers used in different types of power as well as in control industries is PID as it has three diverse control abilities which are “proportional, integral & derivative” and these abilities help the system response to come back to initial value quickly after certain disturbance. The PID work on the concept of feedback system; as PID is connected in feedback and hence it calculates the difference between actual and desired value i.e., error and tries to minimize the error by regulating the input of the system. In present research work, the aim of connecting the PID is to increase or decrease the electrical power in solar PV as well as in thermal power plants as per the requirement of electrical power and hence to attain the balance between the two so that frequency of each area and connecting tie-lines deviations should be minimized. As PID has three diverse control abilities and that is why pickup values of each control need to be calculated correctly. At first, the disturbance of value 0.01 per unit (p.u.). is imposed in area one of an interlinked PV-Thermal and at the same time, the pickup value of proportional control needs to be increased in small steps until the system start showing complete oscillations as per the Ziegler–Nichols (ZN) practice [15].

The pickup after which the system loses its stability is known as extreme pick up (K_u) for thermal region and the time between crests (T_u) is well-known in order to calculate the picks up of PID for different modes.

The same formulation is additionally taken after for PV system also. At last, with the assistance of ZN practice the pick-ups of

different modes of PID are calculated and given in Table 1 for solar PV region and Table 2 for thermal system and calculated value of error i.e., ITAE is shown in Table 3 with and without inclusion of HVDC link.

Table 1: PID Gains for solar PV system

Auxiliary Controller	Kp (Proportional Gain)	Ki (Integral Gain)	Kd (Derivative Gain)
Proportional Integral (PI)	1.79	1.542	
Proportional Derivative (PD)	3.19		0.559
Classic PID	2.39	3.428	0.419
Pessen Integral Rule	2.80	5.000	0.588
Some Overshoot	1.30	1.902	0.622
No Overshoot	0.80	1.15	0.373

Table 2: PID Gains for thermal power

Auxiliary Controller	Kp (Proportional Gain)	Ki (Integral Gain)	Kd (Derivative Gain)
PI	1.79	2.4	
PD	3.19		0.36
Classic PID	2.39	5.33	0.27
Pessen Integral Rule	2.80	7.77	0.37
Some Overshoot	1.33	2.96	0.40
No Overshoot	0.80	1.77	0.24

Table 3: ITAE values with and without HVDC Link

Auxiliary Controller	ITAE	ITAE with HVDC
PI	4.224	0.05129
PD	0.116	0.116
Classic PID	0.0065	0.00104
Pessen Integral Rule	0.0058	0.00099
Some Overshoot	0.0202	0.01547
No Overshoot	0.0565	0.02095

4. Simulation Details and Analysis for LFC

The research work is aimed to check the feasibility of generating electrical energy via means of renewable solar PV in one area and interlinking to power generation via means of thermal power in another area and connected through tie-lines resulting into an interlinked PV-Thermal system used for designing and

analysis of load frequency controllers to regulated frequency and interlinked tie-lines deviations for a certain disturbance.

In addition, the PV-thermal areas are connected via additional HVDC tie-line running parallel to AC tie-line between two interlinked areas. The HVDC tie-lines parallel to AC have the capability to improve the load frequency control responses due to lesser time constant and will show reduce oscillations, better settling time and steady state error to zero value.

The various sub-designs of PID such as “PI, PD & PID” are design and tested for interlinked model to check the superiority of one design over other design. The auxiliary controllers are design to minimize frequency and tie-power deviations to minimum or zero value.

The Zeigler-Nichols tuning method is used to move forward the framework reactions. The picks up of different modes of controllers are assessed with the assistance of ZN practice. The obtained pickup values for various PIDs are given in Table 1 for solar PV and for thermal plants in Table 2. The diverse calculated error values for each mode of auxiliary controllers are given in Table 3. The Table 3 also shows the ITAE with and without inclusion of HVDC link. Now the integral time absolute error (ITAE) definition is chosen to obtain the output of various modes of auxiliary controllers and ITAE is built on the basis of ACE.

The step load is applied in thermal power and PV-Thermal responses for various modes are obtained by considering HVDC parallel to AC tie-line between PV-Thermal regions. The execution of interconnected PV-Thermal is assessed on gotten picks up as given in Table 1 & Table 2 for different strategies and the comparative comes about for frequency, AC tie-power alteration & ACE of each area is appeared in Figures 3-7.

A look at these outcomes about clearly appears that PD mode is unable to take the system results back to reference value within 50 seconds also. The calculated ITAE is 0.116 and it is highest in the group of these control actions.

The results secure through PI and No Overshoot have the supported motions for frequency, AC tie-line power and ACEs for area 1 & 2 which is additionally not alluring seeing the required control and ITAE is 4.224 for PI without HVDC link and it reduces to 0.05129 with HVDC.

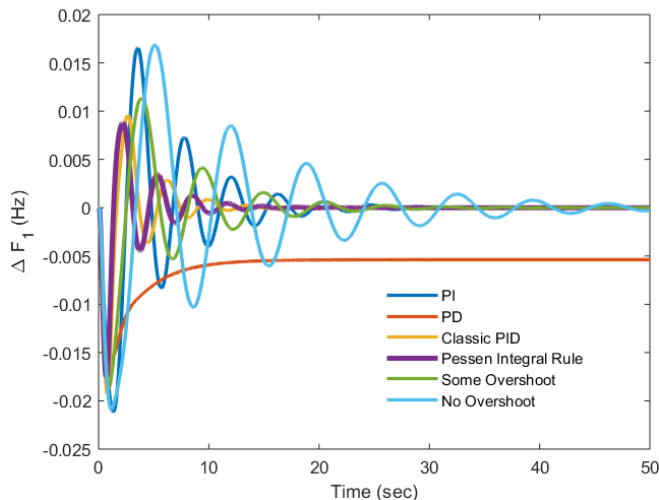


Figure 3: Graphical outcomes of PV-Thermal system

At the same time the ITAE for No Overshoot is 0.0565 without HVDC link & it reduces additionally with HVDC. The results about advertised by Some Overshoot strategy are superior to PI, PD & No Overshoot nevertheless having number of oscillations and settling time is as large as of 20 seconds for all outcomes. The results obtained via classic PID is much better for all graphical results in view of reduced overshoot, lesser oscillations and much lesser time to reach the steady state value when matched with regards to that obtained through other studied auxiliary load frequency controllers.

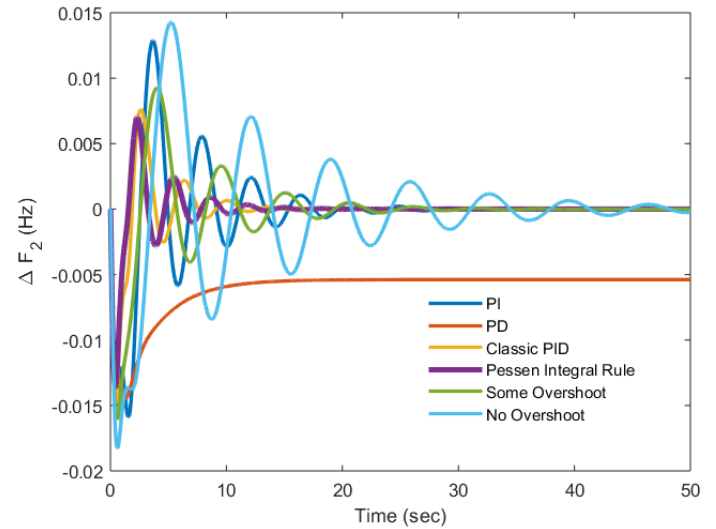


Figure 4: Graphical outcomes of PV-Thermal system

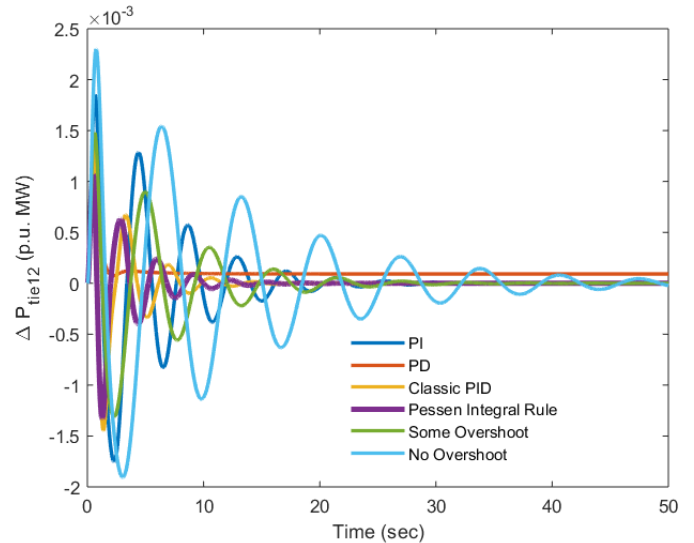


Figure 5: Graphical outcomes of PV-Thermal system

The frequency responses by using the Pessen Integral Rule have (-0.02) Hz of variation from the original value for solar PV area with response settling in 14 seconds. At the same time, the frequency variation is (-0.015) Hz for thermal power plants with settling in 10 seconds & able to go back to the reference or original value much faster than solar PV plants. The same trend is seen for response of tie-line power, ACEs for area 1 and 2 and hence it is concluded that Pessen Integral Rule based auxiliary controller shows much better output in reaching the targets of PV-Thermal system in least conceivable time.

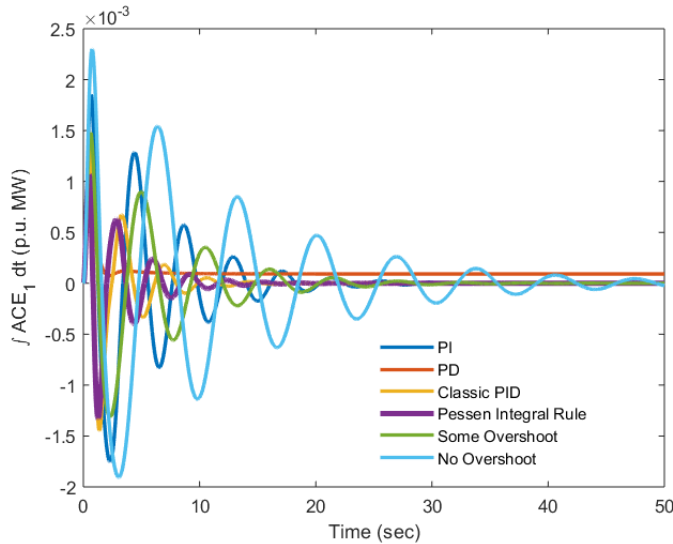


Figure 6: Graphical outcomes of PV-Thermal system

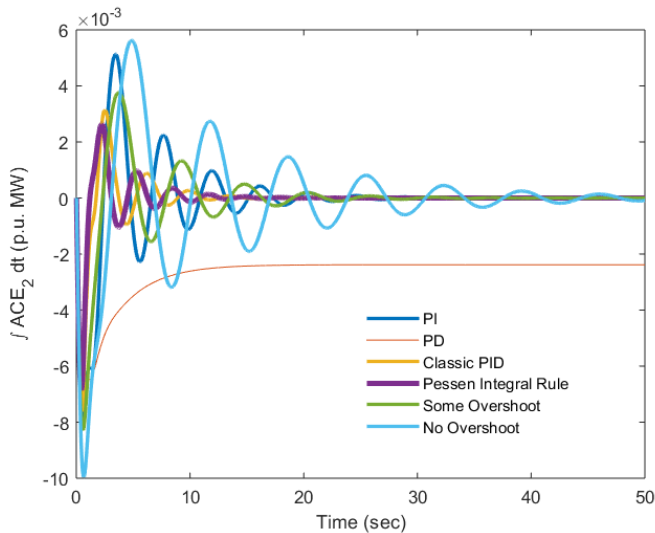


Figure 7: Graphical outcomes of PV-Thermal system

The obtained ITAE is 0.0058 and it comes out to be 0.00099 and this value of ITAE is least ITAE in complete group of investigated auxiliary controllers. It is additionally seen that the settling time and top of overshoot is also less for responses of area-2 when matched with area-1. The reason is that thermal power are well establishing in terms of design and development over the last number of years where as solar PV plants depend highly on solar radiation for generating the output and the solar radiation is highly intermittent in the nature. Further, it is also noted that HVDC link has minimized the ITAE of all auxiliary controllers. When ITAE of various modes are compared and all ITAE values are obtained with respect to HVDC running similar to AC between PV-Thermal regions, it is further verified that ITAE of Pessen Integral Rule outperform all other modes and reach to best possible minimum limit and hence justify the positive impact of this mode for PV-Thermal System.

5. Conclusions

This paper attempts to achieve the of linking of Solar PV power plants with the help of tie-lines to thermal power coming

into an interlinked system. In addition, an impact of HVDC link with AC tie-line is also investigated in this work. The distinctive modes of PID are outlined by developing and checking various PID structures. The design and investigations of various load frequency controllers revealed that the design accomplished by Pessen Integral Rule is quick enough to bring back the responses of PV-Thermal system such as (frequency of area-1 and 2, tie-line power and ACEs of area-1 and 2) deviations to original value after the load disturbance. The output of all responses is smooth with very few oscillations and coming back to original value much faster in comparison to other load frequency controllers. It is also perceiving that error value i.e., ITAE obtain via Pessen method is not as much of when compared with ITAE of other PID controllers. The significant reduction in error values is observed for all auxiliary controllers with inclusion of HVDC link. With HVDC link also, ITAE achieved via Pessen Integral Rule is minimum when compared with other auxiliary controllers and hence this method of PID outperforms over other auxiliary controllers for present studies. However, the research work can be extended to calculate the values of various PIDs by using optimization techniques. The effect of non-linearity and time delay with sensitivity analysis also need to be study for PV-Thermal system. The work may be extended to deregulated environment in view of various market transactions and to study the ancillary services such as LFC in deregulated environment.

Conflict of Interest

The authors declare no conflict of interest.

References

- [1] E. Çelik, N. Ozturk, and E. H. Houssein, "Influence of energy storage device on load frequency control of an interconnected dual-area thermal and solar photovoltaic power system," *Neural Computing and Applications*, 1-17, 2022, doi: 10.1007/s00521-022-07558-x.
- [2] F. T. Tomy, R. Prakash, "Load frequency control of a two-area hybrid system consisting of a grid connected PV system and thermal generator," *Int J Res Eng Technol.*, **3**(7), 573–580, 2014.
- [3] J. Nanda, S. Mishra, and L. C. Saikia, "Maiden application of bacterial foraging based optimization technique in multi-area automatic generation control," *IEEE Trans. Power Syst.*, **24**, 602-609, 2009, doi: 10.1109/TPWRS.2009.2016588.
- [4] Ibraheem, P. Kumar, and D. P. Kothari, "Recent philosophies of automatic generation control strategies in power systems," *IEEE Trans. Power Syst.*, **20**(1), 346–357, 2005, doi: 10.1109/TPWRS.2004.840438.
- [5] Ibraheem, K. R. Niazi, and G. Sharma, "Study on dynamic participation of wind turbines in AGC of power system," *Electric Power Comp. and Syst.*, **43**(1), 44-55, 2014, doi: 10.1080/15325008.2014.963266.
- [6] G. Sharma, Ibraheem, and K. R. Niazi, "Optimal AGC of asynchronous power systems using output feedback control strategy with dynamic participation of wind turbines," *Electric Power Component and Systems*, **43**(4), 384-398, 2015, doi: 10.1080/15325008.2014.949916.
- [7] N. N. Bengiamin, and W. C. Chan, "Variable structure control of electric power generation," *IEEE Trans Power Apparatus Syst.*, PAS-101, 376–380, 1982, doi: 10.1109/TPAS.1982.317117.
- [8] G. Sharma, I. Nasiruddin, K. R. Niazi, and R. C. Bansal, "Robust automatic generation control regulators for a two-area power system interconnected via AC/DC tie-lines considering new structures of matrix Q", *IET-Generation Transmission and Distribution*, **10**(14), 3570-3579, 2016, doi: 10.1049/iet-gtd.2016.0321.
- [9] Y. Wang, R. Zhou, and C. Wen, "Robust load-frequency controller design for power system", *IEE Proc. C*, **140**(1), 11-16, 1993, doi: 10.1049/ip-c.1993.0003.
- [10] E. S. Ali, "Speed control of DC series motor supplied by photovoltaic system via firefly algorithm," *Neural Comput Appl.*, **26**(6), 1321–1332, 2015, doi: 10.1007/s00521-014-1796-5.
- [11] A. S. Oshaba, E. S. Ali, and S. M. Abd-Elazim, "PI controller design for MPPT of photovoltaic system supplied SRM via BAT search algorithm," *Neural*

- Computing Application, **28**(4), 651-667, 2015, doi: 10.1007/s00521-015-2091-9.
- [12] A. S. Oshaba, E. S. Ali, and S. M. Abd-Elazim, "Speed control of SRM supplied by photovoltaic system via ant colony optimization algorithm," *Neural Computing Application*, **28**(2), 365-374, 2015, doi: 10.1007/s00521-015-2068-8.
- [13] S. M. Abd-Elazim, and E. S. Ali, "Load frequency controller design of a two-area system composing of PV grid and thermal generator via firefly algorithm," *Neural Computing Application*, 1-10, 2016, doi: 10.1007/s00521-016-2668-y.
- [14] A. Panwar, G. Sharma, I. Nasiruddin, and R. C. Bansal, "Frequency stabilization of hydro-hydropower system using hybrid bacteria foraging PSO with UPFC and HAE," *Electric Power Systems Res.*, **161**, 74-85, 2018, doi: 10.1016/j.epsr.2018.03.027.
- [15] J. G. Ziegler, and N. B. Nichols, "Optimum setting for automatic controllers," *Transaction ASME*, **64**, 759-768, 1942.

DEM Models Calibration and Application to Simulate the Phosphate Ore Clogging

Bouassale Nasr-Eddine*, Sallaou Mohamed, Aittaleb Abdelmajid, Benaissa Elfahim

Innovation and Systems Engineering Laboratory, M2I Team, ENSAM Meknès Moulay Ismail University, Meknes, Morocco

ARTICLE INFO

Article history:

Received: 30 July, 2022

Accepted: 21 September, 2022

Online: 10 October, 2022

Keywords:

Phosphate ore

Calibration

DEM

Contact model

Angle of Repose

EDEM®

ABSTRACT

In different areas of industry (mining, food processing, pharmaceutical, manufacturing...), the problem of grain, aggregate and clusters flow arises during the handling activities especially loading and unloading. Thus, the study and control of the parameters that govern the flow of the granular medium and its interaction with its environment are key parameters to achieve the desired operational excellence and performance of these activities. The adhesion of granular materials on various surfaces of equipments (trucks surfaces, hoppers, silos...) is one of the major problems facing mining companies. In this paper we presented the Calibration of the Discrete Element Method (DEM) parameters for modeling phosphate ore built on the identification of the repose angle. This will help us to specify the correct inputs parameters that will be introduced for the modeling of adhesion phenomena. First we introduced the model contact which allow us to well define contact between phosphate particles-particles (or clusters-clusters) and phosphate particles (clusters) with tipper surface taking into consideration the cohesive and plastic nature of the contact. Secondly, we presented a calibration method based on the determination of the repose angle of the phosphate ore. This method allowed us, using fractional factorial designs and Box Behnken designs, to determine the optimal parameters for a more accurate simulation. Thirdly, we studied the impact of particle velocities on the tipper surface during charging and discharging of phosphate ore. This study allowed us to predict the areas most affected by the abrasion-erosion phenomenon caused by the impact of particles on the tipper surface. This calibration method allowed us to identify the optimal values for the key parameters that will be used later in the modelling of the phosphate clogging phenomenon on the surfaces of transport truck tippers in the mines.

1. Introduction

In recent years, the global fertilizer market has been characterized by a significant increase in consumption (1.7% /year since 2011), supported mainly by Asia which dominates the market and concentrates about 2/3 of global production and consumption [1]. The lowest possible purchase cost has become an important competitive factor which has led to the relocation of fertilizer production to areas with significant resources at low exploitation costs (Russia, Qatar, Iran, North Africa and probably in the long term the USA with the exploitation of shale gas). Since fertilisation contributes to both the quantity and quality of agricultural production on which the world's food system is based, phosphate mining has become the linchpin of the world food security. Studies show how the consumption of phosphate rock, the origin of phosphorus which is a key element in the manufacture

of fertilisers, will continue to increase over the coming years. In Morocco, it is estimated that phosphate production will reach 262 Mt in 2050 [1–4].

Clogging is one of the main problems that reduce the efficiency of phosphate extraction. This phenomenon results from the adhesion of the phosphate to different surfaces of the transport truck tipper. This blocked portion intensifies during the winter period, especially in the bottom and sides of the tipper [5]. This problem is called granular clogging.

The phosphate rock, used as raw material, comes from Benguerir mine. From a stratigraphic point of view, the Benguerir phosphate series is formed by an alternation of phosphate rock levels and sterile silico-carbonate levels (intercaler) (Figure 1) and the ensemble is capped by a carbonate slab called the Thersity slab.

It is very difficult to explore the charging and discharging for extraction in situ because of high-risk work conditions [6,7]. Thus,

*Corresponding Author: Bouassale Nasr-Eddine, n.bouassale@umi.ac.ma

to minimise the cost of experiments and save time, a number of Discrete Element Method simulations (DEM) have been developed [8–12]. With DEM, we can investigate the mechanical and kinematic behaviour of granular materials. In recent years, researchers have carried out DEM simulations with grain shapes and sizes that are complex enough and large enough to be closer to reality, given that DEM was invented much earlier.[13]. the discrete elements method remains the most used calculation tool for the simulation of the various phenomena that appear during the handling of granular materials [14–21]. In the literature, and up to today, we have found three principal approaches used in the simulation of problems of granular systems: the Monte Carlo approach [22-27], the cellular automation approach [28-31] and the DEM approach [32-34].The cell automation method and the Monte Carlo approaches have enabled the simulation of problems related to granular materials by taking into account only the geometric and statistical aspect, but without considering the real mechanical interactions between grains.. In contrast, the DEM method takes into account the interaction between particles by introducing different contact models. Thus it accurately reflects the mechanical phenomenon of the grain packing. It can generate different particle size distributions, with varying geometric characteristics and surfaces, as well as various material ratios from the analyzed sample.

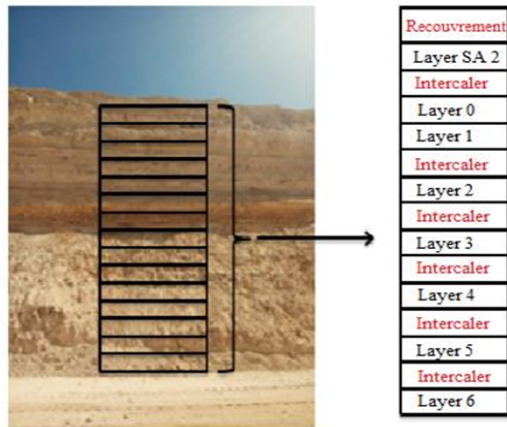


Figure 1: Layered decomposition of Benguerir phosphate [5]

However, what influences the precision of the simulation is the parameter settings [22]. Precise simulations can only be performed if the parameters of the granular materials are well defined. The settings of the process parameters, the nature of the contacts that govern the phenomenon and the behaviour of the materials influences the simulation results [23].

A crucial phase in the development of a discrete element method is the identification of the simulation parameters, namely the specific granular material parameters (Young's modulus, bulk density and Poisson Coefficient) and the parameters related to the nature of the contacts (the particle-wall and particle-particle friction coefficients and the coefficients of restitution). As a result, a calibration of the setup parameters is strongly required to obtain accurate values for the DEM simulation [24–27].

Simulation on software in general requires values for the parameters of the model. For this purpose, there are two main methods for the DEM software to acquire these parameters of contact. The first one is the direct measurement method (DMM),

and the second one is the bulk calibration method (BCM) [22,28–31]. The DMM approach is based on measuring values directly on the particle or contact level. Some properties are easily measured while others remain very difficult, depending on the size of the grains. Almost all attempts have been made at the millimetre level or above [32,33]. Although the values are being directly measured with a certain precision, this does not automatically imply that the DEM model will have the same level of precision at the global level [34–36]. This DMM would be precise if the contact is modelled in an accurate way that captures the physical behaviour of the contact and if both shape and size of the grains are precisely modelled [37,38]. Precise modelling of grain shape and size is too complex when modelling real industrial cases. the calculation time and power limit of the simulators tend to lead to the selection of reasonably large grain sizes, while the shape of the particles cannot be accurately modelled [39–41]. The BCM uses an approach where field measurements or laboratory tests are performed to quantify a specific parameter of the bulk granular material. Experiences are reproduced on software as closely as possible to the configuration and procedures in the laboratory or in the terrain. Simulation values are continuously iterated till the intended response corresponds to the measured one. The difference between the real shape and the virtual model of the grains requires a calibration of the contact parameters [30,31,42,43].

In the DEM simulation, the contact model is a crucial factor that affects the precision level of the simulation. In order to get closer to the actual situation, different contact models appeared in a number of several applications [44–53]. In this study, we used two contact models for our simulation. The Johnson-Kendall-Roberts (JKR) is used for the particle-tipper contact, and the Edinburgh-Elasto-Plastic-Adhesion (EEPA) is used for the particle-particle contact [45]. Furthermore, The modelling of the real shape is important in a discrete element simulation, and the more the geometrical characteristics of the real particles are related to the numerical particles, the closer the results of the numerical simulation are to the real behaviour of the material [54–59]. In the ideal case the grain geometry is retrieved using a rotary scanner as illustrated in the work [58] which allows to obtain the contours of a particle with precision.

In this work we calibrated DEM for phosphate ore in order to define the parameters of the contact models between the phosphate particles themselves and the surface of the tipper of the ore transport truck. This work will allow us to model with DEM the phenomenon of phosphate adhesion during unloading. We presented the contact models we used, followed by the calibration method adopted during this work which is based on the calibration of the angle of repose. The size, shape and distribution of the phosphate particles used in the calibration were studied. We used the fractional factorial designs and Box Behnken designs to determine the influence of the different calibration parameters on the angle of repose.

2. Edinburgh-Elasto-Plastic-Adhesion (EEPA) model for the particle-particle contact

The Edinburgh Elasto-plastic adhesion EEPA model was introduced by Morrissey [60], and implemented in EDEM® as an option [53], to model cohesive materials with elasto-plastic behaviour such as phosphate and clay. It is an extension of the

hysteretic spring model but this time with non-linear behaviour. This model is able to highlight the history of stress dependence of cohesive granular materials with uniaxial consolidation experiments [53]. In [74], the author highlighted the ability of EEPA to generate behaviour that is dependent on the history of previous loads, which is not the case for Hertz-Mindlin, since it's an elastic model. For this purpose, we chose the EEPA to model particle-particle contact of phosphate ore.

2.1. EEPA Force: Normal Direction

This model is an extension of the linear hysteretic model of Walton and Braun [61], allowing tensile forces to develop and also allowing non-linear force-displacement behaviour (overlap) as shown in Figures 2 and 3. The load-displacement curve is defined by the constant pull-off force F_0 , the loading branch stiffness k_1 , the loading-unloading branch stiffness k_2 , the minimum force F_{min} , the adhesion branch stiffness k_a , and the plastic overlap (deformation) δ_p .

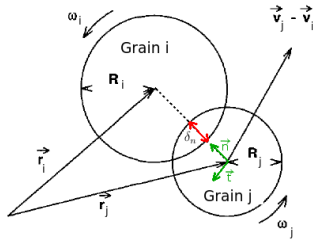


Figure 2 : Formalism used during a contact [62]

The normal force F_n^{EEPA} is composed of two forces, which show its plastic character, namely the hysteretic spring force F_{hys} and the damping force F_{nd} .

$$F_n^{EEPA} = (F_{hys} + F_{nd})\mathbf{n} \quad (1)$$

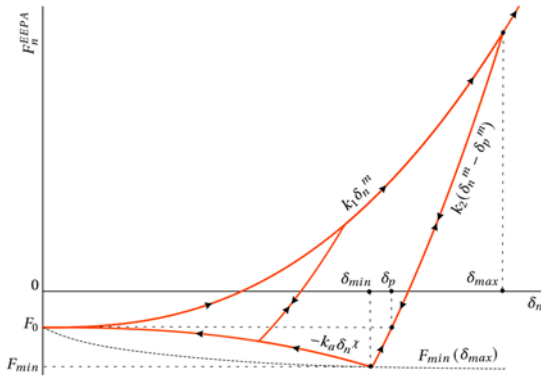


Figure 3 :EEPA model force-displacement relation in the normal direction[63]

where \mathbf{n} is the normal unit vector at the point of contact at the centre of the two particles.

$$F_n^{EEPA} = \begin{cases} F_0 + k_1 * \delta_n^m & \text{if } k_2 * (\delta_n^m - \delta_p^m) \geq k_1 * \delta_n^m \\ F_0 + k_2 * (\delta_n^m - \delta_p^m) & \text{if } k_1 * \delta_n^m > k_2 * (\delta_n^m - \delta_p^m) > -k_{adh} * \delta_n^y \\ F_0 - k_{adh} * \delta_n^y & \text{if } -k_{adh} * \delta_n^y \geq k_2 * (\delta_n^m - \delta_p^m) \end{cases} \quad (2)$$

where F_0 is the adhesion force constant, δ_n^m and δ_p^m are respectively the total normal overlap and the plastic overlap. The loading stiffness k_1 is given by:

$$k_1 = \begin{cases} 2E^*R^* & \text{if } m = 1 \\ \frac{4}{3}\sqrt{R^*}E^* & \text{if } m > 1 \end{cases} \quad (3)$$

where E^* and R^* are the equivalent Young's modulus and radius.

$$R^* = \frac{R_1R_2}{R_1+R_2} \quad (4)$$

R_1, R_2 are radius of particle 1 and 2.

$$E^* = \left(\frac{1-\nu_1^2}{E_1} + \frac{1-\nu_2^2}{E_2} \right)^{-1} \quad (5)$$

E_1, E_2 are Young's modulus of particle 1 and 2.

ν_1, ν_2 are Poisson's ratio of particle 1 and 2.

For our study we took 1.5 as the value of the non-linear slope exponent n . λ_p is defined as the contact plasticity ratio and is given by:

$$\lambda_p = \left(1 - \frac{k_1}{k_2} \right) \quad (6)$$

The damping force F_{nd} can be calculated by:

$$F_{nd} = -\beta_n * v_n \quad (7)$$

where β_n and v_n are respectively the normal damping coefficient and the relative normal velocity.

$$\beta_n = \left(\frac{4m^*k_1}{1+(\pi/\ln e)^2} \right)^{1/2} \quad (8)$$

where e is the coefficient of restitution and m^* is the equivalent mass of the two particles with:

$$m^* = \frac{m_1m_2}{m_1+m_2} \quad (9)$$

2.2. EEPA Force: Force in the Shear Direction

The tangential force F_s is composed of two forces namely tangential damping force F_s^d and tangential spring force F_s^{EEPA} .

$$F_s = F_s^{EEPA} + F_s^d \quad (10)$$

The EEPA force vector is incrementally updated :

$$F_s^{EEPA} = F_s^{EEPA,(dt-1)} - k_t v_t \Delta t \quad (11)$$

The tangential stiffness is given by :

$$k_t = \begin{cases} k_1 & \text{if } n = 1 \\ 8 G^* \sqrt{R^* \delta_n^m} & \text{if } n > 1 \end{cases} \quad (12)$$

where G^* is the effective shear modulus,

$$G^* = \left(\frac{2-\nu_1}{G_1} + \frac{2-\nu_2}{G_2} \right)^{-1} \quad (13)$$

and k_{sf} is the tangential stiffness multiplier. The tangential damping force F_s^d is calculated by :

$$F_s^d = -\beta_t v_t \quad (14)$$

β_t is given by:

$$\beta_t = \sqrt{\frac{4m^*k_t}{1+(\pi/\ln e)^2}} \quad (15)$$

For the stability of the model, tangential force take a critical value f_{ct} :

$$f_{ct} \leq \mu |F_{hys} + k_{adh} \delta_n^m - F_0| \quad (16)$$

where μ is the friction parameter.

3. Johnson-Kendall-Roberts (JKR) Contact Model

Johnson, Kendall and Roberts theory (JKR) [64] introduced adhesion between different surfaces, induced by their surface energies. The (JKR) model is often used to model adherence when caused by capillary forces [60,65–67]. This phenomenon of adhesion has the effect of increasing the contact surface, independently of the load, and justifies the need for a negative force for the release of the surfaces. The theory of the JKR model has been detailed in [68].

For the collision detection, the Sweep and Prune algorithm remains the most famous algorithm used in contact detection when applying the discrete element method [69,70]. This method gives each particle a rectangle parallelepiped that contains it exactly, and the boundaries of this box define on each x, y and z axis a moving interval $[x_{min}, x_{max}]$, $[y_{min}, y_{max}]$ and $[z_{min}, z_{max}]$ respectively (figure 4). The collision of the particles occurred if there is an intersection between the intervals on one of the three axes.

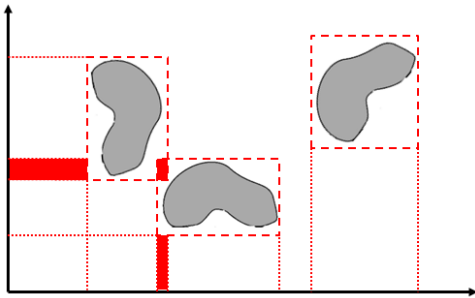


Figure 4: Principle of the Sweep and Prune algorithm

4. Calibration methodology and parameter analysis

4.1. Angle of repose calibration

To generate results close to reality based on simulations of real industrial processes, the inputs relating to the granular materials must be as accurate as possible. The difficulties encountered in the use of DEM lie in the experimental determination of the grain properties (shapes, sizes, coefficient of restitution, rolling friction, grain-grain friction and grain-wall friction, density of gains). Consequently, it is necessary to calibrate the input parameters to achieve satisfactory results [31]. The calibration procedure consists of determining the value of an input parameter by direct measurement such as AoR, bulk density and particle size distribution [71], we then proceed with a series of adjustments until the coincidence between the measured values and the simulated values. A necessary condition is that the tests and measurement method must be reproducible in the laboratory so that the coefficients of interaction can be easily determined.

The angle of repose During a flow, a material forms a natural pile whose slope, defined with the horizontal, forms the natural angle of repose (AoR). It is used to describe the mechanical properties of granular materials. . The natural angle of repose is

constant for a given material, but varies with its moisture content [72]. It is used when studying collapsing, stratifying and segregating. The AoR does not depend only on the mechanical properties of the particles, like density, friction static coefficient and friction dynamic coefficient, but also on the intrinsic properties like shape, geometry and the size of the particles as well as the bulk forming methods [72–75]. When the input values are set, the identification of interaction parameters such as static friction, rolling friction and restitution coefficients must be carried out. These parameters have the ability to considerably affect the nature of the flow. Thus they are very often used as calibration parameters [22, 31,76, 77].

The cylinder lifting (Figure 5) is a common experiment for obtaining the AoR of granular materials [78,79]. The device is basically similar to the one commonly used in litterature, whose principle consists essentially in translating a cylinder suspended upwards [79,80].

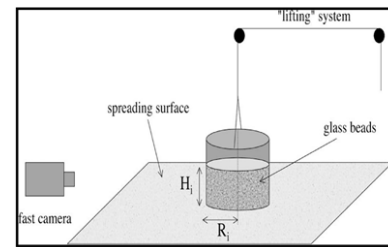


Figure 5: Controlled hollow cylinder test [78]

In [29,73], the author investigated the influence of the dimensions of the test rig and the particle size distribution on the calibration test based on the angle of rest test using a lifting cylinder and they showed that the results remain invariant . The translation speed of the cylinder is considered as a parameter influencing the AoR. Thus the experiment has provided invariant results for granular materials subjected to static stresses when lifting speeds are low.

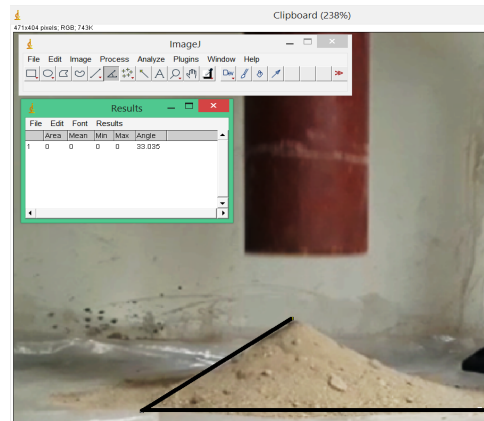


Figure 6: Phosphate AoR test

For our test, 15 kg of mixed phosphate layers (SA2, C1, C2, C3, C4, C5 and C6) is used to carry out the Talus angle test. Inside a cylinder with an internal diameter of 200 mm and a height of 30 cm, a quantity of the Phosphate's particles are glued in such a way that the flow does not interact with the cylinder material. Similarly, on the support on which the phosphate mass will stand, a quantity of phosphate grains is glued to avoid interaction between the particles and the support (Figure 6). Consequently, the interaction

of the particles with the material of the cylinder and the support will be neglected. The cylinder was lifted at a speed of 0.05 m/s [29].

The AoR test was designed to investigate the influence of grain-grain interaction parameters on output variables (angle of repose in our case). We repeated this physical test several times, to have an average of the AoR responses. This average will constitute the target value to be reached during the calibration of the interaction parameters in the EDEM® software. This angle is calculated by measuring the base diameter of the phosphate cone and its height (Figure 7,8).

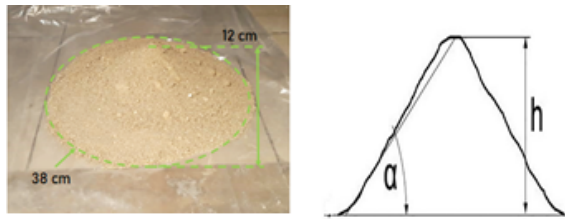


Figure 7: Angle of repose of Phosphate

$$\alpha = \tan^{-1} \left(\frac{2h}{d} \right) = \tan^{-1} \left(\frac{2 \times 12}{38} \right) = 33^\circ \quad (19)$$

h , d are respectively the height and the diameter of the phosphate cone. Thus the characteristic angle of repose of the phosphate is 33° . For the verification we used the software ImageJ [81] and the results are shown in Figure 6. This value will therefore be the calibration target in the following.

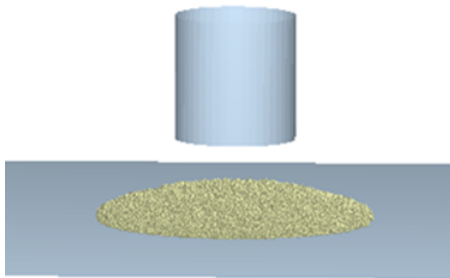


Figure 8: Simulation of the AoR test with EDEM® software

4.2 Particle size distribution and shape

4.2.1 Particle size and distribution

The dimensional distribution of the grains in percentage is determined using dry particle size analysis of samples of phosphate of mass $M=1.5$ Kg (10 samples). This test is the oldest, most common and most economical test described in the NP 18-560 standard. It consists in classifying the different particles constituting the sample by a series of nylon sieves nested one inside the other, with decreasing openings from top to bottom. The phosphate, dried for 24 hours in an oven at $T=120^\circ\text{C}$ to avoid agglomeration of the grains due to the presence of water, is placed at the top and the classification is then obtained by vibrating all the sieves for 5 min. At the end of the test, the rejection from each sieve is weighed (Table1) and the percentage of each size is presented in Figure 9. This study showed that most of the overall mass is concentrated in the $150 \mu\text{m}$ to $500 \mu\text{m}$ range.

Table 1: Results of the particle size analysis of phosphate

Sieve size μm	Retained (g)	Retained (%)	Retained cumulative (g)	Retained cumulative (%)	Cumulative sieve (%)
2000	49.8	3.32	49.8	3.32	96.68
800	172.05	11.47	221.85	14.79	85.21
500	399.45	26.63	621.3	41.42	58.58
250	399	26.6	1020.3	68.02	31.98
150	280.5	18.71	1300.95	86.73	13.27
80	150.3	10.02	1451.25	96.75	3.25
< 80	45.3	3.02	1496.55	99.77	0.23

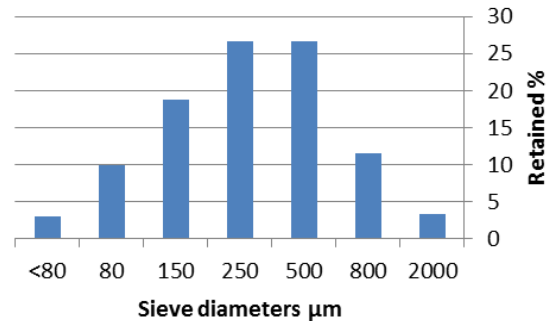


Figure 9: Grain size distribution of phosphate

For the simulation we are asked to enter the particle size distribution of the granular material. For this purpose a statistical test of normality will be carried out to check whether the data in Table 1 follow a normal distribution. The distribution is symmetrical, bell-shaped. It would seem that it can be modelled by a normal distribution. To confirm this, we construct Henry's line. Henry's line is used to approximate the average and standard deviation of the observations of a variable when only the frequencies of its values are available (Figure 10). The distribution can therefore be considered Gaussian. The estimated population average is $390.8 \mu\text{m}$ and the standard deviation is $\sigma = 476.19 \mu\text{m}$. The software results show that the coefficient of determination $R^2 = 0.907$ and the corrected coefficient of determination $R^2_{corr} = 0.91$. These two values indicate that our model is very reliable and can be applied to describe the influence of factors on the response.

4.2.2 Particule shape

The modelling of the real shape is important in a discrete element simulation, and the more the geometrical characteristics of the real particles are related to the numerical particles, the closer the results of the numerical simulation are to the real behaviour of the material [57,59,82]. In the ideal case the grain geometry is retrieved using a rotary scanner [58] which allows to obtain the contours of a particle with precision. In this work, and in order to carry out a three-dimensional modelling of the geometry of an irregular Phosphate particle, samples of each layer of the Benguerir Phosphate are taken to view the structure of their grains under an electronic microscope (Figure 11). Several particle images were taken to select the most representative in terms of size and angularity in order to produce an STL file of the outer shape of a Phosphate particle using CATIA V5 software and which has a geometry roughly gathering almost all the details of the real particles.

The EDEM® software allows users to specify the particle geometry through the so-called "multi-sphere" model, which selects spheres of different sizes to fill the inner volume of the numerical particle geometry, and with the non-linear least squares optimisation the solutions are refined to reach the minimum error value for mass and shape. When the STL file is entered into the software, different types of particles can be generated in such a way that the shape and size of the particle can be modified by changing the number of bonded spheres and their sizes. However, the calculation time increases exponentially with the number of bonded spheres.

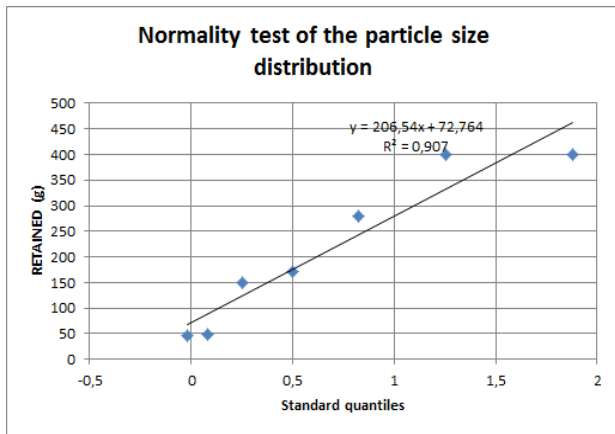


Figure 10: Henry line of particle size distribution

In order to minimise time of simulation [83], consider that combining a number of spheres greater than eight can give satisfactory simulation results (Figure 12).

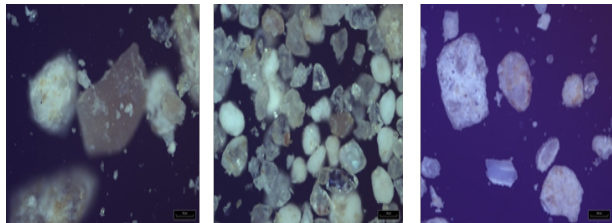


Figure 11: Phosphate grain of sample C1, C3, C6 taken by electronic microscope

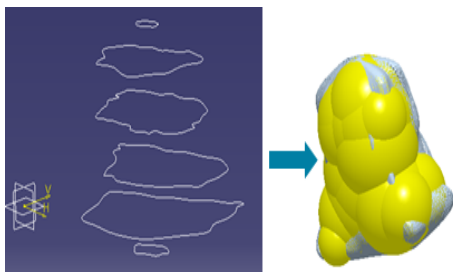


Figure 12: Particle constructed using the 'multi-sphere' method from STL files

5. Test results according to the fractional factorial design

For our simulation process, the DEM was applied, and the EDEM® software was chosen in this research [84]. The EEPA contact model was adopted, with a value of 9.81 m/s² for the gravitational acceleration. The inputs parameters applied in our simulation are presented in Table 2,3,4.

Table 2: Values of some simulation parameters

	Young's modulus E (Pa)	Shear modulus G (Pa)	Poisson Coef. (ν)	Average density ρ (Kg/m ³)
Phosphate	10 ⁶	2.5 10 ⁶	0.25	2404

Table 3: Results of the shear cell test

Reference layer	C (KPa)	φ (°)
C3	30	33

Table 4: Results of the odometer test

Layer reference	shear index (Cc)	Swell index (Cs)
C6	0.193	0.010

The developers of the EDEM® software recommend using a experimental plan to adjust the properties of the granular material. Thus, a fractional factorial design [85,86] with two levels of resolution and five factors will be used to study the five inter-granular interaction factors in sixteen experiments (Figure 13). For this purpose, an initial range of these interaction parameters was determined on the basis of the literature [5,87,88] and on the basis of the GEMM integrated material data library in the EDEM® software.

	Factors														
Essa	2	3	4	5	6	7	8	9	10	11	12	13	14	15	
4	Com III														
8		Com IV	III	III	III										
16			Com V	IV	IV	IV	III	III	III	III	III	III	III	III	
32				Com VI	IV	IV	IV	IV	IV	IV	IV	IV	IV	IV	
64					Com VII	V	IV	IV	IV	IV	IV	IV	IV	IV	
128						Com VIII	VI	V	V	IV	IV	IV	IV	IV	

Figure 13: Choice of experimental plan

Table 5: Model parameter ranges

Parameter	Identifier	Low level	High level
Coefficient of restitution	A	0.15	0.75
Static friction coefficient	B	0.2	1
Rolling resistance coefficient	C	0	0.3
Surface energy (J/m ²)	D	0.3	1.5
Pull-off constant	E	-0.009	0

This library helps the software user through a set of questions (field of application, density, experimental angle of repose) to set likely values of the parameters to model the physical phenomenon (Table 5). The fractional factorial design will be used first to analyse the relationships between the parameters potentially influencing the AoR. Once the influencing factors have been

determined, a response surface design analysis will be carried out to accurately determine the parameter values of the model.

The results of the test according to the fractional factorial design 2^{5-1} are presented in Figure 14. It can be seen that the angle of repose has a large range of variation with a maximum and minimum value of 47.92° and 14.3° respectively, which suggests the influence of certain simulation parameters on the angle of repose.

We conducted a more in-depth analysis of the model results reported on the graph (Figure 15). The significance of the factors can be seen intuitively and is in the following decreasing order: coefficient of static friction > surface energy > coefficient of rolling resistance > coefficient of restitution > pull-off constant.

Based on Figure 16 we state that the four parameters: coefficient of rolling resistance, surface energy and static friction coefficient of the particles have a great influence on the AoR of the phosphate mass, Unlike the other parameters, with an order of influence as follows: coefficient of static friction > surface energy > coefficient of rolling resistance.

Coef. of restitution	Static friction coefficient	Rolling resistance coefficient	Surface energy	Pull-off constant	Angle of Repose
0.15	0.2	0.0	0.3	0.000	14,30
0.75	0.2	0.0	0.3	-0.009	14,30
0.15	1.0	0.0	0.3	-0.009	33,00
0.75	1.0	0.0	0.3	0.000	33,00
0.15	0.2	0.3	0.3	-0.009	20,14
0.75	0.2	0.3	0.3	0.000	20,99
0.15	1.0	0.3	0.3	0.000	36,01
0.75	1.0	0.3	0.3	-0.009	36,01
0.15	0.2	0.0	1.5	-0.009	34,96
0.75	0.2	0.0	1.5	0.000	23,86
0.15	1.0	0.0	1.5	0.000	40,25
0.75	1.0	0.0	1.5	-0.009	40,25
0.15	0.2	0.3	1.5	0.000	27,96
0.75	0.2	0.3	1.5	-0.009	27,96
0.15	1.0	0.3	1.5	-0.009	44,60
0.75	1.0	0.3	1.5	0.000	47,92

Figure 14: Simulation results following the fractional factorial design

As the parameters contact coefficient of restitution and pull-off constant have no significant effect on the response of the angle of repose of the phosphate mass, their values will be set at the low levels shown in Table 6.

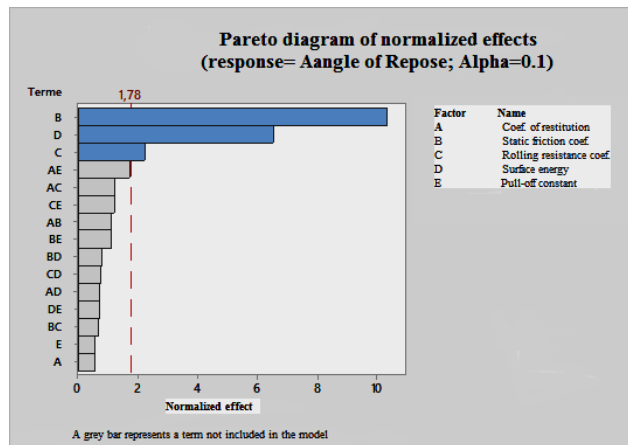


Figure 15: Significance of study factors

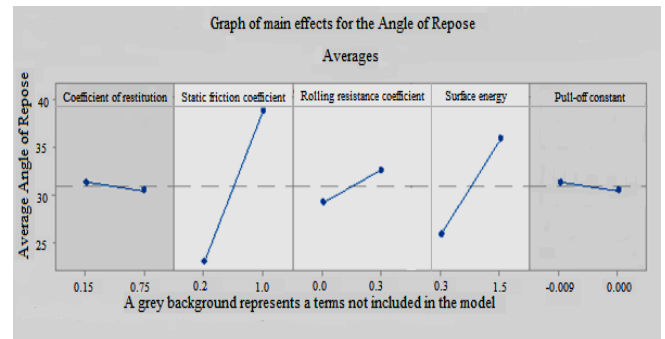


Figure 16: Factors influencing the Angle of Repose

Table 6: Values of non-significant parameters

Non-significant parameter	Value
Coefficient of restitution	0.15
Pull-off constant	-0.009

6. Results of the simulation according to Box Behnken's planTest [89–91]

After the determination of the significant factors for the angle of repose through the fractional factorial design it is necessary to find the exact values of these parameters retained to arrive at a correct modelling of the behaviour of the phosphate. For this purpose the Box Behnken design of experiments are used to find the quadratic relation that links these parameters, considered continuous this time, to the 'angle of repose' response. A three-factor response surface design is chosen and will be studied in 15 trials as recommended by the Minitab software (Figure 17).

Plan		Continuous factors								
		2	3	4	5	6	7	8	9	10
Centred composite (complete)	not divided into blocks	13	20	31	52	90	152			
	divided into blocks	14	20	30	54	90	160			
Centred composite (1/2)	not divided into blocks				32	53	88	154		
	divided into blocks				33	54	90	160		
Centred composite (1/4)	not divided into blocks							90	156	
	divided into blocks							90	160	
Centred composite (1/8)	not divided into blocks									158
	divided into blocks									160
Box-Behnken	not divided into blocks	15	27	46	54	62			130	170
	divided into blocks		27	46	54	62			130	170

Figure 17: Choice of plan of experiments

From an analysis of the responses of simulation the angle of repose in Figure 14, it can be seen that the (AoR) approaches the experimental value for ranges of coefficient of friction, coefficient of rolling resistance and surface energy in the intervals [0.4; 1], [0; 0.4] and [0.8; 1.2] respectively. Thus these intervals will form the basis of the study using Box Behnken plan. The results of the numerical simulation following the test matrix are shown in Figure 18, and it can be seen that the responses are close to the results of the previous fractional plan. In addition, a quadratic regression model is established by the software MiniTab (Equation 20) which has a coefficient of determination of 98.58% close to 1 (i.e.) it has a high reliability.

$$AoR = 2.89 + 50.81 B + 15.66 C + 6.5 D - 23.25 B^2 - 20.43 C^2 \quad (20)$$

Static friction coef.	Rolling resistance coef.	Surface energy	AoR
-1	-1	0	26,36
1	-1	0	37,16
-1	1	0	29,66
1	1	0	39,20
-1	0	-1	26,52
1	0	-1	38,77
-1	0	1	29,05
1	0	1	40,29
0	-1	-1	31,26
0	1	-1	35,43
0	-1	1	35,28
0	1	1	37,76
0	0	0	36,09
0	0	0	35,58
0	0	0	36,47

Figure 18: Simulation results following the Box Behnken plan

7. Analysis of the interaction effect of the regression model

In this test, the AoR of the phosphate mass is used as an indicator for evaluating the regression model. Response surfaces and contour diagram of the pairwise interaction of the different parameters that affect the angle of repose are shown in Figures 19 and 20. An analysis of the parabolas that exist on the response surface curve shows the existence of a non-linear dependence of the AoR on the coefficient of static friction and the coefficient of rolling resistance. These quadratic dependencies are illustrated in the model of Equation 20 with the square term of the coefficient of static friction and rolling resistance. As shown in Figures 19 and 20, the angle of repose increases with the increase in surface energy. When this energy increases, it will lead to a stronger adhesion between the particles, which will lead to the creation of new aggregates that will give more stability to the granular material. This will make particle collapse more difficult and therefore the angle of rest will increase. Similarly the AoR increases with the increase of the coefficient of static friction since the friction contradicts the movement of the particles on each other and thus the angle of the phosphate pile increases. The figures 21 and 22 show that while the rolling resistance coefficient of the particles increases the repose angle of the phosphate volume increases. This is because the rolling resistance prevents the particles from rolling down the slope of the granular cone, which contributes to the increase in the angle of repose.

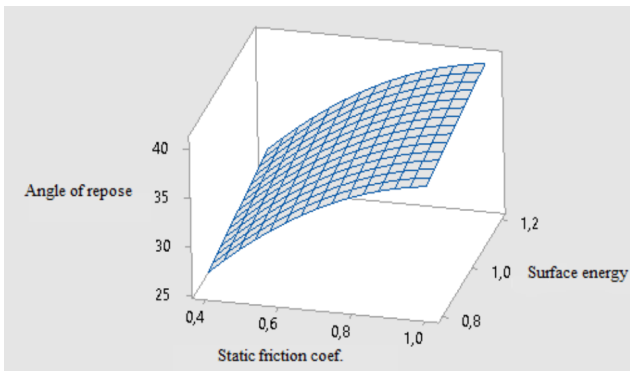


Figure 19: Variation of the angle of repose with surface energy and the static friction coefficient

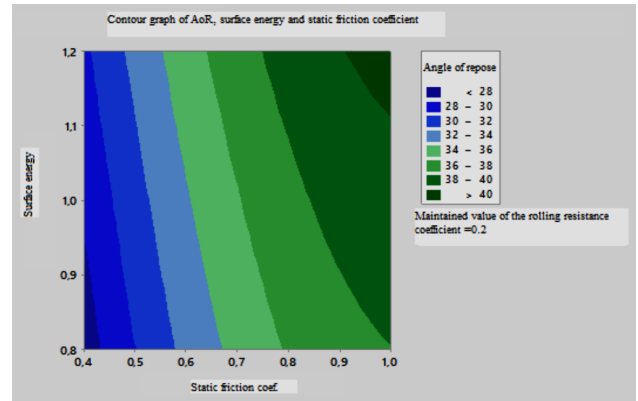


Figure 20 :Contour graph of AoR, surface energy and static friction coefficient

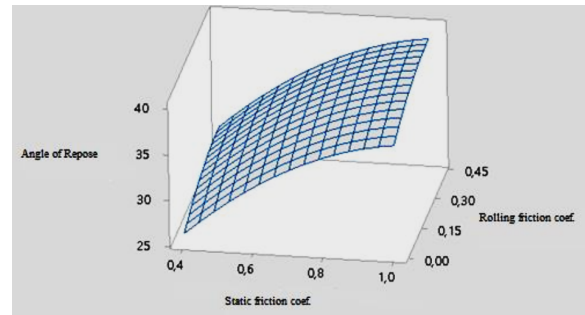


Figure 21 :Variation of the AoR as a function of the surface energy and the rolling resistance coefficient

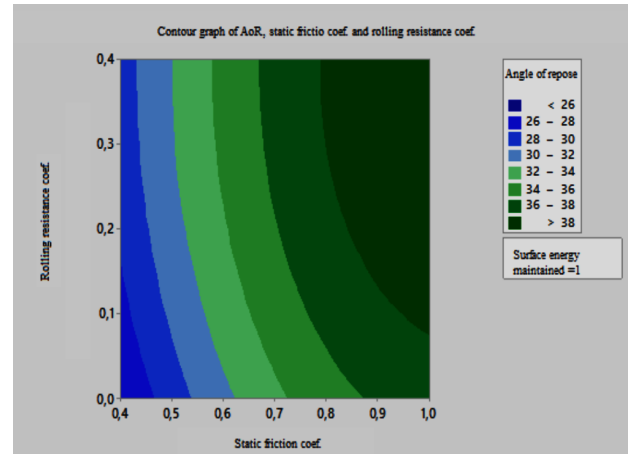


Figure 22: Contour graph of the AoR as a function of the surface energy and the rolling resistance coefficient

8. Results and discussion

The repose angle AoR of the phosphate mass measured by field test was 33°. We took this real angle as the response value and used the contours above and take as values of significant parameters the following values:

Table 7: Optimised values of the simulation parameters

Parameters	Values
Static friction coef.	0.7
Rolling resistance coef.	0.3
Surface energy	1j/m ²

A simulation under EDEM® was performed under the optimised parameters and the angle of repose for phosphate ore was 34.38°. We compared the test results with the simulation results. The relative error was 4.19%. This error value shows that the optimised parameters can be utilised as a reference for the characteristics of the phosphate.

9. Particle velocities

In this section we will investigate the impact of particle velocity on the contact with the tipper surface during loading and unloading. During the first few moments of loading of the tipper by the loader bucket, the simulation results show that the area most affected by the falling grain is in the front part of the tipper as shown in Figure 23. This configuration is quite natural since the particles leaving the bucket are accelerated by gravity to find this area on the tipper first, and then the grains that follow will be oriented towards the sides once the angle of repose exceeds the AoR of the phosphate.

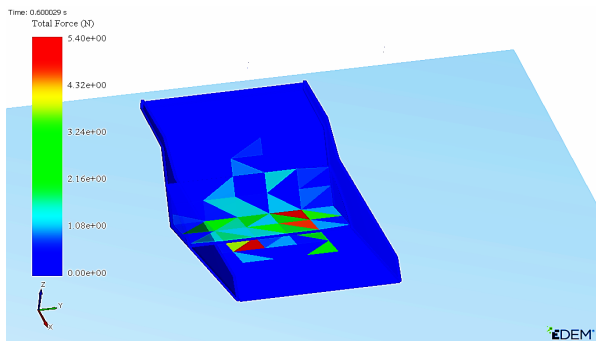


Figure 23: Area of first impact on the tipper

Just before the collision, the particles have a maximum kinetic energy, as they are accelerated by gravity to reach a maximum speed of 3.92 m/s during the first contacts with the tipper (Figure 24). This maximum falling speed starts to decrease as the granular material accumulates in the tipper since the height of fall decreases (figure 25).

Of course, this area of first impact can move on the tipper depending on the position of the loader bucket. Thus, the amplitude of the falling speed will depend on the height of the bucket. Figure 26 shows the decrease in the value of the maximum particle velocity (2.75 m/s) in the case of the reduction of the drop height. However, the position of the filler was fixed according to multiple observations of the truck loading operation in the field or on website videos.

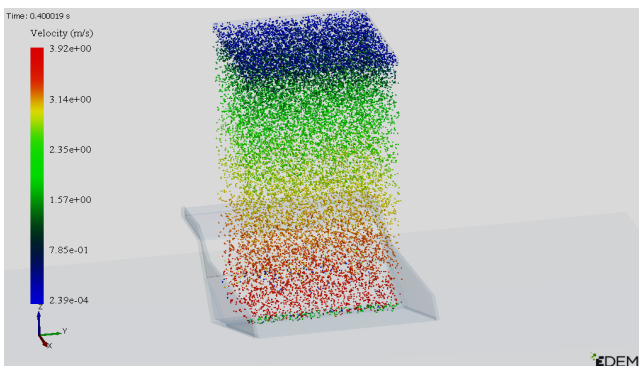


Figure 24: Maximum impact speed

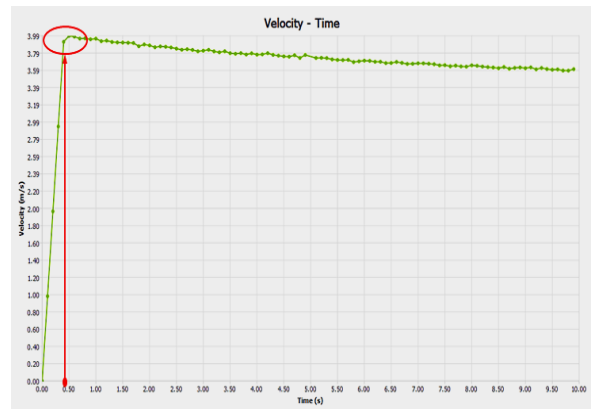


Figure 25: Variation of maximum particle velocities

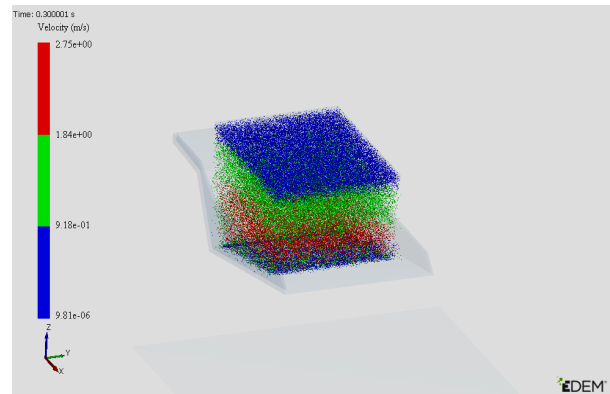


Figure 26: Decrease in particle velocity with decreasing of drop height

This data predicts that the front part of the tipper will be more exposed to abrasive erosion due to the high rates of direct collision of the particles against the tipper during the early loading phase. This is confirmed by the presence of pits and cavities in the same area on the tippers. These pits will increase the flow angle and consequently trap the phosphate grains and give rise to the nucleation of the clogging phenomenon.

10. Conclusion

In this work, we studied phosphate ore using the discrete element method. The study is devoted to the calibration of the DEM based on the angle of repose. The simulation parameters are calibrated and optimized by combining the results from the various physical tests and the DEM simulation with the EDEM® software. We took the value of the angle of repose as the target for the simulation response values, and using the Minitab software, we were able to analyze and optimize the simulation parameters using the response surface method. These physical parameters that significantly affect the AoR were selected, and the interaction between them was analyzed to determine optimal values. We also applied the fractional factorial design test, and the results are analysed to determine the influence of each of the factors and it was found that the angle of repose depends only on the coefficient of static friction, the surface energy and the rolling resistance coefficient. In addition we used Box-Behnken response surface method. The results were analysed and we established the regression model of the significant factors on the angle of repose. This model predicts an increase in the angle of repose as the significant factors increase. The results show that when the surface energy, static friction coefficient and rolling resistance coefficient

take the values: 1 J/m², 0.7 and 0.3 respectively, the simulation results are consistent with the experimental test result and the error in the angle of repose obtained is 4.19%.

A study was conducted on the impact of particle velocity on the surface of the tipper during loading and unloading. This study allowed us to predict that the front part of the tipper will be more exposed to abrasive erosion due to the high speed of direct collision of the particles against the tipper during the beginning of the loading phase, which corresponds perfectly to the reality in the field.

This work constitutes the first part for the study of phosphate or clogging. Indeed, the identification of the different parameters that define phosphate by the calibration method will allow us to better model the phenomenon with the DEM method. The study of the impact velocities will be used to model the stresses and strains on the tipper surface during the loading and unloading of the phosphate in our next work.

Conflict of Interest

The authors declare no conflict of interest.

References

- [1] FAO, *Marché mondial des engrais: bilan du resserrement actuel du marché*, ROME, 2022.
- [2] FAO, *World fertilizer trends and outlook to 2020*, 2017.
- [3] N. Alexandratos, J.B. Fao, "WORLD AGRICULTURE TOWARDS 2030 / 2050 The 2012 Revision ESA Working Paper No. 12-03."
- [4] P. Christmanna, "A forward look into rare earth supply and demand: A role for sedimentary phosphate deposits?," *Procedia Engineering*, **83**, 19–26, 2014, doi:10.1016/j.proeng.2014.09.005.
- [5] M. Medkour, Y. Najih, J. Bengourram, A. El Ghmari, M. Bachaoui, H. Latrache, M. Mabrouki, "Mechanical and thermal characterization of natural phosphate: Clogging understanding (Part 1)," *Materials Today: Proceedings*, **51**, 2032–2039, 2022, doi:10.1016/j.matpr.2021.06.261.
- [6] I. Louw, "Potential radiological impact of the phosphate industry in South Africa on the public and the environment (Paper 1)," *Journal of Environmental Radioactivity*, **217**(February), 106214, 2020, doi:10.1016/j.jenvrad.2020.106214.
- [7] J. Duarte, A.T. Marques, *Occupational Accidents in the Mining Industry — A Short Review*, Springer International Publishing: 61–69, 2019, doi:10.1007/978-3-030-14730-3.
- [8] J. Shen, A. Roberts, C. Wheeler, "Dem simulations on gate loads and bin storage characteristics before discharge," *Powder Technology*, **383**, 280–291, 2021, doi:10.1016/j.powtec.2021.01.028.
- [9] M.J. Mohajeri, W. De Kluijver, R.L.J. Helmons, C. Van Rhee, D.L. Schott, "A validated co-simulation of grab and moist iron ore cargo : Replicating the cohesive and stress-history dependent behaviour of bulk solids," *Advanced Powder Technology*, **32**(4), 1157–1169, 2021, doi:10.1016/j.apt.2021.02.017.
- [10] J. Sun, H. Chen, J. Duan, Z. Liu, Q. Zhu, "Mechanical properties of the grooved-wheel drilling particles under multivariate interaction influenced based on 3D printing and EDEM simulation," *Computers and Electronics in Agriculture*, **172**(July 2019), 105329, 2020, doi:10.1016/j.compag.2020.105329.
- [11] M. Haustein, A. Gladky, R. Schwarze, "Discrete element modeling of deformable particles in YADE," *SoftwareX*, **6**, 118–123, 2017, doi:10.1016/j.softx.2017.05.001.
- [12] C. Ramírez-Aragón, J. Ordieres-Meré, F. Alba-Elías, A. González-Marcos, "Comparison of Cohesive models in EDEM and LIGGGHTS for simulating powder compaction," *Materials*, **11**(11), 1–17, 2018, doi:10.3390/ma11112341.
- [13] B.C. Burman, P.A. Cundall, O.D.L. Strack, "A discrete numerical model for granular assemblies," *Geotechnique*, **30**(3), 331–336, 1980, doi:10.1680/geot.1980.30.3.331.
- [14] J. Jahnke, M. Burger, "PARAMETER IDENTIFICATION FOR SOIL SIMULATION BASED ON THE DISCRETE ELEMENT METHOD AND APPLICATION TO SMALL SCALE SHALLOW PENETRATION TESTS," 332–342, 2019.
- [15] Y. Zhu, J. Gong, Z. Nie, "Particology Shear behaviours of cohesionless mixed soils using the DEM: The influence of coarse particle shape," *Particology*, **55**, 151–165, 2021, doi:10.1016/j.partic.2020.07.002.
- [16] F.-V.D. Luc Scholtès, "A DEM model for soft and hard rocks : Role of grain interlocking on strength," *Journal of the Mechanics and Physics of Solids*, **61**, 352–369, 2013, doi:10.1016/j.jmps.2012.10.005.
- [17] D. Yan, J. Yu, Y. Wang, L. Zhou, K. Sun, Y. Tian, "A Review of the Application of Discrete Element Method in Agricultural Engineering: A Case Study of Soybean," 1–18, 2022.
- [18] L.K. Nordell, "Particle flow modeling: transfer chutes & other applications," *International Materials Handling Conference (BELTCON 9)*, Johannesburg, South Africa, 1–16, 1997.
- [19] D.B.B. Hastie, a. P.P. Grima, P.W.W. Wypych, "Validation of particle flow through a conveyor transfer spoon via particle velocity analysis," *Bulk Europe 2008*, (March 2015), 1–5, 2008.
- [20] T. Gröger, A. Katterfeld, "On the numerical calibration of discrete element models for the simulation of bulk solids," *Computer Aided Chemical Engineering*, **21**(C), 533–538, 2006, doi:10.1016/S1570-7946(06)80100-8.
- [21] M.D. Sinnott, P.W. Cleary, "The effect of particle shape on mixing in a high shear mixer," *Computational Particle Mechanics*, **3**(4), 477–504, 2016, doi:10.1007/s40571-015-0065-4.
- [22] S. Zhang, M.Z. Tekeste, Y. Li, A. Gaul, D. Zhu, J. Liao, "Scaled-up rice grain modelling for DEM calibration and the validation of hopper flow," *Biosystems Engineering*, **194**, 196–212, 2020, doi:10.1016/j.biosystemseng.2020.03.018.
- [23] B. Soltanbeigi, A. Podlozhnyuk, C. Kloss, S. Pirker, J.Y. Ooi, S.A. Papanicopolulos, "Influence of various DEM shape representation methods on packing and shearing of granular assemblies," *Granular Matter*, **23**(2), 1–16, 2021, doi:10.1007/s10035-020-01078-y.
- [24] S. Huang, J.X. Huang, Y.S. Mo, Z.F. Zhang, "Study on Wear Properties of the Flow Parts in a Centrifugal Pump based on EDEM-Fluent Coupling," *Reneng Dongli Gongcheng/Journal of Engineering for Thermal Energy and Power*, **35**(1), 62–69, 2020, doi:10.16146/j.cnki.rndlgc.2020.01.010.
- [25] B.M. Ghodki, M. Patel, R. Namdeo, G. Carpenter, "Calibration of discrete element model parameters: soybeans," *Computational Particle Mechanics*, **6**(1), 3–10, 2019, doi:10.1007/s40571-018-0194-7.
- [26] Y. Tan, Y. Yu, J. Fottner, S. Kessler, "Automated measurement of the numerical angle of repose (aMAoR) of biomass particles in EDEM with a novel algorithm," *Powder Technology*, **388**, 462–473, 2021, doi:10.1016/j.powtec.2021.04.062.
- [27] M. Mousaviraad, M. Tekeste, K.A. Rosentrater, "CALIBRATION AND VALIDATION OF A DISCRETE ELEMENT MODEL OF CORN USING GRAIN FLOW SIMULATION IN A COMMERCIAL SCREW GRAIN AUGER," **60**(4), 1403–1415, 2017.
- [28] M.J. Mohajeri, H.Q. Do, D.L. Schott, "DEM calibration of cohesive material in the ring shear test by applying a genetic algorithm framework," *Advanced Powder Technology*, **31**(5), 1838–1850, 2020, doi:10.1016/j.apt.2020.02.019.
- [29] T. Roessler, A. Katterfeld, "DEM parameter calibration of cohesive bulk materials using a simple angle of repose test," *Particology*, **45**, 105–115, 2019, doi:10.1016/j.partic.2018.08.005.
- [30] A. Boikov, R. Savelev, V. Payor, A. Potapov, "Universal Approach for DEM Parameters Calibration of Bulk Materials," 2021.
- [31] C.J. Coetzee, "Review: Calibration of the discrete element method," *Powder Technology*, **310**, 104–142, 2017, doi:10.1016/j.powtec.2017.01.015.
- [32] N. Kassotakis, V. Sarhosis, M. V Peppas, J. Mills, "Quantifying the effect of geometric uncertainty on the structural behaviour of arches developed from direct measurement and Structure-from-Motion (SfM) photogrammetry," *Engineering Structures*, **230**(December 2020), 111710, 2021, doi:10.1016/j.engstruct.2020.111710.
- [33] M. Marigo, E.H. Stitt, "Discrete element method (DEM) for industrial applications: Comments on calibration and validation for the modelling of cylindrical pellets," *KONA Powder and Particle Journal*, **32**(32), 236–252, 2015, doi:10.14356/kona.2015016.
- [34] S. Kirsch, "Avoiding ambiguity in DEM in-situ calibration for dry bulk materials," *Minerals Engineering*, **145**(July 2019), 106094, 2020, doi:10.1016/j.mineng.2019.106094.
- [35] J. Quist, M. Evertsson, "Framework for DEM Model Calibration and Validation," *Proceedings of the 14th European Symposium on Comminution and Classification*, (September), 103–108, 2015.
- [36] T.A.H. Simons, R. Weiler, S. Strege, S. Bensmann, M. Schilling, A. Kwade, "A ring shear tester as calibration experiment for DEM simulations in agitated mixers - A sensitivity study," *Procedia Engineering*, **102**, 741–748, 2015, doi:10.1016/j.proeng.2015.01.178.

- [37] G. Ma, Z. Sun, H. Ma, P. Li, "Calibration of Contact Parameters for Moist Bulk of Shotcrete Based on EDEM," *Advances in Materials Science and Engineering*, **2022**, 2022, doi:10.1155/2022/6072303.
- [38] G.K.P. Barrios, R.M. de Carvalho, A. Kwade, L.M. Tavares, "Contact parameter estimation for DEM simulation of iron ore pellet handling," *Powder Technology*, **248**, 84–93, 2013, doi:10.1016/j.powtec.2013.01.063.
- [39] C. Chen, J. Gu, Z. Peng, X. Dai, Q. Liu, G.Q. Zhu, "Discrete element modeling of particles sphericity effect on sand direct shear performance," *Scientific Reports*, **12**(1), 1–14, 2022, doi:10.1038/s41598-022-09543-9.
- [40] Z. Zhao, G. Jiang, R. Mao, "Effects of particle sizes of rock phosphate on immobilizing heavy metals in lead zinc mine soils," **14**(2), 258–266, 2014.
- [41] Z. Wang, Y. Fang, W. Feng, X. Tian, J. Lin, "Comparative Study on Particle Size Effect of Crushable Granular Soils through DEM Simulations," **2022**, doi:10.2113/2022/1608454/5558342/1608454.pdf.
- [42] S. Ben Turkia, D.N. Wilke, P. Pizette, N. Govender, N.E. Abriak, "Benefits of virtual calibration for discrete element parameter estimation from bulk experiments," *Granular Matter*, 1–16, 2019, doi:10.1007/s10035-019-0962-y.
- [43] E.X.Z. P.Z. Z.H. Jiang, "Discrete Element Method of Coke Accumulation : Calibration of the Contact Parameter," *IFAC-PapersOnLine*, 241–245, 2018, doi:10.1016/j.ifacol.2018.09.425.
- [44] A.V.B. R.V.S.A.P., "DEM Calibration Approach : Implementing Contact Model," *Journal of Physics: Conf. Series*, 2018.
- [45] Z. Wu, X. Wang, D. Liu, F. Xie, L. George, Z. Zhang, Q. Tang, "Calibration of discrete element parameters and experimental verification for modelling subsurface soils," *Biosystems Engineering*, **212**, 215–227, 2021, doi:10.1016/j.biosystemseng.2021.10.012.
- [46] Y. Su, Y. Xu, T. Cui, X. Gao, G. Xia, Y. Li, "Determination and interpretation of bonded- particle model parameters for simulation of maize kernels," *Biosystems Engineering*, **210**, 193–205, 2021, doi:10.1016/j.biosystemseng.2021.08.022.
- [47] Z. Zhao, H. Li, J. Liu, S.X. Yang, "Control method of seedbed compactness based on fragment soil compaction dynamic characteristics," *Soil and Tillage Research*, **198**(January), 104551, 2020, doi:10.1016/j.still.2019.104551.
- [48] L. Zhang, C.Q. Ru, "A refined JKR model for adhesion of a rigid sphere on a soft elastic substrate," *Journal of Applied Mechanics, Transactions ASME*, **86**(5), 1–11, 2019, doi:10.1115/1.4042574.
- [49] J. Hellwig, R.M.P. Karlsson, L. Wågberg, T. Pettersson, "Measuring elasticity of wet cellulose beads with an AFM colloidal probe using a linearized DMT model," *Analytical Methods*, **9**(27), 4019–4022, 2017, doi:10.1039/c7ay01219e.
- [50] A. Papangelo, R. Lovino, M. Ciavarella, "Electroadhesive sphere-flat contact problem: A comparison between DMT and full iterative finite element solutions," *Tribology International*, **152**(May), 106542, 2020, doi:10.1016/j.triboint.2020.106542.
- [51] S. Richesson, M. Sahimi, "Hertz-Mindlin Theory of Contacting Grains and the Effective-Medium Approximation for the Permeability of Deforming Porous Media," *Geophysical Research Letters*, **46**(14), 8039–8045, 2019, doi:10.1029/2019GL083727.
- [52] M.J. Mohajeri, R.L.J. Helmons, C. van Rhee, D.L. Schott, "A hybrid particle-geometric scaling approach for elasto-plastic adhesive DEM contact models," *Powder Technology*, **369**, 72–87, 2020, doi:10.1016/j.powtec.2020.05.012.
- [53] S.C. Thakur, J.P. Morrissey, J. Sun, J.F. Chen, J.Y. Ooi, "Micromechanical analysis of cohesive granular materials using the discrete element method with an adhesive elasto-plastic contact model," *Granular Matter*, **16**(3), 383–400, 2014, doi:10.1007/s10035-014-0506-4.
- [54] A. Hafez, Q. Liu, T. Finkbeiner, R.A. Alouhali, T.E. Moellendick, J.C. Santamarina, "The effect of particle shape on discharge and clogging," *Scientific Reports*, **11**(1), 1–12, 2021, doi:10.1038/s41598-021-82744-w.
- [55] P. Vangla, N. Roy, M.L. Gali, "Image based shape characterization of granular materials and its effect on kinematics of particle motion," *Granular Matter*, **20**(1), 2018, doi:10.1007/s10035-017-0776-8.
- [56] S.S. Ahmed, A. Martinez, "Effects of Particle Shape on the Shear Wave Velocity and Shear Modulus of 3D Printed Sand Analogs," *Open Geomechanics*, **3**(1), 1–18, 2022, doi:10.5802/ogeo.9.
- [57] D. Höhner, S. Wirtz, V. Scherer, "A numerical study on the influence of particle shape on hopper discharge within the polyhedral and multi-sphere discrete element method," *Powder Technology*, **226**, 16–28, 2012, doi:10.1016/j.powtec.2012.03.041.
- [58] Y. Chen, Z. Chu, X. Yu, "Research of The Influence of The Particle Geometry on The Accumulation of Repose Angle Based on DEM," **154**(Icmia), 38–46, 2017, doi:10.2991/icmia-17.2017.8.
- [59] A. Khazeni, Z. Mansourpour, "Influence of non-spherical shape approximation on DEM simulation accuracy by multi-sphere method," *Powder Technology*, **332**, 265–278, 2018, doi:10.1016/j.powtec.2018.03.030.
- [60] J.P. Morrissey, "Discrete Element Modelling of Iron Ore Fines to Include the Effects of Moisture and Fines," 1–395, 2013.
- [61] O.R. Walton, R.L. Braun, "Viscosity, granular-temperature, and stress calculations for shearing assemblies of inelastic, frictional disks," *Journal of Rheology*, **30**(5), 949–980, 1986, doi:10.1122/1.549893.
- [62] M.J. BOUTELOUP, *Simulation numérique de la dynamique d'un lit granulaire cisailé par un fluide visqueux*, Institut National Polytechnique de Toulouse (INP Toulouse), 2017.
- [63] C.J. Coetzee, *Edinburgh-Elasto-Plastic-Adhesion (EPPA) Contact Model Implementation in PFC, Version 1.1*, 2022, doi:10.13140/RG.2.2.13659.18724.
- [64] K.L. Johnson, K. Kendall, A.D. Roberts, "Surface energy and the contact of elastic solids," *Proceedings of the Royal Society of London. A. Mathematical and Physical Sciences*, **324**(1558), 301–313, 1971, doi:10.1098/rspa.1971.0141.
- [65] J. Hærvig, U. Kleinhans, C. Wieland, H. Spliethoff, A.L. Jensen, K. Sørensen, T.J. Condra, "On the adhesive JKR contact and rolling models for reduced particle stiffness discrete element simulations," *Powder Technology*, **319**, 472–482, 2017, doi:10.1016/j.powtec.2017.07.006.
- [66] S.A. Carr, J. Liu, A.G. Tesoro, "Transport and fate of microplastic particles in wastewater treatment plants," *Water Research*, **91**, 174–182, 2016, doi:10.1016/j.watres.2016.01.002.
- [67] R. Xia, B. Li, X. Wang, T. Li, Z. Yang, "Measurement and calibration of the discrete element parameters of wet bulk coal," *Measurement: Journal of the International Measurement Confederation*, **142**, 84–95, 2019, doi:10.1016/j.measurement.2019.04.069.
- [68] J. Zhou, L. Zhang, C. Hu, Z. Li, J. Tang, K. Mao, X. Wang, "Calibration of wet sand and gravel particles based on JKR contact model," *Powder Technology*, **397**, 117005, 2022, doi:10.1016/j.powtec.2021.11.049.
- [69] T. Capannini, Gabriele and Larsson, "Adaptive Collision Culling for Massive Simulations by a Parallel and Context-Aware Sweep and Prune Algorithm," *IEEE Transactions on Visualization and Computer Graphics*, **24**(7), 2064–2077, 2018, doi:10.1109/TVCG.2017.2709313.
- [70] J.C. Monan Wang, "A review of collision detection for deformable objects," *Computer Animation and Virtual Worlds*, **32**(5), 2021, doi:https://doi.org/10.1002/cav.1987.
- [71] A. Grima, D. Hastie, D. Curry, P. Wypych, R. La Roche, A. Grima, D. Hastie, L. Roche, "The beginning of a new era in design: Calibrated discrete element modelling Publication Details," *Australian Bulk Handling Review*, **16**(6), 14–21, 2011.
- [72] H.M. Beakawi Al-Hashemi, O.S. Baghabra Al-Amoudi, "A review on the angle of repose of granular materials," *Powder Technology*, **330**, 397–417, 2018, doi:10.1016/j.powtec.2018.02.003.
- [73] T. Roessler, A. Katterfeld, "Scaling of the angle of repose test and its influence on the calibration of DEM parameters using upscaled particles," *Powder Technology*, **330**, 58–66, 2018, doi:10.1016/j.powtec.2018.01.044.
- [74] H. Nakashima, Y. Shioji, T. Kobayashi, S. Aoki, H. Shimizu, J. Miyasaka, K. Ohdoi, "Determining the angle of repose of sand under low-gravity conditions using discrete element method," *Journal of Terramechanics*, **48**(1), 17–26, 2011, doi:10.1016/j.jterra.2010.09.002.
- [75] M. Khanal, M. Elmoutie, D. Adhikary, "Effects of particle shapes to achieve angle of repose and force displacement behaviour on granular assembly," *Advanced Powder Technology*, **28**(8), 1972–1976, 2017, doi:10.1016/j.apt.2017.04.016.
- [76] H. Zhou, Z. Hu, J. Chen, X. Lv, N. Xie, "Calibration of DEM models for irregular particles based on experimental design method and bulk experiments," *Powder Technology*, **332**, 210–223, 2018, doi:10.1016/j.powtec.2018.03.064.
- [77] F. Ye, C. Wheeler, B. Chen, J. Hu, K. Chen, W. Chen, "Calibration and verification of DEM parameters for dynamic particle flow conditions using a backpropagation neural network," *Advanced Powder Technology*, **30**(2), 292–301, 2019, doi:10.1016/j.apt.2018.11.005.
- [78] E. Lajeunesse, A. Mangeney-Castelnau, J.P. Vilotte, "Spreading of a granular mass on a horizontal plane," *Physics of Fluids*, **16**(7), 2371–2381, 2004, doi:10.1063/1.1736611.
- [79] R. Cabisco, J.H. Finke, A. Kwade, "Calibration and interpretation of DEM parameters for simulations of cylindrical tablets with multi-sphere approach," *Powder Technology*, **327**, 232–245, 2018, doi:10.1016/j.powtec.2017.12.041.
- [80] H.T. Chou, C.F. Lee, Y.C. Chung, S.S. Hsiau, "Discrete element modelling and experimental validation for the falling process of dry granular steps," *Powder Technology*, **231**, 122–134, 2012,

doi:10.1016/j.powtec.2012.08.001.

- [81] W. Rasband, ImageJ <https://imagej.net/downloads>.
- [82] D. Höhner, S. Wirtz, V. Scherer, "A study on the influence of particle shape and shape approximation on particle mechanics in a rotating drum using the discrete element method," *Powder Technology*, **253**, 256–265, 2014, doi:10.1016/j.powtec.2013.11.023.
- [83] G.R. McDowell, O. Falagush, H.S. Yu, "A particle refinement method for simulating DEM of cone penetration testing in granular materials," *Geotechnique Letters*, **2(7–9)**, 141–147, 2012, doi:10.1680/geolett.12.00036.
- [84] N. Stoimenov, J. Ruzic, "Analysis of the particle motion during mechanical alloying using EDEM software," *IFAC-PapersOnLine*, **52(25)**, 462–466, 2019, doi:10.1016/j.ifacol.2019.12.583.
- [85] X. Li, Y. Du, L. Liu, Y. Zhang, D. Guo, "Parameter calibration of corncob based on DEM," *Advanced Powder Technology*, **33(8)**, 103699, 2022, doi:10.1016/j.appt.2022.103699.
- [86] W. Tinsson, *Plans d'expérience: constructions et analyses statistiques (Mathématiques et Applications, 67)*, 2011.
- [87] E. El Ouardia, "Étude de la calcination du phosphate clair de youssoufia (Maroc)," *Afrique Science: Revue Internationale Des Sciences et Technologie*, **4(2)**, 199–211, 2010, doi:10.4314/afsci.v4i2.61676.
- [88] N. Abdenouri, M. Hasnaoui, H. Mazouz, "Effective moisture diffusivity during the phosphate drying. modeling and experimental study," *Materials Today: Proceedings*, **51**, 2071–2079, 2022, doi:10.1016/j.matpr.2022.01.346.
- [89] D.P. Maurice Pillet, François Louvet, "Plan d'expériences " Definitive Screening Design ", une alternative crédible aux plans composites centrés ?," in *Qualita 2017*, Bourges, France, 2017.
- [90] C.C. Design, I. Variable, R. Surface, J.S. Rao, B. Kumar, "Box-Behnken Design 3D Blade root shape optimization Meta-Model Development," 2018.
- [91] E. Daems, Frédéric and Lognay, Georges and Romnee, Jean-Michel and Froidmont, "Application du plan d'expérience de Box-Behnken et de la méthodologie des surfaces de réponses pour optimiser une méthode de quantification de phyto-œstrogènes dans les fourrages," 2015.

A Self-Adaptive Routing Algorithm for Real-Time Video Transmission in VANETs

Marzouk Hassan*, Abdelmajid Badri, Aicha Sahel

Hassan II University, Electrical Engineering Department, Faculty of Science and Technology - Mohammedia City, Morocco

ARTICLE INFO

Article history:

Received: 03 July, 2022

Accepted: 16 September, 2022

Online: 10 October, 2022

Keywords:

Routing protocols

Self-adaptive

Heuristic algorithm

Video streaming

VANETs

NS2

ABSTRACT

Given the strict Quality of Experience (QoE) and Quality of Service (QoS) criteria for video transmission, such as delivery ratio, transmission delay, and mean opinion Score (MOS), video streaming is one of the hardest challenges in Vehicular Ad-Hoc Networks (VANETs). Additionally, VANET attributes, including environmental impediments, fluctuating vehicle density, and highly dynamic topology, have an impact on video streaming. Creating efficient visual communications in these networks will give drivers access to business and entertainment applications, greater support, safer navigation, and better traffic management. This work particularly investigates the mobility characteristics of autos and the causes of link failure in order to precisely anticipate the dependability of connections between vehicles and build a reliable routing service protocol to satisfy various QoS application demands. Then, a link-time duration model is suggested. Link dependability is assessed and taken into consideration when creating a new self-adaptive routing protocol for video transmission. Due to the quick changes in topology, finding and maintaining the optimum end-to-end route is quite challenging. However, the heuristic Q-Learning algorithm could continually alter the routing path via interactions with the surrounding. This study suggests an algorithm for reliable self-adaptive routing (RSAR). Through changing the heuristic function and integrating the reliability parameter, RSAR works well with VANET. The Network Simulator NS-2 is used to illustrate how well RSAR performs. According to the findings, RSAR is particularly beneficial for many VANET applications since it efficiently addresses the issues brought on by changes in topology.

1. Introduction

Vehicular Ad-hoc Networks (VANETs) are the most important element in building an intelligent transportation system and intelligent city as communication technology advances. Because VANET is a development of conventional Mobile Ad-hoc Networks MANETs, it has sparked a great deal of interest from research organizations, governments, and automakers to offer services like entertainment, consulting, information, and traffic warning; these sectors already have a lot of projects that are already started [1, 2]. According to WHO figures, 1.24 million people die globally each year as a consequence of road accidents. According to World Bank data, transportation accidents cost the global economy \$500 billion a year [3]. Solving traffic congestion has become a global issue since there are more vehicles in cities. Time delays, excessive fuel usage, and environmental pollution

can all be brought on by traffic congestion. In-car entertainment and vehicle-to-vehicle communication have also evolved into necessities that automakers now offer to customers in tandem with the social vehicle network [4]. Vehicle-to-vehicle (V2V) and vehicle-to-infrastructure (V2I) wireless communication are the two categories within VANETs (V2V). Many academics prefer V2V because communication is infrastructure-free, and its implementation is adaptable. VANET, on the other hand, differs from conventional MANETs in a few ways [5]. First, the network topology will frequently change in VANETs because of the fast movement of the network nodes (cars). The links are unreliable due to the short link times maintained between nodes, and vehicle distribution dramatically affects network performance. Second, car nodes are only allowed on roadways and are influenced by a variety of variables, including speed limits and traffic lights. Third, the energy constraints of VANET are no longer a significant problem because cars can generate sufficient power and

*Corresponding Author: Marzouk Hassan, marzouk.hsn@gmail.com

computational capability for themselves. The creation of a reliable routing protocol is now a crucial step in putting VANET applications into practice as an important support technology for the realization of an intelligent transportation system. Old-fashioned routing techniques based on VANETs, such as Dynamic Source Routing (DSR), and Ad-hoc On-demand Distance Vector (AODV) [6, 7], are challenging to apply because of the frequent topology changes and poor connectivity. Since they do not take into account quick topology changes, both the transmission delay and delivery ratio are decreased for these techniques. Recently, various routing algorithms on the basis of geographic location, such as GyTAR and TFOR [8, 9], have been published [10] to address this problem. These routing techniques employ traffic flow estimates, ignore changes in topology, use GPS to find the destination node, and do not take link dependability between nodes into account. Several trustworthy routing algorithms, including EG-RAODV and SLBF [11, 12], have been presented. These algorithms were created by including characteristics like packet error rate and network dependability between nodes. Although the time delay cannot be guaranteed, this method can increase the packet delivery ratio to some amount. Rapid velocity changes are the primary cause of topology changes and faulty links in VANETs. Good evaluation of connection dependability and effective routing algorithm designs can only result from a thorough understanding of vehicle motion characteristics. Assuming that cars are traveling along a set path, a number of variables, including the two vehicles' directions of travel, their distance from one another, their speeds, and their acceleration, can cause a link to be severed between two nodes. Given the low-density, high-speed environment, these aspects must be completely considered in evaluating connection reliability between nodes properly. When maintaining traffic safety and assessing link reliability, the space between vehicles is crucial. Many models of vehicle separation, including the log-normal distribution, the normal distribution model, and the exponential distribution model, have been put forth. In [13], the authors used tests to demonstrate that when the distance between vehicles follows a log-normal distribution, it may be more in line with the way traffic really moves and with safe separations. Effective evaluation of link dependability between nodes requires a thorough grasp of the moving characteristics of moving objects and the traffic flow model. Routing algorithms have been the subject of continuing research, and VANETs have used several efficient algorithms [14] and have outperformed conventional routing algorithms. Q-Learning [15] is a self-learning algorithm that may continuously interact with its surroundings to find the shortest route from a source node to a destination node. This research improves upon the Q-Learning method and suggests a new technique for adaptive routing that is both efficient and trustworthy. It may adaptively modify the Q-table while guaranteeing the dependability of each hop connection, allowing it to conform to changing network architecture like that of a VANET. This paper's major goal is to provide a trustworthy and flexible routing algorithm. The links between each hop determine how reliable a link as a whole is. By carefully examining the motion characteristics of cars, this work creates a trustworthy model of a link between nodes. Once the probability of link dependability has been determined, the Q-Learning algorithm can use it as a parameter to create the RSAR algorithm.

In the first section, the routing method is categorized and then partially explored in the second section. In the third part, we discuss how to create an accurate model for evaluating reliable links. The fourth and fifth section consecutively addresses The RSAR algorithm's fundamental idea and the simulations and analysis that were done. A summary and recommendations for further work are given in the sixth and last sections.

2. Proposed solution

2.1. Q-learning algorithm in VANETs

Standard Q-Learning is an agent-based heuristic learning technique. The three-tuple R, S, and A make up the majority of the learning process for the agent in the widely used Q-Learning algorithm. Where R denotes the instant reward for an action, $A = \{a_1, a_2, \dots, a_n\}$ the activity space, and $S = \{S_1, S_2, \dots, S_n\}$ denotes the state space. The larger the reward gained for the action, the nearer the agent is to the target. The learning process will be thoroughly explained in the following subsections once a few related definitions are presented.

2.1.1. Definitions

- Fundamental elements.

The whole VANET environment is used by the agent as its learning environment.

Learning Agent: Each node of the vehicle functions as its own independent learning agent;

State space (S): All nodes other than this agent make up the state space of a specific agent;

Activity space (A): An activity is the transmission of a beacon packet between two vehicles;

Immediate Reward (R): The instant reward that is given to an agent once they have successfully completed an activity.

- Value of a reward

The instantaneous reward, which has a range of [0,1] and is the reward received by an agent after performing an action, is defined in Definition 1. The reward value for the destination node is 1, as it can directly contact the destination node. Formula (1) specifies the beginning value R of the whole network as follows:

$$R = \begin{cases} 1 & s \in N_d \\ 0 & \text{else} \end{cases} \quad (1)$$

N_d Stands for the set of destination node D's one-hop neighbor's node; the reward value of an action is 1. The Q-value $Q(s, a) (s \in S, a \in A)$, which is in the range [0,1], stands for the potential reward value that is earned while moving from one learning stage.

Q-table definition: Every learner maintains a two-dimensional table with the Q-values of the nodes it can reach and its immediate neighbors. The Q-table is a two-dimensional table (see Table 1).

Table 1: Q-table

	D1	D2	...
N1	Q(D1,N1)	Q(D2,N1)	...
N2	Q(D1,N2)	Q(D2,N2)	...
...

The IDs of every potential destination node are written as D_i in the first line of the Q-table. The one-hop neighbor nodes' IDs, denoted as N_i , are listed in the first column. The value of N_i . $Q(D_1, N_1)$ represents the Q-value between the sending node and its neighbor N1 at the receiving node D_1 . As can be seen in Table 1, the size of the Q-table is dependent on both the number of destination nodes and the number of neighbor nodes. One can see that it can be climbed with relative ease.

Beacon packets are periodically exchanged between nodes to update the values in the Q-table. Each node receives a share of the learning task, which causes the algorithm to swiftly find the best path and allows for prompt adaptation to network topology changes.

2.1.2. Learning process

The aforementioned definitions established each vehicle node as a learning agent. An individual Q-table is associated with each vehicle node, in contrast to conventional learning methods. Nodes complete their learning process by sharing beacon data and updating their Q-tables.

Along with its own speed, position, and other information, each node additionally includes the maximum Q-value of the nearby nodes to the destination node, or the greatest value in a column, in the beacon packet it transmits (as shown in Table 2). Given a VANET topology, $= \{V, E\}$, as shown in Figure 2, we assume that the state space of node A is the series of all nodes that don't include A. The collection of vehicle nodes is represented by $V = \{A, B, C, \dots, H\}$. The set E of edges characterizes a collection of connected nodes that may exchange messages with each other with a single additional hop. As depicted in Figure 3, let's pretend that from node A, we go to node G as the endpoint. The goal now is to use a self-learning algorithm to determine the best route from node A to G, where A is the starting point.

Each vehicle node agent is given learning tasks, and as part of the learning process, the agent's Q-table and the state activity Q-values, $Q(s, a)(s \in S, a \in A)$, are primarily updated.

Table 2: Network parameter settings

Parameter	Value
Size of topology (m*m)	3511m*3009m
Video file frame size	30 fps
Image Resolution	352 * 288
CBR packet size (bytes)	512
Simulation time (s)	300
Propagation model	Two-ray ground

Transmission range (m)	250
MAC standard	IEEE 802.11 MAC (2 Mbps)

Eq. (2) contains the usual Q-Learning function:

$$Q_s(d, x) \leftarrow Q_s(d, x) + \{R + \gamma \cdot \max_{y \in N_x} Q_x(d, y)\} \quad (2)$$

R is the reward value, D represents the destination node, N_x is x^s 's neighbor node, x is its neighbor node, S is the node to go from node x to node D, the maximum Q-value between x and its neighbor is $\max_{y \in N_x} Q_x(d, y)$.

The reward a node gets for completing an action in accordance with Eq is impacted by the discount factor γ , making it a significant parameter (2). Since link stability is an essential factor, we used the between-node link reliability $r(l)$, calculated using Eq. (15) as a discount factor; thus, $r = r. (l)$. The pace of packet transmission in VANETs is a critical metric that depends on the available bandwidth.

The definition of the bandwidth BW is as follows:

$$BW(bps) = \frac{n \times S_B \times 8}{T} \quad (3)$$

where S_B is the packet size in bytes, T is the time interval, and packets sent and received by the node are denoted as n. With the assumption that the node's maximum bandwidth, denoted by \max_{BW} , is a constant Here's how you can figure out your bandwidth:

$$BF = \frac{\max_{BW} - BW}{\max_{BW}} \quad (4)$$

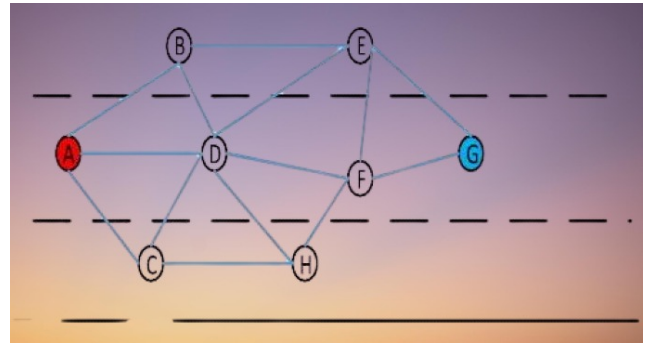


Figure 1: Learning process

Each vehicle node's learning progress is determined by the bandwidth factor. It fluctuates as the element that affects learning speed, depending on variations in effective bandwidth. A new heuristic function can be produced by changing equation (2):

$$Q_s(d, x) \leftarrow (1 - BF) \cdot Q_s(d, x) + BF \cdot \{R + \gamma \cdot \max_{y \in N_x} Q_x(d, y)\} \quad (5)$$

According to Eq. (5), as the hops number rises, the reward value drops. The final reward value depends on the bandwidth, the dependability of the network, and the number of hops. In a dynamic network, By combining bandwidth and connection state,

the most efficient path may be determined between the source and the destination node. The destination node G's one-hop neighbors in Figure 1 are nodes F and E. According to Eq (5), $Q_E(G, G)$ and $Q_F(G, G)$ are the appropriate representations for the reward values from nodes E & F to the destination node G.

It is possible to determine that the ultimate Q-values of $Q_E(G, G)$ and $Q_F(G, G)$ are 0.7 and 0.8, respectively, after accounting for the impacts of bandwidth and link quality. A, B, C, E, F, and H are D's nearby nodes. When node D receives a beacon packet from any neighbor, it processes the packets and extracts the maximum Q-value to node G by using $F, \max_{y \in N_F} Q_F(G, Y)$. Calculate the relevant Q-value, or $Q_D(G, F)$ In accordance with Eq. (5) and update the Q-table.

Being the largest, $Q_F(G, G)$ will have a value of 1 within the beacon packet. Data packets from other nodes will go through the same processes, after which a selected column in the Q-table will be updated. As shown in Figure 2, the remaining neighbor nodes' Q-tables are changed such that $Q_D(G, F) = 0.5$ in compliance with Eq (5). The maximum Q-value between node D and its neighbors is updated in real-time by node D's Q-table as neighbor data packets are constantly received. In a similar vein, when node D transmits a beacon packet, it looks for the maximum Q-value among itself and its neighbors in a certain column of the Q-table. As soon as node A receives the beacon packet from node D, it will send the highest possible Q-value and continue the calculation to update QA. The same procedure is employed when additional nodes send in beacon packets. The outcomes depicted in Figure 4 will ultimately be attained by continuous data packet exchange [16,17].

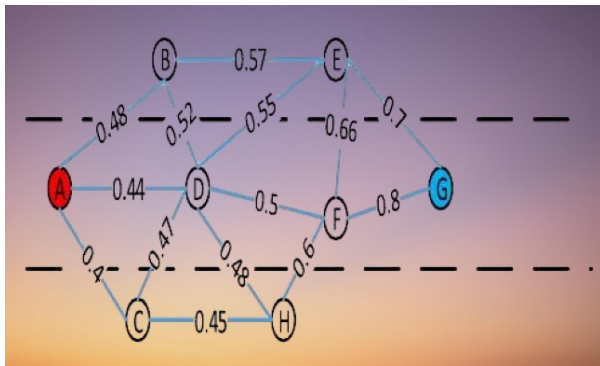


Figure 2: Q-values to the destination node G saved by each node

The best route from A to G may be easily identified, as shown in Figure 2. The best route is the one with the highest Q-value of its nodes. As seen in Figure 4, the best path is ABEG since it has the highest Q-value. The dynamic update-and-save of the Q-table allows the method to quickly, consistently, and robustly react to topology changes.

2.2. The proposed RSAR algorithm

2.2.1. Transmission process

The three actions listed below are carried out by the RSAR algorithm when it routes data packets:

Step 1. Node A checks its internal Q-table before sending a data packet to Node B to see whether Node A is the next hop for Node B. If not, it begins the route development process, which is covered in the next subsection; when this is the case, it picks the node nearest to it that has the greatest Q-value.

Step 2. At the point when the route has been constructed, the fundamental path from the starting node to the ending node has been determined, and the necessary vehicle nodes have been learned. We initiate the route maintenance operation to dynamically keep the end-to-end connection up and running, which is necessary for finding the best path across the whole network topology and resolving the segmentation problem. The next subsection details the route maintenance procedure.

Step 3. The aforementioned procedures establish the best route for the overall network topology. A vehicle node will carry out the first step if it receives or sends data packets; If not, it will proceed to step 2.

2.2.2. Route development and Maintenance Process

Before sending data, a node checks its internal Q-table to determine whether there is a next-hop node between it and the destination. The data packet is sent to the neighboring node with the highest Q-value relative to the target node. If there isn't one, route discovery is initiated. A path request timer is started at the source node, which subsequently sends out a R_req packet to the entire network. Within the R_req data packet, the source node keeps a record of the IDs of all of the nodes that the data packet traveled through while it was being routed across the network. The R_rep packet is saved by the destination node once it has received it for the first time from the source node. Subsequent R_rep packets received by the destination node are deleted. After extracting the ID information that it recorded from the R_rep data packet and flipping it, the node at the end of the route creates a data packet labeled R_req and stores the reversed path information there. Finally, the R_req data packet is discarded. After waiting for an open time window, it sends the R_req data packet via the recorded reverse route. Upon receipt, a node that has been previously recorded will make the necessary adjustments to the data packet's next hop address, refresh its Q-table, and then broadcast the packet using a single hop. When the packet is received by other nodes that are not the destination, those nodes will just alter their Q-tables and then discard the packet. The source node will suspend the request timer as it works on updating its Q-table while waiting for R_rep to be transmitted to the destination node, it also serves as the R_req source node. At this step, a route from the source to the destination node has been identified, and the Q-tables of the nodes on the first path are modified; their starting values are 0.

The values of the Q-tables of some of the nodes that are adjacent to the initial route path are also updated when that path is constructed. It is essential to get the process of route maintenance going as soon as possible in order to guarantee that the path will continue to be useful despite the dynamic changes in the network [18,19]. The maintenance of the Q-tables in a dynamic manner and the resolution of the issue of network segmentation are the primary goals of the process of route maintenance. Each node will, at regular intervals, broadcast

beacon packets in order to keep the Q-tables of its neighboring nodes up to date. The beacon data packet will primarily provide the node's position, speed, and maximum Q-to-Value ratio. max(Q - Value) was discussed in conjunction with the method of education. In the experiment, the beacon packet's transmission delay was set to a random value between [0.5, 1], which was done to guarantee that the update would be effective. For the sake of the Q-table, the actual time at the destination node has been supplied. When a destination node's time hasn't been changed for more than the specified length of time, the data column associated with it is deleted, and the destination node is deemed invalid. In the event of a network split due to a moving vehicle, RSAR initiates the route request timer and makes use of the store-and-forward method to ensure that an R-req data packet is transmitted. In the event that the sending node sometimes doesn't receive the R-rep data packet from the receiving node before the timeout expires, the receiving node is considered inaccessible, and the transmission is aborted. Failure to do so will result in the routing route being restored at the point of disruption.

3. Experimental tests

3.1. System Model

As stated in [20, 21], it is reasonable to assume that the highway is often a straight road and that the broadcasting distance is much greater than the width of the road, both of which are necessary for an accurate evaluation of the connection quality between nodes. The road's width may also be assumed to have negligible effects on forwarding node selection at the following hop and, therefore, may be disregarded. This is essential in order to accurately gauge the quality of inter-node connections. As shown in Figure 3, the simulated highway was created using the above methods.

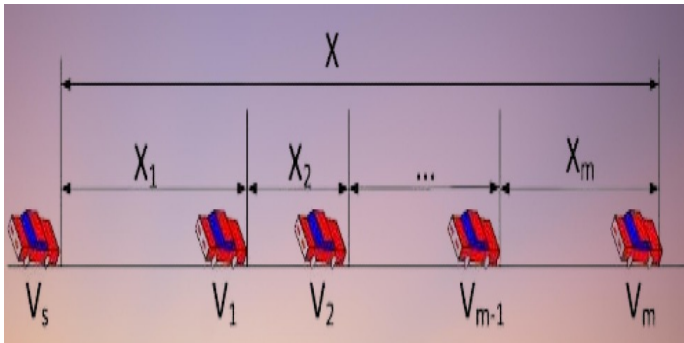


Figure 3: Road model

It is also reasonable to presume that other maneuvers, like speeding up and slowing down, switching lanes, passing other vehicles, and so on, are taking place on the roads. In addition, the distance that separates cars follows a log-normal distribution [22, 23], which can be written as $X_i \in \log N(\mu_i, \delta_i)$. A random variable with a log-normal distribution is depicted in Figure 1 as $X_i = \{X_i(m), m = 0, 1, 2, \dots\}$, where m can take the values 0, 1, or 2. X_i denotes the distance between vehicles i and $i + 1$ and $X_i(m)$ denotes a random variable at moment m, representing the distance between node I and its related nodes. If the node V_s in Figure 1 is considered to be the reference node, then the value X reflects the distance between V_s and any other node. Since X

denotes the distance between other nodes and V_s , and $X = \sum_{i=1}^m X_i$ is also log-normally distributed.

Proposition 1: Let's assume that $X \in \log N(\mu, \delta)$ and that the variable $T = \sqrt{aX + b} + c$ is log-normally distributed, where $a, b, c \in R, a, b, c \neq 0$, and $aX + b \geq 0$.

If the probability distribution function of the t is G_T . Then, for each positive t, $G_T(t) = \Pr \{T \leq t\}$. Apparently, as T is continuous,

$$\begin{aligned}
 G_T(t) &= \Pr \{T \leq t\} \\
 &= \Pr \{\sqrt{aX + b} + c \leq t\} \\
 &= \Pr \{aX \leq (t - c)^2 - b\} \\
 &= \begin{cases} F_X\left(\frac{(t-c)^2 - b}{a}\right) & \text{when } a < 0 \\ 1 - F_X\left(\frac{(t-c)^2 - b}{a}\right) & \text{when } a > 0 \end{cases} \quad (6)
 \end{aligned}$$

F_X is the probability distribution function of X. When $a > 0$, it is evident that T follows a log-normal distribution. When $a < 0$, according to [13], $F(z) = \frac{1}{2} + \frac{1}{2} \operatorname{erf}\left(\frac{z - \mu_z}{\sigma_z \sqrt{2}}\right)$ And letting $z = ((t - c)^2 - b/a)$

$$\begin{aligned}
 1 - F_X(z) &= \frac{1}{2} - \frac{1}{2} \operatorname{erf}\left(\frac{\ln z - \mu(X)}{\sigma(X)\sqrt{2}}\right) \\
 &= F_Y\left(\frac{a}{(t-c)^2 - b}\right) \quad (7)
 \end{aligned}$$

Y is a log-normal random variable with parameters $-\mu(X)$ and $\sigma(X)$. Since the fact $-\operatorname{erf}(x) = \operatorname{erf}(-x)$ is used. Consequently, T conforms to a log-normal distribution, concluding the proof.

The direction of motion is indicated by the black arrows in Figure 2, where two cars are shown in "a" going in the same direction, whereas two vehicles are depicted in "b" moving in the opposite way.

Proposition 2: Assuming that $X \in \log N(\mu, \sigma)$, $T = aX + b$ is log-normally distributed, where $a, b, c \in R$ and $a, b, c \neq 0$. (The reasons offered in the proof of 1 may be used to simply demonstrate this)

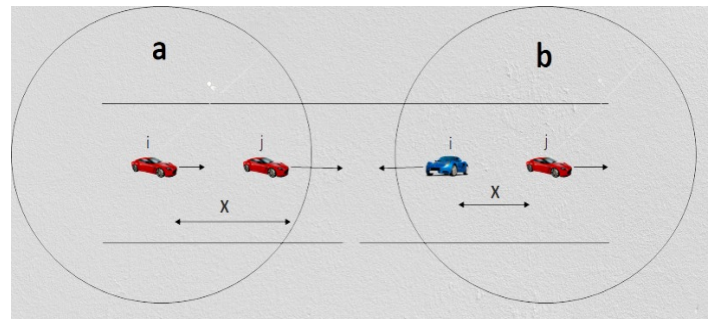


Figure 4: Two cases of link breakage

There are two basic circumstances (shown in Figure 4) in which the connection between two nodes breaks if we assume that the cars are traveling along a fixed route. Both of the vehicles depicted in Figure 4a are moving in the same direction, whereas

both of the vehicles depicted in Figure 4b are progressing in opposing directions. Think of vehicle i as the transfer point and vehicle j as the reference point in this scenario. Under normal circumstances, the longest communication durations between vehicles occur between i and j. The next thing that needs to be done is a comprehensive analysis of the link duration for these two different scenarios.

At time $t_0 = 0$, if the car i is in front of car j, then car i can communicate with car j with just one-hop. This is demonstrated in Figure 4a.

A random variable will be used to determine the initial distance between vehicle X. There is not going to be any change in the maximum communication radius of vehicle R. X fulfills these conditions at the outset:

$$0 \leq X < R \tag{8}$$

On a highway, there will reportedly be instances of accelerating, decelerating, and passing other vehicles in accordance with the system model. On this stretch of road, the maximum speed limit is v_m , which means that all vehicles must travel at a speed that is either lower than or equal to v_m . Consider the fact that the vehicle is moving at a speed of $v(0)$ and that its acceleration is $a(0)$.

When time is less than zero, the acceleration is denoted by the symbol $a(t)$, and the speed is denoted by the $v(t)$. The acceleration, as measured at time t, is calculated as follows:

$$\begin{aligned} 1 \quad & \text{If } a(0) = 0, \text{ for all } t \geq 0, \\ & a(t) = 0. \end{aligned} \tag{9}$$

$$\begin{aligned} 2 \quad & \text{If } a(0) > 0 \\ & a(t) = \begin{cases} a(0) & t \leq \frac{v_m - v(0)}{a(0)} \\ 0 & \text{otherwise} \end{cases} \end{aligned} \tag{10}$$

$$\begin{aligned} 3 \quad & \text{If } a(0) < 0 \\ & a(t) = \begin{cases} a(0) & t \leq \frac{-v(0)}{a(0)} \\ 0 & \text{otherwise} \end{cases} \end{aligned} \tag{11}$$

Based on the analysis presented above, it is reasonable to conclude that when $t_0 = 0$, assuming that the current acceleration $a(0)$ is zero, the instantaneous acceleration would be 0 as well, which is denoted by the equation $a(t) = 0$. If the speed is less than (0) the maximum speed limit, the acceleration is presumed to be $a(0)$; if the speed is more than the maximum speed limit, the acceleration is set to 0. If the speed is above the maximum speed limit, it is changed to 0. Taking into consideration the speed at the beginning, $v(0)$, the instantaneous speed, $v(t)$, can be defined by the following formula at time t:

$$v(t) = v(0) + \int_0^t a(u)du \tag{12}$$

where $u \in [0, t]$, $a(u)$ is the acceleration at time u .

The instantaneous speed may now be calculated by combining Eqs. (6-9):

$$\begin{aligned} 1 \quad & \text{If } a(0) = 0, \text{ for all } t \geq 0, \\ v(t) &= v(0) \\ 2 \quad & \text{If } a(0) > 0 \\ v(t) &= \begin{cases} v(0) + a(0)t & t \leq \frac{v_m - v(0)}{a(0)} \\ v_m & \text{else} \end{cases} \end{aligned} \tag{13}$$

$$\begin{aligned} 3 \quad & \text{If } a(0) < 0 \\ v(t) &= \begin{cases} v(0) + a(0)t & t \leq \frac{-v(0)}{a(0)} \\ v_m & \text{else} \end{cases} \end{aligned} \tag{14}$$

The following formula can be used to calculate the distance traveled by any vehicle traveling at a speed of $v(x)$ during the interval of time represented by $[0, t]$:

$$S(t) = \int_0^t v(x)dx \tag{15}$$

Again, in accordance with the definition presented above, it is possible to determine the gap in space that exists between vehicles i and j at a particular instant in time, as shown in Figure 4.

If we assume that the initial acceleration and speed of i and j vehicles are, respectively $a_i(0), v_i(0), a_j(0)$, and $v_j(0)$, then the instantaneous acceleration and speed of vehicles i and j at time t are, respectively $a_i(t), v_i(t), a_j(t)$, and $v_j(t)$. The following equation can be used to determine the distance between the cars I and j at the time $[0, t]$ if Eqs. 9–15 is followed to their logical conclusions:

$$S_i(t) = \int_0^t v_i(x)dx \tag{16}$$

$$S_j(t) = \int_0^t v_j(x)dx \tag{17}$$

If the distance between vehicles i and j at the beginning of the race is X, the distance $d_{i,j}$ between those two vehicles at the end of the race is:

$$d_{i,j} = \begin{cases} S_j(t) + S_i(t) + X & \text{same direction} \\ S_j(t) - S_i(t) + X & \text{opposite direction} \end{cases} \tag{18}$$

The conclusion that the link is severed can be drawn from Equation 13, which states that when $d_{i,j} > R$, the connection is severed. The following thing that needs to be done is an analysis of the link duration in Figure 2b. This demonstrates how two automobiles meet while traveling in different directions:

$$S_j(t) + S_i(t) + X = R \tag{19}$$

Now it is possible to determine the maximum link duration t. We can calculate the maximum link duration t as follows using

the assumption that $S_j(t) + S_i(t) = \frac{1}{2}a_r t^2 + v_r t$, where $a_r = a_i + a_j$ and $v_r = v_i + v_j$.

$$t = \frac{-v_r + \sqrt{v_r^2 + 2a_r(R-X)}}{a_r} \quad (20)$$

If two vehicles are going in the same direction, as shown in Figure 2a, determine which one is in front by overtaking, decelerating, and accelerating. Vehicle j is in front of vehicle i when $S_j(t) - S_i(t) + X > 0$; conversely, vehicle i precedes vehicle j. A symbolic function was defined as follows to efficiently convey which car is in front:

$$I(i, j) = \begin{cases} 1 & S_j(t) - S_i(t) + X > 0 \\ -1 & \text{otherwise} \end{cases} \quad (21)$$

When the connection is critically disconnected:

$$S_j(t) - S_i(t) + X = R \cdot I(i, j) \quad (22)$$

To compute the link duration at this time, two cases must be taken into account.

When $I(i, j) = 1$, vehicle j is in front of vehicle i. From Eq. (20), $S_j(t) - S_i(t) + X = R$. Similarly, to Eq. (20), because $S_j(t) - S_i(t) = \frac{1}{2}a_r t^2 + v_r t$, where $a_r = a_j - a_i$ and $v_r = v_j - v_i$ The time t can be determined as:

$$t = \frac{-v_r + \sqrt{v_r^2 + 2a_r(R-X)}}{a_r} \quad (23)$$

The position of vehicle i in relation to vehicle j is the same when $I(i, j) = -1$. $S_j(t) - S_i(t) + X = R$, and the link duration t may be calculated from Eq. (1) as follows:

$$t = \frac{-v_r - \sqrt{v_r^2 - 2a_r(R+X)}}{a_r} \quad (24)$$

To calculate the link duration between two nodes within a one-hop range: the transmitting node and the other nodes utilize equations (20), (23), and (24).

Proposition 3: If vehicle i and j's communication link fails at time t , the remaining link duration is a linear or square root function of X .

Proof: It is known that, at a constant speed v_i , $S_i(t) = \int_0^t v_i(x) dx$ is a linear function of t , i.e., $v_i = v_m$, based on the definition of $S_i(t)$ according to Eq. (15), which happens after the connection is lost at time t . $S_i(t) = at + b$. Similarly, it may be inferred that $S_j(t) = ct + d$ is a linear function of t if v_j is a constant. Eq. (23) clearly states that $(a + c)t + b + d + X = R$ when the two cars are moving in different directions. The linear function for the link duration time is $t = \frac{R-b-d-X}{a+c}$. Once a connection is made between two co-directional vehicles i and j, the link duration is also a linear function, as shown by the equation $(c - a)t - b + d + X = R \cdot I(i, j)$. As a result, when v_i and v_j are both constants, and the link duration t is a linear function. A

quadratic polynomial will represent the distance function if either $v_i(t)$ or $v_j(t)$ are not constants. Allow $v_i(t) = v_i(0) + a_i t$ without losing generality. The distance function is, by definition:

$$\begin{aligned} S_i(t) &= \int_0^t v_i(0) + a_i \\ &= v_i(0)t + \frac{1}{2}a_i t^2 \end{aligned} \quad (25)$$

Eqs. (14) and (22) demonstrate that $S_j(t) \pm S_i(t) = \frac{1}{2}a_r t^2 + v_r t$. Consequently, the answer is a square root function of X .

First Theorem Vehicles i and j's link's duration T have a log-normal distribution.

Proof According to Proposition 3, the connection duration can be written as $aX + b$ or $\sqrt{aX + b} + c$. The expression $\sqrt{aX + b} + c$ is log-normally distributed according to Proposition 1. $aX + b$ is distributed log-normally according to Proposition 2. As a result, the link's duration always follows a log-normal distribution. The theorem's proof is now complete.

The link duration of the cars i and j is log-normally distributed as $T \in \log N(\mu_t, \sigma_t)$, where the variance is σ_t and expected is μ_t Based on the link duration between the nodes. The duration of the link may then be used to assess its dependability. The likelihood of two vehicles directly communicating throughout the time period T_p . is known as link reliability. When $t = t_0$ The connection dependability between nodes is, supposing that any two vehicle nodes have a communication link (l):

$$r(l) = P\{t_0 + T_p \mid t_0 \in M\} \quad (26)$$

where M is the time at which the two vehicles' connection began. The link dependability is as a result:

$$r_t(l) = \begin{cases} \int_{t_0}^{t_0+T_p} f(T) dT & T_p > 0 \\ 0 & \text{else} \end{cases} \quad (27)$$

where the probability function for the time period T is expressed by $f(T)$.

3.2. Simulation setup

As seen in Figure 5, the experiment was simulated using NS-2 and a 3511m*3009m square topology using a real-life map of "Anfa District in Casablanca." The topology included intersections and straight roads, each of which had been built up with two-way lanes. To add authenticity to the simulation, each vehicle node in the network employed an intelligent driving model (IDM) that featured waiting, avoiding, overtaking, and lane switching.

The default NS-2 parameter settings are shown in Table 2. we have used a CIF (H.261) video file format with a 352 x 288. UDP was utilized for transmission following the work approach shown in Figure6.

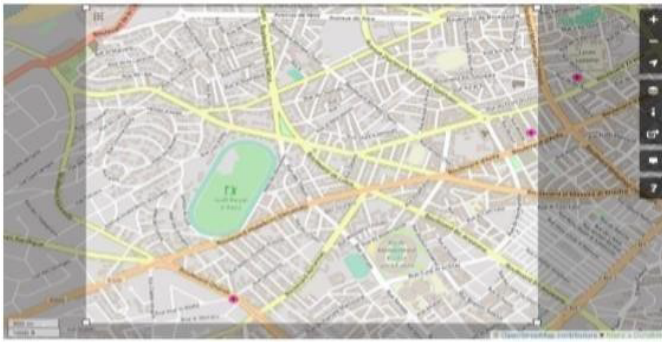


Figure 5: Anfa District Casablanca “OpenStreetMap”

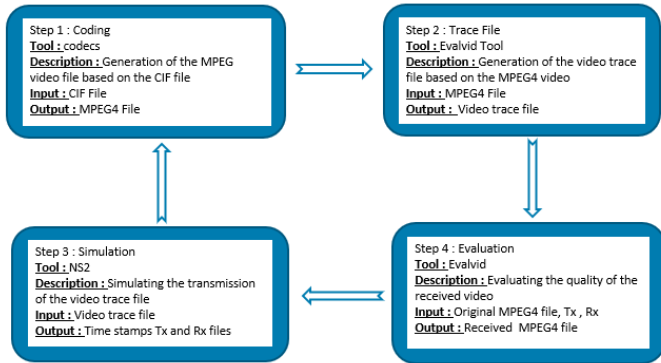


Figure 6: Work approach

In contrast with the Enhanced Distributed Channel Access (EDCA) defined in the 802.11p standard, the video transmission was carried out using an Enhanced Dynamic Cross-layer mechanism for real-time HEVC streaming. This method has proven to deliver improved performance in video quality at reception and end-to-end latency. QoS and QoE calculations have been in use for the verification of the effectiveness of the cross-layer mechanism shown in Figure7 in a separate paper.

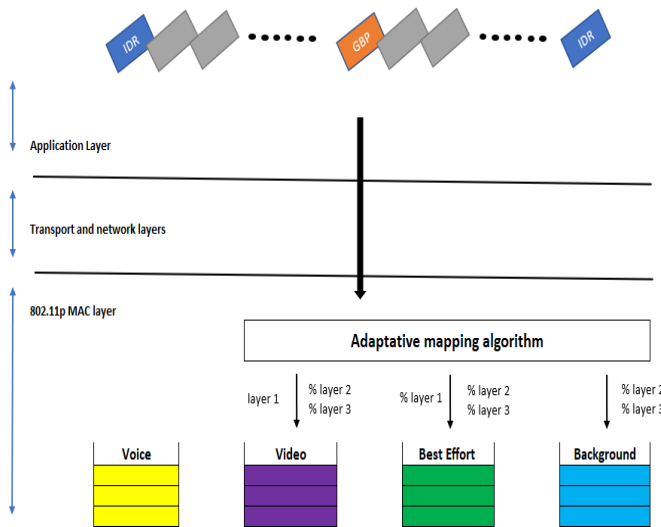


Figure 7: Illustration of the Adaptive mapping algorithm.

Each beacon packet’s size was determined based on the data that was transmitted. Two scenarios that simulated the scenario in Figure 5 were put up to successfully assess the RSAR algorithm’s

performance. The first scenario used a network with 80 nodes and vehicle peak speeds between 30 and 90 kilometers per hour. In this case, we will focus on how the speed of the vehicle impacts the routing protocol and provide an explanation. The alternative scenario went as follows: the cars’ top speed was fixed at 40 km/h, and there was anything between 60 and 120 nodes. The discussion in this instance will center on how vehicle density affects the routing protocol. The nodes were first scattered at random along several roadways and followed a predetermined path.

Each simulation was repeated 20 times with an average value of 300 s between each run. The simulation data were then assembled.

3.3. Simulation results

The QLAODV algorithm, the SLBF algorithm, the GPSR algorithm [11, 14, 17], and the techniques described in [22] were contrasted with the RSAR algorithm suggested in this study. All of these algorithms are examples of routing algorithms. It is feasible to assess the benefits and drawbacks of RSAR thanks to this comparison. The results illustrated in Figs. 8, 9, 10, 11, 12, 13, and 14 were acquired by comparing end-to-end delays; the packet delivery ratios hop number in various scenarios. Figures 8, 9, and 10 show the comparisons of the first test, while figures 11, 12, and 13 show the comparisons in the second test case.

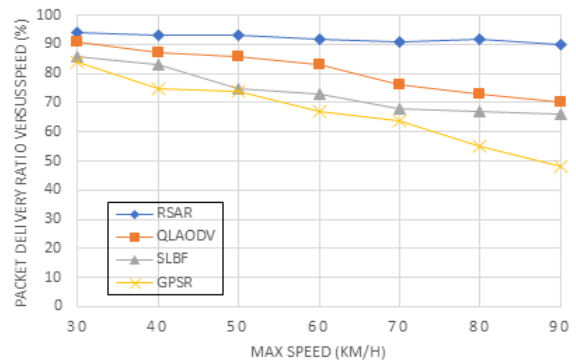


Figure 8: Packet delivery ratio on different speeds

Figure 8 shows that there is a direct association between the speed and packet delivery ratio. A node’s packet delivery ratio is calculated by data packets supplied by that node by the data packets received by the destination node. Figure 8 demonstrates that the RSAR suggested in this paper was able to achieve a consistent and high packet delivery ratio of video data; as speed increased, the average ratio up surged to more than 90%. With increasing speeds, the packet delivery ratios of the other three investigated routing methods dropped dramatically. This enhancement was made possible thanks to RSAR’s careful consideration of how to speed variations affect link reliability. The Q-Learning method uses this information as a learning parameter to make routing decisions by analyzing the links between nodes and determining the dependability of those links. Due to its greedy approach and lack of consideration for connection reliability, while choosing the next hop node, GPSR’s packet delivery ratio decreased quickly. Until the speed reached 54 kilometers per hour, QLAODV’s packet delivery ratio was over 90%, but it rapidly dropped after the speed was exceeded. QLAODV, although using the Q-Learning paradigm, must

constantly repair the route with increasing velocity to provide an always-reliable path from beginning to finish. As a result, the proportion is reduced. Due to its sensitivity to topology changes, SLBF's packet delivery ratio decreased and does not take connection stability into full account. It was more similar to the GSPR algorithm because it used a greedy approach.

Figure 9 shows the connection between speed and end-to-end time delay; In this case, the time delay is measured as the typical amount of time it takes for the receiving node to receive a valid data packet. Figure 9 shows that when the vehicle nodes' speed rose, all four techniques' time delays showed a growing trend. The RSAR algorithm suggested in this paper had a rather constant time delay that fell between SLBF and GSPR. When the maximum speed was greater than 60 km/h, the time delay of SLBF quickly grew and surpassed that of RSAR. The effects of topology modifications and the requirement for a new computation of the re-transmission method or effective forwarding area were the main causes of this trend. While topological modifications have less effect on RSAR, this method ensures that the route with the best Q-value has the most available bandwidth, the least unreliable connection, and the shortest routing distance. Because GSPR solely employs the greedy forwarding method, its time delay was the shortest. The GSPR had the lowest packet delivery ratio since it exclusively employs the greedy mechanism, dropping packets as soon as they don't arrive. Although QLAODV also employs the Q-Learning model, its increased speed requires frequent path switching in order to maintain an efficient routing path.

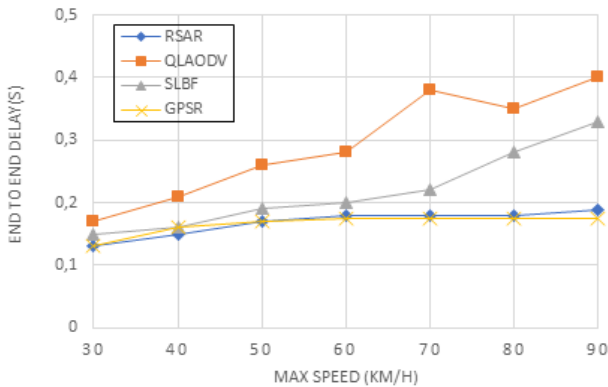


Figure 9: End-to-end delay on different speeds

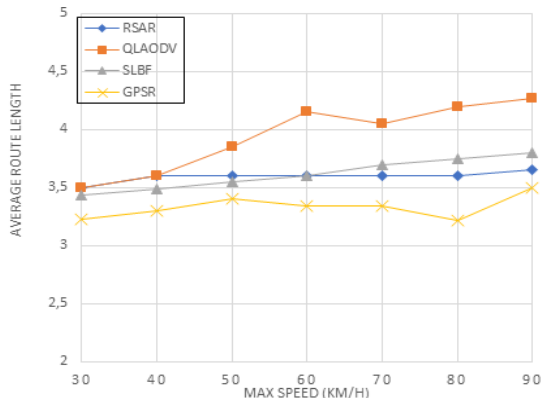


Figure 10: Routing length on different speeds

This resulted in a significant lengthening of the packet delivery time. According to Figure 9, in the context of a topology that was rapidly changing, the RSAR packet delivery ratio ranged from 0.1 to 0.2.

Figure 10 shows the relationship between speed and route length using the average number of hops required by valid data packets to reach their destination. Rather than relying on a route transformation mechanism to ensure that the whole path is maintained, this approach employs a simple forwarding decision to determine which node has the greatest Q-value; as shown in Figure 10, RSAR's route length was less than that of QLAODV. The RSAR suggested in this paper has a consistent route length, as seen in Figure 10. The maximum Q-value and store-and-forward selection mechanisms make this feasible by always using the shortest route possible. Both GSPR and SLBF use a greedy packet forwarding strategy, however when the speed increases over 60 km/h and topological changes become more pronounced, SLBF's route length increases; despite the fact that GSPR employs no trustworthy technique, the lowest number of hops was reached.

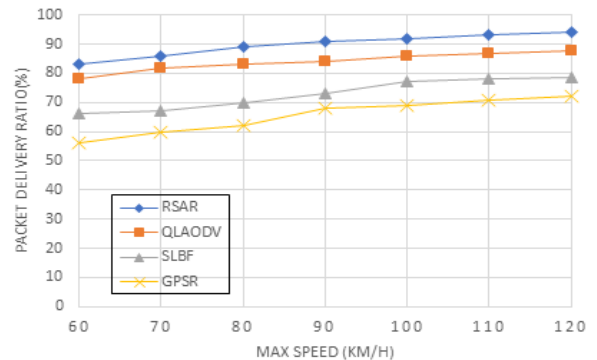


Figure 11: Packet delivery ratio by number of nodes

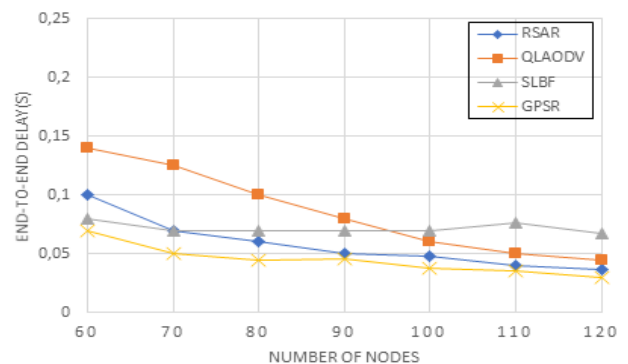


Figure 12: End to end by the number of nodes

The relationship between packet delivery ratios and the number of nodes is seen in Figure 11. Overall, the packet delivery ratio improves with increasing network size across all four approaches as the number of nodes increases. Over 90% packet delivery ratio is achieved in RSAR with 90 nodes, while the packet delivery ratio for QLAODV is 85%. RSAR fully takes into account connection stability between nodes despite the fact that both of these algorithms are based on the Q-Learning concept,

which results in a significantly higher packet delivery ratio. The store-and-forward mechanism makes RSAR's packet delivery ratio superior to that of GPSR and SLBF in the presence of a growing number of nodes. As SLBF employs the retransmission technique, it has a higher packet delivery ratio than GPSR, but because topology has a significant impact because the sending node and vehicle are frequently on different paths, it has a lower packet delivery ratio than RSAR.

Figure 12 describes the link between the end-to-end time delay and the number of nodes. The RSAR's end-to-end latency is quickly catching up to the GPSR's. This is because when nodes are added, RSAR learning nodes are also created, reducing the time delay and shortening the route to the target node. The time delay of QLAODV eventually approaches that of RSAR as the number of nodes rises, but with fewer nodes, it is significantly bigger than that of RSAR. As QLAODV spends so much time maintaining the routes, this behavior arises. Because it employs a scheduled broadcast technique that causes an increase in time delay, SLBF drops slowly with an increase in the number of nodes. As the number of nodes rises, the time delay for each of the four algorithms decreases.

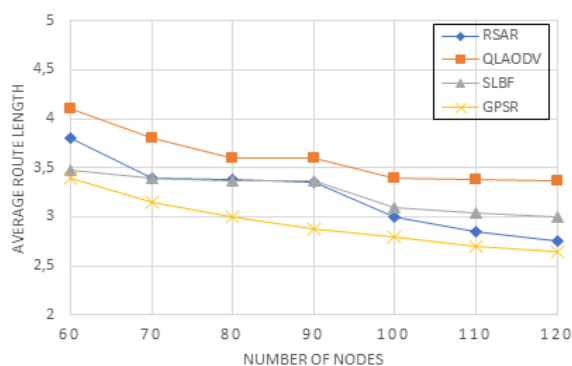


Figure 13: Routing length versus the number of nodes

Figure 13 shows the association between the number of nodes and the average route length. The average route length of all four techniques decreases as the number of nodes rises. The primary reason for this is an increase in the number of effective forwarding nodes. RSAR's route discovery is shorter than QLAODV's path discovery. As GPSR and SLBF both employ a greedy strategy, the path lengths of GPSR, SLBF, and RSAR are near to one another. RSAR chooses the next hop that is closest to the furthest node as the number of nodes increases.

3.4. Summary and discussion

As seen in the previous section, the simulation was based on the two factors that affect the most quality of video transmission those are Speed and the number of nodes.

When speed increases, we have determined that in terms of packet delivery ratio, RSAR was able to achieve a high and consistent packet delivery ratio of video data, with an average ratio of more than 90%, as speed increased. In terms of end-to-end delay, the RSAR algorithm had a rather constant time delay that fell between GSPR and SLBF. In terms of route length, RSAR's route length was less than that of QLAODV, thanks to

the maximum Q-value selection and store-and-forward mechanisms.

In terms of packet delivery ratio, we have concluded that when the number of nodes increases, RSAR kept a ratio above 90%, while the packet delivery ratio for QLAODV was around 85%. In terms of end-to-end delay, The RSAR steadily approaches the GPSRs thanks to the fact that when nodes are added, RSAR's learning nodes are added as well, making the path to the time delay and destination node shorter. Each of the four approaches has a reduced average route length as the number of forwarding nodes increases.

4. Conclusion and future work

In this research, a reliable adaptive routing service method is suggested to address the issues of dramatic topological changes and unstable links brought on by quick vehicle movements in VANET. First, it was established that links had a log-normal distribution in terms of duration after studying the characteristics of vehicle motion and the causes of links' lack of reliability. Second, a link reliability calculation model was created using this information. After the link reliability between nodes was evaluated as a parameter and employed in the Q-Learning process, the RSAR method was then recommended. The effectiveness of four routing methods was then evaluated using simulated trials to measure the number of hops, packet delivery ratios, and end-to-end delays. Under varying circumstances, the findings demonstrated that RSAR achieved a greater packet delivery ratio with a shorter transmission time delay. Due to its self-learning capabilities, RSAR is well-suited to deal with the issues caused by topological changes. Local diffusion is a kind of technique used in learning, and there may be a huge number of nodes involved in choosing the route, so the routing cost in a big network environment will be quite high. As a result, the authors' future work will concentrate on the issue of routing expense.

The creation of the algorithm that was used in finishing tracks at the MAC layer while meeting low latency requirements. Due to the time limit, packages that are not received by the recipient within the time limit do not count towards the total duration of the film. This is done in order to maintain the integrity of the timeline. Because of this, their transmission is completely worthless and does nothing more than burden the network. This feature of the algorithm must be taken into account, as eliminating them at the transmitter would enhance transmission. The technique should form a relationship between the application time constraint, the round-trip time limit, and the transition time represented by the completion of the waiting list to be considered valid.

References

- [1]. M.G. W.L. Junior, D. Rosário, E. Cerqueira, L.A. Villas, "A game theory approach for platoon-based driving for multimedia transmission in VANETs", *Wireless Communications and Mobile Computing*, **2414658**, 1–11, 2018, doi:https://doi.org/10.1155/2018/2414658
- [2]. A.V.V. M. Jiau, S. Huang, J. Hwang, "Multimedia services in cloud-based vehicular networks", *IEEE Intelligent Transportation Systems Magazine*, **7** (3), 62–79, 2015, doi:https://doi.org/10.1109/MITS.2015.2417974
- [3]. X.Z. M. Gerla, C. Wu, G. Pau, "Content distribution in VANETs", *Vehicular Communications*, **1**(1), 3–12, 2014, doi:https://doi.org/10.1016/j.vehcom.2013.11.001
- [4]. R.S. C. Campolo, A. Molinaro, "From today's VANETs to tomorrow's planning and the bets for the day after", *Vehicular Communications*, **2** (3), 158–171, 2015, doi:https://doi.org/10.1016/j.vehcom.2015.06.002

- [5]. R.F.S. D. Perdana, "Performance comparison of IEEE 1609.4/802.11p and 802.11e with EDCA implementation in MAC sublayer", International Conference on Information Technology and Electrical Engineering (ICITEE), 285–290, 2013, doi: 10.1109/ICITEED.2013.6676254
- [6]. N. Mittal, A. Singh, "A Critical Review of Routing Protocols for VANETs", International Conference on Innovative Computing and Communications, Springer Nature Singapore Pte Ltd, 135-142, 2019, doi: doi.org/10.1007/978-981-13-2324-9_14
- [7]. F. Goudarzi, H. Asgari, and H. S. Al-Raweshidy, "Traffic-Aware VANET Routing for City Environments—A Protocol Based on Ant Colony Optimization", IEEE SYSTEMS JOURNAL, 1-11, 2018, doi: 10.1109/JSYST.2018.2806996
- [8]. IEEE P1609.4, "Trial-Use Standard for Wireless Access in Vehicular Environments (WAVE) — Multi-Channel Operation", IEICE transactions on fundamentals of electronics, communications and computer sciences, **12** (2010), 2691-2695, 2006.
- [9]. S. ZAIDI, "Le streaming vidéo dans les réseaux véhiculaires ad-hoc," Doctoral thesis, UNIVERSITE MOHAMED KHIDER- BISKRA, 2018, doi : http://thesis.univ-biskra.dz/id/eprint/3870
- [10]. M. Rouse, "Vehicle-to-vehicle communication (V2V communication)", Internet of Things Agenda, 2014, doi : https://doi.org/10.48550/arXiv.2102.07306
- [11]. M. Zorkany, N.A. Kader, "Vanet routing protocol for v2v implementation: A suitable solution for developing countries", Cogent Engineering, **4**(1), 1362802, 2017, doi : https://doi.org/10.1080/23311916.2017.1362802
- [12]. S. Chakrabarti, L. Technologies, A. Mishra, V. Tech, "QoS Issues in Ad Hoc Wireless Networks" QOS and resource allocation in the 3rd generation wireless networks, IEEE, 142-148, 2001, doi : 10.1109/35.900643
- [13]. G. Ya, S. Olariu, "A probabilistic analysis of link duration in vehicular ad hoc networks", IEEE Intelligent Transportation Systems Magazine, **12** (4), 1227-1236, 2011, doi : 10.1109/TITS.2011.2156406
- [14]. J. Toutouh, "Intelligent OLSR routing protocol optimization for VANETs", IEEE Transactions on Vehicular Technology, **61**(4), 1884-1894, 2012, doi : 10.1109/TVT.2012.2188552
- [15]. Y.N. Zhu, "A new constructing approach for a weighted topology of wireless sensor networks based on local-world theory for the internet of things (IOT)", Computers & Mathematics with Applications, **64** (5), 1044-1055, 2012, doi : https://doi.org/10.1016/j.camwa.2012.03.023
- [16]. YP . Liang, " A kind of novel method of service-aware computing for uncertain mobile applications", Mathematical and Computer Modelling, **57** (3-4), 344–356, 2013, https://doi.org/10.1016/j.mcm.2012.06.012
- [17]. XD Song, X Wang, " Extended AODV routing method based on distributed minimum transmission (DMT) for WSN", AEU - International Journal of Electronics and Communications, **69**(1), 371–381, 2015, doi : https://doi.org/10.1016/j.aeue.2014.10.009
- [18]. Z Ke, Z Ting, " A novel multicast routing method with minimum transmission for WSN of cloud computing service", Soft Computing, **19**(10): 1817-1827, 2015, doi : https://doi.org/10.1007/s00500-014-1366-x
- [19]. XD Song, X Wang, " Extended AODV routing method based on distributed minimum transmission (DMT) for WSN", AEU - International Journal of Electronics and Communications, **69**(1), 371–381, 2015, doi : https://doi.org/10.1016/j.aeue.2014.10.009
- [20]. T Saravanan, N.S. Nithya, " Modeling displacement and direction aware ad hoc on-demand distance vector routing standard for mobile ad hoc networks", Mobile Networks and Applications, **24**(9), 1804–1813, 2019, doi : https://doi.org/10.1007/s11036-019-01390-9
- [21]. T Saravanan, N.S. Nithya, " Energy aware routing protocol using hybrid ANT-BEE colony optimization algorithm for cluster based routing", 4th IEEE international conference on computing communication and automation (ICCCA), 1–6, doi : 10.1109/CCAA.2018.8777662
- [22]. P Sherubha, N Mohanasundaram, " An efficient network threat detection and classification method using ANP-MVPS algorithm in wireless sensor networks", International Journal of Innovative Technology and Exploring Engineering (IJITEE), **8**(11), 2278-3075, 2019, doi : https://www.ijitee.org/wp-content/uploads/papers/v8i11/F3958048619
- [23]. V. Tavares, J.M.R.S. Boulogeorgos, A.A.A. Vuppapapati, " International Conference on Communication, Computing and Electronics Systems", Lecture Notes in Electrical Engineering, Springer, Singapore, 733, doi : https://doi.org/10.1007/978-981-33-4909-4_60

A DC Grid-Connected PV Microgrid Regulated via Digital and MBPC Cascade Control Strategies

Elio Sánchez Gutiérrez*, Sara Judith Ríos Orellana

Faculty of Electrical and Computer Engineering, ESPOL Polytechnic University, Guayaquil, 09-01-5863, Ecuador

ARTICLE INFO

Article history:

Received: 21 July, 2022

Accepted: 21 September, 2022

Online: 18 October, 2022

Keywords:

Microgrid

Inverter

Digital Control

Predictive Control

ABSTRACT

The current paper focuses on the design of cascade control systems employed in photovoltaic (PV) powered microgrids (MG), which have been well received in remote agricultural farms in Ecuador. The study case is composed of a three-phase inverter powered by a DC-DC converter fed by a PV array and its control system. To simulate the effect of MG peak voltage regulation, a comparison of three cascade schemes was done, using MATLAB/SIMULINK®. These schemes are based on digital control, model-based predictive control (MBPC), and a combination of both. It was found that the best stabilization of voltage although with a fast response and a low overvoltage in the MG are reached with a combined scheme, compound by the classical controller combined with the MBPC. The results were validated using the RT-LAB software and the OPAL-RT real-time (RT) simulator, in the tested microgrid.

1. Introduction

This paper is an extension of the work that was originally presented at the *2021 International Conference on Electromechanical and Energy Systems* [1], which was referring to the sizing of components and design of control systems that can be applied in an MG primary control layer powered by solar energy in Ecuador.

Verifiably, one of the principles of large-scale electricity generation is the installation of generators in areas close to energy resources, such as thermoelectric power plants near natural gas deposits. Listing some disadvantages, energy resources are usually non-renewable in several power generation projects, and typical installations are inappropriate when final consumers are far from power plants. Due to these remote destinations, infrastructure costs would rise, this being the construction of one or more substations to mitigate voltage drops in distribution cables.

Several agricultural production farms are in different inaccessible areas along the Ecuadorian coast, which has led several producers to use diesel pumps for irrigation systems. Due to recent studies and the acceptance of PV plants in Ecuador, it is possible to provide a solution with PV MGs for final loads found in distant destinations such as pumps and small residential consumption.

Concurring to a few definitions, an MG is a local and small energy system that can function in a connected mode to the main

grid or a self-regulating disconnected mode. It is made up of several distributed energy sources that supply heterogeneous loads within clearly defined electrical boundaries and by a variety of control criteria [2].

A simple example of an MG architecture is shown in Figure 1, whose main feeders are microgenerators, such as PV arrays, wind turbines, fuel cells, or other micro-turbines. These feeders can operate together with energy storage equipment e.g., lithium or lead-acid batteries. Indisputably, power converters shall be installed, to integrate the energy produced by the micro-generators, such as AC-DC-AC converters needed by wind turbines, and DC-AC converters required by PV arrays. In some instances, to minimize the number of solar panels and reduce the consumption of power converters, low voltage (LV) transformers can be used for coupling with the electricity grid.

Protective devices are required to complement the MG basic scheme, either for short circuits because of single-phase or three-phase faults, energy meters, and intelligent electronic devices. Likewise, a certain number of controllers are usually implemented depending on the MG layers. Regardless of the implemented control system, an MG must be stable in three operating modes: grid-connected, isolated mode, and transitions between these two. All these components can interact with each other through hard-wired signals and/or electrical communication protocols, where Modbus TCP/IP, DNP3, and IEC-61850 [3] are the most used to guarantee reliability and stability.

*Corresponding Author: Elio Sánchez Gutiérrez, eliansan@espol.edu.ec

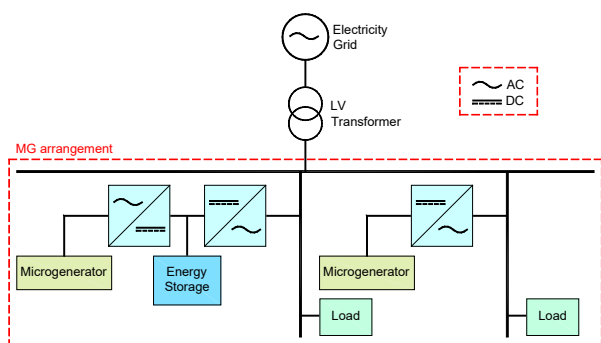


Figure 1: A simple example of MG architecture [2]

2. Comparable Works

The reduced cost of renewable energy generation combined with innovative digital technology contributes to increasing the ubiquity of smart grids, microgrids, and distributed energy generation that integrates renewable energy sources. Since 2000, the consumption of GWh has increased by 1.5 million in hydroelectric plants, 1.13 million in wind farms, and 4.44 million in solar plants. For example, in the next 20 years, renewable energy consumption will be 1.276 TWh in the European Union, 3.382 TWh in China, and 1.750 TWh in India [4].

Around the world, some MGs installations and experimental tests have been developed and updated to understand their operation in diverse topologies. While some of the studies include simply conducting research, others involve disconnecting the electric utility system. The details of very few MG projects, in the last 20 years, which have been put into action are shown in Table 1, where it is evident that the MG concept's adaptability gives experiment settings and goals a broad range.

Table 1: Summary of a few MGs projects worldwide [5–7]

Year	Name	Location	Capacity (MW)	Supply Type
2002	DeMoTec MG	Germany	0.2	Diesel
2004	NTUA MG	Greece	0.01	Wind
2005	Aichi MG	Japan	1.2	Biogas
2008	BC Hydro	Canada	15	Diesel
2009	CERTS Lab.	USA	0.2	Gas
2012	Sevilla University	Spain	0.01	PV
2012	Juiz de Fora Lab.	Brazil	0.015	PV/Wind/ Fuel cell
2013	Hawaii Hydrogen Power Park	USA	0.03	PV/Wind/ Fuel cell
2014	Annobon Island	EG	5	PV
2017	Alcatraz MG	USA	0.305	PV/Diesel
2018	SPORE	Singapore	0.2	Hybrid
2019	FIE-UMSNH Lab.	Mexico	0.003	PV/Wind
2020	Agronim La Bonita	Peru	1	PV
2021	Cuenca University	Ecuador	0.329	PV/Wind/ Diesel/Gas
2022	Kalbarri	Australia	5	PV/Wind

The MG approach is so versatile that has a wide range of applications in remote and off-grid communities. Radiation from the sun can be utilized as an uninterrupted resource that fits appropriately in some applications. Currently, the capacity supplied by PV energy in Ecuador is 27.65 MW, which corresponds to approximately 0.5% of the energy demand, and despite being small, it is gradually developing [8].

The National Institute of Meteorology and Hydrology of Ecuador reported that the average radiation levels were around 4.5 kWh/m² per day, in 2022, also indicating that elevated levels of around 6 kWh/m² per day were reached in some areas of the insular region and inter-Andean [8]. However, other areas such as the coast and the Amazon should not be ignored, especially the province of Guayas located in the southwest of the country, as indicated in Figure 2.

In Ecuador, PV applications have been employed in diverse sectors, such as:

- High-speed alert by small photo radars on highways.
- Water heating in Olympic swimming pools.
- Electrical supply to 370 households in the “Zero houses without electricity” project.
- Fruit drying in Manabi province is fed by PV energy.
- Institutional projects such as ESPOL rectory building where a 1.1 kW operating MG with PV/Wind source.
- The Paragachi PV plant contributes 0.998 MW to the state grid, with 4160 PV panels.
- The approved “El Aromo” PV energy project boosts Ecuador’s PV capacity almost tenfold, adding 258 MW to the current 27.65 MW [9].

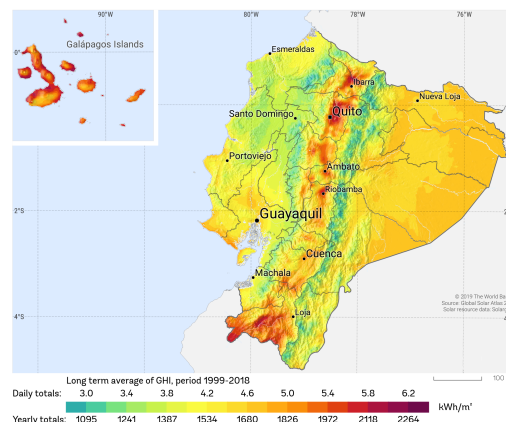


Figure 2: PV power potential in Ecuador [8]

3. Methodology

The current paper's main topic employs a methodical and investigative approach. The area irradiance data and grid nominal electrical parameters must first be acquired to model the grid-connected system. After that, the power converters must be designed. Finally, several simulations will be run, both offline and in RT, and the results will be compared across all cascade control schemes. An MG arrangement is shown in Figure 3 which includes a PV array with a Maximum Power Point Tracking (MPPT)

controller, DC-DC and DC-AC power converters, a grid-connected filter, and capacitors C_{PV} and C_{DC} for minimizing voltage ripples.

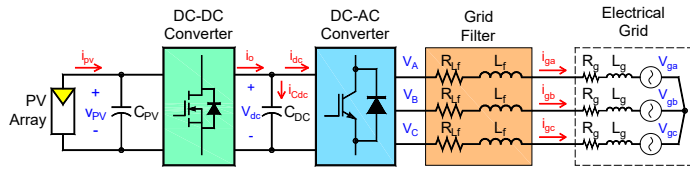


Figure 3: Complete MG sequential power circuit

3.1. PV Panels and Arrays

PV panels, also called PV modules, are comprised of several PV cells, connected, mechanically joined, and resistant to the environmental zone to be installed. In the last years, several studies have been developed, for example in [10], where the impact of new PV panels and their estimated replacement in 10 years versus the 30 years taken as standard useful life is evaluated. That article concludes that the new panels with improved metrics such as efficiency and cost will allow competitive costs even with a 10-year replacement. Regarding PV plant location, in [11] a prediction method based on a cellular computational network to predict PV radiation for large-scale PV plants is studied. It uses geographic information to help predict radiation in neighboring areas.

A PV array made up of multiple PV panels is required to reach higher levels of PV generation. For a higher voltage, PV panels are connected in series and for a higher current they would be connected in parallel, therefore, for a higher power, a series-parallel matrix scheme would be employed. It is significant to mention that the size of PV arrays relies on the PV panels' maximum conditions. In practice, it is standard to use photovoltaic combiner boxes to connect the output of several solar panels, hence optimizing wiring and facilitating maintenance.

3.2. MPPT Algorithm

This algorithm is a regulation to capture the obtainable power from a PV panel during variable working conditions. This technique was implemented in the trigger circuit of the DC-DC converter to repeatedly adjust the PV array's observed impedance and be able to keep its operation as close as possible to the maximum power point (MPP), as pointed out in Figure 4. Additionally, these characteristic curves show the MPP values, when the consumption of the PV panel is I_{MPP} and P_{MPP} at V_{MPP} , and the limit current/voltage values, which are the short-circuit current I_{SC} and the open-circuit voltage V_{OC} .

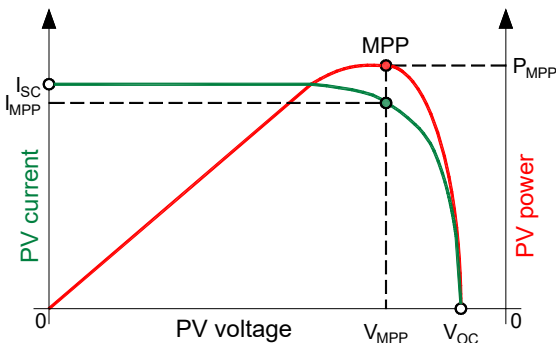


Figure 4: MPP location on Current vs. Voltage and Power vs. Voltage characteristics curves [12]

A widely accepted MPPT algorithm is the "perturb and observe" (P&O) extreme search. In an instant k , it is desired to reach the MPP, in distinction to PV array voltage/current measurements $V_{PV}(k)$ and $I_{PV}(k)$, and modifies its operating point slightly. Then, a comparison between this current power value $P_{PV}(k)$ with the previous one $P_{PV}(k-1)$ will be done, thus modifying the DC-DC converter's duty cycle $d(k)$ until the appropriate conditions are met [12].

Although MPPT algorithms come in various forms, according to [13], neither a deep investigation nor a comparison between various MPPT methods based on predictive control has been conducted. For this reason, in [13] this study is applied to various power converters models. It is possible to determine that the performance of the MPPT based on predictive control is related to the topology and the accuracy of the converter parameters.

The final scheme for this method is sequentially presented in the diagram shown in Figure 5, which can be employed in an algorithmic state machine (ASM), and the goal is that the duty cycle $d(k)$ reaches a nominal value. In [12], a universal RLMPT control method based on a reinforcement learning method is proposed, whose response adjusts the maximum power point of a PV source without any prior knowledge. Their results are close to the optimal point of the MPPT used in this article.

For one PV panel, the MPP data are commonly indicated in the manufacturer datasheet or its characteristic curves. This information and the MG power P_n will be helpful to determine the PV array's size, compound by N_S panels connected in series and N_P panels in parallel as (1).

$$P_{MPP} = P_n = (N_S V_{MPP})(N_P I_{MPP}) \quad (1)$$

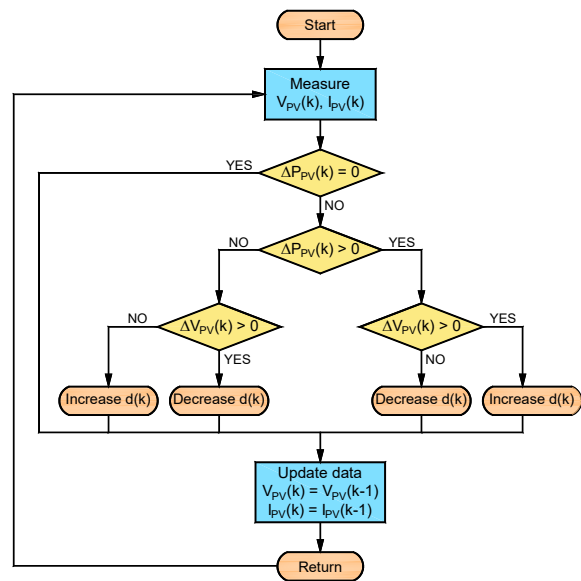


Figure 5: ASM chart of MPPT P&O algorithm [12]

3.3. DC-DC Power Converter

These converters provide a DC voltage that can be changed between different values. The input voltage often is an unregulated DC voltage, and a DC-DC converter is used to convert it into a controlled DC output at the desired level. The operation of DC-DC converters is done with a comparison between a control voltage

and a sawtooth signal v_{st} , oscillating at a switching frequency f_{sw} , and hence a period T_{sw} . Figure 6 shows the respective waveforms and the result of these voltages comparison, and it can be noticed that when the nominal duty cycle (D_0) increases or decreases, the switch control signal pulses shall be wider or narrower, respectively, at a constant frequency. That is the motive why this technique is called Pulse Width Modulation (PWM). It is important to mention that the control signal corresponding to D_0 will be MPPT controller output, as previously indicated in Figure 5.

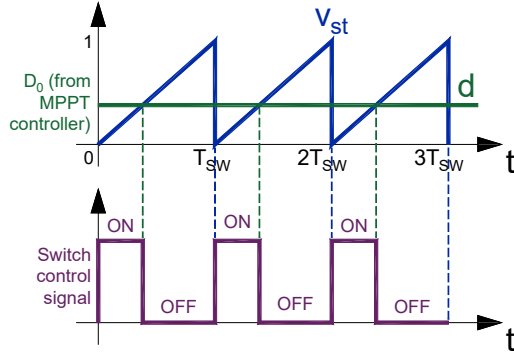


Figure 6: PWM with a comparison between sawtooth and control signals

Depending on how input/output voltage levels are related, these converters can be classified into three types: buck, boost, and buck-boost. A boost DC-DC converter, whose topology is shown in Figure 7, has been chosen to heighten the V_{PV} voltage into a DC link voltage v_{dc} capable of interfacing with the DC-AC converter.

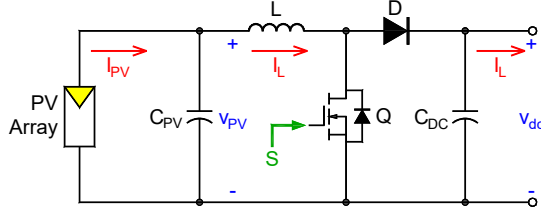


Figure 7: DC-DC boost converter power circuit fed by PV array

In this case, a MOSFET was considered as a switch because of its capacity of handling high voltage/currents. To reduce power losses, Schottky diodes should be used [14], and even these diodes have a peak current greater than typical ranges. In optimal conditions, the output V_{DC} voltage will be chopped according to a switch control signal S , oscillating at a switching frequency f_{sw1} with a duty cycle equivalent to D_0 . This desired value can be calculated as (2).

$$D_0 = 1 - \frac{V_{MPP}}{V_{DC}} \quad (2)$$

The boost converter must operate in continuous conduction mode, or when the inductor current flows continuously, therefore, a minimum value of inductance L_{min} shall be determined as (3), to satisfy this condition [14].

$$L_{min} = \frac{D_0(1-D_0)^2 V_{DC}^2}{2f_{sw1} P_n} \quad (3)$$

For more stable operation, an output capacitance C_{DC} is required. Although C_{DC} has a small resistance in series, it decreases the ripple in V_{dc} voltage, which is normally between 1% to 5%. For a given ripple percentage, the minimum capacitance C_{DCmin} is determined as (4), according to [14].

$$C_{DCmin} = \frac{D_0 P_n}{\left(\frac{\Delta V_{DC}}{V_{DC}}\right) V_{DC}^2 f_{sw1}} \quad (4)$$

To minimize the ripple created with the PV array coupling, an input capacitance C_{PV} is indispensable, and its minimum value C_{PVmin} can be determined as (5), by [14].

$$C_{PVmin} = \frac{\Delta i_{PV}}{8\Delta v_{PV} f_{sw1}} \quad (5)$$

3.4. DC-AC Power Converter

The capacity to convert DC voltage into AC with the required voltage and frequency values to supply power for AC loads, either one-phase or three-phase, makes the DC-AC converter, or inverter, the most crucial component of the MG. Figure 8 illustrates a traditional two-level three-phase inverter with IGBTs for larger loads, such as those greater than 5 kW [15]. This scheme shall be implemented to maintain a balanced electrical grid. For smaller loads, the use of one-phase inverters is acceptable.

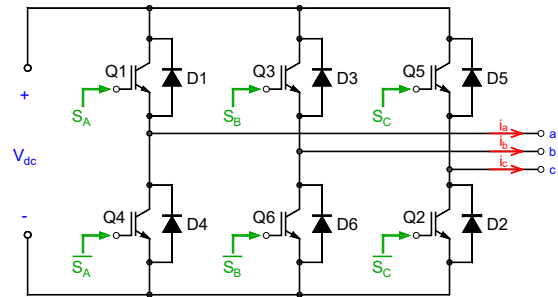


Figure 8: Two-level three-phase inverter power circuit

The IGBTs $Q1, Q2, \dots,$ and $Q6$ are generating square outputs as expected, based on the control signals $S_A, S_B, S_C,$ and their complements, hence using the grid filter is appropriate, which will be explained in detail in the following section 3.5. It is critical to mention that three of the IGBTs are on and the rest are off to avert short-circuits in the DC bus. In these types of converters, the SVPWM modulation scheme is commonly used because it reforms the usage of DC voltage, diminishes the generated harmonic content, and reduces switching losses.

According to (6), the switching/rotating voltage vector U_{ref} has three elements, one for each phase, each of which has two states: open or closed.

$$U_{ref} = \frac{2}{3} (v_A + v_B e^{j(2\pi/3)} + v_C e^{-j(2\pi/3)}) \quad (6)$$

The U_{ref} vector turns counterclockwise at the inverter switching frequency f_{sw} , therefore, inverter behavior must adhere to the eight vectors $U_0, U_1, U_2, \dots,$ and U_7 . It can be demonstrated that these eight vectors, two null and six actives, have a magnitude of $2V_{dc}/3$ and 60° phase [15], therefore six sectors will be only valid, and

identified in Figure 9, where the behaviors of respective control signals S_A , S_B , and S_C are presented too.

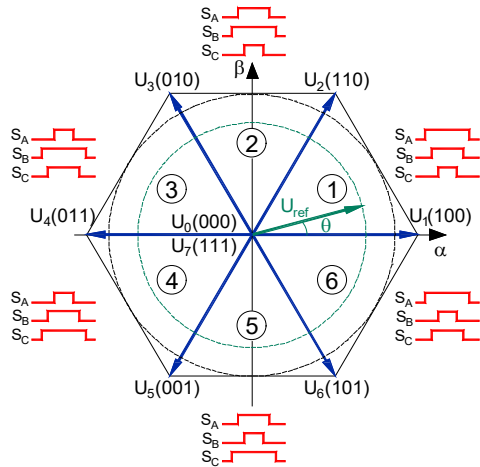


Figure 9: Space vectors for two-level three-phase inverter [15]

3.5. Grid Filter Design

Since inverters produce harmonic content, as was already established, the quality of the energy in the electric grid will be impacted. Due to this, harmonics must be minimized, and total demand distortion must be reduced when designing a low-pass filter. The simplest option for a grid filter is an RL filter where the base inductance per phase is necessary for its calculation [16], as (7) from nominal data, in fact, the MG power P_n of the MG, the grid voltage V_n and the grid frequency f_n .

$$L_{base} = \frac{Z_{base}}{2\pi f_n} = \frac{V_n^2}{2\pi f_n(P_n/3)} \quad (7)$$

For a 10% current ripple, and considering that the value of the resistance R_{Lf} is 25 times greater than that of the inductance L_f , the filter components will be determined as (8) and (9):

$$L_f = 0.1 \frac{V_n^2}{2\pi f_n(P_n/3)} \quad (8)$$

$$R_{Lf} = 25 |L_f| \quad (9)$$

3.6. Control Techniques Premises in MGs

Synchronization with the electrical grid is a priority for any type of control employed in MGs, and with this, the analysis for a grid voltage vector V_{ref} must be turned into a linear invariant system [17] by applying the Clarke transform, to convert it from the time frame (abc frame) to an orthogonal frame ($\alpha\beta$ frame), and then with the Park transform, to convert this vector into an orthogonal rotating frame (dq frame), as detailed in Figure 10.

Additionally, a phase-locked loop (PLL) system is required when the MG is grid-connected, which requires the electrical grid voltage V_q to distinguish the voltage phase and estimate the electrical angle that will be considered in Clarke/Park transforms. [17]. This component can be used to develop some electrical control strategies in MG inverters like:

- Voltage control, where the input voltage of the inverter is measured because this corresponds to the output line-to-line voltage.
- Active/reactive power control, where the inverter injects active/reactive power for a better MG economic operation.
- Droop control is based on voltage droop depending on active power/frequency droop increases, and reactive power decreases.

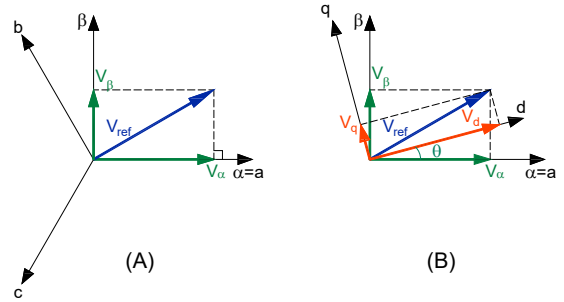


Figure 10: (A) Reference vector components in $\alpha\beta$ frame, and (B) in dq frame

The article [17] presents a description of current control methods for microgrids, especially stand-alone and inverter-based networks. In addition, the control methods are compared presenting the characteristics, control objectives, and their advantages or disadvantages. Regardless of the electrical control chosen, an electrical connection to the grid can cause disturbances, therefore, an appropriate controller must be designed.

Inverter controllers can be classified into classic and advanced. Within the classic control techniques, there is linear control, either by current or voltage, and hysteresis control, either by current or direct power, in the inverter. Furthermore, in advanced control techniques there is predictive control, either hysteresis-based, dead-band control, or model-based; intelligent control either by fuzzy logic, neural networks, or even a combination of both; and sliding mode control by voltage or current in the inverter.

4. Modeling and Control Design

4.1. MG Mathematical Modeling

As mentioned above, the MG key component is the inverter, therefore, the DC-DC converter's power stage will be only analyzed with the voltages and currents of interest, as shown in Figure 3. In the inverter output, the space vector voltage will be:

$$\vec{v}_s = R_{Lf} \vec{i}_s + L_f \frac{di_s}{dt} + \vec{V}_g \quad (10)$$

Applying the Clarke and Park transforms, the following rotational space vectors were obtained in the dq frame: v_s , i_s , and V_g . These vectors contain an electric component with a rotational angle $\theta_g = \omega_g t = 2\pi f_n t$, to represent these expressions in the dq frame [18]:

$$\begin{aligned} \vec{v}_s' &= \vec{v}_s e^{-j\theta_g} = v_d + jv_q \\ \vec{i}_s' &= \vec{i}_s e^{-j\theta_g} = i_d + ji_q \end{aligned} \quad (11)$$

$$\vec{V}_g' = \vec{V}_g e^{-j\theta_g} = V_{gd} + jV_{gq}$$

Then, the voltage space vector will be as (12) with its rotational components, and for MG dq modeling, the identity described in (13) shall be considered [18].

$$\vec{v}_s' = R_{L_f} \vec{i}_s' + L_f \frac{d\vec{i}_s'}{dt} + j\omega_g L_{F'} \vec{i}_s' + \vec{V}_g' \quad (12)$$

$$\frac{d\vec{i}_s'}{dt} e^{-j\theta_g} = \frac{d\vec{i}_s'}{dt} + j\omega_g \vec{i}_s' \quad (13)$$

Considering a zero V_{gq} voltage, and based on the real and imaginary elements, the MG dynamic current models, in the dq frame, will be:

$$v_d = R_{L_f} i_d + L_f \frac{di_d}{dt} - \omega_g L_f i_q + V_{gd} \quad (14)$$

$$v_q = R_{L_f} i_q + L_f \frac{di_q}{dt} + \omega_g L_f i_d$$

On the other hand, the relation between both the DC link power P_c , the grid power P_g and the load power P_L is considered when considering energy conservation [18], and these powers are:

$$v_{dc} i_{cdc} = \frac{3}{2} \vec{v}_s \cdot \vec{i}_s - v_{dc} i_o \quad (15)$$

In the DC link, the i_{cdc} current will be:

$$i_{cdc} = \frac{3}{2v_{dc}} \vec{v}_s \cdot \vec{i}_s - i_o = C_{DC} \frac{dv_{dc}}{dt} \quad (16)$$

And finally, the MG dynamic voltage model in the dq frame will be:

$$i_{cdc} = \frac{3}{2v_{dc}} \vec{v}_s \cdot \vec{i}_s - i_o = C_{DC} \frac{dv_{dc}}{dt} \quad (17)$$

4.2. Digital Cascade Control in MGs

This control strategy is appropriate because SVPWM is frequently performed in digital signal processors, whose outputs match the pulse signals for the IGBTs [19]. These devices rely on microprocessors that run at high frequencies, which are vital in the MG field for microprocessors to contain primary and secondary control systems [20].

The cascade feedback control structure is an effective way to control electrical drives and power converters. The inner loop controllers regulate the dq currents, while the outer loop controls the main desired variable, for instance, the MG voltage, active/reactive power, or mechanical speed in AC motors. The key to the success of cascade control lies in the difference between the time constants of both loops. The response time of dq currents will be much faster.

For this control strategy works properly, some additional components must be included, such as analog to digital data converters, and vice versa, based on holding and sampling circuits. Zero-order holders (ZOH), which are utilized for voltage/current

measurements and operate at a specific sampling time T_s [21], shall be included in digital cascade control schemes, as shown in Figure 11. Additionally, a digital low-pass filter (DLPF) is used to reduce DC link voltage fluctuations. There is a digital Proportional-Integral (PI) controller for the I_q with a null setpoint to give the least amount of reactive power, and the other digital PI controllers are connected in cascade to control I_d internally and V_{dc} externally, this being the desired variable.

For digital controllers' tuning, in the case of I_d , the signals influenced by I_q and V_{gd} will be disturbances, and for I_q , the signal influenced by I_d is a disturbance. In contrast to that, for V_{dc} , the voltage mathematical model shall be simplified, and the voltage behavior will be stable, its component in d axis v_d will be equivalent to the MG maximum voltage, in one phase, and the DC link current i_{dc} will be a disturbance.

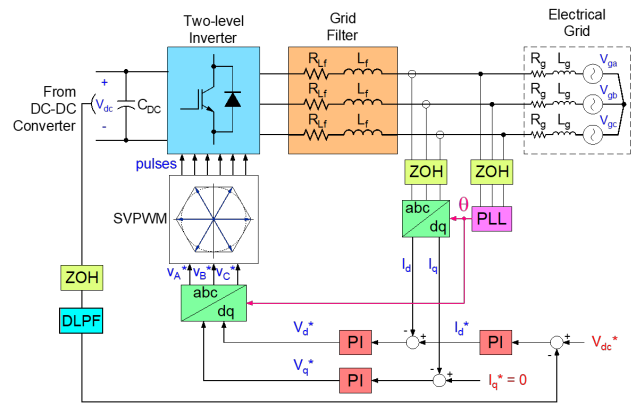


Figure 11: MG v_{dc} voltage regulation with digital cascade control scheme [21]

The transfer functions $I_d(s)/V_d^*(s)$ and $I_q(s)/V_q^*(s)$ will be equal and depend on the RL filter components. Then, I_d closed loop with a current controller $C_i(z)$ will be connected in cascade with a voltage transfer function, and a voltage controller $C_v(z)$. All these control loops are shown in Figure 12.

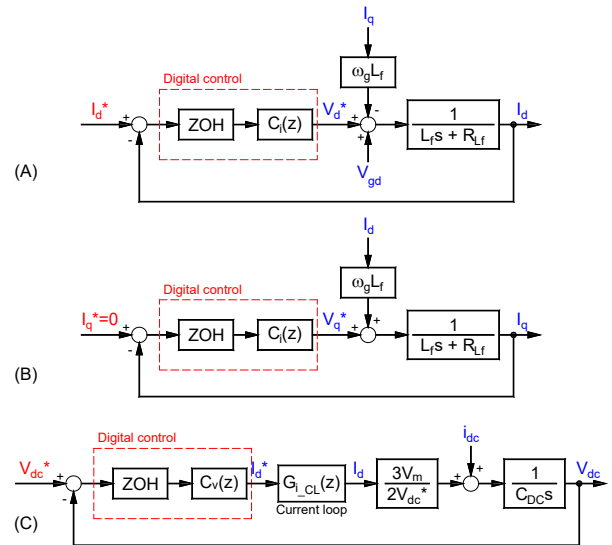


Figure 12: Block diagrams for closed-loop control systems to regulate (A) I_d , (B) I_q , and (C) V_{dc}

4.3. Predictive Cascade Control in MGs

MBPC is model-based, good at predicting future events, and altering the current control strategy optimally, for this reason, MBPC is conducive for inverters since their model is crucial [21]. This strategy is simple and both SISO and MIMO systems can be managed. Other advantages of MBPC strategies over conventional control schemes are that they do not rely on average models, and inverter constraints like overcurrent can be considered while formulating the optimal control issue.

In MG applications, MBPC is widely used. For example, in [22], a predictive control strategy is proposed by an MG model in two layers. The first layer is responsible for optimizing power dispatch and the second layer controls diesel generation. With this method, the weights of the prediction algorithm are also manipulated. Similarly, in [23] an electrical network formed by three MGs that cooperate by sharing their power flows is modeled. Control modeling is based on predictive control, which allows cost function optimization. In that article, the power exchange occurs minimizing the generation from the micro gas turbines.

Figure 13 shows a cascade control scheme where MBPC is implemented, for dq currents regulation and an external digital PI controller for MG voltage regulation. In this case, the MBPC stage can be encapsulated as follows:

- The current prediction process depends on six cases that correspond to the combinations of the inverter's active vectors. The objective is to decrease the errors between the reference values and the present anticipated values, as described by [21].

$$(\Delta I_d^i[k+1] = I_d^*[k] - I_d^i[k+1]) \Big|_{i=1,\dots,6} \quad (18)$$

$$(\Delta I_q^i[k+1] = I_q^*[k] - I_q^i[k+1]) \Big|_{i=1,\dots,6}$$

- The minimization of a dq current cost function J_1 is applied from the dq currents error, and described by [21]:

$$(J_1^i = |\Delta I_d^i[k+1]| + |\Delta I_q^i[k+1]|) \Big|_{i=1,\dots,6} \quad (19)$$

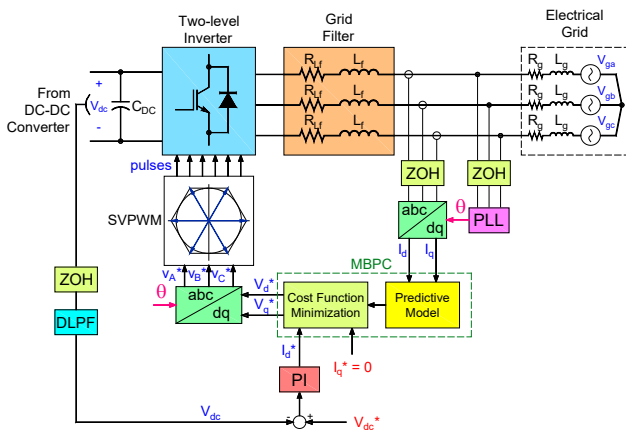


Figure 13: MG v_{dc} voltage regulation with combined cascade control scheme: MBPC inner loop and digital outer loop [21]

To design the MBPC controller, the dq current mathematical model, or its steady space model, must be discretized. Considering all calculated data and V_{gd} as a disturbance, the state matrixes indicated in (20) are obtained. Notably, this controller will manage a MIMO system with two inputs and two outputs.

$$A = \begin{bmatrix} -\frac{R_{Lf}}{L_f} & \omega_g \\ -\omega_g & -\frac{R_{Lf}}{L_f} \end{bmatrix}; B = \begin{bmatrix} \frac{1}{L_f} & 0 \\ 0 & \frac{1}{L_f} \end{bmatrix}; \quad (20)$$

$$C = I_2; D = 0_{2,2}$$

Another available cascade control topology applied in MGs can be obtained by replacing the external digital PI controller with an MBPC controller. This topology provides satisfactory results but requires a lot of computational loads, which several modern hardware is capable of supplying, while a few years ago this activity was feasible but overly expensive.

Figure 14 shows a cascade control scheme where MBPC is implemented for dq currents control and MG voltage regulation. The model described by the simplified voltage transfer function detailed in Figure 12(C) was considered for designing the external MBPC controller, and the d-axis current loop was simplified as a unitary gain because the I_d^* reference is reached much faster than the MG voltage.

Like the previous scheme, the MBPC stage for the outer loop can be summarized as the prediction process for v_{dc} voltage to decrease voltage errors, and the minimization of a voltage cost function J_2 defined by:

$$J_2 = |\Delta v_{dc}[k+1]| = |V_{dc}^*[k] - v_{dc}[k+1]| \quad (21)$$

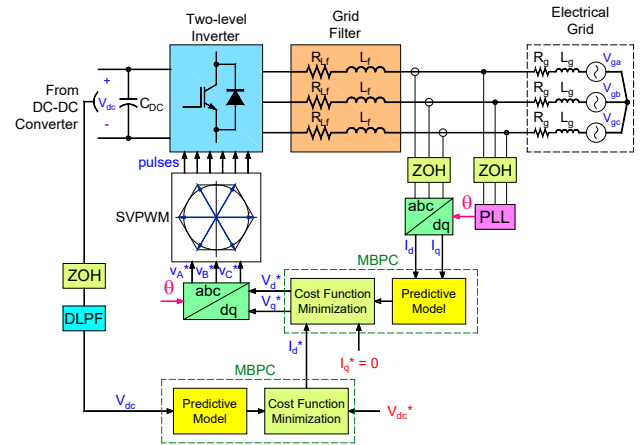


Figure 14: MG v_{dc} voltage regulation with MBPC cascade control scheme

5. Simulation Results

5.1. MG Initial Stages Design

In this paper, MG and its control were modeled and designed to feed a pumping system for agricultural irrigation in a rural area of El Triunfo, province of Guayas, which is situated in the coast region. In 2021, PV radiation had an annual mean value of 6 kWh/m² during the warmest period, in the coast area [24]. Figure 15 illustrates the trend behavior of the PV radiation in this area,

and based on these data, the PV panel from the manufacturer AE SOLAR with P/N AE340SMM6-72 was chosen.

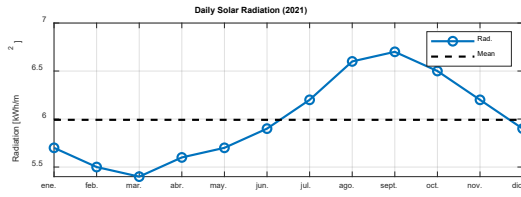


Figure 15: PV data behavior of rural zone located in El Triunfo [24]

The PV panels’ electric parameters must be chosen as a first step. These data are shown in Table 2 and were collected under standard test conditions, which are defined as being 1 kW/m² of full solar noon irradiance at a standard temperature of 25°C, for each PV panel.

By the size of the PV array, the product $N_s N_p$ could be derived as (1) considering the MPP voltage/current values, considering that the MG power is 40 kW or the power of the PV array. In addition, N_s was chosen to be 10 because it is needed that the PV array MPP voltage shall be close to a predefined reference voltage V_{dc}^* of 650 V, and N_p would be 12 for reaching the MPP power of the PV array. According to these predetermined values, the PV array parameters are also indicated in Table 2.

Table 2: PV Panel and PV Array Specifications

Parameter	PV Panel	PV Array
P_{MPP}	340 W	40.81 kW
V_{MPP}	39.09 V	390.9 V
I_{MPP}	8.7 A	104.4 A
V_{OC}	46.94 V	469.4 V
I_{SC}	9.48 A	113.76 A

For the system to be modeled, data from the subsequent stages must be determined in addition to the solar parameters. All gathered results shown in Table 3 were obtained for each indicated stage, where:

- All boost DC-DC converter components were calculated according to (2–5), with a contemplated switching frequency f_{sw1} of 5 kHz.
- MPPT P&O algorithm’s maximum value will be equivalent to the calculated D_0 . Other values were considered for the algorithm execution like the minimum duty cycle D_{min} , the initial duty cycle $D_{initial}$ and the value for duty cycle increment/decrement ΔD .
- A switching frequency f_{sw2} was set at 5 kHz for the inverter.
- The specifications of the Ecuadorian electrical grid, which are the grid voltage V_n of 220 V and the grid frequency f_n equal to 60 Hz, have been used to define the components of the RL filter as (8–9).
- It has been considered that the grid impedance is 10 times less than the impedance of the RL filter.

Table 3: Boost DC-DC Converter, MPPT, and Grid Filter Parameters

Parameter	Value
D_0	0.3986
L	1.5227 mH
C_{DC}	1000 μ F
C_{PV}	100 μ F
$D_{initial}$	0.01
D_{min}	0
ΔD	$\pm 125 \times 10^{-6}$
L_f	0.9629 mH
R_{Lf}	0.0241 Ω
L_g	0.09629 mH
R_g	0.00241 Ω

These data will be helpful for offline and RT simulations in which a 5 kW three-phase RL load with power factor $FP = 0.88$ will be connected after 1 s and disconnected after 2.5 s. The load connection and/or disconnection is to evaluate how well the controllers protect against disturbances while MG is operating.

5.2. Digital Controllers Tuning

Advantageously, the discrete transfer functions for I_d and I_q are equal, and their inner dynamics depend on the RL filter calculated parameters. Therefore, for both cases, the digital PI controllers in inner loops for regulating currents will be the same. The selected gains for the I_d current controller will be essential for voltage controller tuning which depends on the inner closed loop. In the controllers’ tuning process, the best values of proportional gain K_P and integral gain K_I for dq currents and the MG voltage are shown in Table 4 with a sampling time T_s of 10 μ s.

Table 4: Digital controllers’ parameters

Parameter	For I_d / I_q	For V_{dc}
K_P	0.0263	-0.0371
K_I	1.9738	-0.1803

5.3. MBPC Controllers Design

In this instance, the MBPC current controller is designed and simulated with the MATLAB *mpcDesigner* tool with the determined state matrixes of the dq current model, which are indicated in (22). A one-step prediction horizon N_p of 10, a one-step control horizon N_c of 2, and a sampling time T_s of 10 μ s were considered.

$$A = \begin{bmatrix} -25 & 377 \\ -377 & -25 \end{bmatrix}; B = \begin{bmatrix} 1038.5 & 0 \\ 0 & 1038.5 \end{bmatrix} \quad (22)$$

With this sampling time, five tests were run to adjust digital PI controllers for v_{dc} , and the best results came from using $K_P = -0.5$ and $K_I = -1$. During this test, the shortest overshoot OS , and the fastest stabilization time T_{SS} were achieved. This was developed in the cascade control scheme where digital PI control is in the inner loop, and the MBPC is outer.

On the other hand, the MBPC voltage controller design for the cascade control scheme, where both loops are MBPC, was based

on the simplified voltage model. Both prediction and control horizons, N_p and N_c , were the same as those used in the current control, as well as their sampling time.

5.4. MPPT Control Performance

Before running the simulation, it is necessary to enter additional parameters to complete the compilation of the PV array block, like the number of cells per module and the temperature coefficients, and fortunately, the manufacturer’s datasheet also presents these data. In this case, the selected PV panel has 72 cells per module. Besides, the temperature coefficients $\alpha_{I_{sc}}$ and $\beta_{V_{oc}}$, determine the variation of I_{sc} and V_{oc} as a function of temperature when the PV panel operates above the standard temperature of 25°C. For the selected PV panel, the temperature coefficients $\alpha_{I_{sc}}$ and $\beta_{V_{oc}}$ are 0.05%/°C and -0.29%/°C, respectively.

To assess the MPPT controller's effectiveness, Figure 16 shows the PV array voltage, the output current, and the PV power delivered to the DC-DC converter. Notably, the PV array reaches the MPP because its electrical values oscillate around the MPP values listed previously, and even when the RL load is connected at $t = 1$ s, the PV array keeps its operation around the MPP. It can be also observed that when the RL load is disconnected at $t = 2.5$ s, there are no induced oscillations.

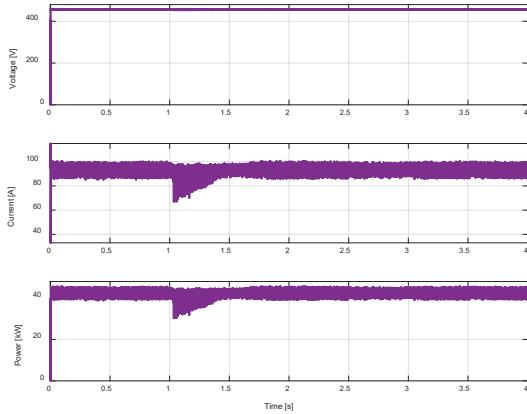


Figure 16: PV array voltage, current, and power behaviors

5.5. Controllers Evaluation in Offline Simulations

In this section, the tests have been conducted with offline simulations, or simulations executed purely in software. To evaluate controllers, Figure 17 illustrates their performance and the behavior of MG voltage v_{dc} around a predefined reference V_{dc}^* equal to 650 V with the following results:

- Initially, v_{dc} reaches an OS equivalent to 2.31% over the reference, with a $T_{ss} \approx 57.1$ ms when digital PI control was implemented. Then, when the RL load is connected, a voltage drop of 170 V appears, and v_{dc} is stabilized almost equal to 0.83 s, after a dead time of 0.5 s, and when the RL load is disconnected, $OS \approx 53.97\%$ and $T_{ss} \approx 0.58$ s.
- Instead, when the inner loop was executed with MBPC and the outer loop with digital PI control, v_{dc} reached a higher $OS \approx 15\%$, with a $T_{ss} \approx 150$ ms. Then, connecting the RL load, the voltage drop is less and equal to 56 V, $T_{ss} \approx 0.33$ s, and there is no presence of any dead time, and after the RL load is disconnected, $OS \approx 7.47\%$ and $T_{ss} \approx 0.25$ s.

- On the other hand, when cascade control was implemented with MBPC, v_{dc} reached a higher OS almost equal to 19.4%, with $T_{ss} \approx 30.27$ ms. Now when the RL load is connected, the voltage drop is 22.9 V and $T_{ss} \approx 1.29$ ms, without dead time too, and after the RL load is disconnected, $OS \approx 1.06\%$ and $T_{ss} \approx 0.52$ s. Unfortunately, a steady-state error (E_{ss}) appears when the RL load is connected, and the MG voltage could not reach the defined reference.

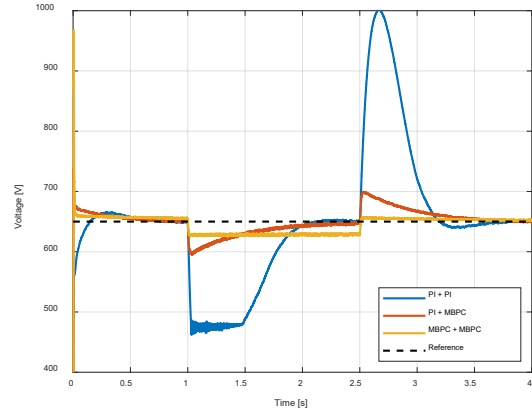


Figure 17: DC voltage behavior with both cascade controllers (Offline simulation)

Table 5 shows all the gathered ripple data present in I_d , I_q , V_d , and V_q for each cascade control scheme during the time intervals, and it is noteworthy that the control actions during MBPC are larger, four times larger for dq currents and 73 times larger for dq voltages specifically, therefore faster responses are obtained.

Table 5: DQ Currents/Voltages Ripples per Time Intervals (Offline Simulation)

PI + PI			
Parameter	$0 < t < 1$ s	$1 \text{ s} < t < 2.5$ s	$t > 2.5$ s
ΔI_d	16.44 A	15.71 A	16.82 A
ΔI_q	15.03 A	13.13 A	13.27 A
ΔV_d	0.44 V	0.43 V	0.42 V
ΔV_q	0.41 V	0.39 V	0.38 V
PI + MBPC			
ΔI_d	47.6 A	44.26 A	46.95 A
ΔI_q	47.42 A	46.39 A	50.74 A
ΔV_d	21.43 V	27.22 V	23.04 V
ΔV_q	29.69 V	31.81 V	30.14 V
MBPC + MBPC			
ΔI_d	38.93 A	36.63 A	40.03 A
ΔI_q	48.91 A	45.06 A	50.8 A
ΔV_d	18.75 V	22.99 V	27.61 V
ΔV_q	29.07 V	26.54 V	29.33 V

5.6. Controllers Evaluation in RT Simulations

When a physical system and the CPU must operate similarly, deterministic answers must be guaranteed, and real hardware may even need to be connected in an interactive loop, RT simulation is required.

Among the advantages of verifying RT implementations, RT testing allows redefinition and verification of control systems with hardware, continuous exploration of the flexible and scalable

platform, and investigation of complex, expensive, or dangerous scenarios that could be held in MGs.

The RT concept can be implemented accurately within the constraints of each system, although sampling would be different for a mechanical system compared to an electrical system. These tests are performed using the sample time $T_{s\ CPU}$, which is the space between data processing. In this paper, it has been determined that this time is $50\mu s$ and that it is equal to all control sampling times.

Currently, ESPOL University has the necessary equipment to conduct R&D projects in advanced industrial and academic solutions for power electronics and power systems sectors. It has the RT-LAB platform with a 32-core OPAL-RT RT simulator, fully integrated with MATLAB/Simulink, one I/O processor based on the Xilinx VC707 Virtex-7 FPGA platform, and one power amplifier OMICRON CMS 356 to exchange voltage/current signals with protection relays, or other electronic devices.

When running these RT simulations, the results tended to get even closer to V_{dc}^* . To evaluate the same controllers, Figure 18 illustrates their performance with the following results:

- First, v_{dc} stabilizes so fast that there is not an *OS* when digital PI control was implemented. Then, when the RL load connection, a voltage drop of 58.83 V appears, and an E_{SS} equal to 45 V. When the RL load is disconnected, $OS \approx 30\%$ and $T_{SS} \approx 0.5$ s.
- When the MBPC inner loop and the digital PI outer loop with, v_{dc} stabilizes so fast that there is not an *OS*. Then, connecting the RL load, the voltage drop is less and equivalent to 56.7 V, v_{dc} stabilized at 0.6 s, and there is no presence of any E_{SS} , and after the RL load is disconnected, $OS \approx 8.8\%$ and $T_{SS} \approx 0.23$ s.
- Finally, with the MBPC cascade control scheme, v_{dc} reached an $OS \approx 5.38\%$, with an $E_{SS} \approx 19.74$ V. Then, with the RL load connection, the voltage drop is 12.22 V and $E_{SS} \approx 12$ V, and with the disconnection of RL load, $OS \approx 3.07\%$ and $E_{SS} \approx 10$ V.

Similarly, to offline simulations, all gathered ripple data present in I_d , I_q , V_d , and V_q is shown in Table 6. The control actions with MBPC are larger, 3.8 times larger for dq currents and 75 times larger for dq voltages specifically.

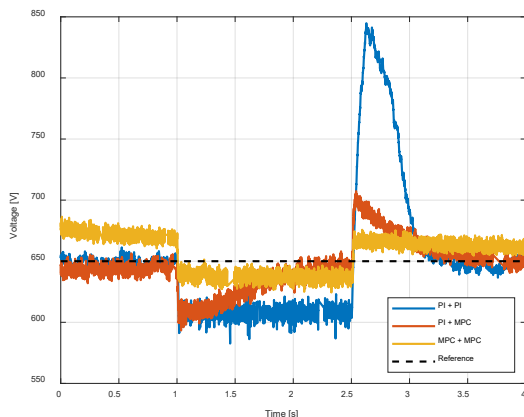


Figure 18: DC voltage behavior with both cascade controllers (RT simulation)

Table 6: DQ Currents/Voltages Ripples per Time Intervals (RT Simulation)

PI + PI			
Parameter	$0 < t < 1s$	$1s < t < 2.5s$	$t > 2.5s$
ΔI_d	37.1 A	26.45 A	39.28 A
ΔI_q	33.9 A	28.1 A	38.2 A
ΔV_d	1.02 V	1.02 V	0.87 V
ΔV_q	1.15 V	0.93 V	1.13 V
PI + MBPC			
ΔI_d	125.7 A	115.51 A	123.41 A
ΔI_q	104.4 A	103.9 A	112.8 A
ΔV_d	99.31 V	93.24 V	98.64 V
ΔV_q	90.6 V	91.4 V	94 V
MBPC + MBPC			
ΔI_d	129.75 A	118.03 A	135.55 A
ΔI_q	138.6 A	118 A	120.4 A
ΔV_d	103.07 V	95.92 V	107.15 V
ΔV_q	111.6 V	100.4 V	101.2 V

6. Conclusion and Further Results

After the performance evaluation of the MG, the correct choice of electrical components has a significant role, because the PV system’s mathematical modeling and the design premises of controllers depend on them. In the case of a component changes value, for example, the operating frequency of the electrical grid, or the V_{dc}^* voltage setpoint, a robust control must be implemented. Even all switching frequencies shall be kept constant.

This article shows that v_{dc} is stabilized using various control techniques (PI + PI, PI + MBPC, and MBPC + MBPC), both in the inner loop and in the outer loop. Although v_{dc} is similarly stabilized using the mentioned control techniques, PI + MBPC cascade control has the best performance. Due to variations in the RL load, it was observed that the voltage spikes are acceptable compared to those that occur when using the other cascade control schemes used and do not produce steady-state voltage errors.

Offline simulations and real-times simulations are presented to validate the effectiveness of the proposed control strategies.

The studied case shows that it would be achievable to connect a 7.5 kW three-phase motor for farm irrigation. It is recommended that this load shall be a maximum of 15% of the MG-rated power.

In the case of digital control systems, it is suggested that PI controllers be used instead of PID (Proportional-Integral-Derivative) controllers, as their design is simpler and provides considerable performance. Additionally, cost savings may be realized in some cases when it is desirable to integrate hardware in the control loop.

For the MBPC design, it is a good practical idea to select an initial prediction horizon N_p and maintain it constantly while modifying other settings, such as cost function weights. N_p should not exceed 50, except when the sampling time of the controller is extremely small, and a little control horizon N_c . Thus, quadratic programming calculates fewer variables in each control interval, promoting faster current controller computations.

The MPPT algorithm with the P&O technique, and the SVPWM stage which generates the IGBT pulses, can be implemented in an FPGA. An FPGA-in-the-loop simulation can be conducted using the RT simulator. With this scenario, the use of MATLAB/Simulink for any current HDL code allows performing MG tests even with a real cascade controller.

Conflict of Interest

The authors declare no conflict of interest.

Acknowledgment

Under the auspices of the R&D Project GI-GISE-FIEC-01-2018, ESPOL Polytechnic University provided support for this research.

References

- [1] G. Elio Sanchez, S.J. Rios, "Digital Control and MBPC design for DC Voltage Regulation in a Grid-Connected PV Microgrid," in 2021 International Conference on Electromechanical and Energy Systems (SIELMEN), IEEE: 219–224, 2021, doi:10.1109/SIELMEN53755.2021.9600409.
- [2] T.S. Ustun, C. Ozansoy, A. Zayegh, "Recent developments in microgrids and example cases around the world—A review," *Renewable and Sustainable Energy Reviews*, **15**(8), 4030–4041, 2011, doi:10.1016/j.rser.2011.07.033.
- [3] A. Bani-Ahmed, L. Weber, A. Nasiri, H. Hosseini, "Microgrid communications: State of the art and future trends," 3rd International Conference on Renewable Energy Research and Applications, ICRERA 2014, 780–785, 2014, doi:10.1109/ICRERA.2014.7016491.
- [4] S. de Dutta, R. Prasad, "Cybersecurity for microgrid," in International Symposium on Wireless Personal Multimedia Communications, WPMC, IEEE Computer Society, 2020, doi:10.1109/WPMC50192.2020.9309494.
- [5] E. Hossain, E. Kabalci, R. Bayindir, R. Perez, "Microgrid testbeds around the world: State of art," *Energy Conversion and Management*, **86**, 132–153, 2014, doi:10.1016/j.enconman.2014.05.012.
- [6] I. Latin, A. Transactions, *A Review of Microgrids in Latin America: Laboratories and Test Systems*, 2022.
- [7] Kalbarri microgrid – Australia's largest launched, Sep. 2022.
- [8] INAMHI, *Pronóstico del Índice Ultravioleta*, Guayaquil, 2022.
- [9] El Aromo Solar PV Park, Ecuador, Sep. 2022.
- [10] J. Jean, M. Woodhouse, V. Bulović, "Accelerating Photovoltaic Market Entry with Module Replacement," *Joule*, **3**(11), 2824–2841, 2019, doi:10.1016/j.joule.2019.08.012.
- [11] I. Jayawardene, G.K. Venayagamoorthy, "Spatial predictions of solar irradiance for photovoltaic plants," in Conference Record of the IEEE Photovoltaic Specialists Conference, Institute of Electrical and Electronics Engineers Inc.: 267–272, 2016, doi:10.1109/PVSC.2016.7749592.
- [12] P. Kofinas, S. Doltsinis, A.I. Dounis, G.A. Vouros, "A reinforcement learning approach for MPPT control method of photovoltaic sources," *Renewable Energy*, **108**, 461–473, 2017, doi:10.1016/j.renene.2017.03.008.
- [13] A. Lashab, D. Sera, J.M. Guerrero, L. Mathe, A. Bouzid, "Discrete Model-Predictive-Control-Based Maximum Power Point Tracking for PV Systems: Overview and Evaluation," *IEEE Transactions on Power Electronics*, **33**(8), 7273–7287, 2018, doi:10.1109/TPEL.2017.2764321.
- [14] T.K. Barui, S. Goswami, D. Mondal, "Design of Digitally Controlled DC-DC Boost Converter for the Operation in DC Microgrid," *Journal of Engineering Sciences*, **7**(2), E7–E13, 2020, doi:10.21272/jes.2020.7(2).e2.
- [15] G. Vivek, J. Biswas, "Study on hybrid SVPWM sequences for two level VSIs," in Proceedings of the IEEE International Conference on Industrial Technology, Institute of Electrical and Electronics Engineers Inc.: 219–224, 2017, doi:10.1109/ICIT.2017.7913086.
- [16] H. Kim, K.H. Kim, "Filter design for grid connected PV inverters," 2008 IEEE International Conference on Sustainable Energy Technologies, ICSET 2008, 1070–1075, 2008, doi:10.1109/ICSET.2008.4747165.
- [17] M.H. Andishgar, E. Gholipour, R. Allah Hooshmand, "An overview of control approaches of inverter-based microgrids in islanding mode of operation," *Renewable and Sustainable Energy Reviews*, **80**, 1043–1060, 2017, doi:10.1016/j.rser.2017.05.267.
- [18] L. Wang, Chai Shan, Yoo Dae, Gan Lu, Ng Ki, *PID and Predictive Control of Electrical Drives and Power Converters using MATLAB / Simulink*, 2015.
- [19] S. Tahir, J. Wang, M. Baloch, G. Kaloi, "Digital Control Techniques Based on Voltage Source Inverters in Renewable Energy Applications: A Review," *Electronics*, **7**(2), 18, 2018, doi:10.3390/electronics7020018.
- [20] M. Valan Rajkumar, P.S. Manoharan, "FPGA based multilevel cascaded inverters with SVPWM algorithm for photovoltaic system," *Solar Energy*, **87**(1), 229–245, 2013, doi:10.1016/j.solener.2012.11.003.
- [21] Maaoui-Ben Ikram, Mohamed Hassine, Naouar Wissem, Mrabet-Bellaaj Najiba, "Model Based Predictive Control For Three-Phase Grid Connected Converter," *Journal of Electrical Systems*, **11**, 463–475, 2015.
- [22] J. Sachs, O. Sawodny, "A Two-Stage Model Predictive Control Strategy for Economic Diesel-PV-Battery Island Microgrid Operation in Rural Areas," *IEEE Transactions on Sustainable Energy*, **7**(3), 903–913, 2016, doi:10.1109/TSSTE.2015.2509031.
- [23] A. Hooshmand, H.A. Malki, J. Mohammadpour, "Power flow management of microgrid networks using model predictive control," in *Computers and Mathematics with Applications*, 869–876, 2012, doi:10.1016/j.camwa.2012.01.028.
- [24] El clima en El Triunfo, el tiempo por mes, temperatura promedio (Ecuador) - Weather Spark, May 2022.

Automatic Counting Passenger System using Online Visual Appearance Multi-Object Tracking

Javier Calle*, Itziar Sagastiberri, Mikel Aramburu, Santiago Cerezo, Jorge García

Fundación Vicomtech, Basque Research and Technology Alliance (BRTA), Donostia-San Sebastián, 20009, Spain

ARTICLE INFO

Article history:

Received: 31 August, 2022

Accepted: 08 October, 2022

Online: 25 October, 2022

Keywords:

People-counting

Multi-object tracking

Fisheye camera

Public transport

Visual appearance modelling

ABSTRACT

In recent years, people-counting problems have increased in popularity, especially in crowded indoor spaces, e.g., public transport. In peak hours, trains move significant numbers of passengers, producing delays and inconveniences for their users. Therefore, analysing how people use public transport is essential to solving this problem. The current analysis estimates how many people are inside a train station by using the number of people entering and leaving the ticket gates or estimating the train occupancy based on conventional CCTV cameras. However, this information is insufficient for knowing the train occupancy. The required data includes vehicle usage: how many people enter or leave a vehicle or which door is the most used. This paper presents a solution to the stated problem based on a multi-object tracker with a sequential visual appearance predictor and a line-based counting strategy to analyse each passenger's trajectory using an overhead fisheye camera. The camera selection inside the train was made after profoundly studying the railway environment. The method proposes a module to compute the total train occupancy. The solution is robust against occlusions thanks to the selected tracker and the fisheye camera field of view. This work shows a proof of concept dataset containing pseudo-real case scenarios of people's affluence in train doors recorded by fisheye cameras. Its purpose is to prove the system's functionality in these scenarios. The proposed approach achieved an overall accuracy of counting people getting on and off of 90.78% in the pseudo-real dataset, proving that this approach is valid.

1 Introduction

In the context of security surveillance, people counting is one of the most interesting tasks in analysing crowds. Although it seems like a simple task, when the crowd density is high, the number of occlusions increases the problem's complexity. During the last few years, this problem has risen significantly in the security field because it allows estimating the number of people in a room, thus limiting access to it. However, people-counting algorithms are also used in outside environments to estimate the number of pedestrians in a specific area.

There are two main circumstances where it is practical to count people in an area. The first one is in an outdoor space, where it is usual to use a CCTV camera on a building wall to overlook pedestrians. This case and the technologies related to it are called crowd counting. For this purpose, it is common to use crowd-density approaches. They behave exceptionally well when dealing with a highly dense crowd. On the contrary, they do not work well with small groups of people, where an error of a single person can mean

a significant change in accuracy.

This paper is an extension of the work initially presented at the IEEE International Conference on Advanced Video and Signal-Based Surveillance [1]. In this case, the multi-object tracker analyses the people's trajectory to count the number of passengers inside a train. Even though the experiments were held in a train-related environment, the offered solution can work in situations where there is a need to count people crossing a narrow space and a limited height to locate the camera. Examples of this may include building doors (banks, shopping centres, stadiums, companies, etc.), other transport (buses) or multitudinous events (festivals, sports events, etc.).

As the objective is to count the number of people inside the train and analyse the influx of people using it, the crowd density approaches are not accurate enough, so other options are considered. The second case is an indoor area CCTV or fisheye cameras. The choice of the camera will depend on the characteristics of the room. Another approach is to know the flow of people getting in and out of a room, especially if there are multiple doors in an area that a single

*Corresponding Author: Javier Calle, email: jcalle@vicomtech.org

camera can not cover. In this case, it is common to use flow-based or detection-based methods to track the people.

In the context of a train, there is a very particular situation; people can only get on and off at train stops. This means that to know the number of people on the train, it is not necessary to count the number of people at all times, just at the train stops.

Another condition to be considered is that, on a train, it is common to find people blocking the door or entering and stopping in the middle of the door. This causes more occlusions and can generate counting errors if the chosen method is not prepared for having a person at the edge of the door.

The next encountered challenge was choosing the counting method. For this, the strategy used is based on route estimation, thus being possible to conclude whether people enter or leave through the door. A multitasking method with a flow door counting strategy has been chosen. All the people in the scene are tracked. And the method can add those who are entering and leaving. So the passenger flow is calculated by comparing the number of people crossing the train door.

Another important point to tackle this issue is the study of the different cameras that could be used. The study was conducted to have the best possible view of the door at the time of entry and exit to ease the video analysis.

The camera that best suited all of the needs was the overhead fisheye camera, as explained in more detail in Section 3. However, using a fisheye camera entails solving a problem of distortion in the shape of people. It is especially challenging at the train's entrance, as it is common to find a different height between the train and the station. That step causes an acceleration in the person's movement through the camera, exacerbated by the camera's distortion. This causes tracking methods based on movement modelling to lose some targets as the complexity of the target's movement increases in this situation.

Given this, the best-suited tracking method is the one that uses visual appearance to aid in the tracking, but it also needs to be robust against the distortion of the cameras. For the detection and tracking of people, the online multi-object tracking approach with an affinity model from previous work [1] is proposed.

This method is based on FairMOT [2]. Still, the addition of the affinity model has been inspired to deal with the visual appearance transformation of the object while it goes through the camera's field of view. This method will allow accurate tracking of people on the scene, as it is fully prepared to deal with the deformation caused by the fisheye cameras.

The model uses a convolutional LSTM encoder-decoder architecture to learn the space-time transformation metric between consecutive re-ID embeddings extracted from the object trajectory. This allows obtaining the next re-ID embedding by considering the long-term appearance information. Furthermore, the tracking algorithm can also handle temporal occlusions in video sequences by feeding back predicted re-ID embeddings into the affinity model.

With the contributions of this work, four problems are solved:

1. Camera positioning and type of camera. After realising a synthetic simulation-based analysis, an overhead fisheye camera is selected to be installed inside the train.
2. The addition of the visual modelling for the tracking to help

the Kalman filter with the issues caused by the distortion of the fisheye camera.

3. Problems caused by the coach step and the train's environment. Solved by the visual appearance-based tracker.
4. Counting people method. The solution is based on all train doors' flow using the tracking results and a counting line.

The report is organised as follows. Section 1 is the current introduction followed by the related work (section 2). This section studies different avant-garde methods to count people based on estimating via area occupancy or trajectory analysis. Additionally, it inspects various people-tracking solutions. Section 3 analyses the railway environment, i.e., it considers the different types and settings of the cameras inside a train car and selects the best option for people counting. Section 4 describes the approach chosen to count people inside a train based on overhead fisheye cameras and the passenger's trajectory. It explores the main stages of the counting people solution, detection, tracking, flow control and occupancy computation. Section 5 presents the obtained results. For this purpose, it first introduces the used datasets for performance evaluation. Straightaway the experimental and global results are given along with a comparison with state-of-the-art works. Section 6 is the conclusion. Here the results are discussed, and conclusions about the people-counting solution are presented. The future work, section 7, describes conceivable improvements and suggestions. Lastly, some acknowledgements for APPRAISE European project are given in Section 8.

2 Related work

As the main method of this article specialises in trajectory-based people counting, this section will first analyse previous SOTA work on occupancy, detection, and trajectory analysis. And it will also present different tracking methods from the SOTA.

2.1 Area occupancy

During the first months of the COVID-19 pandemic, occupancy problems raised their importance as it was essential to prevent disease transmission in closed environments. The main objective was to know how many people were inside an area at a particular moment. These methods are divided into object-detection or density map-based methods. Each person is detected in the first case, while a general estimation is done in the second.

2.1.1 Object based

The approach proposed in [3] uses an overhead video camera. They transform each video frame into a grey-scale picture and subtract the background using the empty scene knowledge. Once verified that the tracked object is a person, they keep track of it, knowing if the person is inside the area.

Another option is the one proposed in [4], where a thermal camera was used to obtain the semantic segmentation for the human. After that, they use a classification model using Adaptive Boosting

(AdaBoost) and a regression model using a shallow neural network to estimate the occupancy.

2.1.2 Density map based

When the pedestrians' density is high, the number of occlusions is also high, and person detection is almost impossible.

In these cases, state of the art is to use methods that estimate a density map and calculate its integral, obtaining the number of objects in the image as [5]–[7]. Also, some "density map" based strategies focus on the most visible part of a human in a crowd, the head, reducing the occlusion effect. The approach made in [8] not only estimates the number of people in a group but localises them with a point in the middle of their heads. They propose a new metric to achieve high localisation errors and counting performances called density Normalised Average Precision (nAP).

2.2 Trajectory analysis

These methods use different strategies to know how many people have entered or left a room. They are divided into image-based or non-image-based methods.

2.2.1 Image based methods

One of the image-based methods is to use a multi-object tracker and analyse the trajectory to count how many people have entered or left a room, as the authors do in [9]. They use a line as a frontier between the inside and the outside of the train. They focus on head detection using a standard overhead camera placed on a train platform roof over the train's door. This method is based on a detector and tracker. Once the trajectory is known, the counting module verifies if the person has crossed the limit line. If the person crosses the line, the counting method checks the direction to determine if the person is entering or leaving the train.

Another similar approach is [10], which tracks heads and uses a frontier line to count people. Their contribution is the analysis of the reference line's height. Alternatively, it is possible to use a region of the image to do the tracking as in [11].

There are different methods to analyse the trajectory. The approach proposed in [12] uses multiple independent lines for counting people. Each line counts the number of people crossing without analysing the direction, just the number of people crossing the lines.

Other methods like [13] propose a strategy that obtains the direction of the trajectories generated by the tracker by computing the angle between the position of the mass centre in the actual frame and its position in a previous frame. In [14], they propose a method consisting of two lines that define an Area of Interest that the person has to cross to be counted. In this case, the direction is determined by which line was crossed first.

In [15], the author defines a Region of Interest (ROI) where they track the objects and obtain the direction by looking at the increasing or decreasing of the y-axis coordinate of the mass centre.

2.2.2 Non image based methods

Some approaches do not use RGB cameras, such as [16], where they use an infrared array sensor. The sensor is equipped with a wide-

angle lens that covers 110° and 75° on each axis, so, if the sensor is placed on the ceiling at 2.6m the sensor will cover 6x3.2meters. The method allows one to count and locate the person in each frame with a margin of 0.3 meters. The dataset used contained data from up to three people simultaneously.

Another method was proposed in [17] using two infrared sensors located at a distance of 15 cm between them. The idea is to use a device that counts how many people have passed through a door. Depending on which IR detect the object first, it is possible to know the direction of that object. This method works with environments that assure that only one person is crossing that door, for example, at ticket gates.

2.3 Tracking

A tracker is needed to be able to analyse the trajectories of people, so different options for tracking were studied. Multi-object tracking approaches are typically categorised into offline and online methods. Offline methods can use all frames in a sequence (present, past and future), whereas online methods only use past and current frames for inference. So the only option to analyse people's trajectory currently getting in or out of the train is to use online methods.

Online methods frequently use the tracking-by-detection approach [18, 19]. In order to connect tracklets or detections between frames, recent online multi-object tracking systems use an affinity model in the data association step. Using pairwise affinity ratings, affinity models attempt to account for occlusions and changes in appearance. These methods can be divided into two categories: (i) robust and discriminant re-ID embeddings-based methods and (ii) sophisticated scoring functions-based methods. For the first, siamese or triplet networks are frequently suggested, as appearance cues are essential. The first approach introduced by [20] proposes a combination of the standard region loss with a triplet loss for maximising and minimising the distance between similar and dissimilar identities. In [21], authors propose deep collaborative reinforcement learning under a unified network.

Sophisticated scoring functions-based methods simultaneously output detected objects and their associated re-ID embeddings, and they focus the attention on an affinity metric design. In [22], a siamese network is explicitly designed to estimate the affinity between the detections by adding the object's appearance. In [23], a quadruplet loss is proposed to emphasise both the object's appearance and its temporal proximity. A more recent proposal is the UMA triplet network, proposed in [24] to learn the single object tracking and affinity prediction tasks simultaneously, creating a unified multi-task learning framework.

Regardless of the approach, it should be noted that all of these algorithms only consider short-term temporal appearance information between successive frames. By teaching an appearance transformation metric, our approach promotes the use of long-term temporal appearance information.

3 Railway environment

Passenger counting in train carriages is a very characteristic problem, as people can only enter and exit at train stops. They also move

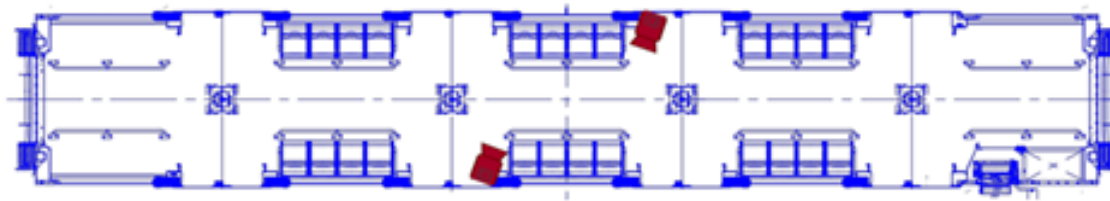


Figure 1: Schema for CCTV use.

together in groups, cross paths, wait at the door until it opens, and move all together at once. Therefore, different situations should be analysed, not only for choosing the best counting strategy but also for setting up the proper type of camera in the correct position to make this task less challenging.

It is important to note that, at certain times of the day, the density of people inside the train can be very high. This implies that the chosen method must be able to operate with a high number of simultaneous objects. In addition, the space inside a coach is minimal, implying that there will be many occlusions. Consequently, finding a counting method that works with high and low densities will be necessary.

While the train is moving, monitoring or tracking people is not necessary, as the train doors are closed, meaning there is no change in the influx of people. Therefore, the trajectory analysis of the users is only necessary when the train stops and the doors to the train open.

As stated before, there is a flow of passengers between carriages in a train, and there is an increased number of occlusions in situations of high occupancy. It would be necessary to count the number of people changing carriages to know the total count in each carriage. The door between carriages is an extra door, which implies a higher number of cameras.

Finally, it is essential to note that it is not necessary to strictly keep each person's ID throughout their journey. It is only needed during their entry or exit of the train, as the objective is to count entries and exits of the carriage through the door. Therefore, considering all this, the number of people will be controlled by focusing on door analysis. To know the total number of people inside the train, counting the number of people entering and exiting at each door is enough. Each door can be analysed separately and then added or subtracted from the people that joined or left the train.

It is crucial to select the best type of camera and its position to make the task easier. So we deeply analysed the possible camera positions and configurations in the wagon to choose the most appropriate for our study.

3.1 Explored camera configurations

It was decided to perform a study based on synthetic simulations to represent the most common and problematic situations in access to a train car. All these simulations were performed with different camera configurations inside the train. Outside will produce more useless tracking due to the people walking near the train but not going in or out. The most representative of which are shown here.

3.1.1 Train's CCTV camera

The first approach is using the CCTV cameras that are already available on the train. For security reasons, these cameras are angled, so the two front doors are checked, and the actions of users are seen to be able to act in case of an emergency, robbery, etc. The layout schematic of the cameras' positions in the coach can be seen in Figure 1.

To check the type of images that would be obtained by this type and the position of the camera, some 3D simulations were carried out. The simulated situations were (i) an empty train with one person entering, (ii) a train with a certain number of passengers already in and a group of people entering through the door.

In the situation where only one passenger is entering, Figure 2, they can be easily monitored. Through analysing images, it is easy to know whether the target is inside or not using this camera.



Figure 2: Example of a CCTV image.

In the second case, Figure 3, there is a greater number of occlusions. Passengers already on the train may occlude the entering people, depending on the distribution of the passengers. If rush hour images were analysed, where the train is almost fully packed before people enter, door visibility would be lost.



Figure 3: Example of a crowded space captured by a CCTV camera.

However, at the moment the group enters the carriage, it is not possible to differentiate whether the passengers in the back have already entered the train or not. There is no visibility of the people in the back of the group. Occlusions with this view will be a big problem, so the position and type of camera must be changed to get a more suitable angle of vision.

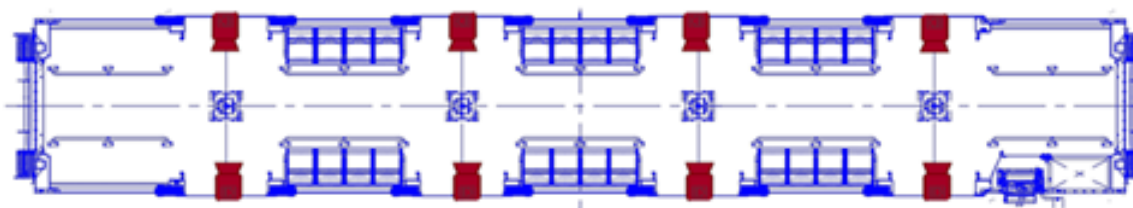


Figure 4: Schema for overhead camera use.

3.1.2 Standard overhead camera

The use of overhead cameras positioned over the doors is considered next. The exact position of the camera is inside the roof of the coach instead of directly above the door, as cameras can not be placed where the door’s mechanism is. This means the camera is slightly displaced towards the inside of the carriage. This position also has the advantage of having the camera at a higher altitude to get a wider field of view of the scene. This kind of view can allow seeing the heads of every person going through the door, reducing the number of occlusions, and it is easier to extract the passenger’s position with respect to the door. A schematic representing the distribution of the cameras can be seen in Figure 4.

The number of cameras is doubled with respect to the previous case, as there is one camera per door.

Figure 5 illustrates a situation where a single person enters the train. The placement of the camera allows for complete visualisation of the passenger. Having complete visibility of the door line allows for distinguishing whether people entered the train or not. However, the field of vision is relatively small, and we can only see the lower part of the door, but the middle and upper parts are not visible. Moreover, the field of view may not be enough to see the entire door if the door is wider or with a lower ceiling.



Figure 5: Example of an overhead camera.

For the second case, in Figure 6, it can be observed that the passengers already in the carriage do not generate any occlusion, as most of them are not visible. Passengers entering the carriage do not occlude each other either, but due to the limited field of vision, we have fewer frames to analyse the trajectory of the passengers.



Figure 6: Example of a crowded space captured by an overhead camera.

3.1.3 Fisheye overhead camera

An overhead camera allows a better perspective of the passengers’ flow through the door. But this solution with a standard camera has a narrow field of view. So, the fisheye camera has been proposed to solve the lack of visibility. The placement is the same as in the previous case (Figure 4), but omnidirectional 180° field of view cameras are used in this one.

Figure 7 illustrates the first experiment, where the person is completely visible. In addition, the image shows a more extensive area inside and outside the train compared to a regular overhead camera. Seeing a larger area of the outside and the coach allows us to analyse the trajectory of the passengers more robustly, as there are more frames where they are visible.

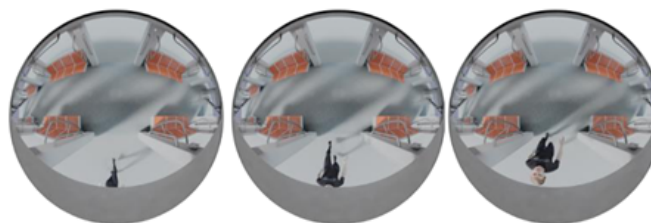


Figure 7: Example of a fisheye overhead camera.

In the second experiment (Figure 8), it can be observed that, similarly to previous cases, occlusions only appear in the case of the group entering the door when they are away from it. At the moment of getting in or out of the carriage, there are no occlusions, although the height of both the person and the camera will affect the perceived distortion.

It should be noted that the camera can only count correctly at the door below the camera, as there will be many occlusions at the opposite door. Hence one camera per door is needed.



Figure 8: Example of a crowded space captured by a fisheye overhead camera.

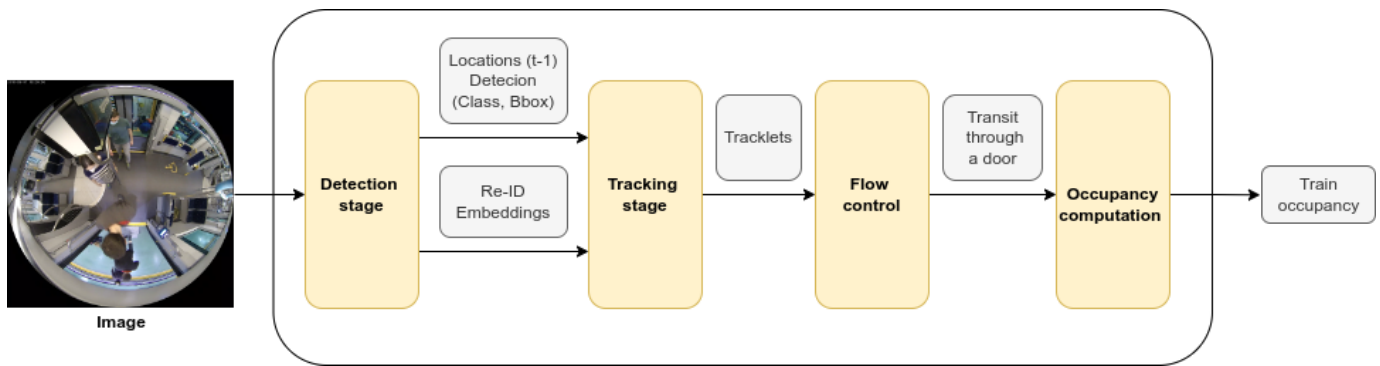


Figure 9: Overview of our overall approach.

3.2 Final configuration of the cameras

The first conclusion is that the camera must be above the door to have a good perspective. Otherwise, the door area is occluded, and the solution can not accurately analyse if a person has boarded or left the train in areas close to the door.

Secondly, after comparing the different types of cameras, it is concluded that both overhead camera options are suitable for the task. As the height of the train ceiling limits the camera location, the best option is to use a fisheye camera to obtain an omnidirectional view, even though the image will be distorted. This camera configuration allows greater flexibility when analysing each person's trajectory since they appear in a more significant number of frames.

In conclusion, the final configuration of our cameras is the one in Figure 4, using overhead fisheye cameras next to each train door.

4 Selected Approach

This section proposes a method to count people inside a train based on overhead fisheye cameras and the passenger's trajectory. Figure 9 shows the schema related to the method.

Both detection and tracking modules are the same as in our previous paper [1], specifically designed to track objects in videos recorded by omnidirectional cameras like the ones in this work. It relies on two main steps for each frame: (i) the detection of the object instances and (ii) the matching of detections to their corresponding tracklets. Once the tracking stage is done, the next step is the counting strategy for each door, where we know the passengers' transit over each doorway. The last step is to count the total number of passengers on the train.

4.1 Detection stage

In keeping with the prior work, the detection pipeline is based on the FairMOT object detection work [2]. This paper's solution uses a network structure which consists of two homogeneous branches to detect the objects and obtain re-ID embeddings in a single step. These embeddings are the feature vector of the detected object, which should ideally give us a smaller distance between the detections of the same object and maximise the space to the other things. For this, the detection network has a convolutional layer with 128

kernels that extract the re-ID features, explained with further detail in the FairMOT work [2].

The essential advantage of this network is that because it does not prioritise object detection over re-ID, the features in the output are ideal for both detection and recognition tasks. Although their work is based on DeepSORT [25], the authors present the results.

4.2 Tracking stage

The structure of this stage can be seen in Figure 10. Notably, the processing pipeline is as follows. Periodically, for each time instant t , any detected object in the scene is represented by $\{c_t^i, r_t^i, e_t^i\}$, where c_t^i is the object class, r_t^i represents the bounding box coordinates $\{x_t^i, y_t^i, w_t^i, h_t^i\}$ and e_t^i is the visual appearance representation of the object, known as re-ID embedding. The bounding box coordinates are given in MOT format [26]; (x,y) represent the top left point of the bounding box, and w and h are the width and height.

Then, depending on the detections in the first frame, a set of tracklets is initialised. As new items enter the scene and new tracklets are created, we continue to associate detections with the scene's existing tracklets for consecutive frames. In the association step, both motion (m) and affinity (a) models are used to calculate the pairwise matching scores s_{ij}^m and s_{ij}^a for every detected object i with every object that has previously been tracked j across successive time instances. A final score s_{ij}^s is calculated by a global scoring function that combines s_{ij}^m and s_{ij}^a scores.

As noted earlier, to link detections with active tracklets, we combine a motion model and an affinity model. This post-processing step is based on DeepSORT [25]. We contribute to this phase by having a single network to predict the embeddings necessary to link active tracklets and detections. As we shall demonstrate in Section 5, the features our network learns are more robust than those of the re-ID module of DeepSORT. Our visual appearance transformation network also learns the appearance evolution over time and estimates the embedding in the next frame once we get the embeddings from detections.

To estimate where the future tracklets will be, the motion model combines a constant velocity model and the Kalman Filter [27]. The scores s_{ij}^m are computed by utilising the squared Mahalanobis distance [28] to calculate the proximity between the predicted and detected bounding boxes. Finally, the unlikely matches are ruled out by thresholding the inverse chi distribution to a 95% confidence interval. In a similar process, the scores s_{ij}^a are computed utilising

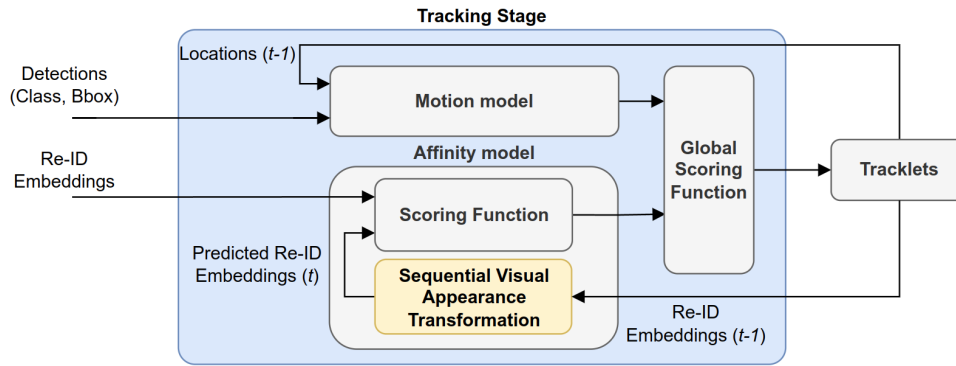


Figure 10: Overview of our online multi-object tracking approach.

the cosine distance to link the visual appearance information between the predicted and detected re-ID embeddings, all of which are based on DeepSORT [25]. The sequential visual appearance transformation network outputs the predicted embeddings online. Finally, using the following equation [25], we combine both distances:

$$s_{ij}^g = \lambda s_{ij}^m + (1 - \lambda) s_{ij}^a \quad (1)$$

where the parameter λ is utilised to balance the impact of the motion and affinity models.

After obtaining the confusion matrix that describes the distances between detections and tracklets, we utilise the Jonker-Volgenant [29] implementation of the linear assignment problem (LAP) algorithm to match pairings that minimise the overall distance. This is a faster implementation of the Hungarian method for LAP. We save a pool of potential active tracks that we keep for n frames when none of the current detections can be matched to them. Although our method is quite similar to DeepSORT [25], we maintain both the new and lost tracks until we get a matching detection for 30 frames. For both new and lost tracks, the number of frames is the same (30). Once the target is detected again, we ought to be able to match it to one of the active tracks visually.

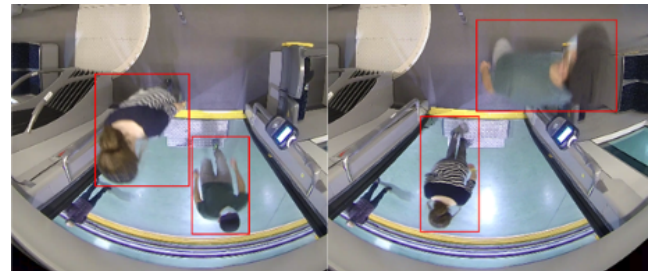
It is crucial to balance the effects of the Kalman and the re-ID embeddings when matching detections with tracks to get accurate results. When examining the image, the Kalman filter can effectively track the targets. Nonetheless, due to the camera's distortion, its constant velocity model causes some problems. The camera is centred on the door, the main area of interest, but that part of the camera is the one that suffers from the highest deformation. This means the target appears to move faster in the central part of the image, so constant velocity can not be assumed. The visual appearance allows us to obtain robustness against occlusions, especially against the high deformation in the door, where we want to know if the passenger is coming into or leaving the train.

4.2.1 Sequential visual appearance transformation network

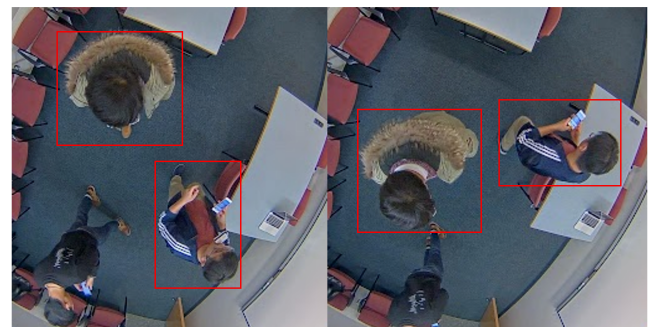
The importance of this model comes from the cameras and environment in which we are developing this work. In the sequence in Figure 11a we can observe the deformation suffered by two people due to the step at the train's entrance. The deformation is more significant when the target is closer to the camera. The height difference created by the step changes the visual appearance of people

more than under normal circumstances. We can see in Figure 11b the deformation in a regular fisheye image taken from the HABBOF [30] public dataset.

In both cases, the people in the sequence have taken only two steps and walked roughly the same distance. But if we look at the person with the green shirt on the right side of the image in Figure 11a, they seem to have moved a lot, and their appearance has changed more when compared to the person in the striped sweatshirt in the right side of the image in Figure 11b.



(a) Position variation by walking on the step.



(b) Position variation by walking on a flat floor.

Figure 11: Compare movement distance due to step

This is the main reason why the visual appearance transformation network is beneficial to model better the change in the person's appearance. The change in appearance is so significant that simply using the embeddings is not enough. We need a dedicated model that learns the visual transformation. On the other hand, we already mentioned that the Kalman filter is not robust enough in this situation. However, it's not only because the main area of interest is the

central part of the image. The step between the train and the ground magnifies the "acceleration" effect. Due to the distortion and the step in the door, our main area of interest, the target's velocity in the image is far from constant when getting in or out of the train.

Now, let us explain the architecture of the proposed network, which we maintained from the previous work. We are working with time data; thus, it makes sense to think about using a recurrent neural network (RNN). RNNs have an internal state known as the hidden state that holds the data relevant to what has been seen, and they sequentially process the new input data to maintain track of the temporal information.

Our sequential visual appearance transformation network has an encoder-decoder structure of deep convolutional long short-term memory (convLSTM) architectures [31]. We can see a graphical representation of a single cell in Figure 12.

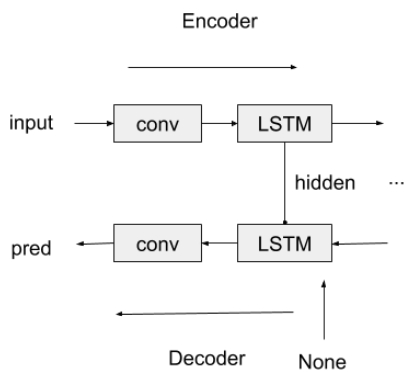


Figure 12: ConvLSTM with an encoder-decoder structure.

As noted, both the encoder and decoder parts are represented by a convLSTM cell. The convLSTM decoder uses the convLSTM encoder's hidden states as its hidden states. The suggested network may be implemented by iteratively concatenating many encoder-decoder structures. We decide to utilise convLSTM since it provides a method for transferring information across sequences. This keeps track of the appearance information for later and stops earlier signals from progressively vanishing. [32]. For this, the encoder captures the context of the visual appearance information, represented by our re-ID embeddings, summarising the previous states of the object trajectory. Conversely, the decoder uses the sequential accumulated transformation, in this instance, the anticipated re-ID embedding for the current frame, to generate the future object appearance.

Using ground truth object sequences, we learn the offline transformation of the visual appearance. We produce a set of re-ID embeddings $e_{gt,j}^i$ for each object identity i that are taken from ground truth detections of the object trajectory. For every $e_{gt,j}^i$, we infer the predicted re-ID embedding $e_{p,j}^i$ by using the proposed network. Finally, we compute the affinity loss as follows:

$$L_{\text{affinity}} = 1 - \left| \frac{1}{N} \sum_{i=1}^N D_c(e_{p,j}^i, e_{gt,j}^i) \right| \quad (2)$$

where D_c represents the cosine distance and N is the batch size. We split the ground truth trajectories into sub-trajectories with a

single length j because the length of the ground truth trajectories is unequal. As a result, we can do the training in batch mode.

4.3 Counting strategy for flow control

Once explained how people are tracked during training, the following section describes how counting people is done. For this purpose, two main factors are taken into account. Firstly, the position and effect of the fisheye camera and how this affects the appearance of people in the image and, therefore, the selection of an appropriate reference point for a person. And, secondly, the logic behind the people counting module.

4.3.1 Fisheye camera effect

Fisheye cameras generate large deformations in objects as they move through space, as explained in section 4.2.1. They specifically produce barrel distortion (Figure 13a), which has more effect at the wide-angle end of the range of the image. The deformation may cause difficulties in developing a good people-counting strategy. So selecting a suitable reference point for a person to identify when he has entered or left a train door is key to obtaining a high hit rate.

Just in the centre of the image of a fisheye camera, an object's appearance will be the least deformed. This can be seen in Figure 13a: the squares located in the middle of the image have no distortion, while the extremes of the image suffer a great distortion. In a real case of a person crossing the door line, only their head and shoulders will be visible in the centre of an image, with no distortion. (Figure 13b).

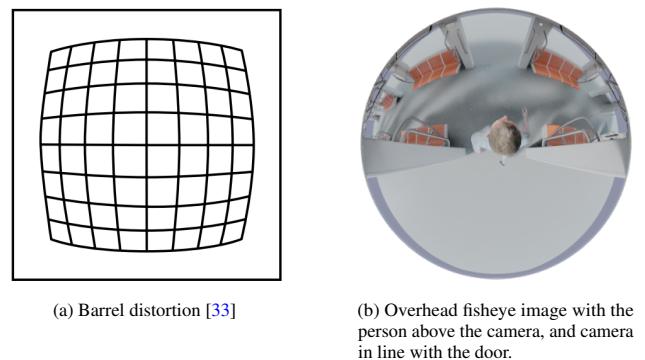


Figure 13: Fisheye camera distortion

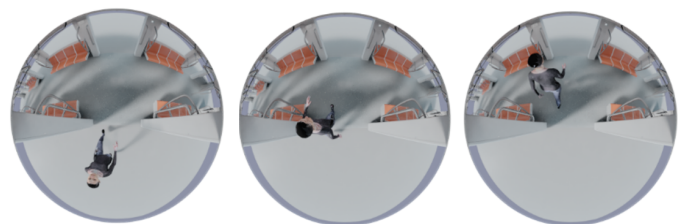


Figure 14: Simulation of an overhead fisheye camera in line with the door. Left: Person approaching the door. Centre: Person below the camera and above the door line. Right: Person walking away from the door.

When an object is further from the centre, the object's image suffers more deformation. For a person, once they are walking away from the camera's centre point, their entire body will appear in the image as long as there are no occlusions. An example can be seen in the left and right images from Figure 14. So the distortion is related to the object's position or person respective to the camera.

Ideally, the best place to locate the camera and detect peoples' positions would be just above the limit line; in this case, the train door axis, as shown in Figure 14. Using the central point of the bounding box would work perfectly as a reference point for the person's position. However, the camera is placed inside the train because of design and structural reasons. Therefore, placing the fisheye camera outside the door axis results in a person's appearance distortion. This makes it somewhat more complicated to define its reference point and to know whether a person is inside or outside the carriage in borderline situations, as in Figure 15. Moreover, this distortion is even increased by some trains' steps that may have at the doors.

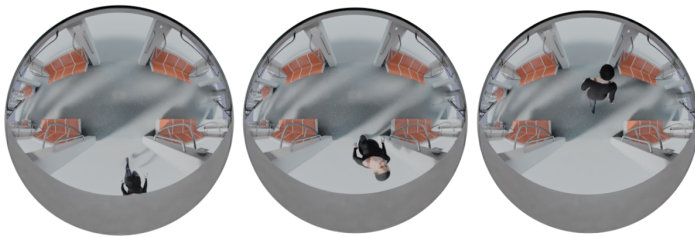


Figure 15: Simulation of an overhead fisheye camera inside the train. Left: Person approaching the door. Centre: Person just above the door line. Right: Person walking away from the door.

The position variation of an object with a constant height moving towards or away from the centre of an overhead fisheye camera is different for the highest and lowest part of the object. This means that when an overhead camera captures the movement of a person, the head's location suffers more variation than the feet' location. For example, in Figure 16 the variation of the head doubles the variation of the feet of the person.

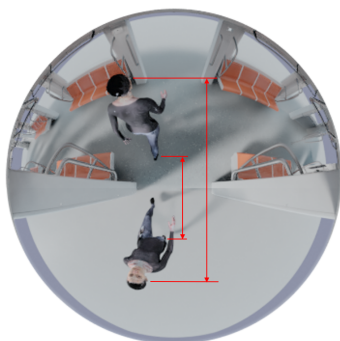
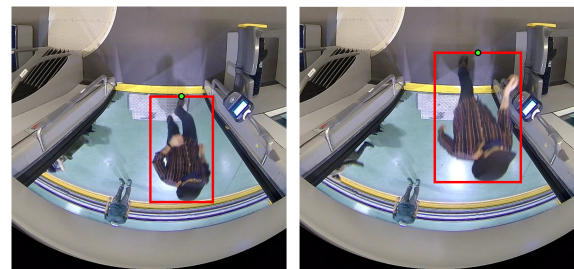


Figure 16: Deformation of top and bottom parts of an object moving in a fisheye camera. In this case, the person's head suffers more variation than the feet.

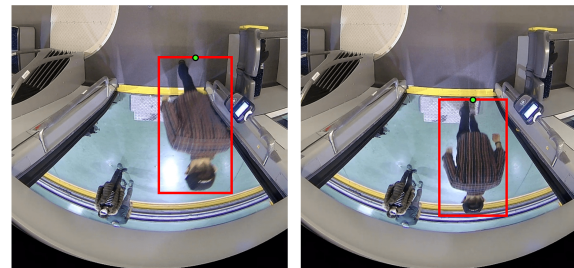
Usually, with standard CCTV cameras, it is common to use the bounding box centre or the person's head as a reference point, as the head is the most visible part. However, based on the problems stated before, with this camera configuration, the most suitable ref-

erence for defining the position of a person is their feet. As for the bounding box, the selected reference point is the upper-centred point related to the feet. Figure 17 shows the entering and exiting conditions picking the feet, located in the upper-centred point of the bounding box, as a reference point to consider that a person has crossed the door line axis.

While entering the train door (Figure 17a) the person is first entirely outside the train. The right image shows that most of the body appears outside the train, but the feet are inside. That means that the person has entered the train. This happens due to the previously explained distortion that depends on the height of an object. While exiting the train (Figure 17b) the left image shows that most of the body is outside the train, but is not considered that the person has left the train until the feet are out of it. This condition is fulfilled in the right image, where the feet are finally outside the train door limit.



(a) Entering condition



(b) Exiting condition

Figure 17: Entering and exiting conditions of a person through a train door (The train door limit is the yellow line).

This way, if a person is standing right at the door's limit, even if their body's bounding box is mostly outside the train, the person will be considered inside the train, as in Figure 18.

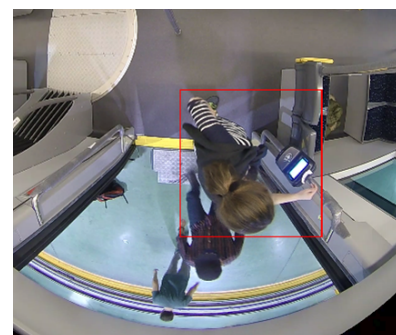


Figure 18: Example of a person standing right under the door.

4.3.2 Counting logic

The counting logic is based on the state-of-the-art of [34]. The main idea is to determine a line and count how many people have crossed it in each direction. The line is defined as a horizontal line in the centre of the image.

To determine if an object has crossed a limit line, the author of the paper mentioned above uses the vertical (y-axis) coordinate of the centre of the bounding box of a person in each frame. Then, the current position and the mean value of the previous positions of the tracked person are considered to evaluate the crossing. As it states, the mean of all the previous points is selected because:

”The reason we take the mean is to ensure our direction tracking is more stable. If we stored just the previous centroid location for the person, we leave ourselves open to the possibility of false direction counting. [...] by taking the mean, we can make our people counter more accurate.”

In the current case of this paper, the limit line will be defined as the limit of the door (notice the yellow line in the Figures 17). So it will also be a horizontal line in the image. A person will be considered that has crossed the line if the limit line’s vertical (y-axis) value is between the current position and the mean of the previous ones. A representation of the stated logic can be seen in Figure 19.

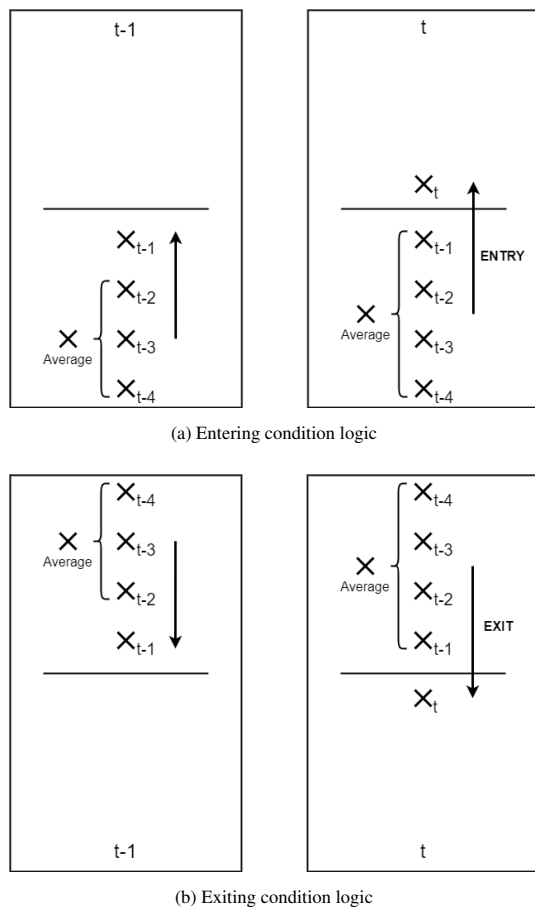


Figure 19: Entering and exiting logic of a person crossing the line.

- **Enter condition logic** (Figure 19a): A person has entered the

train if:

- The current reference point is above the limit line.
- The average of the previous points is below the line.

(The person is moving to the upper part of the image, representing the inside of the train.)

- **Exit condition logic** (Figure 19b): A person has exited the train if:

- The current reference point is below the limit line.
- The average of the previous points is above the line.

(The person is moving to the lower part of the image, representing the outside of the train.)

Some changes were made to the approach mentioned above due to some requisites specific to using the fisheye camera. Instead of using the bounding box centre, the reference point is the top middle point. This point coincides with the location of the feet in the fisheye images, as explained in Section 4.3.1; this reference point is more suitable to determine if a person is inside or outside the train.

The objective of the counting logic is to analyse the flow through the door. If a person goes in or out of the train multiple times in the same recording, the system must count every time the person crosses the line limit (see Figure 20). This may carry problems related to the counting logic, especially with the average of the previous reference points. If the person goes through the door several times, the average point will be unsuitable for the stated logic. That is why the previous tracking points are reset after a person crosses the line limit to avoid further problems. This way, the average position is kept on one side of the limit line, and if the person crosses again, even with the same tracking ID, the logic will still work.

The paper proposes a solution to reset the trajectories based on separating the whole trajectory into sub-trajectories. Every time a tracked person crosses the limit line in either direction, a sub-trajectory containing the previous points of the tracking is saved and set aside. Then, a new sub-trajectory is started, containing only the first reference point of the moment of entering or exiting the door. Figure 21 shows how the trajectory of Figure 20 is separated into four sub-trajectories.

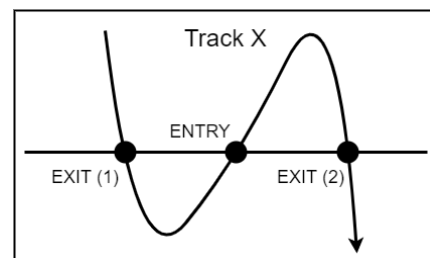


Figure 20: Example of the trajectory of a person entering and exiting multiple times.

This way, the average of the previous points is kept on one side of the line, and as soon as a person crosses the line, the module will count as the entry or exit and reset the previous points for the next sub-trajectory. For example, for the first exit in Figure 21 (Sub-track X_1) the average of the previous points is on the upper side of the

line. Once the person crosses the line (green circle), another sub-trajectory is started (Sub-track X_2). This sub-track ends once the person crosses the line and enters (orange circle). The average point in red is kept on the downside of the line. Similarly happens with the next sub-trajectory (Sub-track X_3), but the average is kept on the upper side. The trajectory ends when the person is no longer tracked (Sub-track X_4).

Finally, the flow of a door is composed of two positive integer numbers:

- **Enter flow:** each person that enters the train counts as a **positive enter**.
- **Exit flow:** each person that exits the train counts as a **positive exit**.

Separating the enter and exit values gives more information about the flow of a door. If a unique number was given as a flow, the information of people who entered or exited the door would be lost. For example, it would be the same for the cases where two people enter and two people exit and for no one entering and exiting the door (flow equal to zero in both cases).

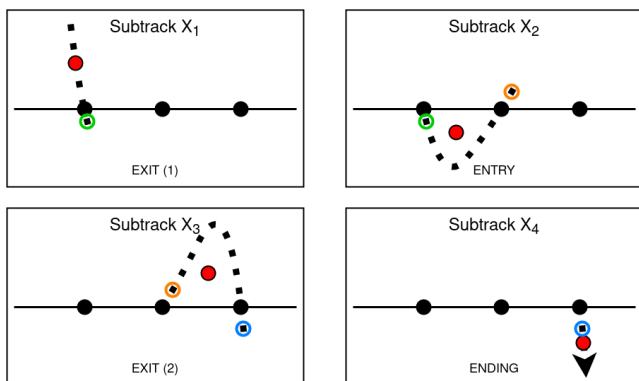


Figure 21: Considered sub-trajectories to evaluate if a person has crossed or not the line in multiple crossings within the same recording. The red dot indicates the average point of the sub-trajectory. The dotted line indicates each person’s step. The coloured circle over a dot indicates the end/beginning of a sub-track.

4.4 Occupancy computation

The methodology for calculating the occupancy of a train is formed by the sum of the people entering minus the sum of the people leaving the train at each door; see Equation 3. It’s important to notice that a particular door’s flow can have either positive, zero or negative value. But the overall train occupancy will be either zero or positive.

$$Total_flow_{door} = Enter_flow_{door} - Exit_flow_{door} \quad (3)$$

Once the total flow of each door is known, to calculate the overall train occupancy, all door flow values are added together, as shown in 4. This particular value will indicate the number of passengers on the train at a given time.

$$Total_occupancy_{train} = \sum_{d=0}^{N_{door}} Total_flow(d) \quad (4)$$

$flow(d)$ is the flow door value, and d is the door number.

5 Results

5.1 Datasets

The next section presents the datasets used for the training and testing of the detection and tracking models and the use case of people counting through trajectory analysis. The datasets are separated into two sections: Public datasets (Section 5.1.1), which were used to train the detection and tracking models; and Proof of concept dataset (Section 5.1.2), which consists of video recordings of a real train fisheye camera where people enter and exit a train.

5.1.1 Public datasets (Detection and Tracking oriented)

The performance of our method is assessed over a certain amount of data obtained from omnidirectional cameras. We considered seven publicly available datasets specifically created to address the problem of people tracking and detection. They combine multiple indoor environments, including a wide range of challenging scenarios: crowded room, severe body occlusions, various body poses, head camouflage (e.g., hoods, hats) and low-light conditions.

Table 1 provides a summary of those datasets, including the number of frames, the number of people (IDs), and the data source for each of them.

It should be noted that the HABBOF, FES, and PIROPO databases lack tracking information.

We added some data captured in trains with the specific camera setting we proposed for these datasets.

Table 1: Public omnidirectional datasets.

Dataset	Images	IDs	Data Source
CEPDOF [35]	25.5k	51	Real
HABBOF [30]	5.8k	-	Real
FES [36]	301	-	Real
Bomni [37]	12.9k	85	Real
THEODORE [36]	100k	2307	Synthetic
Mirror World [38]	7k	63	Real
PIROPO [39]	3k	-	Real
PATHTRACK [40]	276.4k	16,287	Real
Total	430.9k	18,793	-

5.1.2 Proof of concept dataset (People counting)

The dataset for obtaining the results of counting people consists of several video clips. The recordings were captured by a fisheye camera located at the door of a train coach. The videos contain different cases of people entering and exiting the door:

- Cases of one person to multiple people entering and exiting the door one by one.
- People entering or exiting together in groups on the train.
- Video recordings with two or more people, usually crossing their paths.

- Cases where people enter and exit the train at varying walking speeds (Fastly and slowly moving passengers).
- Other actions such as stopping in the middle of the door.

All the clips were classified into three categories depending on the difficulty of the video stream:¹

- **”Low”**: In these videos, there is usually one person who enters and/or exits the train door.
- **”Medium”**: There are usually 2 or 3 people who enter and/or exit the train.
- **”High”**: There are more than five people who enter and/or exit the train.

Once all the clips are grouped in the three types of difficulty, the dataset remains as in Table 2.

Table 2: Number of clips separated into difficulties.

Difficulty	No. of clips
Low	41
Medium	39
High	22

The ground truth data of the different clips consists of the tally of how many people enter and exit the train door, i.e., the total count of people crossing the limit line (door flow). Alongside the difficulty level and the distinction between people entering and exiting the train door, the ground truth data is composed as shown in Table 3.

Table 3: Ground truth data of the count of people crossing the train door line. The difference between entry and exit and the three difficulty levels of clips are reflected.

	People crossing count (GT)		
	Low	Medium	High
Entry	27	47	68
Exit	23	49	68
Total	50	96	136

In total, the dataset contains **282** door flows or entries and exits, which are divided into ”Low”, ”Medium”, and ”High” difficulties.

5.2 Experimental evaluation

Our previous work explained how we obtain the best tracker configuration to achieve a state-of-the-art tracker [1].

Although our main contribution to the tracking stage was proposed in the association part, we also trained the FairMOT object detector network [2] following the same implementation details as the authors. The original network is trained on frontal view images,

¹Even though the video difficulties are separated into three subsets, the ”Low” and ”Medium” video complexities do not differ too much. The major dissimilarity is with the ”High” difficulty videos.

so its performance on omnidirectional data drops dramatically. Consequently, we have used all omnidirectional datasets to fine-tune the pre-trained network.

We select trajectories with a sequence length of $j = 40$ frames for our sequential visual appearance transformation network. This value was chosen because in a camera recording at 15-20 fps, 40 frames are approximately 2 seconds of the recording, and a person will approximately take that time to enter a train; thus, we have 40 consecutive re-ID embeddings for each person’s identity.

The network can keep the identification of the tracked individual for as many frames as they are in the scene, although it was designed to function with as little as 40 frames in training.

The tracklet is retained in the pool of potential identities for 30 frames if the system loses track of a person. If, after 30 frames, the system cannot match the tracklet with any further detections, we assume the individual has departed the scene. This part is important for evaluating the public datasets. However, as the goal is to know whether a person has walked through a door and the direction they walked in, keeping track of them for longer while they are inside the train is not essential.

We have used the same configuration as in our previous work [1] where we prove that using a high λ value and, therefore, giving more weight to the score of the Kalman filter results in a significantly lower outcome. This shows the importance of using appearance-based matching, adding robustness against occlusions. The best option is to use a low λ value but different from zero, so we use $\lambda = 0.1$.

The system’s ability to re-ID people comes from visual information. In case of occlusion, if the target moves through the image, a motion-only model would discard the detection and start a new tracklet. That means we would be unable to count the action if the occlusion happens during an entry or exit if it wasn’t for the visual model.

Following the standard practices in multi-object tracking, we use the multi-object tracking accuracy (MOTA) [41] and the ratio of correctly identified detections over the average number of ground-truth and computed detections (IDF1) for rigorously evaluating re-ID features with ground-truth detections.

To evaluate the performance of our tracker, we have considered a unique scenario containing the test set from all datasets that include ground truth tracking information, meaning: CEPDOF, MWR, and Bomni, with six different sequences in total. Also, to achieve a better performance, we train our tracker with the PATHTRACK dataset [40]. This dataset is one of the largest publicly available multiple objects tracking data sets.

Following the same implementation details as in our previous work [1], we obtain three proposed networks. Table 4 shows the MOTA and IDF1 results for the baseline FairMOT method and our three proposed networks. The convLSMT-Enc-Dec-3 achieves the best MOTA and IDF1 results with 88.21% and 87.77%, respectively.

Table 4: Evaluation of our online tracking by detection approach including PATH-TRACK dataset [40]

Model	MOTA (%)	IDF1 (%)
FairMOT	82.94	80.25
FairMOT + convLSMT-Enc-Dec-1	87.85	87.73
FairMOT + convLSMT-Enc-Dec-3	88.21	87.77
FairMOT + convLSMT-Enc-Dec-5	87.15	87.55

We compare the performance of our approach on the Bomni [37] and Mirror World [38] datasets as we only found results for these two datasets. Table 5 demonstrates the benefits of our affinity model concerning state-of-the-art methods. As state-of-the-art methods do, we also include multi-object tracking precision (MOTP) for this comparison. Results show that our approach outperforms all existing methods considering the omnidirectional perspective. In particular, it improves the best performance (93.5%) obtained by BTLD [42] by almost 2% using the Bomni dataset. Similarly, we outperform the best performance (38.4%) obtained so far by SORT [38] by more than 40% using the Mirror World dataset.

Due to the lack of recent results for omnidirectional datasets, we decided to compare ourselves with DeepSORT [25]. We use the detections of our model and perform the tracking with their approach. Table 5 and 6 show results across the six test sequences. We used the model with $\lambda = 0$ for comparison, as that is the value they used in their final implementation. Table 5 shows that using FairMOT instead of DeepSORT yields slightly better results, proving the re-ID embeddings of their work are better than those of the original DeepSORT. Table 6 shows that our method improves tracking given the increase in the number of mostly and partially tracked people.

Table 5: Comparison with state-of-the-art methods.

Approach	MOTA (%)	MOTP (%)	IDF1 (%)
Bomni Dataset			
FTMO [37]	73.52	72.00	-
FTMO (updated) [43]	86.27	72	-
RTMOT [42]	78.55	76.74	-
BTLD [44]	93.5	-	-
Ours	94.27	92.14	95.14
Mirror World Dataset			
SORT [38]	38.4	-	32.1
Ours	84.14	81.93	88.68
Across all datasets (MW, Bomni and CEPDOF)			
DeepSORT[25]	81.37	80.15	79.98
FairMOT[2]	82.94	80.34	80.25
Ours	88.03	84.25	86.87

Finally, Figure 22 shows that the presented method is more robust to the appearance distortion caused by overhead cameras than DeepSORT. Moreover, it can recognise the target in the centre of the image, whereas DeepSORT changes its ID due to appearance distortion.

Taking all of these results into account, we prove that adding the sequential visual appearance transformation network helps with the reidentification task in the case of fisheye cameras. Due to the deformation, the appearance of the objects is less constant than with regular cameras, so we need the aid of a model specialised in predicting the object’s appearance and comparing the embeddings. We can’t use the embeddings directly because the appearance changes between frames.

Table 6: Tracking quality compared with DeepSORT.

Model	Mostly tracked	Partially tracked	Totally lost
DeepSORT	16	13	6
FairMOT + convLSMT-Enc-Dec-3	20	11	4

5.3 Global results

The proof of concept dataset defined in Section 5.1.2 is used to obtain the results of the people counting method. This dataset is exclusively used to get the results of the people counting module because it is the closest dataset to a real-case scenario, the main objective is to check the feasibility of the people counting logic from Section 4.3.2. The dataset is not considered significant enough to present the results of the detection and tracking module due to its size.

The accuracy results for each difficulty level were based on the total count of entries and exits from each video divided by its ground truth (GT), as shown in Equation 5. The following Table 7 shows the accuracy results of the people counting logic.

$$accuracy_{Entry/Exit}(\%) = \frac{\sum Output}{\sum GT} \tag{5}$$

Table 7: People counting accuracy (%).

	People counting accuracy (%)		
	Low	Medium	High
Entry	100.00	97.87	91.18
Exit	100.00	89.80	79.41
Mean	100.00	93.75	85.29

The overall accuracy of counting people getting on and off is **90.78%**. The worst results are presented with "High" difficulty clips, as the detector may fail in crowded situations or when people cross their paths. Even though the dataset used to obtain these results is based on real case scenarios (recorded with fisheye cameras and with people entering and exiting the train door), the number of door flows is not representative enough for a generalization. So the results might not be reliable. Future work aims to create a more extensive dataset with more realistic scenarios to validate the people-counting module alongside the detection and tracking models.

The approach proposed in [9] was similar to this project’s strategy. As the author uses a tracker and a counting line to know how

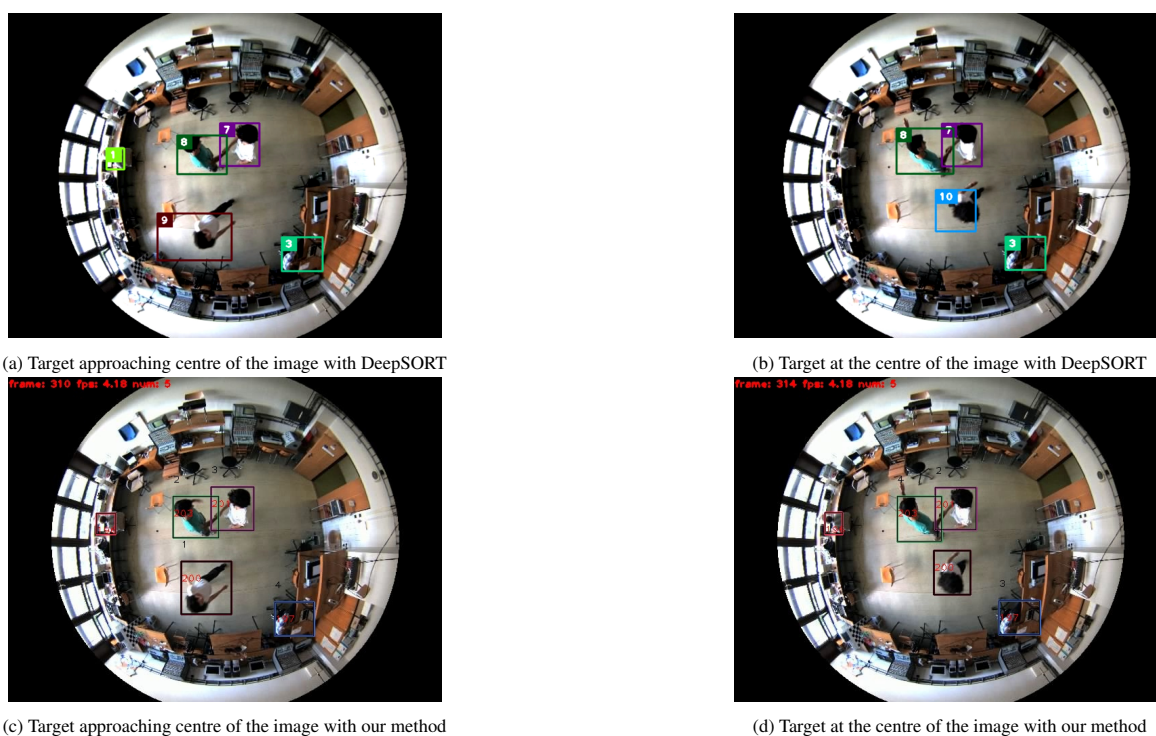


Figure 22: One of the scenarios where our method can keep track of a target compared to state-of-the-art methods.

many people entered or left the train. In this case, it uses a standard overhead camera, so there is no image distortion. This type of camera needs a higher position to have enough vision to analyze the passengers' flow, so the point of view (camera location) is outside the train, on the roof of a train platform. The accuracy metric used in this proposal is based on a confusion matrix. The ground truth data of the videos specifies when a person has entered or exited the train. The proposal achieves an accuracy of 92.01% and 92.47% in counting people leaving and entering the train, respectively.

The approach in this paper instead is based on an overhead fisheye camera inside the train. A fisheye camera can be located in a lower position maintaining a wide viewing angle, and, therefore, inside the train, close to the door. This location's advantage is that the cameras can follow the passengers' trajectory inside and outside the train at the expense of having distortion. But, as explained in section 4.3.1, the tracker solves the fisheye camera's image distortion problem. The accuracy metric used in this paper is based on counting entries and exits, achieving an overall accuracy of 90.78% against the proof of concept dataset.

Comparing the results and affirming which method is better does not make sense since the cameras and the databases are different. The only viable comparison is to evaluate the accuracy of the two solutions and check that the results are similar. It is impossible to affirm that one methodology is better than the other, as their goal is only to count people, but we also want to analyze the trajectory and the influx of people using the train.

6 Conclusions

This paper presents a method based on video sequences to count the number of people inside a train car based on the doors' flow. The technique can be applied in environments with narrow spaces and a limited height to locate the camera, such as buildings, transports or events where a door limits the entry. The proposed approach is based on an appearance-based multi-object tracker and a door's flow counting method that analyze the trajectory of each passenger, counting how many times the people enter or leave the coach.

A study of the best camera type and its location was done to obtain the best possible vision of the passengers at the door. After analyzing the train's environment and carrying out different simulations, the best results were given by an overhead fisheye camera. This camera causes distortion, which our appearance model can handle, improving the performance achieved by the motion modelling-only models. Moreover, the selected trackers can also handle the step acceleration problem.

Once the trajectory was known, a flow control module based on a counting line was developed to calculate the number of times the passengers crossed the line in each direction. Different options for the reference point of a bounding box were regarded, and the central upper point was selected as the best reference point to decide whether a person was on either side of the line. Finally, the overall train occupancy module knows the train occupancy based on all the door's flow information.

After all this work, it is possible to affirm that using fisheye cameras allows for better tracking of people thanks to their broader field of view. The selected tracker can solve the distortion problems caused by the fisheye camera. Moreover, the counting method is robust against the different situations found on a train, and it is

successfully tested on a proof-of-concept dataset. Finally, it is confirmed that the previous tracker [1] works as well as expected in a different and more complex environment.

7 Future work

It has been proven that the method works, but its accuracy cannot be confirmed because the dataset used is small and in a controlled environment. The future line of work is to obtain a dataset taken in a real environment, annotate it and check its absolute precision. As for the algorithm, the next step would be to try a Generative adversarial network (GAN) [45] to model the appearance of the detections, as this model has proven to be a very effective way of predicting visual appearance in a time sequence.

8 Acknowledgments

This work has been partially funded by the European Union's H2020 research and innovation programme under grant agreement 101021981, project APPRAISE (Facilitating public & private security Operators to mitigate terrorism scenarios against soft targets).

References

- [1] I. Sagastiberri, N. v. d. Gevel, J. García, O. Otaegui, "Learning Sequential Visual Appearance Transformation for Online Multi-Object Tracking," in 2021 17th IEEE International Conference on Advanced Video and Signal Based Surveillance (AVSS), 1–7, 2021, doi:10.1109/AVSS52988.2021.9663809.
- [2] Y. Zhang, C. Wang, X. Wang, W. Zeng, W. Liu, "FairMOT: On the Fairness of Detection and Re-Identification in Multiple Object Tracking," arXiv preprint arXiv:2004.01888, 2020.
- [3] E. Khoumeri, H. Fraoucene, E. Khoumeri, C. Hamouda, R. Cheggou, "People Counter with Area Occupancy Control for Covid-19," 405–415, 2021, doi:10.1007/978-3-030-63846-7_38.
- [4] A. Naser, A. Lotfi, J. Zhong, "Adaptive Thermal Sensor Array Placement for Human Segmentation and Occupancy Estimation," IEEE Sensors Journal, **21**(2), 1993–2002, 2021, doi:10.1109/JSEN.2020.3020401.
- [5] Z.-Q. Cheng, J.-X. Li, Q. Dai, X. Wu, A. Hauptmann, "Learning Spatial Awareness to Improve Crowd Counting," in 2019 IEEE/CVF International Conference on Computer Vision (ICCV), 6151–6160, 2019, doi:10.1109/ICCV.2019.00625.
- [6] Y. Li, X. Zhang, D. Chen, "CSRNet: Dilated Convolutional Neural Networks for Understanding the Highly Congested Scenes," 1091–1100, 2018, doi:10.1109/CVPR.2018.00120.
- [7] Y. Miao, Z. Lin, G. Ding, J. Han, "Shallow Feature Based Dense Attention Network for Crowd Counting," in The Thirty-Fourth AAAI Conference on Artificial Intelligence, AAAI 2020, The Thirty-Second Innovative Applications of Artificial Intelligence Conference, IAAI 2020, The Tenth AAAI Symposium on Educational Advances in Artificial Intelligence, EAAI 2020, New York, NY, USA, February 7–12, 2020, 11765–11772, AAAI Press, 2020.
- [8] Q. Song, C. Wang, Z. Jiang, Y. Wang, Y. Tai, C. Wang, J. Li, F. Huang, Y. Wu, "Rethinking Counting and Localization in Crowds: A Purely Point-Based Framework," 2021.
- [9] S. A. Velastin, R. Fernández, J. E. Espinosa, A. Bay, "Detecting, Tracking and Counting People Getting On/Off a Metropolitan Train Using a Standard Video Camera," Sensors, **20**(21), 2020, doi:10.3390/s20216251.
- [10] D. Kuplyakov, Y. Geraskin, T. Mamedov, A. Konushin, "A Distributed Tracking Algorithm for Counting People in Video by Head Detection," paper26–1, 2020, doi:10.51130/graphicon-2020-2-3-26.
- [11] J.-W. Kim, K.-S. Park, B.-D. Park, S.-J. Ko, "Real-time vision-based people counting system for the security door," in Proceedings of the IEEE Conference, 1416–1419, The Institute of Electronics and Information Engineers, 2002.
- [12] J. Barandiaran, B. Murguia, F. Boto, "Real-time people counting using multiple lines," in 2008 Ninth International Workshop on Image Analysis for Multimedia Interactive Services, 159–162, IEEE, 2008.
- [13] J. Ahmad, H. Larijani, R. Emmanuel, M. Mannion, A. Javed, "An intelligent real-time occupancy monitoring system using single overhead camera," in Proceedings of SAI Intelligent Systems Conference, 957–969, Springer, 2018.
- [14] S. Yu, X. Chen, W. Sun, D. Xie, "A robust method for detecting and counting people," in 2008 International conference on audio, language and image processing, 1545–1549, IEEE, 2008.
- [15] P. Chato, D. J. M. Chipantasi, N. Velasco, S. Rea, V. Hallo, P. Constante, "Image processing and artificial neural network for counting people inside public transport," in 2018 IEEE Third Ecuador Technical Chapters Meeting (ETCM), 1–5, IEEE, 2018.
- [16] M. Bouazizi, C. Ye, T. Ohtsuki, "Low-Resolution Infrared Array Sensor for Counting and Localizing People Indoors: When Low End Technology Meets Cutting Edge Deep Learning Techniques," Information, **13**(3), 2022, doi:10.3390/info13030132.
- [17] R. L. dos Santos, H. C. de Oliveira, M. C. de Almeida, D. F. Vieira, E. P. L. Junior, T. Ji, "A Low-Cost Bidirectional People Counter Device for Assisting Social Distancing Monitoring for COVID-19," Journal of Control, Automation and Electrical Systems, **33**(4), 1148, 1160, 2022, doi:10.1007/s40313-022-00916-z.
- [18] P. Bergmann, T. Meinhardt, L. Leal-Taixe, "Tracking Without Bells and Whistles," in Proceedings of the IEEE/CVF International Conference on Computer Vision (ICCV), 2019.
- [19] W. Tian, M. Lauer, L. Chen, "Online Multi-Object Tracking Using Joint Domain Information in Traffic Scenarios," IEEE Transactions on Intelligent Transportation Systems, **21**(1), 374–384, 2020, doi:10.1109/ITITS.2019.2892413.
- [20] W. V. Ranst, F. De Smedt, J. Berte, T. Goedemé, "Fast Simultaneous People Detection and Re-identification in a Single Shot Network," in 2018 15th IEEE International Conference on Advanced Video and Signal Based Surveillance (AVSS), 2018, doi:10.1109/AVSS.2018.8639489.
- [21] L. Ren, J. Lu, Z. Wang, Q. Tian, J. Zhou, "Collaborative Deep Reinforcement Learning for Multi-object Tracking," in V. Ferrari, M. Hebert, C. Sminchisescu, Y. Weiss, editors, Computer Vision – ECCV 2018, 2018.
- [22] X. Dong, J. Shen, "Triplet Loss in Siamese Network for Object Tracking," in Proceedings of the European Conference on Computer Vision (ECCV), 2018.
- [23] J. Son, M. Baek, M. Cho, B. Han, "Multi-object Tracking with Quadruplet Convolutional Neural Networks," in 2017 IEEE Conference on Computer Vision and Pattern Recognition (CVPR), 3786–3795, 2017, doi:10.1109/CVPR.2017.403.
- [24] J. Yin, W. Wang, Q. Meng, R. Yang, J. Shen, "A Unified Object Motion and Affinity Model for Online Multi-Object Tracking," in Proceedings of the IEEE/CVF Conference on Computer Vision and Pattern Recognition (CVPR), 2020.
- [25] N. Wojke, A. Bewley, D. Paulus, "Simple Online and Realtime Tracking with a Deep Association Metric," 2017.
- [26] P. Dendorfer, H. Rezatofighi, A. Milan, J. Shi, D. Cremers, I. D. Reid, S. Roth, K. Schindler, L. Leal-Taixé, "MOT20: A benchmark for multi object tracking in crowded scenes," CoRR, **abs/2003.09003**, 2020.
- [27] R. E. Kalman, "A New Approach to Linear Filtering and Prediction Problems," Transactions of the ASME–Journal of Basic Engineering, **82**(Series D), 35–45, 1960.

- [28] P. C. Mahalanobis, "On the Generalised Distance in Statistics," *Proceedings of the National Institute of Sciences of India*, **2**(1), 49–55, 1936.
- [29] R. Jonker, A. Volgenant, "A shortest augmenting path algorithm for dense and sparse linear assignment problems," *Computing*, **38**(4), 325–340, 1987.
- [30] S. Li, M. Tezcan, P. Ishwar, J. Konrad, "Supervised People Counting Using An Overhead Fisheye Camera," in *2019 16th IEEE International Conference on Advanced Video and Signal Based Surveillance (AVSS)*, 1–8, 2019, doi:10.1109/AVSS.2019.8909877.
- [31] X. Shi, Z. Chen, H. Wang, D.-Y. Yeung, W. kin Wong, W. chun Woo, "Convolutional LSTM Network: A Machine Learning Approach for Precipitation Nowcasting," 2015.
- [32] S. A. Rahman, D. A. Adjeroh, "Deep Learning using Convolutional LSTM estimates Biological Age from Physical Activity," *Scientific Reports*, 2019, doi:10.1038/s41598-019-46850-0.
- [33] G. Vass, "Applying and removing lens distortion in post production," 2003.
- [34] A. Rosebrock, "OpenCV People Counter," <https://pyimagesearch.com/2018/08/13/opencv-people-counter/>, 2018, [Online; accessed 12- Aug- 2022].
- [35] Z. Duan, M. O. Tezcan, H. Nakamura, P. Ishwar, J. Konrad, "RapiD: Rotation-Aware People Detection in Overhead Fisheye Images," 2020.
- [36] T. Scheck, R. Seidel, G. Hirtz, "Learning from THEODORE: A Synthetic Omnidirectional Top-View Indoor Dataset for Deep Transfer Learning," *2020 IEEE Winter Conference on Applications of Computer Vision (WACV)*, 2020, doi:10.1109/wacv45572.2020.9093563.
- [37] B. E. Demiroz, I. Ari, O. Eroglu, A. A. Salah, L. Akarun, "Feature-based tracking on a multi-omnidirectional camera dataset," in *2012 5th International Symposium on Communications, Control and Signal Processing*, 1–5, 2012, doi:10.1109/ISCCSP.2012.6217867.
- [38] R. B. Knapp, N. F. Polys, J.-B. Huang, A. Ibrahim, N. Ma, C. Hurt, Y. xiao, "MW-18Mar Dataset," .
- [39] U. P. d. M. G.-U. Grupo de Tratamiento de Imágenes, "PIROPO Database: People in Indoor ROoms with Perspective and Omnidirectional cameras," .
- [40] S. Manen, M. Gygli, D. Dai, L. V. Gool, "PathTrack: Fast Trajectory Annotation with Path Supervision," 2017.
- [41] R. Stiefelhagen, K. Bernardin, R. Bowers, J. Garofolo, D. Mostefa, P. Soundararajan, "The CLEAR 2006 Evaluation," in R. Stiefelhagen, J. Garofolo, editors, *Multimodal Technologies for Perception of Humans*, 1–44, Springer Berlin Heidelberg, Berlin, Heidelberg, 2007.
- [42] H. S. P. Brauer, *Camera based Human Localization and Recognition in Smart Environments*, Ph.D. thesis, University of the West of Scotland, 2014.
- [43] B. Demiroz, A. Salali, L. Akarun, "Multiple person tracking using omnidirectional cameras," 1231–1234, 2014, doi:10.1109/SIU.2014.6830458.
- [44] G. Gemignani, *BTLD+: A Bayesian Approach to Tracking Learning Detection by Parts*, Ph.D. thesis, UNIVERSIT'A DEGLI STUDI DI MILANO, 2013.
- [45] I. Goodfellow, J. Pouget-Abadie, M. Mirza, B. Xu, D. Warde-Farley, S. Ozair, A. Courville, Y. Bengio, "Generative adversarial nets," in *Advances in neural information processing systems*, 2672–2680, 2014.

Long-term Bottom-up Modeling of Renewable Energy Development in Morocco

Jabrane Slimani^{*1}, Abdeslam Kadrani¹, Imad EL Harraki², El hadj Ezzahid³

¹Research Laboratory in Information Systems, Intelligent Systems and Mathematical Modeling, National Institute of Statistics and Applied Economics, Rabat, Morocco

²Research Laboratory in Information Systems, Intelligent Systems and Mathematical Modeling, National School of Mines of Rabat, Rabat, Morocco

³Faculty of Legal, Economic and Social Sciences of Rabat–Agdal, Mohammed V University of Rabat, Rabat, Morocco

ARTICLE INFO

Article history:

Received: 04 September, 2022

Accepted: 04 October, 2022

Online: 25 October, 2022

Keywords:

Energy system modelling

Power system

Renewable energies

OSeMOSYS

Optimization model

Morocco

ABSTRACT

Renewable energy is an essential source of green growth for countries facing a shortage of fossil fuels. They offer a sustainable, inexhaustible, carbon-free solution to the future energy dependency of nations. Morocco, which has no traditional energy resources, depends entirely on the international primary energy market to meet its growing demand. For this reason, Morocco launched the National Energy Strategy in 2009 to reach 42% renewable production by 2020. This strategy has been renewed to 52% by 2050. Thanks to this policy, the country has been able to address most of its energy challenges. This study analyzes the energy mix of Morocco from 2010 to 2050. The methodology adopted is to simulate Morocco's electricity mix for this period. We assumed we were at the beginning of deploying the country's energy policy to assess the adopted strategic decisions. The analysis shows that the different technological solutions for electricity production chosen at the beginning of Morocco's energy transition could be better. Indeed, the decision to develop concentrated solar power as the leading renewable source and coal as a backup option, for example, appears to be contested. However, according to the third scenario of our study, renewables have the potential to become the main source of energy for the Moroccan power grid.

1 Introduction

This paper is an extension of work initially reported in the “2021 International Conference on Electrical, Computer and Energy Technologies (ICECET)” [1].

The Kingdom of Morocco relied primarily on foreign supplies to meet its growing energy needs during the first decade of the 21st century [2]. Forecasts for 2008 suggested that the country's high rates of population growth and urbanization, as well as its economic prosperity, would contribute to higher energy consumption and a greater mismatch between supply and demand [3]. This dependence on imported fossil fuels has widened the country's trade and financial deficits [4]. On the other hand, Morocco has significant potential to meet its energy needs through renewable sources such as hydroelectricity, solar energy, and wind power [5].

Considering the country's greatest renewable energy potential

and the significant scarcity of fossil-fuel reserves, the kingdom initiated a new national energy policy in 2009 [6]. This strategy prioritized supply security, energy mix diversity, low cost, safety, efficiency, and environmental cleanliness [7]. This strategy intended to raise renewable energy's installed capacity share to 42% in 2020 and 52% in 2030 [8].

Although it has a percentage of renewable energy (RE) that is around 36.8%, Morocco has not yet accomplished the goal it set for itself in the energy transformation field. The target was to achieve a share of renewable energy in the power sector equal to 42 percent by the end of 2020 [9]. Despite this, the renewable energy targets specified have been increased to exceed the current goal of 52% of the national power mix by 2030 [10, 11].

The most significant delay was in the implementation of the Solar Plan [12]. This enormous project, with a significant capacity for electric energy production, has provided Morocco with a valid

*Corresponding Author: Jabrane SLIMANI, Research Laboratory in Information Systems, Intelligent Systems and Mathematical Modeling, National Institute of Statistics and Applied Economics, Rabat, Morocco, Email: jslimani@insea.ac.ma

energy alternative and a tool for socioeconomic growth, allowing it to become a “reference” in Africa for renewable energy production! In addition, the accomplishments in the hydroelectricity field follow the goals. Towards the wind side, we expect to surpass the goals barely. Despite this, the cumulative impact of the two, whose targets will be surpassed in 2021, will not be sufficient to compensate for the delay in the solar plan [13]. Because of this circumstance, we began to wonder whether the decisions and approaches suggested in the Moroccan solar plan, developed after the energy strategy implementation, were especially relevant. In addition, we questioned the reliability of the guidance of the subject-matter experts who supported these choices.

In light of this, this article provides a historical and projected assessment of Morocco’s electricity system. The plan is to simulate the power mix in Morocco from 2010 to 2050 as though we were at the beginning of the country’s energy policy rollout. The analysis is based on OSeMOSYS (Open-Source Energy Modeling System), a long-term planning model that allows us to compute the energy supply mix that best fulfills the energy service demands in each year and a time step of the investigated scenario while reducing total discounted costs.

The remainder of this work will be organized as follows: First, we will go through the OSeMOSYS model and the applied analytical approach. In this section, we will go over the changes made to the model code’s initial version. These changes provided a more accurate picture of Moroccan energy policy. Section 03 then presents our model’s various input data and assumptions. We also recall the scenarios’ assumptions and attributes. Then, in Section 04, we will present and debate the key findings of the simulated scenarios, and ultimately, we will give the study’s primary conclusions. The final purpose of our analysis is to evaluate Morocco’s judgments made between 2010 and 2020, as well as the best solutions that should be chosen. Furthermore, would it be possible to speed the shift away from fossil fuels between 2020 and 2050, and what would the costs be?

2 Material and Methods

2.1 Tool: Open-Source energy Modelling System

Bottom-up modeling approaches are applied to optimize power systems in developing nations with suitable technology and supply resources [14]. One example of a model that fits this description is the bottom-up, dynamic, linear optimization model known as the Open-Source Energy Modelling System (OSeMOSYS), which is used for integrated evaluation and energy planning [15]. OSeMOSYS seeks to accomplish this by considering various technological, economic, and environmental factors, all while striving to achieve the lowest possible total discounted cost [16]. This model’s designers constructed it to divide its functionality into several “blocks.” These features are connected to the following aspects: prices, capacity adequacy, energy balance, emissions, and provisions for renewable energies [17]. What distinguishes one block from another are the equations, the formulae and the restrictions, the intermediate variables, and the parameters introduced by the analyst. [15, 16, 18].

Initially, the code for OSeMOSYS was developed in GNU Math-

Prog. More recently, it has been rewritten in the GAMS (General algebraic modeling system) and Python programming languages [19]. Within the context of the conference publication [1], we carried out the simulation utilizing the GAMS implementation of the model. However, in this version, with the additional information we were able to obtain throughout our research project, we could carry out the simulation using the Python version that was running under pyomo.

2.2 Basic Code Adjustments

Our modeling of the Moroccan power system aims to determine the most efficient way to meet the country’s predicted long-term electricity demand, while also considering Morocco’s energy strategy targets in terms of the amount of renewable capacity that may be built. In the original version of OSeMOSYS, constraints relating to the availability of resources, the characteristics of renewable technologies, and the development of demand were already incorporated. Although, the requirements of EnR integration into the power system are stated in terms of yearly renewable energy production considerations.

The modeler may introduce the integrative constraint for RES in the energy system by using Equation 1. The different terms of the equation are detailed in Table 1. “r” and “y” represent the data sets for the region and the modeling year, respectively. This equation is encoded using the Pyomo coding scheme, as in box 01. Nevertheless, applying this equation to the specific situation of Morocco’s energy strategy is not an ideal solution.

$$\forall_{r,y} \quad REmpT_{r,y} \times RETPA_{r,y} \leq TREPA_{r,y} \quad (1)$$

$$\forall_{r,y} \quad REmCT_{r,y} \times TPCA_{r,y} \leq TRECA_{r,y} \quad (2)$$

Therefore, to accurately represent the constraints imposed by the renewable installed capacity, we had to convert the previous mathematical “equation (1)” into the new “equation (2)”. The different terms of the “equation (2)” are detailed in Table 2. Additionally, constraints were introduced to the original code, as demonstrated in “box 02”. The technique of obtaining the TotalRECapacityAnnual variable is determined by “equation (3)”, “t” symbolizes technologies’ power plants. The different terms of “equation 3” are detailed in Table 3. The second term in “equation (2)” is the variable TotalPowerCapacityAnnual derived from the TotalCapacityAnnual variable and the PowerTagTechnology parameter as shown in “equation (4)”. The additional parameter PowerTagTechnology was included to allow the model to distinguish between electricity-generating technologies and other technologies defined in the model. The different terms of the “equation (4)” are detailed in Table 4. The REMinCapacityTarget(r, y) parameter is the third component of the “equation (2)”. It was created in order to set a minimum target for renewable capacity.

$$\forall_{r,t,y} \quad \sum_t TCA_{r,t,y} \times REtgT_{r,t,y} = TRECA_{r,y} \quad (3)$$

$$\forall_{r,t,y} \quad \sum_t TCA_{r,t,y} \times PtgT_{r,t,y} = TPCAnnual_{r,y} \quad (4)$$

Table 1: Summary of datasets used

Abbreviation	OSeMOSYS designation	Description
REmPT	REMinProductionTarget	The minimum renewable production target desired by the analyst (parameter)
RETPA	RETotalProductionOfTargetFuelAnnual	The Annual Production of the fuels marked as renewable in the model (variable)
TREPA	TotalREProductionAnnual	The annual production of all technologies marked as renewable in the model
REmCT	REMinCapacityTarget	The minimum renewable capacity target desired by the analyst (parameter)
TPCA	TotalPowerCapacityAnnual	Annual capacities of technologies that convert primary energy into power (new variable)
TRECA	TotalRECapacityAnnual	A new variable introduced to the system to identify the total annual renewable capacity
REtgT	RETagTechnology	A binary parameter indicating renewable technologies, with a value of 1 indicating renewable technologies and 0 otherwise (parameter)
TCA	TotalCapacityAnnual	The existing total capacity of technology “t” for year “y” (variable).
PtgT	PowerTagTechnology	A binary parameter indicating power technologies, with a value of 1 indicating electricity-generating technologies and 0 otherwise (parameter)

3 Data Collection and Analysis Approach

3.1 Base year data

The year 2010 will serve as the foundation for building our analysis, as was said earlier. As a result, when the model was created, the current properties of the power system were used as starting parameters for the optimization process. Consequently, the treatment got off to the most effective beginning point imaginable. As a result, our model considers the electricity generation industry in Morocco at the end of 2009 [20]. There is information supplied on the capacity that was built before the year 2010. (Figure 1).

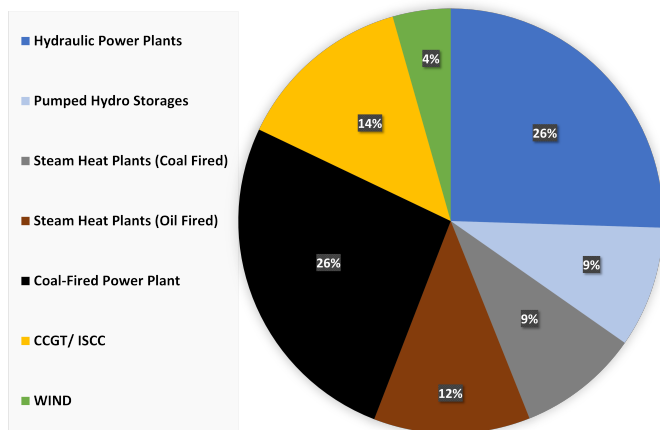


Figure 1: Installed capacity at the end of 2009 in Morocco [20]

It is important to note that the electricity system in Morocco does not cover the entire kingdom territory. This is mainly some generation capacity installed on the demand side in remote areas,

such as the kingdom’s south. These regions are supplied with power by gas turbines and diesel generators connected to a local grid. In our research, we did not take into consideration these capacities. Instead, we have considered the fact that the electricity fleet must connect to the national grid to meet the demand associated with this region.

3.2 Reference Energy System

When modeling energy systems, it is common practice to employ a representation in the form of a network for all the practical tasks required to provide end-users with a variety of energy sources. The term “Reference Energy System” (RES) refers to this particular representation [21]. In the context of our study, the selected RES is shown in Figure 2. The block denotes the various technologies in the RES, while the lines stand in for the various energy carriers. Technologies can refer to all kinds of processes performed on certain energy carriers, such as extraction, refinement, conversion, transportation, distribution, and usage of that energy carrier.

In the case of Morocco, where energy is primarily obtained through imports, we have not considered the relatively insignificant sector of primary energy extraction. On the other hand, the refinery has not been considered because its activity level dropped significantly after 2010 and stopped in 2015. As we had stated previously, when it came to converting primary energy into electricity, we depended on the technologies already in place at the beginning of 2010. These include coal-fired power plants, natural gas-fired power plants, oil-fired power plants, grid-connected diesel generators, wind farms, hydroelectric power plants, and a pumped storage power station. We have included in this mixture two technologies that are candidates for the development of renewable capacity. These technologies are photovoltaic and solar concentration.

The capacity of these power stations has been aggregated in a

modeled setting. In other words, we do not simulate each power plant isolated. Instead, a block of power plants that convert one type of primary energy into power will be depicted together. Decision-makers can then pick the size of the new capacity required after obtaining the total ideal capacity required. In the case of transmission and distribution networks, precisely the same method was taken. These grids were modeled as a single technology that transforms the electricity from these plants into transmission electricity for the transmission grid, and then another technology that transforms this electricity into electricity for end users for the distribution grid. The transmission grid and the distribution grid were both modeled as separate technologies. On the demand side, each type of electricity consumption was combined into a single estimate for the national electricity demand.

3.3 Inputs and assumptions

OSeMOSYS's simulation of the Moroccan power system relied on several assumptions to generate accurate results.

3.3.1 Temporal precision

In the conference paper [1], we decided to sequence the modeling horizon over five years. In this extended essay paper, however, we have chosen annual modeling. In addition, to simulate the seasonal and daily variation of electricity demand and the intermittent nature of renewable energy sources, we divided each year of the model into a total of six-time steps. There are two periods each day: day and night. There are also three seasons: winter, intermediate, and summer. This gives us a total of six periods: WD and WN for the daytime and the night of a day during the winter; ID and IN for the daytime and the night of a day during the intermediate season; and SD and SN for the daytime and the night of a day during the summer.

3.3.2 Electricity Demand

According to the data provided by ONEE in its numerous activity reports [22], the yearly increase rate of energy consumption was around 6% from 2010 to 2016. This growth rate was observed throughout the entire period. Thereafter, this rate continued to fall until it reached 5% in 2018. Furthermore, the Moroccan Ministry of Energy analyzed energy demand until 2050 [23], which established three different demand evolution scenarios for the time spanning from 2020 to 2050. A trend macroeconomic scenario, in which the Moroccan economy maintains the same trend (3.5%) recorded from 2009 to 2018; a high macroeconomic scenario, in which a gradual economic recovery is expected to reach 5% in 2050; and a pessimistic macroeconomic scenario, in which the downward trend recorded from 2009 to 2018 is expected to continue to 2% in 2050. ONEE statistics have been used as the basis for our examination of demand from 2010 through 2018. On the other hand, for 2019-2050, we have decided to go with the findings of the trend scenario developed through the research carried out by the Ministry of Energy (Figure 3).

3.3.3 Costs

Any such study relies highly on the investment prices selected for the technologies being considered, in addition to the costs of fuel, operation and maintenance (O&M), and non-operational expenditures. The investment costs and fixed operation and maintenance (O&M) expenses were expressed in USD per kW of installed capacity, with variable O&M costs stated in US dollars per gigajoule and fuel costs expressed in US dollars per unit. These costs were gathered from various sources [24–30], and we have displayed them in Figures 4, 5, and 6, respectively.

3.3.4 Common data and hypothesis

Several other statistics and assumptions are shared in all scenarios. These figures were obtained from a variety of sources [24, 31–33]. Table 2 summarizes the various values estimated during the modeling period.

The capacity factor is the most crucial criterion to consider in this category. It represents the available capacity for each period, usually given as a proportion of the total installed capacity. This value remains constant throughout the year for conventional technologies, making it possible to consider unplanned disruptions. On the other hand, the value of renewable energy sources fluctuates depending on the period in question. Thus, the intermittent nature of these technologies is also represented here. Figure 7 provides a visual representation of the various capacity factors of renewable energy that were taken into account in our research.

The second parameter is the Availability Factor. It represents the most extended period that a particular technology can function throughout an entire year, represented as a percentage of the year ranging from 0 to 1. It enables breaks to be scheduled in advance. The third one is the operational Life Cycle, which is the usable life of a technology measured in years. The other metrics include each technology's efficiency and CO₂ emission rate.

To establish certain constraints, we had to make some additional assumptions. Among these assumptions is the discount rate, set at 5%, based on the average rate applied to loans by Moroccan banks [34]. Furthermore, the reserve margin was set at 20% of the installed capacity, and no emission limits were imposed.

3.3.5 Assumptions and Scenario characteristics

Under the Moroccan energy plan approved in 2009, three scenarios have been selected for implementation. The main difference between these scenarios is the share of renewable energy in the installed electricity capacity. The first scenario is a Business As Usual (BAU) scenario that does not impose a lower limit on the share of renewables. This scenario reflects a trend in the electricity mix. At the same time, the optimization model is proposed to incorporate renewable energies. The second scenario is the one that matches the target of the Moroccan energy policy, which is to reach a rate of 42% of installed renewable power in 2020 and 52% in 2030. The third scenario is the scenario that estimates the feasibility of increasing the rate of integration of renewable energy in the electricity mix. For this purpose, the Moroccan energy strategy's objective has been revised to 60% of installed renewable power in 2030 and 80% in 2050.

4 Results and Discussion

To fully comprehend the results of the Moroccan energy policy, the findings are contrasted with the real situation that occurred on the reality in Morocco from 2010 to 2018. Recommendations will be based on the research done for the years 2019–2050.

4.1 Power Generation Capacity

If we look at the three scenarios together, we see that, in the first scenario, the proportion of renewable energy sources is relatively low (Figures 8;9;10). Indeed, renewable energy is scarce from 2010 to 2035; This results from the very high cost of these technologies at the onset of the modeling period and the unavailability of a minimum renewable capacity target. In this scenario, solar energy has not been chosen to be included, but the incorporation of wind energy into the mix will begin in earnest in the year 2035. This can be explained by the fact that technology relating to wind energy

has become more economically mature than those relating to solar energy.

On the other hand, one can make the observation that the total capacity required to fulfill the demand in the third scenario is more significant than that required in the first two scenarios. The high integration rate of RE, which reached 60% in 2030 and 80% in 2050, is the reason for this gap in capacity. In addition, it appears that the retirement of coal-fired power plants is happening faster as a result of investments in RE. In fact, coal-fired generation capacities are still present until 2040 in the first scenario; however, in the second and third scenarios, these capacities are almost nonexistent beyond 2030. Regarding the utilization of natural gas, we can observe that this production method is present in each scenario. Furthermore, the supremacy of this conventional technology over its alternatives can be attributed to the reliability of the technology and the low cost of the commodity, in this case, natural gas, compared to the cost of fuel oil.

Table 2: Data and hypothesis common to all scenarios [24, 31–33]

	Units	Technology							
		Coal_PP	Oil_PP	GAS_PP	WIND	PV	CSP	HYD	PHS
Average capacity factor	%	85	90	87	35	27	70	51	100
Availability factor	%	84	89	91	100	100	100	95	100
Life cycle	Years	40	25	30	25	25	25	80	50
Efficiency	%	39	35	54	100	100	100	32	100
CO2 emissions	ton/PJ	0.0905	0.0589	0.0503	0	0	0	0	0

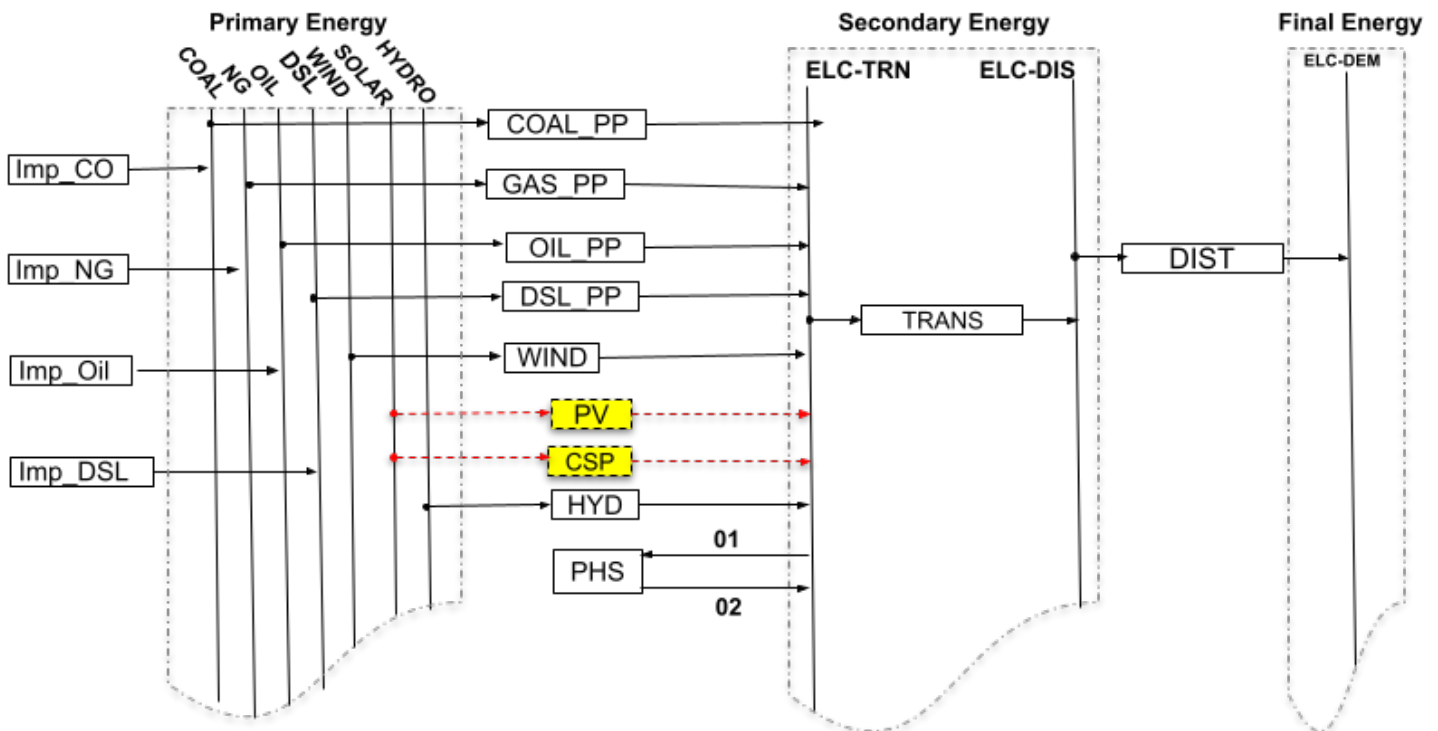


Figure 2: Electricity supply model of Morocco's reference energy system in OSeMOSYS/ source : illustration, made by the authors

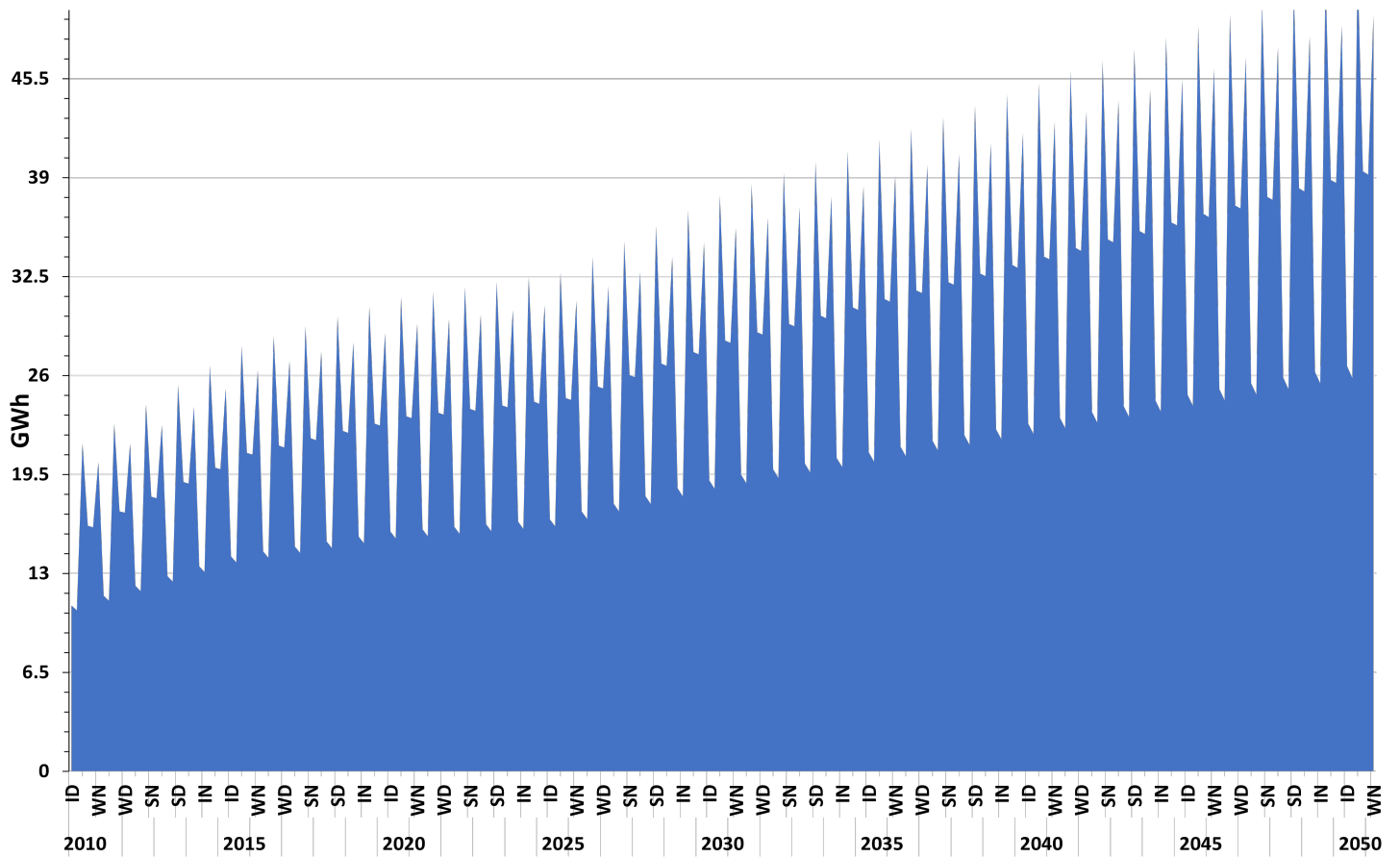


Figure 3: Electricity demand 2010-2050 in GWh

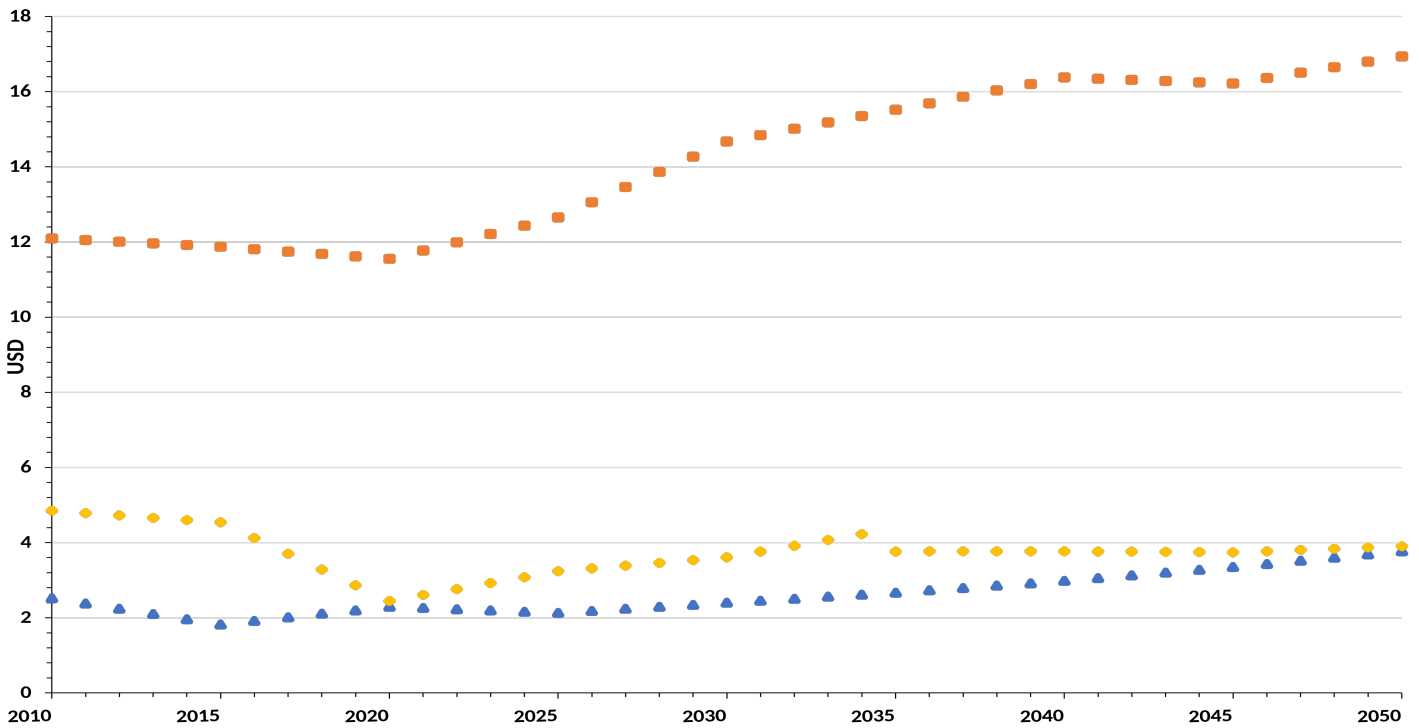


Figure 4: Energy Prices by Source, 2010-2050

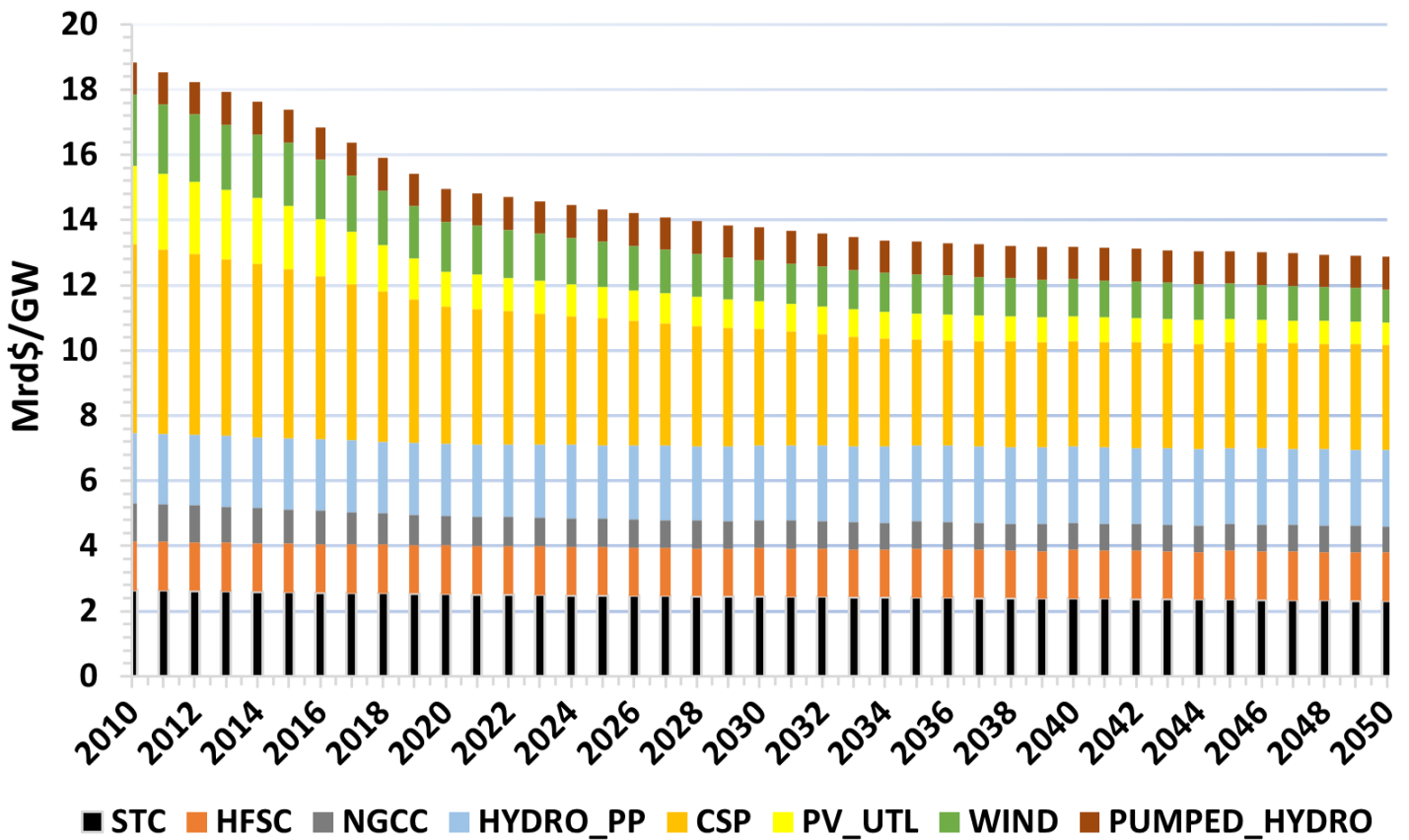


Figure 5: Capital cost for power plants 2010-2050

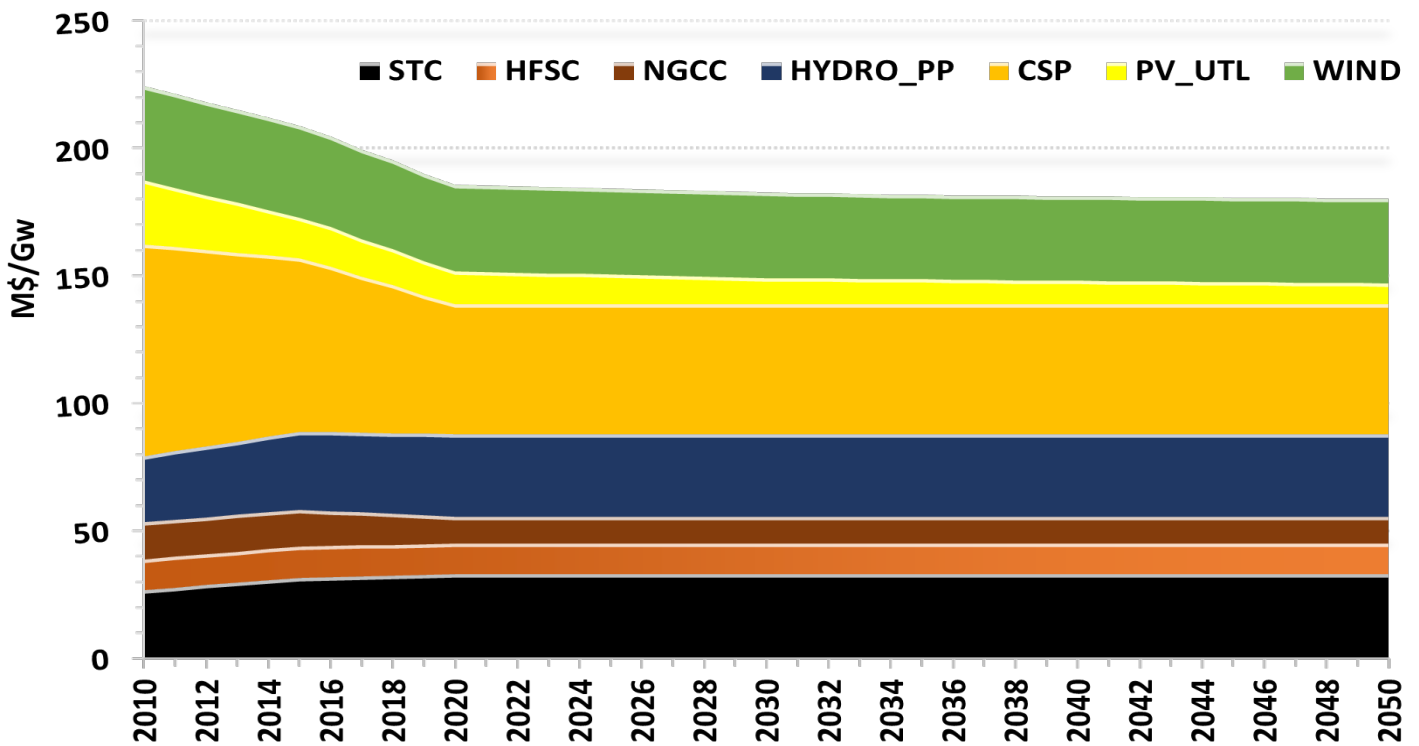


Figure 6: Fixed O&M costs for power plants, 2010-2050

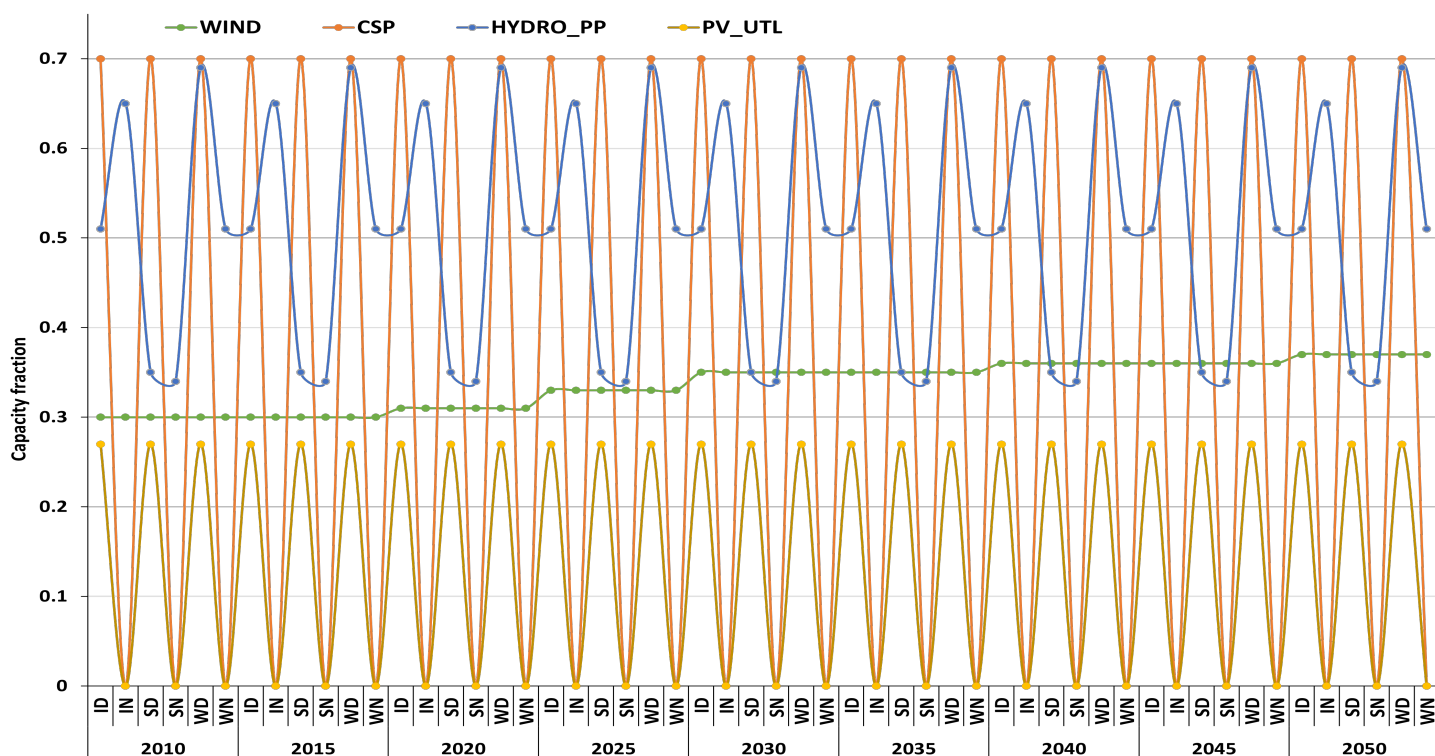


Figure 7: Capacity Factor Renewable Energy

Furthermore, we note that only two of the three possible renewable technologies were chosen, Wind energy and solar photovoltaic energy. However, none of the possible results involve using concentrated solar electricity. A finding that sheds light on Morocco's decisions in 2010 regarding the technologies it plans to deploy.

Figure 4 demonstrates that the majority of the electricity mix in the BAU scenario is composed of conventional technologies. Renewable energy sources account for just 6% of the total capacity in the year 2030, and this percentage will not reach 42% until the year 2050. In 2035, pumped storage technology will account for 48% percent of total installed capacity, making it one of the technologies with the most significant proportion of installed capacity. This focus on PHS can be explained by the fact that the capacity and availability factors were estimated at 100%. In addition, the model did not stipulate an upper capacity limit for the system. In light of these assumptions, one can question the veracity of the results. These assumptions, however, may be appropriate even in the lack of reliable facts on the issue. For starters, pumped storage power stations can run as long as the upstream reservoir is adequately replenished. This can be achieved by either flowing water from a river or pumping water from the downstream tank. Then, for the availability factor and unexpected shutdowns and maintenance, two pumping units and two turbine units are sufficient to ensure the station's operation. Furthermore, regarding available capacity, Morocco has a relatively vast coastline that may be utilized as marine PHS, considerably improving Morocco's potential in this technology.

In contrast to scenario 01, solar PV is the first renewable technology to be integrated into the electricity mix in the 2e scenario (Figure 9), with wind beginning to gain a significant role from 2035 to 2050. We also find that the share of gas power plants is directly proportional to the integration rate of renewable energy sources. Indeed, in 2050, the share of NG-PP approaches 50% in scenario 02, whereas it does not exceed 40% in scenario 01. This result demonstrates the significance of this technology in the context of the vast development of renewable energies.

This observation is corroborated in scenario 03 (Figure 10), when the rates of renewable energy integration rise substantially. This is owing to the model's need to meet significant minimum capacity demand. This is also something we observe at this time. The built wind capacity had expanded dramatically at the start of the modeling period, in contrast to what we stated in Scenario 2. It should be highlighted that, based on current price trends, solar PV will be pretty competitive for average renewable energy integration between 2020 and 2040. However, technology to offer backup is required. Wind power, however, is critical for rapid integration with a high percentage of renewable energy. Indeed, with rates reaching 60% from the start of the projected period, significant investments in natural gas power plants have been made, highlighting the critical potential of this technology to offer the necessary reserve to deal with renewable energy's intermittent nature. Once the integration rate reaches 80%, establishing PHS facilities becomes imperative. This is what we notice in the year 2050.

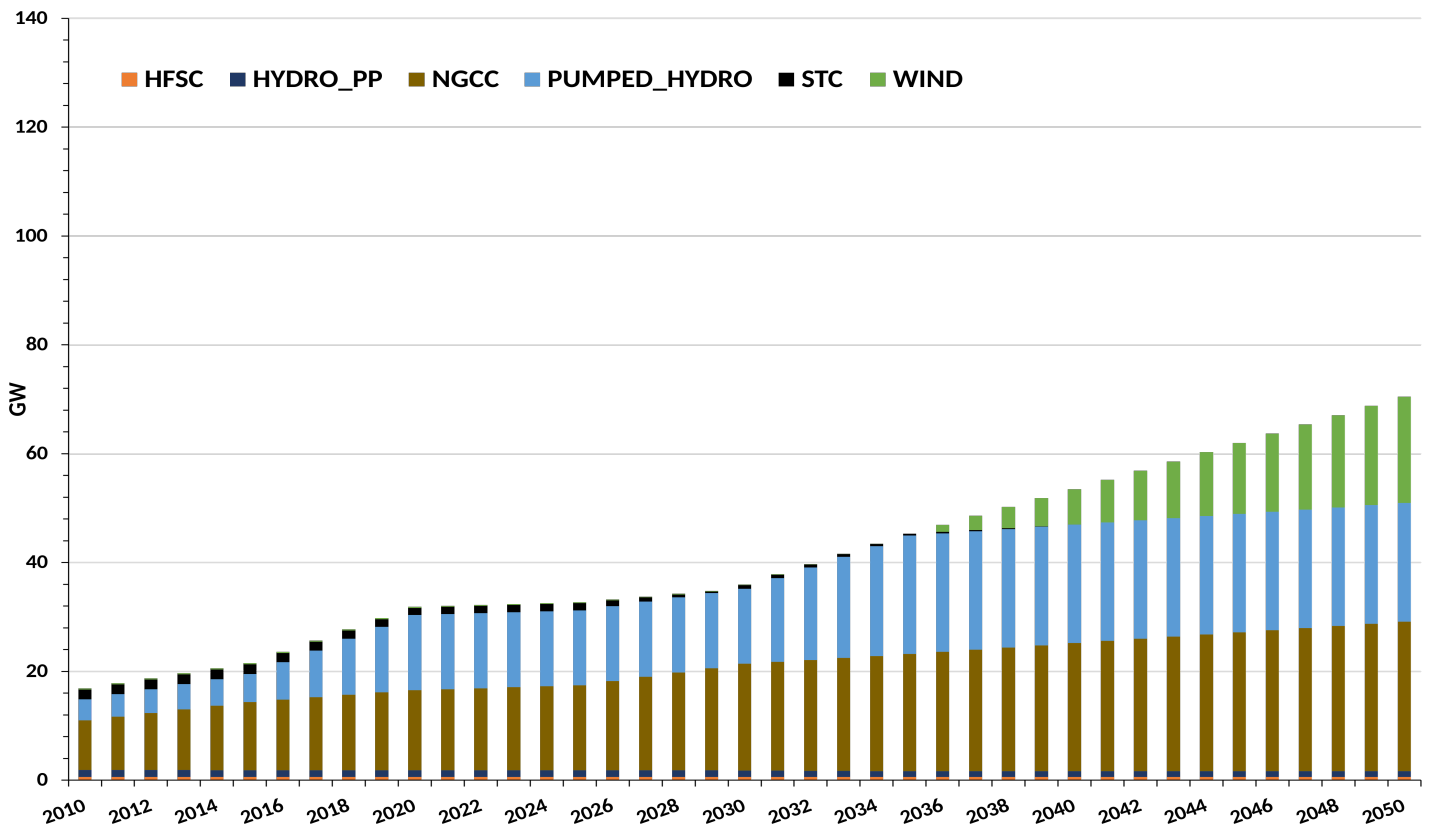


Figure 8: Total Annual Capacity (Scenario 1)

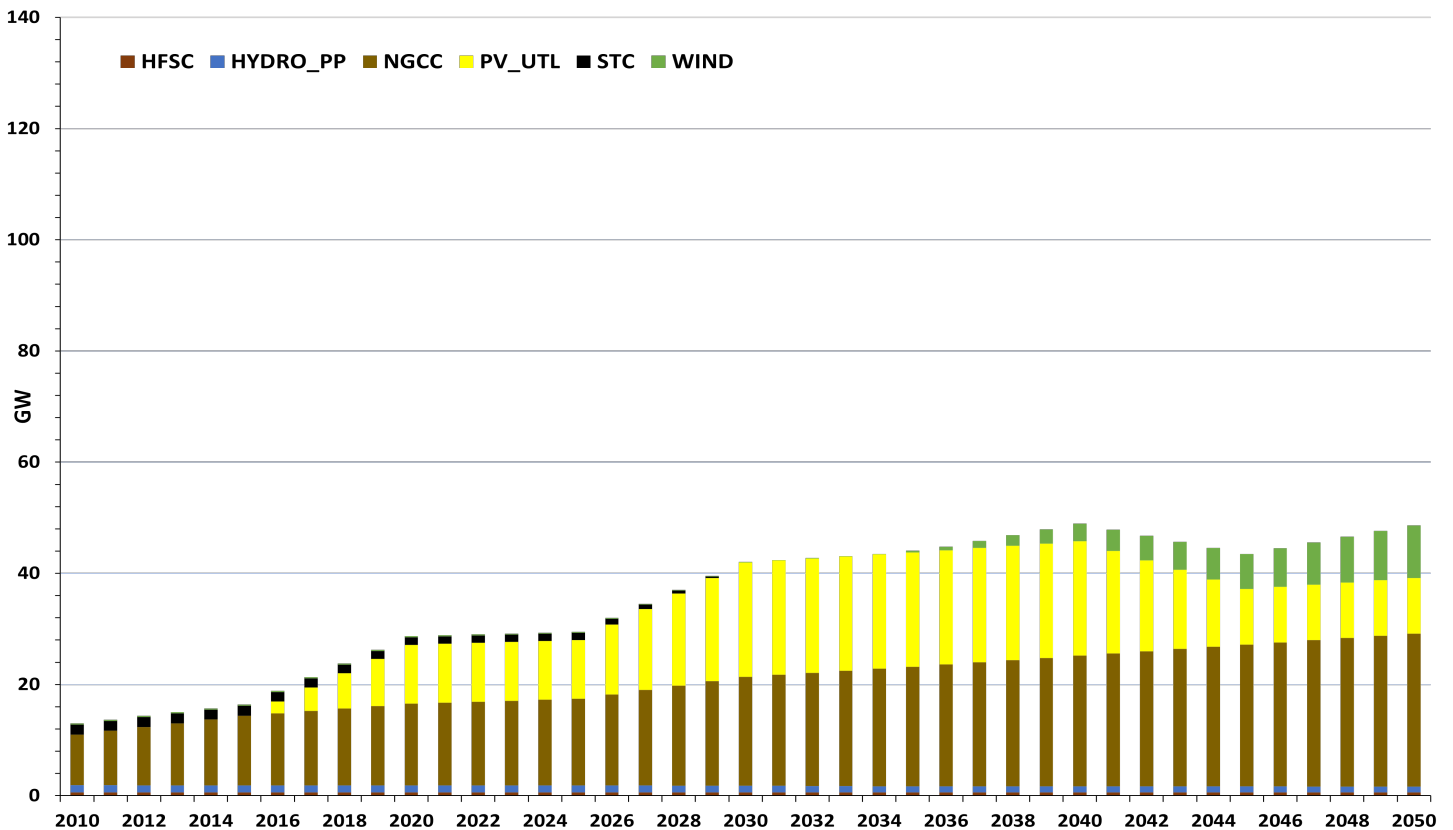


Figure 9: Total Annual Capacity (Scenario 2)

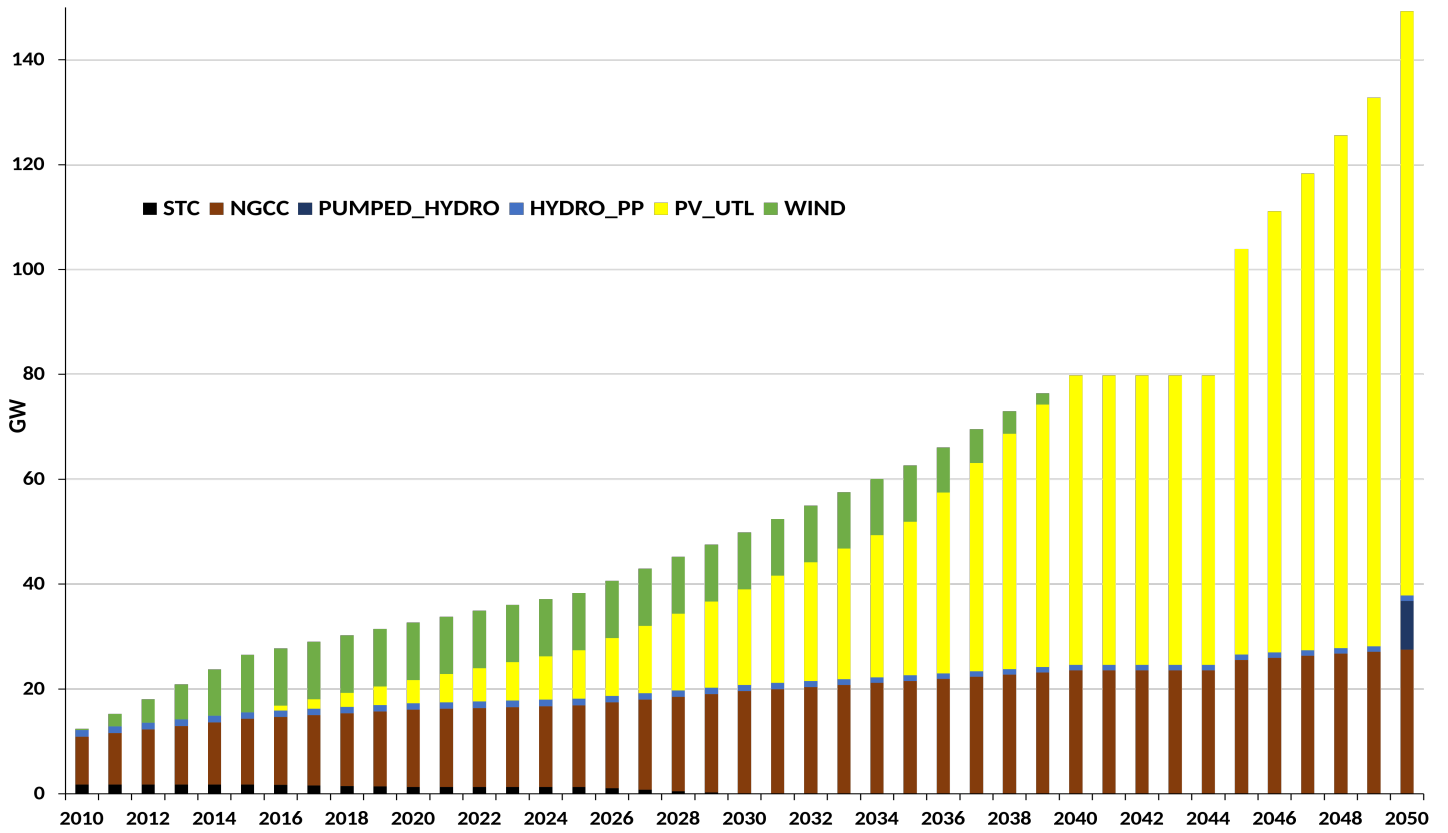


Figure 10: Total Annual Capacity (Scenario 3)

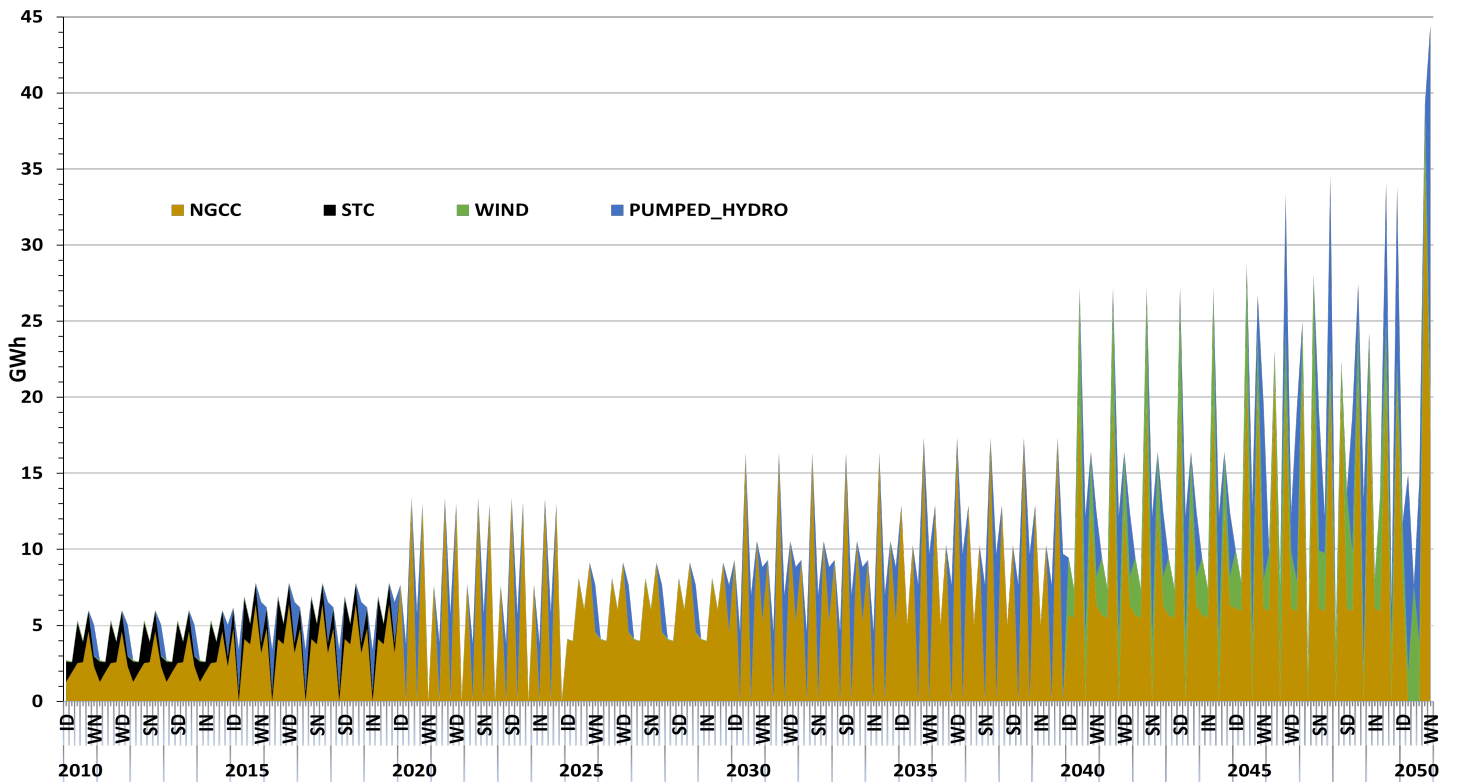


Figure 11: Technology Production by Time Slice (Scenario 1)

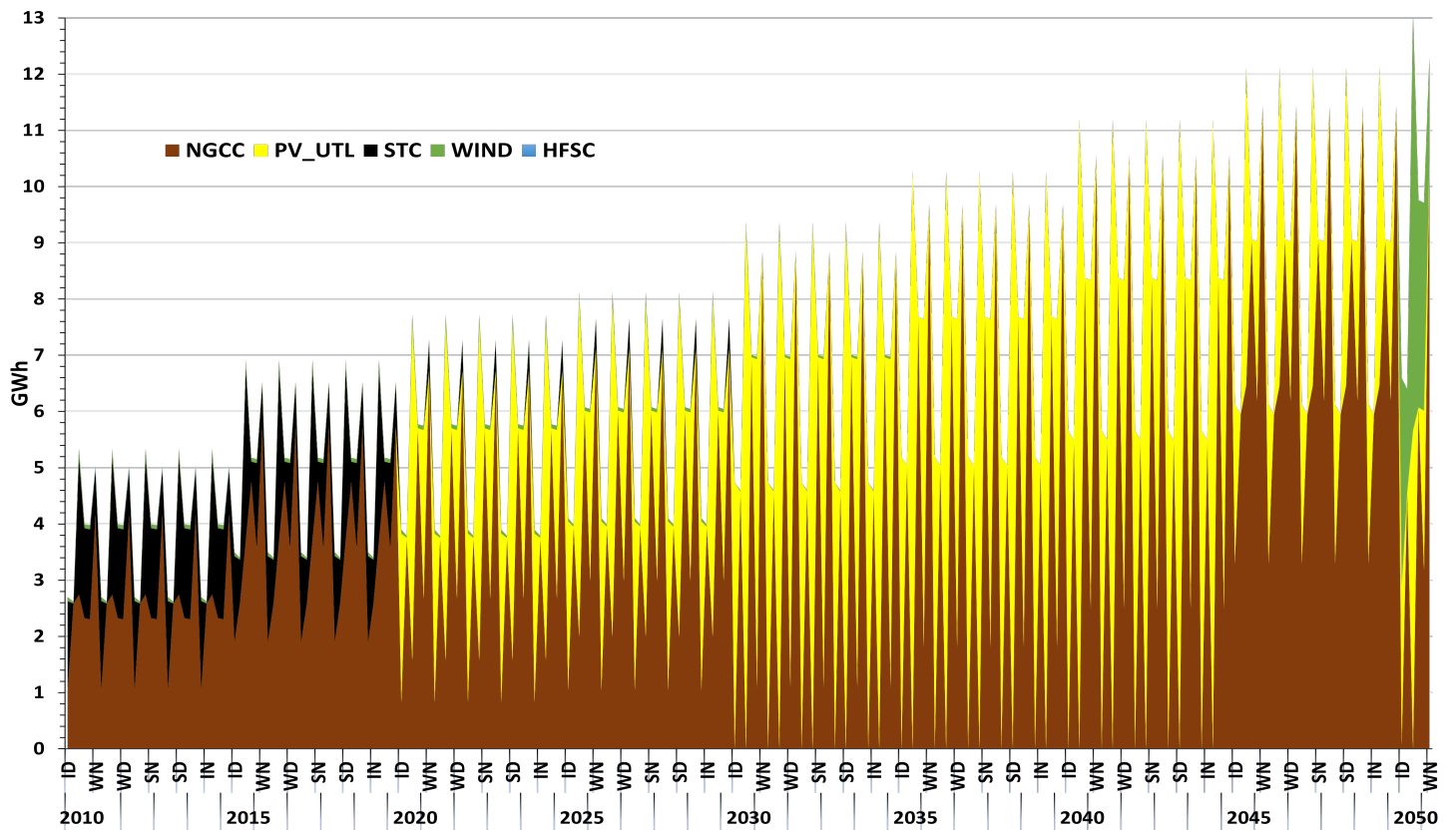


Figure 12: Technology Production by Time Slice (Scenario 2)

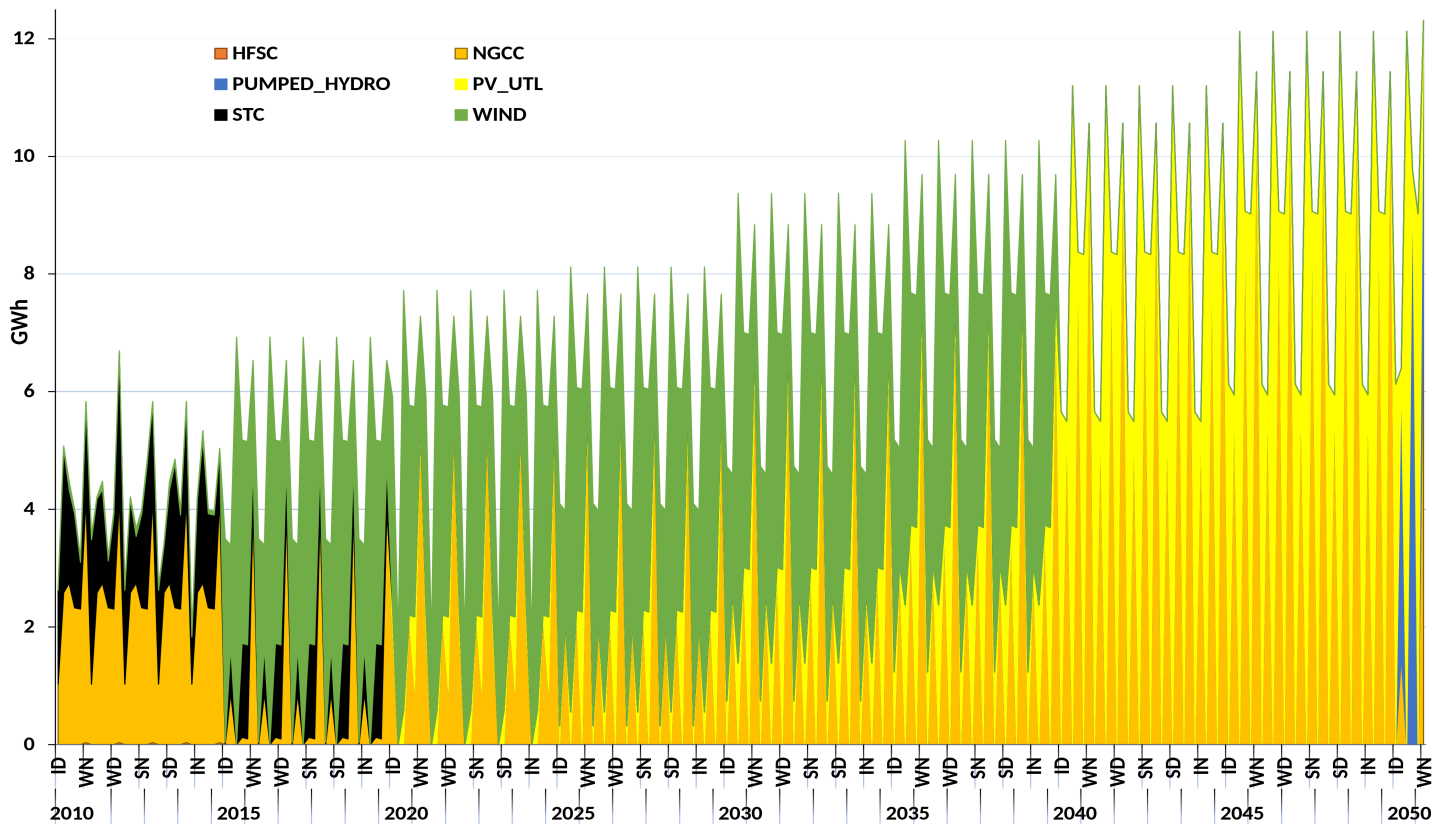


Figure 13: Technology Production by Time Slice (Scenario 3)

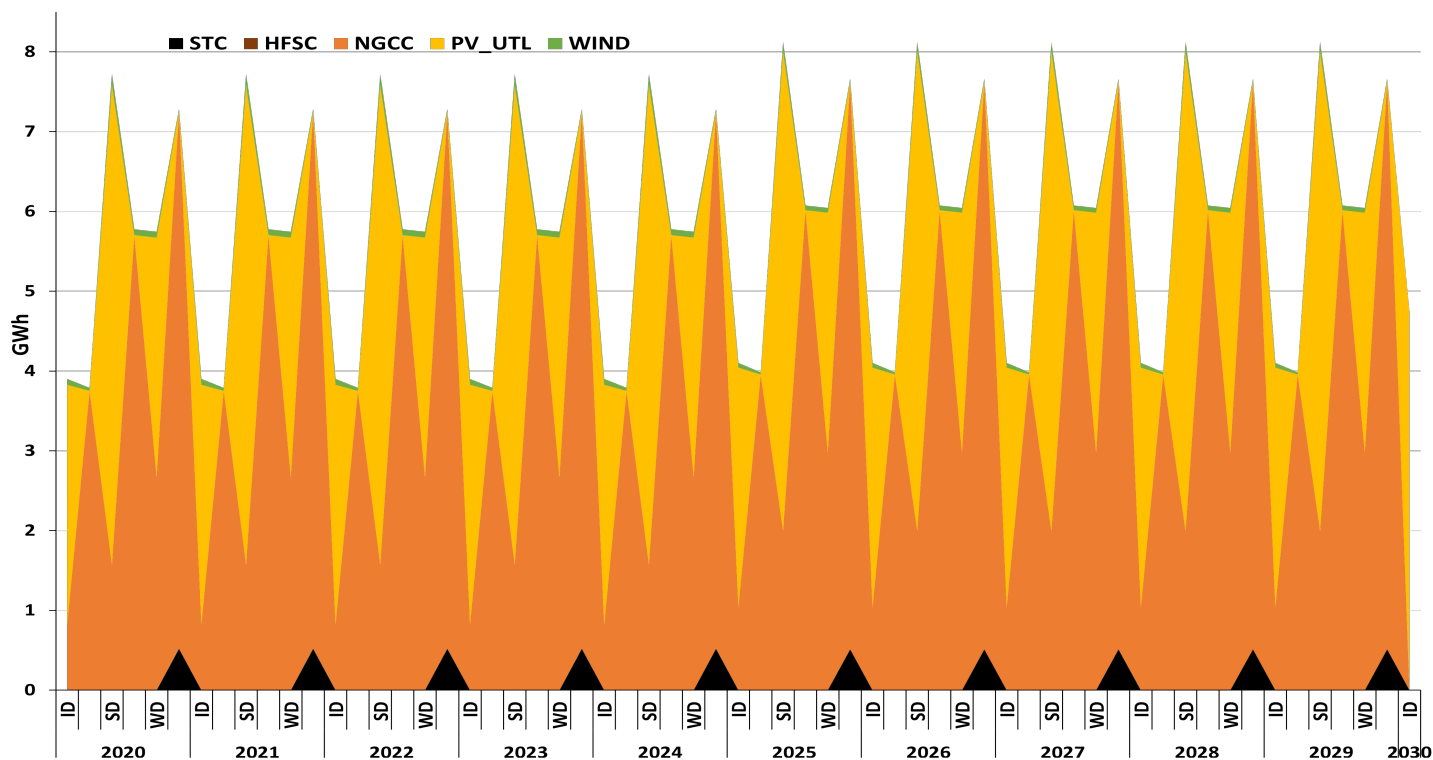


Figure 14: Technology Production by Time Slice 2020-2030 (Scenario 02)

4.2 Electricity Production Aspects

Figures 11, 12, and 13 shows how energy output is allocated in three scenarios; We can instantly see that scenario 1 produces substantially more energy than the other two situations. Indeed, scenario 01's total output is 17% higher than scenario 02's and 22% higher than scenario 03's. Although all three scenarios have the same overall demand that must be satisfied, Scenario 01's high use of PHS causes additional demand to be met through the pumping required to fill the quantity tanks. When we look at the breakdown of power generated to fulfill demand between 2010 and 2015, coal and gas come out on top. Second, in Scenarios 02 and 03, conventional generation facilities are predominantly centered on natural gas-fired plants. The second point to note is the variation in generation by time slice in the 02 and 03 scenarios. Because renewable energy sources are intermittent, this was to be expected.

We already mentioned in Scenario 01 that natural gas and coal will be the dominant energy generation sources, as seen in Figure 5. Indeed, the competitiveness of renewable energy in electricity production remains questionable because no minimum production constraint or installed capacity limit is imposed. Wind energy, on the other hand, will become more competitive by 2040 and will naturally be included in the optimal electricity mix. This is attributed to lower wind energy costs and higher generating capacity.

On the modeled days, photovoltaic (PV) generation is the primary contributor to satisfying power demand first thing in the morning in the second scenario. Gas-fired power plants increase output to meet the increased demand for electricity in the evening. Between 2010 and 2020, there will be virtually no visible difference in power generation between conventional and renewable energy sources. However, between 2020 and 2030, the difference between

the two will expand slightly. The fundamental cause of this increase is the amplitude of photovoltaic generation, which decreases dramatically when the sun sets. Figure 14, which focuses solely on this period, clearly illustrates this argument. Wind farms will be used to compensate for the decreasing amount of solar power available in the evenings beginning in 2040. As a result, it is less likely that gas-fired power plants will be used to the same extent until the end of the period predicted.

When compared to the conclusion of the period evaluated in Scenario 2, the amount of power generated by NG-PP plants falls at a much steeper and faster pace in Scenario 3. Furthermore, as illustrated in Figure 7, which depicts the distribution of electricity generation by time slice for Scenario 03, the utilization of NG-PP is primarily related to peak load. The latter is mainly used during peak demand or at night to compensate for the fact that renewable energy sources often do not produce at night.

4.3 Carbon emissions

Figure 15 exemplifies this notion. The simulation findings reveal that the initial scenario causes the most severe pollution. Compared to the first scenario, CO₂ emissions reported for scenarios 2 and 3 were reduced by 25% and 72%, respectively. It is possible to avoid between 62 and 135 Ktonnes of CO₂ emissions. The operation of thermal power plants is a significant source of carbon dioxide emissions. Given that the 1st scenario is dominated by power plants of this sort and that pulverized coal is a significant component of the production mix, it is not unexpected that these emissions are at their highest level. Consider the objectives that the Moroccan government has set for itself. We can see that Scenarios 2nd and 3rd will considerably contribute to the desired carbon intensity reduc-

tion. It would also be interesting to see how the model reacts when environmental limitations are introduced to the basic scenario.

4.4 Total Costs

As shown in Figure 15, the BAU scenario will result in the lowest total expenditure. In this scenario, the cost of fossil fuels represents more than 80% of the total expenditure, taking into account the absence of any intervention on the installed capacity. The total discounted costs of scenario 3 are 2% higher than the total discounted costs of scenario 1. The total discounted cost of Scenario 2 is only 0.5% higher than the total cost of Scenario 1.

The lower fuel prices almost fully compensate for the investments in the second scenario. This also results in a positive energy independence benefit, at a cost almost comparable to that of Scenario 1. However, this result would not have been achieved without the lower fossil fuel prices. In the third scenario, the discounted costs are the highest of the other scenarios. This is because the model has been forced to make large investments in renewable technologies, the relatively high costs.

Scenarios 02 and 03 are distinguished by considerable growth in the use of renewable energy sources. This results in less dependence on fossil fuels and greater self-sufficiency in imports. On the other hand, scenario 01 is characterized by an increased sensitivity to fluctuations in fossil fuel prices, which have been unstable in recent years and which may create a precarious situation in the long term. Therefore, Morocco relies on policymakers to consider that, even if the scenarios with efficient RE integration are slightly more expensive than those without renewable limits, they will reduce the country's dependence on fossil fuels.

Currently, more studies are being conducted to determine the best integration rates for each renewable energy option. This includes photovoltaics and wind power and selecting the best combination of reserve systems. The aim is to manage the effects of these renewables' intermittent nature while maintaining the national grid's stability [35].

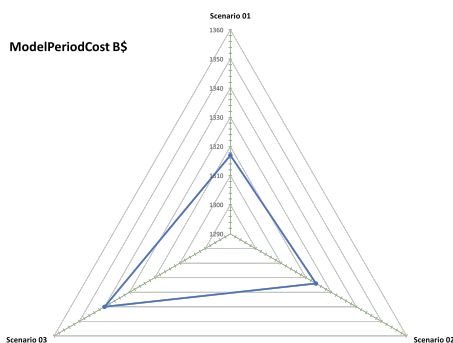


Figure 15: Total discounted cost of the scenarios

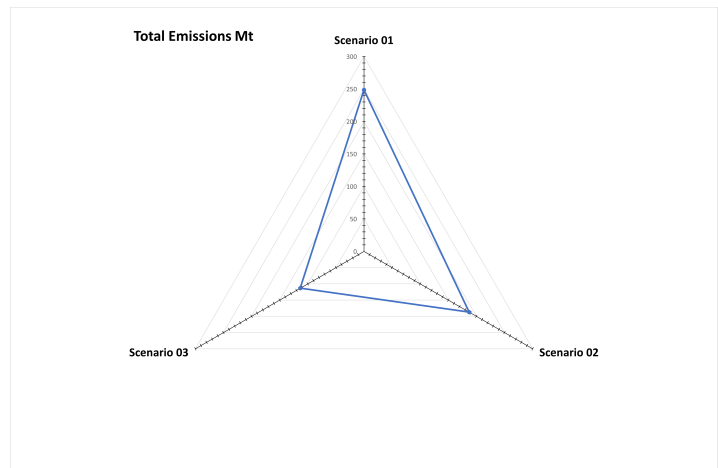


Figure 16: CO2 Emissions by scenario

In view of the results of this study, the following question arises: why has Morocco not created more natural gas power plants and made do with the two power plants of Ain Bnimathar and Tahadart, which have played an important role in meeting demand and ensuring the stability of the network?

The answer to this question is based on two axes. The first is the absence of this resource on the national territory, while coal has long been extracted from the mines of Jerrada, in the east of the kingdom [36]. The second is the low level of gas infrastructure. Indeed, in our analysis, the infrastructure necessary for the use of natural gas for electricity generation has not been considered, notably in terms of storage capacity and delivery network from the port. This is justified by the fact that the gas-fired power plants in operation so far have benefited from the proximity of the GME (Gazoduc Maghreb Europe) and from the fee in kind paid by Algeria for allowing the use of Moroccan territory for the transport of its natural gas to Europe. All these parameters, as well as others such as the required electrical storage capacity and the optimal storage technology, as well as electricity exchanges with Europe, power to X, and demand management, will be the subject of future analysis.

5 Conclusion

According to the results of this study, the different technological options for electricity generation chosen at the beginning of Morocco's energy transition are not always ideal. Indeed, the decision to develop CSP as the leading renewable source and coal as a backup load source appear controversial. This result leads us to question the primary basis for this choice. This result leads us to question the primary basis for this choice. Actually, at the time, cost reductions of solar PV, derived from its three-decade learning curves, were already far more promising than the modest cost reductions of solar thermal power. These results are from several feedback reports from the Kramer Junction solar thermal power plants in the United States [37].

In addition, while CSP offers enormous storage capacity at acceptable costs, its large-scale growth is limited by the demand for land, making it a centralised power generation technology that requires the creation of a large grid to transmit the output [38].

Furthermore, while coal-fired power plants are an attractive technology for meeting demand and maintaining grid stability, they cannot be used as a back-up technology with a large share of renewables in the electricity mix [39]. This will limit the use of renewable capacity because coal is not very flexible. The third scenario also showed that RE has the potential to become the main source of energy in the Moroccan electricity system. However, for this to happen, they will need to be integrated with flexible generation systems such as gas-fired power plants and energy transfer stations [40, 41].

Besides, as the third scenario shows, increases in renewable energy capacity targets have not always been reflected in total costs. In fact, the total costs remained relatively similar to those in the second scenario. Our results are consistent with the findings of experts in the field. For example, [42] estimated that if Morocco had made the necessary efforts to accelerate the development of power transfer stations, notably the Abdelmoumen project, which was to be commissioned in 2008, it would not have needed as much storage as the CSP plants offer. Moreover, PHS could have been used to compensate for the intermittency of wind power, which is not possible with CSP storage. On the other hand, [42] states that if Morocco had advanced the wind projects, it could have had about 3,000 GWh/year of wind energy, acquired at a price (0.03 USD/kWh). This amount corresponds to the 1050 GWh/year of solar thermodynamic energy currently purchased (at about 0.14 USD/kWh on average).

Further Research Other concerns regarding the energy sector in Morocco will be studied in the near future as part of our ongoing research. A new configuration of the model will be carried out to achieve this objective. This will involve taking into account new parameters, such as the possibility of exporting electricity and the impact that this option will have on the Kingdom's trade balance. In addition, other new parameters will be analyzed, such as the exchange of electricity with neighboring countries. In addition, we will study the storage capacities needed to support the development of renewable energy sources, among others.

Various improvements will also be made to the OSeMOSYS model to analyse concepts such as the stochastic aspect of raw material costs, the fluctuations of RE, as well as the impact of the energy strategy on other sectors such as air quality and environmental preservation, water resource management, or industry and its competitiveness in the context of new carbon taxes introduced and planned by the European market.

Conflict of Interest The authors declare no conflict of interest.

Acknowledgment This project would not have been possible without the assistance of many people. I'd like to thank my three advisors, Abdeslam KADRANI, Imad EL HARRAKI, and El Hadj EZZAHID, for their invaluable support. I would like to take this opportunity to acknowledge the time and effort devoted by reviewers to improving the quality of this work.

References

- [1] J. Slimani, A. Kadrani, I. E. Harraki, E. H. Ezzahid, "Renewable Energy Development in Morocco: Reflections on Optimal Choices through Long-term Bottom-up Modeling," *International Conference on Electrical, Computer, and Energy Technologies, ICECET 2021*, 2021, doi:10.1109/ICECET52533.2021.9698630.
- [2] M. Chentouf, M. Allouch, "Renewable and alternative energy deployment in Morocco and recent developments in the national electricity sector," *Open Access Journal Photoenic*, **2**(1), 00017, 2018.
- [3] R. Madomercandy, "Investigation of The Feasibility of Renewables in Meeting The Moroccan Primary Energy Demand," Napier University, 2007.
- [4] B. J. Sellers, J. A. Voltaire, S. M. Gustafson, W. A. Hartman, "Energy Sustainability in Morocco," *Energy*, 2015.
- [5] T. Kousksou, A. Allouhi, M. Belattar, A. Jamil, T. El Rhafiki, A. Arid, Y. Zeraouli, "Renewable energy potential and national policy directions for sustainable development in Morocco," *Renewable and Sustainable Energy Reviews*, **47**, 46–57, 2015.
- [6] A. Haddouche, M. Taoumi, "Turning energy constraints into opportunities: the case of Morocco; Transformer la contrainte energetique en opportunités: le cas du Maroc," *Liaison Energie-Francophonie*, 2008.
- [7] H. Ben Sassi, C. Alaoui, F. Errahimi, N. Es-Sbai, H. B. Sassi, C. Alaoui, F. Errahimi, N. Es-Sbai, "Vehicle-to-grid technology and its suitability for the Moroccan national grid," *Journal of Energy Storage*, **33**(October), 102023, 2021, doi:10.1016/j.est.2020.102023.
- [8] M. Chentouf, M. Allouch, "Assessment of renewable energy transition in Moroccan electricity sector using a system dynamics approach," *Environmental Progress and Sustainable Energy*, **40**(4), 0–2, 2021, doi:10.1002/ep.13571.
- [9] "Stratégie énergétique: Trois ans de retard — L'Economiste," .
- [10] LesEco.ma, "Énergies renouvelables : objectif (presque) atteint ! - LesEco.ma," .
- [11] "Point de vue : Le Maroc va-t-il réaliser ses objectifs en production d'énergies renouvelables d'ici 2020 ?" .
- [12] T. Amegroud, "Morocco's power sector transition: Achievements and potential," 2018.
- [13] "Au Maroc, les ratés de la stratégie solaire," .
- [14] C. A. Floudas, P. M. Pardalos, *Encyclopedia of optimization*, Springer Science & Business Media, 2008.
- [15] T. Niet, A. Shivakumar, F. Gardumi, W. Usher, E. Williams, M. Howells, "Developing a community of practice around an open source energy modelling tool," *Energy Strategy Reviews*, **35**, 100650, 2021, doi:10.1016/J.ESR.2021.100650.
- [16] M. Howells, H. Rogner, N. Strachan, C. Heaps, H. Huntington, S. Kyreos, A. Hughes, S. Silveira, J. DeCarolis, M. Bazillian, A. Roehrl, "OSeMOSYS: The Open Source Energy Modeling System: An introduction to its ethos, structure and development," *Energy Policy*, **39**(10), 5850–5870, 2011, doi:10.1016/J.ENPOL.2011.06.033.
- [17] M. Welsch, M. Howells, M. Bazilian, J. F. DeCarolis, S. Hermann, H. H. Rogner, "Modelling elements of Smart Grids – Enhancing the OSeMOSYS (Open Source Energy Modelling System) code," *Energy*, **46**(1), 337–350, 2012, doi:10.1016/J.ENERGY.2012.08.017.
- [18] A. Dhakouani, E. Znouda, C. Bouden, "Impacts of energy efficiency policies on the integration of renewable energy," *Energy Policy*, **133**, 110922, 2019.
- [19] "Introduction to OSeMOSYS — OSeMOSYS 0.0.1 documentation," .
- [20] ONEE, "Chiffres Clés," 2019.
- [21] A. Hermelee, "Regional Reference Energy Systems: electric utility applications," 1979, doi:10.2172/6301105.

- [22] ONEE, “Depliant Statistiques FR 2019,” 2019.
- [23] “Analyse de la demande énergétique à l’horizon 2050,” .
- [24] “Annual Energy Outlook 2020,” .
- [25] “Welcome to ENERGYDATA.INFO - ENERGYDATA.INFO,” .
- [26] “Homepage - U.S. Energy Information Administration (EIA),” .
- [27] “Data — Electricity — 2021 — ATB — NREL,” .
- [28] “Welcome to TAQAMOROCCO — TAQAMOROCCO,” .
- [29] P. A. Bennouna, “19 Avril 2021,” 2021.
- [30] I. International Energy Agency, I. E. Agency, “Energy Policies Beyond IEA Countries: Morocco 2019 Review,” 2019.
- [31] C. Cannone, L. Allington, “Selected ‘Starter Kit’ energy system modelling data for Morocco (CCG),” 2021, doi:10.21203/RS.3.RS-480023/V2.
- [32] B. Amin, “Nul besoin de nouvelles centrales thermiques électriques - ni charbon ni fuel ni gaz naturel,” Technical report, 2021, doi:10.13140/RG.2.2.29241.90720.
- [33] P. Sullivan, W. Cole, N. Blair, E. Lantz, V. Krishnan, T. Mai, D. Mulcahy, G. Porro, “2015 Standard Scenarios Annual Report: U.S. Electric Sector Scenario Exploration,” 2015.
- [34] A. Derbali, “Determinants of the performance of Moroccan banks,” *Journal of Business and Socio-economic Development*, **1**(1), 102–117, 2021, doi:10.1108/JBSED-01-2021-0003.
- [35] J. Slimani, A. Kadrani, I. El Harraki, E. H. Ezzahid, “Long-Term Wind Power Development in Morocco: Optimality Assessment using Bottom-up Modeling,” *Proceedings of the 2021 Ural-Siberian Smart Energy Conference, USSEC 2021*, 215–220, 2021, doi:10.1109/USSEC53120.2021.9655736.
- [36] H. Ez-zaki, A. Diouri, A. Bouregba, F. Amor, S. Chhaiba, O. Sassi, Y. E. Rhaffari, “Ecofriendly bricks elaborated from coal waste of Moroccan Jer-rada Mining,” *MATEC Web of Conferences*, **149**, 01043, 2018, doi:10.1051/MATECONF/201814901043.
- [37] C. Philibert, “The present and future use of solar thermal energy as a primary source of energy,” *International Energy Agency*, 1–16, 2005.
- [38] M. T. Islam, N. Huda, A. B. Abdullah, R. Saidur, “A comprehensive review of state-of-the-art concentrating solar power (CSP) technologies: Current status and research trends,” *Renewable and Sustainable Energy Reviews*, **91**, 987–1018, 2018, doi:10.1016/J.RSER.2018.04.097.
- [39] Y. Zhao, M. Liu, C. Wang, X. Li, D. Chong, J. Yan, “Increasing operational flexibility of supercritical coal-fired power plants by regulating thermal system configuration during transient processes,” *Applied energy*, **228**, 2375–2386, 2018.
- [40] M. Simão, H. M. Ramos, “Hybrid Pumped Hydro Storage Energy Solutions towards Wind and PV Integration: Improvement on Flexibility, Reliability and Energy Costs,” *Water* 2020, Vol. 12, Page 2457, **12**(9), 2457, 2020, doi:10.3390/W12092457.
- [41] M. A. Gonzalez-Salazar, T. Kirsten, L. Prchlik, “Review of the operational flexibility and emissions of gas- and coal-fired power plants in a future with growing renewables,” *Renewable and Sustainable Energy Reviews*, **82**, 1497–1513, 2018, doi:10.1016/J.RSER.2017.05.278.
- [42] “Stratégie énergétique nationale : Interview avec M. Amin BENNOUNA,” .

Appendix

```
1 # Parameters
2 model.RETagTechnology = Param(model.REGION, model.TECHNOLOGY, model.YEAR, default=0)
3 model.RETagFuel = Param(model.REGION, model.FUEL, model.YEAR, default=0)
4 model.REMinProductionTarget = Param(model.REGION, model.YEAR, default=0)
5 # Model Variables
6 model.TotalREProductionAnnual = Var(model.REGION, model.YEAR, initialize=0.0)
7 model.RETotalProductionOfTargetFuelAnnual = Var(model.REGION, model.YEAR, initialize=0.0)
8
9 def FuelProductionByTechnologyAnnual_rule(model, r, t, f, y):
10     return (
11         sum(
12             model.ProductionByTechnology[r, l, t, f, y]
13             for l in model.TIMESLICE
14         )
15         == model.ProductionByTechnologyAnnual[r, t, f, y]
16     )
17
18 model.FuelProductionByTechnologyAnnual = Constraint(
19     model.REGION, model.TECHNOLOGY, model.FUEL, model.YEAR, rule=FuelProductionByTechnologyAnnual_rule
20 )
21
22 def TechIncluded_rule(model, r, y):
23     return (
24         sum(
25             model.ProductionByTechnologyAnnual[r, t, f, y]
26             * model.RETagTechnology[r, t, y]
27             for t in model.TECHNOLOGY
28             for f in model.FUEL
29         )
30         == model.TotalREProductionAnnual[r, y]
31     )
32
33
34 model.TechIncluded = Constraint(
35     model.REGION, model.YEAR, rule=TechIncluded_rule
36 )
37
38
39 def FuelIncluded_rule(model, r, y):
40     return (
41         sum(
42             model.RateOfProduction[r, l, f, y]
43             * model.RETagFuel[r, f, y]
44             * model.YearSplit[l, y]
45             for f in model.FUEL
46             for l in model.TIMESLICE
47         )
48         == model.RETotalProductionOfTargetFuelAnnual[r, y]
49     )
50
51
52 model.FuelIncluded = Constraint(
53     model.REGION, model.YEAR, rule=FuelIncluded_rule
54 )
55
56
57 def EnergyConstraint_rule(model, r, y):
58     return (
59         model.REMinProductionTarget[r, y]
60         * model.RETotalProductionOfTargetFuelAnnual[r, y]
61         <= model.TotalREProductionAnnual[r, y]
62     )
63
64
65 model.EnergyConstraint = Constraint(
66     model.REGION, model.YEAR, rule=EnergyConstraint_rule
67 )
```

Listing 1: Original Renewable energy constraint coding on Pyomo

```

1 # Parameters
2 model.PowerTagTechnology = Param(model.REGION, model.TECHNOLOGY, model.YEAR, default=0)
3 model.REMinCapacityTarget = Param(model.REGION, model.YEAR, default=0)
4
5 # Model Variables
6 model.TotalRECapacityAnnual = Var(model.REGION, model.YEAR, initialize=0.0)
7
8 ##### RE Capacity Target equations #####
9 def PWTechIncluded_rule(model, r, y):
10     return(
11         sum (
12             model.TotalCapacityAnnual[r, t, y]
13             * model.PowerTagTechnology[r, t, y]
14             for t in model.TECHNOLOGY
15         )
16         == model.TotalPowerCapacityAnnual[r, y]
17     )
18 model.PWTechIncluded = Constraint(
19     model.REGION, model.YEAR, rule=PWTechIncluded_rule
20 )
21
22 def RETechIncluded_rule(model, r, y):
23     return (
24         sum(
25             model.TotalCapacityAnnual[r, t, y]
26             *model.RETagTechnology[r, t, y]
27             for t in model.TECHNOLOGY
28         )
29         == model.TotalRECapacityAnnual[r, y]
30     )
31 model.RETechIncluded = Constraint(
32     model.REGION, model.YEAR, rule=RETechIncluded_rule
33 )
34
35 def RECapacityConstraint_rule(model, r, y):
36     return (
37         model.REMinCapacityTarget[r, y]*
38         model.TotalPowerCapacityAnnual[r, y]
39         <= model.TotalRECapacityAnnual[r, y]
40     )
41 model.RECapacityConstraint = Constraint(
42     model.REGION, model.YEAR, rule=RECapacityConstraint_rule
43 )

```

Listing 2: New Renewable energy constraint coding on Pyomo

Model Order Reduction and Distribution for Efficient State Estimation in Sensor and Actuator Networks

Ferdinand Friedrich*

University of Augsburg, Chair of Control Theory, Augsburg, 86159, Germany

ARTICLE INFO

Article history:

Received: 31 August, 2022

Accepted: 04 October, 2022

Online: 25 October, 2022

Keywords:

Model Order Reduction
Sensor and Actuator Network
Distributed State Estimation

ABSTRACT

We present in this contribution the distribution of a global multi-input-multi-output system in a sensor and actuator network. Based on controllability and observability, the global system is decentralized and the system properties are preserved as a result. This results in multiple decentralized local single-input-single-output systems with the same system order as the global system. As these local systems are implemented on decentralized CPUs in the network, the computational effort of the nodes has to be minimized. This is achieved by approximating the input and output behavior and reducing the system order of the decentralized local systems. For this purpose, the two most common techniques, Balanced Truncation and Krylov subspace methods, are presented. Kalman filters are used for state reconstruction. To approximate the input/output behavior of the global system, information from all decentralized reduced local systems is necessary, thus a fully interconnected network is used for communication. By decentralized fusion algorithms in the network nodes, the Kalman filter algorithm is separated and distributed in the network.

1 Introduction

This paper is an extension of "Reduced and Distributed Estimation in Sensor and Actuator Networks - Automated Design Based on Controllability and Observability" presented at the IEEE Conference on Control Technology and Applications (CCTA) 2021 in San Diego (virtual) and "Model-Order Reduction and System Distribution Using Krylov Subspaces - An Approach for Efficient State Estimation in Sensor and Actuator Networks" presented at the IEEE Conference on Control Technology and Applications (CCTA) 2022 in Trieste [1], [2].

The requirements for the accuracy of mathematical models are constantly increasing. Also large-scale MIMO¹ systems are not protected from the increasing requirements. These and the increasing complexity of the systems enhance the system order of the dynamic large-scale MIMO systems [3], [4]. The use of such complex and large-scale models in simulation is very cumbersome and sometimes impossible. Moreover, system analysis and controller design using known methods is also impossible. For this reason, methods for linear and nonlinear systems are developed to reduce large models to a manageable size and to approximate the characteristic properties related to the input/output behavior [5]. Memory and computational requirements are reduced by distributing the system so that only

parts of the model are available for local systems [6]. However, this requires decentralized estimation procedures.

If the internal model relationships (e.g. mechanical and electrical) are known, the distribution into local systems is performed manually [6]. Furthermore, system digraphs and cut-point sets are used for model distribution [7]. In [8], a manual method for distributing large systems is also presented. In this method, reduced local systems with overlapping state vectors are created. All described manual methods share the property that the actual system order of the global system is preserved in the network despite the distribution into local systems.

In contrast, we use decentralization for distribution based on the controllability and observability of the global MIMO system. By decoupling the inputs and outputs, several local SISO² systems are formed from the global MIMO system. These decentralized local systems are implemented in a fully interconnected network. Moreover, we use model order reduction techniques, resulting in the decentralized local systems with much lower order and preserving the system properties [9]. Further, the computational effort in each network node is reduced.

Several techniques for reducing the model order are known [10]. The most common techniques for approximating the input and output behavior are Balanced Truncation and Krylov subspace methods.

* Corresponding Author: Ferdinand Friedrich, University of Augsburg, Chair of Control Theory, Universitaetsstrasse 2, 86159 Augsburg, ferdinand.friedrich@uni-a.de¹Multi-Input-Multi-Output²Single-Input-Single-Output

In Balanced Truncation, the Hankel singular values are analyzed and the states with a small impact on the energy transport are neglected and truncated [11]. In *Krylov* subspace methods, to approximate the input and output behavior, the transfer functions of the global and reduced systems are expanded at an arbitrary development point. In this process, the first coefficients, also called moments, of the Taylor series of the transfer function are matched [12], [13].

Therefore, the methods are also called moment matching with the *Padé*-type approximation method based on rational interpolation [14], [15]. If only a single development point (several are also possible) $s = 0$ is chosen, the reduction is ascribed to an *padé*-approximation [16]. A more extensive background on *Krylov* subspace methods is given in [10], [17], and [18]. Model order reduction with *Krylov* subspaces requires less memory and computational effort (compared to Balanced Truncation) [19]. Meanwhile, several algorithms for the *Krylov* subspaces are known. In this paper, we only use the *Arnoldi* algorithm with its extension to MIMO systems [20], [21].

This paper is organized as follows. In Section 2, the systems under consideration are defined. The methods used to reduce the model order are presented in Section 3. The distribution and deployment in a network are demonstrated in Section 4. A demonstrator is used for detailed real-time experimental evaluation of the presented methods and the results are presented in Section 5.

2 Preliminaries

In this contribution, we refer to global multi-input-multi-output linear time-invariant systems of the form

$$\Sigma_G = \begin{cases} \dot{\mathbf{x}}(t) = \mathbf{A}\mathbf{x}(t) + \mathbf{B}\mathbf{u}(t) \\ \mathbf{y}(t) = \mathbf{C}\mathbf{x}(t) \end{cases} \quad (1)$$

Here, $\mathbf{A} \in \mathbb{R}^{n \times n}$ is the system matrix and $\mathbf{B} \in \mathbb{R}^{n \times p}$ is the input matrix. The matrix $\mathbf{C} \in \mathbb{R}^{q \times n}$ is the output matrix and \mathbf{x} , \mathbf{u} as well as \mathbf{y} are the state vector, the inputs and the outputs of the global continuous-time system Σ_G .

3 Model Order Reduction

Precise modeling of technical systems often leads to large systems of differential equations, requiring a high computational effort. For this reason, methods are used to reduce the order of the systems. Thereby the characteristic properties are supposed to be preserved and the input/output behavior has to be maintained as exactly as possible. The linear reduction methods can be categorized into three classes. One class is the modal reduction methods, in which less dominant eigenvalues and eigenmodes are removed from the system representation. The second class of reduction methods, which is also used in this contribution, are the balanced methods. Here, energy-oriented analyses are used to remove an unimportant subsystem. The third class describes the *Krylov* subspace methods. In this method, certain parameters of the transfer function, the so-called moments, are preserved in the reduced model. This class is also used for decentralization and distribution in this contribution.

3.1 Balanced Truncation

The Balanced Truncation (BT) method is based on the system properties of controllability and observability. Different methods for determining controllability and observability are known. For balanced truncation, the *Gramian* controllability matrix and the *Gramian* observability matrix shall be used.

A system (1) is controllable if a control vector $\mathbf{u}(t)$ exists that transforms the system from an initial state $\mathbf{x}(t = 0) = \mathbf{0}$ to a final state in finite time. The controllability *Gramian* is defined as

$$\mathbf{W}_c = \int_0^\infty e^{\mathbf{A}t} \mathbf{B} \mathbf{B}^T e^{\mathbf{A}^T t} dt. \quad (2)$$

Furthermore, a system (1) is fully observable if the system state $\mathbf{x}(t = 0)$ can be determined by observing the output $\mathbf{y}(t)$ over a finite time interval. The *Gramian* observability matrix is derived as follows

$$\mathbf{W}_o = \int_0^\infty e^{\mathbf{A}^T t} \mathbf{C}^T \mathbf{C} e^{\mathbf{A}t} dt. \quad (3)$$

For the transfer of the system (1) from the initial position \mathbf{x}_0 to the final position \mathbf{x}_e in infinite time, the energy $\mathbf{x}_e^T \mathbf{W}_c^{-1} \mathbf{x}_e$ must be applied. In contrast, the energy $\mathbf{x}_0^T \mathbf{W}_o \mathbf{x}_0$ is generated when the system (1) in the initial position \mathbf{x}_0 can oscillate uninfluenced ($\mathbf{u}(t) = 0$) to its rest position. This energy-based approach reveals that a difficultly controllable state requires a high level of energy to achieve. This can also be observed in the eigenvalues of the matrix \mathbf{W}_c^{-1} . The more energy is needed to reach a specific state, the larger is its eigenvalue. This analysis can also be used for observability. However, here a small eigenvalue of the state determines that it is badly observable, because only a small amount of energy is visible.

By a state transformation the system Σ_G with order n is transformed into a balanced state-space representation, whereby the *Gramian* matrices

$$\mathbf{W}_c = \mathbf{W}_o = \begin{bmatrix} \sigma_1 & & 0 \\ & \ddots & \\ 0 & & \sigma_n \end{bmatrix} \quad (4)$$

are diagonal and identical [22]. In [23] it was demonstrated that any complete controllable and observable system can be transformed into a balanced state-space representation. The diagonal elements σ_i of (4) are the *Hankel singular values* (HSV). The HSV can be determined by

$$\sigma_i = \sqrt{\lambda_i \mathbf{W}_c \mathbf{W}_o}. \quad (5)$$

Here, λ_i represents the eigenvalues of the system Σ_G . The HSVs are invariant to transformations, so small HSVs correspond to badly controllable and observable states [22], [24]. The transformation matrix to the balanced state-space representation of (1) are determined in four steps:

1. In [25] it is shown that the controllability (2) and the observability matrix (3) are also solutions of the *Lyapunov* equation

$$\mathbf{A} \mathbf{W}_c + \mathbf{W}_c \mathbf{A}^T + \mathbf{B} \mathbf{B}^T = \mathbf{0} \quad (6)$$

$$\mathbf{A}^T \mathbf{W}_o + \mathbf{W}_o \mathbf{A} + \mathbf{C}^T \mathbf{C} = \mathbf{0} \quad (7)$$

2. After solving the *Lyapunov* equation, *Gramian* matrices are positive definite and can be decomposed into *Cholesky* factors: For the solution of the *Lyapunov* equation, one positive

definite solution for \mathbf{W}_c and \mathbf{W}_o exists for every fully controllable and observable system. The *Gramian* matrices can be decomposed into *Cholesky* factors

$$\mathbf{W}_c = \mathbf{S}^T \mathbf{S} \quad (8)$$

$$\mathbf{W}_o = \mathbf{R}^T \mathbf{R} \quad (9)$$

3. The product $\mathbf{S}\mathbf{R}^T$ is subjected to a singular value decomposition (SVD),

$$\mathbf{S}\mathbf{R}^T = \mathbf{U}\mathbf{\Sigma}\mathbf{V}^T, \quad (10)$$

which yields the orthogonal matrices \mathbf{U} and \mathbf{V} , and the diagonal matrix $\mathbf{\Sigma}$ of HSVs.

4. The matrix \mathbf{T} for transformation to balanced state-space representation is

$$\mathbf{T} = \mathbf{\Sigma}^{-\frac{1}{2}} \mathbf{V}^T \mathbf{R} \quad (11)$$

and its inverse is

$$\mathbf{T}^{-1} = \mathbf{S}^T \mathbf{U} \mathbf{\Sigma}^{-\frac{1}{2}} \quad (12)$$

In [26] it is presented that these matrices (11) and (12) transform a fully controllable and observable system in balanced state-space representation.

$$\mathbf{\Sigma}_{Bal} = \begin{cases} \dot{\mathbf{x}}_{Bal}(t) &= \mathbf{T}^{-1} \mathbf{A} \mathbf{T} \mathbf{x}_{Bal}(t) + \mathbf{T}^{-1} \mathbf{B} \mathbf{u}(t) \\ \mathbf{y}(t) &= \mathbf{C} \mathbf{T} \mathbf{x}_{Bal}(t) \end{cases} \quad (13)$$

The HSVs reveals that not all states are equally well controllable and observable. If only the states which contributes much to the energy transfer are used, then only the first r HSVs of $\mathbf{\Sigma}$ and the first r columns of \mathbf{U} as well as \mathbf{V} need to be considered. BT can also be interpreted as a *Petrov-Galerkin* projection into a reduced subspace [22]. For this projection, the transformation matrices (11) and (12) are modified.

$$\mathbf{W}_{BT}^T = \mathbf{\Sigma}^{-\frac{1}{2}} \mathbf{U}^T \mathbf{R}^T \quad (14)$$

$$\mathbf{V}_{BT} = \mathbf{S} \mathbf{V} \mathbf{\Sigma}^{-\frac{1}{2}} \quad (15)$$

Where $\mathbf{W}_{BT} \in \mathbb{R}^{r \times n}$ and $\mathbf{V}_{BT} \in \mathbb{R}^{n \times r}$ are the biorthogonal projection matrices. By the projection matrices only the first r columns are considered, thus the system order $r < n$ is reduced. This truncates only the HSVs with a small participation in the energy transfer, thus the input/output behavior is only marginally affected.

3.2 Krylov Subspaces

If numerically robust and efficient computations are required for model order reduction, the reduction must be performed by *Krylov* subspaces. Additionally, this method is used for very large systems. In [21] and [27] the *Krylov* subspace is generally defined. Let \mathbf{M} be an arbitrary constant matrix and \mathbf{v} a constant vector, called starting vector, then the *Krylov* subspace is defined as follows

$$\mathcal{K}_r(\mathbf{M}, \mathbf{v}) = \text{span} \{ \mathbf{v}, \mathbf{M}\mathbf{v}, \dots, \mathbf{M}^{r-1}\mathbf{v} \}. \quad (16)$$

Here, $\mathbf{M} \in \mathbb{R}^{n \times n}$, $\mathbf{v} \in \mathbb{R}^n$ are the arbitrary matrix and vector as well as $\mathcal{K}_r \subseteq \mathbb{R}^n$ is a r -dimensional subspace. For model order reduction with *Krylov* subspaces also transformation matrices \mathbf{W} and \mathbf{V} are used. The matrices are composed of column vectors, which are also

the basis of the *Krylov* subspaces.

Referring to the system (1), the transformation matrix \mathbf{V} as an arbitrary basis of the input subspace is determined by

$$\mathcal{K}_{r_1}(\mathbf{A}^{-1}, \mathbf{A}^{-1}\mathbf{B}). \quad (17)$$

In addition, the transformation matrix \mathbf{W} is derived as the basis of the output subspace

$$\mathcal{K}_{r_2}(\mathbf{A}^{-T}, \mathbf{A}^{-T}\mathbf{C}^T). \quad (18)$$

For the reduction, $r_1 = r_2 = r$ must be required, whereby it must be ensured that both transformation matrices \mathbf{V} and \mathbf{W} have full rank r . The *Arnoldi* algorithm is used to determine the transformation matrices \mathbf{V} and \mathbf{W} . Algorithm 1 shows the calculation of the transformation matrix \mathbf{V} based on (17).

Algorithm 1: MIMO Arnoldi Algorithm [21]

Result: Transformation matrix \mathbf{V}

Set $\mathbf{v}_1 = \frac{\mathbf{b}_1}{\sqrt{\mathbf{b}_1^T \mathbf{b}_1}}$ and \mathbf{b}_1 is the first starting vector;

for $i=2,3,\dots$ **do**

if $i \leq m_i$ **then**

 Next vector is the i -th starting vector

else

$\mathbf{r}_i = \mathbf{A}_1 \mathbf{v}_{i-m_1}$

end

 Set $\hat{\mathbf{v}}_i = \mathbf{r}_i$

 > Orthogonalization

for $j = 1, \dots, i-1$ **do**

$\mathbf{h} = \hat{\mathbf{v}}_i^T \mathbf{v}_j$

$\hat{\mathbf{v}}_i = \hat{\mathbf{v}}_i - \mathbf{h} \mathbf{v}_j$

end

if $\hat{\mathbf{v}}_i = 0$ **then**

 Reduce m_1 to $m_1 - 1$

m_1 is nonzero calculate new \mathbf{r}_i

else

$\mathbf{v}_i = \frac{\hat{\mathbf{v}}_i}{\sqrt{\hat{\mathbf{v}}_i^T \hat{\mathbf{v}}_i}}$

 > i -th column of matrix \mathbf{V}

end

end

The same algorithm and (18) is used to determine the matrix \mathbf{W} . The columns of the transformation matrices are spanning the corresponding *Krylov* input and output subspace (Fig. 1). If the model order reduction is performed based on (17) and (18) with matrices \mathbf{V} and \mathbf{W} , the reduction procedure is called two-sided. Obviously, only one of the two matrices can be used. The remaining transformation matrix is chosen arbitrarily, but it must have full rank. The reduction procedure is then called one-sided.

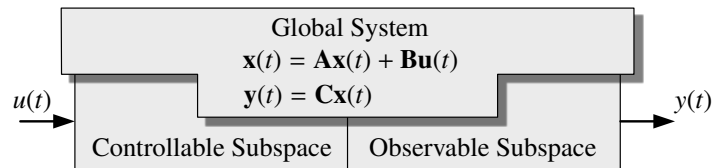


Figure 1: Controllability and observability are major properties and subspaces of dynamical control systems.

In *Krylov* subspace methods, the transfer functions of the original system and the reduced system are expanded at an arbitrary development point s_0 , thus the first moments (coefficients of the *Taylor*

series) match. In this contribution, the development point $s_0 = 0$ is chosen, whereby the transfer function of (1) is described by a *Taylor* series around the developing point. The resulting i -th moment of the series around $s = 0$ is

$$\mathbf{m}_i = \mathbf{C}\mathbf{A}^{-(i+1)}\mathbf{B} \quad (19)$$

with $i = 0, 1, \dots$

One-sided *Krylov* reduction methods reduce the original system to order r . In this case, the first r moments of the original system and the reduced system are matched. In the case of a two-sided method, the first $2r$ moments are matched.

The moment \mathbf{m}_0 corresponds to the stationary gain and is preserved in the *Krylov*-based reduction, so the reduced system is equally stationary accurate. Two-sided *Krylov* methods adjust two times as many moments for the same reduction size compared to one-sided methods. For this reason, two-sided methods are usually preferable. In addition, they offer the advantage that the reduction is independent of the representation of the original model. In contrast, regular state transformations and other equivalent transformations of the original model in one-sided reduction affect the transfer behavior in the reduced model [28]. Using a projection, the state vector $\mathbf{x}(t)$ is approximated by the reduced state vector $\mathbf{x}_r(t)$ as follows

$$\mathbf{x}(t) = \mathbf{V}\mathbf{x}_r(t). \quad (20)$$

Here, $\mathbf{V} \in \mathbb{R}^{n \times r}$ is the basis of the *Krylov* input subspace and is determined using algorithm 1. $\mathbf{x}_r \in \mathbb{R}^r$ is the state vector of the reduced system.

By applying the *Arnoldi* algorithm twice with different subspaces (17) or (18), the reduced system with the transformation matrices can be determined as follows.

$$\Sigma_r = \begin{cases} \dot{\mathbf{x}}_r(t) &= \mathbf{W}^T \mathbf{A} \mathbf{V} \mathbf{x}_r(t) + \mathbf{W}^T \mathbf{B} \mathbf{u}(t) \\ \mathbf{y}_r(t) &= \mathbf{C} \mathbf{V} \mathbf{x}_r(t) \end{cases} \quad (21)$$

4 Model Distribution

Decentralization and distribution of global large-scale MIMO systems in a sensor and actuator network achieve order reduction, as individual nodes never need to estimate the entire global state vector. Often, this distribution occurs due to internal system relationships or due to physical system boundaries. In this section, we present two approaches for decentralization and distribution, both based on controllability and observability of the global system. One approach demonstrates decentralization into local SISO systems based on the inputs and outputs of the global MIMO system. The order of the local systems is reduced to further minimize the computational effort using model order reduction techniques. In a further approach, the local SISO systems will be generated based on the controllable and observable subspace. The order reduction resulting from decentralization and distribution is reflected in a reduced computational effort for each node. As a consequence, the required computational effort in a local node is lower than in a centralized system.

4.1 Input-/Output-based

By decentralizing the inputs and outputs of (1), m local systems with an equal number of sensors and actuators are derived. Thereby, the

outputs of the global system (1) are decentralized without further considerations. To decentralize the inputs, the physical couplings must be considered. For this purpose, the decoupling method from [29] can be used. It is assumed that the inputs have a localized impact in large-scale systems. The inputs of the global system are decentralized into local systems as in [1]. Decentralization and distribution provides the ability to distribute the system in a network. In a fully connected network, minimal non-modeled couplings between the inputs are considered by communication.

Thus, m local SISO systems are derived from the global system Σ_G . During decentralization, local systems with one input and one output each are expanded, but the system order n is not reduced (Fig. 2).

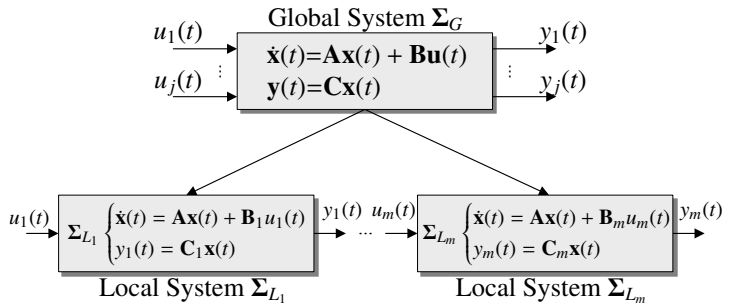


Figure 2: Decentralization of the global MIMO system with j inputs and outputs into m local systems.

The controllability and observability of the global system were not modified by decentralization. It can be demonstrated that by superposing the local *Gramian* controllability matrix \mathbf{W}_{c_j} and the local observability matrix \mathbf{W}_{o_j} , the global controllability \mathbf{W}_c and observability \mathbf{W}_o are recovered. The local systems are described as follows

$$\Sigma_{L_j} = \begin{cases} \dot{\mathbf{x}}(t) &= \mathbf{A}\mathbf{x}(t) + \mathbf{B}_j u_j(t) \\ y_j(t) &= \mathbf{C}_j \mathbf{x}(t) \end{cases} \quad (22)$$

with $j = 1, \dots, m$.

Where m describes the number of sensors and actuators. The index j at the input matrix \mathbf{B} and at the output matrix \mathbf{C} represents the corresponding column and row of the matrices. This defines local SISO systems Σ_{L_j} with one sensor and actuator each.

The local systems (22) are implemented on different decentralized CPUs, which communicate through a fieldbus system, and are used in a network.

4.1.1 Application in a Sensor and Actuator Network

Each local system Σ_{L_j} describes a network node where a Kalman Filter (KF) is used for state reconstruction [30]. The computational effort in the network nodes is further reduced if the KF algorithm is separated [1]. In the prediction step the system inputs are used and in the correction step, the observations are processed. Both filter steps communicate through a priori and a posteriori estimation $\hat{\mathbf{x}}(k)$ and covariance $\mathbf{P}(k)$. As the inputs are only applied in the prediction step, this part of the algorithm is implemented in the actuator nodes. In the sensor nodes, the observations are applied and only the correction step of the KF algorithm is executed. *Splitting the Kalman Filter* (SKF) provides the distribution of the local system (22) in a

network of sensor and actuator nodes. Each network node only has to calculate a part of the KF algorithm. By exchanging the a priori and a posteriori information, both filtering steps are connected in the network.

Therefore, the continuous-time dynamics of (22) must be transformed into discrete-time dynamics. To further minimize the computational effort, it is necessary to reduce the order of the discrete decentralized local systems. For this purpose, the model order reduction techniques presented in Section 3 are used.

$$\Sigma_{Lr,j} = \begin{cases} \dot{\mathbf{x}}_r(t) = \mathbf{W}^T \mathbf{A} \mathbf{V} \mathbf{x}_r(t) + \mathbf{W}^T \mathbf{B}_j u_j(t) \\ y_{r,j}(t) = \mathbf{C}_j \mathbf{V} \mathbf{x}_r(t) \end{cases} \quad (23)$$

with $j = 1, \dots, m$.

The decentralized reduced local systems (23) can also be used in the SKF. Depending on the reduction method, the projection matrices \mathbf{V} and \mathbf{W} are determined by Section 3.1 or Section 3.2. However, this turns the SKF into the *Splitted Reduced Kalman Filter* (SRKF)

Prediction

$$\hat{\mathbf{x}}_r^-(k) = \mathbf{A}_r(k-1) \hat{\mathbf{x}}_r^+(k-1) + \mathbf{B}_r(k-1) u_j(k-1) \quad (24)$$

$$\mathbf{P}_r^-(k) = \mathbf{A}_r(k-1) \mathbf{P}_r^+(k-1) \mathbf{A}_r^T(k-1) + \mathbf{Q}(k-1) \quad (25)$$

Correction

$$\mathbf{K}_r(k) = \mathbf{P}_r^-(k) \mathbf{C}_r^T(k) [\mathbf{C}_r(k) \mathbf{P}_r^-(k) \mathbf{C}_r^T(k) + \mathbf{R}(k)]^{-1} \quad (26)$$

$$\hat{\mathbf{x}}_r^+(k) = \hat{\mathbf{x}}_r^-(k) + \mathbf{K}_r(k) [y_j(k) - \mathbf{C}_r(k) \hat{\mathbf{x}}_r^-(k)] \quad (27)$$

$$\mathbf{P}_r^+(k) = [\mathbf{I} - \mathbf{K}_r(k) \mathbf{C}_r(k)] \mathbf{P}_r^-(k) [\mathbf{I} - \mathbf{K}_r(k) \mathbf{C}_r(k)]^T + \mathbf{K}_r(k) \mathbf{R}_r(k) \mathbf{K}_r^T(k). \quad (28)$$

The index r expresses that a reduced model $\Sigma_{Lr,j}$ is used in the decentralized local nodes. The index j in (24) and (27) refers to the corresponding local system.

The distribution of prediction (24), (25) and correction (26),(27) as well as (28) of the local reduced systems (23) in sensor and actuator network nodes, is connected by the communication of the reduced a priori and a posteriori information. A fully connected network is formed if all m local reduced systems $\Sigma_{Lr,j}$ communicate. This requires each sensor node to communicate its reduced a posteriori information to all local actuator nodes. This information is processed in the actuator nodes in a fusion step of the SRKF and used in determining the reduced a priori information. The SRKF becomes the *Decentralized Splitted Reduced Kalman Filter* (DSRKF) (Fig. 3). In [31], [32] and [33], a different notation is proposed for the a posteriori values, as the correction is performed using only the local observation.

$$\tilde{\mathbf{P}}_{r,j}^+(k) = \left[(\mathbf{P}_{r,j}^-(k))^{-1} \mathbf{C}_{r,j}^T(k) \mathbf{R}_{r,j}^{-1}(k) \mathbf{C}_{r,j}(k) \right]^{-1} \quad (29)$$

$$\tilde{\mathbf{x}}_{r,j}^+ = \hat{\mathbf{x}}_{r,j}^-(k) + \mathbf{K}_{r,j}(k) [y_i(k) - \mathbf{C}_{r,j}(k) \hat{\mathbf{x}}_{r,j}^-] \quad (30)$$

For the interaction in the network between each local system, the information of the reduced covariance error and the reduced state error are used. These errors are determined in the corresponding local sensor nodes and transmitted to the actuator nodes. Thus, all actuator nodes receive the reduced error information of the sensor nodes. The reduced covariance error and reduced state error for the

decentral reduced local system $\Sigma_{Lr,j}$ is determined by

$$\mathbf{E}_{r,j}(k) = (\tilde{\mathbf{P}}_{r,j}^+(k))^{-1} - (\mathbf{P}_{r,j}^-(k))^{-1} \quad (31)$$

$$\mathbf{e}_{r,j}(k) = (\tilde{\mathbf{P}}_{r,j}^+(k))^{-1} \tilde{\mathbf{x}}_{r,j}^+(k) - (\mathbf{P}_{r,j}^-(k))^{-1} \hat{\mathbf{x}}_{r,j}^-(k) \quad (32)$$

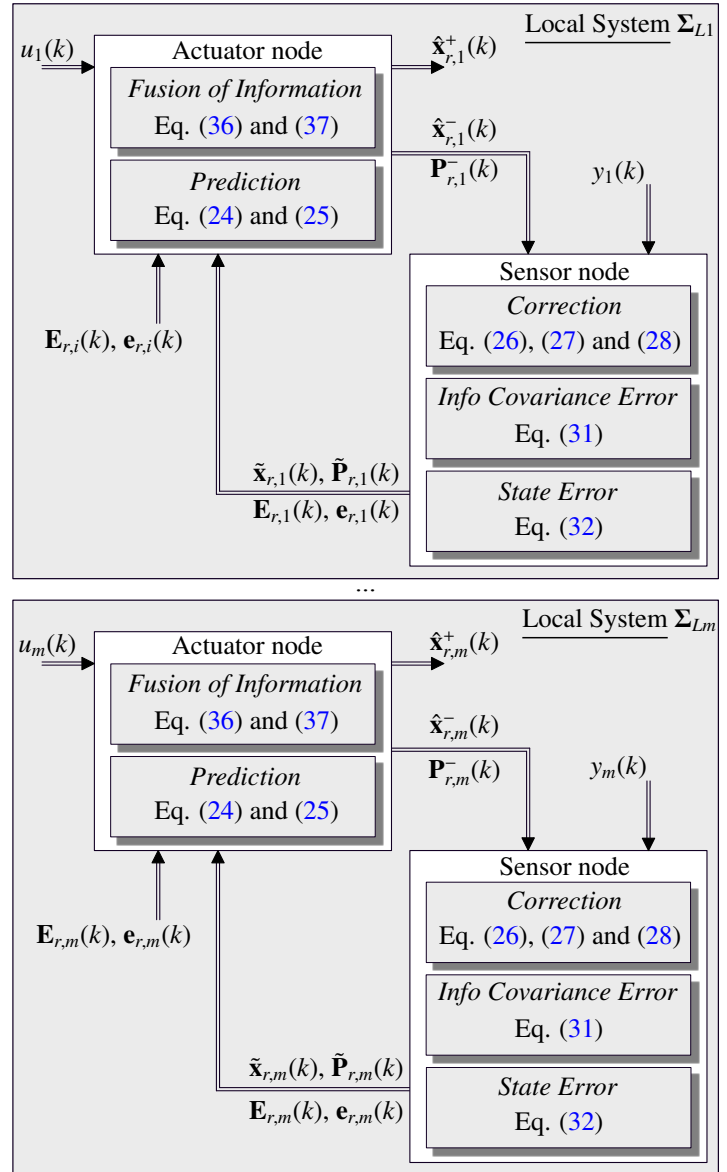


Figure 3: Splitting the KF algorithm on the actuator and sensor nodes. In all nodes reduced models are implemented (SRKF).

Each local system is projected by the matrices \mathbf{V} and \mathbf{W} into its own reduced subspace. In order to exchange information between the subspaces, the information, for instance the reduced error covariances $\mathbf{E}_{r,j}$ and the reduced state error vectors $\mathbf{e}_{r,j}$, must be transformed. The transformation from the transmitter subspace to the receiver subspace is performed in the receiving local actuator node. For the transformation matrices proposed in [31], we use the matrices already determined by the model order reduction in Section 3. These matrices are not symmetric, thus the *Moore-Penrose* inverse is used and specified by the superscript \dagger . If the projection matrices

are determined by the method of Section 3.1, the transformation between the local subspaces are performed as follows

$$\mathbf{V}_{r,ji} = \mathbf{W}_{BT,i} \mathbf{W}_{BT,j}^\dagger \quad (33)$$

For the state of clarity, the transformation using the methods form Section 3.2 is identical. As mentioned above, small couplings between inputs are considered in a fully networked sensor and actuator network. The error information of local system j are transformed by

$$\mathbf{E}_{r,ji}(k) = (\mathbf{V}_{r,ji}^T)^\dagger \mathbf{E}_{r,j}(k) \mathbf{V}_{r,ji}^\dagger \quad (34)$$

$$\mathbf{e}_{r,ji}(k) = (\mathbf{V}_{r,ji}^T)^\dagger \mathbf{e}_{r,j}(k) \quad (35)$$

into the subspace of the system i . By adding fusion equations

$$(\mathbf{P}_{r,j}^+(k))^{-1} = (\mathbf{P}_{r,i}^-(k))^{-1} + \sum_{j=1}^m \mathbf{E}_{r,ji}(k) \quad (36)$$

$$\hat{\mathbf{x}}_{r,j}^+(k) = \mathbf{P}_{r,j}^+(k) \left[(\mathbf{P}_{r,j}^-(k))^{-1} \hat{\mathbf{x}}_{r,j}^-(k) + \sum_{j=1}^m \mathbf{e}_{r,ji}(k) \right] \quad (37)$$

to each actuator node, a fully interconnected network can be created.

Another approach uses for fusion all state estimates and covariance matrices of the decentralized reduced local systems (23). Here, the estimated a posteriori state vectors $\hat{\mathbf{x}}^+$ and a posteriori covariance matrix \mathbf{P}^+ are transmitted to a central fusion center. There is no direct communication between the locally reduced systems. The fusion is performed in the center by the *Generalized Millman's Formula* (GMF). The GMF combines $\hat{\mathbf{x}}^+$ and \mathbf{P}^+ for multisensor systems [34], [35]. Assuming that m local systems estimate the vector $\mathbf{x} \in \mathbb{R}^n$ with $\hat{\mathbf{x}}$, these estimates are applied to determine the related local error covariance

$$\mathbf{P}_{i,j} = \text{cov}(\tilde{\mathbf{x}}_i, \tilde{\mathbf{x}}_j) \quad (38)$$

$$\tilde{\mathbf{x}}_i = \mathbf{x} - \hat{\mathbf{x}}_i \quad (39)$$

$$i, j = 1, \dots, m.$$

The objective of GMF is to find the optimal estimate of \mathbf{x} . [35] presents that this is achieved if the individual ξ_i are weighted and summed

$$\hat{\mathbf{x}} = \sum_{i=1}^m \xi_i \hat{\mathbf{x}}_i. \quad (40)$$

In addition, it is shown that the weighting matrix ξ_i is found by minimizing the mean square error criterion, and that the minimization leads to linear equations

$$\sum_{i=1}^{m-1} \xi_i (\mathbf{P}_{i,m-1} - \mathbf{P}_{i,m}) + \xi_m (\mathbf{P}_{m,m-1} - \mathbf{P}_{m,m}) = \mathbf{0} \quad (41)$$

$$\sum_{i=1}^m \xi_i = \mathbf{I}. \quad (42)$$

Therefore, the fusion of two local state vectors is proved to be equivalent to the well known *Bar-Shalom-Campo* formula. A more detailed background is given by [34] and [36].

Each decentralized reduced local system uses a KF for state reconstruction and communicates the estimated states and covariances to a fusion center (Fig. 4).

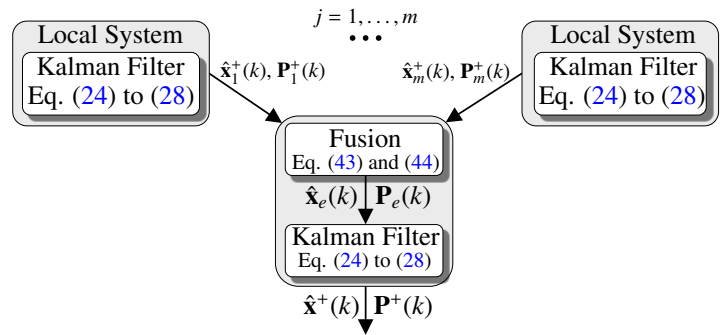


Figure 4: The state reconstruction in the local nodes is performed by a KF with a reduced model.

For independent estimates, GMF has a simple closed form

$$\hat{\mathbf{x}}_e = \mathbf{P}_e \sum_{j=1}^m \mathbf{P}_j^{+1} \hat{\mathbf{x}}_j^+ \quad (43)$$

$$\mathbf{P}_e^{-1} = \sum_{j=1}^m \mathbf{P}_j^{+1}. \quad (44)$$

Due to decentralization and model order reduction, the decentralized reduced systems are transformed into different subspaces. The decentralized reduced estimates of the local systems have to be transformed into a common subspace for fusion. For this purpose, a reference system is derived from the global system (1). The reference system is described as follows

$$\Sigma_{Ref} = \begin{cases} \dot{\mathbf{x}}_{Ref}(t) = \mathbf{W}^T \mathbf{A} \mathbf{V} \mathbf{x}_{Ref}(t) + \mathbf{W}^T \mathbf{B} \mathbf{u}(t) \\ \mathbf{y}_{Ref}(t) = \mathbf{C} \mathbf{V} \mathbf{x}_{Ref}(t). \end{cases} \quad (45)$$

In the model order reduction, the reference system is adapted to the order of the decentralized reduced local systems. In deriving the reference system, attention was given only to the stability and not to the quality of the approximation. At the fusion center, the transmitted information are considered as uncorrelated as they originate from different subspaces. After the received information is transformed into the reference system subspace, it is fused (43) and (44). Based on the reference model, a KF is implemented in the fusion center. This interprets the fusion $\hat{\mathbf{x}}_e$ as an observation and this improves the fusion result.

4.2 Subspace based

Using the input subspace \mathcal{K}_{r1} and the output subspace \mathcal{K}_{r2} separately as well as algorithm 1, the global system Σ_G is reduced and distributed. Here, a one-sided method is chosen, thus the controllable subspace is determined only by using the transformation matrix \mathbf{V} [37]. For reduction, $\mathbf{W}^* = \mathbf{V}$ is chosen so that \mathbf{W}^* has maximum rank. Thus, a reduced order model is found,

$$\Sigma_{r,C} = \begin{cases} \dot{\mathbf{x}}_{r,C}(t) = \mathbf{W}^{*T} \mathbf{A} \mathbf{V} \mathbf{x}_{r,C}(t) + \mathbf{W}^{*T} \mathbf{B} \mathbf{u}(t) \\ \mathbf{y}_{r,C}(t) = \mathbf{C} \mathbf{V} \mathbf{x}_{r,C}(t) \end{cases} \quad (46)$$

which describes the controllable subspace. The application of algorithm 1 is repeated for the Krylov output space. Thus the matrix \mathbf{W} is determined. For this reduction $\mathbf{V}^* = \mathbf{W}$ is chosen, thus also here the second matrix has maximal rank. The reduced model

$$\Sigma_{r,O} = \begin{cases} \dot{\mathbf{x}}_{r,O}(t) = \mathbf{W}^T \mathbf{A} \mathbf{V}^* \mathbf{x}_{r,O}(t) + \mathbf{W}^T \mathbf{B} \mathbf{u}(t) \\ y_{r,O}(t) = \mathbf{C} \mathbf{V}^* \mathbf{x}_{r,O}(t) \end{cases} \quad (47)$$

describes the observable subspace. Using (46) and (47), the global system is approximated over the controllable and observable subspace. A reduced system is obtained by the system matrix $\mathbf{A}_{r,C}$ and the input matrix $\mathbf{B}_{r,C}$, of the controllable subspace, and by the output matrix $\mathbf{C}_{r,O}$, of the observable subspace

$$\begin{aligned} \mathbf{A}_{r,C} &= \mathbf{W}^{*T} \mathbf{A} \mathbf{V} \\ \mathbf{B}_{r,C} &= \mathbf{W}^{*T} \mathbf{B} \\ \mathbf{C}_{r,O} &= \mathbf{C} \mathbf{V}^* \end{aligned} \quad (48)$$

4.2.1 Application in a Sensor and Actuator Network

A KF is also used for state reconstruction in the subspace-based distribution. After the transformation from continuous to discrete time, the system is used in KF. By distributing into the controllable and observable subspace, this method can also be used in a network. Applying the SKF presented in Section 4.1, the computational effort in the decentralized CPUs is reduced because each network node only needs to determine a part of the KF algorithm. By using the reduced model (48), the SKF becomes the SRKF as described above (Fig. 5). However, information from both subspaces is necessary for a complete approximation. By communicating a priori estimates $\hat{\mathbf{x}}_r^-$ and covariance matrices \mathbf{P}_r^- as well as a posteriori state vectors $\hat{\mathbf{x}}_r^+$ and covariance matrices \mathbf{P}_r^+ , a interconnected network is created. To achieve this objective, the orthonormal bases from Section 3 are used. For communication between the reduced controllable and reduced observable subspace, the transmitted data must be transformed into the target subspace.

$$\mathbf{T}_c^o = \mathbf{W} \mathbf{V}^\dagger. \quad (49)$$

The index of \mathbf{T} describes the starting point and the superscript indicates the target point of transformation. Due to the lack of symmetry of the orthonormal bases, the Moore-Penrose inverse is here also necessary. As in the previous section, we assume that no packets are lost and that both nodes operate with the same sampling time.

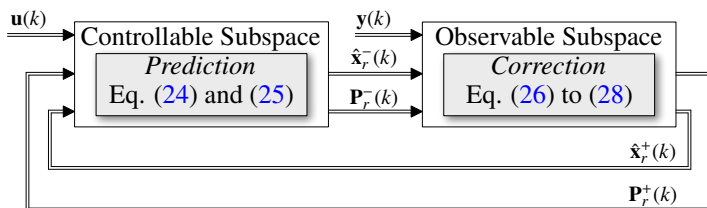


Figure 5: Distribution of the global linear system on the basis of controllability and observability

5 Experimental Evaluation and Results

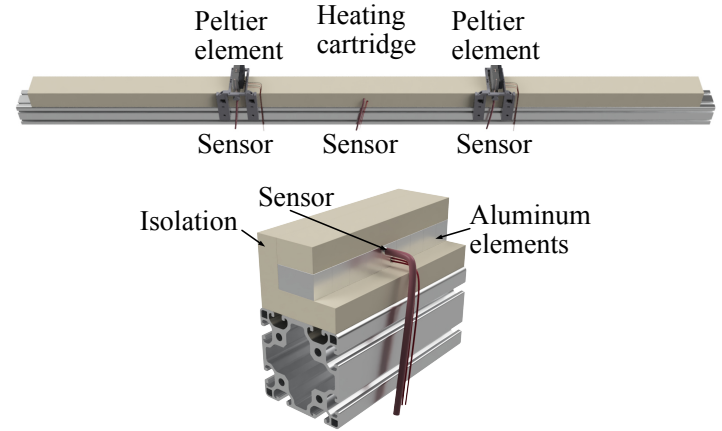


Figure 6: Visualization of a large scaled system. The discrete aluminum rod ($l = 2\text{m}$) is cooled on two elements and heated on another.

We have experimentally evaluated the presented methods on an example published in [1] and [2]. Here we analyzed the temperature distribution in a discrete heating rod.

The aluminum rod consists of $n = 100$ elements. The contact surfaces of the aluminum elements have been thermally insulated, minimizing the influence of ambient temperature. The heat conducting rod is cooled by two Peltier elements and heated by a heating cartridge. In addition, the temperature distribution in the aluminum elements is monitored by three PT1000 sensors. The global system of the thermal rod can be described as follows

$$\begin{aligned} \mathbf{x}_q(k+1) &= p_1 \mathbf{x}_{q-1}(k) + (2p_2 + p_3) \mathbf{x}_q(k) + p_1 \mathbf{x}_{q+1}(k) + \mathbf{w}_q \\ &\text{with } q = 1, \dots, n \end{aligned} \quad (50)$$

Where the index q is the number of the aluminum element. The parameters p_1 and p_2 represents the element geometry, heat capacity as well as the heat transfer coefficient. The elements $q = 1$ and $q = 100$ have only one neighboring element, thus the heat emitting surface is larger than for the other elements. For this purpose, $2p_2 + p_3 \implies p_2 + p_4$ is chosen for the elements at the end of the rod. The parameter p_3 and p_4 are the product of the heat transfer coefficient and the heat emitting surface. \mathbf{w}_q is a normally distributed noise, describing uncertainties in the process.

The system order is $n = 100$ and is determined by the elements of the rod. Thus the system matrix is $\mathbf{A} \in \mathbb{R}^{100 \times 100}$. Here, the system has three actuators and three sensors, so the input matrix is $\mathbf{B} \in \mathbb{R}^{n \times 3}$ and the output matrix is $\mathbf{C} \in \mathbb{R}^{3 \times n}$. The sensors and actuators are placed in the same aluminum element (25, 50, 75). So the input matrix \mathbf{B} is a zero matrix and is only assigned at the positions $B_{25,1} = -1$, $B_{50,2} = 1$ and $B_{75,3} = -1$ and the output matrix \mathbf{C} is also a zero matrix and is also only assigned at the elements $C_{1,25} = 1$, $C_{2,50} = 1$ and $C_{3,75} = 1$. The global system can be described as follows

$$\Sigma_{Rod} = \begin{cases} \mathbf{x}(k+1) &= \mathbf{A} \mathbf{x}(k) + \mathbf{B} \mathbf{u}(k) \\ \mathbf{y}(k) &= \mathbf{C} \mathbf{x}(k) \end{cases} \quad (51)$$

5.1 Parameter Identification

The unknown parameters of the global system are determined by identification in two steps. In the first step, the parameter p_2 is identified by the homogeneous solution of the state space equation. For this purpose, a single aluminum element is used to determine the main diagonal of the system matrix \mathbf{A} (Fig. 7).

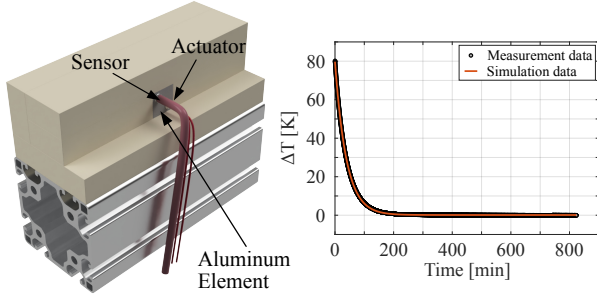


Figure 7: Parameter identification of the main diagonal elements.

This element is equipped with the heating cartridge and a sensor, and the isolation minimizes the influence of the ambient temperature. The heating cartridge will heat the temperature in the element to $T=80^\circ\text{C}$. When the temperature reaches $T=80^\circ\text{C}$, the power of the heating cartridge is switched off and the cooling curve is recorded until the steady state is reached (Fig. 7).

For the identification procedure, a first-order linear model and a *Nelder-Mead* simplex are used in combination with an ode4 solver. The least squares method is used to evaluate the output error and the *Nelder-Mead* simplex minimizes the cost function

$$\min J = \min_{\hat{\mathbf{p}} \in \mathbb{R}^n} \sum_{k=1}^N [y(k) - \hat{y}(k)]^2. \quad (52)$$

so that the behavior of the model is fitted to the real system. In the second identification step, the secondary diagonal elements of the system matrix \mathbf{A} are determined. For this purpose, seven aluminum elements are used to reduce the discretization error (Fig. 8). The elements at the edge are equipped with a sensor. The middle element is also equipped together with the heating cartridge. With constant heating power, the elements are heated until the steady state is reached. A seventh order model is used for identification and least squares is used to evaluate the output error. The cost function (52) is also minimized using a *Nelder-Mead* simplex in combination with an ode4 solver.

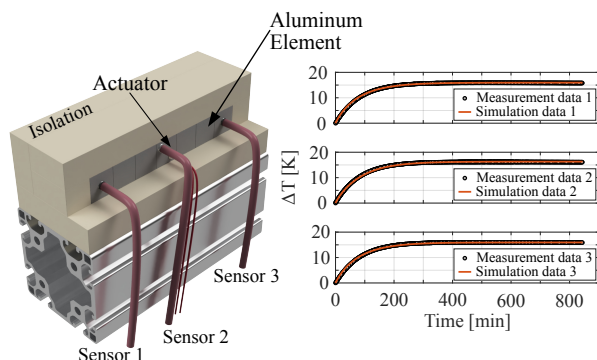


Figure 8: Parameter identification of the secondary diagonal elements.

These identified parameters can be used in the global system

$$\begin{aligned} p_1 &= 4.2812 \cdot 10^{-4} \frac{1}{s} & p_2 &= 4.3048 \cdot 10^{-4} \frac{1}{s} \\ p_3 &= 1.8067 \cdot 10^{-4} \frac{1}{s} & p_4 &= 2.2561 \cdot 10^{-4} \frac{1}{s} \end{aligned} \quad (53)$$

5.2 Input-/Output-based Distribution

The starting point is a global MIMO system (51) with three actuators and three sensors and a system order of $n = 100$. Considering the controllability and observability of the global system Σ_{Rod} , $m = 3$ local systems are decentralized with one actuator and sensor each.

$$\begin{aligned} \Sigma_{L_1} \begin{cases} \mathbf{x}(k+1) &= \mathbf{A}\mathbf{x}(k) + \mathbf{B}_j u_1(k) \\ y_1(k) &= \mathbf{C}_j \mathbf{x}(k) \end{cases} \\ \Sigma_{L_2} \begin{cases} \mathbf{x}(k+1) &= \mathbf{A}\mathbf{x}(k) + \mathbf{B}_j u_2(k) \\ y_2(k) &= \mathbf{C}_j \mathbf{x}(k) \end{cases} \\ \Sigma_{L_3} \begin{cases} \mathbf{x}(k+1) &= \mathbf{A}\mathbf{x}(k) + \mathbf{B}_j u_3(k) \\ y_3(k) &= \mathbf{C}_j \mathbf{x}(k) \end{cases} \end{aligned} \quad (54)$$

The index $j = 1, \dots, m$ is the corresponding column of the global input matrix \mathbf{B} and the corresponding row of the global output matrix \mathbf{C} . The system order is not changed, thus the decentralized local systems are also $n = 100$.

Analyzing the HSVs reveals, that order $r = 6$ is achieved (Fig. 9). The order $r = 6$ allows 93.1217% of the energy to be transported from the inputs to the outputs. Based on the analysis, states with a small impact on the energy transport are cut off and the system order is reduced to $r = 6$. The model order reduction reduces the computational effort in the network node.

The decentralized reduced local systems are extended by the DSRKF presented in Section 4, providing communication between the network nodes and generating a fully interconnected network.

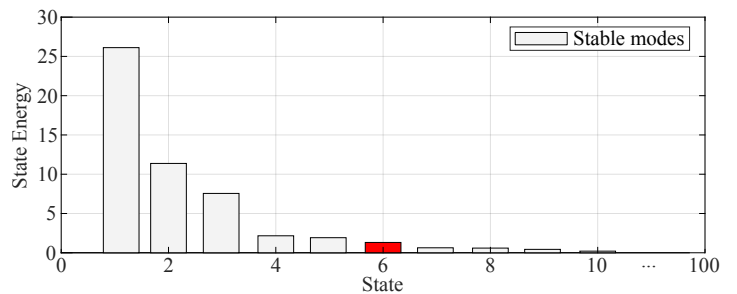


Figure 9: Visualization of the state energy of the global system (50). It is illustrated that the energy decreases strongly with the sixth state. Red bar illustrates the cut-off system order r .

Fig. 3 illustrates that the sensor nodes communicate with the actuator nodes by means of the exchanged a priori and a posteriori information. The full interconnectivity of the network is achieved by exchanging the error information (31) and (32) between the decentralized reduced local systems. This error information is already used in the prediction, so a fusion step has to be added to the algorithm in the actuator nodes (36) and (37).

By using BT, the physical interpretability of the states is lost, thus, for an analysis, the reduced state vector has to be transformed back

to the global state space. For this transformation of the a priori and a posteriori information, the following equations are used

$$\hat{\mathbf{x}}^-(k) = \mathbf{V}_{BT} \hat{\mathbf{x}}_r^-(k) \quad (55)$$

$$\hat{\mathbf{x}}^+(k) = \mathbf{V}_{BT} \hat{\mathbf{x}}_r^+(k). \quad (56)$$

The transformation matrix \mathbf{V}_{BT} is determined by (15).

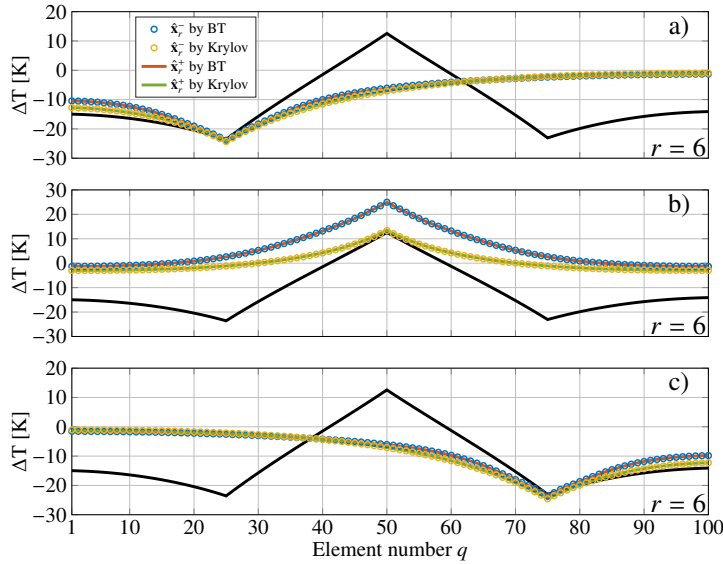


Figure 10: A priori and a posteriori estimated state vectors of local systems reduced by BT (3.1) and *Krylov* (3.2).

Fig. 10 demonstrates that the local SISO systems satisfy the characteristics of the decentralized inputs and outputs of the global system. Hereby, the global temperature profile (50) is shown in black and the a priori estimation $\hat{\mathbf{x}}_r^-$ after the reduction by BT/*Krylov* of the actuator node, is represented in blue/orange dots as well as the a posteriori estimation $\hat{\mathbf{x}}_r^+$ in red/green lines of the sensor node. In a), b) and c) the estimates based on measurement data of the reduced local systems after the transformation into the original SISO subspace ($n = 100$) are illustrated.

In addition, it is presented that despite the lost interpretability of the states due to the model order reduction as well as the distribution of the estimation algorithms in a interconnected network, the controllability and observability of the global system is approximated by the decentralized reduced local systems.

The input-/output-based distribution from Section 4.1 is also analyzed using the model order reduction method from Section 3.2, the two-sided *Krylov* method. Although the model order reduction with *Krylov* subspace methods is numerically efficient, the stability of the reduced system is not guaranteed. Therefore, the stability must be checked in the preprocessing. Based on the stability analysis of the decentralized local systems, the reduction with *Krylov* subspace methods also yields stable reduced systems for $r = 6$.

This approach also illustrates that the characteristics of the sensors and actuators of the global system is approximated by the decentralized reduced local systems (Fig. 10). Furthermore, the described method for decentralization is used independently of the two model order reduction methods presented.

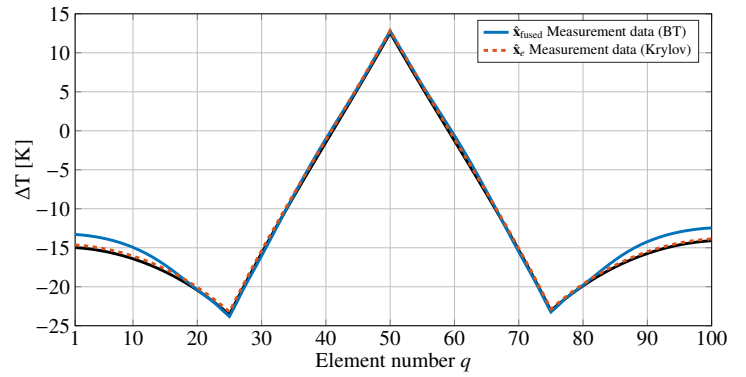


Figure 11: By BT and *Krylov* reduced estimated a posteriori state vectors with (57) and (58) as well as (43) and (44) fused in a center.

If the a posteriori information of the decentralized SISO system reduced by BT is provided to a fusion center, the original Σ_{Rod} is reconstructed. For this purpose, the reduced a posteriori state vector $\hat{\mathbf{x}}_r^+$ and the a posteriori covariance matrix \mathbf{P}_r^+ of the $m = 3$ local systems must be transformed into the local model space and fused by

$$\mathbf{P}_{fused}(k) = \left(\sum_{j=1}^m \mathbf{P}_j^-(k) \right)^{-1} \quad (57)$$

$$\hat{\mathbf{x}}_{fused}(k) = \mathbf{P}_{fused}(k) \sum_{j=1}^m \left(\mathbf{P}_j^-(k) \right)^{-1} \hat{\mathbf{x}}_j^-(k). \quad (58)$$

For the reconstruction of the global system Σ_{Rod} based on the second method of model order reduction, a reference system (45) is derived. The stability and the equivalent system order ($r = 6$) as for the $m = 3$ decentralized reduced local systems have to be considered. Before the decentrally reduced local a posteriori information is used for fusion, a transformation into a known common subspace is required. For this purpose, the decentrally reduced local a posteriori information is transformed into the subspace of the reference system. For further improvement a KF is used, which achieves an increase of the reconstruction $\hat{\mathbf{x}}_e$ of the global system Σ_{Rod} with the reference system and the fusion result as observation.

In contrast to Fig. 10, a fusion center is used in Fig. 11. The global temperature profile according to (50) with the identified parameters is shown in black. The decentralized local a posteriori states, reduced by BT, are shown in blue after fusion by (57) and (58) and transformation ($n = 100$), while the dashed red line represents the decentralized local a posteriori states, reduced by the method of *Krylov* subspaces.

Here, the global system is fully reconstructed despite decentralization and distribution in a sensor and actuator network. Additionally, it is demonstrated that the presented methods are independent of the model order reduction techniques. The decentralization and distribution would be implemented for both model order reduction methods (BT and *Krylov* subspace methods) on BECKHOFF® CX6030 CPUs (Intel® Core™ i7 7700, 3.6GHz) and tested in real-time approaches.

The deviation of the approximation by Balanced Truncation in the ranges $q = 1, \dots, 25$ and $q = 75, \dots, 100$ is accounted for by the reduction of the system order. With an increase of the order this

deviation is minimized.

The communication effort is directly dependent on the system order. For clarification, the system (51) was manually distributed into several local systems. The order of the local systems is $n_1 = 35$, $n_2 = 20$ and $n_3 = 45$. If these decentralized local systems are used to reconstruct the global system without further reduction, all local systems must communicate with each other. The communication overhead is significantly higher than in the presented methods with the reduction methods BT and Krylov subspace methods (Fig. 12). Thus, the presented methods reduce not only the computational effort in the network nodes but also the communication effort.

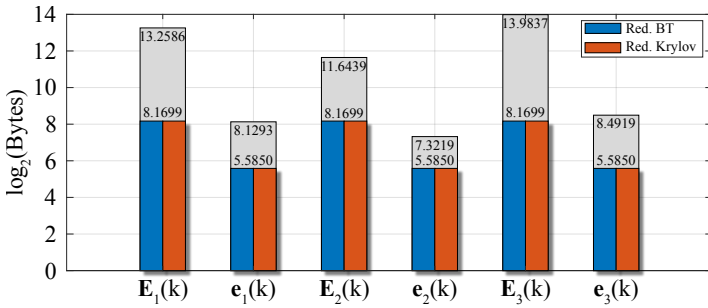


Figure 12: The information of the covariance error and state error sent by manual splitting is illustrated as grey and for DSRKF as blue/red bars (logarithmic scale).

5.3 Subspace based Distribution

Without decentralization, the controllable and observable *Krylov* subspace is derived directly from the global system (51). For this purpose, the repeating of the one-sided method for the *Krylov* input space and the *Krylov* output space is proposed in Section 4.2. The resulting reduced systems (46) and (47) describe the corresponding subspace. However, to approximate the global input and output behavior, information from both subspaces are required. For state reconstruction in the subspace-based distribution, a SRKF from Section 4.1.1 is used with the matrices (48). By separating the controllable and observable subspace, this distribution can also be used in a network.

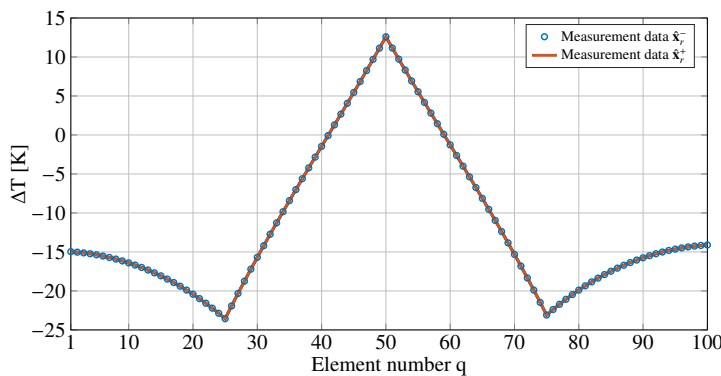


Figure 13: Reconstructing the global temperature profile by communicating the reduced a priori and a posteriori states according to the distribution of the controllability and observability subspace in a sensor and actuator network.

The network nodes transmit the a priori and a posteriori state vectors and covariance matrix, so no fusion steps are required in the

algorithms. However, the information received in the subspaces must be transformed (49). Even when *Krylov* methods are used without decentralization, the stability of the reduced system must be analyzed in preprocessing. Fig. 13 demonstrates that also in this case, for $r = 6$, a stable reduced system is present and used.

In contrast to the previous method (Section 5.2), only two network nodes are used here. One network node uses the complete information of the inputs for the prediction of the KF and another network node uses all observations for the correction step of the reconstruction of the global system behaviour.

The minimization of the communication effort is not depicted, as in this distribution only the prediction and correction is separated (SKF). Using the model order reduction (SRKF), there will be a lower communication effort with each reduced system order, since a manual division cannot be performed when separating prediction and correction.

6 Conclusion

In this paper, we have shown the decentralization into SISO systems of large-scale MIMO systems. We have also presented an input/output-based and a subspace-based method for system distribution. Both methods focus on the controllability and observability of the global MIMO system. By applying the two best known model order reduction methods (balanced truncation and *Krylov* subspaces), the system order of the generated decentralized local systems was reduced. By adding a DSRKF to the decentralized reduced local systems, they are used in a network. The reduced decentralized local systems describe different subspaces, so it is assumed that the reduced information is communicated in the network. It could be demonstrated that the transformation matrices resulting from the two presented methods can also be used for communication. Their distribution in a connected network in combination with the model order reduction methods significantly reduced the computational and communication effort required for state estimation of the large-scale linear MIMO system.

In the future, the presented methods will also be applied for decentralized distributed control. In future practical approaches, the methods will also be used in tracking dynamic targets and applied to the decentralized distributed multi-laser tracker system (DDMLTS) [38].

Conflict of Interest The authors declare no conflict of interest.

References

- [1] F. Friedrich, J. Mayer, C. Ament, "Reduced and Distributed Estimation in Sensor and Actuator Networks - Automated Design Based on Controllability and Observability," in 2021 IEEE Conference on Control Technology and Applications (CCTA), 666–672, IEEE, San Diego, CA, USA, 2021, doi:10.1109/CCTA48906.2021.9659129.
- [2] F. Friedrich, J. Mayer, C. Ament, "Model-Order Reduction and System Distribution Using Krylov Subspaces - An Approach for Efficient State Estimation in Sensor and Actuator Networks," accepted for CCTA2022.
- [3] R. D'Andrea, G. Dullerud, "Distributed control design for spatially interconnected systems," IEEE Transactions on Automatic Control, 48(9), 1478–1495, 2003, doi:10.1109/TAC.2003.816954.

- [4] B. Bamieh, F. Paganini, M. Dahleh, "Distributed control of spatially invariant systems," *IEEE Transactions on Automatic Control*, **47**(7), 1091–1107, 2002, doi:10.1109/TAC.2002.800646.
- [5] L. A. Montestruque, P. J. Antsaklis, "Model-Based Networked Control Systems - Stability," 58.
- [6] J. Lunze, *Regelungstechnik 2*, Springer Berlin Heidelberg, Berlin, Heidelberg, 2016, doi:10.1007/978-3-662-52676-7.
- [7] U. A. Khan, J. M. F. Moura, "Model Distribution for Distributed Kalman Filters: A Graph Theoretic Approach," in 2007 Conference Record of the Forty-First Asilomar Conference on Signals, Systems and Computers, 611–615, IEEE, Pacific Grove, CA, USA, 2007, doi:10.1109/ACSSC.2007.4487286, iSSN: 1058-6393.
- [8] B. Noack, J. Sijs, U. D. Hanebeck, "Fusion Strategies for Unequal State Vectors in Distributed Kalman Filtering," *IFAC Proceedings Volumes*, **47**(3), 3262–3267, 2014, doi:10.3182/20140824-6-ZA-1003.02491.
- [9] J. Lunze, *Control Theory of Digitally Networked Dynamic Systems*, Springer International Publishing, Heidelberg, 2014, doi:10.1007/978-3-319-01131-8.
- [10] A. C. Antoulas, *Approximation of large-scale dynamical systems*, Advances in design and control, Society for Industrial and Applied Mathematics, Philadelphia, 2005, doi:10.1137/978-0-89871-871-3.
- [11] P. Benner, A. Schneider, "Balanced Truncation Model Order Reduction for LTI Systems with many Inputs or Outputs," in Proceedings of the 19th International Symposium on Mathematical Theory of Networks and Systems – MTNS 2010, 4, MTNS, Budapest, Hungary, 2010.
- [12] E. F. Yetkin, H. Dag, "Parallel implementation of iterative rational Krylov methods for model order reduction," in 2009 Fifth International Conference on Soft Computing, Computing with Words and Perceptions in System Analysis, Decision and Control, 1–4, IEEE, Famagusta, 2009, doi:10.1109/ICSCCW.2009.5379421.
- [13] Z. Bai, "Krylov subspace techniques for reduced-order modeling of large-scale dynamical systems," *Applied Numerical Mathematics*, **43**(1-2), 9–44, 2002, doi:10.1016/S0168-9274(02)00116-2.
- [14] P. Feldmann, R. Freund, "Efficient linear circuit analysis by Pade approximation via the Lanczos process," *IEEE Transactions on Computer-Aided Design of Integrated Circuits and Systems*, **14**(5), 639–649, 1995, doi:10.1109/43.384428.
- [15] K. Gallivan, E. Grimme, P. Van Dooren, "Asymptotic waveform evaluation via a Lanczos method," *Applied Mathematics Letters*, **7**(5), 75–80, 1994, doi:10.1016/0893-9659(94)90077-9.
- [16] G. A. Baker, P. R. Graves-Morris, *Padé approximants*, number v. 59 in *Encyclopedia of mathematics and its applications*, Cambridge University Press, Cambridge [England] ; New York, 2nd edition, 1996.
- [17] D. Rafiq, M. A. Bazaz, "Model Order Reduction via Moment-Matching: A State of the Art Review," *Archives of Computational Methods in Engineering*, **29**(3), 1463–1483, 2022, doi:10.1007/s11831-021-09618-2.
- [18] L. Feng, "Review of model order reduction methods for numerical simulation of nonlinear circuits," *Applied Mathematics and Computation*, **167**(1), 576–591, 2005, doi:10.1016/j.amc.2003.10.066.
- [19] H. K. F. Panzer, T. Wolf, B. Lohmann, " \mathcal{H}_2 and \mathcal{H}_∞ error bounds for model order reduction of second order systems by Krylov subspace methods," in 2013 European Control Conference (ECC), 4484–4489, IEEE, Zurich, 2013, doi:10.23919/ECC.2013.6669657.
- [20] S. Gugercin, *Projection Methods for Model Reduction of Large-Scale Dynamical Systems*, Dissertation, Rice University, Rice, 2003.
- [21] B. Salimbahrami, B. Lohmann, T. Bechtold, "Two-Sided Arnoldi in Order Reduction of Large Scale MIMO Systems," 9.
- [22] B. Moore, "Principal component analysis in linear systems: Controllability, observability, and model reduction," *IEEE Transactions on Automatic Control*, **26**(1), 17–32, 1981, doi:10.1109/TAC.1981.1102568.
- [23] S. Gugercin, A. C. Antoulas, "A Survey of Model Reduction by Balanced Truncation and Some New Results," *International Journal of Control*, **77**(8), 748–766, 2004, doi:10.1080/00207170410001713448.
- [24] D. Hinrichsen, H.-W. Philippsen, "Modellreduktion mit Hilfe balancierter Realisierungen / Model reduction using balanced realizations," at - *Automatisierungstechnik*, **38**(1-12), 460–466, 1990, doi:10.1524/auto.1990.38.112.460, publisher: De Gruyter (O).
- [25] S. L. Brunton, J. N. Kutz, *Data-Driven Science and Engineering*, Cambridge University Press, 1st edition, 2019.
- [26] A. Laub, M. Heath, C. Paige, R. Ward, "Computation of system balancing transformations and other applications of simultaneous diagonalization algorithms," *IEEE Transactions on Automatic Control*, **32**(2), 115–122, 1987, doi:10.1109/TAC.1987.1104549, conference Name: IEEE Transactions on Automatic Control.
- [27] I. Jaimoukha, "A general minimal residual Krylov subspace method for large-scale model reduction," *IEEE Transactions on Automatic Control*, **42**(10), 1422–1427, 1997, doi:10.1109/9.633831.
- [28] B. Lohmann, B. Salimbahrami, "Introduction to Krylov subspace methods in model order reduction," *Methods Applications in Automation*, 1–13, 2003.
- [29] P. Falb, W. Wolovich, "Decoupling in the design and synthesis of multivariable control systems," *IEEE Transactions on Automatic Control*, **12**(6), 651–659, 1967, doi:10.1109/TAC.1967.1098737.
- [30] D. Simon, *Optimal state estimation: Kalman, H [infinity] and nonlinear approaches*, Wiley-Interscience, Hoboken, N.J, 2006, doi:10.1002/0470045345.
- [31] A. G. Mutambara, *Decentralized Estimation and Control for Multisensor Systems*, Routledge, 1st edition, 2019, doi:10.1201/9781315140803.
- [32] P. Hilgers, C. Ament, "Distributed and decentralised estimation of non-linear systems," in 2010 IEEE International Conference on Control Applications, 328–333, 2010, doi:10.1109/CCA.2010.5611300, iSSN: 1085-1992.
- [33] B. S. Rao, H. F. Durrant-Whyte, "Fully decentralised algorithm for multisensor Kalman filtering," *IEE Proceedings D (Control Theory and Applications)*, **138**(5), 413–420, 1991, doi:10.1049/ip-d.1991.0057, publisher: IET Digital Library.
- [34] V. Shin, Y. Lee, T.-S. Choi, "Generalized Millman's formula and its application for estimation problems," *Signal Processing*, **86**(2), 257–266, 2006, doi:10.1016/j.sigpro.2005.05.015.
- [35] H. B. Mitchell, *Multi-sensor data fusion: an introduction*, Springer, Berlin ; New York, 2007, doi:10.1007/978-3-540-71559-7.
- [36] J. Ajgl, "Millman's Formula in Data Fusion," in The 10th International PhD Workshop Young Generation Viewpoint, 6.
- [37] B. Salimbahrami, R. Eid, B. Lohmann, "On the choice of an optimal interpolation point in Krylov-based order reduction," in 2008 47th IEEE Conference on Decision and Control, 4209–4214, IEEE, Cancun, 2008, doi:10.1109/CDC.2008.4739219.
- [38] F. Friedrich, J. Brandl, C. Ament, "Absolute Distance Measurement by a Decentralized and Distributed Multi-Lasertracker-System," in 2022 IEEE/ASME International Conference on Advanced Intelligent Mechatronics (AIM), 1249–1255, IEEE, Sapporo, Japan, 2022, doi:10.1109/AIM52237.2022.9863275.

Detection of Event-Related Potential Artifacts of Oddball Paradigm by Unsupervised Machine Learning Algorithm

Rafia Akhter*, Fred Beyette

School of Engineering, Electrical Computer Engineering, University of Georgia, Athens, USA

ARTICLE INFO

Article history:

Received: 26 July, 2022

Accepted: 08 October, 2022

Online: 31 October, 2022

Keywords:

Electroencephalography (EEG)

Event-Related Potential (ERP)

Oddball Paradigm

Artifact Corrupted Epochs

Artifacts

Detection

ABSTRACT

Electroencephalography (EEG) is one of the most common and benign methods for analyzing and identifying abnormalities in the human brain. EEG is an incessant measure of the activities of the human brain. In contrast, when the measurement of EEG is bounded by time and the EEG is synchronized to an exterior stimulus, is known as Event-Related Potential (ERP). ERP has the capability to perceive and explore the human brain's responses to specific sensitive, cognitive, or motor events in real time with high temporal resolution. Among the various techniques, the oddball paradigm is very famous in EEG studies. In an oddball paradigm experiment, brain responses to frequent and infrequent stimuli are measured. However, the success of ERP research is very much dependent on the analysis of clean data sets and unfortunately, EEG is a combination of both neural and non-neural activities which introduce significant sources of noise that are not related to the brain's response to the external stimulus. These unrelated non-EEG components are acknowledged as artifacts and due to these, the quality of the EEG may damage by decreasing SNR (signal-to-noise ratio). In addition, these artifacts may mislead the actual information in the study. Addressing this problem, the purpose of this research is to introduce a machine learning algorithm (ML) that can screen EEG/ERP data to remove data epochs that are disrupted by artifacts and thus produce a clean data set. Overall, three unsupervised ML algorithms are applied to identify noisy epochs and it is found that the DBScan method performs best with 93.43% accuracy. Finally, the success of this study will allow the ERP study to have a cleaner ERP data set in normal laboratory conditions with less complexity in the ERP studies.

1. Introduction

This study is an extension of our previously published [1] paper and was presented at the 7th International Conference on Data Science and Machine Learning Applications (CDMA, 2022). In this paper, we identified and detected the auditory ERP artifacts by unsupervised Machine Learning Algorithms (MLAs) and compared the results and features with the visual Event-Related Potential (ERP) artifacts that were presented at the CDMA conference.

Electroencephalography (EEG) is a safe and painless method of measuring the human brain's electrical activities in real-time. In medical research, EEG experiments are very convenient. EEG

measures the electric potential of the brain over a continuous time and EEG activities over a bounded time are acknowledged as Event-Related Potential (ERP) [2]. ERPs can explore the brain's response to a specific sensory input with a high temporal resolution. In addition, ERPs are potential for the use of human biomarker, and other cerebral processes [3-5].

The oddball paradigm is one of the common experimental methods in ERP research. In the oddball paradigm, there is a sequence of monotonous stimuli, and it is irregularly interrupted by an uncommon stimulus [6]. In this study, the experimental work is comprised of a typical auditory oddball paradigm. Here, the test subject heard a series of tones with two different pitches. One of the tones is played much more frequently than other. For example, a common tone played 80% of the time with a randomly interspersed

*Corresponding Author: Rafia Akhter, email: Rafia.Akhter@uga.edu

uncommon tone making up the remaining 20% of tones. It has been established by different studies that ERP gives a maximum positive peak of around 300 ms- 600 ms and the peak is higher for target/oddball stimuli compared with standard stimuli. This component is known as the P300 component [7].

However, EEG in its raw form is a mixture of neural and non-neural activities. Any non-neural activities are unnecessary in EEG research and recognized as artifacts in EEG/ERP research [8]. These artifacts may produce erroneous results in ERP studies in various ways. For example, may damage the ERP signal quality by reducing the signal-to-noise ratio, there could be some arbitrary artifacts which occur infrequently for one certain condition for one test subject while for other test subjects it may occur rarely. As a result, there might be huge differences in the evaluation of two test subjects for the same experiments [9]. There are many more reasons for artifacts that may mislead the conclusion of any ERP study.

There are a huge number of sources of EEG artifacts but the most common artifacts are related to eye and body movements. In this study, our goal is to detect eye-blink artifacts, eye-movement artifacts, and body movement artifacts in normal laboratory conditions. Although much research has been done, there is no standard technique for detecting and eliminating artifacts. Addressing this, the aim of this study is to introduce a method of machine learning (ML), in which we can identify artifact corrupted ERP epochs and by removing those from the dataset, we will have a clean dataset. This experiment is done with the addition of some external effort to create artifacts. So that we could detect these artifacts. As a result, the outcomes from this study will improve the signal quality of the ERP experiment.

We applied the anomaly or outlier detection method of MLA and our data was unlabeled i.e. we applied, unsupervised MLA. Unsupervised MLAs find uncommon data points which have different properties compared to others, in any dataset. We applied three unsupervised MLAs for the detection of artifacts. They are Density-Based Spatial Clustering of Applications with Noise (DB-Scan), Isolation Forest (IsoF), and Local Outlier Factor (LOF). We measured the artifact-mixed ERP epochs detection efficiency of these methods and compared the accuracy of efficiency with the standard EEGLab method. We found the DBScan method is most efficient with 93.43% accuracy while the other methods also showed a good efficiency, ranging from 85% to 87%.

EEG is frequently utilized to analyze epilepsy, which causes variations from the norm in EEG readings. It is additionally utilized to analyze rest clutters, the profundity of anesthesia, coma, encephalopathies, and brain passing [10]. In general, EEG produces amplitude with respect to time and it is a very sensitive measurement. These measures are very important for clinical decisions. But artifacts may change or hide the information in EEG and removing these artifacts may take a long time for analyzing the data by extracting features. But MLAs have shown faster learning to process EEG signals [11] by outlier or anomaly detection method. Isolation Forest is an effective MLA for this detection with linear computational complexity. Screening anomaly is useful for the detection of epileptic seizures [12]. LOF can identify artifacts by producing abnormal scores using statistical methods [13]. DBScan uses a clustering-based algorithm to detect

artifacts [14]. Overall, MLAs have shown effective importance in analyzing epilepsy and other neurological diseases.

The organization of the paper is as follows: section 2 consists literature review, the experimental setup and procedure are explained in Section 3, identification of artifacts are in section 4, Section 5 contains practical implementations, and finally, results and conclusions are in Sections 6 & 7.

2. Literature Review

A lot of research has been done to remove artifacts but most methods require labeling the artifacts manually or requiring additional hardware. For example, Electrooculography electrodes may require to place around the eyes or may necessitate data-sets containing a huge amount of data, and many more [15]. The involvement of humans to label artifacts in EEG data may be not desirable as it might be a tedious and time-consuming process [16].

In [17], the author described an unsupervised EEG artifact detection algorithm. It shows that this algorithm is effective to identify eyeblinks with 98.15% accuracy. They collected their dataset with the OpenBCI system and used EEGLab. In their experiment, subjects were instructed to watch a video and read articles, each for 5 minutes. They compared the methods with SVM and k-NN which are learning-based methods. But the accuracy of the performances of these methods was very low, 46.49% 67.82% comparatively.

In [18], the author established a deep learning method using Bayesian and attention modules to improve the performance of the classifier. Here, after the filtering process, to remove line noise, the artifact subspace reform (ASR) technique [19] was revised to remove an artifact that is dispersed throughout the entire scalp with a huge variance. The infomax-ICA technique was then directed to get a set of ICs establishing EEG and artifacts [20]. To end, topographic plots were drawn and labeled by EEG experts. The classification accuracy was very high, around 95% but this method needs an attention module, task-dependent, and an EEG expert is required.

In [21], the author depicted an EEG noise-reduction scheme that customizes representation knowledge to perform patient- and task-specific discovery of artifacts and correction. More specifically, their method is dependent on a given task and extracted 58 features from the signals.

3. Experimental Setup and Procedure

3.1. Dataset

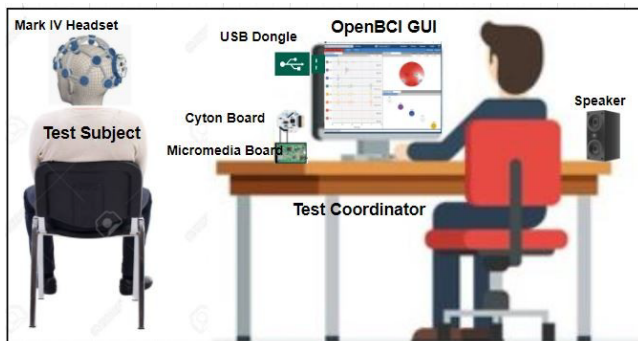
This auditory oddball paradigm EEG data set is approved by the Institutional Review Board (IRB) at the University of Georgia, Athens. All of the participants provided knowledgeable permission. In this study, the number of test subjects was 13 (both male and female). They all were a minimum of 18 years of age. They had no psychiatric conditions and no hearing or eye-sight weakening. The EEG experiment had 3 setups and for every test subject, there were 3 data sets. The first data set is a mind wandering data set and the last two are artifact corrupted/test data sets. For 13 subjects, there is 13 mind wandering data sets and 26 test data sets. However, in 3 of the test data sets, almost all the ERP epochs were characterized by

test subject distraction, and those 3 data sets were not considered in our study. So, there was a total of 26 test data sets.

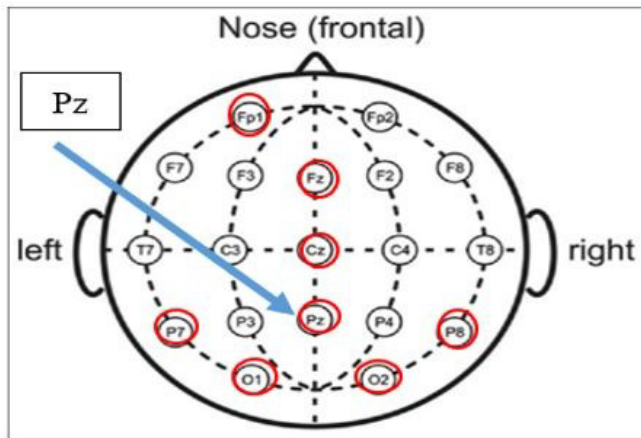
For the recording and collection of data, an OpenBCI EEG capture system with an Ultracortex Mark IV headset was used. Here, the electrodes were connected according to the international 10-20 system along the surface of the scalp [22]. The 8-channel Cyton board was mounted to the headset. We connected electrodes to the frontal (FP1, Fz), central (Cz, C4), parietal (Pz, P7, P8), and occipital portion (O1, O2) in the human scalp (Fig. 1B). The Cyton Board was wirelessly connected via a Bluetooth (4.0 Low Energy BLE) to a data collection computer. To generate the auditory stimuli for the ERP oddball experiments, we used a Mikromedia PIC24EP board, available from MikroElektronika Inc [23].

3.2. Data Collection Procedure

In this auditory oddball paradigm, subjects hear a sequence comprised of 2 tones with a different pitch where one of the tones is played much more frequently than the other (ex. a common tone played 80% of the time with a randomly interspersed uncommon tone making up the remaining 20% of tones).



(a)



(b)

Figure 1: (a) The experimental setup of auditory oddball task. There were a series of tones with two different frequencies of 1000Hz and 2000Hz. The tones were played randomly with the stimuli duration of 200 ms and ISI of 3s 50 ms); (b) The International 10/20 system of electrode positions. The red-colored electrode positions were used to record the data in this experiment. For all the calculations, the measurements of the Pz location (marked in blue) were used.

In this experiment, to record EEG (as shown schematically in Fig. 1A), the Ultracortex Mark IV headset was used. There were 50 tones with two different pitches. One tone with 1000 Hz is known as a “common” tone and the other with 2000 Hz, is “uncommon or

oddball”. The subject was instructed to concentrate on the uncommon tones and ignore the frequent tones. The proportion of frequent and uncommon tones was 80:20. The stimuli or tone duration was 200 ms and the Inter-stimulus Interval was 3s 50 ms.

There were 3 experimental setups. In the 1st setup, there was no instruction for the test subjects. The subject heard the tones and data were recorded. The data set from this setup is named a mind-wandering data set. At the 2nd setup, the subjects were instructed to give their special concentration to counting the uncommon/oddball tones and try to overlook the common tones. In the 3rd setup, the experimental condition was the same as in the 2nd, but we made an unexpected disturbance. For example, we made an abrupt flash on another monitor to divert the mind of the test subject, so that he/she would have somebody’s movements or blink their eyes.

The data sets collected for the last two setups are named artifact corrupted/test data sets. After completion of each dataset collection procedure, there was a 1–3-minute break of “mental rest” before initiating the next data collection interval.

3.3. Processing of Dataset

There were 3 data collection intervals for every subject and there was a total of 26 test data sets, as described in section 3.1. After recording, the data sets were protected in CSV format and EEGLab (a tool of MATLAB) was used for the primary analysis [24]. The DC offsets were uninvolved, and a band-pass filter (non-causal) of 0.1 Hz-30 Hz was used for the filtering of the EEG signals. For the ERP epochs extraction, a time window of -1000 ms to 2000 ms was bounded and ERP features were extracted in an adequate window of 200 ms to 600 ms after the commencement of the stimulus for the ERP evaluation. For further calculation, all measures (amplitude and latency) were evaluated from the uncommon stimuli at the Pz electrode position.

4. Artifacts Detection

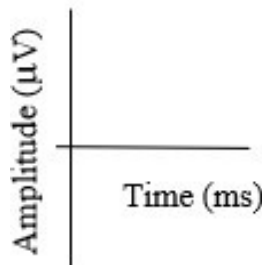
The signal recorded in ERP experiments is a combination of EEG plus the non-neural source of activities. These non-neural sources are mainly from the induced electrical signals of the recording environment (e.g., line noise from lights and computers) and human biological activities. For example, it is very usual that while recording EEG, a test subject may blink his eye, moves his eye, he may move his head, or body, there may be muscle activities, have skin potential, and many more [25]. All of these may create non-neural signals in EEG recording and these are considered artifacts. As a result, EEG signals are often contaminated by several artifacts such as the electrooculogram (EOG), the electromyogram (EMG), electrocardiogram (ECG) and motion artifacts are a result of, for example, an eye-blink activity is an EOG artifact.

In this study, we tried to detect eye-blink, eye-movement, and body-movement artifacts. Due to the spontaneous movement of eyelids, the EOG artifact is normally always present in EEG signals. When a subject blinks his eyes, an eye-blink artifact appears as a high amplitude spike in the EEG signal [26]. Eyeblink responses are opposite in polarities compared to EEG signals and usually consist of a deflection of 50-100 V with a typical duration of 200-400 ms.

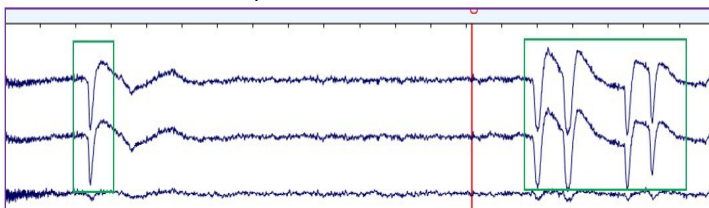
In addition, there are either horizontal eye movements or vertical ones. For a horizontal movement of eyes (HEOG), there is a higher

positive voltage over the side of the head that the eyes now point toward. For a leftward eye movement, a positive-going voltage deflection is shown on the left side of the scalp, and a negative-going voltage on the right. In the case of vertical eye movements (VEOG), higher deflection shows between the electrodes below and above the eyes[27,28].

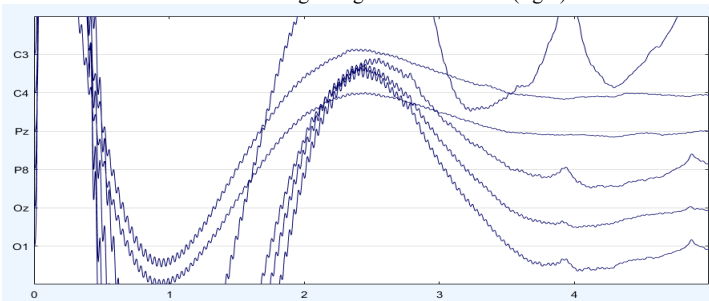
The movement of the body is very obvious for a test subject. Body movements create huge fluctuation of voltage levels and there may be high voltage levels which may shift upward or/and downward drift [29]. If these artifacts are not removed from the dataset, then the measurement or the values of the ERP features may be totally in the wrong format. All of these create huge artifacts in EEG and change the measurement levels of ERP features. Fig.2 shows the artifacts in EEG recording for subject 1.



Axis description of the figures. x-axis: time in millisecond (ms); y-axis : EEG voltage amplitudes in the microvolt



(a) EEG eye blink artifacts shows in green box (left) and artifacts due to eye-movement shows right in green colored box (right)



(b)EEG body movement artifacts

Figure 2: Examples of artifacts in EEG recordings for Subject 1

5. Practical Implementation

At first, we detected the artifact corrupted ERP epochs by a standard method (EEG Lab) and after that, identified by unsupervised Machine Learning Algorithms (MLA). For detecting artifact corrupted ERP epochs , a maximum of 150 V (+/-) was set for peak-amplitude detection and 25 V(+/-) maximum for mean amplitude. The overall process of this study is shown in the following block diagram (Fig. 3).

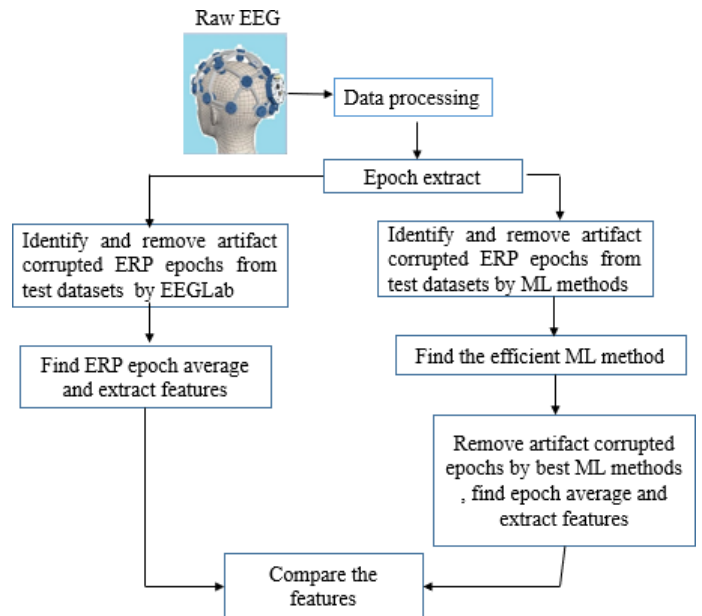
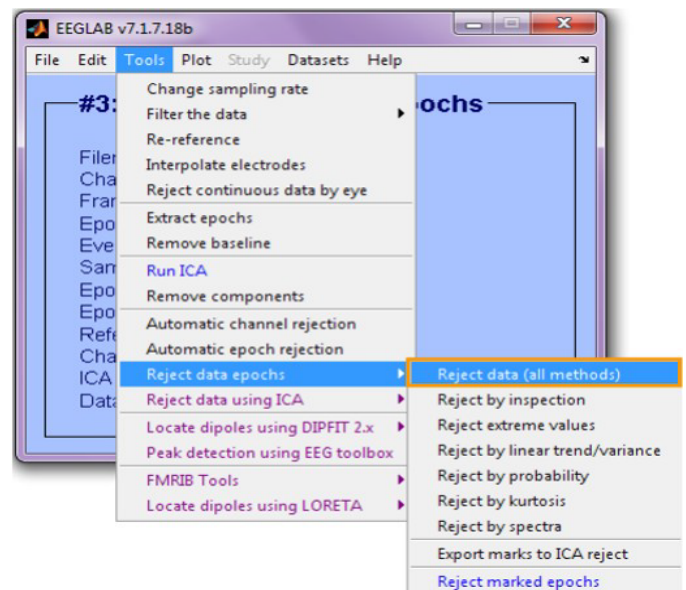


Figure 3: The block diagram of this research shows all the steps of the auditory oddball paradigm experiment and the comparison step with the visual oddball paradigm experiment

1.1 EEGLab: Standard method of ERP artifacts detection

EEGLab is one of the most popular EEG software for EEG analysis [30]. It is a freely available open-source toolbox [31] that provides an interactive graphical user interface (GUI), allows users to flexibly and interactively process their high-density EEG, is capable to do the dynamic brain data using independent component analysis (ICA), and able to spectral time/frequency and coherence analysis, as well as standard methods including event-related potentials (ERP) [32] and many more. For all of these reasons, we used EEGLab as a standard method of EEG/ERP analysis. Fig. 4 shows how these parameters for artifact rejection can be set for automatic artifact identification in EEGLab. Beyond these simple approaches, there are many other methods to detect and reject artifacts in the EEG dataset.

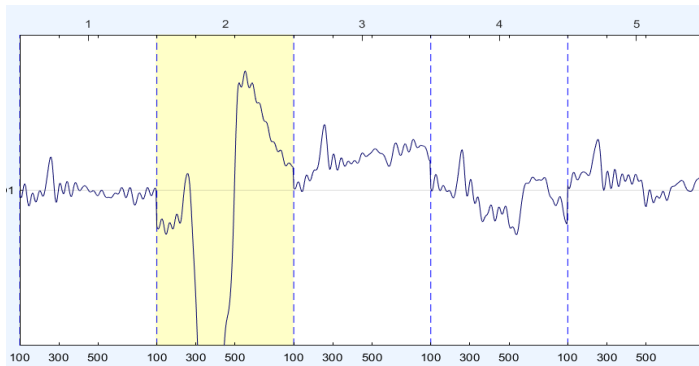


(a) EEG Lab Menu bar shows the methods of detecting and rejecting abnormal ERP epochs

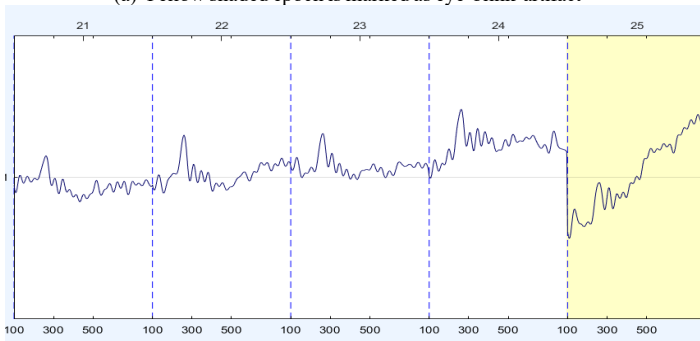


(b) Shows the parameters selection options for rejecting ERP epochs

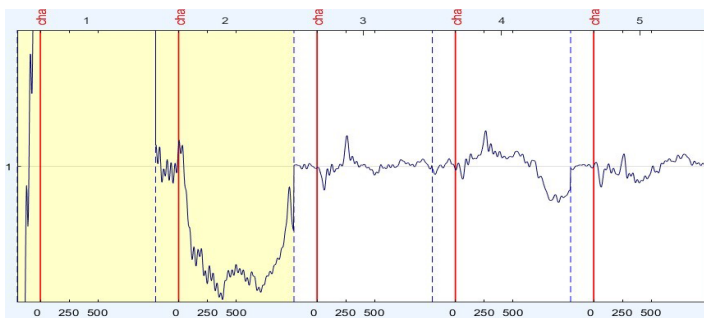
Figure 4: EEGLab processing steps for artifact corrupted ERP epochs detection



(a) Yellow shaded epoch is marked as eye-blink-artifact



(b) Yellow shaded epoch is marked as body movement-artifact



(c) Yellow shaded epoch is considered as an artifact corrupted epoch due to abnormal spectra

Figure 5: Examples of ERP artifacts detected by EEGLab (yellow shaded)

We performed the following steps by EEGLab [33] Toolbox:

- Filter
- Run ICA
- Remove components
- Extract epochs
- Reject Data epochs

In this study, we applied the method “Reject Data Epochs” by:

- Reject extreme values
- Reject by abnormal spectra
- Reject by the linear trend

The artifact corrupted ERPs detected by EEGLab methods, following the above steps are shown in Fig. 5. Among the three figures, in every figure, the yellow shaded epochs are not similar to other epochs. These are detected as anomalous ERPs by EEGLab “Reject Data Epochs” methods. For example, in fig 5A, the yellow shaded epoch (2nd from left) are showing a much higher peak compared to others. It is known that, for eye blink, EEG amplitudes give a higher peak. For this reason, it is marked as an eye-blink corrupted epoch.

5.1. Machine Learning Algorithms

Machine Learning Algorithms (MLAs) generally can predict output from the given input values [34-36]. In addition, MLAs can identify the outliers in the data-set in a very fast and with good efficiency. Outlier points are significantly different from the majority of the other data points[37] and the process of finding the outliers in the data-set is known as anomaly detection. MLAs have both supervised and unsupervised learning approaches. Supervised learning uses labeled data to help predict outcomes. On the other hand, unsupervised learning does not use labeled data [38]. They analyze and discover hidden patterns and return the data points with abnormal behavior. In this study, to detect the artifact corrupted ERP epochs, the following 3 features were used. i. Mean of ERP amplitude (mean), ii. The peak of ERP amplitude (peak P300), and iii. latency of the peak ERP (known as P300) (peak latency) in the window of 200 to 600 ms. In this study, we applied three unsupervised MLAs for identifying artifact corrupted ERP epochs based on anomaly detection. They are:

1. Isolation Forest (IsoF)
2. Local Outlier Factor (LOF)
3. DBScan

The Local Outlier Factor (LOF) algorithm is an unsupervised anomaly detection method that calculates the region density aberration of a definite data point concerning its neighbors. It considers as deviations from the norm the samples that have a noticeably lesser density compared to the neighbors[39]. In Fig. 6, there are two neighbors, C1 C2. and there are two outliers, P1, and P2. The neighbor’s numbers are a typical set of (i)more prominent than the least number of tests a cluster must contain so that other tests can be nearly exceptions relative to another cluster, and (ii) smaller

than the supreme number of close-by tests and these are termed theoretically as local outliers.

Isolation Forest (IsoF) is an unsupervised MLA that separates observations by selecting random features and returns the unusual score of each test point. This algorithm describes that anomalies are data points with unusual behavior and they are few. IsoF could be a tree-based show where segments are formed by randomly selecting a feature and after that picking an arbitrary split value between the minimum and supreme worth of the chosen feature[40]. Fig. 7 shows that red circles are separated from other normal points (blue) due to unusual behavior.

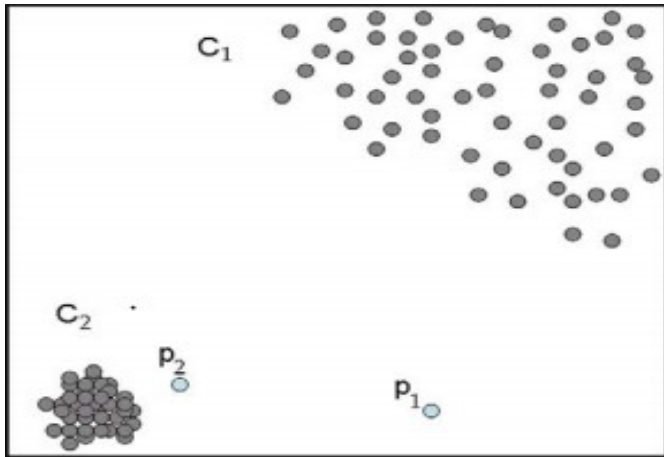


Figure 6: Local Outlier Factor. There are two neighbors, C1 C2. and there are two outliers, P1, and P2. [source: Arun Mohan, "Local Outlier Factor", Medium.com, Dec 31, 2008]

		Actual Values	
		Positive (1)	Negative (0)
Predicted Values	Positive (1)	TP	FP
	Negative (0)	FN	TN

Figure 7: Isolation Forest. In this figure, red circles are separated from other normal points (blue) due to unusual behavior.

DBScan Clustering is an unsupervised MLA that's used to gather data into clusters. It is a famous outlier detection method based on density. This process reveals central samples of high density and expands cluster density. More accurately, this algorithm sees clusters as a region of high density isolated by low density. For this relatively basic view, clusters found by DBSCAN can be in any form[41]. In this procedure, there are two sorts of parameters and three sorts of information focus. One parameter is "eps" (maximum range of the area) and another is "minpts" (least number of facts in the eps-area of a central point).

When any data point contains at least "minpts", are known as "core points" and when the quantity of points is less than "minpts", are known as "border points". In addition, within the "eps" range, when there are any points not surrounded by other points, i.e., absolutely alone in the eps range, those data point is known as an outlier, In Fig.8, there are two clusters, colored as deep-blue and green where outlier is marked as a red circle.

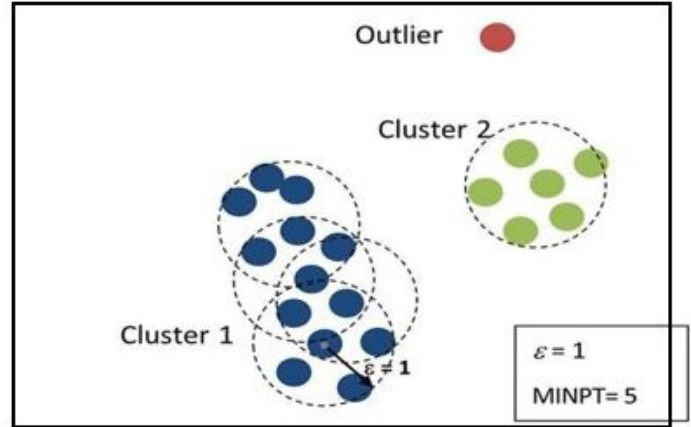


Figure 8: DBScan Cluster Technique . There are two clusters, colored as deep-blue and green where the outlier is marked as red circles. Also, eps are equal to 1 and the minimum number of points is 5.

5.2. Confusion Matrix

A confusion matrix is very useful to present the performance of any model [Fig. 9]. It consents to the visualization of the performance of the subsequent procedure. It is a table with two rows and two columns that calculates the number of true positives, true negatives, false positives, and false negatives [42]. For our calculation, we measured the accuracy (Table I) of artifact corrupted epochs for the unsupervised MLAs by the following equation:

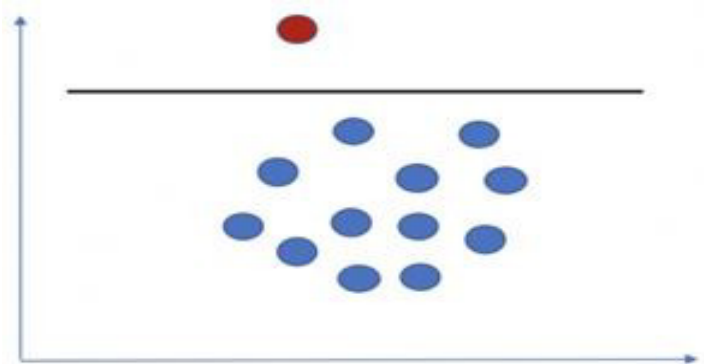


Figure 9: Confusion Matrix

$$\alpha = (TP + TN)/(TP + TN + FP + FN) \quad (1)$$

In the above equation, $\alpha = Accuracy$,
 $TP = True Positive$, $TN = True Negative$,
 $FP = False Positive$, $FN = False Negative$

6. Results

6.1. Artifact corrupted Epoch Detection Accuracy

In Fig. 10, the artifact corrupted ERP epochs, detected by Isolation Forest, DBScan, and LOF methods are shown for our test

subject 1. The orange colors are indicating the artifact corrupted ERP epochs.

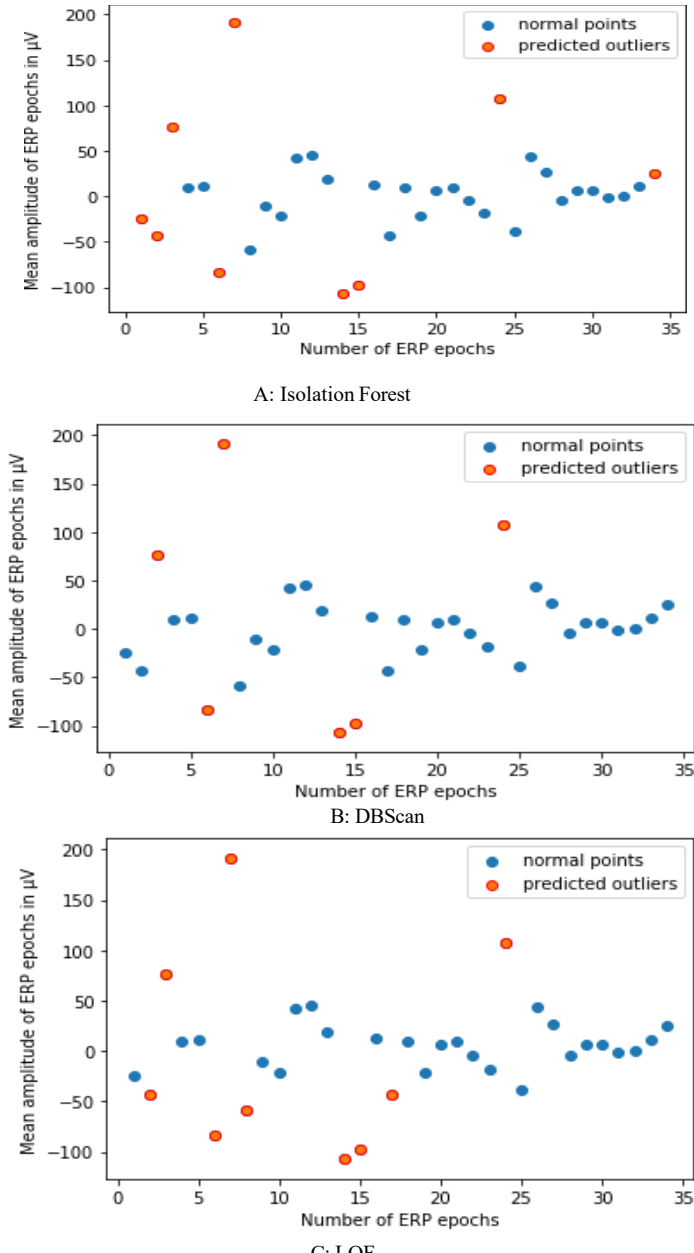


Figure 10: Three unsupervised MLAs. Here, orange circles are artifact corrupted ERP epochs and blue circles are normal ERP epochs, for the test subject 1.

Table 1: Comparison of the detection of accuracy of the artifact corrupted epoch (in %) with eeglab

Dataset	Isolation Forest	DBScan	LOF
D1	76	91	94
D2	88	91	88
D3	94	97	88
D4	94	91	88
D5	74	88	85
D6	94	97	97
D7	94	97	94
D8	91	97	91
D9	95	88	82

D10	94	97	94
D11	91	97	94
D12	76	94	79
D13	82	94	85
D14	91	94	88
D15	62	94	74
D16	97	94	94
D17	91	94	82
D18	91	91	82
D19	88	91	88
D20	88	97	82
D21	79	88	85
D22	82	95	84
D23	81	92	86
Average	85.54%	93.43%	87.18%

Table-I shows the detection accuracy of the artifact corrupted ERP epoch of the auditory oddball paradigm. There, artifact corrupted ERP epoch detection accuracy of three unsupervised machine learning algorithms is compared with EEGLab’s “Reject data epochs” method.

There are 23 test data-sets and named D1, D2, . . . , D23 (as described in section 3.1). Each data-set contains 50 epochs. At first, we detected the artifact corrupted epochs of the D1 data-set by EEGLab (named Data-set E1). After that, we applied 3 unsupervised MLAs (Isolation Forest, DBScan, and LOF) to detect the outlier and named the data-sets as M1, M2 M3, respectively. Then, by confusion matrix, we compared the accuracy of M1, M2 M3 with E1 for the detection of artifact corrupted epochs. We repeated this procedure for all the remaining 23 data-sets. All of the comparative results are shown in Table-I. All the methods showed good detection accuracy and the DBScan achieved a maximum of 93.43%. The LOF method detection accuracy was 87.18% and the Isolation Forest performed with 85.54%.

Table 2: Comparison of visual and auditory oddball paradigm artifact corrupted epoch detection accuracy

	Isolation Forest	DBScan	LOF
Audi ERP	85.34%	93.43%	87.13%
Visu ERP	79.7%	90.15%	77.95%

Table 2, shows the comparison between the auditory oddball paradigm (Audi ERP) and visual oddball paradigm (Visu ERP) for the detection of artifact corrupted ERP epochs. In our previously published paper [1], there is detail about the procedure and results of the visual oddball paradigm. The dataset is a publicly available IRB-approved dataset by the University of California, Davis. The dataset contains 30 subjects’ data. In that experiment, each subject saw five letters (A, B, C, D & E) randomly and one of these letters was assigned as a target letter, and its probability of appearance was 20%. The subject had to identify if the visual stimuli were a target or not, for every block of letters (Fig. 11). The duration of visual stimuli was 200 ms and the gap between each stimulus was 1200 – 1400 ms.

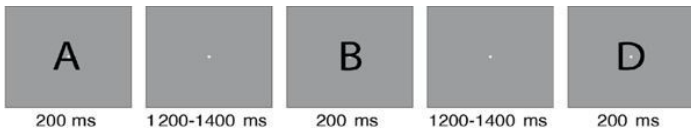


Figure 11: Visual Oddball task (Each subject saw five letters: A, B, C, D & E, randomly, and one of these letters was assigned as a target letter, and its probability of appearance was 20%. The subject had to identify if the visual stimuli were a target or not, for every block of letters (Fig. 11). The duration of visual stimuli was 200 ms and the gap between each stimulus was 1200 – 1400 ms.);

For this visual oddball paradigm data-set, we detected three artifacts corrupted epochs. They are artifacts due to eye blinks, due to eye-movement, and due to body movement. Both EEGLab and MLAs are applied to detect artifact corrupted epochs and compared the accuracy as we did in this study. In Fig. 12, it is shown that, for both (visual and auditory) oddball paradigms, the DBScan performed with maximum accuracy while the other two methods are inconsistent with their positions.

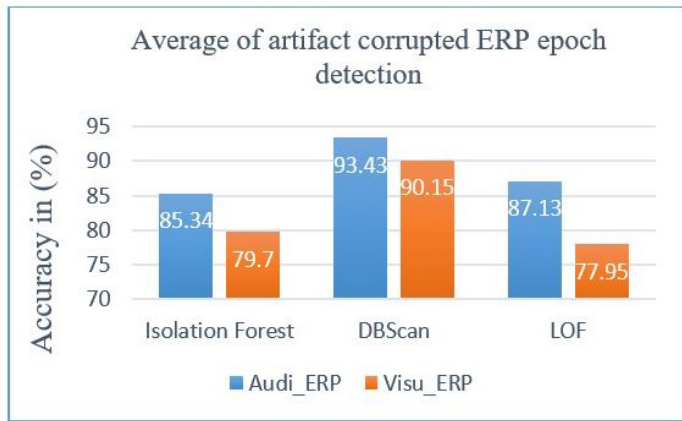


Figure 12: Comparison of artifact corrupted ERP epoch detection accuracy (on average) for both auditory oddball paradigm (Audi ERP) and visual oddball paradigm (Visu ERP) ERP Signal Analysis

6.2. ERP Parameter Analysis

At first, the mean of ERP amplitude, the peak value of ERP amplitude, and the latency of ERP peak were measured in a time window of 200ms to 600ms from the test data sets. Then we identified and removed the artifact corrupted ERP epochs (as described in Section V: A) from the test data sets. After that, we again measured the same values. After comparing the values, before and after removing the artifacts, we found a clear change in values for ERP mean and peak amplitude measures but there were no noticeable changes for the ERP peak latency measures. In Fig. 13 and Fig. 14, it is clearly shown that, for both mean and peak amplitudes, the values become lower after removing the artifact mixed epochs. For mean amplitudes it became 16.14 V from 35.4 V and, for peak amplitudes, it became 142.81 V from 223.9 V.

We also compared the values with our previously published visual oddball paradigm data set [1]. In Tables 3 & 4, values of auditory(Audi ERP) and visual(Visu ERP) ERP mean and peak amplitudes (in micro-volt) are given. In Table 3, mean ampl is the mean amplitude before artifact corrupted ERP epochs removal and mean AR means the mean amplitude after artifact corrupted ERP epochs removal. Same meanings are applicable to Table4. From these tables and Fig. 15 Fig. 16, it is clearly shown that for both

mean and, peak amplitude, the value levels were higher before the artifact corrupted ERP epochs were removed. More specifically, there are sharper differences in the auditory oddball paradigm.

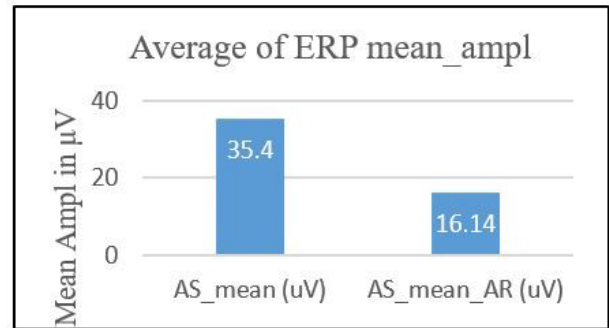


Figure 13: Comparison of the auditory mean amplitude of ERP data before and after (AR) the artifact corrupted EEG epochs are removed (uV: microvolt)

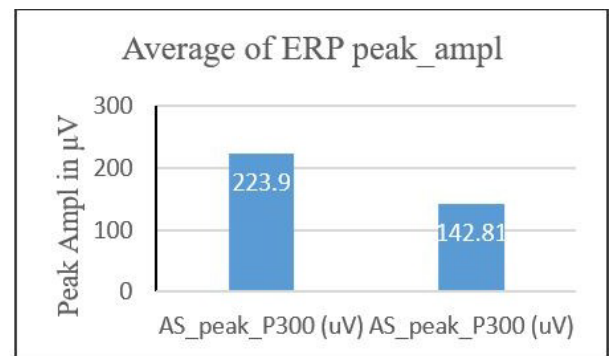


Figure 14: Comparison of the auditory peak amplitude of ERP data before and after (AR) the artifact corrupted EEG epochs are removed (uV: microvolt)

Table 3: Values of auditory and visual erp mean amplitudes in a time window of 200 to 600 ms before (mean) and after (mean ar) artifact corrupted epochs are removed

	Visu ERP	Audi ERP
mean(micro-volt)	9.28	35.4
mean AR(micro-volt)	8.59	6.14

Table 4: Values of auditory and visual erp peak amplitudes in a time window of 200 to 600 ms before (peak ampl) and after (peak ampl ar) artifact corrupted epochs are removed

	Visu ERP	Audi ERP
Peak ampl(micro-volt)	27.75	223.9
Peak ampl AR(micro-volt)	26.33	142.81

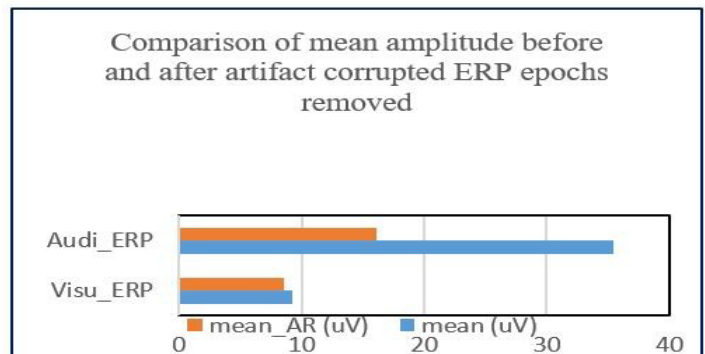


Figure 15: Comparison of the auditory ERP mean amplitude in a time window of 200 to 600 ms before and after the removal of artifact corrupted epochs (V: microvolt)

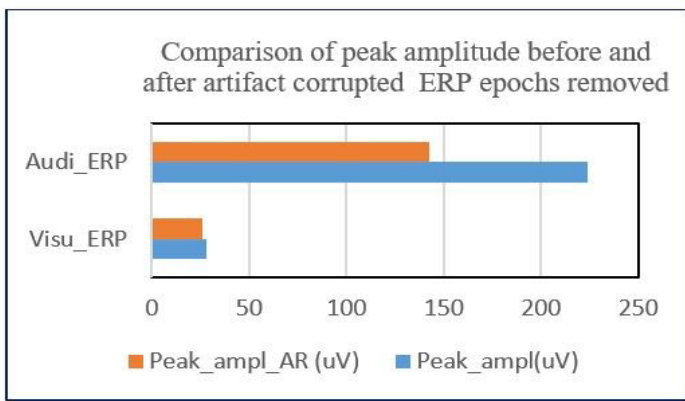


Figure 16: Comparison of the auditory ERP peak amplitude in a time window of 200 to 600 ms before and after the removal of artifact corrupted epochs (V: microvolt)

7. Conclusion

In this study, we detected ERP artifacts of the auditory oddball paradigm by unsupervised machine learning algorithms and compared the results with the visual oddball paradigm experiment which is our previously completed experiment. Our data were unlabeled and we found unsupervised machine learning algorithms are fairly efficient to distinguish the artifacts due to eye and body movement. Among the applied unsupervised machine-learning algorithms, the DBScan method performed with the most efficiency for distinguishing artifacts in ERPs for both audio and visual oddball paradigms. For the auditory ERP experiment, the accuracy is 93.43%, and for the visual ERP experiment, is 90.15%. In addition, the Isolation Forest and LOF method also showed good efficiency for the audio ERP experiment, 85.34%, and 87% respectively. On the other hand, they showed moderate efficiency for the visual ERP experiment, 79.7% and, 77.95% respectively (Table II). So, with the DBScan algorithm, we will have a cleaner ERP dataset in normal laboratory conditions with less complexity in data processing which may improve the quality of the EEG experiments.

It is very obvious that there is a huge change in amplitude levels of ERPs for the eye and body movement corrupted artifacts and normally amplitude levels lift up or down. From Tables 3 & 4, it is clear that ERP means and amplitude become lower after removing artifact corrupted epochs. In addition, there are specific differences between the audio ERP oddball paradigm experiment. On the other hand, no substantial changes were found for the peak latency, before and after artifact corrupted epoch removal.

For future research, there can be added more complexity to detect artifacts. Also, experiments can be designed to detect muscle artifacts which are one of the other common artifacts. Overall, this study may enable the use of ERPs as a strong bio-marker in EEG research in real-world experiments.

Conflict of Interest

There is not any conflict of interest.

References

[1] R. Akhter, F.R. Beyette, "Machine Learning Algorithms for Detection of Noisy/Artifact-Corrupted Epochs of Visual Oddball Paradigm ERP Data," in Proceedings - 2022 7th International Conference on Data Science and Machine

Learning Applications, CDMA 2022, Institute of Electrical and Electronics Engineers Inc.: 169–174, 2022, doi:10.1109/CDMA54072.2022.00033.

[2] S. Luck, "An Introduction to the Event-Related Potential Technique," Chapter 6, 2nd ed., MIT press, 2014.

[3] A.K.M.A. Siddique, R. Azim, A. Islam, "Analysis of the temperature effect on the P300 component by the left and right-hand movement," *16*(1), 45–49, Oct. 2022, doi:10.9790/1676-1601014549.

[4] P. Kadambi, J.A. Lovelace, F.R. Beyette, "Audio based brain computer interfacing for neurological assessment of fatigue," in International IEEE/EMBS Conference on Neural Engineering, NER, 77–80, 2013, doi:10.1109/NER.2013.6695875.

[5] M.T. Giovanetti, F.R. Beyette, "Physiological health assessment and hazard monitoring patch for firefighters," Midwest Symposium on Circuits and Systems, 2017-August, 1168–1171, 2017, doi:10.1109/MWSCAS.2017.8053136.

[6] Y.A. W de Kort L J M Schlangen Drir K C H J Smolders E Gecer, by Lotte Sap, The Influence of Light on the ERP P300 Waveform Sap, Lotte The Influence of Light on the ERP P300 Waveform THE EFFECT OF LIGHT ON THE ERP P300 WAVEFORM 1 Acknowledgement.

[7] R. Akhter, K. Lawal, M.T. Rahman, S.A. Mazumder, "Classification of Common and Uncommon Tones by P300 Feature Extraction and Identification of Accurate P300 Wave by Machine Learning Algorithms," *IACSA International Journal of Advanced Computer Science and Applications*, *11*(10), 2020.

[8] M.G. Asogbon, W. Samuel, X. Li, K. Dabbakuti, "Methods for removal of artifacts from EEG signal: A review You may also like A linearly extendible multi-artifact removal approach for improved upper extremity EEG-based motor imagery decoding Methods for removal of artifacts from EEG signal: A review 1,2 ShailajaKotte and," *12093*, 2020, doi:10.1088/1742-6596/1706/1/012093.

[9] M.K. Islam, A. Rastegarnia, Z. Yang, "Methods for artifact detection and removal from scalp EEG: A review," *Neurophysiologie Clinique/Clinical Neurophysiology*, *46*(4–5), 287–305, 2016, doi:10.1016/j.neucli.2016.07.002.

[10] J.A. Urigüen, B. Garcia-Zapirain, "EEG artifact removal-state-of-the-art and guidelines," *Journal of Neural Engineering*, *12*(3), 2015, doi:10.1088/1741-2560/12/3/031001.

[11] R. Akhter, F. Ahmad, F.R. Beyette, "Automated Detection of ERP artifacts of auditory oddball paradigm by Unsupervised Machine Learning Algorithm," in 2022 IEEE Conference on Computational Intelligence in Bioinformatics and Computational Biology, CIBCB 2022, Institute of Electrical and Electronics Engineers Inc., 2022, doi:10.1109/CIBCB55180.2022.9863055.

[12] D. Steyrl, G. Krausz, K. Koschutnig, al -, L. Fiedler, M. Wöstmann, Y. Roy, H. Banville, I. Albuquerque, A. Gramfort, T.H. Falk, J. Faubert, "Deep learning-based electroencephalography analysis: a systematic review," *Journal of Neural Engineering*, *16*(5), 051001, 2019, doi:10.1088/1741-2552/AB260C.

[13] Y. Guo, X. Jiang, L. Tao, L. Meng, C. Dai, X. Long, F. Wan, Y. Zhang, J. van Dijk, R.M. Aarts, W. Chen, C. Chen, "Epileptic Seizure Detection by Cascading Isolation Forest-Based Anomaly Screening and EasyEnsemble," *IEEE Transactions on Neural Systems and Rehabilitation Engineering*, *30*, 915–924, 2022, doi:10.1109/TNSRE.2022.3163503.

[14] Z. Lin, F. Wen, Y. Ding, Y. Xue, "Data-Driven Coherency Identification for Generators Based on Spectral Clustering," *IEEE Transactions on Industrial Informatics*, *14*(3), 1275–1285, 2018, doi:10.1109/TII.2017.2757842.

[15] M. Piorecký, J. Štrobl, V. Krajca, "Automatic EEG classification using density based algorithms DBSCAN and DENCLUE," *Acta Polytechnica*, *59*(5), 498–509, 2019, doi:10.14311/AP.2019.59.0498.

[16] N. Bigdely-Shamlo, K. Kreutz-Delgado, C. Kothe, S. Makeig, "EyeCatch: data-mining over half a million EEG independent components to construct a fully-automated eye-component detector," Annual International Conference of the IEEE Engineering in Medicine and Biology Society. IEEE Engineering in Medicine and Biology Society. Annual International Conference, 2013, 5845–5848, 2013, doi:10.1109/EMBC.2013.6610881.

[17] M. Agarwal, R. Sivakumar, "Blink: A Fully Automated Unsupervised Algorithm for Eye-Blink Detection in EEG Signals," 2019 57th Annual Allerton Conference on Communication, Control, and Computing, Allerton 2019, 1113–1121, 2019, doi:10.1109/ALLERTON.2019.8919795.

[18] S.S. Lee, K. Lee, G. Kang, "EEG Artifact Removal by Bayesian Deep Learning & ICA," in 2020 42nd Annual International Conference of the IEEE

- Engineering in Medicine & Biology Society (EMBC), IEEE: 932–935, 2020, doi:10.1109/EMBC44109.2020.9175785.
- [19] C.J.T. Kothe, “Artifact removal techniques with signal reconstruction,” Google Patents. US Patent App. 14/895,440, 2016.
- [20] A.K. Maddirala, K.C. Veluvolu, “Eye-blink artifact removal from single channel EEG with k-means and SSA,” *Scientific Reports*, **11**(1), 2021, doi:10.1038/s41598-021-90437-7.
- [21] S. Sadiya, T. Alhanai, M.M. Ghassemi, “Artifact detection and correction in EEG data: A review,” *International IEEE/EMBS Conference on Neural Engineering, NER*, 2021-May, 495–498, 2021, doi:10.1109/NER49283.2021.9441341.
- [22] P. Schembri, M. Pelc, J. Ma, “The Effect That Auditory Distractions Have on a Visual P300 Speller While Utilizing Low-Cost Off-the-Shelf Equipment,” *Computers* 2020, **9**(3), 68, 2020, doi:10.3390/COMPUTERS9030068.
- [23] LUCIO. di JASIO, “Graphics, touch, sound and usb, user interface design for embedded applications,” 2014.
- [24] A. Delorme, S. Makeig, “EEGLAB: An open source toolbox for analysis of single-trial EEG dynamics including independent component analysis,” *Journal of Neuroscience Methods*, **134**(1), 9–21, 2004, doi:10.1016/j.jneumeth.2003.10.009.
- [25] M. Fatourechi, A. Bashashati, R.K. Ward, G.E. Birch, “EMG and EOG artifacts in brain computer interface systems: A survey,” *Clinical Neurophysiology*, **118**(3), 480–494, 2007, doi:10.1016/j.clinph.2006.10.019.
- [26] A.K. Maddirala, K.C. Veluvolu, “Eye-blink artifact removal from single channel EEG with k-means and SSA,” *Scientific Reports* 2021 11:1, **11**(1), 1–14, 2021, doi:10.1038/s41598-021-90437-7.
- [27] D.W. Frank, R.B. Yee, J. Polich, “P3a from white noise,” *International Journal of Psychophysiology*, **85**(2), 236–241, 2012, doi:10.1016/J.IJPSYCHO.2012.04.005.
- [28] C.J. Ochoa, J. Polich, “P300 and blink instructions,” *Clinical Neurophysiology*, **111**(1), 93–98, 2000, doi:10.1016/S1388-2457(99)00209-6.
- [29] R. Martínez-Cancino, A. Delorme, D. Truong, F. Artoni, K. Kreutz-Delgado, S. Sivagnanam, K. Yoshimoto, A. Majumdar, S. Makeig, “The open EEGLAB portal Interface: High-Performance computing with EEGLAB,” *NeuroImage*, **224**, 116778, 2021, doi:10.1016/j.neuroimage.2020.116778.
- [30] A. Delorme, R. Oostenveld, F. Tadel, A. Gramfort, S. Nagarajan, V. Litvak, “Editorial: From Raw MEG/EEG to Publication: How to Perform MEG/EEG Group Analysis With Free Academic Software,” *Frontiers in Neuroscience*, **16**, 359, 2022, doi:10.3389/FNINS.2022.854471/BIBTEX.
- [31] C. Brunner, A. Delorme, S. Makeig, “Eeglab - an Open Source Matlab Toolbox for Electrophysiological Research,” *Biomedizinische Technik. Biomedical Engineering*, **58** Suppl 1, 2013, doi:10.1515/BMT-2013-4182.
- [32] J. Lopez-Calderon, S.J. Luck, “ERPLAB: an open-source toolbox for the analysis of event-related potentials,” *Frontiers in Human Neuroscience*, **8**(1 APR), 2014, doi:10.3389/FNHUM.2014.00213.
- [33] R. Martínez-Cancino, A. Delorme, D. Truong, F. Artoni, K. Kreutz-Delgado, S. Sivagnanam, K. Yoshimoto, A. Majumdar, S. Makeig, “The open EEGLAB portal Interface: High-Performance computing with EEGLAB,” *NeuroImage*, **224**, 2021, doi:10.1016/J.NEUROIMAGE.2020.116778.
- [34] T. Jiang, J.L. Gradus, A.J. Rosellini, “Supervised Machine Learning: A Brief Primer,” *Behavior Therapy*, **51**(5), 675–687, 2020, doi:10.1016/j.beth.2020.05.002.
- [35] M.T. Rahman , R. Akhter, “Forecasting Stock Market Price Using Multiple Machine Learning Technique,” Preprint, 2021.
- [36] M.T. Rahman, R. Akhter, “Forecasting and Pattern Analysis of Dhaka Stock Market using LSTM and Prophet Algorithm,” Preprint, 2021.
- [37] S. Sing, “Anomaly Detection Using Isolation Forest Algorithm,” *Analytics Vidhya Medium*, 2020.
- [38] M.Y. Pusedan, J.L. Bulialli, R.V.H. Ginardi, “Optimum partition in flight route anomaly detection,” *Indonesian Journal of Electrical Engineering and Computer Science*, **14**(3), 1315–1329, 2019, doi:10.11591/IJEECS.V14.I3.PP1315-1329.
- [39] M.M. Breunig, H.-P. Kriegel, R.T. Ng, J. Sander, “LOF: Identifying Density-Based Local Outliers,” 2000, doi:10.1145/335191.
- [40] A. Mavuduru, “How to perform Anomaly Detection with the Isolation Forest Algorithm, Toward Data Science,” 2021.
- [41] E.E.M. Schubert, “DBSCAN revisited, revisited: why and how you should (still) use DBSCAN,” *ACM Transactions on Database Systems (TODS)*, **1**–21, 2017.
- [42] F. Demir, “Deep autoencoder-based automated brain tumor detection from MRI data,” Elsevier: 317–351, 2022, doi:10.1016/B978-0-323-91197-9.00013-8.

Blockchain Applications in Suning and PingAn

Cong Qi*, Yue Lei, Yuejun Cai

The Hong Kong Polytechnic University, Department of Management and Marketing, Hong Kong, China

ARTICLE INFO

Article history:

Received: 27 May, 2022

Accepted: 15 October, 2022

Online: 31 October, 2022

Keywords:

Blockchain applications

Suning

PingAn

ABSTRACT

The emergence of blockchain technology has facilitated the digital transformation of many businesses and thereby increased the competitiveness of China in the global market. As a cutting-edge technology, Blockchain has significantly influenced the practices across all business sectors. Focusing on the retail and insurance sectors, this paper analyzes the blockchain technology applications in two companies - Suning and PingAn. Success factors in blockchain implementation were discussed by using TOE framework. Similarities and differences in the implementation and development processes are compared. Features from the two corresponding industries - retail and insurance are also summarized. The major results revealed that retail and insurance industries are two of the most important application sectors of blockchain technology, and Suning and PingAn are both pioneers in blockchain technology development and implementation in their specific sectors. However, there are still distances between Chinese blockchain providers and world leading providers of blockchain, even though China has the largest number of blockchain patents in the world. The research results provide meaningful insights and practical implications to the blockchain application fields.

1. Introduction

This paper is an extension of work [1] initially presented at the conference of Artificial Intelligence and Blockchain Technology (2021). Starting from a boom in the crypto-asset speculative movement in 2017, blockchain technology has kept an ascending trend in recent years [2]. Due to the high fever of Bitcoin, blockchain as a novel technology is also gradually gaining popularity in various industries. Blockchain consists of a peer-to-peer (P2P) network, a private key cryptography, and a protocol to make transactions secure [3]. Blockchain shares some unique characters, such as decentralization, persistency, anonymity and suitability [4], and was widely applied in multiple prevalent areas [5].

Although blockchain technology has been studied in various industries, its primary applications exist in the finance industry. Due to the use of blockchain, the labor costs are significantly reduced, and information system security is substantially increased [6]. Retail industry is another industry with a higher penetration rate of blockchain, it can be used to trace veraciously transactional records [7]. Though industry papers have discussed and listed the implementation facts of both industries, little research has been done to systematically

summarize the similarities and differences between the two industries, specifically with exemplary cases. With the above, this study examines the blockchain applications in these two industries and thoroughly analyzes two exemplars - Suning holdings group and PingAn insurance group. The Technology-Organization-Environment framework is also used to summarize the success factors of blockchain implementation in both companies. In sum, our paper aims to address the following research questions:

1. How do Suning holdings group and PingAn insurance adopt and provide blockchain technology in their businesses?
2. What are the similarities and differences between both companies regarding to the development and implementation of blockchain technologies? What are the common factors leading to blockchain application success?
3. How was blockchain technology developed in retail and insurance industries on a large scale?

2. Blockchain Technology

Blockchain is a system for recording information, and it is essentially a distributed ledger technology. The decentralized and immutable nature makes it difficult to disrupt. A blockchain is a chained database containing fixed-length blocks in which every

*Corresponding Author: Cong Qi, Email: cong.qi@polyu.edu.hk

www.astesj.com

<https://dx.doi.org/10.25046/aj070518>

transaction record is included. Newly generated incompressible transactions need to be verified before being inserted into the block. Users manage the data stored in the public blockchain autonomously through a P2P network and a distributed timestamp server, they also have free access to the transactions between two parties permanently recorded in the blockchain [8].

From the perspective of information technology, a blockchain is a distributed database in the form of multiple nodes, and a complete copy is available on each node. If more than 50% of the nodes reach consensus, the chain is entirely trustworthy [9]. In addition to the transaction record and timestamp, each block contains a hash value of the previous block and a new random number that can be used to verify the hash. The hash value exists to prevent fraud caused by changes to the content stored in the blockchain, and it follows each block to change [10]. Blockchain also determines whether a block contains a valid transaction. It uses the proof of work algorithm, which empowers data stored in the blockchain to be unaffected by the collapse of one node and thus maintains the authenticity of the data. On an overall basis, such a transparent system helps record the detailed sequence of events [6].

From the perspective of business transactions, blockchain technology offers a shared ledger for all companies involved in transaction. These new ledgers can hardly result in data loss, change or deletion, and can exclude the presence of a trusted third-party company as in traditional transactions [11]. In this study, we discuss the applications of blockchain technology in the retail and insurance industries. Suning holdings group and PingAn insurance are selected in this paper as typical cases due to their pioneer positions in blockchain technology adoption and implementation. Furthermore, we extend our study and discuss the general phenomena of applying blockchain technology in retail and insurance industries. Last, the comparison of successful factors, similarities and differences between the two companies are presented, and the features of the two industries are summarized.

3. Blockchain in Suning holdings group

Suning holdings group (hereafter Suning) has been ranked as the second-largest civilian-run enterprise in mainland China. As a large ecological, platform-based company, Suning's industry chain involves retail, finance, logistics, Internet of things (IoTs), cultural creation, and sports. With an online and offline customer base of over 600 million, Suning is well-positioned to use big data to build consensus collaboration networks. A large amount of data provided blockchain technology a suitable environment. This amount of data also contributed to establish a blockchain lab by Suning Financial Research Institute in 2017, and thereupon, Suning integrated the blockchain technology into the group's business [12]. After that, Suning launched the domestic credit information transmission system, blockchain blocklist sharing platform, "blockchain + IoTs" financing platform for cars, blockchain anti-counterfeiting technology, and blockchain asset securitization service system between 2017 and 2018. After a series of practices of blockchain, Suning released the Suning blockchain white paper in July 2018. The white paper elaborated the development path and application areas of blockchain in Suning and announced Suning's prediction of the future development of blockchain [12].

A year later, Suning launched Blockchain as a Service (BaaS), a cloud-based infrastructure platform to provide developers and users with an ecosystem for creating and managing blockchain applications. The BaaS platform is also committed to provide a series of blockchain financial solutions such as data sharing, IoTs, supply chain finance, and payment settlement. In 2020, Suning launched an external empowerment plan to enhance digital and intelligent financial services, which has accelerated the research and development of blockchain technologies and expanded the blockchain application scenarios to its major partners. It is worth mentioning that Suning's financial blockchain technology has won various industry awards, including being selected for the 2020 FAT Blockchain fintech leading 100 list. These show that Suning's blockchain applications are forward-looking in the industry [13].

3.1. Suning's blockchain in Retail and E-Commerce

Suning's blockchain application in the retail industry originated from the concept of smart retailing [14]. Compared to traditional retailing, smart retailing tends to predict consumers' preferences and customize services by using big data. It involves drawing a user portrait, building a membership ecosystem, and supplying products according to market demand.

3.1.1. User portraits and member ecology

Consumers inevitably reveal their privacy when engaging in consumer behavior. To prevent user information from being leaked to third parties intentionally or unintentionally, Suning introduced blockchain technology to store users' information. Moreover, since the data in the blockchain is available to authorized users only, consumers are able to self-manage the information stored in the blockchain, thus eliminate the possibility of information leakage [15]. Suning's business involves diverse aspects of retail industry, such as clothing, food, housing, and transportation. Building a member ecology can strengthen communication and enhance the sense of user experience. The ecology enables consumers, retailers, and suppliers to join the same blockchain network to avoid the unnecessary cost due to information asymmetry.

3.1.2. Smart logistics

Smart logistics is mainly reflected in supply chain management. Most traditional supply chains use one single approach - bulk goods reach the distributors through the supply chain and are distributed to smaller sales stores [16]. However, Blockchain technology allows factories to supply according to customers' demand, eliminating the need for customers to wait for replenishment and travel to physical stores. The supply chain no longer adjusts passively based on customer demand but proactively predicts consumer demand and market trends [17].

Blockchain technology can also monitor products throughout the logistics process to ensure that goods are traceable. On one hand, real-time logistics records track each transaction and delivery environment, avoiding incidents such as goods lost or replaced in the middle of the process. It strengthens the management of employees and reduces the possibility of

corruption. On the other hand, blockchain technology can implement precise regulation of cargo transportation. All parties involved in the transportation process can exchange real-time data and electronic documents without barriers [18]. Thus, the most optimal transportation route can be filtered out. In 2018, Suning collaborated with Baidu to develop driverless delivery vans. This has made uploading logistics information to the blockchain network easier [19].

According to statistics, Suning's smart logistics network has covered 95% of the areas in mainland China. The company also plans to reach 20 million square meters storage area by 2025. In August 2020, Suning, China Logistics, and other partners jointly released the "5G smart logistics innovation demonstration white paper", in which Suning's experience in exploring smart logistics using blockchain and 5G technology was made public [19].

3.2. Suning's blockchain in financial trade

Since the invention of Bitcoin, the financial industry was the first sector to achieve a breakthrough in blockchain. Suning's blacklist sharing platform is one of the influential application areas of blockchain [12]. Traditional blacklists are used to record individuals or organizations with serious adverse credit problems, and are used mainly by financial institutions. However, most traditional blacklist data are non-public. It is thus difficult to investigate whether the other party commits credit problems before a transaction, which results in inevitable losses for both parties. Suning took the initiative to use blockchain technology to build a decentralized blacklist sharing platform. Blacklists in the industry are pooled and published to authorized organizations. This list is shared with other nodes in the blockchain network through smart contracts [12]. After one year's implementation, the platform gathered 11 million pieces of data, including 7 financial institutions on the blacklist [20]. In September 2020, Suning bank officially joined forces with Citic bank and Minsheng bank to create a blockchain consortium that used the blacklist sharing platform of Suning.

3.3. Suning's blockchain in IoT

Traditional IoTs relies on a centralized structure where all devices are authenticated by accessing a centralized cloud server. When the IoTs applications expand, it is highly prone to a system collapse, and lead to high financial and human resources costs. Meanwhile, the highly centralized nature makes all data stored in the IoTs hub. Once the hub is attacked, all users' private data will be lost or maliciously exploited [12]. Blockchain technology can solve this problem. In the following, we will introduce Suning's two applications of blockchain in IoTs.

3.3.1. Smart home

As a company that promotes smart retail ecology, Suning has taken the lead in the industry to build an ecological intelligence platform to introduce smart home applications. Suning built a Biu+ ecological system based on artificial intelligence technologies, and blockchain technology in the Biu+ smart home system realizes the goal of information interoperability [21].

3.3.2. IoTs financing platform for cars

Suning launched the "Blockchain + IoTs" financing platform for cars in March 2019. Blockchain technology solves the problem

of poor credibility supervision of movable assets pledge and inventory pledge financing business. Business process data can be uploaded to the blockchain platform, while sensors can monitor the goods in the warehouse in real-time to ensure the safety of goods during the pledge period. Suning claims that using the platform, the credit volume of the inventory financing business is expected to have a tenfold increase [22].

3.4. Blockchain in culture and creativity

Cultural creation involves film and television, audio-visual, media, and craft design. The degree of copyright protection directly affects the motivation of creators. The major problem with copyright protection is that the certification mechanism is time-consuming and costly. Inspired by the feature of blockchain, Suning uploads the creators' content to the blockchain, and the generated timestamp is a unique proof of work. Subsequent modifications to the work are recorded in the block in chronological order. When the work faces the problem of copyright protection, the data in the blockchain will become a critical source to prove the originality. Meanwhile, smart contracts allow creators and consumers to transact directly without the presence of a third party (e.g., record label and broker). The privacy of the entire sales process is protected, and third-party profit sharing can be largely avoided [12].

The key milestones of the implementation process are summarized in Table 1.

Table 1: Milestones of Blockchain implementation in Suning

Time	Milestones of implementation
April 2017	Suning launched a blockchain-based Letter of the credit system (BCLC), a blockchain financial blacklist data service system.
February 2018	Suning launched the blacklist sharing platform system.
July 2018	<ul style="list-style-type: none"> Suning and SAP carry out technological innovation and industry practice and promote the digital economy. Suning officially published Suning's blockchain white paper and blueprinted different application scenarios of blockchain technology in retail, logistics, finance, culture, and creative industries. The Suning blockchain commodity traceability platform was launched.
September 2018	Suning Bank successfully granted pledge credit to the coal of Taihe port services through a chattel pledge financing platform based on blockchain and IoTs.
March 2019	Suning finance's "Blockchain + Internet of Things" finance platform was launched.
April 2019	The Suning blockchain forfeiting platform was launched.
June 2019	Suning demonstrated its ambition for blockchain technology in smart homes by deploying Suning's Biu+ ecology.
End of 2019	Suning launched Suning's Blockchain as a Service (BaaS) cloud infrastructure platform.

Beginning of 2020	Suning financial technology launched the blockchain asset securitization service system, cooperating with the initial issuance of RMB 800 million first way asset-backed security loans.
February 2020	The Suning logistics "5G Wolong" unmanned vehicle empowered by blockchain successively completed unmanned terminal delivery deployments in Beijing, Nanjing, and Suzhou.
August 2020	The "5G smart logistics innovation demonstration white paper" that shares the strategic acumen of the combination between blockchain and 5G technology in smart logistics was jointly released by Suning and its alliances.
September 2020	<ul style="list-style-type: none"> The Suning blacklist sharing platform buttressed the development and launch of the blockchain consortium, established by Suning bank, Citic bank, and Minsheng bank. Suning was invited to be a member of the official Jiangsu Internet society blockchain standardization technical committee.
November 2020	The blockchain information sharing platform of anti-money laundering led by Suning bank started its services.

Suning has benefited from the large-scale adoption of blockchain technology. User retention has dramatically increased as a result of blockchain's utilization in user profiling, and Suning is now able to proactively predict customer demand and market trends. Meanwhile, the expenditures brought on by information asymmetry were decreased [15, 17]. Suning was able to quickly upgrade information systems and achieve 95% coverage of the national smart logistics network thanks to blockchain applications in IoT. The presence of blockchain eliminated the volatility of conventional IoT systems and decreased the expenditure on building infrastructure and maintaining systems. Additionally, Suning has been able to grow its business into industries like intellectual property protection due to the application of blockchain in cultural protection, which started in 2018 [12, 23].

As a comparison, Amazon - one of the world's best retailers in US, also has a unique insight into the expansion of its blockchain business. Its Amazon Managed Blockchain (AMB) makes it easy for clients to join public networks or create and manage scalable private networks using the popular open-source frameworks. Many famous companies in the world employed AMB services. Examples include: BMW, Sage, SonyMusic, and Nestle. AMB solutions were also used to facilitate supply chain management, international transactions, digital right protection, record keeping of all kind and more. In sum, Amazon developed a simpler and more efficient blockchain program that significantly reduces operational time and offers more than 70 solutions for customers [24]. Compared with Suning, Amazon provided more international services with a larger capacity across multiple areas to its clients, whereas Suning focuses more on the Chinese business, but still having an advantage in a wide application area of blockchain. It

will take Suning a longer time to develop its blockchain technology to reach the maturity level of Amazon.

4. Blockchain in the retail industry

In the post-epidemic era, the challenges faced by retailers, such as supply chain maintenance, product sales, and employee safety, urged the development of blockchain technology in retail industry [25]. The application of blockchain technology is mainly reflected in three aspects. Firstly, it builds consumer confidence in the brand: blockchain has significantly reduced customer concerns about information security leaks. Likewise, supply chain management with blockchain participation ensures the quality of goods. Secondly, it improves the ability of suppliers to meet market demand: the supply chain under blockchain management actively adjusts the production quantity and inventory of goods according to market demand, reducing unnecessary costs. Finally, it creates additional competitive advantages for firms: customer profiling based on customer information, understanding consumer preferences, and designing products to meet market demand.

Alibaba and Jingdong are the industry leaders ahead of Suning in terms of blockchain technology applications. The blockchain competition between these three top companies started with the "618" (an online shopping festival organized by e-commerce platforms in China on June 18th) promotion in 2018. Jingdong generated CNY259.8 billion turnover, and Ali Group's Tmall reached CNY213.5 billion. The high turnover has led to concerns about the quality of goods. Using blockchain technology to trace the originality of goods became a key to solve this concern. Jingdong firstly applied blockchain technology for anti-counterfeit traceability of mother and child, global purchase, and alcohol products. It made the total number of traceable commodities increased by more than 200 times within the 18 days of the "618" campaign. The platform has also attracted more than 400 companies worldwide, which further increased the number of traceable goods to 1 billion pieces [26].

In sum, for the retail industry, the significance of blockchain mainly lies in protecting user information, anti-counterfeit traceability of products, and monitoring the logistics process. A reasonable implementation of blockchain technology can help retail merchants win customers' trust and save unnecessary costs.

5. Blockchain in PingAn insurance

Ping An Insurance Co. of China Ltd (hereafter PingAn) is a Shenzhen-based Chinese holding company engaged in insurance, banking, and financial services, with thirty subsidiaries located domestically and oversea. PingAn was ranked No. 7 on the Forbes Global 2000 list of companies in 2021 and No. 29 on the Fortune Global 500. PingAn has generated \$107 billion in gross premiums as China's largest insurer in 2018 alone. In July 2019, PingAn became the second-largest insurer globally, with a market capitalization of \$220 billion [27]. PingAn joined the R3 Blockchain Alliance in 2016 to collaborate with a global consortium on how to apply blockchain technology to the financial market, which was PingAn Group's first attempt at blockchain technology [28]. As a traditional insurance and finance company, PingAn aspires to be positioned more as a technology company providing cutting-edge technologies [29].

In the traditional insurance industry, policies are primarily documented in paper-based contracts, and consumers would call or meet the customer representative to finalize the contract. This process relies on manual operations and is subject to the risk of information loss, tampering, and misinterpretation. It is stated that fraud accounts for 10 percent of all property and casualty losses and creates at least \$80 billion in losses in the U.S. [30]. Additionally, the lack of security, efficiency, and customer satisfaction in traditional insurance sales are issues that cannot be ignored. Blockchain technology could be an intelligent solution here [30].

Realizing the significant impact of blockchain in insurance business, PingAn increased the investment of research and development in blockchain. 2021's knowledge asset management report shows that PingAn has obtained 1,749 blockchain patent families, implying a significant increase compared to the 291 in 2019 [31]. PingAn's powerful blockchain technologies have created a new financial ecosystem covering five substantial areas: finance, real estate, automotive, healthcare, and smart cities. The blockchain system developed by PingAn has attracted 13.32 million Internet users in 2020 and reached 225 million currently [32].

5.1. PingAn's blockchain in finance

PingAn OneConnect is an associate company of the PingAn insurance conglomerate. It has perfectly solved the challenges of privacy protection and system performance with its self-developed FiMAX S3C cryptographic blockchain structure. In addition to basic blockchain application methods such as trade finance, supply chain finance, and asset-backed securities, PingAn OneConnect also offers customized blockchain solutions for enterprises. Unlike traditional blockchain nodes generated by multiple accounts, the BNaaS (Blockchain Network as a Service) platform developed by PingAn allows users to independently create and publish new blockchain networks and join existing commercial blockchain networks through the BNaaS marketplace [13].

The blockchain-enabled platform, jointly built by OneConnect and UBX Philippines, targets Micro, Small, and Medium Enterprises (MSME) banking needs. It aggregates blockchain, face recognition, micro-expression, big data, and AI technologies and covers many business finance needs. Therefore, it can integrate more MSMEs into the financial system [33]. In addition, OneConnect developed a new smart legal contracting system in 2019, and actively rolled out ALFA smart contracts. The contracts cover seven major financial sectors: banking, funds, securities, trusts, leasing, futures, and insurance across PingAn Group's various divisions. Using this smart contract, managing Asset-Backed Securities (ABS) scheme contracts that would initially take two employees two to three weeks can now be completed in half an hour. After a wide-range use, ABS assets traded through ALFA reached CNY100 billion (\$13 billion). The technology has significantly reduced the contracting time by 85% [34].

5.2. Blockchain in real estate, automobile, medical care, and smart city

PingAn, one of China's largest real estate investors, spends CNY50 billion (\$7.7 billion) of its annual budget on new physical asset investments, representing 10% of its total investments each

year [35]. Lease transactions and property registration in the real estate business involve preserving confidential information such as property rights, management rights, and transaction prices. With the help of blockchain technology, the accuracy and efficiency of the above activities can be improved.

In the automotive industry, where PingAn is involved, blockchain technology enables the traceability of the sources of auto parts and improves operational transparency. Moreover, blockchain allows the automation of processes in car-sharing services. For instance, with the assistance of smart contracts, blockchain will help two parties create an agreement, after all the conditions of the agreement are fulfilled, this agreement will be automatically executed [36].

PingAn's healthcare ecosystem, released in 2020, contains one of the largest healthcare databases in the world. The database holds the second largest number of health technology patent applications globally, covering 30,000 disease profiles, 300 million apps, and over 1 billion medical consultation records [37]. Blockchain technology is mainly used for anti-counterfeit traceability of drugs and storage of patient electronic profiles.

PingAn signed an agreement with the Sanya city government to build a "smart city" based on blockchain, artificial intelligence, big data, and cloud computing technologies. PingAn group invested CNY30 billion (\$4 billion) to construct Sanya's smart city [38]. The key milestones of the implementation process in PingAn are summarized in Table 2.

Table 2: Milestones of Blockchain implementation in in PingAn

Time	Milestones of implementation
May 2016	PingAn became the first Chinese financial services institution to join the R3 consortium.
October 2016	PingAn OneConnect successfully registered the patent for "blockchain-based transaction verification method and system", "permission control method and system based on blockchain transaction", and "blockchain-based transaction processing method and system."
January 2017 – May 2018	PingAn OneConnect successfully registered a series of patents for a Blockchain related systems and methods.
August 2018	PingAn unveiled China's first "1+N" smart city integrated platform, supported by blockchain technology.
October 2018	HKMA uses PingAn's FiMAX blockchain to establish an eTradeConnect platform for seven international banks in Hong Kong.
December 2018	PingAn Good Doctor started integrating blockchain technology in their smart severe disease monitoring system, AI-based medical system, PASS and smart medical safety monitoring platform to improve the data security of the healthcare ecosystem.
March 2019	PingAn OneConnect works with IFAB to establish a blockchain-based IFAB trade finance network for SMEs.

April 2019	PingAn OneConnect established the Tianjin port blockchain-based verification pilot project.
May 2019	PingAn OneConnect built and operated a blockchain-enabled integrated Gamma Platform, allowing clients to migrate, manage and enhance their technology infrastructure and simplify the digital transformation process.
June 2019	<ul style="list-style-type: none"> • PingAn OneConnect started managing the contracts by the ALFA smart contract cloud platform, which supported 1,000 standard contract templates and 80,000 tags stored in the blockchain. • PingAn FiMAX won the Best Blockchain or Distribution Ledger Technology Award from the Asian Banker, the Outstanding FinTech Achievement and the Best Application of Advanced Technology in a Product or Service from bank administration institution.
July 2019	PingAn OneConnect officially launched the Blockchain Network-as-a-Service (BNaaS) for customers to create their blockchain-based networks or take part in existing networks established by others.
December 2019	<ul style="list-style-type: none"> • PingAn’s International Smart City subsidiary launched iShenzhen blockchain electronic license application platform. • PingAn integrated the blockchain witness function and launched the “PingAn Good Lawyer” smart legal compliance assessment systems.
April 2020	PingAn OneConnect and China merchants’ port group created a blockchain-based system with Shenzhen customs to serve the Guangdong-Hong Kong-Macao Greater Bay Area.
May 2020	PingAn was one of the pioneers utilizing the blockchain technology to develop a tax-industry alliance chain for the sake of reducing tax costs and trade finance risk.
August 2020	PingAn’s International Smart City subsidiary was invited to be the chief compilation team as recorded in the bluebook of blockchain application innovation in the area of Beijing government services.
October 2020	PingAn launched the intelligent transportation integration platform- “155C” to resolve traffic congestion-related issues.
November 2020	<ul style="list-style-type: none"> • PingAn filed the largest number of blockchain-related patents in 2020 [31]. • PingAn FiMAX was listed on the Top 30 list of the 2020 China Blockchain entities and was rewarded by 5th Golden Gyro Awards for its contribution to the Blockchain industry.

September 2021	<ul style="list-style-type: none"> • PingAn OneConnect had collaborated with 62 government agencies and regulators and 41 IT service providers to benefit over two million SMEs through its financial ecosystem. • PingAn’s FiMax architecture has been widely recognized and won 22 technology awards [39].
----------------	--

In PingAn’s insurance business, blockchain technology has significantly advanced the digital transformation, improved traditional insurance paper-based transactions and enhanced employee efficiency. As a result, there has been a corresponding reduction in errors and frauds previously caused by manual labor. PingAn OneConnect is also very good in developing blockchain platforms and offers blockchain services to other companies. The applications of blockchain in other areas has automated procedures and increased operational transparency in various ways. Due to the increased accuracy of confidential information and transaction efficiency, PingAn has won the trust of investors and clients [36]. Statistics show that after blockchain technology was adopted, the total number of users surged to 225 million [32].

As a comparison, United Health Group (UHG) U.S. - the benchmark for blockchain technology adoption in the health insurance sector was chosen. UHG uses the blockchain alliance the same way as PingAn. However, UHG's alliance brings together significant, industry-leading businesses from several sectors and encompasses multiple commercial relations, including suppliers and rivals. In contrast to PingAn's blockchain alliance, which is more homogeneous and is mostly constituted of insurance businesses, UHG's blockchain alliance deploys a multi-company, multi-site, permissioned blockchain. Each alliance member has the flexibility to deploy its nodes in accordance with its corporate demands. To this extend, PingAn's blockchain technology applications are yet to be as innovative and diversified as those of international leaders [40].

6. Blockchain in the insurance industry

Blockchain technology is used in the insurance industry mainly as a decentralized and shared distributed ledger to prevent the risk of fraud in the insurance business by providing immutable and time-stamped records of transactions. In recent years, insurance companies have gradually benefited from blockchain technologies in their insurance business and have significantly increased their investment in developing new models of blockchain technologies.

The insurance market size of blockchain was estimated to be \$1,393.8 million by 2023, with an 84.9% compound annual growth rate (CAGR) [41]. The applications of blockchain are reflected in the following aspects: (1) fraud monitoring and risk prevention: insurance companies can keep all transaction records permanently on a distributed ledger and can use public data to predict and analyze fraudulent activities, (2) increasing customer trust in the brand: cryptographic principles in blockchain are used to authenticate customers and ensure transaction security and customer privacy, (3) claim processing: use blockchain technology to analyze data and significantly speed up claim processing, (4) smart contracts: blockchain's smart contracts automatically fulfill contracts when all conditions are met, reducing back-end

paperwork and lowering insurance company management and operating costs.

The current situation shows that insurers are more cautious in blockchain deployment compared with the retailers, and blockchain is primarily applied to prevent fraud risks and manage information. However, some start-up insurers are trying to expand blockchain operations to other areas such as accessing and auditing electronic health records and verifying settlements. These activities are expected to save costs and improve operational efficiency [36].

7. Comparison between the two cases and two industries

So far, we have introduced the implementation of blockchain technology in two companies - Suning and PingAn, and described the trend of blockchain applications in the retail and insurance industries. In this session, we will first use Technology-Organization-Environment (TOE) framework to summarize the factors leading to blockchain implementation success, and then compare the similarities and differences between these two companies. The summarized features of blockchain applications in both industries will be presented at last.

7.1. TOE framework and common factors to blockchain applications success

With the analysis of the two cases, we argue that Suning and PingAn share several commensurate characteristics that lead to their success in blockchain implementations. We draw on the Technology-Organization-Environment (TOE) framework to explicate how and why these characteristics are essential and generalizable rather than domain-specific to all industries and types of organizations.

TOE framework was initiated by Tornatzky and Fleishcer in 1990 [42], and further extended to suit different contextual and/or situational analyses. The main principle of the TOE framework advocates the contextual congruence of technology itself, organization, and external environment to the technology adoption and implementation [43]. In this paper, we draw on the TOE framework extended by [44], which is believed to be more appropriate and deliberately designed for information and communication technology studies. Further, our analysis responds to [44]’s call to examine the external support and user-centric view in different contexts [44].

In TOE, the technological context highlights not only the significant characteristics of technology but also the “compatibility” and “interoperability” elements of the current system [45]. Three sub-factors are conceptualized in the technology context, including system configuration, technology hardware readiness, and technology compatibility. Firstly, system configuration refers to the technical architecture configuration and integration of both software and hardware [44]. Suning and PingAn have done well in this aspect, evidence can be found from the different awards they have received. For example, Suning has been selected for the 2020 FAT blockchain fintech leading 100 lists. PingAn FiMAX won the outstanding Fintech achievement and the best application of advanced technology from a bank administration institution. Secondly, technology readiness refers to the maturity and capability in technology deployment [46]. PingAn has tried to integrate blockchain technology into current business

practices and exercises; Suning has pioneered in transforming its businesses with blockchain. Though there might be slight differences, we believe such a difference can be attributed partially to the unique business nature. Thirdly, technology compatibility refers to how technology is perceived as consistent with the current organizational values and practices [47]. We argue that both companies did more than embracing blockchain technology alone; they tried to align it at a strategic level to explore any potential competitive advantages brought by blockchain.

Regarding to the organizational context, the organizational support to the new technologies, the readiness for the technology implementation, resource investments and supportive corporate culture can impact the success of technology implementation to a greater extent [43]. According to the TOE framework, the organizational support can be categorized into two factors: organization fit and user barrier. It is believed that Suning and PingAn’s success in blockchain applications is never possible if they have not invested enough time, resources and training for all relevant users, including employees, clients and business partners. Both companies proactively distributed and shared the information with different stakeholders and invited them to get involved in their platform and ecosystem development. For instance, Suning advanced blockchain development by integrating 5G technology with allies in the “5G smart Logistics Innovation Demonstration White Paper”, and PingAn developed the tax-industry alliance chain with other partners. On the other hand, we found that both companies spontaneously value users’ acceptance of product and service change. They released the news about their new businesses with blockchain and benefits their customers can acquire from these new businesses through different channels such as newspapers, daily news, social media, and even state media, which have significantly cultivated customers' confidence on the new business and technologies in China.

Finally, the environmental context considers the views of external stakeholders seriously, organization should engage in the prosperity of the ecosystem with high commitment [43]. External support is the overarching factor in the organizational context of technology implementation success. In addition to clients and business allies, government plays a critical role in Suning and PingAn’s success in blockchain implementation. Specifically, the Chinese central government clearly encourages blockchain industrial ecosystem establishment and blockchain industrial applications. It issued 217 policies, regulations, and program documents pertaining to blockchain technology, clarifying the legal boundary of blockchain application and implementation [48]. For instance, one of the initiators of PingAn’s tax-industry alliance chain is the Shenzhen government. In short, based on the TOE framework, we argue that Suning and PingAn share some common characteristics of success in blockchain applications. These commonalities are theoretically and practically generalizable to other fields. Table 3 summarizes these common factors.

Table 3: Common factors to blockchain application success based on TOE framework

<i>Technological context</i>	
System Configuration	Suning and PingAn both have well-developed technical architecture and

	integration systems on both software and hardware.
Technology Readiness	Suning and PingAn both demonstrated maturity and capability in technology deployment. Correspond to different business natures, Suning focused more on blockchain adoption whereas PingAn is more on development and implementation.
Technology Compatibility	Suning and PingAn not only integrated blockchain technology into their current business coherently, but also embedded it into their business strategies.
<i>Organization context</i>	
Organizational Fit	Suning and PingAn's invested much time and resources to train users to process and handle the change brought by blockchain in their business. Both organizations also proactively distributed and shared the information with different stakeholders, and invited them getting involved in their platform and ecosystem development.
User Barrier	Suning and PingAn maximized the benefits from different information channels to promote their blockchain technology and related new business for the sake of aggrandizing customers' acceptance.
<i>Environmental context</i>	
External Support	Suning and PingAn both benefited from blockchain-related national regulations and policies as well as the collaboration with state and/or provincial government.

7.2. Similarities and differences between two companies

First, though Suning and PingAn belong to two different industries, they share some common features. The similarities are summarized in Table 4.

Table 4: Similarities between the two companies

The scale of blockchain application	Large scale covers multiple fields
Application areas	Focus on finance, real estate, supply chain, smart home or smart city, data management, and customer information management
Blockchain features used	Secure, unanimous, distributed, immutable, time-stamped
Government support	Both are based in China and strongly supported by the Chinese government [48]
Patent	Both are obtained patents in blockchain technology
Blockchain provider	Provide blockchain service (BaaS) to other companies [13]

Cooperation with other companies	Both are collaborating with other companies to develop blockchain technology
Common benefits	<ul style="list-style-type: none"> • Enhance information reliability • Process a large quantity of data automatically • Increase information transparency • Improve security and accountability in transaction • Reduce financial risk • Reduce labor costs
Common challenges	<ul style="list-style-type: none"> • Solve the relations of production but not productivity itself • Optimize algorithmic capabilities to analyze data • Prevent crime due to the anonymity of the blockchain • Expand potential uses of blockchain • Interoperability between blockchains • System performance • Ecosystem development

Second, the differences between the two companies are presented in Table 5.

Table 5: Differences between the two companies

	Suning	PingAn
Application areas	Retailing and retailing-related service	Insurance business and blockchain technology development (blockchain service provider)
Blockchain in IoT	Real-time monitoring of pledged goods in the warehouse and uploading business process data to the blockchain	Collecting insured vehicle data and uploading it to a blockchain-based insurance network
Independently developed cryptographic blockchain structure	FiMAX S3C [13]	No independently developed cryptographic blockchain structure
Vision	Domestic e-commerce business development	International business development
Strategic management	Establish a strategic alliance	Improve product innovation

7.3. Summarized features of retail and insurance industries

The major features of blockchain technology applications in retail and insurance industries are summarized below (Table 6.)

Table 6: Summarized features of blockchain applications in retail and insurance industries

	Retail industry	Insurance industry
Application areas	<ul style="list-style-type: none"> • Build customer confidence in the brand • Supply chain management • Enhancing the market competitiveness 	<ul style="list-style-type: none"> • Fraud monitoring and risk prevention • Increasing customer trust • Customer retention • Claim processing • Smart contract
Major limitation of blockchain applications	<p>Scalability</p> <ul style="list-style-type: none"> • Difficult to store the growing amount of data • Decrease transaction processing speed [49] 	<p>Security</p> <ul style="list-style-type: none"> • Inaccurate data cannot be repaired • Private keys are easily lost [50]
Compound annual growth rate	84.6% [51]	84.9% [41]
Investment Return	<ul style="list-style-type: none"> • Strong revenue growth: including factors that support volume and price • Better operating margins: including factors that support the selling and administrative side as well as cost of goods sold [52] 	Reduction of administrative and operations cost: blockchain can deliver reinsurance industry-wide savings up to \$10 billion [53]
Influence on industry	<ul style="list-style-type: none"> • Reduce retail costs and waste of resources • Optimize customer-retailer relationships 	<ul style="list-style-type: none"> • Replace the role of insurance companies as intermediaries • Reduce insurance fraud losses

Outlook on next step	<ul style="list-style-type: none"> • Reduce the risk of data breaches • Focus blockchain development resources on use-cases with a clear path to commercialization • Push for standardization in technology, business processes and talent skill sets [52] 	<ul style="list-style-type: none"> • Shape a stimulating and regulatory environment • Identify the challenges around blockchain's open and decentralized nature [54]
-----------------------------	---	--

8. Conclusion

Blockchain technology has gone beyond the early hype of Bitcoin and evolved into an emerging technology commonly adopted by governments and industries with the general goal of improving productivity and reducing costs. China always keeps an open and positive attitude towards developing and using blockchain, especially in the retail, insurance, and finance sectors. Since the year of 2017, China has dominated global blockchain development market.

For the future, the data breach risks will be the main focus of the future blockchain technology development in retail. Regarding to the current cryptocurrency landscape, most retail industry employees expressed their confusion and distrust of blockchain technology. Therefore, developing a trustworthy and secured blockchain information systems will be a key priority to advance in the retail sector [55]. User or customer education is also necessary. Meanwhile, most company would like to embrace below two approaches: focusing blockchain development resources on use - cases with a clear path to commercialization and pushing for standardization in technology, business processes and talent skill sets [54].

For insurance industry, the way forward for blockchain technology will be to shape a stimulating and regulatory environment. While blockchain technology can provide technical proofs of ownership, consensuses and responsibilities, these proofs still lack legal support. For example, smart contracts can technically bind both parties to the contract, but the law does not explicitly acknowledge the contract's legitimacy. Therefore, the next step for blockchain in the insurance industry should be establishing and implementing specific rules and regulations [56]. Moreover, collaborating with consortia, technologists, startups, and regulators to identify challenges around the open and decentralized nature of blockchain is critical to the insurance industry. The areas include: the limitations of the technology, the development of the market, data protection, and the standardization of operational requirements [54].

This paper firstly introduced the origin and background of blockchain technology and briefly described the technical characteristics of blockchain. It then analyzed the implementation of blockchain in two companies from two industries - Suning in the retail industry and PingAn in the insurance industry. We summarized the success factors of blockchain implementation by

using TOE framework. For technological context, both companies are well developed in system configuration; both of them demonstrated maturity and capability in technology deployment; and both technology deployments are compatible with the companies' long time strategic development. In terms of organizational context, both companies' blockchain developments fit their organizational development and are welcomed by their clients. At last, the blockchain technology implementations are both strongly supported by government. We also compared the similarities and differences between the two companies in blockchain applications. Both companies are pioneers in their specific domain, though sharing slightly different missions or goals in blockchain implementation and development. Compared with US firms, China's leading companies still have some distances in terms of the kind of blockchain services provided and the maturity level. At last, the summarized features of blockchain applications in two industries were presented. The investment of return and future outlook were discussed. In sum, this study provided deep insights in understanding the development of blockchain technology in China, especially in the retail and insurance industries.

Conflict of Interest

The authors declare no conflict of interest.

References

- [1] Y. Cai, C. Qi, "Blockchain Technology Applications in Retail and Insurance Sectors: Cases from Suning and PingAn," in 2021 International Conference on Artificial Intelligence and Blockchain Technology (AIBT), IEEE: 80–84, 2021, doi:10.1109/AIBT53261.2021.00020.
- [2] M. Quiniou, "Blockchain: The Advent of Disintermediation.," Newark: John Wiley & Sons, Inc, 2019, doi: 10.1002/9781119629573.
- [3] K. Kulkarni, *Learn Bitcoin and Blockchain*, Packt Publishing Limited, 2018, available at: <https://www.packtpub.com/product/learn-bitcoin-and-blockchain/97811789536133>.
- [4] Z. Zheng, S. Xie, H. Dai, X. Chen, H. Wang, "An Overview of Blockchain Technology: Architecture, Consensus, and Future Trends," in 2017 IEEE International Congress on Big Data (BigData Congress), IEEE: 557–564, 2017, doi:10.1109/BigDataCongress.2017.85.
- [5] F. Casino, T.K. Dasaklis, C. Patsakis, "A systematic literature review of blockchain-based applications: Current status, classification and open issues," *Telematics and Informatics*, **36**, 55–81, 2019, doi:10.1016/j.tele.2018.11.006.
- [6] A. Hayes, *Blockchain Definition: What You Need to Know*, 2022, available at: <https://www.investing.com/academy/crypto/blockchain-definition/>.
- [7] A.K. Kar, L. Navin, "Diffusion of blockchain in insurance industry: An analysis through the review of academic and trade literature," *Telematics and Informatics*, **58**, 101532, 2021, doi: 10.1016/j.tele.2020.101532.
- [8] M. Belotti, N. Božić, G. Pujolle, S. Secci, "A vademecum on blockchain technologies: When, which, and how," *IEEE Communications Surveys & Tutorials*, **21**(4), 3796–3838, 2019, doi: 10.1109/COMST.2019.2928178.
- [9] J.J. Bambara, P.R. Allen, K. Iyer, R. Madsen, S. Lederer, M. Wuehler, *Blockchain: A practical guide to developing business, law, and technology solutions*, McGraw Hill Professional, 2018, available at: https://books.google.com.hk/books/about/Blockchain_A_Practical_Guide_to_Developi.html?id=tg7dswEACAAJ&redir_esc=y.
- [10] M. Nofer, P. Gomber, O. Hinz, D. Schiereck, "Blockchain," *Business & Information Systems Engineering*, **59**(3), 183–187, 2017, doi:10.1007/s12599-017-0467-3.
- [11] G. Strawn, "Blockchain," *IT Professional*, **21**(1), 91–92, 2019, doi:10.1109/MITP.2018.2879244.
- [12] Birost, "Suning releases blockchain white paper, Suning blockchain will be applied to multiple scenarios of smart retail ecology", 2022, available at: <https://blog.birost.com/a?ID=01000-5640385f-a6a0-4b08-9cb7-e9d60c5e5743>
- [13] A. Frosinini, *DLT solutions for trade and finance China focus*, 2020, available at: [file:///D:/Users/mslaurel/Downloads/DLT%20solutions%20for%20trade%20and%20finance%20-%20China%20focus%20-%20Final%20\(2\).pdf](file:///D:/Users/mslaurel/Downloads/DLT%20solutions%20for%20trade%20and%20finance%20-%20China%20focus%20-%20Final%20(2).pdf)
- [14] English.Wimc.Org.Cn, "Zhang Jindong: To Drive Intelligent Manufacturing with Intelligent", 2022, available at: https://english.wimc.org.cn/ennews_show.aspx?id=85.
- [15] Xinhua, "Suning releases blockchain white paper", 2018, available at: <https://en.imsilkroad.com/p/103916.html>
- [16] J. Sell, "How Omni-Channel Commerce Is Changing Traditional Supply Chains", *Inbound Logistics*, 2015, available at: <https://www.inboundlogistics.com/articles/how-omni-channel-commerce-is-changing-traditional-supply-chains/>.
- [17] G.R. Sheffield, "An examination of e-commerce and its influence on the traditional and e-commerce supply chain models", 2019, available at: <https://www.proquest.com/docview/2191207183?pq-origsite=gscholar&fromopenview=true>.
- [18] Y. Cai, C.M.I. Cheung, K.W. Chan, X. Ou, "Be more specific! An exploratory study of 5g and blockchain application on retailing industry with suning limited case," *J Huma Soci Scie*, **5** (1): 21, 32, 688–2690, 2022, available at: <https://opastpublishers.com/open-access/be-more-specific-an-exploratory-study-of-5g-and-blockchain-application-onmretailing-industry-with-suning-limited-case.pdf>.
- [19] VisionNav Robotics, "818 Suning Smart Logistics Enlarges The Move! 5G Automated Warehouse Opens to The Media For The First Time", 2020, available at: <https://www.visionnav.com/news/index-8.html#news>.
- [20] Cindy, "Suning Financial Blockchain Blacklist Sharing Platform has collected 11 million blacklist data - , BTC Trade", 2019, available at: <https://www.ibctrade.co/application/2667.html?lang=en>.
- [21] C.U. Inc, "Suning Unmanned "Biu" Store to make International Debut at CES 2018 to Showcase Smart Retail Worldwide", 2018, <https://en.pmasia.com/releases/global/suning-unmanned-biu-store-to-make-international-debut-at-ces-2018-to-showcase-smart-retail-worldwide-199089.shtml>.
- [22] V. He, "Suning was Praised for Its "Blockchain + Internet of Things" Financing Platform for Cars, 8BTC.COM", 2019, available at: <https://news.8btc.com/suning-was-praised-for-its-blockchain-internet-of-things-financing-platform-for-cars>.
- [23] Suning Holding Group, "Suning Holdings Group Ranks Second on China's Top 500 Non-state Owned Enterprises List in 2020, Cision PR Newswire", 2020, available at: <https://www.prnewswire.com/news-releases/suning-holdings-group-ranks-second-on-chinas-top-500-non-state-owned-enterprises-list-in-2020-301129798.html>.
- [24] Amazon Web Services, "AWS's blockchain", 2022, <https://docs.aws.amazon.com/whitepapers/latest/aws-overview/blockchain.html>.
- [25] H. Anwar, "Blockchain in Retail: Use Cases and Potential Applications, 101 Blockchains", 2020, available at: https://101blockchains.com/blockchain-in-retail/?gclid=Cj0KCQjwteOaBhDuARIsADBqRq36L-4X5UJsJk1fX-HKaWCwV14QwJLTrvWwkBbazf7NLw7XOAJEaAuRZEALw_wcB.
- [26] Blocking, "Ali, Jingdong, Suning, "chain" battle double eleven Blockchain Network", 2020, available at: <https://blocking.net/21987/ali-jingdong-suning-chain-battle-double-eleven/>.
- [27] F. Lu, "Ep. 144 – A new approach to blockchain – Ping An's Insights , Insureblocks", 2021, available at: <https://podcasts.apple.com/in/podcast/ep-144-a-new-approach-to-blockchain-ping-ans-insights/id1361820676?i=100050557258>.
- [28] J. Kelly, "Ping An becomes first Chinese member of R3 blockchain consortium", *Reuters*, 2016, available at: <https://group.pingan.com/media/news/News-2016/Ping-An-becomes-first-Chinese-member-of-R-blockchain-consortium.html>.
- [29] Bloomberg News, "China's Ping An Insurance to Spend \$22B on Tech, From AI to Blockchain", *Insurance Journal*, 2019, available at: <https://www.insurancejournal.com/news/international/2019/10/24/546474.htm#:~:text=Insurance%20Giving%20Back-,China's%20Ping%20An%20Insurance%20to%20Spend%20%2422,Tech%2C%20From%20AI%20to%20Blockchain&text=Ping%20An%20Insurance%20wants%20to,intelligence%20to%20blockchain%20will%20work..>
- [30] J. Tropea, "Insurance Disruption: How Blockchain Is Transforming the Industry | Bankrate", *Bankrate*, 2021, available at: <https://www.bankrate.com/insurance/car/blockchain-disruption/>.
- [31] H. Partz, "Chinese holding firm Ping An overtakes Tencent in blockchain patents race", *Cointelegraph*, 2021, available at: <https://cointelegraph.com/news/chinese-holding-firm-ping-an-overtakes-tencent-in-blockchain-patents-race>.
- [32] Ping An Group, "Ping An business case series: How integrated finance ecosystems are empowering millions in China", *Financial Times*, 2021,

- available at: <https://www.ft.com/partnercontent/ping-an-insurance/how-integrated-finance-ecosystems-are-empowering-millions-in-china.html>.
- [33] S. Writer, "UBX taps OneConnect for blockchain-enabled platform for MSMEs", *Frontier Enterprise*, 2019, available at: <https://www.frontier-enterprise.com/ubx-taps-oneconnect-for-blockchain-enabled-platform-for-msmes/>.
- [34] Ledger Insights, "China's Ping An rolls out OneConnect blockchain smart legal contracts", *Ledger Insights*, 2019, available at: <https://www.ledgerinsights.com/china-ping-an-oneconnect-blockchain-smart-legal-contracts/>.
- [35] S. He, "Ping An to add \$7.7bn in real assets despite China property headwind | Asset Owners", *AsianInvestor*, 2021, available at: <https://www.asianinvestor.net/article/ping-an-to-add-7-7bn-in-real-assets-despite-china-property-headwind/472156>.
- [36] D. Turpitka, "Blockchain In The Automotive Sector: Three Use Cases And Three Challenges", *Forbes*, 2021, available at: <https://www.forbes.com/sites/forbestechcouncil/2021/12/22/blockchain-in-the-automotive-sector-three-use-cases-and-three-challenges/?sh=3df5c9a82508>.
- [37] Ping An Insurance Group, "Ping An Unveils Health Care Ecosystem Strategy - A Growth Engine for the Group Empowered by World-leading Healthtech", 2020, available at: <https://www.prnewswire.com/news-releases/ping-an-unveils-health-care-ecosystem-strategy-301136665.html>.
- [38] M. Yakubowski, "China: Insurance Giant Ping An, Sanya City Gov't to Build 'Smart City' with Blockchain", *COINTELEGRAPH*, 2018, available at: <https://cointelegraph.com/news/china-insurance-giant-ping-an-sanya-city-govt-to-build-smart-city-with-blockchain>.
- [39] OneConnect Financial Technology Co., Ltd. "Annual Report 2021", Hong Kong, 2022, available at: https://www.annualreports.com/HostedData/AnnualReports/PDF/NYSE_OCFT_2021.pdf.
- [40] United Health Group, "Improving provider data accuracy: a collaborative approach using a permission blockchain", 2018, available at: <https://blockchainhealthcaretoday.com/index.php/journal/article/view/62>.
- [41] MarketsandMarkets, "Blockchain in Insurance Market Size, Share and Global Market Forecast to 2023", 2018, available at: <https://www.marketsandmarkets.com/Market-Reports/blockchain-in-insurance-market-9714723.html>.
- [42] L.G. Tornatzky, M. Fleischer, A.K. Chakrabarti, *The processes of technological innovation*, Lexington books, 1990, doi: <https://doi.org/10.1007/BF02371446>
- [43] R. Depietro, E. Wiarda, M. Fleischer, "The context for change: Organization, technology and environment," in the *Processes of Technological Innovation*, 199(0), 151–175, 1990, doi: <https://doi.org/10.1007/BF02371446>.
- [44] T. Masood, J. Egger, "Augmented reality in support of Industry 4.0—Implementation challenges and success factors," *Robotics and Computer-Integrated Manufacturing*, **58**, 181–195, 2019, doi: [10.1016/j.rcim.2019.02.003](https://doi.org/10.1016/j.rcim.2019.02.003).
- [45] M. Gattullo, G.W. Scurati, M. Fiorentino, A.E. Uva, F. Ferrise, M. Bordegoni, "Towards augmented reality manuals for industry 4.0: A methodology," *Robotics and Computer-Integrated Manufacturing*, **56**, 276–286, 2019, doi: [10.1016/j.rcim.2018.10.001](https://doi.org/10.1016/j.rcim.2018.10.001).
- [46] K. Zhu, K.L. Kraemer, S. Xu, "The process of innovation assimilation by firms in different countries: a technology diffusion perspective on e-business," *Management Science*, **52**(10), 1557–1576, 2006, doi: [10.1287/mnsc.1050.0487](https://doi.org/10.1287/mnsc.1050.0487).
- [47] Y.-M. Wang, Y.-S. Wang, Y.-F. Yang, "Understanding the determinants of RFID adoption in the manufacturing industry," *Technological Forecasting and Social Change*, **77**(5), 803–815, 2010, doi: [10.1016/j.techfore.2010.03.006](https://doi.org/10.1016/j.techfore.2010.03.006).
- [48] L. Cai, Y. Sun, Z. Zheng, J. Xiao, W. Qiu, "Blockchain in China," *Communications of the ACM*, **64**(11), 88–93, 2021, doi: [10.1145/3481627](https://doi.org/10.1145/3481627).
- [49] U. Klarman, S. Basu, A. Kuzmanovic, E.G. Sirer, "bloxroute: A scalable trustless blockchain distribution network whitepaper." 2018, available at: <https://bloxroute.com/wp-content/uploads/2018/03/bloXroute-whitepaper.pdf>.
- [50] J. Chen, W., Xu, Z., Shi, S., Zhao, Y., & Zhao, "A survey of blockchain applications in different domains," in 2018 International Conference on Blockchain Technology and Application, 17–21, 2018, doi: [10.1145/3301403.3301407](https://doi.org/10.1145/3301403.3301407).
- [51] B. Jagtap, R. Rake, S. Baul, "Blockchain in Retail Market Statistics - 2026," *Applied Market Research*, 2019, available at: <https://www.alliedmarketresearch.com/blockchain-in-retail-market>.
- [52] Deloitte, "New tech on the block: Planning for blockchain in the retail and Consumer Packaged Goods industries", 2018, available at: <https://www2.deloitte.com/content/dam/Deloitte/uk/Documents/Consumer/IndustrialProducts/deloitte-uk-blockchain-in-retail-and-cpg.pdf>.
- [53] PwC, Blockchain, "Blockchain, A catalyst for new approaches in insurance", 2018, available at: <https://www.pwc.com/gx/en/industries/financial-services/publications/blockchain-a-catalyst.html>.
- [54] McKinsey&Company, "Blockchain in insurance opportunity or threat", 2016, available at: <https://www.mckinsey.com/~media/mckinsey/industries/financial%20services/our%20insights/blockchain%20in%20insurance%20opportunity%20or%20threat/blockchain-in-insurance-opportunity-or-threat.ashx>.
- [55] M.T. Nuseir, "Potential impacts of blockchain technology on business practices of bricks and mortar (B&M) grocery stores," *Business Process Management Journal*, 2020, doi: [10.1108/BPMJ-06-2020-0267](https://doi.org/10.1108/BPMJ-06-2020-0267).
- [56] J. Al-Jaroodi, N. Mohamed, "Blockchain in industries: A survey," *IEEE Access*, **7**, 36500–36515, 2019, doi: [10.1109/ACCESS.2019.2903554](https://doi.org/10.1109/ACCESS.2019.2903554).

Association Rules for Knowledge Discovery From E-News Articles: A Review of Apriori and FP-Growth Algorithms

Thilini Lakshika*, Amitha Caldera

Department of Information Systems Engineering, University of Colombo School of Computing, Colombo, 00700, Sri Lanka

ARTICLE INFO

Article history:

Received: 15 July, 2022

Accepted: 12 October, 2022

Online: 31 October, 2022

Keywords:

Association Rule Mining

Apriori algorithm

FP-Growth algorithm

Frequent Pattern Mining

Knowledge Discovery

ABSTRACT

Owing to technological development, the internet has become the world's largest platform where an unaccountable amount of e-news information is freely available to use. Most of the time, e-newspaper readers have to examine the massive collection of e-news articles to locate necessary information relevant to them. Massive semi-structured and unstructured texts usually mislead the readers when they search and understand data for some knowledge. Furthermore, manually reading a collection of e-news articles for some knowledge is tedious and unproductive. The literature related to Knowledge Discovery from text documents has had a substantial improvement in this regard and Association Rule Extraction using text documents, in particular, has become a more frequent and imperative research approach to finding out the most significant information, patterns, and features in the text documents while diminishing the time for reading all the documents. This study provides a comprehensive review of Association Rule extraction using textual data covering the essential topics; Pre-processing, steps in Association Rule Mining, and rule mining algorithms. Out of the various existing association rule mining algorithms, the two most important algorithms, Apriori and FP Growth, are chosen for the experiment using e-news articles. Based on the experimental results, this study discusses the performance, significant bottlenecks, recent breakthroughs of rule mining algorithms, and finally the perspective directions to facilitate future research.

1. Introduction

Due to the rapid growth of web technologies and data repositories, 80% of the world's data is now available in electronic format [1,2]. The internet is the most common platform where an enormous amount of semi-structured and unstructured texts is freely available in reports, news articles, web pages, log files, data transaction files, and other types of electronic documents to satisfy human information desires. The escalating nature of the internet lets many documents first appear online before printing, which is a major reason for the availability of a valuable source of knowledge. Hence, information in the printed medium is slowly losing its gleam. In contrast, the information in the electronic medium continues to grow with the easy availability of quick and obsolete data to the world with only a few snaps.

Due to the overloaded information on news websites, it is tough and tedious for e-news readers to remember all important

information to get some knowledge to satisfy their information desires [1–4]. Even searching the internet for exact details is time-consuming. The resultant information may confuse users to deal with it due to both relevant and irrelevant information. Extracting knowledge from e-news articles in semi-structured and unstructured formats becomes more arduous, but it is worthwhile to explore those because of the necessity of obtaining knowledge. But, manual analysis of bulky information available in e-news articles for effective extraction of useful information is not conceivable [3]. Similarly, manual knowledge discovery has a very little guarantee of generating enough details to support decision-making compared to automated knowledge discovery [3]. This issue leads e-news article readers to make decisions based on applications in knowledge discovery.

An automatic text analysis tool based on techniques such as Knowledge Discovery, called Text Mining or Text Data Mining from textual data sources, is the most demanding solution to address this problem [1, 2]. The higher availability of massive amounts of electronic documents has been a great motivation for

*Corresponding Author: Thilini Lakshika, Department of Information Systems Engineering, University of Colombo School of Computing, Colombo, 00700, Sri Lanka, +94713179029, tlv@ucsc.cmb.ac.lk

automatically introducing new knowledge acquisition approaches. Hence, the automatic extraction of knowledge from a large number of e-news articles available on the web using Text Mining (TM) concepts has become an increasingly important research topic [1-3].

Data Mining (DM) is the process of extracting, exploring, and analysing large blocks of information to gather meaningful patterns and trends that can consider knowledge in the data sources. Applying DM techniques to extract interesting and useful knowledge is challenging because of the information overloading, higher duplication rates, and ambiguities of data [5]. DM in the text is known as Text Mining (TM) and is generally used to extract meaningful patterns in a collection of text data using Natural Language Processing (NLP) techniques such as Information Extraction (IE) to transform unstructured data into a structured format [6, 7]. One of the main operations in TM is frequent itemset mining for identifying frequent patterns, hidden patterns, themes, and the context in large datasets that are very easy to understand and interpret by data analysts and normal users [1-5]. Frequent itemset mining plays an essential role in many data mining tasks. Algorithms such as Apriori and FP-Growth are the more frequently used Association Rule Mining (ARM) algorithms for mining sequential and emerging patterns.

Researchers typically use data mining techniques such as classification, clustering, regression analysis, and ARM to discover knowledge from massive data sets by applying novel experimental approaches. TM is a precious and beneficial process for organizations with large textual datasets as it supports expanding the decision-making process of organizations, leading to better business outcomes. However, the richness and vagueness of natural language is the most complex challenge in applying TM techniques [2].

So, the research questions (RQs) that we aim to cover with the study are:

- RQ1: What tasks are currently being solved with association rules using textual data?
- RQ2: What areas of applications currently have been addressed with association rules using textual data?
- RQ3: Which pre-processing steps need to be applied for ARM using textual data?
- RQ4: Which ARM algorithm: Apriori or FP Growth has fast execution in association rule generation using e-news articles?
- RQ5: What are the current trends and future problems to be faced by Apriori and FP Growth algorithms in textual data?

The main contributions of this study are,

- Discuss the diverse areas of ARM along with its applications and motivate research on TM.
- A detailed discussion of the main phases in ARM including the most important text pre-processing steps.
- An experiment conducted using the major rule generation algorithms including Apriori and FP-Growth, their usage,

performance, and limitations in TM using a collection of e-news articles.

- Discuss the Apriori and FP-Growth algorithm perspective directions to facilitate future research in TM.

The organization of this paper is as follows. Overview in section 2 explores the fundamental ideas related to ARM. Further elaborations on the role of Association Rules, including Apriori and FP-Growth algorithms in Text applications, are presented in section 3. The significant phases in ARM are discussed in section 4. Our experimental application of Apriori and FP Growth algorithms for association rule generation using e-news articles is described in section 5. Section 6 includes the results and discussion, and the directions for future research are presented in section 7. Finally, section 8 concludes the research work.

2. Overview

2.1. Introduction to Data Mining

The automatic knowledge discovery from text documents using TM concepts has become an emerging research topic [1-3]. Extracting, exploring, and analyzing information to discover meaningful patterns and trends in data is the main focus of DM approaches. Even though the DM supports different techniques such as ARM, frequent itemset mining, and pattern mining, applying those techniques for the extraction of interesting and useful knowledge is challenging because of the information overloading, higher duplication rates, and ambiguities of data [5]. The most common issues in DM are handling many patterns, finding relationships between keywords, and generating knowledge using keyword relationships. Typically, DM techniques discover a rich set of patterns that can consider knowledge in the data sources. However, effective analysis of such discovered patterns for making decisions becomes more complicated due to the meaningless patterns and noises present in the discovered patterns. Even though data mining techniques directly deal with structured data, they may be adapted to mine unstructured text data that presents unique characteristics [2].

2.2. Introduction to Text Mining

Text Mining or Document Mining is an emerging field of research due to the need to retrieve important non-trivial information or knowledge and features by transforming a collection of unstructured text data into a structured format [3, 5, 6]. Data Mining using textual data, also known as Text Mining and is generally used to identify meaningful patterns in a collection of text data using Natural Language Processing (NLP) techniques such as Information Extraction (IE) to transform unstructured data into a structured format [6,7]. TM is generally used to extract semantic logic in the textual data while DM is used to discover novel insights and hidden patterns in text data. Even though many DM tools and applications are designed to work on structured data from databases, many TM tools and applications are designed to work with both unstructured and semi-structured databases such as full-text documents, emails, and HTML files. The lack of explicit structure in the unstructured text data

increases the difficulties of discovering the documents' implicit knowledge. Natural language may express the same concept in multiple ways, making it harder to extract and represent the conceptual concepts in the natural text [1].

Hence, text data mining approaches are still attracting more attention in designing novel TM models to retrieve the users' expected data [6]. Association rule discovery is one of the main techniques in TM, and existing rule discovery approaches are categorized as sequential patterns, maximal patterns, and closed patterns [5]. The various applications such as information extraction, summarization, document classification, and document clustering are the more commonly used applications in the research field of text data analysis.

2.3. Basic Text Pre-processing steps

Generally, e-news articles comprise information in an unstructured format that cannot be straightly used for further processing and cause inaccurate results in text mining [3]. Thus, mining extensive e-news article collections in unstructured text format to extract valuable patterns requires applying essential pre-processing steps and converting the information into a more appropriate data format than keeping the information in a plain text file [3]. The required pre-processing steps for the text data are more important before- applying any DM techniques. Text pre-processing steps typically compromise transformation, tokenization, filtration of keywords, and stemming and indexing of the keywords [2,3].

Transformation: Information on the web presents in different document formats and structures, which requires converting them into Extensible Markup Language (XML) format that is amenable to further processing [1,2].

Tokenization: The unstructured text formats in e-news articles cause inaccurate results in text mining [3] and are required to convert them into structured formats and proceed with only valid tokens by removing inappropriate information such as special characters, parentheses, commas, etc. Tokenization plays a significant role in increasing accuracy in knowledge discovery.

Filtration: Finding out the relationship between all the keywords in the e-news articles is required to generate accurate knowledge from a collection of e-news articles. When the document is not filtered well, filtration becomes complex. The filtration of stop words and suffixes is essential to find the relationship between the keywords. Manual filtration of e-news articles will take much time, and users may miss track of what they are searching for.

Stemming: Stemming reduces the ambiguous association rule generation due to suffixes in the natural text and further reduces the complexity and extra memory consumption while refining the effectiveness and performance of knowledge discovery systems [3]. Many works of literature [3] use a well-known rule-based stemming algorithm; Porter stemmer since it meets both the satisfaction and effectiveness in attaining more relevant information in the text.

Indexing: It is required to index the text to use the unordered words in the text documents [1,2]. Manually or automatically generated indexes using textual data can be considered the foundation for the knowledge discovery process [2]. However, it is not easy to apply manual indexing to large-scale textual data in e-news articles due to its limitations such as heavy time consumption [2]. To address these issues, automated indexing procedures have been examined as a technique that allows association extraction techniques on large-scale textual data [2,3]. Many pieces of research follow the most widely used frequency-based automated indexing weighting scheme which is known as TF-IDF (Term Frequency - Inverse Document Frequency) to calculate and assign higher weights to differentiate terms in a source document [2,3]. Extracting association rules using text documents are based on keyword features in the text, and correlations between those keyword features are based on the weights calculated using the TF-IDF method [1-8].

3. Role of Association Rules in Text Applications

The continued growth in large databases emphasizes the necessity of improving mining performance and precision. Hence, many studies develop novel mining algorithms, theories, and improvements to existing methods. ARM is an exciting DM research domain and raises the interest of many researchers to develop highly efficient algorithms to mine association rules from text documents. ARM concepts span across many domains as per the nature of the problem and demand.

The medical field is a universal domain that requires excessive effort in terms of knowledge management. Most medical applications are daily producing a bulk of medical data in free text formats, which is a very time-consuming task for medical professionals to read and interpret. Hence, applications of TM are widely used in the biomedical field to automatically extract medical findings in these free-text reports based on functional keywords [6]. In [6], the author integrated the Apriori algorithm to find interesting medical data patterns and easily understand the results.

The application of ARM for Knowledge discovery in the newspaper domain is very useful since newspaper readers can easily discover knowledge from a collection of documents without reading all the documents manually [3]. For example, in recent studies [1,2], the authors describe their experimental results of applying Extracting Association Rules from Text (EART) using a set of medical documents related to the epidemic of H5N1 avian influenza virus taken from the MEDLINE bibliographic database. EART uses XML technology with TF-IDF Information Retrieval (IR) scheme for feature selection and the DM techniques for association rules extraction using web documents. As a solution to the time-consuming manual itemsets generation, EART identifies the most essential word features such as the name of the disease, reported outbreak location, current status, and type of the victim, etc. for use in association rules extraction. EART consists of four phases; (1) structural phase (2) indexing phase (3) TM phase and (4) visualization phase.

The main focus of the EART system [1,2] is on the keywords that appear in the extracted association rules and their statistical

distributions without considering the order in which the words occur in a sentence. The ERAT system uses extracted association rules to identify the relations between features in the text document collection. The EART system analyses the keywords in the extracted association rules from two perspectives. (1) The co-occurrence of a keyword in one sentence in the original text document. (2) The existence of a keyword in one sentence without co-occurrence. The EART system outperforms other systems that extract and evaluate the association rules using the Apriori algorithm [1,2]. Experimentation results in [1,2] accepting the challenge of extracting association rules from multidimensional information presented in web news documents.

Another study in [3] discovers association rules and thereby enables the user to generate knowledge from a collection of web news articles related to diseases such as Cholera and Dengue. However, the process of association rule extraction has an expanding growth and a massive number of rules can be extracted from the database [2]. To enhance the efficiency in discovering knowledge from the large number of association rules based on user queries, this study includes an association rule training system that contains pre-defined details about each disease such as impacts of those diseases, reasons for spreading diseases, locations, and victims. This system supports reliable decisions makings due to the knowledge discovered by identifying significant association rules depending on the keywords in the query supplied.

Due to the comprehensive, up-to-date, and valuable information, which contains many broad and collective types of concepts or features, many pieces of literature [1–3] use web news documents as their experimental datasets. Furthermore, web news can more easily be adapted to TM as it does not require the involvement of a subject matter expert to understand and interpret the text features and concepts present in news documents.

In [7], the author deviated from traditional ARM techniques and presented a fuzzy framework for identifying association rules in a text document. This fuzzy framework consists of a fuzzy extended Boolean model, and generated fuzzy association rules are applied to query refinement in Information Retrieval. The generated fuzzy association rules let users query the text document and refine it by showing them a list of candidate terms. Furthermore, this study presented different procedures to apply fuzzy association rules automatically and semi-automatically.

A recent study in [5] accepts the challenge of handling duplications and ambiguities in text data by explaining the relationship between rough set-based decision rules and association rules. The rough association rule-based approach in their study improves ARM effectiveness. The specific information included in rough association rules distinguishes them from standard association rules. The rough association rule comprises a set of terms and their frequency distributions. It is also feasible to dynamically update these rough association rules to increase the effectiveness of the results [5].

The demand for text classification is increasing with the increasing number of online texts. In [9], the author presents a novel fast algorithm for classifying textual data using the concept of ARM. This algorithm is capable of deriving feature sets from pre-classified text documents. Later, the Naïve Bayes classifier

applies to the derived features to get the final output of the classification. The algorithm's accuracy in classifying a new document directly depends on the associated word sets generated from pre-classified text documents and performs better with the nonoverlapping text categories.

Detecting and displaying topics from a group of documents is another ARM application. For example, in [4], the author presented a novel approach that uses the visualization of generated association rules to identify the topics from a collection of documents. This approach [4] extends the Apriori algorithm-based approach described in [10]. The experimental results in [4] have shown a reliable match between extracted topics to those present in the data set.

3.1. Role of Apriori Algorithm in Text Applications

The preliminary concept of the Apriori algorithm was the supermarket shopping cart transactions with a set of frequently purchased items [11]. Apriori is one of the well-recognized ARM algorithms that find the frequent items in transactional data sources [1–12]. Association rule mining or discovery using the traditional Apriori algorithm is the most common approach in retrieving hidden rules in the data sources [1–12] but has to pay with immense resources and time.

In [10], the author implements two extending algorithms to discover association rules that are primarily different from the traditional Apriori algorithm. The evaluation results in [10] show that these algorithms perform better for problems with small itemsets than large ones compared to the Apriori algorithm. Furthermore, their study elaborates on another algorithm; Apriori-hybrid [10] by combining the best features in the initially proposed two algorithms to increase the performance in ARM-based applications. Experiments on the Apriori-hybrid algorithm show that it has a linear relationship with the number of items in an association rule and the number of transactions in the database.

Another study in [11] implements Apriori MSG-P, a modified association rule mining technique to demonstrate rare association rules in an operational databank taken from a hospital. During the evaluation process, they examine different characteristics in support values by applying multiple minimum support value approaches for discovering rare itemsets. Experimental results prove that these rare itemsets are more effective than the traditional Apriori algorithms in identifying widespread knowledge and patient behaviors in their databank.

In [2,3], the authors used GARW (Generating Association Rule based on Weighting Scheme) algorithm to overcome the multiple passes over the chosen data, which is another major problem in the Apriori algorithm. The GARW algorithm scans only an XML file containing all the keywords above the given threshold values and their frequencies in each document to generate large frequent keywords. The execution time of the GARW algorithm is less than the Apriori algorithm [1,2].

In recent research, the algorithms for ARM implement numerous optimization techniques to minimize space utilization

and save time in computing frequent itemsets and their support values. The novel scalable algorithm presented in [8] proposes a solution for the existing problems in frequent itemset mining by partitioning the search space. This [8] algorithm discovers closed frequent itemsets which are the lossless and concise presentation of all the frequent itemsets that can be mined from a transactional database. The adaptation of the bitwise vertical representation of the database and the divide-and-conquer approach makes this a fast and memory-efficient scalable algorithm. Moreover, this algorithm addresses the main problems in generating the same closed itemset multiple times using an effective and memory-efficient pruning technique. Mainly, this algorithm does not require keeping the extracted closed patterns in the main memory and enables each visited partition of the search space to be mined independently in any sequence or parallelly.

3.2. Role of FP-Growth Algorithm in Text Applications

Frequent Pattern Growth (FP-Growth) is a frequently used alternative algorithm for generating Frequent Item Sets in a data set. This algorithm enhances the Apriori algorithm that overcomes many of the major problems associated with the Apriori algorithm [13]. Theoretical research in [14] has proven that the FP-growth algorithm resolves two significant complications of the traditional Apriori algorithm. The experimental results in [14] demonstrate that the FP-growth algorithm has higher frequent pattern mining efficiency, less memory usage, and less CPU utilization than the Apriori algorithm. The FP-Growth algorithm accompanies the divide-and-conquer strategy and does not generate candidates because it uses FP-Tree. This dense tree data structure can compress the original transaction database to extract Frequent itemsets [14]. Frequent pattern mining using the FP-Growth algorithm works very well in many broad applications [13-29], including software bug detection, clustering, classification, and recommender systems, and supports selecting the best patterns while reducing time and cost.

The FP-Growth algorithm is mainly used for mining complicated patterns from graph databases [15]. This algorithm is designed for itemset mining, not for graph mining and it does not mine frequent subgraphs well [15]. Hence, finding the frequent subgraphs that support is greater than the given minimum support using a collection of graphs is one of the main problems of frequent subgraph mining [15]. Thus, it is required to make necessary variations in the algorithm so it can be efficiently used for graph mining.

Many of the existing document mining methods for document clustering are based on the frequency of keywords presented in the document [15]. Such methods identify a document as a vector and keywords with their frequency as its elements. However, a document has no way to possess relationships among the keywords. Hence, these methods are not adequate in representing the document's ideas. Clustering documents using the FP-Growth algorithm for association rule mining is a novel approach that overcomes the issues in existing approaches [15]. In [15], the author used the FP-Growth algorithm

to mine text documents, find association rules, check the similarity between generated association rules using clustering, and use those results to determine frequent subgraphs. This study modified the FP-Growth algorithm to find the frequent subgraph with clustering affinity propagation in a graph. The ability to evaluate the large-scale graph paths improves the performance of this modified algorithm.

The performance of frequent pattern mining algorithms is affected by many factors, including the databases' characteristics. The FEM (FP-growth & Eclat Mining) algorithm proposed in [26] takes advantage of both FP-tree and TID-list (transaction ID list) data structures to efficiently mine short and long frequent patterns from datasets. The experimental results of the FEM algorithm show a significant improvement in the performance of mining frequent patterns compared to the FP-Growth algorithm. Another experiment presented in [25] concluded that the Dynamic FP-tree construction/reordering algorithm (DynFP-growth algorithm) presented by them behaves better than the FP-growth algorithm.

This algorithm modified the original structure of the FP-Growth algorithm by replacing the single linked list which was used to link the tree nodes to the header with a doubly-linked list and further adding a master table to the same header. Even though the existing database is getting updated, the generated FP-tree in the DynFP-growth algorithm doesn't rebuild the tree. Instead, the algorithm has to be performed considering both new transactions in the database and the initially generated FP tree. Hence, this approach can provide speedy responses to any queries even on the databases that are being repeatedly updated.

The N Painting-Growth and Painting-Growth algorithms developed in [28] are two different improved versions of the FP-Growth algorithm which use two-item permutation sets to extract association rules. The N Painting-Growth algorithm builds two-item permutation sets while the Painting-Growth algorithm builds an association picture based on the two-item permutation sets to find out association sets of all frequent items and then extract all the frequent itemsets according to the association sets. These algorithms reduce the overhead of scanning the database twice in traditional FP-Growth algorithms up to once while increasing the time efficiency. Furthermore, using two-item permutation sets gives several advantages such as lesser memory consumption, running faster, low complexity, and being easy to maintain.

4. Association Rule Mining (ARM)

Association Rule Mining (ARM) is an imperative research area to discover frequent patterns by highlighting correlations between word features in the texts [13-18]. In general, ARM is a process with three major phases; (1) the Text Pre-processing phase, (2) the Association Rule Mining phase, and finally (3) the Visualization phase.

4.1. Text Pre-processing phase

The massive amount of information available in unstructured text format cannot be directly used for further processing. Mining

large document collections to extract useful patterns requires applying essential pre-processing steps to the source documents and storing the information in source documents in a more appropriate data structure for further processing than a plain text file [3]. Text pre-processing steps typically compromise tokenization, filtration of keywords, and stemming and indexing of the keywords [3] to improve the performance in the ARM phase.

4.1.1. Text Transformation

Information on the web presents in different document formats and structures which requires converting them into a machine-processable format that can be easily processed by computers [1,2]. The Extensible Markup Language (XML) is a metalanguage that is used to display documents on the internet based on a user-defined markup language that is amenable to further processing. Supporting techniques in XML help automate the indexing of documents and thus make machines processable [1]. The ERAT system [2] initially saved the Web news pages as text documents and later transformed them into XML format for further processing.

4.1.2. Tokenization

Generally, unstructured data in web pages cause inaccurate results in TM [3]. Thus, it is required to convert unstructured data formats into structured formats by splitting the text in documents into words or terms and selecting only valid tokens by removing inappropriate information such as parentheses, commas, special characters, etc., using tokenization. Tokenization is crucial in removing irrelevant tokens, as it can reduce unnecessary memory and time consumption in the knowledge discovery process. MySQL data structures [3] and matrixes developed using MATLAB software [6] can be used to store tokenization operation results, making it easier to perform further operations such as filtration and stemming, etc.

4.1.3. Filtration

Finding out the relationship between all the keywords present in the text is required for generating accurate knowledge from the collection of text documents. But finding relationships becomes complex if the document is not filtered well. Due to the morphological richness of language, text documents contain many suffixes and stop words [3] which occur frequently likewise "a ", "the", "so" and so on. The careful disregard of stop words without losing the sentence's meaning is required as they do not add much meaning to a sentence and the suffixes may attach to the same word but with different forms. Without filtering such suffixes and stop words in the input documents, finding relationships in text documents and generating accurate knowledge using keywords may become an inefficient and complex process [3]. Unimportant words such as articles, determiners, pronouns, prepositions, common adverbs, non-informative verbs, and conjunctions get discarded. Only the more

significant words from the document content are used for further processing [2,3].

Manual filtration will take much time and may miss the track quickly. EART [2] used a list of stop words that are frequently used in English document scripts. Moreover, the EART [2] system replaces parentheses, commas, and special characters with whitespaces.

4.1.4. Stemming

Stemming is reducing the variant forms of the same word to its word stem or root which is known as a lemma. This process happens by removing a word's prefixes and suffixes [2]. Suffixes are single or sets of letters added at the end of a word to generate different forms of the initial word while prefixes are single or sets of letters added at the beginning of a word to generate different forms of the same word. Applying the process of stemming is vital in applications with Natural Language Understanding (NLU), Natural Language Processing (NLP), and Information Retrieval (IR). Applying stemming operation before retrieving information from the documents is much important as it reduces the size of the dataset and the ambiguous association rules generated due to the presence of suffixes and prefixes, and further reduces the complexity and extra memory consumption while refining the effectiveness and performance of knowledge discovery systems [3].

Several types of stemming algorithms attempt to convert a word into its stem or root form. Still, they differ concerning performance and accuracy. Many works of literature [3] use a well-known rule-based stemming algorithm; Porter stemmer since it meets both the satisfaction and effectiveness in attaining more relevant information in the text. One of the common problems in porter's stemmer is that it does not give precise root words at all times. But still, the Porter algorithm was found to be the best algorithm to perform stemming among diverse stemming algorithms such as Paise and Krovitz [3] that are described in the literature [3]. The studies in [1,2] designed a novel stemming dictionary (lexicon) which is suitable for use in the medical domain.

4.1.5. Indexing

Indexing using a weighting scheme comes after the filtration and stems in the text documents. Manually or automatically generated indexes using textual data can be considered the foundation for the knowledge discovery process [2]. However, it is not easy to apply manual indexing to large-scale textual data due to its limitations such as heavy time consumption [2]. Hence, automated indexing procedures have to be considered in applications that use ARM techniques on a large scale [2,3]. In automated indexing techniques, each text document is represented by a set of keywords known as index terms where each index term is a single word or a phrase whose semantics support representing the central theme in the document [2]. Thus, each index term has varying relevance in representing and expressing the document's

theme in a document collection. A numerical weight is assigned to each index to capture its effectiveness.

Definition and Notations in TF-IDF

Many pieces of research [2,3] on extracting association rules follow the most widely used frequency-based weighting scheme; TF-IDF (Term Frequency - Inverse Document Frequency) to identify and filter the terms assigning higher weights to differentiate terms in a source document.

The Term Frequency (TF) is the count that denotes the frequency of a term (keyword) in a collection of documents. TF can be calculated using (1),

$$(tf)_{i,j} = \sum_{i=j=1}^n (Nt_i, d_j) \quad (1)$$

Where Nt_i, d_j represents the number of times the term t_j occurs in a document d_j .

Inverse Document Frequency (IDF) is the count that denotes the frequency of source documents that contains the term (keyword) at least once. IDF can be calculated using (2),

$$(idf)_{i,j} = \sum_{i=j=1}^n \log_2 \left(\frac{|D|}{Nt_j} \right) \quad (2)$$

Where Nt_j denotes the document frequency(df) of the term t_j which is the number of documents included in the document collection D in which t_j occurs at least once. The total number of documents in the document collection is denoted using $|D|$.

TF-IDF value for each term (keyword) can be calculated using (3),

$$w(i,j) = tfidf(d_i, t_j) = Nt_i, d_j * \sum_{i=j=1}^n \log_2 \left(\frac{|D|}{Nt_j} \right) \quad (3)$$

$$w(i,j) = tfidf(d_i, t_j) = (tf)_{i,j} * \log_2 \left(\frac{|D|}{df_j} \right) \quad (4)$$

The simplified version of (3) is in (4) and it calculates the $w(i,j)$ only if $Nt_i, d_j \geq 1$. When the words that do not appear in D, the $Nt_i, d_j = 0$ and thereby $w(i,j) = 0$.

The value of the Document Frequency (df) scales the d logarithmically. Hence, the formula $\log_2 \left(\frac{|D|}{Nt_j} \right)$ gives the full weight for $tfidf$ if a term occurs in only one document and if a term occurs in all the documents, then the value of $tfidf$ would get zero.

The two important aspects reveal from the TF-IDF weighting scheme are,

1. By considering the tf values, the more often occurring terms in a document can be identified as the representative terms of the content of the document.
2. By considering the idf values, a term that occurs in more documents can be identified as less discriminative.

Many applications based on Information Retrieval (IR), Text summarization, and association rule extraction from text

documents use TF-IDF to weight terms. In [2], the author applies a statistical relevance-scoring function to collecting web news documents to assign scores for each keyword based on maximal TFIDF. Depending on the user's requirement, the top N terms with the highest TF-IDF values can be occupied as the final list of keywords used in the ARM phase [1-3]. The major advantage of automated indexing based on TF-IDF is that it reduces the indexing cost [2].

4.2. Association Rule Mining (ARM) phase

Association Rule Mining (ARM) technique automatically finds information by extracting association rules which contain relationships such as "one implies the other" or "occur together" associated within a list of keywords in a collection of indexed documents. Following the user's requirement, the high-frequency keywords in the indexed documents are selected to generate association rules.

4.2.1. Definition and Notations in ARM

Given a set of keywords $A = \{w_1, w_2, \dots, w_n\}$ and a collection of indexed documents $D = \{d_1, d_2, \dots, d_m\}$, where each document d_i is a collection of keywords such that $d_i \subseteq A$. Let W_i be a set of keywords. A document d_i is said to contain W_i if and only if $W_i \subseteq d_i$. The general expression of an association rule is an implication of the form $W_i \Rightarrow W_j$ where W_i (antecedent) and W_j (consequent) are sets of keywords in a collection of indexed documents such that $W_i \subset A, W_j \subset A$ and $W_i \cap W_j = \emptyset$.

The most significant two measures used in the Association Rule evaluation process are support(s) and confidence(c).

If s% of documents in the collection of indexed documents D contain $W_i \cup W_j$, then the Association rule $W_i \Rightarrow W_j$ is said to have support (W_i, W_j) that can be calculated using (5).

$$Support(W_i W_j) = \frac{Support\ count\ of\ W_i W_j}{Total\ number\ of\ documents\ (D)} \quad (5)$$

If C % of indexed documents in the collection of documents D that contain W_i also contain W_j , then the Association rule $W_i \Rightarrow W_j$ holds in D is said to have confidence (W_i, W_j) that can be calculated using (6).

$$Confidence\ (W_i \setminus W_j) = \frac{Support\ (W_i W_j)}{Support\ (W_i)} \quad (6)$$

The general definition of the above two basic measures depends on how a transaction is defined based on the domain. As an example, a transaction can be the records in the dataset or database, each document in the collection of documents [2].

The two threshold values, minimum support, and minimum confidence are the constraints of support and confidence values that the user establishes. An association rule whose support and confidence values are higher than the user-defined thresholds is said to be a strong association rule.

Association rules extraction is a two-step process [1-7]: First, find frequent itemsets, all the itemsets that have support above

minimum support value. Secondly, use the identified frequent keyword sets in step 1 to generate the association rules by discarding those rules below minimum confidence. The later step in the Association Rule generation process is more straightforward than step one, requiring more time and effort [2].

4.2.2. Apriori Algorithm in ARM

Apriori is one of the well-recognized ARM algorithms which supports finding frequent items in transactional data sources [1,2] using two main phases, where the first phase counts item or keyword occurrences to determine the large 1-itemsets and the second phase (k) is again two-fold. In the first fold, the large itemsets L_{k-1} found in the (k-1)th pass are used to generate the candidate itemsets C_k by the Apriori function. The database is scanned and the support of candidates in C_k is counted in the second fold.

The below steps demonstrate the general workflow in the Apriori algorithm associated with the terms in Table I.

Table 1. Notations Used in The Apriori Algorithm

Term	Description
k-keywordsets	A keyword set with k- keywordsets
L_k	Set of large k- keywordsets that satisfy min_{sup} value (in the k th pass)
C_k	Set of candidate k- keywordsets generated from potentially large k- keywordsets
min_{sup}	User-specified minimum support value
min_{conf}	User-specified minimum confidence value

Step 1: Scan the indexed documents or database and find all their accumulated counts. Select the set of frequent 1-itemsets that satisfy the threshold min_{sup} value which is known as L_k .

Step 2: Uses L_k to find the candidate 2- itemsets (C_{k+1}) set. This is a two-step process where step 1 is to use the L_k found in the kth pass to generate the candidate 2-itemsets C_{k+1} . The second step is to scan the indexed documents or database and calculate each candidate's support in C_{k+1} .

Step 3: Calculate the support count for all the itemsets in C_{k+1} and select the frequent 2-itemsets that satisfy the threshold min_{sup} value known as L_{k+1} .

Step 4: Continues steps 2 and 3 until no new frequent (k+1)-itemsets are found.

Step 5: Find all the association rules that satisfy the threshold min_{conf} for each frequent itemsets.

Apriori follows an iterative level-wise search approach, where k-itemsets are used to explore (k+1)-itemsets [1,2,9].

As described in Table II, the input to the above algorithm is a transaction database where each entry is a transaction of the form <Transaction_id, Set of Items> which is also known as horizontal data format.

Table 2: Horizontal Data Format

Transaction_id	Set of Items
1	a,b,c,d
2	b,c,d
3	A c
4	c,d

The Apriori algorithm will encounter two problems when the frequencies in a set of items have a great variation.

- If the value of min_{sup} is set too high, then the association rules that involve rare items will not be detected. To find out the association rules that involve both frequent and rare items, the value of min_{sup} has to be set very low. Since the frequent itemsets will be associated with each other in all possible combinations, this may cause the generation of a large number of candidate sets [13,14].
- Apriori requires a repeated scan of the database for calculating the support count for candidate sets [13,14].

The vertical format was applied to solve the above issues arising in the DM field by transforming the horizontal data layout described in Table II into the vertical data layout described in Table III by scanning the data set for mining frequent itemsets [13,29,30]. The vertical data format in Table III shows the 1-itemset and it contains entries like <Item, Set of Transactions containing the item>.

Table 3: Vertical Data Format

Item	Transaction Ids	Frequency
a	1,3	2
b	1,2	2
c	1,2,3,4	4
d	1,2,4	3

Every item in Table II is considered as a candidate 1-itemset in the above transaction. This layout employed an intersection between the Transaction_id lists to calculate the support value of the 'candidate's itemset identified in subsequent steps. After counting their support values, all the candidate itemsets which are lesser than the minimum support are discarded.

The vertical layout is a refinement of the traditional Apriori algorithm because it substantially reduces the number of database scans [13,29,30]. This improvement is because the support count (Frequency) is stored in vertical data format just computing the cardinality of each Transaction Id set. Hence, the mining

efficiency is increased and the processing time is decreased compared to the default horizontal layout.

4.2.3. FP-Growth Algorithm in ARM

The FP-Growth is an efficient algorithm that has been proposed as an alternative to the Apriori algorithm for mining frequent itemsets without generating candidates [19–24]. It stores the database transactions in a tree structure which are denoted as FP-tree [19–24] where every item in a transaction has a linked list going through all other transactions that contain the item. The FP-tree structure uses a vertical and horizontal database layout to set aside the transactional database in the main memory. Every node in the FP-tree has a counter value that maintains the number of transactions shared by the node. All occurrences of an item in the FP-tree are linked with the next occurrence of the respective item in the FP-tree using links. Apart from that, a header table contains each item in the FP-tree and its support value and a link to refer to the first occurrence of the item in the FP tree. All the items in the FP tree are stored in the descending order of the support value. Hence, more frequently occurring items are organized closer to the root node of the FP-tree and such items are more likely to be shared than others.

The FP-Growth algorithm consists of 3 main stages:

- Generation of conditional pattern base
- Generation of conditional FP-Tree
- Searching for the frequent itemsets

Algorithm 1 demonstrates the general workflow in the FP-Growth algorithm that incorporates the above 3 main stages.

Algorithm 1: FP-Growth algorithm

Input: FP-Tree

Output: The complete set of frequent patterns

Method: FP-Growth (Tree, null)

Procedure: FP-Growth (Tree, α)

```

if the Tree consists of a single path P then;
    for each combination (denoted  $\beta$ ) of the nodes in the path,
        P do
            generate patterns  $\beta \cup \alpha$  with support = min support of
            nodes in  $\beta$ 
    else
        for each  $a_i$  in the Header of Tree do
            generate patterns  $\beta = a_i \cup \alpha$  with support =  $a_i$ .support
            construct  $\beta$ 's conditional pattern base and FP-Tree,
            Tree $\beta$ 
            if Tree $\beta \neq$  null then
                CALL FP-growth (Tree $\beta$ ,  $\beta$ )
    end
    
```

The algorithm first compresses the database into a highly condensed FP-tree structure, avoiding costly database scans [23]. Next, it applies the divide-and-conquer approach to decompose the ARM tasks into smaller ones avoiding candidate generation [23, 24].

The FP-GrowthThe FP-Growth algorithm has overcome one major problem of the Apriori algorithm. It has overcome one major

problem the Apriori algorithm does not generate a great number of candidate itemsets [13]. Furthermore, this algorithm transformed the entire text database into an FP-tree that holds all the database's information. Hence it requires only two scans of the database and does not scan it again and again as in Apriori [14–19]. The first scan is to find out the frequent words and their support count and the second scan is to sort out each transaction according to their descending support count. Moreover, searching frequent itemsets in FP-Tree does not use generated candidates as it is done on the Apriori algorithm. Hence, the FP-Growth algorithm becomes faster than the traditional Apriori algorithm [13–29].

4.3. Visualization phase

ARM often results in a massive number of association rules which requires the user to go through all the generated rules to discover the interesting rules. Manually analyzing such a massive number of rules is a time-consuming, tough, and tiring activity [20,21]. These issues can be addressed by interactive visualization of the extracted association rules in a textual or graphical format. Association rule visualization has an extensive history of transforming bulky amounts of data into a better accessible method for analysis. Interactive visualization techniques fall under three important categories named scatter plots, matrix visualization, and graph-based visualization [31]. The main elements used in these visualization categories are shown in Figure 1.

As shown in Figure 1, scatter plots utilize different interest measures such as confidence and support on the x and y-axis, and association rules with similar values for such interest measures are placed adjacent to each other. The graph-based visualization demonstrates how association rules are shared by individual items while matrix visualizations demonstrate association rules that have the same antecedent or consequent in the same column or row. The association rules in Figure 1 are shown in blue color.

The literature introduced different visualization techniques such as scatter plots, double-decker plots, mosaics, and parallel coordinates plots to visualize and analyze association rules [21]. Nevertheless, most of such techniques are still falling short with the presence of a large number of association rules [21,22]. However, the most traditional visualization techniques are not much appropriate for visualizing massive sets of association rules since they generally consist of many unique antecedents and consequents [21].

In [21], the author introduced a novel visualization method, a grouped matrix-based representation, which automatically creates nested groups of association rules by applying the k-means clustering algorithm to handle the massive number of generated rules. The hierarchical structure formed by these nested groups of association rules can be interactively explored down to each rule. This Matrix-based visualization [20,21] technique represents the antecedent and consequent of the association rule on the x and y-axes while any selected interest measure is displayed at the intersection of the x and y-axes of a given rule.

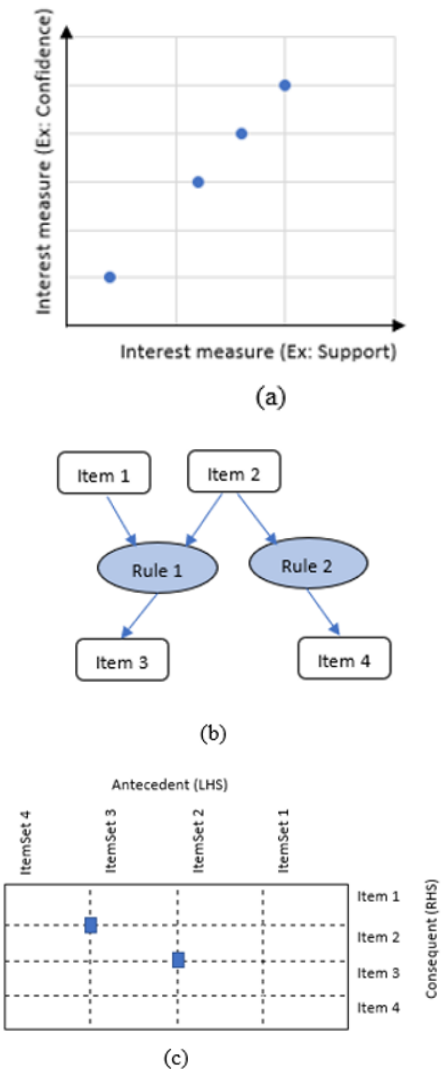


Figure 1. The main elements of association rule visualization using (a) a scatter plot, (b) graph-based visualization, and (c) matrix visualization.

This technique addresses the typical problem that is aroused with huge sets of association rules by grouping antecedents together and letting the end users explore the most interesting groups automatically using different colors and the position of elements in the plot. Grouped matrix-based visualization is easy to understand and unique [21] since most other visualization methods are not able to efficiently deal with huge sets of association rules.

The graph-based techniques [22] visualize the most important extracted association rules using vertices and directed edges where vertices represent each item or itemsets. In contrast, edges represent the relationships in terms of rules. Any selected interest measures are added to the edges of the graph as labels on the edges or as edges with different colors or edges with varying widths of the arrows. These graph-based techniques present a very comprehensible representation of association rules for relatively small sets of association rules selected based on their corresponding confidence score ($\min_{conf.}$) value. Graph-based visualization techniques are well suited when the end users are

concerned with an aggregated perspective on the most important rules [22]. But this technique offers a clear representation only for relatively small sets of rules, which can be easily chosen based on the selected interest measure.

5. ARM using e-news articles

This section describes the implementation details of the Apriori and FP Growth algorithm for a collection of e-news articles.

5.1. Environment and Dataset

The implementation and testing of Apriori and FP Growth algorithms were done in Python (version 3.7.0) using a workstation with Intel(R) Core (TM) i3-8130U CPU @ 2.20 GHz and 4 GB main memory.

This study evaluated the two algorithms: Apriori and FP Growth using the collection of e-news documents written in the English language released by the Document Understanding Conference (DUC) – 2002 which uses Text REtrieval Conference (TREC) data as the experimental dataset. This dataset comprises 128 topics-related e-news article sets and each article set has between 5 and 15 e-news articles, with an average of 10 articles. The news article must be at least 10 sentences long, but there is no maximum length. The list of topics-related e-news article sets used for the experiment is described in Table IV.

Table 4: The list of topics-related e-news article sets used for the experiment (DUC 2002)

Document set ID	No. of news articles	Total No. of sentences
d113h	5	82
d083a	6	95
d061j	7	124
d063j	8	136
d094c	9	137
d075b	10	183
d070f	11	208
d081a	12	210
d072f	13	229
d069f	14	237

5.2. Methodology

As shown in Figure 2, firstly the basic text pre-processing steps described in section 4.1 including filtration, stemming, and indexing was applied to the collection of e-news articles.

Next, the two algorithms: Apriori and FP Growth were applied to the indexed e-news article collections for generating association rules. We used the TF-IDF numerical statistic to generate index terms from the e-news articles and the count of such generated index terms which are above the threshold value of 0.6 are shown in Table V. All the calculations for identifying index terms were done following (1) to (4) described in the section 4.1.5. Depending on the user’s requirement, the top N terms with

the highest TF-IDF values can be occupied as the final list of keywords used in the ARM phase [1–3].

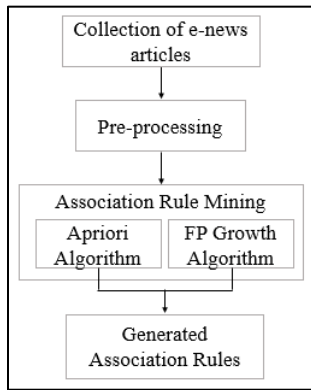


Figure 2. The process of Association Rule Generation

We generated the association rules with different combinations of min_{sup} (values: 60,70,80,90,100) and min_{conf} (values: 80,85,90,95,100) values. All the generated association rules that satisfy each combination of min_{sup} and min_{conf} values were taken for the experiment.

Table 5: The count of index terms (keywords) generated for each topics-related e-news article sets used for the experiment (DUC 2002)

Document set ID	No. Index Terms
d113h	528
d083a	593
d061j	789
d063j	847
d094c	698
d075b	1180
d070f	1271
d081a	1420
d072f	1542
d069f	1782

Table 6: Association Rules generated for the document set ID: d113h using the Apriori algorithm

$min_{sup} \backslash min_{conf}$	80	85	90	95	100
60	2909	2221	1912	1459	1127
70	2793	2442	1789	1009	808
80	2543	1992	1405	828	576
90	2046	1551	1079	518	251
100	1506	1119	731	385	73

Our experiment generated the association rules for document sets in Table V using different value combinations of min_{sup} and min_{conf} . Support and Confidence value for each generated association rule were calculated using (5) and (6) in section 4.2.1. All the association rules that satisfy each combination of min_{sup} and min_{conf} values were taken for evaluation.

Table 7: Association Rules generated for the document set ID: d113h using the FP Growth algorithm

$min_{sup} \backslash min_{conf}$	80	85	90	95	100
60	2329	2110	1794	1391	978
70	2172	1825	1490	1121	873
80	1856	1513	1201	705	584
90	1621	1297	903	561	240
100	1349	1067	871	378	81

The total number of Association Rules generated using the document set ID: d113h which satisfy the specified min_{sup} and min_{conf} values are listed in Table VI and Table VII.

6. Results & Discussion

The major concern of the experiment described in this study includes a comparison of the execution time of both algorithms for each document set listed in Table V to identify the most effective algorithm for e-news articles.

We monitored the complete execution time taken by each algorithm for generating the set of association rules with different combinations of min_{sup} and min_{conf} values. The execution time taken by each algorithm for generating association rules for the document set ID: d113h with 100% support and 100% confidence is listed in Table VIII.

Table 8: Execution time of Apriori and FP-Growth algorithms for the document set ID: d113h

Document set ID	Apriori Algorithm		FP Growth Algorithm	
	Execution time	No. of rules	Execution time	No. of rules
d113h	40 minutes	73	3 minutes	81
d083a	50 minutes	70	4 minutes	76
d061j	65 minutes	81	5 minutes	80
d063j	70 minutes	85	6 minutes	91
d094c	63 minutes	72	5 minutes	68
d075b	75 minutes	88	6 minutes	76
d070f	87 minutes	89	7 minutes	93
d081a	116 minutes	107	9 minutes	98
d072f	125 minutes	114	11 minutes	91
d069f	146 minutes	123	13 minutes	126

Our implementations of the Apriori and FP Growth algorithms consider each sentence in the e-news article as one database transaction. Hence, each document collection generates a large number of TF-IDF weighted index terms (Table V) or keywords to be considered in association rule generation.

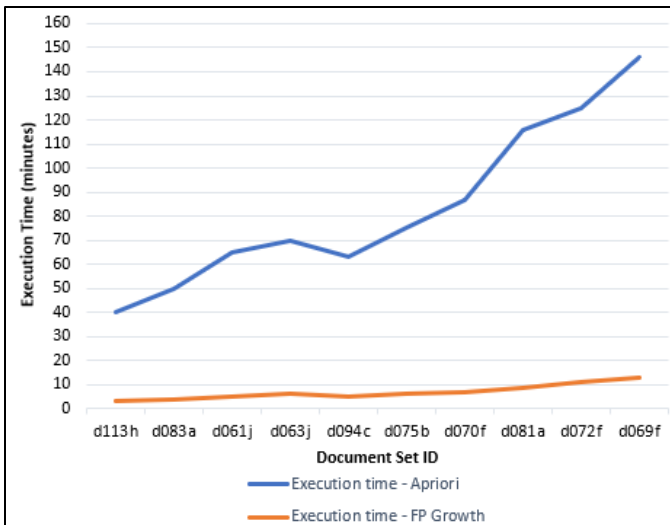


Figure 3: The comparison of algorithm execution time for generating association rules with 100% support and 100% confidence

When the number of generated association rules getting increased, the execution time of both algorithms also getting increased. The details presented in Table VIII and the comparison of execution time in Figure 3 represent that out of these two algorithms, the FP Growth algorithm always performs much better than the Apriori algorithm disregarding the number of generated association rules and several index terms. Mainly this happens due to the major weaknesses in the Apriori algorithm such as several transactional database scans, large memory utilization, and higher execution time.

6.1. The complications in Apriori Algorithm in ARM

Following the experimental results, we evident the below compilations in the Apriori algorithm for association rule generation using textual data.

The Apriori algorithm requires a repeated scan of the database for calculating the support values for each generated candidate set [1-14] which is one of the major problems in the Apriori algorithm. The literature describes the GARW algorithm [1-3] as a solution to this issue since it 'doesn't scan the original documents multiple times as in the Apriori algorithm. Instead, it scans the generated XML file, which includes only the keywords identified during the large frequent keyword sets generation in each document. It also includes only the keywords identified during the large frequent keyword sets generation in each document and satisfies the user-defined threshold values. Therefore, the execution time of the GARW algorithm is less than the Apriori algorithm [1,2].

Another major bottleneck in the Apriori algorithm is candidate set generation by handling extremely large candidate sets. Moreover, frequent pattern matching using such massive candidates by searching through each transaction in the database is very expensive and time-consuming. When the frequencies in a

set of items have a significant variation and if the value of min_{sup} is set too high, then the association rules that involve infrequent items will not be detected. To identify the association rules that involve both frequent and infrequent items, the value of the min_{sup} has to be set very low. Since each frequent item is getting associated with other frequent items making all possible combinations, this may cause the generation of a massive number of candidate sets [13,14].

As a solution to this issue, the study in [8] presented a fast and memory-efficient scalable algorithm that uses the divide-and-conquer approach. This algorithm uses the bitwise vertical representation of the original database and formalizes the problems that arise in closed itemsets mining by partitioning the search space. This algorithm presents a condensed but lossless representation of all the extracted frequent itemsets in the transactional database and then identifies all the possible closed frequent Itemsets for discovering closed frequent itemsets. Furthermore, this algorithm uses several optimization techniques to reduce space and time utilization in generating itemset closures and their support values. But, one major drawback encountered in this algorithm is the generation of the same closed itemset multiple times [8]. Apart from this algorithm, in [8] the author proposes an effective and efficient pruning technique that does not require storing the set of extracted closed patterns in the main memory. Moreover, this technique allows each visited partition of the search space to be mined parallelly or separately despite the order.

The pruning technique used in the Apriori algorithm does not assure an effective pruning of candidates due to the rapid growth in the frequent itemsets. In this case, the proposed algorithm in [8] ensures that frequent closed itemsets extract all frequent closed itemsets in the transactional database without any duplications while saving memory space and reducing the execution time in itemset closures generation [8].

Association rule generation using the Apriori algorithm considers all the keywords without considering the importance of each keyword. Owing to this, a large collection of association rules will be generated, becoming a tedious and time-consuming task. More importantly, the knowledge discovery using these association rules will not be so worthwhile as it considers all the keywords in the transactional database, including lower-weight keywords [3]. Applying the Apriori algorithm to the vertical data format described in Table III instead of the horizontal data format addresses most of the limitations discussed above [2,3].

6.2. The complications in FP-Growth Algorithm in ARM

Following the experimental results, we evident the below compilations in the FP Growth algorithm for association rule generation using textual data.

The major complication in the FP-Growth algorithm is the cost and time consumption in constructing the FP-Tree. The FP-tree construction in this algorithm has a high requirement for memory space. Hence, the algorithm may not fit in the shared memory when the transactional database gets larger. Apart from that, the observations explained in [25] state that the resulting FP-tree cannot be considered a unique representation of the same logical database that is used in FP-tree generation. But once the construction of the FP-tree is over, it can be easily used to read off the itemsets [19].

The other complication is that the support value can only be calculated after the entire FP-Tree is constructed. Furthermore, when the threshold value of support is getting higher, extensive time is wasted since the pruning can be applied only to one item at once [19,24]. Also, the FP-growth algorithm requires at most two complete database scans [13-29], and scanning the database twice reduces the efficiency of the FP-Growth algorithm.

Even though the Painting-Growth and N Painting-Growth algorithms [28] only scan the database once and are easy to implement, there are still several complications in them. The Painting-Growth algorithm builds the association picture, leading to a large memory overhead. The N Painting-Growth algorithm performs well with macroscale datasets and the implementation of the algorithm is more complex than the Painting-Growth algorithm. Third, these two algorithms repeatedly scan the generated frequent item association sets and extract multi-item frequent sets. This results in reducing the time efficiency of these algorithms [28].

The exponential growth in association rule extraction produces a large number of rules. Association rule extraction approaches are also broadly expanding, and novel algorithms such as Apriori-hybrid are increasing their performance in many real-world applications [6]. Generally, the existing data mining techniques discover innumerable patterns or knowledge from a training data set. Furthermore, noise in the discovered patterns makes the effective knowledge discovery process a big challenge. The concept of closed patterns [8] deals with the noise up to a significant level, but the discovered knowledge still retained many meaningless patterns. Apart from that, the generation and identification of only the interesting patterns based on pre-defined constraints improve the quality of the ARM process [5].

7. Future Directions

Knowledge discovery is an increasing field of research. Still, there is a tremendous need to develop TM approaches using AMR which can guide the user on knowledge discovery in text documents such as web articles identifying important information, and how to generate knowledge. Even though knowledge refinement has been carried out in the literature, the refinements in the ARM are still comparatively less [27].

7.1. Refinements to the Apriori Algorithm

Support and confidence are the two factors considered by the Apriori algorithm to measure the statistical strength of the generated association rules. However, these factors are not useful in deciding the generated rules' convenience or detecting conflicts between the generated rules [27]. Hence, a refinement of the existing factors by introducing a novel factor that considers the convenience of generated rules and identification of conflicts between rules is important for obtaining consistent and interesting patterns.

A few of the major future directions in the Apriori algorithm are,

- Reducing the multiple passes over the chosen data to speed up the algorithm execution.
- Identifying only the most important keywords for generating association rules to reduce generating a large collection of association rules which will not be so meaningful.
- Generating efficient candidate sets by handling exceedingly large candidate sets and matching frequent patterns with a large number of candidates.

Furthermore, the current pruning technique used in the Apriori algorithm does not assure an effective pruning of candidate sets due to the rapid growth in the frequent itemsets.

7.2. Refinements to the FP-Growth Algorithm

The most needed refinement in the FP-Growth algorithm is reducing the cost of development and time consumption in constructing the FP-Tree. Another primary direction in the FP-Growth algorithm is to enhance the algorithm to fit in the shared memory when the transactional database gets larger.

N Painting-Growth and Painting-Growth algorithms developed in [28] provide a direct link for the subsequent ARM research. Enhancing the performance of the Painting-Growth and N Painting-Growth algorithms [28] while increasing the efficiency in infrequent item removal and multi-item frequent sets mining will be some of the leading future works.

8. Conclusion

Effective information extraction using text documents is a massive challenge due to the duplications and ambiguities of data values in the text. The works of literature related to Knowledge Discovery from text documents using Association Rule Extraction have become a more frequent and imperative research approach to finding out the most significant information, patterns, and features in the text documents. This survey provides a comprehensive review of Association Rule extraction using text documents covering a comprehensive review of multiple aspects.

Furthermore, the experimental results discussed in this study answer the question ‘Which ARM algorithm: Apriori or FP Growth has fast execution in association rule generation using e-news articles?’. Out of the Apriori and FP Growth algorithms, the FP Growth algorithm always performs much better than the Apriori algorithm disregarding the number of textual contents included in E-news articles. Mainly this happens due to the major weaknesses in the Apriori algorithm such as several transactional database scans, large memory utilization, and higher execution time.

The main outcomes of the study we have conducted are,

- A thorough review of extracting knowledge in text sources using Association Rules.
- A review of the most popular application domains of ARM along with its usage and applications.
- A review of more frequently used association rule extraction algorithms, mainly the Apriori and FP-Growth algorithms in ARM, their usage, recent breakthroughs, advantages, and major bottlenecks in TM.
- Detailed information on the ARM process including a comprehensive review of the Text Pre-processing phase, Association Rule Mining phase, and Visualization phase.
- Detailed information on the perspective directions to facilitate future research.

The major complications in the Apriori algorithm were addressed by introducing a novel compact data structure, FPtree. The FP-growth algorithm that uses the FP tree allows efficient discovery of frequent itemsets and is faster than other ARM algorithms. Even though the value of the support factor influenced the performance of the Apriori algorithm, the performance of the FP-growth algorithm is not influenced by the value of the support factor. Thus, the algorithms with candidate set generation behave well with small databases with the size of a maximum number of transactions of around 50,000 and a support factor of at least 30% [25].

Later, FP-tree-based pattern recognition algorithms such as FEM [26], and DynFP-growth algorithm [25] were developed based on the completeness and compactness of the FP-growth structure. DynFP-growth [25] and FP-growth algorithms that don't require candidate generation perform much better. The experimental results of the FEM [26] and FP-growth [25] algorithms have shown a significant improvement in the performance of mining frequent patterns compared to the FP-Growth algorithm. N Painting-Growth algorithm and Painting-Growth algorithm presented in [28] reduce the overhead of scanning a database multiple times. The use of two-item permutation sets in these algorithms gives several advantages: running faster, occupying less memory space, having low complexity, and being easy to maintain. Based on the survey presented in our paper, it's evident that pattern-based growth

algorithms like FP-Growth and their refinements based on the FP-tree are more efficient than algorithms based on candidate generation such as Apriori.

Conflict of Interest

The authors declare no conflict of interest.

Acknowledgment

I am grateful to the University of Colombo School of Computing (UCSC), Sri Lanka for all the facilities provided for this research work.

References

- [1] H. Mahgoub, “Mining association rules from unstructured documents”, *International Journal of Applied Mathematics and Computer Sciences*, **1** (4), 201-206, 2008, doi:10.5281/zenodo.1330457.
- [2] H. Mahgoub, D. Rösner, N. Ismail, F. Turkey, “A text mining technique using association rules extraction”, *International Journal of Computer, Electrical, Automation, Control, and Information Engineering*, **2**(6), 2044-2051, 2008.
- [3] M. Kulkarni, S. Kulkarni, “Knowledge discovery in text mining using association rule extraction”, *International Journal of Computer Applications*, **143**(12), 30–35, 2016, doi: 10.5120/ijca2016910144.
- [4] A. A. Lopes, R. Pinho, F. V. Paulovich, R. Minghim, “Visual text mining using association rules”, *Comput. Graph.*, **31**(3), 316–326, 2007, doi: 10.1016/j.cag.2007.01.023.
- [5] Y. Li, N. Zhong, “Rough association rule mining in text documents for acquiring web user information needs”, in 2006 IEEE/WIC/ACM International Conference on Web Intelligence (WI 2006 Main Conference Proceedings) (WI'06), Hong Kong, China, 226–232, 2006, doi: 10.1109/WI.2006.151.
- [6] J. Manimaran, T. Velmurugan, “A survey of association rule mining in text applications”, in 2013 IEEE International Conference on Computational Intelligence and Computing Research, Enathi, Tamilnadu, India, 1–5, 2013, doi: 10.1109/ICCIC.2013.6724258.
- [7] M. Delgado, M. J. Martín-Bautista, D. Sánchez, J. M. Serrano, M. A. Vila, “Association rule extraction for text mining”, In: Carbonell, J.G., Siekmann, J., Andreasen, T., Christiansen, H., Motro, A., Legind Larsen, H. (eds) *Flexible Query Answering Systems - FQAS 2002*, Lecture Notes in Computer Science(), Springer, Berlin, Heidelberg, **2522**, 154-162, 2002, doi: https://doi.org/10.1007/3-540-36109-X_12.
- [8] C. Lucchese, S. Orlando, R. Perego, “Fast and memory-efficient mining of frequent closed itemsets”, *IEEE Trans. Knowl. Data Eng.*, **18**(1), 21–36, 2006, doi: 10.1109/TKDE.2006.10.
- [9] C. M. Rahman, F. A. Sohel, P. Naushad, S. M. Kamruzzaman, “Text classification using the concept of association rule of data mining”, in 2010 Proceedings of the International Conference on Information Technology, Kathmandu, Nepal, 234-241, 2010, doi: <https://doi.org/10.48550/arXiv.1009.4582>.
- [10] R. Agrawal, R. Srikant, “Fast algorithms for mining association rules”, in Proceedings of the 20th International Conference of very Large Data Bases, VLDB, Santiago, Chile, 487-499, 1994.
- [11] T. Ouyoumkochoagorn, “Mining rare association rules on Banpheo Hospital (Public Organization) via Apriori MSG-P algorithm”, *ECTI Transactions on computer and information Technology*, **6**(2), 156–165, 1970, doi: 10.37936/ecti-cit.201262.54337.
- [12] V. Chandola, V. Kumar, “Summarization - compressing data into an informative representation”, in 2005 5th IEEE International Conference on Data Mining (ICDM'05), 1-8, 2005, doi: 10.1109/ICDM.2005.137.
- [13] Ali Ikhwan, Milfa Yetri, Yohanni Syahra, Jufri Halim, Andysah, Putera Utama Siahaan, Solly Aryza, Yasmin Mohd Jacob, “A novelty of data mining for promoting education based on FP-Growth algorithm”, in 2018 *International Journal of Civil Engineering and Technology (IJCET)*, **9**(7), 1660-1669, 2018.
- [14] Wei Zhang, Hongzhi Liao, Na Zhao, “Research on the FP Growth algorithm about association rule mining”, in 2008 International Seminar on Business and Information Management, Wuhan, 315–318, 2008, doi: 10.1109/ISBIM.2008.177.
- [15] R. K. Soni, N. Gupta, A. Sinhal, “An FP-Growth approach to mining

- association rules”, *International Journal of Computure Science and Mobile Computation*, **2**(2), 1-5, 2013.
- [16] Satya Wacana Christian University, I. S. Rajagukguk, S. Y. J. Prasetyo, I. Sembiring, “The analysis and implementation of algorithm of Frequent Pattern – Growth to support the promotion strategy in Victory University Sorong”, *International Journal of Comput. Sci. Eng.*, **4**(10), 24–31, 2017, doi: 10.14445/23488387/IJCSE-V4I10P106.
- [17] J. Panjwani, “Application of FP Tree Growth algorithm in text mining”, M.S. thesis, Department of Computer Science and Engineering, Jadavpur University, Kolkata, India, 2010.
- [18] K. Gadia, K. Bhowmick, “Parallel text mining in multicore systems using FP-tree algorithm”, in 2015 International Conference on Advanced Computing Technologies and Applications (ICACTA), *Procedia Computer Science*, **45**, 111–117, 2015, doi: 10.1016/j.procs.2015.03.100.
- [19] A. Kauri, G. Jagdev, “Analyzing working of FP-Growth algorithm for frequent pattern mining”, *International Journal of Research Studies in Computer Science and Engineering (IJRSCSE)*, **4**(4), 22-30, 2017, doi: <http://dx.doi.org/10.20431/2349-4859.0404003>.
- [20] Zulham Zulham, Ibnu Rusydi, Ananda H Elyas, “Pattern analysis of health equipment procurement system using the FP-Growth algorithm”, in 2nd International Conference on Inovations in Social Sciences Education and Engineering (ICoISSEE), **1**(1), 2021.
- [21] M. Hasler, R. Karpienko, “Visualizing association rules in hierarchical groups”, *Journal of Business Economics*, **87**(3), 317–335, 2017, doi: 10.1007/s11573-016-0822-8.
- [22] M. Hasler, S. Chelluboina, “Visualizing association rules in hierarchical groups”, in 42nd Symposium on the Interface: Statistical, Machine Learning, and Visualization Algorithms (Interface 2011), Intelligent Data Analysis group, Southern Methodist University, 2011.
- [23] O. Netzer, R. Feldman, J. Goldenberg, M. Fresko, “Mine your own business: market-structure surveillance through text mining”, *Marketing Science*, **31**(3), 521–543, 2012, doi: 10.1287/mksc.1120.0713.
- [24] J. Arora, “An efficient ARM technique for information retrieval in data mining”, *International Journal of Engineering Research & Technology (IJERT)*, **2**(10), 1079-1084, 2013, doi: 10.17577/IJERTV2IS100229.
- [25] A. Bala, M. Z. Shuaibu, “Performance analysis of Apriori and FP-Growth algorithms (Association Rule Mining)”, *International Journal of Computer Technology & Applications*, **7**(2), 279-293, 2016.
- [26] C. Gy, “A comparative study of association rules mining algorithms”, in 2004 1st Romanian- Hungarian Joint Symposium on Applied Computational Intelligence (SACI), 1-10, 2004, doi:10.13140/2.1.1450.3365.
- [27] G. Alaghband, L. Vu, “A fast algorithm combining FP-tree and TID-list for frequent pattern mining”, in 2011 Proceedings of Information and Knowledge Engineering, 472-477, 2011.
- [28] M. N. M. García, S. Segrera, V. F. López, “Association rules: problems, solutions, and new applications”, in 2005 Proceedings of the III National Workshop on Data Mining and Learning, 317-323, 2005.
- [29] Y. Zeng, S. Yin, J. Liu, M. Zhang, “Research of improved FP-Growth algorithm in association rules mining”, *Scientific Programming*, **2015**, 1–6, 2015, doi: 10.1155/2015/910281.
- [30] I. Aqra, N. Abdul Ghani, C. Maple, J. Machado, N. Sohrabi Safa, “Incremental algorithm for association rule mining under dynamic threshold”, *Applied Sciences*, **9**(24), 5398, 2019, doi: 10.3390/app9245398.
- [31] M. Hasler, “arulesViz: interactive visualization of association rules with R”, *The R Journal*, **9**(2), 163-175, 2017, doi: 10.32614/RJ-2017-047.

Hybrid Neural Network Method for Predicting the SOH and RUL of Lithium-Ion Batteries

Brahim Zraibi^{*1}, Mohamed Mansouri¹, Salah Eddine Loukili², Said Ben Alla²

¹National School of Applied Sciences of Berrechid, Laboratory LAMSAD, Hassan First University of Settat, Morocco

²Faculty of Science and Technology, Laboratory VTE, Hassan First University of Settat, Morocco

ARTICLE INFO

Article history:

Received: 28 August, 2022

Accepted: 25 October, 2022

Online: 31 October, 2022

Keywords:

Lithium-ion Batteries

Remaining Useful Life

Deep Neural Network

State-of-Health

ABSTRACT

The use of a battery to power an electrical or electronic system is accompanied by battery management, i.e. a set of measures intended to preserve it for preventative maintenance, thus the cost reduction. This management is generally based on two key parameters, the (remaining useful life) RUL and the (State-of-health) SOH, which relate respectively to the charge output and the aging of the Lithium-ion battery. The issue will be resolved and advances in production, battery utilization, and optimization will be made possible by accurate SOH determination and dependable RUL prediction. The CNN-BGRU-DNN hybrid strategy, which we suggest in this study, integrates Convolutional Neural Networks (CNN), Bidirectional Gated Recurrent Units (BGRU), and Deep Neural Networks (DNN) to increase the precision of SOH and RUL estimates for Lithium-ion batteries. To that purpose, the performance of the prediction findings is assessed using the MAE, RMSE, AE, and RE as well as the NASA datasets of lithium-ion batteries for experimental validation. The verification tests' findings show that, in comparison to existing approaches in the literature, the suggested method may greatly reduce prediction error and achieve high estimation accuracy of the battery's state of health.

1. Introduction

Electric vehicles are a promising technology for reducing the increasing air pollution such as decreasing CO₂ emission from worldwide transportation. They are operated by battery packs [1]. The accelerated electrification of vehicles is significantly facilitated by batteries [2]. There are five key considerations for EV batteries: longevity, specific energy, specific power, cost, and safety. Over the past ten years, the first four factors have greatly aided in the optimization of electrode and electrolyte materials. Many researchers worldwide, however, have not fully addressed the question of safety [3]. The repeated operation of batteries leads to loss of capacity and increase the resistance, which allow some catastrophes to happen like explosion and combustion resulted on the excessive usage. The solution will enable advancements in battery production, use, and optimization through accurate state of health (SOH) determination and reliable remaining useful life (RUL) prediction. For instance, end users can make an estimation of the predicted battery life to ensure that batteries are used to their greatest capability before being replaced or discarded. To expedite the testing, validation, and production

processes, manufacturers might group new cells according to their anticipated lifetime [4]. As a result, the complete electrification system requires an intelligent BMS capable of forecasting and monitoring battery behavior, which are very important for the safety and reliability of EVs and ESS [5]. Among different batteries, Li-Bs are widely regarded as potential options for a variety of applications, owing to their high energy density, power density, low self-discharge rate, and extended lifespan. Recently, many researches have started to focus on parameters of the BMS battery to estimate each of them. Many factors, including the state of charge (SOC), SOH, RUL, the charge capacity, and the internal resistance, must be monitored to ensure that Li-ion batteries are used efficiently and safely [6] [7]. Throughout the life cycle of lithium batteries in electrified vehicles, SOH is an essential parameter for problem diagnostics and safety early warnings in addition to its capacity to precisely predict the remaining mileage of EVs [8]. The RUL prediction of Li-Bs considers a significant choice for reliability, safety, and efficient battery operations, which is the number of cycles (charge/discharge) left before the battery fails, which is between 70 and 80% of its maximum capacity [7], [9], [10]. The equivalent circuit model [11], electrochemical model, data-driven model, and hybrid method

*Corresponding Author: Brahim Zraibi, b.zraibi@uhp.ac.ma

model are the four primary models that have been used in recent decades to perform substantial research on RUL estimate and SOH prediction of lithium batteries. The approach of the data model is receiving increasing amounts of attention as a result of the growth in lithium battery data [12], [13].

An accurate state of health (SOH) estimate helps ensure dependability and safety while the battery is operating. There are several ways to estimate it, including hybrid techniques based on neural networks [14], [15]. In 2017 [16], the author proposed the OS-ELM method and they utilized the discharge time of equal voltage interval as the HI. In 2019 [17], the author focused on their paper on the SOH estimation of lithium-ion battery using PKNN and Markov Chain. For verification, they compared the PKNN with other methods, which it obtained a high prediction accuracy. Besides, in [18], the author propose a method that combines the partial incremental capacity and ANN. Additionally, in [19], the author combine the ANN method with the PF algorithm for estimating the SOH, where they obtained an accurate estimation. In 2020 [20], the author integrated the deep Boltzmann machines and LSTM for obtaining the health prediction of a medical Li-ion battery. The empirical results obtain a good of SOH prediction. In [21], the author proposed a combination between GRU and CNN. While, in [8], the author combined the WNN with UPF. The performance results demonstrate their capability in improving the accuracy of SOH prediction.

The goal of this paper is to estimate the SOH and RUL of a lithium-ion battery using a hybrid method named CNN-BGRU-DNN. The comparison is performed between the proposed hybrid method and various prediction methods. The experiment obtained good results for the proposed method that achieved high predictive accuracy for the SOH and estimation compared to the other results.

The remaining parts of this essay are written as follows: The tools and methods for forecasting the RUL and SOH of battery lithium-ion batteries using the suggested method are presented in Section 2. A comparison of the SOH estimate accuracy is shown in Section 3. A conclusion is then offered.

2. RUL and SOH Prediction

2.1. CNN-BGRU-DNN architecture

The SOH and RUL of Li-ion batteries have been predicted using the CNN, BGRU, and DNN methods in prior literary works, where they performed well. By merging CNN, BGRU, and DNN, our study aims to enhance and attain high accuracy of SOH and RUL estimate.

In terms of feature extraction, CNN is proficient and benefits from both scale invariance and local dependence. Its feature extraction process is organized hierarchically. Through the use of many feature planes and neurons, the first layer of convolution extracts various input characteristics. In order to acquire continuous spatial features, the second layer, known as secondary feature extraction, decreases the feature surface dimension and its resolution. The outputs of the convolution layer are the inputs of the pooling layer, and the two layers are mapped one to one and each to the other. The data from the first two levels can be

combined in the third layer. Full connection outputs are delivered to the last layer. [22].

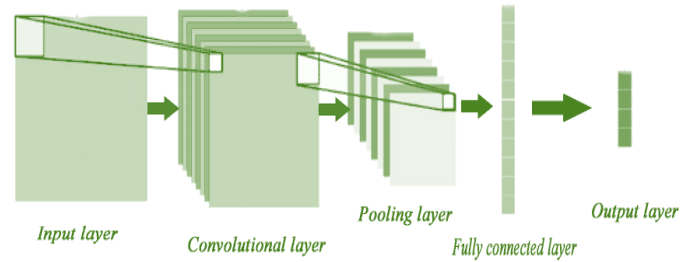


Figure 1: CNN structure

The RNN is one of the most well-liked deep learning (DL) algorithms since it makes use of the temporal correlations between neurons, although it suffers from the gradient vanishing issue [23]. Two RNN variations, LSTM and GRU, are utilized to regulate the propagation of gradient information and remember the parameters as successive inputs during the long-term sequence in order to solve this problem. [13].

GRU is classified as one of the RNN's variants. Its ability to regulate the propagation of gradient information and retain the parameters as future inputs over the long-term sequence is a core element. GRU consists of two gates: update gate z , which regulates the updating of the hidden state, and reset gate r , which determines whether or not to ignore the prior hidden state.

GRU's equations can be defined as follow:

$$z_t = \sigma(W_z[h_{t-1}, x_t])$$

$$r_t = \sigma(W_r[h_{t-1}, x_t])$$

$$\tilde{h}_t = \tanh(W_h[r_t * h_{t-1}, x_t])$$

$$h_t = ((1 - z_t) * h_{t-1}) + (z_t * \tilde{h}_t)$$

where, \tilde{h}_t is the candidate gate and h_t is output activation, the unit output as (h), W is the weight matrices, and σ is the sigmoid function represented [24].

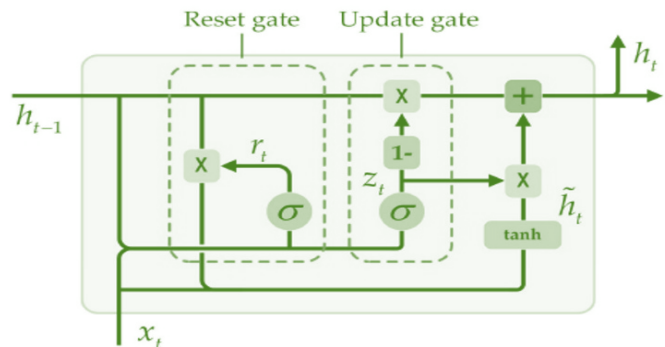


Figure 2: GRU structure

A GRU neural network with a two-layer structure is known as a Bidirectional Gate Recurrent Unit (BGRU) neural network. They have the ability to process the data inputs in both directions,

i.e. the forward and backward temporal sequences, with the outputs of both connected in the same output layer, allowing these bidirectional algorithms to be more efficient with defining the relationship between the sequences and its model. BGRU can save cost and time by reducing the amount of calculations required.

To benefit from the advantages of each algorithm and enhance the performance, they were combined with each other. The results of the integration of CNN, bidirectional of GRU, and DNN into one framework obtained good performance. The DL technology uses multiple layers to extract higher-level features from the raw input progressively.

Data processing is the initial step. We chose the discharge data from datasets that we extract from specific batteries that comprise charge, discharge, and impedance features. For each cycle of our experiment, where the input is the prior capacity and the output is the current capacity, we only choose one feature from this data, the capacity. We then used a window size of eight values to organize this data for the training step, which predicts data sequences. Finally, we split the data into test and training sets using the same split ratios for each battery. To predict the RUL of the Li-ion battery, we used the CNN-BGRU-DNN technique based on univariate time series.

We try to profit from their advantages where CNN is applied to extract local features, capture the spatial relationship, and use shared weights structure to reduce the amount of the weights and try to find the shared information from the measurement of data. Where we use one convolutional layer with 64 filters inclusive of the kernel size of 4, also we employ in this structure one default stride, causal padding, and Relu activation function. Then, the BGRU is applied to understand the temporal relationships in the feature sequence and it uses their internal state (memory) to learn features and time dependencies from the sequential data, and capture temporal features. Where we utilize two layers from each of them, which consist of 160 nodes then a flatten layer comes next. While DNN maps the features by choosing 3 dense layers, containing the Relu activation functions of each layer, with 128 nodes. Then we use one dense layer with one node to employ as a regression layer for getting the final SOH output and contribute to accurate prediction. Thus, the architecture of the proposed method shown in figure 3 is chosen after numerous experiments.

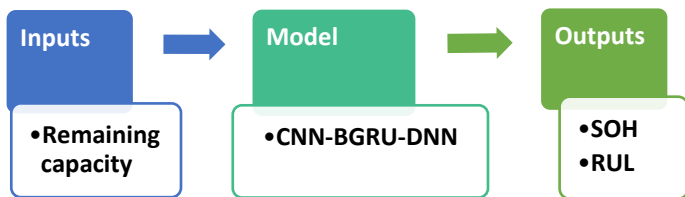


Figure 3 : The framework of proposed method

2.2. Experiment description

This research validates its findings using experimental data from the NASA Prognostics Center of Excellence [25], which includes of aging information 18650 Li-ion batteries. Where Table 1 provides the following information regarding these batteries:

Table 1: NASA Lithium-Ion Batteries description

Batteries	NASA
Temperature (C)	24
Constant charge current	1.5 (A)
Cut-off voltage of Charge/Discharge	4.2/ 2.5 (V)
Minimum charge current	20 (mA)
Rated capacity (Ah)	2
Cycles	168 (B5,B6,B7)

The proposed approach, CNN-BGRU-DNN, was implemented using the hyper-parameters presented in table 2 and using the following environment and tools:

- Google Colaboratory notebook
- 1 CPU Core: Intel(R) Xeon(R) CPU @ 2.20GHz
- Physical memory: 12G
- GPU: Tesla K80 - 11441MiB memory
- CUDA Version: 11.2
- TensorFlow version: 2.7.0
- Python version: 3.7.12.

Table 2: Hyper-parameters values

Hyper parameters	values
Window size	8
Batch size	32
Shuffle buffer size	1000
Epochs	1400
Learning rate	8e-4
Regularization	without
Activation function	ReLU
Optimizer	Adam
Loss function	Huber

We utilize MAE and RMSE [24] to assess how well the algorithms execute SOH estimation, while AE and RE are used to assess RUL prediction accuracy. These are their definitions [26] :

$$MAE = \frac{1}{K} \sum_{k=1}^k |y_k - \hat{y}_k| \quad (2)$$

$$RMSE = \sqrt{\frac{1}{N} \sum_{i=1}^N (y_k - \hat{y}_k)^2} \quad (3)$$

$$AE = |RUL_{real} - RUL_{predicted}| \quad (4)$$

$$RE = |RUL_{real} - RUL_{predicted}| / RUL_{real} \times 100\% \quad (5)$$

Where \widehat{y}_k is the predicted value and y_k is the actual value. The accuracy of the SOH forecast is greater when the MAE and RMSE are near to zero.

2.3. RUL and SOH estimation

The major of this section is to present the ability of the proposed hybrid method CNN-BGRU-DNN to estimate the SOH and RUL of different Li-ion batteries; it is also for confirming our method's prediction accuracy.

The battery's capacity, performance, and state of health are shown by SOH indicator. It is the ratio of a battery's actual capacity (Ca) to its rated capacity (Cr), where actual capacity refers to how much of the battery's capacity is actually used when it is fully charged. The rated capacity of a totally charged battery is 100%, whereas the capacity of a totally failed battery is 0%. The battery's SOH is defined as follows [27]:

$$SOH = \frac{Ca}{Cr} \tag{6}$$

The remaining number of cycles of battery capacity to reach at its failure threshold that means the time between now and the end-of-life "EOL" is defined as RUL, showing as follows [7]:

$$RUL = C_{EOL} - C_{cc} \tag{7}$$

C_{cc} is the number of cycle at the actual capacity and C_{EOL} is the cycle number when the capacity of battery arrives at the EOL.

The experiment were terminated only when battery attained their EOL, as seen in figure 4, where the line of EOL represented by a red color, which considered as the time when the capacity reaches 70% in rated capacity for the NASA batteries. The EOL is calculated as:

$$EOL = Cr * 0.7 = 1.4 \text{ Ah} \tag{8}$$

In this study, we separated the datasets into training and prediction data with the identical beginning prediction point of each dataset, which is 80 cycles. We utilized three batteries, B0005, B0006, and B0007, to establish the degradation sample of the battery's capacity.

Figure 4 above displays the outcomes of the SOH and RUL predictions, where Real values are displayed in blue and predicted values are shown in orange. The SOH and RUL predictions for NASA batteries demonstrate how the suggested hybrid technique, CNN-BGRU-DNN, practically always results in almost identical actual and predicted curves for all batteries. As a result, the hybrid method's SOH estimation accuracy is good. The point of failure at the end of life (EOL) for all batteries is when both curves almost exactly meet. As a result, CNN-BGRU-DNN achieves the maximum level of RUL prediction accuracy.

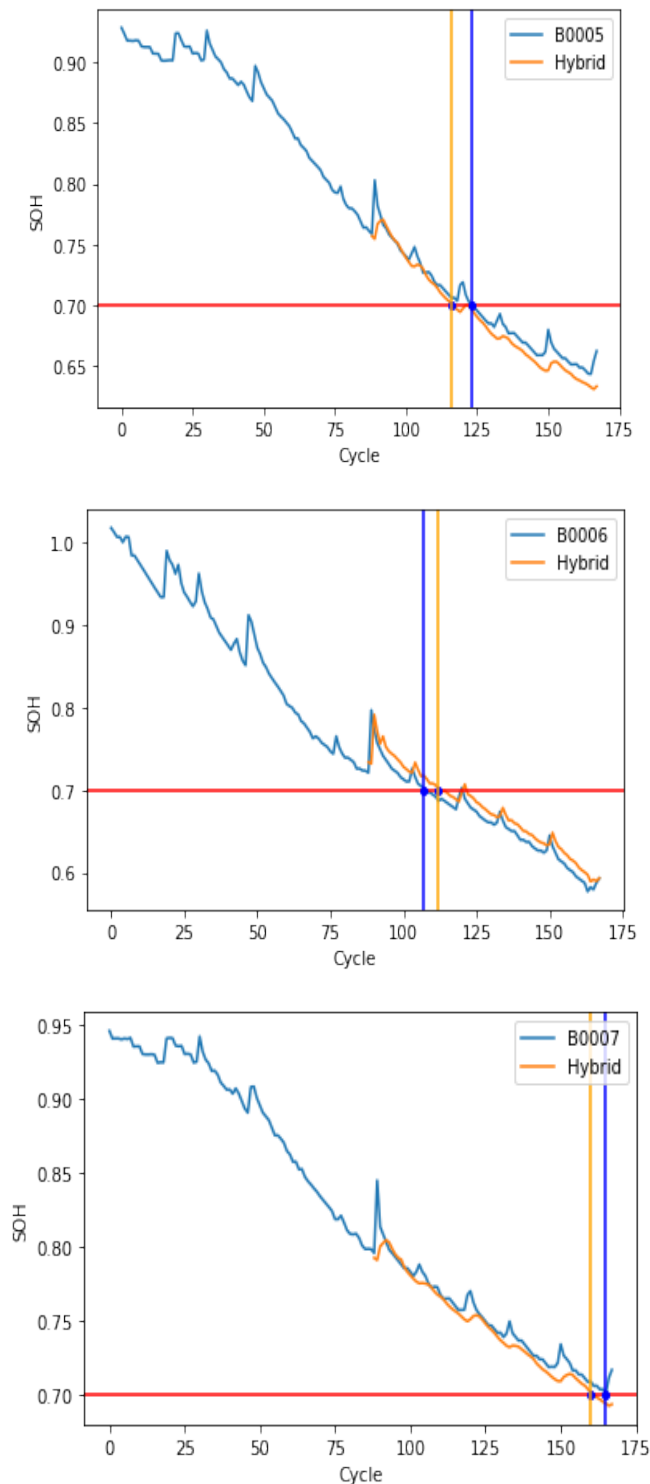


Figure 4: The SOH and RUL prediction results using CNN-BGRU-DNN.

Table 3: SOH estimation results

Batteries	Methods	RMSE	MAE
B0005	CNN-BGRU-DNN	0.01165	0.00884
B0006	CNN-BGRU-DNN	0.00884	0.01334

B0007	CNN-BGRU-DNN	0.00990	0.00667
-------	--------------	---------	---------

Table 4: RUL estimation results

CNN-BGRU-DNN				
Batteries	RUL _{real}	RUL _{predicted}	AE	RE %
B0005	123	116	7	5.69
B0006	107	112	5	4.67
B0007	165	160	5	3.03

The values for MAE, AE, and RMSE are extremely low, as seen in Tables 3 and 4. The CNN-BGRU-DNN approach helps minimize error during SOH deterioration, as this experiment shows. Furthermore, the Li-ion battery RUL estimation using the CNN-BGRU-DNN method is accurate. This demonstrates that CNN-BGRU-DNN approach is the best at predicting battery SOH, and the experiment illustrates perfectly the hybrid method's capacity for having greater forecast accuracy.

3. Comparison between proposed method and other methods in literature

This subsection provides a comparison of the SOH prediction accuracy of different other studies' predictions. We use performance method findings from earlier papers to compare more widely with other forms of prediction, since these approaches use the same NASA datasets and performance measures.

Table 5: SOH estimation results of some papers

Batteries	Methods	RMSE
B0005	UPF	1.088
	Elman NN	0.210
	WNN-UPF [8]	0.027
	GPR- LSTM [28]	0.012
	CNN-BGRU-DNN	0.011
B0006	CGTSSA_Cat_Boost [29]	0.0268
	SSA_Cat_Boost	0.0317
	PSO_Cat_Boost	0.0531
	Cat_Boost	0.0708
	CGTSSA-SVM	0.0362
	CGTSSA-ELM	0.0579
	UPF	1.115
	Elman NN	0.223
	WNN-UPF [8]	0.050
	GPR- LSTM [28]	0.013
CNN-BGRU-DNN	0.008	
B0007	UPF	1.161

Elman NN	0.145
WNN-UPF [8]	0.024
CGTSSA_Cat_Boost [29]	0.0118
SSA_Cat_Boost	0.0147
PSO_Cat_Boost	0.0263
Cat_Boost	0.0465
CGTSSA-SVM	0.0178
CGTSSA-ELM	0.0447
GPR- LSTM [28]	0.009
CNN-BGRU-DNN	0.009

From the results of table 5, we can clearly see that the RMSE value of our proposed method is smaller than the values reported by the studies, the RMSE metric is widely used in regression problems where we predict continues values, which is the case is the prediction of the SOH of Ion-Lithium batteries.

We can conclude based on the results of table 5 that the proposed suggested named CNN-BGRU-DNN is a good estimator with its high accuracy for predicting the RUL and SOH.

Conclusion

This study proposes a hybrid approach known as CNN-BGRU-DNN to predict Li-ion battery SOH and RUL. A dataset received from NASA is used to experimentally validate the suggested strategy. The results of the proposed hybrid method demonstrate that we achieved a big performance improvement and satisfying results evaluated by the performance indicators called MAE, RE %, AE and RMSE, where error rates are reduced and accuracy increased. In comparison to the outcomes of previous publications, four prediction performance indices show that CNN-BGRU-DNN has the greatest accuracy.

Nomenclature

AE	absolute error
ANN	artificial neural network
BMS	battery management system
BGRU	bidirectional gated recurrent units
CNN	convolutional neural network
DNN	deep neural networks
DL	deep Learning
ELM	extreme learning machine
LSTM	long short-term memory
Li-B	lithium-ion battery
MAE	mean absolute error
ML	machine learning
NASA	national aeronautics and space administration
PF	particle filter
RE	relative error
RNN	recurrent neural network
RMSE	root mean square error
RUL	remaining useful life
ReLU	rectified linear unit
UKF	unscented Kalman filter
WNN	wavelet neural network
UPF	unscented Kalman particle filter

References

- [1] M.U. Ali, A. Zafar, S.H. Nengroo, S. Hussain, G.S. Park, H.J. Kim, ‘Online remaining useful life prediction for lithium-ion batteries using partial discharge data features’, *Energies*, **12**(22), 2019, doi:10.3390/en12224366.
- [2] R. Xiong, Y. Zhang, J. Wang, H. He, S. Peng, M. Pecht, ‘Lithium-Ion Battery Health Prognosis Based on a Real Battery Management System Used in Electric Vehicles’, *IEEE Transactions on Vehicular Technology*, **68**(5), 4110–4121, 2019, doi:10.1109/TVT.2018.2864688.
- [3] H. Chaoui, C.C. Ibe-Ekeocha, ‘State of Charge and State of Health Estimation for Lithium Batteries Using Recurrent Neural Networks’, *IEEE Transactions on Vehicular Technology*, **66**(10), 8773–8783, 2017, doi:10.1109/TVT.2017.2715333.
- [4] W. Luo, C. Lv, L. Wang, C. Liu, ‘Study on impedance model of Li-ion battery’, *Proceedings of the 2011 6th IEEE Conference on Industrial Electronics and Applications, ICIEA 2011, 1943–1947, 2011*, doi:10.1109/ICIEA.2011.5975910.
- [5] J. Fan, J. Fan, F. Liu, J. Qu, R. Li, ‘A Novel Machine Learning Method Based Approach for Li-Ion Battery Prognostic and Health Management’, *IEEE Access*, **7**(1), 160043–160061, 2019, doi:10.1109/ACCESS.2019.2947843.
- [6] B. Zraibi, M. Mansouri, C. Okar, ‘Comparing Single and Hybrid methods of Deep Learning for Remaining Useful Life Prediction of Lithium-ion Batteries’, *E3S Web of Conferences*, **297**, 01043, 2021, doi:10.1051/e3sconf/202129701043.
- [7] B. Zraibi, C. Okar, H. Chaoui, M. Mansouri, ‘Remaining Useful Life Assessment for Lithium-ion Batteries using CNN-LSTM-DNN Hybrid Method’, *IEEE Transactions on Vehicular Technology*, 2021, doi:10.1109/TVT.2021.3071622.
- [8] J. Jianfang, W. Keke, P. Xiaoqiong, S. Yuanhao, W. Jie, Z. Jianchao, ‘Multi-Scale Prediction of RUL and SOH for Lithium-Ion Batteries Based on WNN-UPF Combined Model’, *Chinese Journal of Electronics*, **30**(1), 26–35, 2021, doi:10.1049/cje.2020.10.012.
- [9] Y. Toughzaoui, S. Bamati, H. Chaoui, H. Louahlia, ‘State of health estimation and remaining useful life assessment of lithium-ion batteries : A comparative study’, **51**(March), 2022, doi:10.1016/j.est.2022.104520.
- [10] J. Wei, G. Dong, Z. Chen, ‘Remaining Useful Life Prediction and State of Health Diagnosis for Lithium-Ion Batteries Using Particle Filter and Support Vector Regression’, *IEEE Transactions on Industrial Electronics*, **65**(7), 5634–5643, 2018, doi:10.1109/TIE.2017.2782224.
- [11] C. Chang, Q. Wang, J. Jiang, T. Wu, ‘Lithium-ion battery state of health estimation using the incremental capacity and wavelet neural networks with genetic algorithm’, *Journal of Energy Storage*, **38**(September 2020), 102570, 2021, doi:10.1016/j.est.2021.102570.
- [12] L. Yao, S. Xu, A. Tang, F. Zhou, J. Hou, Y. Xiao, Z. Fu, ‘A Review of Lithium-Ion Battery State of Health Estimation and Prediction Methods’, 2021.
- [13] B. Zraibi, M. Mansouri, S.E. Loukili, ‘Comparing deep learning methods to predict the remaining useful life of lithium-ion batteries’, *Materials Today: Proceedings*, (xxxx), 2022, doi:10.1016/j.matpr.2022.04.082.
- [14] S. Yang, C. Zhang, J. Jiang, W. Zhang, L. Zhang, Y. Wang, ‘Review on state-of-health of lithium-ion batteries : Characterizations , estimations and applications’, *Journal of Cleaner Production*, **314**(May), 128015, 2021, doi:10.1016/j.jclepro.2021.128015.
- [15] A. Basia, Z. Simeu-abazi, E. Gascard, P. Zwolinski, ‘Review on State of Health estimation methodologies for lithium-ion batteries in the context of circular economy’, *CIRP Journal of Manufacturing Science and Technology*, **32**, 517–528, 2021, doi:10.1016/j.cirpj.2021.02.004.
- [16] Y. Zhu, F. Yan, J. Kang, C. Du, ‘State of health estimation based on OS-ELM for lithium-ion batteries’, *International Journal of Electrochemical Science*, **12**(7), 6895–6907, 2017, doi:10.20964/2017.07.35.
- [17] H. Dai, G. Zhao, M. Lin, J. Wu, G. Zheng, ‘A novel estimation method for the state of health of lithium-ion battery using prior knowledge-based neural network and markov chain’, *IEEE Transactions on Industrial Electronics*, **66**(10), 7706–7716, 2019, doi:10.1109/TIE.2018.2880703.
- [18] S. Zhang, B. Zhai, X. Guo, K. Wang, N. Peng, X. Zhang, ‘Synchronous estimation of state of health and remaining useful lifetime for lithium-ion battery using the incremental capacity and artificial neural networks’, *Journal of Energy Storage*, **26**(July), 100951, 2019, doi:10.1016/j.est.2019.100951.
- [19] W. Qin, H. Lv, C. Liu, D. Nirmalya, P. Jahanshahi, ‘Remaining useful life prediction for lithium-ion batteries using particle filter and artificial neural network’, *Industrial Management and Data Systems*, **120**(2), 312–328, 2019, doi:10.1108/IMDS-03-2019-0195.
- [20] C.C. Liu, T. Wu, C. He, ‘State of health prediction of medical lithium batteries based on multi-scale decomposition and deep learning’, *Advances in Mechanical Engineering*, **12**(5), 2020, doi:10.1177/1687814020923202.
- [21] Y. Fan, F. Xiao, C. Li, G. Yang, X. Tang, ‘A novel deep learning framework for state of health estimation of lithium-ion battery’, *Journal of Energy Storage*, **32**(August), 101741, 2020, doi:10.1016/j.est.2020.101741.
- [22] X. Song, F. Yang, D. Wang, K.L. Tsui, ‘Combined CNN-LSTM Network for State-of-Charge Estimation of Lithium-Ion Batteries’, *IEEE Access*, **7**, 88894–88902, 2019, doi:10.1109/ACCESS.2019.2926517.
- [23] Y. Zhang, R. Xiong, H. He, Z. Liu, ‘A LSTM-RNN method for the lithium-ion battery remaining useful life prediction’, *2017 Prognostics and System Health Management Conference, PHM-Harbin 2017 - Proceedings*, (51507012), 2017, doi:10.1109/PHM.2017.8079316.
- [24] M. Sajjad, Z.A. Khan, A. Ullah, T. Hussain, W. Ullah, M.Y. Lee, S.W. Baik, ‘A Novel CNN-GRU-Based Hybrid Approach for Short-Term Residential Load Forecasting’, *IEEE Access*, **8**, 143759–143768, 2020, doi:10.1109/ACCESS.2020.3009537.
- [25] K.G. Saha, ‘Battery data set’, *NASA AMES Prognostics Data Repository*.
- [26] D. Liu, Y. Luo, J. Liu, Y. Peng, L. Guo, M. Pecht, ‘Lithium-ion battery remaining useful life estimation based on fusion nonlinear degradation AR model and RPF algorithm’, *Neural Computing and Applications*, **25**(3–4), 557–572, 2014, doi:10.1007/s00521-013-1520-x.
- [27] X. Bian, Z. Wei, J. He, F. Yan, ‘A Novel Model-based Voltage Construction Method for Robust State-of-health Estimation of Lithium-ion Batteries’, (December), 2020, doi:10.1109/TIE.2020.3044779.
- [28] J. Zhao, Y. Zhu, B. Zhang, M. Liu, J. Wang, C. Liu, Y. Zhang, ‘Method of Predicting SOH and RUL of Lithium-Ion Battery Based on the Combination of LSTM and GPR’, 2022.
- [29] M. Zhang, W. Chen, J. Yin, T. Feng, ‘Health Factor Extraction of Lithium-Ion Batteries Based on Discrete Wavelet Transform and SOH Prediction Based on CatBoost’, 2022.